Imaging Ultrafast Dynamics on the Atomic Scale with a Terahertz Scanning Tunneling Microscope

by

Vedran Jelic

A thesis submitted in partial fulfillment of the requirements for the degree of

Doctor of Philosophy

Department of Physics

University of Alberta

© Vedran Jelic, 2018

Abstract

The combination of ultrafast laser pulses with atomic resolution microscopy has been actively pursued for the last few decades. Its achievement unlocks a new age in modern science where the fundamental interactions between individual atoms and molecules can be investigated at their intrinsic operating timescales. Conventional scanning probe techniques have demonstrated unprecedented imaging of atoms and molecules on surfaces, but they struggle to resolve any events that occur faster than a few hundred microseconds. Conversely, state-of-the-art lasers can generate sub-femtosecond pulses, but diffraction prevents their localization to nanoscale dimensions.

In this thesis, ultrafast time-resolved imaging and tunneling spectroscopy is demonstrated by coupling free-space-propagating single-cycle terahertz pulses to the metallic tip of a scanning tunneling microscope (THz-STM). For the surfaces that were imaged here, a spatial resolution of 0.3 nm is achieved together with a temporal resolution of 500 fs. A thorough review of the THz-STM is presented from its early beginnings in ambient conditions, to atomic-scale imaging of semiconductor surfaces in ultrahigh vacuum. At first, the performance of the THz-STM is assessed in ambient air by imaging the picosecond dynamics of photoexcited InAs nanodots on a GaAs surface. Then, the THz-STM system is re-designed for an ultrahigh vacuum environment that enables the highly reactive Si(111)-(7×7) surface to be investigated. THz-STM imaging

of this surface reveals that ultrafast THz pulses can coherently tunnel several hundred electrons across the STM junction within a few hundred femtoseconds in a manner that preserves the ultimate spatial resolution of the microscope. The THz pulses generate extreme transient current densities across the tunnel junction in excess of 10^{11} A/cm^2 due to a fundamentally different terahertz tunneling conductance compared to the steady-state. This unique tunneling conductance is due to reduced screening of the THz pulse electric field at the silicon surface, which leads to subsurface THz-pulse-induced band bending and non-equilibrium charging of the poorly conducting Si(111)-(7×7) surface. Next, the ultrafast carrier dynamics of an optically excited GaAs(110) surface are imaged with the time-resolved THz-STM. The local transient surface photovoltage is found to be strongly modulated near charged defects on the sample surface. Two different regimes of the THz pulse electric field amplitude are identified. In the nearly-linear regime, the photoexcited transient surface photovoltage directly samples the THz pulse near-field waveform at the tip apex. However, at high THz pulse electric fields, ultrafast non-equilibrium charging of the GaAs subsurface dominates the response of the transient tunnel current. The high THz pulse electric field can also induce significant structural modifications to the tip apex and sample surface, but the onset of these effects is strongly dependent on the sample temperature.

Preface

The research conducted for this thesis was performed from September 2012 to November 2018 at the University of Alberta under the supervision of Professor Frank A. Hegmann. It has led to three collaborative refereed publications, two non-refereed publications, and I have personally contributed five invited presentations, three invited seminars and eleven conference abstracts on these results. The three refereed publications as of November 2018 are listed below, along with their corresponding author contributions.

T. L. Cocker, V. Jelic, M. Gupta, S. J. Molesky, J. A. J. Burgess, G. De Los Reyes, L. V. Titova, Y. Y. Tsui, M. R. Freeman & F. A Hegmann. "An ultrafast terahertz scanning tunnelling microscope," *Nat. Photon.* **7**, 620–625 (2013). With guidance from F. Hegmann, T. Cocker designed and built the set-up, acquired/analyzed the data, and wrote the manuscript. I contributed to data acquisition and developed the tunneling model simulation with assistance from T. Cocker. M. Gupta provided the sample and assisted with interpretation of the measurements. S. Molesky, G. De Los Reyes and L. Titova contributed to data acquisition, while J. Burgess, Y. Tsui and M. Freeman contributed to interpretation of the data. These results are described in chapter 4.

P. H. Nguyen, C. Rathje, G. J. Hornig, V. Jelic, C. Ropers & F. A. Hegmann. "Coupling terahertz pulses to a scanning tunneling microscope," *Physics in*

Canada **71**, 157–160 (2015). P. H. Nguyen performed the electromagnetic simulation, data analysis and composition of the manuscript with support from C. Rathje and G. J. Hornig. I assisted with interpretation of the results and contributed to discussions.

V. Jelic, K. Iwaszczuk, P. H. Nguyen, C. Rathje, G. J. Hornig, H. M. Sharum, J. R. Hoffman, M. R. Freeman & F. A. Hegmann. "Ultrafast terahertz control of extreme tunnel currents through single atoms on a silicon surface," *Nat. Phys.* **13**, 591–598 (2017). With guidance from F. Hegmann, I designed and built the optical setup, prepared the samples, acquired/analyzed the data, interpreted the results and wrote the manuscript. J. R. Hoffman assisted with construction of the optical setup. The theoretical model was developed with assistance from K. Iwaszczuk. P. Nguyen, H. Sharum and G. Hornig contributed to preliminary measurements with the THz-STM. P. Nguyen and D. Mildenberger assisted with chemical etching of the the tips. M. Freeman and K. Iwaszczuk assisted with interpretation of the data. The electromagnetic simulation that is described in chapter 6 was performed by P. H. Nguyen with support from C. Rathje, G. J. Hornig, F. Hegmann and myself. This work is described in chapter 6.

The work presented in chapters 7 and 8 will be published in upcoming articles. I am responsible for the data acquisition, data analysis, interpretation and manuscript composition, while T. Wang, D. Mildenberger, J. A. M. Calzada and Y. Luo assisted with the measurements.

It is remarkable how often success is the reward for trying the unknown.

– Heinrich Rohrer, 1992. [1]

Acknowledgements

A huge thank you to my supervisor Frank Hegmann for his enthusiastic support, stimulating discussions and countless memorable adventures outside of the lab. Next, I would like to thank all the wonderful people that have worked with me on the THz-STM project: Tyler Cocker, Reginald Miller, James Hoffman, Peter Nguyen, Haille Sharum, Christopher Rathje, Graham Hornig, Krzysztof Iwaszczuk, Kaylee Biggart, Tianwu Wang, Jesus Alejandro Marin Calzada, Daniel Mildenberger, Yang Luo, Jianqiang Gu and Ray Liu. Thank you to my labmates for refreshing discussions and experimental assistance: Lyuba Titova, David Purschke, Mary Narreto, Charles Jensen and Cameron Hough. I am grateful for the support and guidance of my committee members Robert Wolkow and Mark Freeman, and thankful for the thoughtful insights of my examining committee members Carsten Krauss, John Davis and Rupert Huber. Thank you Kailey Robertson for all of your administrative help. Thank you Greg Popowich, James Chaulk, Beipei Shi, Mark Salomons, Dave Fortin and Don Mullin for your brilliant technical expertise. Thank you Moe Rashidi, Jason Pitters, Radovan Urban, Roshan Achal, Taleana Huff, John Wood and Jacob Burgess for helping me with various aspects of scanning tunneling microscopy. Thank you to my funding sources Alberta Innovates and the Natural Sciences and Engineering Research Council of Canada. Thank you to all my friends who were always supportive and inquisitive. I am forever grateful to my parents Srećko Jelić and Verica Jelić, and my partner Danielle Jenson for all of their love and support.

Contents

1 Introduction **1**

2 Scanning Tunneling Microscopy **7**
2.1 Tunneling Spectroscopy . . . 12
2.2 Taking Images of Atoms . . . 15
2.3 STM Tunneling Models . . . 21
2.3.1 Simmons Tunneling Model . . . 21
2.3.2 Image Potential . . . 24
2.3.3 Bardeen Tunneling Model . . . 25

3 Ultrafast Terahertz Pulses **27**
3.1 Generation . . . 28
3.1.1 Ultrafast Photocurrent . . . 28
3.1.2 Nonlinear Optics . . . 29
3.1.3 Laser-Induced Gas Filamentation . . . 31
3.2 Detection . . . 32
3.2.1 Photoconductive Sampling . . . 33
3.2.2 Electro-Optic Sampling . . . 34
3.2.3 Air-Biased Coherent Detection . . . 36

4 Terahertz Scanning Tunneling Microscopy **38**
4.1 Experimental Details . . . 39
4.2 Coupling THz Pulses to the STM . . . 45
4.3 Modeling the THz-Pulse-Induced Current . . . 51
4.4 Ultrafast THz-STM Imaging . . . 55
4.5 Optical Pump – THz-STM Probe Imaging . . . 57

5 Ultrahigh Vacuum THz-STM **63**
5.1 Experimental Details . . . 64
5.1.1 Tunnel Current Detection . . . 67
5.1.2 Optical Setup . . . 70
5.2 Tip Preparation . . . 72
5.3 Sample Preparation . . . 80
5.3.1 Si(111)-(7×7) . . . 81
5.3.2 H-Si(100)-(2×1) . . . 83
5.3.3 Ag-Si(111)-($\sqrt{3}\times\sqrt{3}$) . . . 85
5.3.4 GaAs(110) . . . 86

6 THz-STM of Si(111)-(7×7) **87**
6.1 Atomic Resolution THz-Driven STM . . . 90
6.2 Modeling THz-STM on Si(111)-(7×7) . . . 99

6.3 Ultrafast Band Bending . . . 110
6.4 THz Pulse Electric Field Penetration . . . 114
6.5 Charge Transport Dynamics . . . 117
6.6 Steady-State Bias Voltage Dependence . . . 120
6.7 Hot Electron Effects . . . 125
6.8 Subsurface Features . . . 129

7 Optical Pump – THz-STM Probe of GaAs(110) 133
7.1 Sampling the THz-STM Near-Field . . . 139
7.2 Modeling Pump-Probe THz-STM . . . 154
7.3 Imaging Ultrafast Carrier Dynamics . . . 159

8 THz-Pulse-Induced Structural Modifications 171
8.1 Structural Modifications with the STM . . . 171
8.2 Si(111)-(7×7) . . . 178
8.3 H-Si(100)-(2×1) . . . 188
8.4 GaAs(110) . . . 191

9 Summary and Outlook 194

References 197

Appendix A Ultrafast Movie of an InAs Nano-Island 233

Appendix B Ultrafast Laser System Details 235
B.1 RegA Laser . . . 235
B.2 Optical Setup for the Delay Stages . . . 239

Appendix C UHV THz-STM System Details 241
C.1 Equipment . . . 241
C.1.1 Ultrahigh Vacuum System . . . 241
C.1.2 STM Control Console . . . 252
C.2 Preparing Tips . . . 253
C.2.1 Etching Tips . . . 253
C.2.2 Mounting Tips . . . 254
C.2.3 *In situ* Tip Conditioning . . . 255
C.3 THz-STM Data Acquisition . . . 257
C.3.1 Point Spectroscopy . . . 257
C.3.2 Imaging . . . 259
C.3.3 Electro-Optic Detection . . . 260
C.4 THz-STM Data Analysis . . . 261

List of Tables

1.1 A summary of the spatio-temporal resolutions of various ultrafast scanning probe microscopy techniques reported in literature. STM – scanning tunneling microscopy; AFM – atomic force microscopy; s-SNOM – scattering-type scanning near-field optical microscopy; LTEM – laser terahertz emission microscopy; FWM – four-wave-mixing; OPP – optical pump-probe; JM – junction-mixing; PG – photoconductively-gated; SPPX – shaken-pulse-pair-excited; N/A – not applicable. 3

6.1 Experimental and theoretical relative heights between inequivalent adatoms on the Si(111)-(7×7) surface. This table is a partial summary of the Si(111)-(7×7) inequivalent adatom heights reported in literature. Several results were graphically interpolated and should be considered estimates to within a few picometers. If an experimental condition was not specified, a dash is displayed. The faulted corner (F-Co), faulted-centre (F-Ce) and unfaulted-corner (UF-Co) adatom heights are relative to the unfaulted-centre-adatom. 98

C.1 A list of common residual gases in ultrahigh vacuum chambers and their corresponding atomic mass units (amu). CH_2 – methylene; CH_4 – methane; NH_3 – ammonia; C_2H_2 – acetylene; C_2H_4 – ethylene; C_2H_2 – methylene; C_2H_6 – ethane; C_3H_3OH – methanol; C_3H_8 – propane; C_4H_{10} – butane; C_3H_6O – acetone; C_3H_8O – isopropanol; C_6H_6 – benzene. 250

List of Figures

2.1 Schematic of the essential equipment for scanning tunneling microscopy. A d.c. bias voltage, $V_{\text{d.c.}}$, is applied to the sample, generating a tunnel current, $I_{\text{d.c.}}$, which flows through a sharp metal tip. The tip is attached to a set of piezoelectric crystals that can control its spatial location. The tunnel current is amplified by several orders of magnitude and directed into a feedback loop that controls the tip-height, z, through a d.c. voltage, V_z, which is applied to the z-direction piezoelectric crystal. Two additional piezo crystals are used to scan the tip laterally across the sample by sweeping the voltages V_x and V_y. 8

2.2 Schematic 1D metal–vacuum–semiconductor energy profile. A negative sample bias shifts the Fermi level ($\varepsilon_{\text{F,sample}}$) of the degenerately doped semiconductor $e|V|$ above the Fermi level of the tip, ($\varepsilon_{\text{F,tip}}$). Green arrows represent tunneling of electrons, while a longer arrow indicates a higher tunneling probability. The tip and sample density of states are represented by $\rho_{\text{t}}(\varepsilon)$ and $\rho_{\text{s}}(\varepsilon)$, respectively (filled states are shaded). This schematic has been adapted from figure 20.8 in [67]. 12

2.3 **a**, Measured I–V curves and **b**, I–z curves acquired with a tungsten tip on the Si(111)-(7×7) surface. The I–V curves were acquired with the tip–sample separation set by $V_{\text{d.c.}} = -1$ V and $I_{\text{d.c.}} = -20$ pA. The I–z curves were acquired with the initial tip–sample separation, z_0, set by $V_{\text{d.c.}} = 1$ V and $I_{\text{d.c.}} = 50$ pA. The inset shows the I–z curve on a semilog plot. Applying Eq. 2.6 to **b** finds $\phi_{\text{exp}} = 3.5$ eV. 13

2.4 Atomically-resolved topography of a Si(111)-(7×7) surface that was acquired in constant-current mode at $V_{\text{d.c.}} = +1.2$ V and $I_{\text{d.c.}} = +200$ pA. Image size 230 nm × 340 nm (inset 15 nm × 15 nm); 180 minute scan for the original square image at 4096 × 4096 pixels; scan speed 300 nm/s. 18

2.5 Atomically-resolved topography of a Si(111)-(7×7) surface that was acquired in constant-current mode at $V_{\text{d.c.}} = -1.2$ V and $I_{\text{d.c.}} = -200$ pA. Image size 230 nm × 340 nm (inset 15 nm × 15 nm); 220 minute scan for the original square image at 4096 × 4096 pixels; scan speed 250 nm/s. 19

2.6 **a**, Atomically-resolved topography of a Si(111)-(7×7) surface along with **b**, the simultaneously acquired differential conductance ($\mathrm{d}I/\mathrm{d}V$) image at a modulation frequency of 7177 Hz, modulation amplitude of ± 50 mV and a current amplifier with 10^8 gain and 15 kHz bandwidth. The images were acquired in constant-current mode at $I_{\mathrm{d.c.}} = -100$ pA and $V_{\mathrm{d.c.}}$ as shown above the topography images. Image size 9 nm × 9 nm; 256 × 256 pixels; scan speed 9.1 nm/s. The colourmap is 22 pm (brown) to 160 pm (gold) for **a** and −75 pS (brown) to +210 pS (gold) for **b**. 20

2.7 Schematic metal–vacuum–metal energy profile including image potential effects. A negative bias on the sample shifts the Fermi level ($\varepsilon_{\mathrm{F,sample}}$), above the Fermi level of the tip ($\varepsilon_{\mathrm{F,tip}}$) by an amount $e|V|$. The tip is positioned $z = 6$ Å above the sample surface, while the tip and sample barrier heights ($\phi_{\mathrm{t}}, \phi_{\mathrm{s}}$) are both 5 eV. The standard 1D trapezoidal barrier, $\phi(x, \phi_{\mathrm{t}}, \phi_{\mathrm{s}}, V, z)$, Eq. 2.11 (red solid line), is modified by the applied field and its interaction with the image potential, $\phi_{\mathrm{img}}(x, z)$, resulting in a reduced barrier-height (Eq. 2.17 and Eq. 2.18), $\phi_{\mathrm{eff}}(x, \phi_{\mathrm{t}}, \phi_{\mathrm{s}}, V, z) = \phi(x, \phi_{\mathrm{t}}, \phi_{\mathrm{s}}, V, z) + \phi_{\mathrm{img}}(x, z)$, and a reduced barrier-width (Eq. 2.20), $\delta = z_2 - z_1$ (black solid line). The blue solid line was calculated using a polynomial approximation for the image potential (Eq. 2.19). The constants $\overline{\phi}$ and $\overline{\phi}_{\mathrm{eff}}$ are the average values of $\phi(x)$ and $\phi_{\mathrm{eff}}(x)$ between z_1 and z_2. 24

3.1 THz pulse electric field waveform generated by an interdigitated photoconductive antenna and electro-optically sampled using a 1 mm thick ZnTe crystal. Inset: corresponding amplitude spectrum. 28

4.1 Photograph of the experimental setup for ambient THz-STM. Free-space-propagating terahertz pulses are focused onto the tip of a scanning tunneling microscope using an off-axis parabolic mirror with a focal length of 4 inches. The red banana clip on the right applies a d.c. bias voltage, $V_{\mathrm{d.c.}}$, to the sample. . . . 39

4.2 Electronics setup for data acquisition with the ambient THz-STM. The red solid line represents the optical-pulse-train, while the thick green solid line represents the THz-pulse-train. The orange and light blue lines represent electronic connections that carry the measured current, $I_{\mathrm{THz,avg}}$, and relative tip height, $z_{\mathrm{measured}} = z - z_0$, respectively. The black and dark blue solid lines represent electronic connections between instruments in the form of BNC connectors. 41

4.3 Optical setup for ambient THz-STM where the red solid line represents the optical-pulse-train and the thick green solid line represents the THz-pulse-train. 42

4.4 Ultrafast THz pulses were focused to 2 mm spot size at the base of a mechanically cut Pt/Ir(90:10) STM tip at an angle of 40° above the horizontal plane. This angle was chosen to match the geometry of the ultrahigh vacuum chamber that is introduced in chapter 5. A steady-state bias voltage, $V_{\text{d.c.}}$, was applied to the sample, while a feedback loop controlled the tip height and maintained a constant total tunnel current, $I_{\text{total}} = I_{\text{d.c.}} + I_{\text{THz,avg}}$. 44
4.5 THz pulse electric field waveform generated by a photoconductive antenna with a 1 mm gap and electro-optically sampled using a 1 mm thick ZnTe crystal. The electric field calibration was performed using Eq. 3.8. Inset: corresponding amplitude spectrum. The THz pulse peak electric field is denoted by $E_{\text{THz,pk}}$. For a symmetric pulse there is no dominant polarity and thus, $E_{\text{THz,pk}} = E_{\text{THz,max}} = |E_{\text{THz,min}}|$. 44
4.6 The total voltage across the tunnel junction is determined by the sum of $V_{\text{d.c.}}$ and the time-dependent THz-pulse-induced voltage, $V_{\text{THz}}(t)$. 46
4.7 Schematic of the nonlinear tunneling I–V curve of an STM (black solid line), where the d.c. bias, $V_{\text{d.c.}}$, drives a d.c. current, $I_{\text{d.c.}}$. A free-space-propagating THz pulse couples to the STM tip and generates a time-dependent voltage, $V_{\text{THz}}(t)$ (green solid line), that drives an ultrafast THz-pulse-induced tunnel current, $I_{\text{THz}}(t)$ (blue solid line), which results in an average rectified tunnel current of $I_{\text{THz,avg}} = f_{\text{rep}} \times \int I_{\text{THz}}(t)\, \mathrm{d}t$. . . . 47
4.8 Measured I–V curves for an HOPG surface using a Pt/Ir tip with vertically polarized THz pulses incident onto the STM tip at $E_{\text{THz,pk}} = 120$ V/cm (blue solid line). Horizontally polarized THz pulses at the same electric field strength do not couple to the tip and thus, the measured I–V curve (red solid line) matches the I–V curve with the pulses blocked (black dashed line). The feedback loop was disengaged at $V_{\text{d.c.}} = +0.03$ V, $I_{\text{d.c.}} = +1$ nA, and $E_{\text{THz,pk}} = 0$ V/cm. 47
4.9 Tip height retraction as a function of the incident energy per pulse at, **a**, THz and **b**, optical frequencies. During acquisition the feedback loop is engaged and its bandwidth is much larger than the modulation frequency of 20 Hz that was used to chop the optical and THz pulses. The optical pulse had a center wavelength of 800 nm and a pulse duration of 150 fs. The scans were acquired under ambient conditions in constant-current mode at $V_{\text{d.c.}} = +30$ mV and $I_{\text{d.c.}} + I_{\text{THz,avg}} = +1$ nA for **a** and $I_{\text{d.c.}} + I_{\text{Optical,avg}} = +1$ nA for **b**. For both scans the pulse energy was gradually changed over a ~ 5 minute period and the pulses were polarized vertically along the tip-axis. . . 48
4.10 THz pulses were sent through a Michelson interferometer to enable autocorrelation measurements. A high-resistivity two-side-polished silicon wafer separated the single THz pulse into two nearly-equal-amplitude pulses with the path-length of one pulse modulated by a computer-controlled delay stage in order to adjust the relative temporal delay between the two pulses, $\Delta\tau$. 49

4.11 **a**–**f**, THz-pulse-induced tunnel current as a function of the arrival of two equal amplitude THz pulses (coloured squares). The THz-STM autocorrelations were performed at $E_{\mathrm{THz,pk}} = 74$ V/cm (**a**), $E_{\mathrm{THz,pk}} = 78$ V/cm (**b**), and $E_{\mathrm{THz,pk}} = 83$ V/cm (**c**) for gold, and $E_{\mathrm{THz,pk}} = 87$ V/cm (**d**), $E_{\mathrm{THz,pk}} = 92$ V/cm (**e**), and $E_{\mathrm{THz,pk}} = 97$ V/cm (**f**) for HOPG. The measurements were acquired at $V_{\mathrm{d.c.}} = +30$ mV and $I_{\mathrm{d.c.}} + I_{\mathrm{THz,avg}} = +1$ nA, while in constant-current mode ($I_{\mathrm{THz,avg}} \ll I_{\mathrm{d.c.}}$), and with the feedback loop bandwidth below the modulation frequency of the THz-pulse-train. The solid lines are fits based on the Simmons model (see section 4.3). **g**, Full-width-half-maxiumum (FWHM) of Gaussian fits to the data in **a**–**f**. 50
4.12 THz-pulse-induced tunnel current versus incident peak electric field (THz I–E) curves over gold nanoislands (black circles) and HOPG (red triangles). The data points are peaks of Gaussian fits to the autocorrelations in Fig. 4.11. The red and black solid lines are Simmons model fits to the data (see section 4.3). . . 51
4.13 **a**, **b**, Simulated Simmons model I–V curves for STM of gold nanoislands (black solid line) and HOPG (red solid line) plotted on a linear scale (**a**) and a log scale (**b**). The model parameters are determined from a global fit to measured I–z curves and THz-STM autocorrelations on gold and HOPG. The simulation parameters that were used to generate the I–V curves shown here were, $\phi_{\mathrm{Au}} = 0.2$ eV, $\phi_{\mathrm{HOPG}} = 0.25 \pm 0.04$ eV, $z_{\mathrm{Au}} = 5.9 \pm 0.6$ nm, $z_{\mathrm{HOPG}} = 5.6 \pm 0.6$ nm, $I_0 = +1$ nA and $V_0 = +30$ mV. 52
4.14 **a**, Simulated THz pulse voltage waveform, $V_{\mathrm{THz}}(t)$, (Eq. 4.4) and **b**, its corresponding amplitude spectrum. 53
4.15 Simulation of the THz-pulse-induced tunnel current using the Simmons model (Eq. 4.2). The free parameters are defined in the text. **a**, THz-pulse-induced voltage $V_{\mathrm{THz}}(t)$, between tip and sample for an incident THz pulse with $E_{\mathrm{THz,pk}} = 83$ V/cm. **b**, The THz-pulse-induced current transient, $I_{\mathrm{THz}}(t)$. **c**, The number of electrons that tunnel across the junction (running integral of **b**). After the THz pulse has passed (beyond 2 ps), the number of electrons rectified is 3800. At 250,000 terahertz pulses per second, this is equivalent to $I_{\mathrm{THz,avg}} = +150$ pA. . 54
4.16 THz-STM spatio-temporal autocorrelation of gold nanoislands on HOPG. **a**, STM topography images a junction between two gold nanoisland and **b**, the simultaneously acquired THz-pulse-induced tunnel current images, $N_{\mathrm{e^-}}(x, y)$. Each pair of images (topography and THz-STM) was acquired with a relative time delay between THz pulses equal to -500 fs, -250 fs, 0 fs, $+250$ fs and $+500$ fs from left to right, respectively. **c**, THz-STM autocorrelations acquired with the tip located over the top-left nanoisland (black circle, black solid line) and the HOPG substrate (red circle, red solid line. **d**, The THz pulse electric field waveforms for time delays of -500 fs, -250 fs, 0 fs, $+250$ fs and $+500$ fs from left to right, respectively. The THz-STM measurements were acquired in air and at room temperature while in constant-current mode at $V_{\mathrm{d.c.}} = +30$ mV and $I_{\mathrm{d.c.}} + I_{\mathrm{THz,avg}} = +1$ nA. The feedback loop bandwidth was kept well below the modulation frequency of the THz-pulse-train and also, $I_{\mathrm{THz,avg}} \ll I_{\mathrm{d.c.}}$. 56

4.17 Scanning electron microscope (SEM) image of InAs nanodots on a GaAs wetting layer. This sample was used for the THz-STM measurements in Fig. 4.18, Fig. 4.19 and Fig. 4.20. . . . 57
4.18 Optical pump – THz-STM probe time delay scans (OPP-THz-STM scans) acquired with the tip positioned over an InAs nanodot (black circles connected by the red solid line) and over the GaAs wetting layer (blue circles connected by the blue solid line). The measurements in **a** were acquired with the tip positioned above the InAs nanodot and wetting layer shown in Fig. 4.19. The measurement in **b** was acquired with the tip positioned above the InAs nanodot in Fig. 4.20b. The pump–probe scans were acquired with the same settings as their respective figures. Both pump–probe scans in **a** were acquired using two averages, while the scan in **b** was acquired using five averages. The solid green line in **b** is a single exponential fit with a decay time of 1 ps and an offset of 440 rectified electrons. 59
4.19 Ultrafast optical pump – THz-STM probe imaging of photoexcited InAs nanodots on GaAs. **a**–**d**, At $\tau_{\text{Optical–THz}} = -500$ fs before photoexcitation, the topography image (**a**) reveals a nanodot on the surface but the THz-STM image (**b**) does not exhibit any features. **c**, **d**, At negative time delay, the THz-pulse-induced current, $I_{\text{THz}}(t)$, was below the noise floor. **e**–**h**, At $\tau_{\text{Optical–THz}} = +500$ fs after photoexcitation, both of the topography (**e**) and THz-STM (**f**) images reveal an InAs nanodot. **g**, **h**, Electron trapping by the InAs nanodot resulted in a local enhancement of the bias voltage and led to an enhanced THz-pulse-induced current, $I_{\text{THz}}(t)$. The optical pulse has a center wavelength of 800 nm, a pulse duration of 150 fs and a fluence of 110 µJ/cm^2. The images were acquired under ambient conditions in constant-current mode at $V_{\text{d.c.}} = -3.5$ V, $I_{\text{d.c.}} + I_{\text{THz,avg}} = -0.5$ nA and $E_{\text{THz,pk}} = +100$ V/cm ($E_{\text{THz,max}} \approx -E_{\text{THz,min}}$). 61
4.20 Spatial resolution of optical pump – THz-STM probe imaging of photoexcited InAs nanodots on GaAs. **a**, Topography image, **b**, THz-STM image and **c**, corresponding line scans (blue solid lines in **a** and **b**) for a photoexcited InAs nanodot at $\tau_{\text{Optical–THz}} = +1$ ps. A spatial resolution of 2 nm is estimated from the line scan. **d**, Topography image, **e**, THz-STM image and **f**, corresponding line scans (blue solid lines in **d** and **e**) for another photoexcited InAs nanodot at $\tau_{\text{Optical–THz}} = +0.5$ ps. A spatial resolution of 4 nm is estimated from the line scan. The optical pump pulse has a center wavelength of 800 nm, a pulse duration of 150 fs and a fluence of 200 µJ/cm^2. The images were acquired in air and at room temperature while in constant-current mode at $V_{\text{d.c.}} = -3$ V, $I_{\text{d.c.}} + I_{\text{THz,avg}} = -0.5$ nA and $E_{\text{THz,pk}} = +70$ V/cm. 62

5.1 Photographs of the ultrahigh vacuum scanning tunneling microscope system. **a**, The STM chamber (without the STM scanhead in place) is in the foreground along with the large 6" and 8" windows for *in situ* manipulation with the wobble stick (which is visible in the middle left of the image). Three small 2.75" windows are used for coupling the optical pump pulse to the STM and setting up the two alignment cameras. The laser-alignment camera is angled at 35° above the horizontal plane, while the tip-exchange-alignment camera is placed horizontal to the tip–sample tunnel junction. The preparation chamber is visible in the background. **b**, The loadlock chamber is visible in the foreground, while the inverted xyz-viewport and open-flow cryostat are located in the middle left of the image. 64
5.2 Electronics setup for data acquisition with the ultrahigh vacuum THz-STM. The red solid line represents the optical-pulse-train, while the thick green solid line represents the THz-pulse-train. The orange and light blue lines represent electronic connections that carry the measured current, $I_{\mathrm{THz,avg}}$, and relative tip height, $z_{\mathrm{measured}} = z - z_0$, respectively. The black and dark blue solid lines represent electronic connections between instruments in the form of BNC connectors. 65
5.3 Photograph of the IVP-PGA second stage current amplifier. The red rectangle on the bottom highlights the potentiometer that was used to zero the tunnel current with the tip retracted (via a d.c. offset) to within approximately ± 40 fA. The yellow rectangle in the middle highlights the potentiometer that controls the fine-adjust-gain of the second-stage amplifier. This potentiometer has never been adjusted from its initial setting of $\times 1.04$ (this value was determined from calibration with a GΩ resistor). The blue rectangle on the left highlights the pins that control the coarse-adjust-gain of the second-stage amplifier, from top to bottom the settings are: $\times 100$, $\times 10$ and $\times 1$ (setting in the image). The green rectangle on the right highlights the pins that control the low-pass-filter setting of the second-stage amplifier, from left to right the settings are: No Filter, 150 kHz, 50 kHz, 15 kHz, 5 kHz (setting in the image), 1.5 kHz and 0.5 kHz. 66
5.4 Measured frequency response of the first-stage current amplifiers for the different filter settings that are described in Fig. 5.3. **a**, IVP-100, **b**, IVP-200 and **c**, IVP-300. The amplifiers were connected to a GΩ resistor that was driven by a sine-wave modulation with a peak amplitude of ± 3 V. The time constant on the lock-in amplifier was at least 5 cycles of the modulation, while the acquisition time per frequency step was set to 3 times the lock-in time constant. The lock-in amplifier output was set to R-mode. 67
5.5 Optical setup for the UHV THz-STM system. 70
5.6 Photograph of the UHV THz-STM setup where the optical-pulse-train is represented by red lines and the THz-pulse-train is represented by thicker yellow lines. The optical-pulse-train is focused onto the tip at an angle of 120° (top-down view) with respect to the THz-pulse-train. 71

5.7 Scanning electron microscope images of tungsten tips that were used with the THz-STM. The images were all acquired using the in-lens detector with a 5 keV electron beam propagating at 90° with respect to the tip axis. The bottom-middle image was acquired at 10° with respect to the tip axis. 73
5.8 Electronics setup for electron bombardment of the STM tip. A floating power supply (Prevac Heat-2PS) sourced a constant-current output of a few amperes through a thoriated-tungsten filament, while floating several hundred volts below ground (negative voltage). The voltage V_{C} was measured using a multimeter and used to determine the the current travelling through the tip via $I_{\mathrm{EB}} = (1\ \mathrm{mA/V}) \times V_{\mathrm{C}}$. The 10 kΩ resistor was a safety precaution in the case of an electrical short, $R_{\mathrm{EB}}(V) \approx 0$. The resistor can support 11 W of power dissipation at 1080 V, and transiently 110 W for 5 seconds. Caution: do note raise the current through the thoriated-tungsten filament much more than 1.4 A as it will evaporate considerable amounts of tungsten onto the surrounding ceramic insulation, eventually creating an electrical short that requires breaking vacuum to remove. For reference, this layer was easily removed by placing the ceramic insulation into a beaker of 3 M NaOH and placing the beaker into an ultrasonic bath for several hours. 74
5.9 Electronics setup for field emission of the tip. A field emission bias voltage up to +5000 V was provided by the high voltage power supply (Stanford Research Systems PS350). The voltage V_{B} was measured using a multimeter and used to determine the the current travelling through the tip via $I_{\mathrm{FE}} = (1.1\,\mu\mathrm{A/V}) \times V_{\mathrm{B}}$. The 10 MΩ resistor was a safety precaution in the case of an electrical short, $R_{\mathrm{FE}}(V) \approx 0$. The resistor can support 0.75 W of power dissipation at 7500 V. An oscilloscope may be used to monitor the field emission current. If the oscilloscope was connected, the overall effective resistance was lowered from 0.909 MΩ to 0.476 MΩ, changing the calibration factor to 2.1 µA/V. A simplified equivalent circuit representation is shown on the right, it was used to find $V_{\mathrm{FE}} = V_{\mathrm{A}} - V_{\mathrm{B}}$. 75
5.10 Measured Fowler-Nordheim plots for several polycrystalline tungsten tips that were prepared for use with the THz-STM. The legend shows the radius of curvature estimate for each tip apex based on the slope of its corresponding Fowler-Nordheim plot (see text for details). 76
5.11 Measured electron bombardment current versus time with 1.3 A travelling through the tungsten filament (see Fig. 5.8). The floating voltage supply was turned to –900 V after 75 seconds, changed to –800 V after 225 seconds and then turned off after 525 seconds. 77
5.12 Measured field emission current versus time at $V_{\mathrm{FE}} = 700$ V. The current was sampled every 200 ms for more than 20 hours. The high field emission current induced numerous structural changes to the tip apex (between 5 and 10 hours), until eventually a stable configuration was reached. 78

5.13 Electronics setup for field emission of the tip while mounted in the STM scanhead and located several hundred nanometers above the sample surface. A field emission bias voltage up to −600 V was provided by the high voltage power supply (Stanford Research Systems PS350). The voltage V_B was measured using a multimeter and used to determine the the current travelling through the tip via $I_{FE} = (1.1\,\mu A/V) \times V_B$. The 10 MΩ resistor was a safety precaution in the case of an electrical short, $R_{FE}(V) \approx 0$. The resistor can support 0.75 W of power dissipation at 7500 V. An oscilloscope may be used to monitor the field emission current. If the oscilloscope was connected, the overall effective resistance was lowered from 0.909 MΩ to 0.476 MΩ, changing the calibration factor to 2.1 µA/V. A simplified equivalent circuit representation is shown on the right, it was used to find $V_{FE} = V_A - V_B$. 79
5.14 Electronics setup for direct current resistive heating of the sample, $R_s(V)$. The in-series variable resistor, R_{var} = 0.1–500 Ω, can only support a power dissipation of 0.5 W and should be circumvented by using the switch when necessary. Both constant-current and constant-voltage power supplies were used, depending on the value of $R_s(V)$ (see text for details). 82
5.15 STM image of the Si(100)-(2×1) surface acquired in constant-current mode at $V_{d.c.} = -1.4$ V and $I_{d.c.} = -50$ pA. Image size 20 nm × 20 nm. 83
5.16 STM image of the H-Si(100)-(2×1) surface acquired in constant-current mode at $V_{d.c.} = -1.5$ V and $I_{d.c.} = -100$ pA. Image size 15 nm × 15 nm. 84
5.17 STM images of the Ag-Si(111)-($\sqrt{3} \times \sqrt{3}$) surface with only partial coverage of the underlying Si(111)-(7×7) layer. The images were acquired in constant-current mode at $V_{d.c.} = -1$ V and $I_{d.c.} = -100$ pA. **a**, image size 50 nm × 50 nm. **b**, image size 10.5 nm × 14.4 nm. 85
5.18 Photograph of the tip during THz-STM of a freshly cleaved GaAs(110) surface in ultrahigh vacuum. 86

6.1 Ultrafast THz pulses are focused by a lens in an inverted viewport (left) onto an STM tip in ultrahigh vacuum (center), inducing a tunnel current at the junction (inset). 88
6.2 THz pulse electric field waveform and its corresponding frequency spectrum peaked at 0.4 THz (inset). 89
6.3 Schematic of the nonlinear tunneling I–V curve of an STM (black solid line), where the d.c. bias, $V_{d.c.}$, drives a d.c. current, $I_{d.c.}$ and an ultrafast THz pulse with asymmetric half-cycle amplitudes generates a time-dependent voltage, $V_{THz}(t)$ (red solid line), that drives an ultrafast terahertz-induced current, $I_{THz}(t)$ (blue solid line), resulting in a rectified average tunnel current, $I_{THz,avg}$. 89
6.4 **a**, Measured I–V curves and **b**, I–z curves acquired without THz pulses incident (black solid line) and with THz pulses incident (red solid line). The measurements were acquired with the tip positioned over an unfaulted centre adatom and the tip–sample separation set by $V_{d.c.} = -0.25$ V, $I_{d.c.} = -20$ pA, and $E_{THz,pk} = 0$ V/cm. 90

6.5 The THz pulse polarity (0°, 90°, 180°) is used to control the THz-pulse-induced rectified tunnel current. Electrons flow from the sample to the tip for a negative THz polarity and from the tip to the sample for a positive THz polarity. 91
6.6 Terahertz pulse polarization dependence at $|E_{\mathrm{THz,pk}}| = 500$ V/cm and $V_{\mathrm{d.c.}} = 0$ V, demonstrating terahertz control of positive (red solid line) and negative (green solid line) extreme transient currents. For $I_{\mathrm{THz,avg}} = 0.1$ nA, 2500 electrons are rectified by each THz pulse at a rate of 250 kHz. The measurements were acquired with the feedback loop disengaged at $V_{\mathrm{d.c.}} = 0$ V, $I_{\mathrm{THz,avg}} = -20$ pA, and $E_{\mathrm{THz,pk}} = -150$ V/cm 92
6.7 Measured THz I–E curves (THz-pulse-induced current versus peak THz pulse electric field) as a function of $V_{\mathrm{d.c.}}$. The measurements were acquired with the feedback loop disengaged at $V_{\mathrm{d.c.}} = -1.3$ V, $I_{\mathrm{d.c.}} = -20$ pA, and $E_{\mathrm{THz,pk}} = 0$ V/cm, maintaining $|I_{\mathrm{d.c.}}| < 10$ pA at $V_{\mathrm{d.c.}} = \pm 1$ V. 92
6.8 Topographic images of the Si(111)-(7×7) surface measured in constant-current mode with **a**, standard STM at $V_{\mathrm{d.c.}} = -0.5$ V, $E_{\mathrm{THz,pk}} = 0$ V/cm, $I_{\mathrm{d.c.}} = -20$ pA and **b**, TD-STM of the same region with $V_{\mathrm{d.c.}} = 0$ V, $E_{\mathrm{THz,pk}} = -200$ V/cm and $I_{\mathrm{THz,avg}} = -20$ pA. Image size 8.5 nm × 8.5 nm; scan speed 13 nm/s; low-pass-filtered with a 3×3 smoothing matrix. 93
6.9 Large area TD-STM image acquired at $V_{\mathrm{d.c.}} = 0$ V, $E_{\mathrm{THz,pk}} = -200$ V/cm and $I_{\mathrm{THz,avg}} = -20$ pA. Image size 40 nm × 40 nm; scan speed 25 nm/s; colourmap range 0.2 nm. 94
6.10 **a**, Unit cell for the Si(111)-(7×7) surface reconstruction with adatoms as yellow circles. The orientation of faulted and unfaulted unit cell halves matches the orientation in the images. **b**, Cross-sectional linescans through the 7×7 unit cell (dashed line in **a**) for STM (blue solid line) and TD-STM (red solid line), showing a spatial resolution of 0.3 nm. 95
6.11 Constant-height spatio-temporal autocorrelation at $E_{\mathrm{THz,pk}} = -100$ V/cm for each pulse. The time delay between THz pulses is given by $\Delta\tau$ for each image. Image size 13 nm × 13 nm; scan speed 12 nm/s; colourmap −25 e^-/pulse (brown) to −450 e^-/pulse (gold). 95
6.12 **a**, 2D-FFT of the TD-STM image in Fig. 6.9. **b**, The same 2D-FFT with small white and black circles as guides to the eye for locating peaks in k-space. The large white circle has a radius of 3.33 nm^{-1}. 96
6.13 **a**, High resolution TD-STM image acquired at $V_{\mathrm{d.c.}} = 0$ V, $I_{\mathrm{THz,avg}} = -20$ pA and $E_{\mathrm{THz,pk}} = -200$ V/cm. Image size 4.8 nm × 5.5 nm; scan speed 13 nm/s; low-pass-filtered with a 3×3 smoothing matrix. **b**, **c**, Constant-current TD-STM linescans for nearest-neighbour adatoms (**b**) and next-nearest-neighbour adatoms (**c**). 96

6.14 **a**, Constant-height total current image, low-pass-filtered during acquisition and **b**, the simultaneously acquired THz-STM image, $N_{e^-}(x, y)$. The average total current is −12 pA, while the average terahertz current is −4 pA (or equivalently 100 rectified electrons per pulse tunneling from the sample to the tip). $V_{d.c.}$ = −0.30 V; $E_{THz,pk}$ = −200 V/cm; image size 10 nm × 10 nm; scan speed 11 nm/s. 97
6.15 Constant-height THz pulse autocorrelations on Si(111)-(7×7). **a**, The feedback loop was disengaged at $V_{d.c.}$ = −1.20 V, $I_{d.c.}$ = −30 pA, $E_{THz,pk}$ = 0 V/cm and the parameters during acquisition were $V_{d.c.}$ = −1.20 V, $E_{THz,pk}$ = −115 V/cm (each pulse). **b**, The feedback loop was disengaged at $V_{d.c.}$ = +1.00 V, $I_{d.c.}$ = +200 pA, $E_{THz,pk}$ = 0 V/cm and the parameters during acquisition were $V_{d.c.}$ = 0 V, $E_{THz,pk}$ = −90 V/cm (each pulse). 97
6.16 Simulated temporal profile of the THz-pulse-induced tunnel current using the Bardeen model. **a**, Total applied voltage $V_{THz}(t)$ between tip and sample ($V_{d.c.}$ = 0 V). **b**, The THz-induced current transient, $I_{THz}(t)$, calculated using Eq. 6.1. **c**, The number of electrons that tunnel across the junction (running integral of **b**). After the THz pulse has passed (beyond 6 ps), the number of electrons rectified is 570. At 250,000 terahertz pulses per second, this is equivalent to $I_{THz,avg}$ = +23 pA. 100
6.17 Density of states (DOS) used in the tunneling model for STM (black solid line) and THz-STM (red solid line). 103
6.18 *I*–*V* curves obtained from a global fit of multiple data sets to the Bardeen tunneling model for STM (black solid line) and THz-STM (red solid line). Experimental STM *I*–*V* curves (circles) were acquired at five different tip–sample separations (Δz = z − z_0 = 500 pm, 375 pm, 250 pm, 125 pm and 0 pm for blue, red, green, magenta and cyan circles, respectively) and then normalized to the initial tip height. The dashed line represents the quantum of conductance, $G_0 \approx 77.5\,\mu$A. The initial tip–sample separation, z_0, was set by $V_{d.c.}$ = −0.25 V, $I_{d.c.}$ = −20 pA, $E_{THz,pk}$ = 0 V/cm over an unfaulted-centre-adatom and measurements were performed over the same atom. 104
6.19 Simulated and experimental *I*–*V* curves taken without (black triangles, green solid line) and with (red circles, blue solid line) THz pulses incident on the tip. The initial tip–sample separation was set by $V_{d.c.}$ = −0.25 V, $I_{d.c.}$ = −20 pA, $E_{THz,pk}$ = 0 V/cm over an unfaulted-centre-adatom and measurements were performed over the same atom. 105
6.20 Simulated and experimental *I*–*z* curves taken without (black triangles, green solid line) and with (red circles, blue solid line) THz pulses incident on the tip. The initial tip–sample separation was set by $V_{d.c.}$ = −0.25 V, $I_{d.c.}$ = −20 pA, $E_{THz,pk}$ = 0 V/cm over an unfaulted-centre-adatom and measurements were performed over the same atom. 105

6.21 Simulated (blue solid line) and experimental (red circles) THz I–E curves. The initial tip–sample separation was set by $V_{\mathrm{d.c.}} = -0.25$ V, $I_{\mathrm{d.c.}} = -20$ pA, $E_{\mathrm{THz,pk}} = 0$ V/cm over an unfaulted-centre-adatom and measurements were performed over the same atom. 106
6.22 Simulated (blue solid line) and experimental (red circles) THz I–E curves measured with the THz pulse silicon beamsplitter in place (see Fig. 5.2). The initial tip–sample separation was set by $V_{\mathrm{d.c.}} = -0.25$ V, $I_{\mathrm{d.c.}} = -20$ pA, $E_{\mathrm{THz,pk}} = 0$ V/cm over an unfaulted-centre-adatom and measurements were performed over the same atom. Inset: Electro-optically measured THz pulse waveform with the silicon beamsplitter in place. 106
6.23 Simulated (solid lines) and experimental (circles) THz pulse autocorrelations with the THz pulse peak electric field in each arm of the autocorrelator denoted by $E_{\mathrm{THz,pk}}$. The THz pulse waveform in Fig. 6.22 was used to model $V_{\mathrm{THz}}(t)$ for the autocorrelation fits in this figure. The initial tip–sample separation was set by $V_{\mathrm{d.c.}} = -0.25$ V, $I_{\mathrm{d.c.}} = -20$ pA, $E_{\mathrm{THz,pk}} = 0$ V/cm over an unfaulted-centre-adatom and measurements were performed over the same atom. 107
6.24 THz pulse voltage transient (red solid line) and simulated ultrafast THz-pulse-induced current transient (blue solid line) based on the THz-STM I–V curve in a for $E_{\mathrm{THz,pk}} = -200$ V/cm (**a**), $E_{\mathrm{THz,pk}} = +300$ V/cm (**b**) and $E_{\mathrm{THz,pk}} = +400$ V/cm (**c**), reaching peak THz-pulse-induced tunnel currents of 1 mA over 240 fs (full-width half-maximum). The rectified terahertz current ($I_{\mathrm{THz,avg}}$) is negative for **a**, **b** and positive for **c**. 108
6.25 Modeling TD-STM on Si(111)-(7×7) in the extreme tunnel current regime. **a**, Experimental and simulated THz I–E curve exhibiting three distinct regimes designated by I (blue), II (green) and III (red) (see also Fig. 6.21). **b**–**d**, Schematic of $V_{\mathrm{THz}}(t)$ (red solid line) superimposed on the THz-STM I–V (black solid line), generating an ultrafast tunnel current, $I_{\mathrm{THz}}(t)$ (blue solid line) for $E_{\mathrm{THz,pk}} < 0$ V/cm (**b**), 0 V/cm $< E_{\mathrm{THz,pk}} < +360$ V/cm (**c**) and $E_{\mathrm{THz,pk}} > +360$ V/cm (**d**). The rectified terahertz current ($I_{\mathrm{THz,avg}}$) is negative for **b**, **c** and positive for **d**. 109
6.26 **a**, Constant-current STM image at $V_{\mathrm{d.c.}} = -1$ V, $I_{\mathrm{d.c.}} = -100$ pA and $E_{\mathrm{THz,pk}} = 0$ V/cm. Image size 9 nm × 9 nm; scan speed 9 nm/s. **b**, Band diagram for steady-state equilibrium tunneling from occupied surface states (occupied states are shaded). Green arrows indicate the direction and magnitude of electron tunneling. Fermi levels for bulk, tip and surface are given by $\varepsilon_{\mathrm{F,B}}$, $\varepsilon_{\mathrm{F,tip}}$ and $\varepsilon_{\mathrm{F,S}}$, respectively, where $eV_{\mathrm{d.c.}} = \varepsilon_{\mathrm{F,tip}} - \varepsilon_{\mathrm{F,B}}$. . 110
6.27 **a**, Constant-current STM image at $V_{\mathrm{d.c.}} = +1$ V, $I_{\mathrm{d.c.}} = +100$ pA and $E_{\mathrm{THz,pk}} = 0$ V/cm. Image size 9 nm × 9 nm; scan speed 9 nm/s. **b**, Band diagram for equilibrium tunneling into unoccupied surface states. Green arrows indicate the direction and magnitude of electron tunneling. Fermi levels for bulk, tip and surface are given by $\varepsilon_{\mathrm{F,B}}$, $\varepsilon_{\mathrm{F,tip}}$ and $\varepsilon_{\mathrm{F,S}}$, respectively, where $eV_{\mathrm{d.c.}} = \varepsilon_{\mathrm{F,tip}} - \varepsilon_{\mathrm{F,B}}$. 111

6.28 **a**, Constant-height image of the THz-pulse-driven tunnel current at $V_{\mathrm{d.c.}} = 0$ V and $E_{\mathrm{THz,pk}} = -200$ V/cm. **b**, Constant-height TD-STM image at $V_{\mathrm{d.c.}} = 0$ V and $E_{\mathrm{THz,pk}} = +400$ V/cm. Image size 9 nm × 9 nm; scan speed 12 nm/s. 112
6.29 Band diagrams for THz-pulse-induced non-equilibrium tunneling at $E_{\mathrm{THz,pk}} = -200$ V/cm during the initial positive THz pulse half-cycle (**a**) and final negative THz pulse half-cycle (**b**). Green arrows indicate the direction and magnitude of electron tunneling. Fermi levels for bulk, tip and surface are given by $\varepsilon_{\mathrm{F,B}}$, $\varepsilon_{\mathrm{F,tip}}$ and $\varepsilon_{\mathrm{F,S}}$, respectively, where $eV_{\mathrm{d.c.}} = \varepsilon_{\mathrm{F,tip}} - \varepsilon_{\mathrm{F,B}}$. $\varepsilon_{\mathrm{F,S}}$ is shifted from $\varepsilon_{\mathrm{F,B}}$ due to a transient surface charge, where $eV_{\mathrm{THz}}(t) = \varepsilon_{\mathrm{F,tip}} - \varepsilon_{\mathrm{F,B}}$. 112
6.30 Band diagrams for ultrafast non-equilibrium tunneling at $E_{\mathrm{THz,pk}} = +400$ V/cm during the initial negative THz pulse half-cycle (**a**) and final positive THz pulse half-cycle (**b**). Green arrows indicate the direction and magnitude of electron tunneling. Fermi levels for bulk, tip and surface are given by $\varepsilon_{\mathrm{F,B}}$, $\varepsilon_{\mathrm{F,tip}}$ and $\varepsilon_{\mathrm{F,S}}$, respectively, where $eV_{\mathrm{d.c.}} = \varepsilon_{\mathrm{F,tip}} - \varepsilon_{\mathrm{F,B}}$. $\varepsilon_{\mathrm{F,S}}$ is shifted from $\varepsilon_{\mathrm{F,B}}$ due to a transient surface charge, where $eV_{\mathrm{THz}}(t) = \varepsilon_{\mathrm{F,tip}} - \varepsilon_{\mathrm{F,B}}$. 113
6.31 Simulated THz pulse at STM tip apex. The temporal profile of an electro-optically (EO) measured THz pulse waveform (black solid line) is used as an input for the electromagnetic (EM) simulation of THz pulse coupling to an STM tip. The electric field transient at the tip apex is extracted from the simulation (red solid line). Inset: corresponding amplitude spectra. . . . 114
6.32 Electromagnetic simulation of THz pulse coupling to an STM tip. **a**, Simulation geometry and **b**, finite element mesh. **c**, THz pulse electric field enhancement (red circles) and THz pulse peak voltage (blue circles) at the STM junction for several tip–sample separations. **d**, THz pulse peak electric field at the tip apex (red circles) and THz pulse peak voltage at the tip apex (blue circles) for several incident fields. 115

6.33 Electric field spatial profiles obtained from 3D electromagnetic simulations. **a**, Simulation geometry with a tip–sample separation of 10 nm and tip radius of curvature of 100 nm. The bulk was modeled using a conductivity of 20,000 S/m, while the 7×7 surface was approximated as a 10 nm slab with a conductivity of 500 S/m (10 nm × 500 S/m = 5 µS/□) [316]. The red dashed line outlines a 30 nm radius half-sphere in the silicon bulk that contains 500 electrons and the arrows illustrate carriers within tens of nanometers of the tunnel junction being accelerated by the THz pulse electric field. The free-space THz pulse has a field strength of $E_{\mathrm{THz,pk}} = 100$ V/cm and is incident onto the tungsten tip at 35° above the x-axis (see Fig. 6.32 for details). **b**, Simulated spatial profile of the vertical component of the steady-state electric field, $[E_{\mathrm{d.c.}}]_{\mathrm{Z}}$, with $V_{\mathrm{d.c.}} = 1$ V applied to the sample. The d.c. electric field does not penetrate significantly into the bulk under steady-state. **c**, **d**, Simulated spatial profile of the THz pulse electric field for the vertical component, $[E_{\mathrm{THz,pk}}]_{\mathrm{Z}}$ (**c**), and horizontal component, $[E_{\mathrm{THz,pk}}]_{\mathrm{X}}$ (**d**), when the larger THz pulse half-cycle undergoes maximum enhancement at the junction. The colourmap range was chosen to emphasize the terahertz electric field penetration into the bulk (the electric field in the gap is saturated dark red/blue). For a 0.7 nm tunnel gap and an incident field free-space THz pulse electric field of $E_{\mathrm{THz,pk}} = 200$ V/cm, the electric field obtained from the simulation is enhanced by a factor of 28. 116

6.34 Simplified equivalent circuit representation of the tunnel current pathways at THz frequencies and in steady-state. The impedance of the tunnel junction is given by $Z_{\mathrm{Tip\text{-}Surf}}$, while the impedance between the surface and the bulk is given by $Z_{\mathrm{Surf\text{-}Bulk}}$. Charge carriers on the Si(111)-(7×7) surface can either propagate along the surface, or travel directly from surface states into bulk states. The conductivity of the Si(111)-(7×7) surface is approximately 1 µS/□ [318, 319, 330, 334], corresponding to a resistance of ∼ 1 MΩ. **a**, A free-space THz pulse induces a transient voltage at the tunnel junction, $V_{\mathrm{THz}}(t)$, that drives an ultrafast transient current, $I_{\mathrm{THz}}(t)$, with peak currents up to 1 mA. The impedance for electrons tunneling from surface states to bulk states is small at high frequencies due to THz-pulse-induced band bending ($Z_{\mathrm{Surf\text{-}Bulk}} \ll 1$ MΩ). **b**, Under steady-state operation the depletion layer prevents charge carriers from accessing the bulk directly ($Z_{\mathrm{Surf\text{-}Bulk}} \gg 1$ MΩ). The charge carriers propagate on the Si(111)-(7×7) surface before eventually scattering into the bulk. 119

6.35 STM and TD-STM constant-current topographs. **a**, TD-STM image from Fig. 6.8b acquired at $V_{\mathrm{d.c.}} = 0$ V and $E_{\mathrm{THz,pk}} = -200$ V/cm. **b**, STM image from Fig. 6.8a acquired at $V_{\mathrm{d.c.}} = -0.5$ V. **c**, **d**, STM images of the same region at $V_{\mathrm{d.c.}} = -0.7$ V (**c**) and $V_{\mathrm{d.c.}} = -1$ V (**d**). Image size 8.5 nm × 8.5 nm; scan speed 13 nm/s; low-pass filtered with a 3×3 smoothing matrix; feedback loop setpoint −20 pA. 122

6.36 Constant-current topography of Si(111)-(7×7) at several $V_{\text{d.c.}}$ and $E_{\text{THz,pk}} = -200$ V/cm. The images are acquired at a feedback loop setpoint of −20 pA ($I_{\text{d.c.}} + I_{\text{THz,avg}} = -20$ pA). At $V_{\text{d.c.}} = 0$ V, the 50% duty cycle THz pulse modulation is switched off, doubling $I_{\text{THz,avg}}$ at constant tip height. Image size 40 nm × 40 nm; scan speed 40 nm/s. 123
6.37 THz-STM of Si(111)-(7×7) at several $V_{\text{d.c.}}$ and $E_{\text{THz,pk}} = -200$ V/cm. The THz-STM images, $N_{\text{e}^-}(x, y)$, are acquired simultaneously with the constant-current topography images in Fig. 6.36. The lock-in time constant was set to 1 ms with an average pixel-time during scanning at 2.4 ms. The colourmap ranges from 80 to 350 rectified electrons per pulse for brown to gold, respectively. 124
6.38 Hot electrons in the THz-pulse-induced current. **a**, I–z curves measured at $V_{\text{d.c.}} = 0$ V for several $E_{\text{THz,pk}}$. The initial tip–sample separation was set by $V_{\text{d.c.}} = 0$ V, $I_{\text{THz,avg}} = -20$ pA, $E_{\text{THz,pk}} = -225$ V/cm. **b**, I–z curves measured at $V_{\text{d.c.}} = 0$ V for several $E_{\text{THz,pk}}$ with the initial tip–sample separation set by $V_{\text{d.c.}} = 0$ V, $I_{\text{THz,avg}} = -20$ pA, $E_{\text{THz,pk}} = -240$ V/cm. **c**, A bi-exponential fit was used if the I–z curve exhibited fast and slow decay components. **d**, A plot of the apparent barrier-height obtained from the exponential decay of experimental (symbols) and simulated (green solid line) I–z curves in **a** and **b**. The error bars are determined from an uncertainty in the z-piezo calibration and exponential fits to the I–z curves. Inset: non-equilibrium band diagram for large negative terahertz fields. Incorporating an image potential into the modeling (dashed line) lowers the effective barrier height and width (see section 6.2 for details). 126
6.39 Simulated I–z curves for a hot electron energy distribution. **a**, Hot electrons are modeled as a density of states above the Fermi level using Gaussians centered at 0 eV (A), 1.5 eV (B) and 2.3 eV (C). **a**, Simulated I–z curves and their corresponding apparent barrier-heights. The apparent barrier-heights are 2.7 eV, 1.1 eV and 0.3 eV for electron energies centered at 0 eV (A), 1.5 eV (B) and 2.3 eV (C), respectively. The Bardeen tunneling model parameters are: $V_{\text{THz,pk}} = -3$ V, z = 1 nm and $\phi_{\text{sim}} = 5$ eV. . 127
6.40 Constant-current TD-STM image with increasing and decreasing $E_{\text{THz,pk}}$. **a**, 3D perspective view of TD-STM topography acquired at $V_{\text{d.c.}} = 0$ V, $I_{\text{THz,avg}} = -20$ pA and various $E_{\text{THz,pk}}$. The topography appears stepped because the tip jumps when $E_{\text{THz,pk}}$ is changed (constant-current mode). Topography z-range, 0.4 nm. **b**, Processed image where the average of every line is set to zero. $E_{\text{THz,pk}}$ is changed fourteen times throughout the scan. Image size 9 nm × 9 nm; scan speed 14 nm/s. . . . 128
6.41 THz-STM revealing subsurface features on Si(111)-(7×7). **a**, Constant-current topography image at $V_{\text{d.c.}} = -1.2$ V and **b**, simultaneously acquired THz-STM at $E_{\text{THz,pk}} = -60$ V/cm and $I_{\text{d.c.}} + I_{\text{THz,avg}} = -200$ pA. Image size 80 nm × 80 nm; scan speed 72 nm/s; $I_{\text{THz,avg}}$ is less than 10% of the total current ($I_{\text{d.c.}} \gg I_{\text{THz,avg}}$). **c**, **d**, Cross-sectional linescans for the topography image in **a** and THz-STM image in **b**, as indicated the by the blue lines in the insets. 130

6.42 Comparison between topography, THz-STM and differential conductance images on Si(111)-(7×7). **a**, Constant-current topography image at $V_{\mathrm{d.c.}} = -1.2$ V. **b**, The simultaneously acquired THz-STM image at $E_{\mathrm{THz,pk}} = -110$ V/cm. **c**, The simultaneously acquired differential conductance ($\mathrm{d}I/\mathrm{d}V$) image at 25 mV $\mathrm{d}I/\mathrm{d}V$ modulation amplitude. Image size 340 nm × 280 nm; scan speed 160 nm/s; $I_{\mathrm{d.c.}} + I_{\mathrm{THz,avg}} = -200$ pA with $I_{\mathrm{d.c.}} \gg I_{\mathrm{THz,avg}}$. **d**, **e**, **f**, Cross-sectional linescans as indicated by the blue lines in **a**–**c** for topography (**d**), THz-STM (**e**) and $\mathrm{d}I/\mathrm{d}V$ (**f**). 131

6.43 Subsurface features on Si(111)-(7×7) at two different $E_{\mathrm{THz,pk}}$. **a**, Constant-current topography image at $V_{\mathrm{d.c.}} = -1.2$ V. **b**, The simultaneously acquired THz-STM image at $E_{\mathrm{THz,pk}} = -100$ V/cm. **c**, The simultaneously acquired differential conductance image. **d**, Constant-current topography image at $V_{\mathrm{d.c.}} = -1.2$ V. **e**, The simultaneously acquired THz-STM image at $E_{\mathrm{THz,pk}} = -165$ V/cm. **f**, The simultaneously acquired differential conductance image. The average of every line was set to zero for the topography images because of minor tip changes (instead of plane-fit-subtraction). For both sets of scans: image size 150 nm × 150 nm; scan speed 120 nm/s; $I_{\mathrm{d.c.}} + I_{\mathrm{THz,avg}} = -200$ pA with $I_{\mathrm{d.c.}} \gg I_{\mathrm{THz,avg}}$; 25 mV $\mathrm{d}I/\mathrm{d}V$ modulation amplitude. **g**, **h**, **i**, Cross-sectional linescans as indicated by the blue lines in **a**–**f** for topography (**g**), THz-STM (**h**) and $\mathrm{d}I/\mathrm{d}V$ (**i**). The linescans for topography and $\mathrm{d}I/\mathrm{d}V$ were shifted along the y-axis for clarity. 132

7.1 STM image of the GaAs(110) surface acquired in constant-current mode at $V_{\mathrm{d.c.}} = +1.5$ V, $I_{\mathrm{d.c.}} = +150$ pA and $T = 295$ K. A red rectangle with dimensions 5.6 Å × 4.0 Å shows the unit cell of the surface. Image size 3.9 nm × 3.4 nm; scan speed 15 nm/s; colourmap range 100 pm. 135

7.2 Band diagrams for STM of n-type GaAs(110) under reverse bias at $V_{\mathrm{d.c.}} = +2$ V. **a**, **b**, A pair of band diagrams for an atomically clean GaAs(110) surface before (**a**) and after (**b**) photoexcitation by an optical pulse that creates electron–hole pairs in the sample. **c**, **d**, A pair of band diagrams for a negatively charged surface defect on GaAs(110) before (**c**) and after (**d**) photoexcitation. The two small Gaussians represent the intrinsic surface states of GaAs(110), while a solid black bar represents a negatively charged (D^-) or neutral (D^0) extrinsic in-gap surface state. Green arrows indicate the direction of electron tunneling, with thicker arrows indicating a higher tunneling probability. Small blue and white circles are used to represent electrons and holes, respectively. The Fermi levels of the tip and sample bulk are given by $\varepsilon_{\mathrm{F,tip}}$ and $\varepsilon_{\mathrm{F,B}}$, respectively, where $eV_{\mathrm{d.c.}} = \varepsilon_{\mathrm{F,tip}} - \varepsilon_{\mathrm{F,B}}$. The dashed grey lines in **b** and **d** show the change in band bending due to the surface photovoltage (SPV). The occupied states for the sample, surface and tip are colored red, pink and blue, respectively. 137

7.3 Photoconductive sampling of the THz pulse in the far-field and the STM near-field. **a**, Electro-optically sampled THz pulse electric field waveform and its corresponding frequency spectrum (inset). The magnitude of the smaller THz pulse half-cycle is approximately $\sim$ 75 % of the larger half-cycle. **b**, Measured THz-pulse-induced rectified tunnel current, I_{THz} (e^-/pulse) = $N_{\mathrm{e}^-} = I_{\mathrm{THz,avg}}/(e\, f_{\mathrm{rep}})$, as a function of arrival time between the optical pulse and THz pulse onto the STM junction (OPP-THz-STM waveform). The measurements were acquired on a GaAs(110) surface at $V_{\mathrm{d.c.}} = +2$ V, $I_{\mathrm{d.c.}} + I_{\mathrm{THz,avg}} = +50$ pA, $E_{\mathrm{THz,pk}} = +40$ V/cm and $\varepsilon_{\mathrm{Optical}} = 1$ nJ. 141

7.4 Nonlinear behaviour in optical pump – THz-STM probe waveforms on GaAs. **a**, Measured OPP-THz-STM waveforms that were acquired at two different locations on the sample surface with $V_{\mathrm{d.c.}} = +2$ V, $I_{\mathrm{d.c.}} + I_{\mathrm{THz,avg}} = +50$ pA, $\varepsilon_{\mathrm{Optical}} = 2.6$ nJ and $E_{\mathrm{THz,pk}} = -120$ V/cm. **b**, Measured THz-pulse-driven OPP-THz-STM waveforms that were acquired with the tip gently contacted to the sample surface at $V_{\mathrm{d.c.}} = 0$ V and $\varepsilon_{\mathrm{Optical}} =$ 100 nJ. The feedback loop was disengaged after the tip–sample separation had established equilibrium due to the optical-pulse-induced thermal expansion. 143

7.5 Coherent control of photoexcited carriers on the GaAs(110) surface with the THz-STM. All of the waveforms were acquired in constant-current mode at $V_{\mathrm{d.c.}} = +2$ V, and $E_{\mathrm{THz,pk}}$ as shown in the legend. **a**, **b**, OPP-THz-STM waveforms acquired with tip #1 at $I_{\mathrm{d.c.}} + I_{\mathrm{THz,avg}} = +50$ pA and $\varepsilon_{\mathrm{Optical}} = 1$ nJ. **c**, **d**, OPP-THz-STM waveforms acquired with tip #2 at $I_{\mathrm{d.c.}} + I_{\mathrm{THz,avg}} = +300$ pA and $\varepsilon_{\mathrm{Optical}} = 2.6$ nJ. **e**, **f**, OPP-THz-STM waveforms acquired with tip #3 at $I_{\mathrm{d.c.}} + I_{\mathrm{THz,avg}} = +50$ pA and $\varepsilon_{\mathrm{Optical}} = 2.4$ nJ. The vertical dashed lines represent the temporal location of each half-cycle of the THz-pulse-induced tunnel current waveform. The relative position of the larger half-cycle was set to 0 ps for each data set, while the smaller-half cycle occurred at –0.6 ps for **a** and **b**, –0.9 ps for **c** and **d**, and –1 ps for **e** and **f**. 146

7.6 Time-resolved THz I–E curves acquired on the GaAs(110) surface. **a**, The measurements were acquired at $V_{\mathrm{d.c.}} = +2$ V, $I_{\mathrm{d.c.}} + I_{\mathrm{THz,avg}} = +200$ pA, $\tau_{\mathrm{THz–Optical}} \approx +50$ ps and $\varepsilon_{\mathrm{Optical}} = 3.6$ nJ. **b**, THz I–E curves acquired using tip #3 with the same settings as Fig. 7.5e,f. **c**, **d**, The data points for **c** and **d** were extrapolated from the OPP-THz-STM waveforms in Fig. 7.5c,d and Fig. 7.5a,b, respectively. 147

7.7 The effect of a microscopic tip restructuring on the measured THz-STM near-field waveform. **a**, STM and THz-STM images of the GaAs(110) surface after the tip restructuring event. The images were acquired at $V_{\mathrm{d.c.}} = +2$ V, $I_{\mathrm{d.c.}} + I_{\mathrm{THz,avg}} = +50$ pA, $E_{\mathrm{THz,pk}} = -500$ V/cm, $\varepsilon_{\mathrm{Optical}} = 2.6$ nJ and $\tau_{\mathrm{THz–Optical}} =$ 0 ps. Image size 300 nm $\times$ 300 nm. **b**, Measured OPP-THz-STM waveforms before and after the tip restructuring event, acquired at $V_{\mathrm{d.c.}} = +2$ V, $I_{\mathrm{d.c.}} + I_{\mathrm{THz,avg}} = +50$ pA, $E_{\mathrm{THz,pk}} = +60$ V/cm and $\varepsilon_{\mathrm{Optical}} = 2.6$ nJ. 148

7.8 Near-field photoconductive sampling of a complex temporal structure. **a**, Measured OPP-THz-STM waveforms acquired at $V_{\text{d.c.}} = +2$ V, $I_{\text{d.c.}} + I_{\text{THz,avg}} = +50$ pA, $E_{\text{THz,pk}} = \pm 60$ V/cm and $\varepsilon_{\text{Optical}} = 2.6$ nJ. Normalized amplitude spectra are shown for the incident THz pulse (green line), before the restructuring event (black line), after the restructuring event (blue line), and the full waveform in **a** (red line). The amplitude spectrum for the full waveform had notable peaks at 60 GHz, 125 GHz and 260 GHz. **b**, Electro-optically sampled THz pulse electric field waveform. **c**, Measured OPP-THz-STM waveforms with the same settings as **a** except with $E_{\text{THz,pk}} = \pm 25$ V/cm. . . . 149
7.9 **a**, Incident optical pulse energy, $\varepsilon_{\text{Optical}}$, dependence of OPP-THz-STM waveforms on GaAs(110) using tip #1 at $V_{\text{d.c.}} = +2$ V, $I_{\text{d.c.}} + I_{\text{THz,avg}} = +50$ pA and $E_{\text{THz,pk}} = +105$ V/cm. A vertical dashed line is shown at $\tau_{\text{THz–Optical}} = -0.6$ ps and $\tau_{\text{THz–Optical}} = 0$ ps. **b**, A single scan was acquired at $\tau_{\text{THz–Optical}} = 0$ ps with the same settings as **a**. The inset shows the relative tip height throughout the acquisition; a steady 0.5 pm/s background drift towards the sample was subtracted from the measurement. 151
7.10 Optical pulse polarization dependence of OPP-THz-STM waveforms on GaAs(110). The measurements were acquired with tip #3 at $V_{\text{d.c.}} = +2$ V, $I_{\text{d.c.}} + I_{\text{THz,avg}} = +50$ pA, $E_{\text{THz,pk}} = \pm 105$ V/cm and $\varepsilon_{\text{Optical}} = 0.64$ nJ. The vertical dashed lines are centered at $\tau_{\text{THz–Optical}} = -0.85$ ps, $\tau_{\text{THz–Optical}} = 0$ ps, and $\tau_{\text{THz–Optical}} = +2.3$ ps. 152
7.11 Constant-tip-height d.c. bias voltage dependence of THz-STM on GaAs(110). **a**, Current–voltage characteristic (I–V) acquired with the feedback loop disengaged at $V_{\text{d.c.}} = +2$ V, $I_{\text{d.c.}} + I_{\text{THz,avg}} = +110$ pA, $E_{\text{THz,pk}} = +50$ V/cm, $\varepsilon_{\text{Optical}} = 2.6$ nJ and $\tau_{\text{THz–Optical}} = 0$ ps. **b**, The simultaneously acquired rectified electrons per THz pulse. $I_{\text{THz,avg}}$ only contributes about 2% of the total measured current at $V_{\text{d.c.}} = +2$ V. 153

7.12 Modeling time-resolved THz-STM on GaAs(110) in the extreme tunnel current regime. **a**–**c**, Experimental (red circles) and simulated (green solid lines) OPP-THz-STM waveforms at three different $E_{\mathrm{THz,pk}}$. The experimental waveforms are from the data set in Fig. 7.5a,b, where they were acquired at $V_{\mathrm{d.c.}} = +2$ V, $I_{\mathrm{d.c.}} + I_{\mathrm{THz,avg}} = +50$ pA and $\varepsilon_{\mathrm{Optical}} = 1$ nJ. **d**–**f**, The optically-induced transient carrier density, $n(\varepsilon, t)$, of the local GaAs(110) surface for carrier-decay time-constants of 0.16 ps (**d**), 1.3 ps (**e**) and 3 ps (**f**), where τ is the relative time delay of the optically-induced transient carrier density with respect to the THz pulse. **g**–**i**, The THz pulse waveform incident onto the tip as measured by free-space electro-optic sampling. **j**–**o**, The simulated instantaneous THz-pulse-induced tunnel current, $I_{\mathrm{THz}}(t, \tau)$, generated by the THz voltage transient, $V_{\mathrm{THz}}(t)$, at time delays of $\tau = -0.7$ ps for **j**–**l** and $\tau = 0$ ps for **m**–**o**. The simulated OPP-THz-STM waveforms, $N_{\mathrm{e^-}}(\tau) = e^{-1} \times \int_{-\infty}^{+\infty} I_{\mathrm{THz}}(t, \tau)\, \mathrm{d}t$, were acquired with similar parameters as in section 6.2: barrier-height $\phi_{\mathrm{t}} = \phi_{\mathrm{s}} = 4.9 \pm 0.5$ eV, tip–sample separation $z = 0.8 \pm 0.2$ nm, THz pulse field enhancement $F = 275{,}000 \pm 25{,}000$, and the time-dependent carrier densities in **d**–**f**, which were calculated using Eq. 7.1, with $\rho_{\mathrm{s}}(\varepsilon) = 1$, $\varepsilon_{\mathrm{c}} = 0$ eV, $\gamma_{\mathrm{rt}} = 70$ fs, $\sigma = 1.8 \pm 0.3$ eV, and $A_0 = 10^6 \pm 10^5$. . . 157

7.13 Ultrafast THz-STM imaging of gallium vacancies on the silicon-doped GaAs(110) surface. **a**, Measured optical pump – THz-STM probe time delay scan acquired at $V_{\mathrm{d.c.}} = +2$ V, $I_{\mathrm{d.c.}} + I_{\mathrm{THz,avg}} = +50$ pA, $E_{\mathrm{THz,pk}} = +40$ V/cm and $\varepsilon_{\mathrm{Optical}} = 1$ nJ at two different locations on the surface. **b**, Atomic-row-resolved STM constant-current topographic images of the GaAs(110) surface acquired at $V_{\mathrm{d.c.}} = +1.5$ V, $I_{\mathrm{d.c.}} + I_{\mathrm{THz,avg}} = +75$ pA, $E_{\mathrm{THz,pk}} = +70$ V/cm and $\varepsilon_{\mathrm{Optical}} = 1$ nJ, at three different time delays, $\tau_{\mathrm{THz–Optical}}$. **c**, Rectified THz-pulse-induced tunnel current images, $N_{\mathrm{e^-}}(x, y)$, acquired simultaneously with the corresponding topography images in **b**. All topographic data has been plane-fit-subtracted to account for the piezo thermal drift throughout the scan. Image size 10 nm × 10 nm; scan speed 21 nm/s. 160

7.14 Ultrafast defect-enhanced carrier trapping for two types of surface defects. **a**, **b**, STM images and **c**, **d**, ultrafast THz-STM images of the photoexcited GaAs(110) surface at time delays of $\tau_{\mathrm{THz–Optical}} = 0$ ps (**a**, **c**) and $\tau_{\mathrm{THz–Optical}} = -0.7$ ps (**b**, **d**). The images were acquired at $V_{\mathrm{d.c.}} = +1.5$ V, $I_{\mathrm{d.c.}} + I_{\mathrm{THz,avg}} = +75$ pA, $\varepsilon_{\mathrm{Optical}} = 1$ nJ and $E_{\mathrm{THz,pk}} = +60$ V/cm. Image size 19 nm × 19 nm; scan speed 20 nm/s. 161

7.15 Band diagrams for THz-STM of a photoexcited n-type GaAs(110) sample under a steady-state reverse bias, $V_{\text{d.c.}}$, with the THz pulse electric field strength in the **a**, **b**, weak-field regime and **c**, **d**, strong-field regime. Electrons and holes are represented as small blue and white circles, respectively. The two small Gaussians represents the intrinsic surface states of GaAs(110), while a solid black bar represents the extrinsic in-gap surface state (D^-, D^0, D^+). The dashed grey lines show the change in band bending due to the transient THz-current-modified surface photovoltage. Green arrows indicate the direction of electron tunneling, while blue arrows indicate the non-equilibrium transport of electrons and holes through the surface states. The Fermi levels of the tip, surface and sample bulk are given by $\varepsilon_{\text{F,tip}}$, $\varepsilon_{\text{F,S}}$ and $\varepsilon_{\text{F,B}}$, respectively, where $eV_{\text{d.c.}} + eV_{\text{THz}}(t) = \varepsilon_{\text{F,tip}} - \varepsilon_{\text{F,B}}$ and $\varepsilon_{\text{F,S}} = \varepsilon_{\text{F,B}} - eV_{\text{SVP}}(t-\tau, I_{\text{THz}})$. The occupied states for the sample, surface and tip are colored red, pink and blue, respectively. 164

7.16 Time-resolved THz-STM imaging of ultrafast carrier dynamics near surface defects on GaAs(110). **a**, STM topography and **b**, the ultrafast THz-STM image acquired at $V_{\text{d.c.}} = +2.5$ V, $I_{\text{d.c.}} + I_{\text{THz,avg}} = +200$ pA, $\varepsilon_{\text{Optical}} = 2.6$ nJ, $\tau_{\text{THz–Optical}} = -0.7$ ps and $E_{\text{THz,pk}} = -105$ V/cm. Image size 40 nm × 20 nm; scan speed 70 nm/s. **c**, OPP-THz-STM waveforms that demonstrate how a bipolar THz-pulse-induced rectified tunnel current can occur at particular time delays for different values of the carrier-decay time-constant, θ. The vertical dashed lines are centered at $\tau_{\text{THz–Optical}} = -0.7$ ps and $\tau_{\text{THz–Optical}} = 0$ ps. . 166

7.17 Comparison between constant-current and constant-height ultrafast THz-STM images of atomic-scale defects on the GaAs(110) surface. **a**, Constant-current STM topography $z(x, y)$, and **b**, the simultaneously acquired THz-STM image $I_{\text{THz,avg}}(x, y)$. **c**, Constant-height total current image $I_{\text{d.c.}}(x, y) + I_{\text{THz,avg}}(x, y)$, and **d**, simultaneously acquired THz-STM image $I_{\text{THz,avg}}(x, y)$. The images were acquired at acquired at $V_{\text{d.c.}} = +2.5$ V, $\varepsilon_{\text{Optical}} = 2.6$ nJ, $E_{\text{THz,pk}} = +90$ V/cm and $\tau_{\text{THz–Optical}} = 0$ ps. For **a** and **b**, the tunnel current was regulated at +50 pA, while for **c** and **d**, the feedback loop was disengaged at +50 pA and $V_{\text{d.c.}} = +2.5$ V on the defect-free GaAs(110) surface. Image size 11 nm × 11 nm; scan speed 130 nm/s. 167

7.18 High spatial resolution THz-STM imaging of atomic-scale defects on the GaAs(110) surface. **a**, STM topography and **b**, the ultrafast THz-STM image acquired at $V_{\text{d.c.}} = +1.5$ V, $I_{\text{d.c.}} + I_{\text{THz,avg}} = +75$ pA, $\varepsilon_{\text{Optical}} = 1$ nJ, $\tau_{\text{THz–Optical}} = 0$ ps and $E_{\text{THz,pk}} = +70$ V/cm. Image size 12 nm × 12 nm; scan speed 8.5 nm/s. **c**, **d**, Cross-sectional linescans for two different regions of the STM image (solid blue lines) and THz-STM image (solid gold lines). 168

7.19 **a**, **b**, STM images and **c**, **d**, ultrafast THz-STM images of the photoexcited GaAs(110) surface acquired at $V_{\text{d.c.}} = +2.5$ V, $I_{\text{d.c.}} + I_{\text{THz,avg}} = +200$ pA, $\varepsilon_{\text{Optical}} = 2.6$ nJ, $\tau_{\text{THz–Optical}} = 0$ ps and $E_{\text{THz,pk}} = -105$ V/cm. **a**, **c**, Image size 50 nm × 50 nm; scan speed 75 nm/s. **b**, **d**, Image size 100 nm × 100 nm; scan speed 45 nm/s. 169
7.20 Ultrafast THz-STM imaging of surface defects on silicon-doped GaAs(110) using tip #2. All of the measurements were acquired at $V_{\text{d.c.}} = +2$ V, $I_{\text{d.c.}} + I_{\text{THz,avg}} = +50$ pA, $\varepsilon_{\text{Optical}} = 2.6$ nJ and $E_{\text{THz,pk}} = +105$ V/cm. **a**, Measured OPP-THz-STM waveforms at the two different locations on the sample surface shown by the red and black circles in the topography image of the middle frame. **b**, STM images and **c**, ultrafast THz-STM images of the photoexcited GaAs(110) surface at time delays of $\tau_{\text{THz–Optical}} = -3$ ps (left), $\tau_{\text{THz–Optical}} = -0.9$ ps (middle) and $\tau_{\text{THz–Optical}} = 0$ ps (right). Image size 45 nm × 45 nm; scan speed 23 nm/s. 170

8.1 THz-pulse-induced single-adatom removal from the Si(111)-(7×7) surface. STM images of the same surface were acquired at $V_{\text{d.c.}} = -0.9$ V and $I_{\text{d.c.}} = -100$ pA, before (**a**) and after (**b**) exposing the STM tip to THz pulses for $t_{\text{dmg}} \approx 5$ s at $E_{\text{THz,pk}} = -150$ V/cm, $V_0 = V_{\text{d.c.}}$ and $I_0 = I_{\text{d.c.}}$. Image size 7.0 nm × 5.4 nm. Note: the adatom that was actually removed in **b** was positioned directly northeast of the brown topographic depression. This was revealed by STM images of the defect at other bias voltages. 179
8.2 Imaging voltage dependence of an atomic-scale THz-pulse-induced surface modification. STM images of the same Si(111)-(7×7) surface were acquired at $|I_{\text{d.c.}}| = 150$ pA, and a range of bias voltages before (**a**) and after (**b**–**f**) exposing the STM tip to THz pulses for $t_{\text{dmg}} \approx 3$ s at $E_{\text{THz,pk}} = -200$ V/cm, $V_0 = -0.5$ V and $I_0 = I_{\text{d.c.}}$. Image size 10 nm × 10 nm. 180
8.3 Imaging voltage dependence of a nanometer-scale THz-pulse-induced surface modification. STM images of the same Si(111)-(7×7) surface were acquired at $|I_{\text{d.c.}}| = 35$ pA, and a range of bias voltages before (**a**) and after (**b**–**d**) exposing the STM tip to THz pulses for $t_{\text{dmg}} \approx 3$ s at $E_{\text{THz,pk}} = -400$ V/cm, $V_0 = +1$ V and $I_0 = I_{\text{d.c.}}$. Image size 35 nm × 35 nm. 181
8.4 Imaging voltage dependence of a nanometer-scale THz-pulse-induced surface modification. STM images of the same Si(111)-(7×7) surface were acquired at $|I_{\text{d.c.}}| = 35$ pA, and a range of bias voltages before (**a**) and after (**b**–**d**) exposing the STM tip to THz pulses for $t_{\text{dmg}} \approx 3$ s at $E_{\text{THz,pk}} = -450$ V/cm, $V_0 = +1$ V and $I_0 = I_{\text{d.c.}}$. Image size 40 nm × 30 nm. 182
8.5 THz-pulse-induced surface modification and tip material deposition. An STM image of the Si(111)-(7×7) surface was acquired at $I_{\text{d.c.}} = 150$ pA and $V_{\text{d.c.}} = +1.5$ V, after the STM tip was exposed to THz pulses for $t_{\text{dmg}} \approx 5$ s at $E_{\text{THz,pk}} = -400$ V/cm for the top middle event and $E_{\text{THz,pk}} = -500$ V/cm for the other two events. Image size 100 nm × 100 nm. 183

8.6 THz-pulse-induced surface modifications and tip material depositions. An STM image of the Si(111)-(7×7) surface was acquired at $I_{\text{d.c.}} = 50$ pA and $V_{\text{d.c.}} = +1$ V, after the STM tip was exposed to THz pulses at $E_{\text{THz,pk}} = -350$ V/cm, $V_0 = +0.5$ V and $I_0 = I_{\text{d.c.}}$ for $t_{\text{dmg}} \approx 5$ s. Image size 50 nm × 50 nm. 184
8.7 **a**, **b**, Local and nonlocal THz-pulse-induced surface modifications on the nanometer-scale. STM images of the same Si(111)-(7×7) surface were acquired at $V_{\text{d.c.}} = +2$ V and $I_{\text{d.c.}} = 50$ pA, before (**a**) and after (**b**) exposing the STM tip to THz pulses for $t_{\text{dmg}} \approx 3$ s at $E_{\text{THz,pk}} = -350$ V/cm, $V_0 = V_{\text{d.c.}}$ and $I_0 = I_{\text{d.c.}}$. Image size 40 nm × 40 nm. The red circles are guides to the eye for locating the THz-pulse-induced modifications. . . . 185
8.8 **a**, **b**, STM images of THz-pulse-induced nano-patterned circles on the Si(111)-(7×7) surface acquired at $I_{\text{d.c.}} = +30$ pA and $V_{\text{d.c.}} = +2$ V. Prior to the image acquisition, the STM tip was exposed to THz pulses at $V_0 = V_{\text{d.c.}}$, $I_0 = I_{\text{d.c.}}$ and $E_{\text{THz,pk}} = -400$ V/cm for $t_{\text{dmg}} \sim 60$ s as the tip was translated along a 40 nm diameter circle (**a**) and a 25 nm diameter circle (**b**). Image size 70 nm × 70 nm for **a** and 45 nm × 45 nm for **b**. 186
8.9 STM image of THz-pulse-induced nano-patterning on the Si(111)-(7×7) surface acquired at $V_{\text{d.c.}} = +1.7$ V and $I_{\text{d.c.}} = +200$ pA. Prior to the image acquisition, the STM tip was exposed to THz pulses at $V_0 = V_{\text{d.c.}}$, $I_0 = I_{\text{d.c.}}$ and $E_{\text{THz,pk}} = -300$ V/cm for $t_{\text{dmg}} \sim 30$ s. Image size 100 nm × 100 nm. 187
8.10 Large-scale atomically-resolved STM image of THz-pulse-induced nano-patterning on the Si(111)-(7×7) surface acquired at $V_{\text{d.c.}} = +1$ V and $I_{\text{d.c.}} = +50$ pA. Prior to the image acquisition, the STM tip was exposed to THz pulses at $V_0 = V_{\text{d.c.}}$, $I_0 = I_{\text{d.c.}}$ and $E_{\text{THz,pk}} = -300$ V/cm for $t_{\text{dmg}} \sim 60$ s. Image size 210 nm × 60 nm. 188
8.11 An STM image of the H-Si(100)-(2×1) surface that was acquired after THz-pulse-induced hydrogen desorption was performed during the previous scan, where the THz pulse electric field, $E_{\text{THz,pk}}$, was increased progressively throughout the scan. The fast scan direction is leftward-travelling and the slow scan direction is downward-travelling. The image was acquired at $V_{\text{d.c.}} = -1.5$ V and $I_{\text{d.c.}} = -100$ pA, and the same settings were used during the THz-pulse-induced hydrogen desorption. Image size 30 nm × 30 nm. 189
8.12 STM images of the H-Si(100)-(2×1) surface that were acquired **a**, before, and **b**, **c**, after THz-pulse-induced hydrogen desorption was performed at $E_{\text{THz,pk}} = -300$ V/cm, $V_0 = -1.5$ V and $I_0 = -100$ pA. The images were acquired in constant current mode at $|I_{\text{d.c.}}| = 100$ pA. Image size 17 nm × 23 nm. 190
8.13 STM images of the H-Si(100)-(2×1) surface that were acquired **a**, before, and **b**, **c**, after THz-pulse-induced hydrogen desorption was performed at $E_{\text{THz,pk}} = -450$ V/cm, $V_0 = -1.5$ V and $I_0 = -100$ pA. The images were acquired in constant-current mode at $|I_{\text{d.c.}}| = 100$ pA. Image size 19 nm × 21 nm. 190

8.14 Spontaneous creation of atomic chains during time-resolved THz-STM imaging of GaAs(110). **a**, **b**, STM topography and **c**, **d**, the ultrafast THz-STM images of the same surface acquired at $V_{\text{d.c.}} = +2.5$ V, $I_{\text{d.c.}} + I_{\text{THz,avg}} = +200$ pA, $\varepsilon_{\text{Optical}} = 2.6$ nJ, $\tau_{\text{THz–Optical}} = -0.7$ ps and $E_{\text{THz,pk}} = -105$ V/cm. Image size 40 nm × 40 nm; scan speed 70 nm/s. 191
8.15 Spontaneous removal of a single gallium atom from the GaAs(110) surface during THz-STM imaging at $V_{\text{d.c.}} = +1.5$ V, $I_{\text{d.c.}} + I_{\text{THz,avg}} = +75$ pA, $\varepsilon_{\text{Optical}} = 1$ nJ, $\tau_{\text{THz–Optical}} = 0$ ps and $E_{\text{THz,pk}} = +70$ V/cm. Image size 4.7 nm × 4.7 nm; scan speed 21 nm/s. 192

A.1 Ultrafast movie of an InAs nano-island. The STM images (first and third rows) and THz-STM images (second and fourth rows) were acquired with the tip travelling in the right scan direction at $V_{\text{d.c.}} = -2.1$ V, $I_{\text{d.c.}} = -500$ pA, $E_{\text{THz,pk}} = 100$ V/cm and the time delay, $\tau_{\text{Optical–THz}}$, as given below the pairs of images. Image size 400 nm × 400 nm; scan speed 1300 nm/s. 233
A.2 Ultrafast movie of an InAs nano-island. The STM images (first and third rows) and THz-STM images (second and fourth rows) were acquired with the tip travelling in the left scan direction at $V_{\text{d.c.}} = -2.1$ V, $I_{\text{d.c.}} = -500$ pA, $E_{\text{THz,pk}} = 100$ V/cm and the time delay, $\tau_{\text{Optical–THz}}$, as given below the pairs of images. Image size 400 nm × 400 nm; scan speed 1300 nm/s. 234

B.1 **a**, Photograph and **b**, schematic of the Ti:sapphire regenerative amplifier laser (Coherent RegA 9050). The green beam is a 532 nm c.w. 15 W pump laser (Coherent Verdi-V18), while the thin red beam is a seed pulse from the oscillator (Coherent Micra) that gets coupled into the cavity and then amplified for approximately 22 round trips (thick red beam). The input seed pulse and output amplified pulse are routed into and out-of the cavity by an acousto-optic modulator. A Faraday Isolator separates the two beam paths. 237
B.2 Photograph of the optical beam path through the delay stages for the new setup that has 80% of the full laser power going towards THz pulse generation. The red beam is the electro-optic sampling pulse, the green beam is the pump pulse, and the orange beam goes to the autocorrelator and photodiode trigger (see also Fig. 5.2). 239
B.3 Photograph of the optical beam path through the delay stages for the old setup that had only 64% of the full laser power going towards THz pulse generation. The red beam is the electro-optic sampling pulse, the green beam is the pump pulse, the yellow beam is used by another experiment, and the orange beam goes to the autocorrelator and photodiode trigger (see also Fig. 4.2). 240

C.1 Photographs of the three THz-STM electronics racks. 1 – controller for the vibration isolation system (TMC Stacis 2100), 2 – ionization gauge controllers (Granville-Phillips 350), 3 – turbomolecular pump controller (Leybold), 4 – electron bombardment heater (Prevac Heat-2PS), 5 – temperature controller (Lakeshore 331), 6 – electron evaporator controllers (SPECS), 7 – low voltage power supply (Agilent 6542A), 8 – argon gun controller (SPECS), 9 – ion pump controller (Gamma Vacuum). 10 – digital multimeter (Agilent 34401A), 11 – oscilloscope (Tektronix DPO2002B), 12 – THz source power supply (BK Precision 9122A), 13 – high voltage power supply (Stanford Research PS350), 14 – voltage pulser (Directed Energy HV1000), 15 – delay generator (Stanford Research Systems DG645), 16 – function generator (BK Precision BK4052), 17 – multi-range power supply (BK Precision 9206), 18 – variable resistor, 19 – temperature controller, 20 – external loadlock heater, 21 – 50 Ω load resistor, 22 – digital multimeters (Agilent 34401A), 23 – oscilloscope (Tektronix MSO2024B), 24, 25, 26 – lock-in amplifier (Stanford Research Systems SR830), 27 – single-shot THz pulse controller, 28 – STM control console (RHK SPM1000), 29 – data acquisition analog-to-digital converter (National Instruments USB6212DAQ), 30 – low-noise voltage amplifier (Stanford Research Systems SR560). 242
C.2 Photographs of the various equipment used to operate instruments inside the Preparation Chamber of the UHV system. 1 – main water valve, 2 – nitrogen purge inlet, 3 – main return valve, 4 – water purge valve, 5 – argon gun (SPECS IQE-11/35), 6 – controller for the quartz crystal thickness monitor inside the deposition chamber (Inficon FTM-2400), 7 – quartz crystal oscillator (Inficon OSC-100A), 8, 9 – controllers and power supplies for the atomic hydrogen source (TDK-Lambda GEN 40-38), 10 – residual gas analyzer (Extorr XT100M), 11 – atomic hydrogen source (RIBER), 12 – hydrogen gas inlet valve, 13 – electron evaporator (SPECS EBE-1), 14 – deposition chamber, 15 – water-cooled leads from the high ampere power supply (RD Mathis LV400), 16, 17, 18, 19 – manual and electronic valves of the mass-flow-controller (Bronkhorst), 20 – hydrogen gas purifier, 21, 22, 23 – manual valves and regulator for the hydrogen gas cylinder. 243
C.3 Schematic of the vacuum system for the THz-STM. The inlet valve, purge valve, turbomoleular pump and roughing pump+valve are operated electronically using the turbo pump controller (#3 in Fig. C.1), while the green purge valve and the UHV gate valves are operated manually. 245
C.4 Photograph of the vacuum suitcase and the ion pump controller. 251
C.5 Back panel of the RHK SPM100 control console. 252

C.6 Photographs of the new tip etching station. **a**, The entire assembly rests on a vibration isolation table (TMC 66-501). **b**, A small beaker is used to hold solution of 2 M NaOH, while electrical connections are made to the etching wire and the platinum wire. **c**, The platinum wire is bent into the shape of a ring, orientated parallel to the surface of the etchant, and gently submersed into the solution. 254
C.7 Photographs of the **a**, tip holder **b**, unlocked and empty tip-exchange-holder, and **c**, locked and loaded tip-exchange-holder. 255
C.8 Photographs of the electrical connections for *in situ* tip conditioning. **a**, The three safe high-voltage (SHV-5) connections into the UHV chamber. The top two connections are for the high voltage, while the bottom connection is for floating ground. **b**, The electrical breakout box for electron bombardment. The color-coded connections from the power supply are attached to the red, black and green connections on the box. **c**, The electrical breakout box for electron field emission. The high voltage is connected at the bottom right, just before the 10 MΩ safety-resistor. 256
C.9 Calibrating the THz Waveform. **a**, Electro-optically sampled THz waveform as measured using a lock-in amplifier (black solid line) and the raw signal from the balanced photodiode detectors (red solid line). **b**, Relationship between the applied voltage to the THz pulse source and the peak THz electric field $E_{\mathrm{THz,pk}}$. The measurement was acquired at $t = 0$ ps. 260
C.10 Filtering noise in the STM image. **a**, STM image acquired at $V_{\mathrm{d.c.}} = +1.5$ V and $I_{\mathrm{d.c.}} = +150$ pA. Image size 130 nm × 130 nm. **b**, 2D-FFT of the image in **a** with white arrows in the center highlighting the frequency peaks of the noise. Image size 3.5 nm^{-1} × 3.5 nm^{-1}. **c**, Inverse FFT of **b** after filtering out the frequency peaks due to the noise. 261

Chapter 1

Introduction

Our ability to generate extremely short pulses of light is essential for studying the evolution of physical systems at ultrafast timescales. The term ultrafast informally refers to a temporal duration on the order of picoseconds or less. Ultrafast laser technology was developed during the 1970s using mode-locked dye lasers that could produce sub-picosecond pulses with energies of about 1 nanojoule [2]. By the early 1990s, ultrafast lasers were able to generate pulses with a temporal duration in the femtosecond regime, and with pulse energies that were starting to reach the millijoule regime. By depositing such large energies over ultrafast timescales, the transient peak power achievable by table-top lasers was starting to reach several gigawatts, and eventually several terawatts [2]. Laboratories from around the world began to comprehensively explore nonlinear optical phenomena across a wide range of materials [3–5], leading to the development of several new sub-fields that have had a major impact on modern technology and scientific research, including femtochemistry [6–9], frequency comb spectroscopy [10–12], optical telecommunications [13], super-resolved fluorescence microscopy [14–16], chirped pulse amplification [17], optical tweezers [18], high harmonic generation in gases [19–22] and in solids [22–28], attosecond technology [20, 29–33], and terahertz (THz) technology [34–43]. While lasers are readily used to measure transient dynamics with an extremely high temporal resolution, their spatial resolution is determined by the diffraction-limited spot-size of the focused laser beam. However,

this fundamental principle only applies to free-space-propagating light and it can be circumvented by coupling the electromagnetic pulses to nanostructures that can localize the light fields to extremely small spatial dimensions. This simple concept has opened the door to an entirely new branch of science called nanophotonics [44, 45].

As these historic developments in laser technology were occurring, several other branches of physics were pursuing another major scientific goal – imaging the atomic structure of matter. Several complimentary techniques were developed towards this goal including transmission electron microscopy [46–49], atomic force microscopy [50–55], field ion microscopy [56–58] and scanning tunneling microscopy (STM) [1, 59–67]. An inevitable encounter was set to occur between the burgeoning field of nanophotonics and these various microscopy techniques, with the ultimate goal of designing several new platforms for probing the dynamics of matter at the smallest of lengthscales and the fastest of timescales, simultaneously[1]. While, there have been numerous advances over the years in time-resolved electron microscopy of bulk materials [6–9] and time-resolved scanning probe microscopy of surfaces (Table 1.1) [68–138], researchers have only recently developed an ultrafast (sub-picosecond) scanning probe microscope[2] that can maintain the same ångström-scale spatial resolution as conventional scanning probe techniques.

Several challenges have to be overcome when using optical pulses with scanning probe techniques because they deposit a large amount of energy (and thus heat) to the tip–sample junction [139–142]. This can lead to transient surface potentials and thermovoltages [142], generating displacement currents that limit the attainable spatio-temporal resolution of the ultrafast microscope [96]. Furthermore, with an optical-pulse-coupled STM, the excitation of electrons

[1]Spatio-temporal imaging with a scanning probe technique requires that the physical process under investigation can be repeatedly triggered by the laser pulses (it is not some random event). The measurements are acquired stroboscopically and represent a time-resolved average over many excitations of the same event.

[2]In general, scanning probe microscopy (SPM) refers to any technique that raster scans a very sharp tip across a sample surface while mapping out some measurable quantity.

	Technique	Spatial Resolution	Temporal Resolution	Incident Power	Notes
[68–77]	s-SNOM	90 nm	∼ps	∼ µW	best spatial resolution: [77]
[78, 79]	s-SNOM	10 nm	0.010 ps	40 mW	
[80–82]	s-SNOM	20 nm	0.200 ps	10 mW	
[83]	LTEM	20 nm	0.500 ps	35 mW	
[84]	FWM-AFM	50 nm	0.002 ps	8 mW	
[85, 86]	OPP-AFM	10 nm	1 ps	5–30 mW	
[87]	Ultrafast STM	∼ µm	∼ µs	4 mW	
[88–92]	JM-STM	1 nm	20 ps	30–100 mW	requires transmission lines on the sample
[93–98]	PG-STM	20 nm	2 ps	∼40 mW	the measured signal is capacitively coupled [96]
[99]	OPP-STM	∼ µm	0.040 ps	100 mW	
[100]	OPP-STM	∼ µm	0.060 ps	0.4 mW	up to 8 µJ per pulse at 5 mJ/cm^2
[101]	OPP-STM	2 nm	0.040 ps	10 mW	
[102]	two-photon OPP-STM	0.5 nm	0.070 ps	0.084 mW	
[103]	two-color OPP-STM	∼nm	0.200 ps	0.2 mW	excitation at 800 nm and 400 nm
[104]	nonlinear OPP-STM	0.3–10 nm	0.100 ps	0.50–0.85 mW	requires a transparent sample
[105]	OPP-STM	1 nm	0.130 ps	200 mW	circularly polarized pulses
[106–112]	SPPX-STM	$<$ 1 nm	0.140 ps	0.01–0.1 mW	best spatial resolution: [110]
[113–115]	electronic SPPX-STM	$<$ 1 nm	1 ns	0.01–0.07 mW	electronically modulated continuous-wave laser
[116, 117]	electronic STM	atomic	∼ms	N/A	
[118–120]	electronic STM	atomic	∼ µs	N/A	
[121–123]	electronic STM	atomic	∼ns	N/A	
[124–127]	electronic STM	atomic	∼ns	N/A	
[128]	electronic STM	atomic	300 ps	N/A	
[129]	electronic STM	atomic	120 ps	N/A	
[130–134]	THz-STM	atomic (0.3 nm)	0.500 ps	∼ µW	this work, see chapter 6 and chapter 7
[135]	THz-STM	atomic (0.06 nm)	0.115 ps	∼ µW	
[136, 137]	THz-STM	∼nm	$<$ 1 ps	∼ µW	
[138]	THz-STM	atomic (0.15 nm)	0.500 ps	∼ µW	

Table 1.1: A summary of the spatio-temporal resolutions of various ultrafast scanning probe microscopy techniques reported in literature. STM – scanning tunneling microscopy; AFM – atomic force microscopy; s-SNOM – scattering-type scanning near-field optical microscopy; LTEM – laser terahertz emission microscopy; FWM – four-wave-mixing; OPP – optical pump-probe; JM – junction-mixing; PG – photoconductively-gated; SPPX – shaken-pulse-pair-excited; N/A – not applicable.

across the tunnel junction is typically a photon-driven process (for example, a field-driven process is demonstrated in [104] and [143]). At low intensities this results in a hot electron population that has an increased probability to tunnel due to the absorption of photons [101–103], while at high intensities multi-photon photoemission occurs and reduces the spatial resolution to the micrometer regime [99, 100]. For an ultrafast STM, a field-driven process is desirable because the electrons remain in thermal equilibrium, and the ultrafast laser field simply acts as a quasi-static bias voltage that drives electron tunneling across the junction. Field-driven processes require that every laser pulse has the same carrier-envelope-phase (CEP). These types of ultrafast lasers, which are labeled as 'CEP stable', have only recently emerged at optical frequencies [29–32, 143–145]. Their application to field-driven electron tunneling at optical frequencies appears to be promising [143], even as the half-cycle duration (1.3 fs at 800 nm) approaches the transit time for an electron across the barrier ($\lesssim$ 2 fs [143, 146–150]). On the other end of the spectrum, at microwave frequencies, nanosecond-scale phase-stable pulses can be efficiently generated and propagated along transmission lines that are connected to the tip and sample. This has led to the development of several all-electronic time-resolved STMs that can maintain the same spatial resolution as conventional STM, while supporting a nanosecond-scale temporal resolution [119–129].

Coupling ultrafast THz pulses to scanning probe microscopes dates back to the early 2000s [68–72], after the appearance of compact and efficient first-generation THz sources and detectors [151–156]. By illuminating a sharp metal tip with ultrafast THz pulses, the incident electric field becomes concentrated around the tip apex, whereby a local interaction occurs with the sample that spectrally and temporally alters the THz pulse. The spatio-temporal dynamics that occur at the tip–sample junction are encoded in the reflected THz pulse, which is measured by sampling of the THz pulse electric field [68–78], or intensity [79–82]. This technique is known as scattering-type scanning near-field optical microscopy (s-SNOM), and since it probes the local dielectric function of the sample, it is a complementary measurement to the STM, which probes

the local density of electronic surface states.

Intense THz pulses have been used to non-resonantly control the motion of charged particles[3] [24, 26, 43, 157–159] and induce electron tunneling from a bulk solid [160–164]. Ultrafast THz pulses that are coupled to the surface of a metal manifest as delocalized terahertz surface plasmon polaritons (THz-SPPs), also known as Sommerfeld-Zenneck waves [165–168]. The generation of THz-SPPs from free-space-propagating THz pulses can be accurately described using antenna theory [71, 72, 83, 165, 168–170]. On a highly conductive and smooth metallic surface, a THz-SPP can propagate for several centimeters with minimal dispersion [165, 167]. Field enhancement and subwavelength confinement occur when a THz-SPP propagates down a sharp taper [166–168, 171], such as the tip of a scanning tunneling microscope. In this case, the THz pulse electric field is localized to very small spatial dimensions and an extremely large field enhancement occurs due to the atomically sharp tip that is positioned within 1 nm of a conductive sample. Following these principles, ultrafast THz pulses with a relatively low electric field in free-space can be strongly enhanced at the tip of a scanning tunneling microscope (THz-STM) and used to coherently drive electron tunneling across the junction with sub-cycle precision.

The field of THz-STM has seen rapid growth since its initial development in 2013 ([130, 131] and chapter 4). Several new THz-STM experiments have emerged showing coherent control of electron tunneling [136], state-selective ultrafast tunneling through molecular orbitals [135], the effect of the tip geometry on the THz pulse CEP [137], and high-resolution imaging of the charge-density-wave dynamics on 2H-$NbSe_2$ [138].

The outline of this thesis is as follows. First, an introduction to the scanning tunneling microscope is presented in chapter 2, followed by an introduction to ultrafast terahertz pulses in chapter 3. The first experiments with the THz-

[3] A THz pulse with a center frequency of 1 THz and a peak electric field of 300 kV/cm can accelerate an electron to 1 eV within a half-cycle of an oscillation [43].

STM at ambient pressure and temperature, which were performed together with Tyler Cocker [130, 131], are summarized in chapter 4. The remaining experiments with the THz-STM were all performed under ultrahigh vacuum, using the experimental setup that is described in chapter 5. In chapter 6, the THz-STM was used to comprehensively explore the Si(111)-(7×7) surface at very high THz-pulse-induced tunnel currents [134]. The ultrafast THz pulses were used to drive hundreds of electrons through single atoms at subpicosecond timescales, while maintaining atomic-scale resolution without a steady-state bias present. In chapter 7, the THz-STM was used to sample the THz pulse near-field at the tip apex, image the ultrafast surface photovoltage of single atom defects, and drive non-equilibrium charging of the GaAs(110) subsurface. In chapter 8, THz-pulse-induced surface modifications were investigated on the Si(111)-(7×7), H-Si(100)-(2×1) and GaAs(110) surfaces.

Chapter 2

Scanning Tunneling Microscopy

Quantum mechanical tunneling is a universal phenomena that plays a fundamental role in several scientific fields such as condensed matter physics [58, 59, 146–149, 172–176], nuclear physics [177], astrophysics [178], and even photosynthesis [179]. For several decades, tunneling-based microscopes such as the field emission microscope [174] and field ion microscope [58] have employed the large field enhancement of sharp metal tips to image atomic-scale features near the tip apex[1]. However, this effect was limited to features on the apex of very sharp metal tips and incapable of imaging a smooth surface. A predecessor to the STM was developed in 1972, the topografiner [180], but it was limited to the field emission regime due to a lack of key technological advances regarding vibration isolation. However, in the 1980s, it was realized that the tunneling process could be used to locally probe the surfaces of materials using a sharp scanning metal tip [60], even down to the atomic scale [61]. This ultimately led to the development of the scanning tunneling microscope in 1982 by Gerd Binnig, Heinrich Rohrer, Christoph Gerber and Edmund Weibel [1, 59–62].

The essential elements of a standard STM experimental setup are shown in Fig. 2.1. An atomically sharp metal tip is scanned laterally (x, y) across a flat sample, while applying a steady-state direct current (d.c.) bias voltage between the tip and sample. A conventional single-probe STM will typically

[1]Typically a kilovolt-scale d.c. voltage applied to the tip is sufficient to generate the necessary V/Å electric fields.

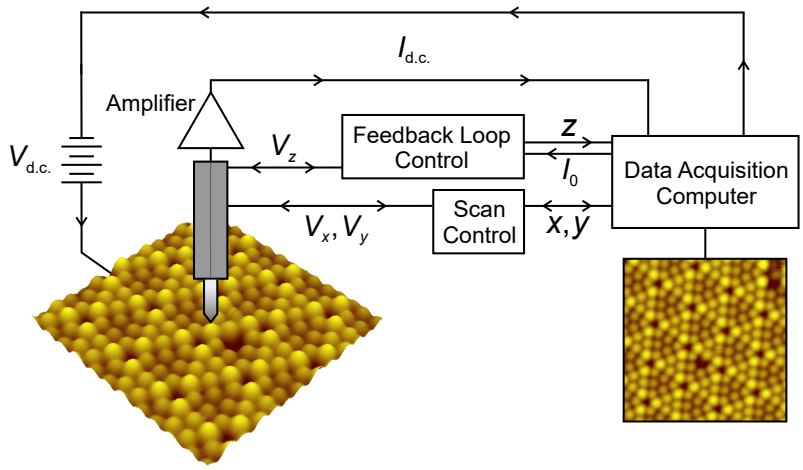

Figure 2.1: Schematic of the essential equipment for scanning tunneling microscopy. A d.c. bias voltage, $V_{\mathrm{d.c.}}$, is applied to the sample, generating a tunnel current, $I_{\mathrm{d.c.}}$, which flows through a sharp metal tip. The tip is attached to a set of piezoelectric crystals that can control its spatial location. The tunnel current is amplified by several orders of magnitude and directed into a feedback loop that controls the tip-height, z, through a d.c. voltage, V_z, which is applied to the z-direction piezoelectric crystal. Two additional piezo crystals are used to scan the tip laterally across the sample by sweeping the voltages V_x and V_y.

bias the sample and ground the tip. In this case, a negative bias voltage raises the Fermi level of the sample, $\varepsilon_{\mathrm{F,sample}}$, above the Fermi level of the tip, $\varepsilon_{\mathrm{F,tip}}$, by $e|V_{\mathrm{d.c.}}|$. Electrons tunnel with a high probability through the sub-nanometer wide vacuum barrier that separates the tip and sample, generating a d.c. tunnel current, $I_{\mathrm{d.c.}}$, with a typical magnitude between 10^{-12}–10^{-8} A. The tunnel current is directed into a feedback circuit that adjusts the height of the tip, $z(x, y)$, in order to maintain a constant tunnel current, $I_0(x, y)$. This is the primary mode of operation with the STM because the feedback loop can maintain a safe tip–sample distance that avoids crashing the delicate tip apex. However, occasionally the feedback loop is disengaged (opened) and the tip is scanned in a horizontal plane above the sample surface, as the tunnel current, $I_{\mathrm{d.c.}}(x, y)$ is measured. An advantage to constant-height scans is that the measurements are easier to interpret and simulate when the tip–sample distance (z) does not continuously change throughout the acquisition.

Drift is an extremely important consideration for STM. The amount of lat-

eral drift (xy-drift) determines the stability of single-point-spectroscopy and in extreme cases it causes skewing of the image during 2D measurements. Meanwhile, vertical drift (z-drift) determines how long the acquisition time can be with the feedback loop disengaged. Most 2D scans require several minutes of acquisition, severely restricting the amount of z-drift that can be tolerated. A typical STM tunnel junction has a tip–sample separation between 5 Å $< z <$ 10 Å, but it is not sufficient to simply avoid contact with the sample during constant-height measurements. This is because the tunnel current varies exponentially with the tip–sample distance (Eq. 2.4). So even a 1 Å drift over several minutes will be detected as a gradual increase of the tunnel current across the STM image. Accordingly, for constant-height measurements, the STM tip is often left hovering above the sample for several hours (or even overnight) prior to the acquisition.

Imaging artifacts and xyz-drift also arise due to the inherent hysteretic behaviour of the piezoelectric crystals that control the position of the tip (their response depends on both past and present conditions) [67]. Piezoelectric crystals are expanded and contracted by directly applying an electric potential to them. This causes the ions in the crystal lattice to be displaced by an amount that is linearly proportional to the applied voltage (for small voltages). Today, piezoelectric actuators are routinely used across a wide range of scanning probe microscopes. However, in the early days of STM, it was not known whether piezoelectric crystals would continue to work at the picometer scale, as Heinrich Rohrer recalls:

> *With atomic resolution in sight, the tip position had to be controlled within a fraction of an ångström not just of a nanometer. Only the experiments themselves showed afterwards that the response of the piezo to an applied material was continuous and reasonably linear down to at least the picometer level. It is remarkable how often success is the reward for trying the unknown.*
>
> – Heinrich Rohrer, 1992 [1]

Measurement artifacts can arise when using piezoelectric crystals for nanoscale

or picoscale displacement [67]. When a voltage change, ΔV, is applied to the piezoelectric crystal, the expansion or contraction that occurs is due to the displacement of ions inside the crystal lattice, along with ferroelectric domain reorientation and the subsequent build-up of strain over time. This leads to a time-dependence for the displacement of a piezoelectric crystal, $x(V,t)$, also known as piezo-creep. After an instantaneous voltage change, $\Delta V = V_1 - V_0$, the position of the crystal will only move from x_0 to x_1 in the limit of $t \to \infty$. These effects are addressed by ensuring that the STM image is composed of horizontal linescans that are all acquired with the tip travelling along the same scan direction. In other words, the STM tip always goes back and forth along each line (fast scan direction), before taking a single step in the perpendicular direction (slow scan direction). This means that every 2D acquisition with the STM always has an image with the tip travelling in the left (up) direction, and an image with the tip travelling in the right (down) direction[2]. These two images are nearly-identical, but they contain minor offsets in the fast scan direction due to piezo-creep. As the dimensions of the STM scan are increased, the measurement artifacts become more pronounced. These artifacts lead to additional precautions when performing single-point STM spectroscopy. If the STM tip needs to move several nanometers to some point of interest, a brief image should be acquired upon arrival of the tip to ensure that the tip is actually positioned at the desired location.

The tunnel current carries with it information about the local electronic wavefunction of both the tip and the sample. While the concept of a wavefunction can be easily applied to single atoms and molecules, for bulk crystal structures, the STM is understood to probe the electronic local density of states (LDOS). The general behaviour of the tunnel current flowing across the STM junction can be understood at a basic level using the standard solutions of a 1D square barrier potential, as typically solved by undergraduate students in a quantum mechanics class [181]. In this simplified model, the tunnel current is proportional to the electron transmission probability through a 1D square

[2]The scan window can be arbitrarily rotated to any angle.

barrier potential (Fig. 2.2) with a height of ϕ_0 (relative to the Fermi level, ε_F; approximately equal to the material work function [182], $\phi_0 = \phi_\mathrm{s} = \phi_\mathrm{t}$). The probability of an electron tunneling across the barrier is determined by solving the 1D time-independent Schrödinger equation

$$\left[\phi_0 - \varepsilon\,\right]\psi(z) = \frac{\hbar^2}{2m}\frac{\mathrm{d}^2}{\mathrm{d}z^2}\,\psi(z)\,, \tag{2.1}$$

inside the three separate regions (left, right and inside the potential barrier with $\varepsilon < \phi_0$), where, m is the electron mass, ε is the electron energy relative to the Fermi level, $\hbar$ is the reduced Planck constant, z is the position coordinate and $\psi(z)$ is the wavefunction. The transmission probability is found to be exponentially dependent on the barrier width, z_0, and decay constant, κ, as given by [67]

$$T = \frac{4k^2\kappa^2}{(\kappa^2+k^2)^2\,\sinh^2(\kappa\,z_0) + 4k^2\kappa^2} \approx \left(\frac{4k\kappa}{k^2+\kappa^2}\right)^2 e^{-2\,\kappa\,z_0}\,, \tag{2.2}$$

where $k = \sqrt{2m\varepsilon}\,/\hbar$ is the wavenumber of the incident and transmitted electrons with respect to the Fermi wavenumber,

$$\kappa = \sqrt{2m(\phi_0 - \varepsilon\,)}/\hbar\,, \tag{2.3}$$

is the $1/e$ decay constant for the wavefunction inside the barrier and

$$I = I_0\,\exp\!\left(-\,2\,z_0\sqrt{\frac{2m(\phi_0-\varepsilon)}{\hbar^2}}\right), \tag{2.4}$$

is the tunnel current (see section 2.3 for more accurate models that also take into account the applied bias voltage and local density of electronic states). It is precisely this exponential dependence of the tunnel current on the tip–sample separation that enables the STM to locally probe surfaces with an extremely high spatial resolution. This can be understood from an approximation of the spatial extent of the tunnel current as a function of lateral position, Δx, and tip radius of curvature, R [66]

$$I(\Delta x) \;\approx\; I_0\,\exp\!\left(\frac{-(\Delta x)^2}{R}\sqrt{\frac{2m\phi_0}{\hbar^2}}\right). \tag{2.5}$$

For a standard barrier-height of $\phi_0 = 5$ eV, and a tip radius of curvature of 10 Å, at $\Delta x = 5$ Å the tunnel current drops by 94%. While this simple calculation assumes a rather small radius of curvature for the tip apex, this can be readily achieved with delicate tip preparation and *in situ* reformation of the tip apex (see section 5.2 for details). In practice, the STM lateral resolution exceeds these predicted values, with modern designs capable of reaching the sub-ångström regime [135, 138, 183–188].

2.1 Tunneling Spectroscopy

Local tunneling spectroscopy is most often performed by disengaging the feedback loop and varying the bias voltage, $V_{\text{d.c.}}$, while measuring the tunnel current, $I_{\text{d.c.}}$, in order to produce a current–voltage (I–V) characteristic for the tunnel junction (Fig. 2.3a). The precise curvature of the I–V characteristic is modulated by the energy-dependent LDOS(ε) of the tip and sample. In particular, the tunnel current flowing through the STM junction is a product

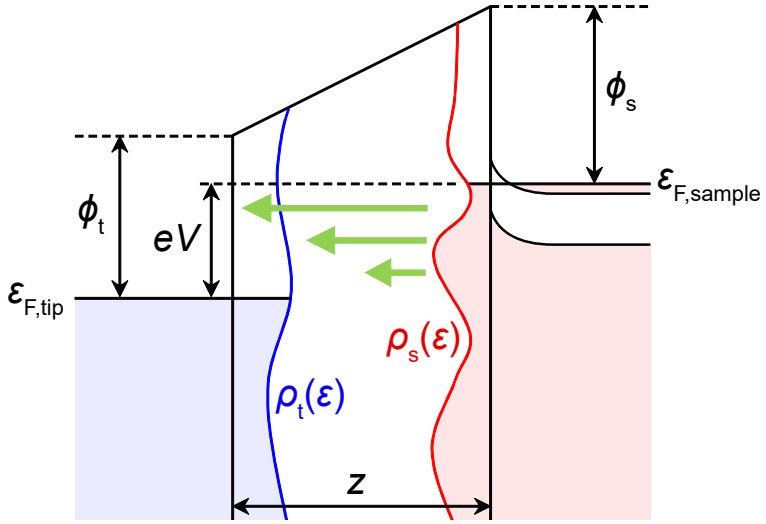

Figure 2.2: Schematic 1D metal–vacuum–semiconductor energy profile. A negative sample bias shifts the Fermi level ($\varepsilon_{\text{F,sample}}$) of the degenerately doped semiconductor $e|V|$ above the Fermi level of the tip, ($\varepsilon_{\text{F,tip}}$). Green arrows represent tunneling of electrons, while a longer arrow indicates a higher tunneling probability. The tip and sample density of states are represented by $\rho_t(\varepsilon)$ and $\rho_s(\varepsilon)$, respectively (filled states are shaded). This schematic has been adapted from figure 20.8 in [67].

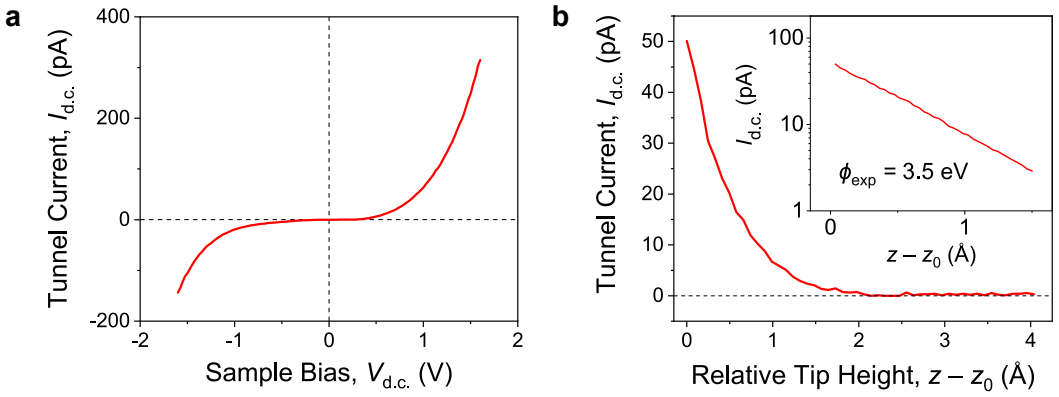

Figure 2.3: **a**, Measured I–V curves and **b**, I–z curves acquired with a tungsten tip on the Si(111)-(7×7) surface. The I–V curves were acquired with the tip–sample separation set by $V_{\text{d.c.}} = -1$ V and $I_{\text{d.c.}} = -20$ pA. The I–z curves were acquired with the initial tip–sample separation, z_0, set by $V_{\text{d.c.}} = 1$ V and $I_{\text{d.c.}} = 50$ pA. The inset shows the I–z curve on a semilog plot. Applying Eq. 2.6 to **b** finds $\phi_{\text{exp}} = 3.5$ eV.

of the both the tip LDOS, $\rho_{\text{t}}(\varepsilon)$, and sample LDOS, $\rho_{\text{s}}(\varepsilon)$, in the energy range $[\varepsilon_{\text{F,tip}},\ \varepsilon_{\text{F,sample}} = \varepsilon_{\text{F,tip}} + eV]$ (see Fig. 2.2). Here, $\varepsilon_{\text{F,tip}}$ and $\varepsilon_{\text{F,sample}}$ are the tip and sample Fermi levels, respectively and e is the elementary charge. The ideal tip material should have a near-constant LDOS ($\rho_{\text{t}}(\varepsilon) \approx \rho_0$) in order to minimize tip-induced artifacts in the measurements (the geometry of the tip apex also contributes to the LDOS shape). In practice, the transition metals tungsten, gold, silver, platinum and iridium are typically used for STM tips and the tip LDOS is often characterized by performing tunneling spectroscopy on a well known sample.

While $\rho_{\text{s}}(\varepsilon)$ and $\rho_{\text{t}}(\varepsilon)$ certainly modulate the I–V curve, the induced variations are quite small and it can be difficult to extract meaningful quantitative information from the I–V curve alone. This is because the tunnel current increases monotonically with increasing bias voltage, creating a strong background signal that obscures features in the I–V curve that are due to $\rho_{\text{s}}(\varepsilon)$ and $\rho_{\text{t}}(\varepsilon)$. A solution to this problem is to first determine the differential conductance, $\mathrm{d}I/\mathrm{d}V$ and then normalize it with the I–V curve via $(\mathrm{d}I/\mathrm{d}V)/(I/V)$ [189]. This normalized differential conductance curve is approximately proportional to to $\rho_{\text{s}}(\varepsilon)$. In fact, the quantitative connection between ρ_{s} and

$(\mathrm{d}I/\mathrm{d}V)/(I/V)$ is an active area of research with the STM community [67, 190–193]. The differential conductance $(\mathrm{d}I/\mathrm{d}V)$ can be straight-forwardly acquired from numerical differentiation of the I–V curve; however, this can significantly decrease the signal-to-noise of the measurement. An alternative method for acquiring the differential conductance is to use a lock-in amplifier together with a small a.c. sine-wave voltage modulation, $V_{\mathrm{a.c.}}(t)$, added to the overall d.c. bias voltage, $V_{\mathrm{d.c.}}$ (see [67] for a detailed explanation). In this case, the $\mathrm{d}I/\mathrm{d}V$ is acquired simultaneously with the raw tunnel current (I). An important consideration for $\mathrm{d}I/\mathrm{d}V$ spectroscopy using a lock-in amplifier is to set the lock-in phase such that the capacitive component is entirely in one channel, while the 90° out-of-phase resistive component is entirely in the other channel. This latter channel is localized to the tunnel junction, while the capacitive component is delocalized and can be measured even with the tip retracted several centimeters away from the sample. If the bias voltage modulation frequency is kept well-above the feedback loop bandwidth, the feedback loop can be re-engaged and the differential conductivity measurement remains valid because the tip height does not respond to $V_{\mathrm{a.c.}}(t)$.

The current–distance (I–z) characteristic is another form of tunneling spectroscopy. Here, the feedback loop is opened and the tip–sample separation, z, is varied, while recording the tunnel current, $I_{\mathrm{d.c.}}$ (I–z curve). The current decays exponentially with the tip–sample separation (Fig. 2.3b). Accordingly, I–z curves can be used to determine the characteristic decay constant, κ, which is related to the barrier-height of the tunnel junction (ϕ_0) via Eq. 2.3. The experimentally measured apparent barrier-height, ϕ_{exp}, is typically defined by rearranging Eq. 2.4 into

$$\phi_{\mathrm{exp}} = \frac{\hbar^2 \kappa^2}{2m} = \frac{\hbar^2}{8m}\left(\frac{\mathrm{d}\ln I}{\mathrm{d}z}\right)^2, \tag{2.6}$$

and assuming only electrons at the Fermi level contribute to tunneling ($\varepsilon = 0$ eV). Recent work has demonstrated that measurements of $\mathrm{d}I/\mathrm{d}z$ and $\mathrm{d}^2I/\mathrm{d}z^2$ can be used to more accurately describe the relationship between κ and ϕ [194]. Similar to the case of $\mathrm{d}I/\mathrm{d}V$ spectroscopy, $\mathrm{d}I/\mathrm{d}z$ and $\mathrm{d}^2I/\mathrm{d}z^2$ can also be

acquired through the use of a lock-in amplifier and a tiny $z_{\mathrm{a.c.}}(t)$ modulation applied to the z-piezo, typically no more than a few picometers. However, recent measurements with a dual AFM/STM system have shown that $\mathrm{d}I/\mathrm{d}z$ spectroscopy is strongly dependent on the bias voltage, and difficult to fully interpret [195].

A third type of spectroscopy is sometimes performed that combines both I–V and I–z spectroscopy by varying the bias voltage, $V_{\mathrm{d.c.}}$, with the feedback loop engaged [196–198]. In this way, the bias voltage can be freely varied without any undesirable tip or surface modifications occurring due to the large currents that can occur with an unregulated tip–sample separation. This form of tunneling spectroscopy produces what are known as z–V curves. However, while z–V curves are less prone to tip–sample contact during acquisition, interpretation of the data becomes more difficult as any spatial variations in κ will also modulate the tip-height, which can easily obscure features that are due to $\rho_{\mathrm{t}}(\varepsilon)$. This type of tunneling spectroscopy has been used to detect standing waves in the vacuum gap due to field emission resonances [65, 199]

2.2 Taking Images of Atoms

The first report on tunneling through a controllable vacuum gap by G. Binnig, H. Rohrer, C. Gerber and E. Weibel in 1982 described the distinctive exponential dependence of the tunnel current with tip–sample separation [59]. Then, by laterally scanning the tip while in constant-current mode, the resulting topography of the Au(110) electronic surface states was mapped out [60]. This initial demonstration of the STMs capabilities did not achieve atomic resolution on Au(110). In fact, the original STM did not have enough lateral resolution to measure a difference between Au(110)-(1×2) and Au(110)-(1×3), until improvements were made to the design in 1983 [200]. However, by switching the sample under investigation to one with a much larger surface reconstruction, Binnig et al. were able to demonstrate for the first time atomic resolution with the STM on the Si(111)-(7×7) surface [61]. The Si(111)-(7×7) surface

was chosen because of a large spacing between adatoms[3] (7 Å), as compared to a close-packed metal surface such as Au(111) (3 Å). Also, Si(111)-(7×7) has a much larger surface corrugation of 2 Å, compared to 0.3 Å for a close-packed-metal like gold. Atomic resolution on a close-packed metal surface was finally achieved in 1987 by Hallmark et al. on Au(111) [63]. It was noted that the atomic corrugation of the surface ($\sim$ 30 pm) was an order of magnitude larger than the theoretically predicted corrugation of the surface LDOS at the Fermi level ($\sim$ 1 pm) [63, 65, 66]. Subsequent theoretical developments and experimental studies determined that the increased surface corrugation is due to the d_{z^2} tip state of transition metal atoms [66, 201] and elastic deformation of the tip–surface junction through adhesion forces [202].

> *STM graphs are not simply reproductions of surface-atom corrugation. They rather reflect the corrugation of the electron wave functions near the Fermi level, roughly in the middle of the vacuum gap. To make a quantitative connection with the corrugation of the surface cores, a detailed tunnel theory on the atomic scale is required.*
>
> – Gerd Binning and Heinrich Rohrer, 1982 [203]

A high quality tip is essential for acquiring highly corrugated images of atoms [61, 63, 201, 202, 204–206] and molecules [135, 183–185, 195, 206–213] on surfaces. The wavefunction of the apex atom on the STM tip can be approximated using the hydrogenic atomic orbitals (s, p_z, d_{z^2}, d_{xz}, $d_{x^2-y^2}$, etc.), where each of these tip-state wavefunctions has a unique 3D shape that overlaps with the local 3D wavefunction of the sample surface. The hydrogenic orbitals are a good approximation, but there are subtle differences such as the d-state electron wavefunction being relatively close to the nucleus for a free atom, whereas atoms in a bulk-state have their d-state electron wavefunction protrude out much farther [214]. In fact, it is now widely accepted that the sharp d-band orbitals of a transition metal tip apex are what provide the atomic resolution in STM [65, 66, 214, 215]. However, different wavefunctions at the tip apex can

[3] An adatom is an adsorbed atom that lies on the surface of a crystal.

lead to a wide variety images for the same sample surface [216]. One such example finds that tip states with a quantum number $m \neq 0$ completely invert the topographic contrast (tunnel current contrast) during constant-current (constant-height) imaging [66, 217]. Additional complications arise in the interpretation of STM images due to the principle of reciprocity, which states that features in the image can be interpreted as the tip imaging the sample, or the sample imaging the tip. This is evident experimentally when a very sharp feature is lying on the sample surface; a blunt tip that images this feature will produce an image that reveals the topographic nature of the tip apex [67]. If STM measurements are to be performed on an unknown sample, these experimental complications can be overcome by calibrating the tip-state with a well-known sample like copper or gold. For these reasons, great care must be taken when preparing the STM tip (see section 5.2), and then subsequently interpreting the imaging and tunneling spectroscopy results.

STM images are acquired by sampling either the tunnel current (constant-height mode), or the tip-height (constant-current mode), while raster scanning the tip across the sample surface. Every data channel of the STM (z, I, $\mathrm{d}I/\mathrm{d}V$, $\mathrm{d}^2I/\mathrm{d}V^2$, $\mathrm{d}I/\mathrm{d}z$ etc.) outputs two arrays, typically between 128 $\times$ 128 and 512 $\times$ 512 in pixel size, for both left-travelling and right-travelling scan directions (or up and down). Very large arrays (1024 $\times$ 1024 pixels or even 8092 $\times$ 8092 pixels) require significantly longer acquisition times, limiting their applicability. However, with a clean environment, minimal thermal drift, and long-term tip stability, it is possible to acquire atomically-resolved images that are several hundred nanometers in size[4]. This is demonstrated in Fig. 2.4 and Fig. 2.5 for positive and negative voltages, respectively, on the Si(111)-(7×7) surface. In Fig. 2.4 three different incommensurate domains are visible (top, left, right), each having nucleated independently, before finally meeting and forming the domain walls along the center of the image. The surface

[4]All constant-current topography images, $z(x, y)$, that are presented in this thesis have been plane-fit-subtracted in order to account for any thermal drift that may have been present throughout the acquisition.

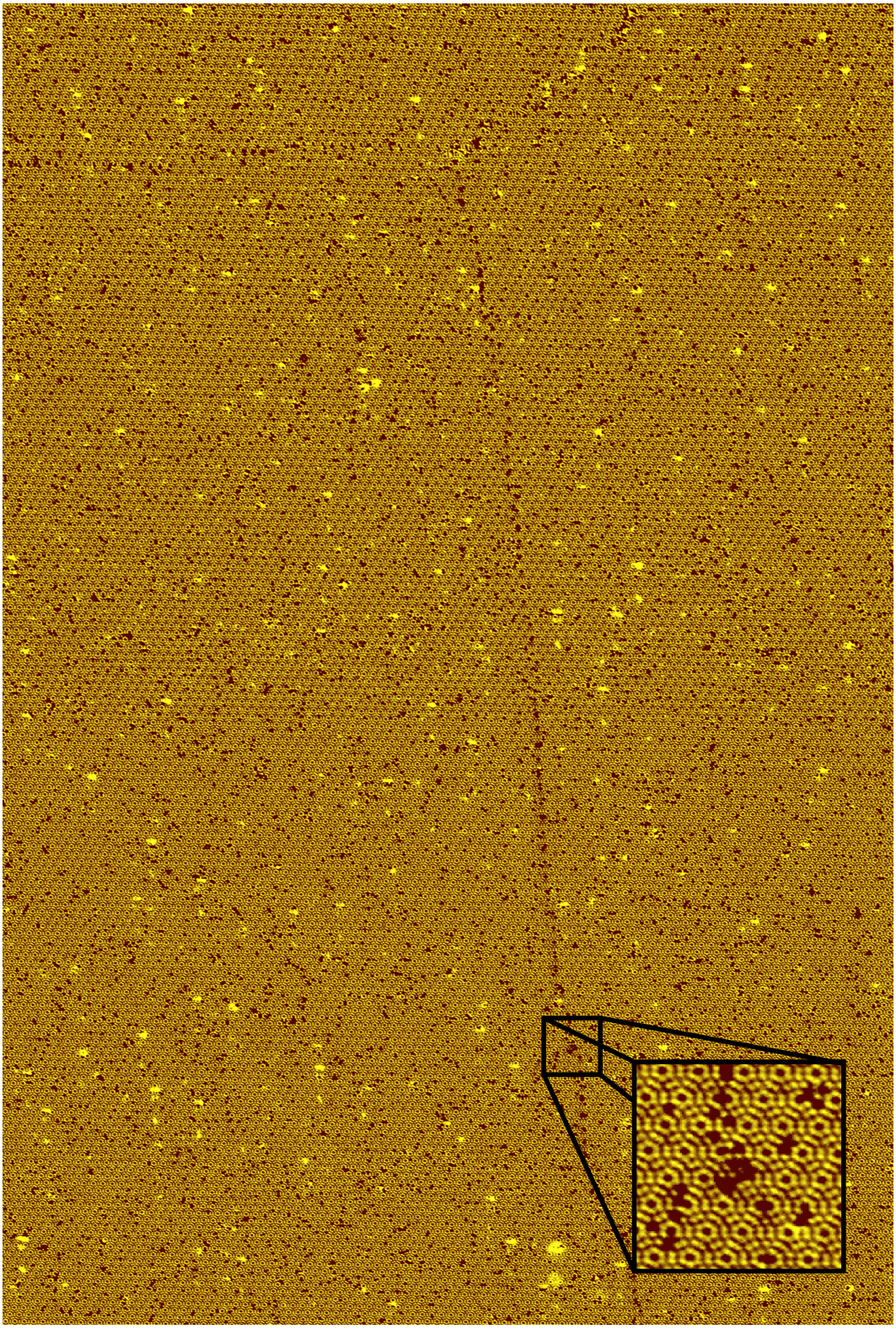

Figure 2.4: Atomically-resolved topography of a Si(111)-(7×7) surface that was acquired in constant-current mode at $V_{\mathrm{d.c.}} = +1.2$ V and $I_{\mathrm{d.c.}} = +200$ pA. Image size 230 nm × 340 nm (inset 15 nm × 15 nm); 180 minute scan for the original square image at 4096 × 4096 pixels; scan speed 300 nm/s.

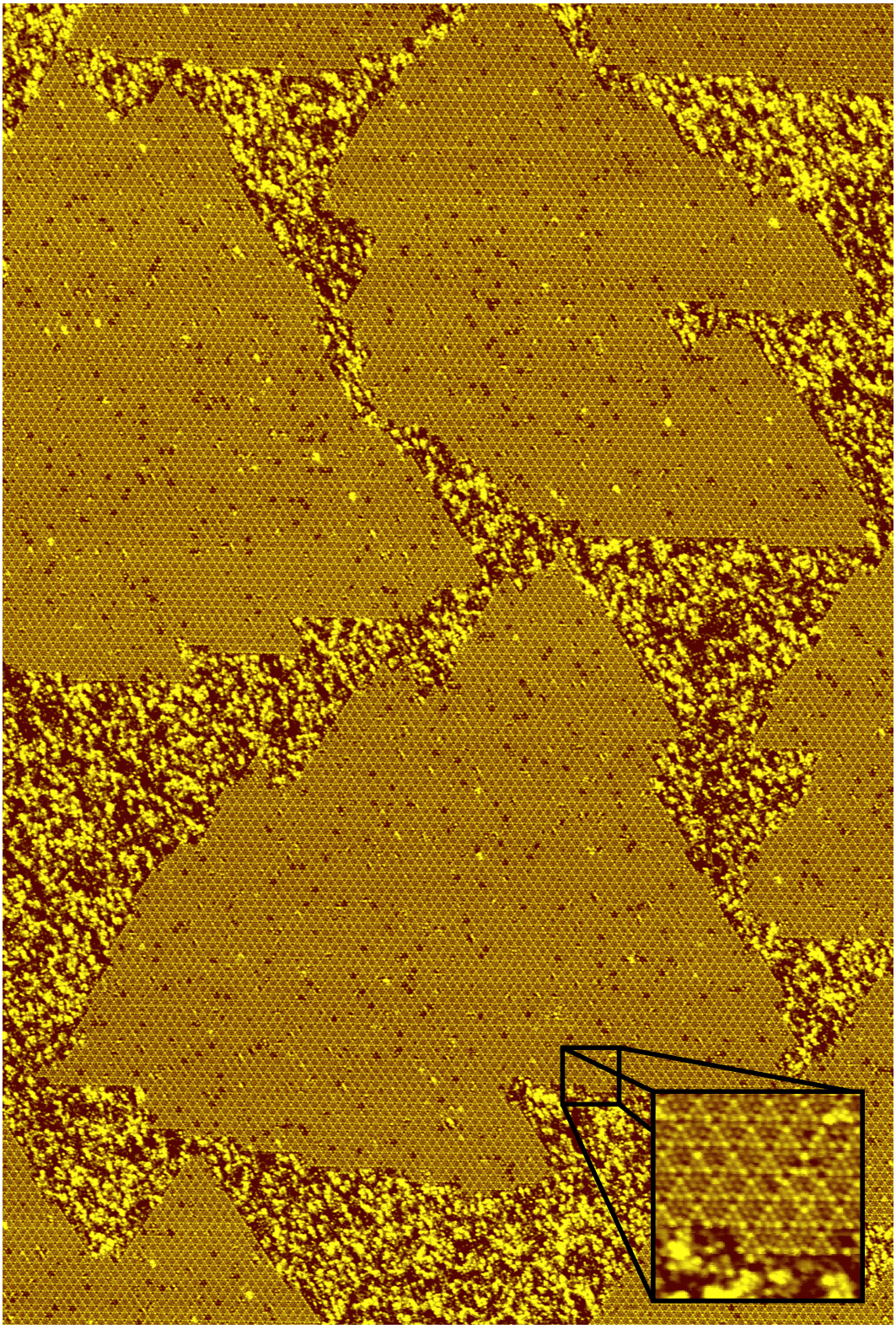

Figure 2.5: Atomically-resolved topography of a Si(111)-(7×7) surface that was acquired in constant-current mode at $V_{\text{d.c.}} = -1.2$ V and $I_{\text{d.c.}} = -200$ pA. Image size 230 nm × 340 nm (inset 15 nm × 15 nm); 220 minute scan for the original square image at 4096 × 4096 pixels; scan speed 250 nm/s.

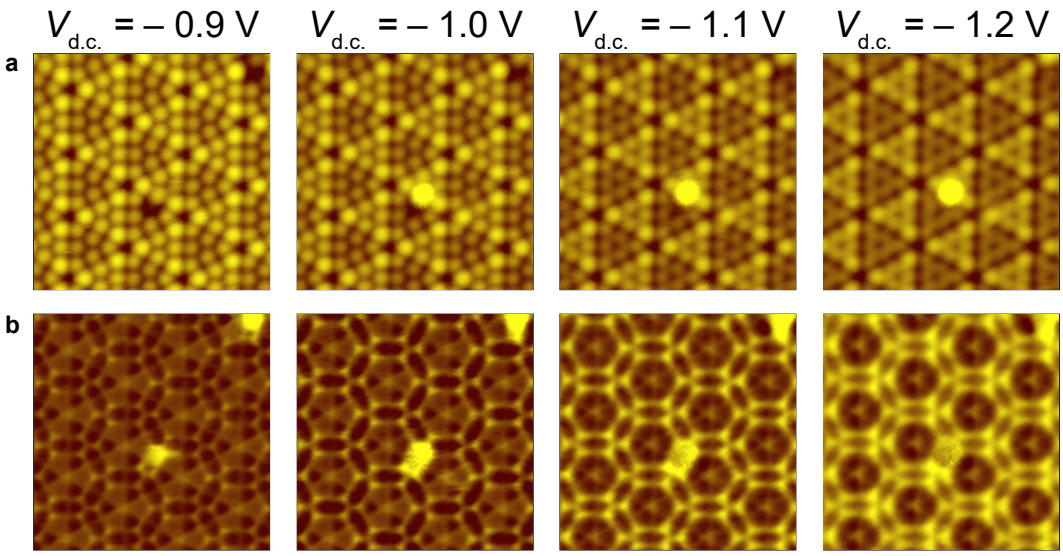

Figure 2.6: **a**, Atomically-resolved topography of a Si(111)-(7×7) surface along with **b**, the simultaneously acquired differential conductance ($\mathrm{d}I/\mathrm{d}V$) image at a modulation frequency of 7177 Hz, modulation amplitude of ± 50 mV and a current amplifier with 10^8 gain and 15 kHz bandwidth. The images were acquired in constant-current mode at $I_{\mathrm{d.c.}} = -100$ pA and $V_{\mathrm{d.c.}}$ as shown above the topography images. Image size 9 nm × 9 nm; 256 × 256 pixels; scan speed 9.1 nm/s. The colourmap is 22 pm (brown) to 160 pm (gold) for **a** and −75 pS (brown) to +210 pS (gold) for **b**.

in Fig. 2.5 was prepared with a shorter annealing time (see section 5.3.1 for details), resulting in multiple independently-nucleated domains of 7×7 with non-crystalline regions spaced inbetween.

Constant-current $\mathrm{d}I/\mathrm{d}V$ imaging of the Si(111)-(7×7) surface using the lock-in amplifier technique is shown in Fig. 2.6. A missing center-adatom is evident in the images for both topography (Fig. 2.6a) and differential conductance (Fig. 2.6b). For a detailed explanation of STM imaging on the Si(111)-(7×7) surface see section 6.6 and [64–67, 218, 219]. When using a lock-in amplifier to collect the data, it is important to ensure that the acquisition time per pixel is greater than the integration-time-constant on the lock-in amplifier. Furthermore, if the feedback loop is engaged during lock-in amplifier measurements of the tunnel current, the modulation frequency that is used for lock-in detection must be kept beyond the bandwidth of the STM feedback loop, and within the bandwidth of the high-gain current amplifier.

2.3 STM Tunneling Models

The STM exhibits spectacular spatial resolution, but interpretation of the data can be quite challenging. Accordingly, it has become routine to support the measured data with theory and simulation. Several models have been proposed with varying levels of theoretical sophistication. Basic models are confined to one spatial dimension and explore the behaviour of the tunnel current as a function of the tip–sample separation, bias voltage and barrier heights of the tip and sample, whereas complex three-dimensional models such as *ab initio* density functional theory are well-suited for directly simulating STM images [220–227].

The theoretical models used throughout this thesis are strictly one-dimensional and used to simulate the tunnel current flowing through the tip–sample junction. In section 2.3.1, the tunneling model developed by John G. Simmons is considered, where any effects due to the LDOS are assumed to be constant [228–230]. The effect of an image potential on the tunnel current calculations is presented in section 2.3.2. At very close tip–sample separations ($z < 10$ Å), the image potential is found to greatly alter the magnitude of the tunnel current. Section 2.3.3 presents a tunneling model that was first introduced by John Bardeen, which accounts for the effects of the tip and sample LDOS. The one-dimensional Bardeen tunneling model described in section 2.3.3 was modified to account for image potential effects in section 6.2.

2.3.1 Simmons Tunneling Model

The original Simmons tunneling model [228, 229] derives the current density that is produced when a voltage is applied between two planar metal electrodes separated by a nanometer-scale insulating film. Even though the model was derived two decades before the invention of the STM, and it assumes an entirely planar geometry, the Simmons model has been effectively used as a first-approximation for modeling the tunnel current flowing through the STM junction [88, 91, 92, 136, 137]. The Simmons model assumes zero temperature,

one spatial dimension and a density of states that is constant with energy. The tunnel current is given as [228–230]

$$I = \frac{meA}{2\pi^2\hbar^3}\left[eV\int_0^{\varepsilon_\mathrm{F}-eV} T(\varepsilon)\,\mathrm{d}\varepsilon + \int_{\varepsilon_\mathrm{F}-eV}^{\varepsilon_\mathrm{F}} (\varepsilon_\mathrm{F}-\varepsilon)\,T(\varepsilon)\,\mathrm{d}\varepsilon\right], \tag{2.7}$$

where m is the electron mass, e is the elementary charge, A is the spatial area of the tunnel current, $\hbar$ is the reduced Planck constant, V is the applied voltage, ε_F is the Fermi level energy and $T(\varepsilon)$ is the tunneling transmission probability. $T(\varepsilon)$ is determined from the WKBJ approximation via (see [64–67, 228–230])

$$T(\varepsilon) = \exp\!\left(-\frac{2\sqrt{2m}}{\hbar}\int_{z_1}^{z_2}\sqrt{\varepsilon_\mathrm{F}-\varepsilon+\phi(x)}\;\mathrm{d}x\right), \tag{2.8}$$

where in general, $\phi(x)$ is the height of the barrier as a function of position between the tip and sample, and z_1, z_2 are positions where the barrier height crosses the Fermi level energy (of the tip at positive bias and of the sample at negative bias). The tunneling probability is approximated as [228–230]

$$T(\varepsilon) \approx \exp\!\left(-\frac{2\beta\delta\sqrt{2m}}{\hbar}\sqrt{\varepsilon_\mathrm{F}-\varepsilon+\overline{\phi}}\right), \tag{2.9}$$

where $\overline{\phi}$ is the average barrier-height given by

$$\overline{\phi}(\phi_\mathrm{t},\phi_\mathrm{s},V,z) = \frac{1}{\delta}\int_{z_1}^{z_2}\phi(x,\phi_\mathrm{t},\phi_\mathrm{s},V,z)\,\mathrm{d}x\,, \tag{2.10}$$

where ϕ_t is the barrier height of the tip (determined by the material work function, see [182]), ϕ_s is the barrier height of the sample, z is the tip–sample separation, β is a correction factor near unity and $\delta = z_2 - z_1$ is the effective barrier-width. For a standard trapezoidal barrier shape, ($z_1 = 0$, $z_2 = z$, red solid line in Fig. 2.7), the following expressions define the barrier-height

$$\phi(x,\phi_\mathrm{t},\phi_\mathrm{s},V,z) = \begin{cases} \phi_\mathrm{t} + \dfrac{x}{z}(\phi_\mathrm{s}-\phi_\mathrm{t}-e|V|) & , \quad V \geq 0 \\ \phi_\mathrm{t} + \dfrac{x}{z}(\phi_\mathrm{s}-\phi_\mathrm{t}+e|V|) & , \quad V < 0 \end{cases} \tag{2.11}$$

and the effective barrier-width

$$\delta(\phi_\mathrm{t},\phi_\mathrm{s},V,z) = \begin{cases} z & , \quad -\phi_\mathrm{t} < eV < \phi_\mathrm{s} \\ \dfrac{z\,\phi_\mathrm{t}}{\phi_\mathrm{t}-\phi_\mathrm{s}+e|V|} & , \quad \phi_\mathrm{s} \leq eV \\ \dfrac{z\,\phi_\mathrm{s}}{\phi_\mathrm{s}-\phi_\mathrm{t}+e|V|} & , \quad eV \leq -\phi_\mathrm{t} \end{cases} \tag{2.12}$$

The average barrier-height, $\overline{\phi}$, is determined by placing Eq. 2.11 into Eq. 2.10, yielding

$$\overline{\phi}(\phi_{\mathrm{t}},\phi_{\mathrm{s}},V)=\begin{cases}(\phi_{\mathrm{t}}+\phi_{\mathrm{s}}-e|V|)/2 & , \quad -\phi_{\mathrm{t}}<eV<\phi_{\mathrm{s}} \\ \phi_{\mathrm{t}}/2 & , \quad \phi_{\mathrm{s}}\leq eV \\ \phi_{\mathrm{s}}/2 & , \quad eV\leq-\phi_{\mathrm{t}}\end{cases} \tag{2.13}$$

The correction factor, β, in Eq. 2.9 is very close to unity and in general, it is given by the expression [228–230]

$$\beta(\phi_{\mathrm{t}},\phi_{\mathrm{s}},V)=\begin{cases}1-\dfrac{1}{8\delta}\displaystyle\int_{z_1}^{z_2}\left(\frac{\phi(x)}{\overline{\phi}}-1\right)^2\mathrm{d}x & , \quad V\geq 0 \\ 1-\dfrac{1}{8\delta}\displaystyle\int_{z_1}^{z_2}\left(\frac{\phi(x)-e|V|}{\overline{\phi}-e|V|}-1\right)^2\mathrm{d}x & , \quad V<0\end{cases} \tag{2.14}$$

For a trapezoidal barrier (Eq. 2.11) this yields ($23/24\leq\beta\leq 1$)

$$\beta(\phi_{\mathrm{t}},\phi_{\mathrm{s}},V)=\begin{cases}1-\dfrac{1}{24}\left(\dfrac{e|V|-\phi_{\mathrm{s}}+\phi_{\mathrm{t}}}{e|V|-\phi_{\mathrm{s}}-\phi_{\mathrm{t}}}\right)^2 & , \quad 0\leq eV<\phi_{\mathrm{s}} \\ 1-\dfrac{1}{24}\left(\dfrac{e|V|+\phi_{\mathrm{s}}-\phi_{\mathrm{t}}}{e|V|-\phi_{\mathrm{s}}-\phi_{\mathrm{t}}}\right)^2 & , \quad -\phi_{\mathrm{t}}<eV<0 \\ \dfrac{23}{24} & , \quad \phi_{\mathrm{s}}\leq eV \\ \dfrac{23}{24} & , \quad eV\leq-\phi_{\mathrm{t}}\end{cases} \tag{2.15}$$

After substituting Eq. 2.9 into Eq. 2.7, taking advantage of the approximation $\alpha\sqrt{\overline{\phi}+e|V|}\gg 1$, and ignoring any terms with $\sqrt{\overline{\phi}+\varepsilon_{\mathrm{F}}}$, $\sqrt{\overline{\phi}+\varepsilon_{\mathrm{F}}-\varepsilon}/\alpha^3$ or $1/\alpha^4$, where $\alpha=2\beta\delta\sqrt{2m}/\hbar$ (see [228, 229] for details), the final expression for the tunnel current becomes

$$\begin{aligned}I=\frac{\pm eA}{\hbar(2\pi\beta\delta)^2}\Bigg[&\overline{\phi}\cdot\exp\left(-\frac{2\beta\delta\sqrt{2m}}{\hbar}\sqrt{\overline{\phi}}\right)\ldots \\ &\ldots-\left(\overline{\phi}+e|V|\right)\cdot\exp\left(-\frac{2\beta\delta\sqrt{2m}}{\hbar}\sqrt{\overline{\phi}+e|V|}\right)\Bigg],\end{aligned} \tag{2.16}$$

where A is the tunnel junction contact area and the top case of $\pm$ occurs at positive bias (V > 0), while the bottom case occurs at negative bias (V < 0).

2.3.2 Image Potential

Simmons also considered the effect of an image charge on the potential barrier height and width (black and blue solid lines in Fig. 2.7) [228, 229]. The result is that the barrier height, $\phi(x, \phi_t, \phi_s, V, z)$, is reduced by an amount

$$\phi_{img}(x, z) = -\frac{e^2}{8\pi\epsilon_0}\left[\frac{1}{2x} + \sum_{n=1}^{\infty}\left(\frac{nz}{(nz)^2 - x^2} - \frac{1}{nz}\right)\right], \tag{2.17}$$

where ϵ_0 is the permittivity of free space. This expression is equivalent to [230]

$$\phi_{img}(x, z) = -\frac{e^2}{16\pi\epsilon_0 z}\left[2\psi(1) - \psi\left(\frac{x}{z}\right) - \psi\left(1 - \frac{x}{z}\right)\right], \tag{2.18}$$

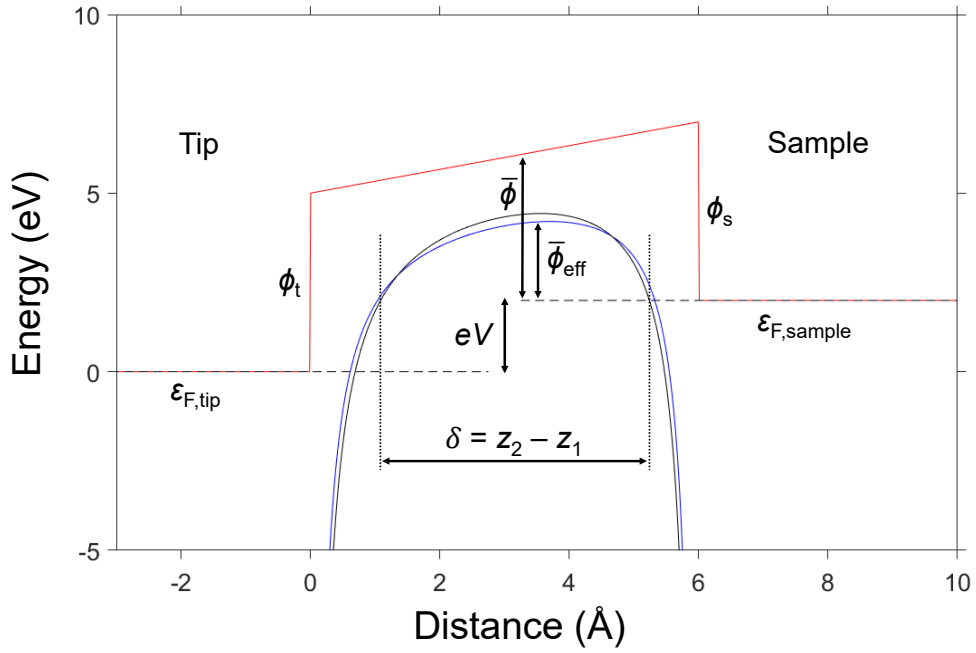

Figure 2.7: Schematic metal–vacuum–metal energy profile including image potential effects. A negative bias on the sample shifts the Fermi level ($\varepsilon_{F,sample}$), above the Fermi level of the tip ($\varepsilon_{F,tip}$) by an amount $e|V|$. The tip is positioned $z = 6$ Å above the sample surface, while the tip and sample barrier heights (ϕ_t, ϕ_s) are both 5 eV. The standard 1D trapezoidal barrier, $\phi(x, \phi_t, \phi_s, V, z)$, Eq. 2.11 (red solid line), is modified by the applied field and its interaction with the image potential, $\phi_{img}(x, z)$, resulting in a reduced barrier-height (Eq. 2.17 and Eq. 2.18), $\phi_{eff}(x, \phi_t, \phi_s, V, z) = \phi(x, \phi_t, \phi_s, V, z) + \phi_{img}(x, z)$, and a reduced barrier-width (Eq. 2.20), $\delta = z_2 - z_1$ (black solid line). The blue solid line was calculated using a polynomial approximation for the image potential (Eq. 2.19). The constants $\bar{\phi}$ and $\bar{\phi}_{eff}$ are the average values of $\phi(x)$ and $\phi_{eff}(x)$ between z_1 and z_2.

where $\psi(x)$ is the digamma function (the logarithmic derivative of the gamma function). These two equivalent expressions (Eq. 2.17 and Eq. 2.18, solid black line in Fig. 2.7) can be approximated as (solid blue line in Fig. 2.7)

$$\phi_{\mathrm{img}}(x,z) \approx -\frac{1.15\, e^2 \ln 2}{16\pi\epsilon_0}\left[\frac{z}{x(z-x)}\right]. \tag{2.19}$$

The effective barrier-width, $\delta = z_2 - z_1$ (Fig. 2.7), is calculated from the two positive roots of

$$\phi(x,\phi_{\mathrm{t}},\phi_{\mathrm{s}},V,z) + \phi_{\mathrm{img}}(x,z) = \begin{cases} 0 & , \quad V \geq 0 \\ e\,|V| & , \quad V < 0 \end{cases} \tag{2.20}$$

2.3.3 Bardeen Tunneling Model

The original Bardeen tunneling model [175] incorporates three-dimensional wavefunctions to solve the time-independent Schrödinger equation for the tip and sample subsystems independently, then combines the two subsystems and applies time-dependent perturbation theory to approximate the tunneling probability between two superconductors separated by a thin film. It has been applied to scanning tunneling microscopy [66, 67, 231] and in its most general form, the tunnel current, I, is given by

$$I = \frac{4\pi e}{\hbar}\sum_{i,f} |M_{fi}|^2 \delta(\varepsilon_f - \varepsilon_i)\,, \tag{2.21}$$

where e is the elementary charge, $\hbar$ is the reduced Planck constant and E_i, E_f are the initial and final energy of the electron, respectively. The term $|M_{fi}|^2$ is the tunneling probability for each transition ($i \rightarrow f$; it is also referred to as the tunneling matrix element) and it is given by

$$M_{fi} = \frac{\hbar^2}{2m}\int_S \Big[\psi_i(\boldsymbol{r})\,\nabla\psi_f^*(\boldsymbol{r}) - \psi_f^*(\boldsymbol{r})\,\nabla\psi_i(\boldsymbol{r})\Big]\cdot \mathrm{d}\boldsymbol{S}\,, \tag{2.22}$$

where ψ_i and ψ_f are the wavefunctions of the tip and sample, respectively, and the integration is performed over the surface, S, lying within the barrier region. The tip and surface wavefunctions are generally unknown; however, the Bardeen tunneling model can be simplified by applying the energy-dependent,

zero temperature and one-dimensional approximations that replace the sum of states in Eq. 2.21 into an integral over the bias window [67]

$$I = \frac{4\pi e}{\hbar} \int_0^{eV} \rho_{\mathrm{t}}(\varepsilon - eV)\, \rho_{\mathrm{s}}(\varepsilon)\, T(\phi_{\mathrm{t}}, \phi_{\mathrm{s}}, \varepsilon, V, z)\, \mathrm{d}\varepsilon\,, \tag{2.23}$$

where ε is the energy, $\rho_{\mathrm{t}}(\varepsilon)$ is the energy-dependent tip density of states, $\rho_{\mathrm{s}}(\varepsilon)$ is the sample density of states, and V is the sample bias (see Fig. 2.2). The tunneling matrix element $|M_{fi}|^2$ is reduced to the transmission factor (see equation 20.53 in [67])

$$T(\phi_{\mathrm{t}}, \phi_{\mathrm{s}}, \varepsilon, V, z) \;=\; \xi \cdot \overline{\phi}(\phi_{\mathrm{t}}, \phi_{\mathrm{s}}, \varepsilon, V, z) \cdot e^{-2z\sqrt{\frac{2m}{\hbar^2}\overline{\phi}(\phi_{\mathrm{t}}, \phi_{\mathrm{s}}, \varepsilon, V, z)}}\,, \tag{2.24}$$

where ϕ_{t}, ϕ_{s} are the tip and sample barrier-heights, respectively, z is the tip–sample separation, m is the electron mass and $\xi = 2[\hbar\, A\, \psi_i(0)\, \psi_f(z)]^2/m$, where A is the tunneling area. The average barrier-height, $\overline{\phi}$, is calculated from $\phi(x)$ via Eq. 2.10 with $z_1 = 0$ and $z_2 = z$. The spatially-dependent barrier-height, $\phi(x)$, for a standard 1D trapezoidal barrier is given by

$$\phi(x, \phi_{\mathrm{t}}, \phi_{\mathrm{s}}, \varepsilon, V, z) = \phi_{\mathrm{t}} \pm e|V| \mp |\varepsilon| + \frac{x}{z}(\phi_{\mathrm{s}} - \phi_{\mathrm{t}} \mp e|V|)\,, \tag{2.25}$$

resulting in an expression for the average barrier-height given by

$$\overline{\phi}(\phi_{\mathrm{t}}, \phi_{\mathrm{s}}, \varepsilon, V) = \left(\frac{\phi_{\mathrm{t}} + \phi_{\mathrm{s}} \pm e|V|}{2}\right) \mp |\varepsilon|\,. \tag{2.26}$$

In Eq. 2.25 and Eq. 2.26, the top case ($\pm$, $\mp$) is used for positive bias (V > 0) and the bottom case is used for negative bias (V < 0). Also at negative bias, the substitution $|\varepsilon| \rightarrow e|V| - |\varepsilon|$ is made. If the density of states is flat for both the tip and sample, the Bardeen model (Eq. 2.23) agrees with the Simmons model (Eq. 2.16). As the voltage is increased, there is a gradual transition from the tunneling regime to the field emission regime and finally to the space-charge-limited regime [136, 232, 233].

Chapter 3

Ultrafast Terahertz Pulses

The wide-spread use of femtosecond lasers in the late 1980s [2] led to the development of new techniques for generating and detecting free-space propagating ultrafast THz pulses [151–156]. Prior to this, the terahertz band of the electromagnetic spectrum was largely unexplored and often labeled the 'THz gap', lying between the familiar mid-infrared and microwave regions. The on-going development of efficient and compact THz sources [234–249] and detectors [249–255] has helped to accelerate the considerable interest in ultrafast THz science and technology [34–43]. The two major applications that have attracted significant attention from various scientific disciplines are THz pulse spectroscopy [38–42, 256–259], and non-resonant THz control over matter [24, 26, 43, 157–164]. The low photon energy and non-contact nature of THz pulses make them well-suited for probing the electron dynamics of materials, or non-resonantly controlling the motion of charged carriers. Another unique aspect of THz technology is the ability to directly sample the amplitude and phase of the THz pulse electric field using a variety of processes. This chapter briefly summarizes the most commonly used techniques for generating and detecting ultrafast THz pulses using tabletop laser systems.

3.1 Generation

3.1.1 Ultrafast Photocurrent

A picosecond duration burst of current will radiate electromagnetic waves at THz frequencies (Fig. 3.1). Externally biased photoconductive antennas are widely used for accelerating charge carriers in photo-active semiconductors such as GaAs [155, 156, 244, 249, 250, 255] and silicon-on-sapphire [151, 152, 256]. In a traditional photoconductive antenna, femtosecond laser pulses irradiate a semiconductor surface and generate charge carriers. These charge carriers are subsequently accelerated by a static d.c. bias that is applied across two metal electrodes that have been etched onto the semiconductor surface. The applied bias is typically pulsed in order to minimize the power dissipation within the photoconductive antenna and prolong its lifetime. The power dissipation of the antenna is also minimized naturally because the photoexcited charge carriers become trapped and recombine with lifetimes between microseconds and picoseconds, depending on the material and its concentration of trapping sites. A photoconductive emitter can be modeled as a Hertzian

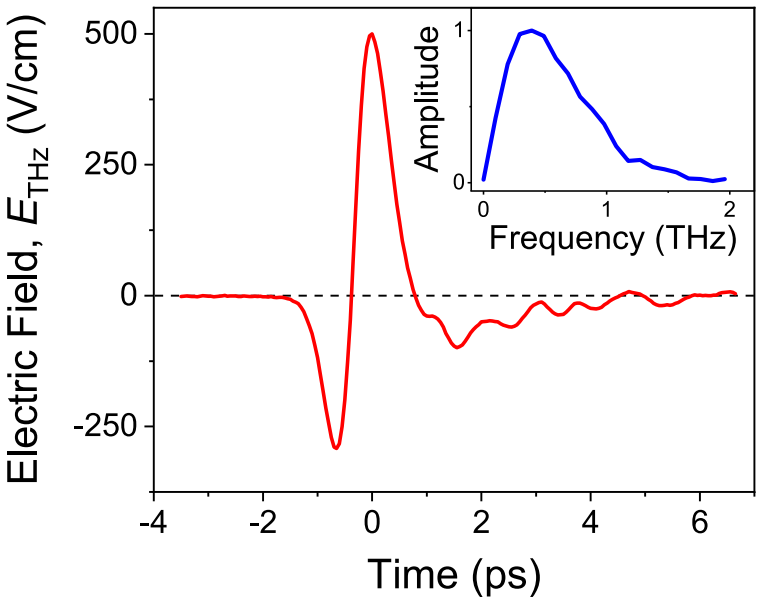

Figure 3.1: THz pulse electric field waveform generated by an interdigitated photoconductive antenna and electro-optically sampled using a 1 mm thick ZnTe crystal. Inset: corresponding amplitude spectrum.

dipole with $x \ll \lambda$, where x is the length of the dipole ($\sim$ optical spot size) and λ is the wavelength (300 µm at 1 THz). In the far-field, $r \gg x$, the THz pulse electric field amplitude, $E_{\mathrm{THz}}(t)$, is proportional to the time derivative of the photo-induced current, I_{PC}, as expressed by the equation [36]

$$E_{\mathrm{THz}}(t) = \frac{\mu_0 \, d_0}{4\pi} \frac{\sin(\theta)}{r} \frac{\mathrm{d}I_{\mathrm{PC}}}{\mathrm{d}t_{\mathrm{r}}} \, \hat{\theta} \,, \tag{3.1}$$

where μ_0 is the permeability of free space, d_0 is the spot size of the optical beam, r & θ define the position in space and $t_{\mathrm{r}} = t - r/c$ is the retarded time, where c is the speed of light.

Terahertz pulses have also been observed from femtosecond photoexcitation of semiconductor surfaces without an externally applied bias [83, 260–263]. In this case, charge carrier separation occurs naturally due to the built-in depletion field of the semiconductor surface, or the photo-Dember effect, or both. For most semiconductor surfaces, the polarity of the depletion field switches sign upon changing the type of dopant (acceptor or donor). This property proves useful for distinguishing between electron acceleration due to the built-in depletion field and the photo-Dember effect. This latter phenomena originates from differences in the mobilities for electrons and holes[1], resulting in a transient electric dipole near the semiconductor surface. The photo-Dember field can either complement or oppose the built-in field from the surface states. The photo-Dember effect is more significant for narrow gap semiconductors such as InAs [83, 262] and InSb [262]. This is because of a shorter penetration depth at infrared frequencies and a higher mobility for electrons as compared to holes, resulting in a large carrier density gradient that produces a strong photo-Dember field [262].

3.1.2 Nonlinear Optics

A non-resonant high intensity optical pulse that is propagating through a transparent medium can excite a multitude of nonlinear processes through

[1]The ratio $\mu_{\mathrm{e}}/\mu_{\mathrm{h}}$ for undoped samples in $\mathrm{cm}^2/(\mathrm{V{\cdot}s)}$: Si 1300/500; GaAs 8800/400; InAs 33,000/460; InSb 77,000/750 [264]

different phase-matching conditions [5]. These processes can generate phase-stable ultrafast THz pulses with center frequencies ranging from the far-infrared [153, 240–243] to the mid-infrared [246–248, 251]. Nonlinear processes can be understood by perturbatively expanding the electric-field-induced polarization, $\boldsymbol{P}$=(P_x, P_y, P_z), of a medium as

$$P_i = \epsilon_0 \sum_{j,k,l...}^{3} \left[\chi_{ij}^{(1)} E_j + \chi_{ijk}^{(2)} E_j E_k + \chi_{ijkl}^{(3)} E_j E_k E_l + ... \right], \tag{3.2}$$

where $j, k, l, ...$ are summed over the three Cartesian components, E_j is the component of the field in the j direction, ϵ_0 is the permittivity of free space, $\chi_{ij}^{(1)}$ is first order electric susceptibility tensor (rank 2), $\chi_{ijk}^{(2)}$ is the second order electric susceptibility tensor (rank 3) and $\chi_{ijkl}^{(3)}$ is the third order electric susceptibility tensor (rank 4). In general, for a lossless medium, the electric susceptibility tensors, $\chi_{ij}^{(1)}$, $\chi_{ijk}^{(2)}$ and $\chi_{ijkl}^{(3)}$, are composed of 9, 27 and 81 independent matrix elements, respectively. However, most crystal structures will have symmetries that reduce these large tensors to only a few non-zero elements. For example, ZnTe is a very common source for ultrafast THz pulses and due to its highly symmetric zincblende structure (crystal class $\overline{4}3m$), the second order susceptibility, $\chi_{ijk}^{(2)}$ has only six elements, all of which have the same value [5]. Accordingly, the electric susceptibilities, $\chi^{(1)}$, $\chi^{(2)}$ and $\chi^{(3)}$, are often written as scalar quantities and if we consider a monochromatic driving field, $E = E_0 \sin(\omega\, t)$, that is polarized in the z direction, then the total polarization can be written as

$$\begin{aligned} P_z \; = & \frac{\epsilon_0 \, {E_0}^2}{2} \, \chi^{(2)}(\omega - \omega = 0) \, ... \\ & ... + \epsilon_0 \, E_0 \Big[\, \chi^{(1)} \; + \frac{3 \, {E_0}^2}{4} \chi^{(3)}(\omega + \omega - \omega = \omega) \, \Big] \sin(\omega\, t) \, ... \\ & ... - \frac{\epsilon_0 {E_0}^2}{2} \, \chi^{(2)}(\omega + \omega = 2\,\omega) \cos(2\,\omega\, t) \, ... \\ & ... - \frac{\epsilon_0 {E_0}^3}{4} \, \chi^{(3)}(\omega + \omega + \omega = 3\,\omega) \sin(3\,\omega\, t) \, ... \end{aligned} \tag{3.3}$$

where the electric susceptibilities are, in general, frequency dependent, and for reference they are shown here with emphasis on the corresponding nonlinear optical process that occurs between the monochromatic photons. The

first term in Eq. 3.3, $\chi^{(2)}(\omega - \omega = 0)$, is known as optical rectification. It manifests as a d.c. polarization that is induced by the monochromatic electromagnetic wave propagating inside the medium. For a non-dispersive optical pulse with a time-dependent field amplitude, $E = E_0(t)\sin(\omega\, t)$, and a long temporal envelope as compared to ω^{-1}, the induced polarization will follow the temporal envelope of the optical pulse. Optical pulses with a temporal envelope in the range of 10–1000 fs can produce single-cycle THz pulses inside a non-centrosymmetric medium via optical rectification [5, 34, 36, 37]. In the far-field, the generated THz pulse electric field amplitude is proportional to $\partial^2\mathbf{P}^{(2)}/\partial t^2$.

The second term in Eq. 3.3 is the a.c. Kerr effect, $\chi^{(3)}(\omega + \omega - \omega = \omega)$. It results in an intensity-dependent-refractive-index at the carrier frequency, ω, and due to the Gaussian-like beam shape of most lasers, it leads to self-focusing of the laser beam inside the medium [5]. The third and fourth terms in Eq. 3.3 produce second harmonic radiation $(\omega + \omega = 2\,\omega)$ and third harmonic radiation $(\omega + \omega + \omega = 3\,\omega)$, respectively. If the driving field is a superposition of two frequencies, $E = E_1\sin(\omega_1\, t) + E_2\sin(\omega_2\, t)$, a similar expression to Eq. 3.3 can be formulated, but containing an additional frequency term at $|\omega_1 - \omega_2|$. This nonlinear process is known as difference frequency generation ($|\omega_1 - \omega_2| = \omega_3$), and it can generate THz photons (ω_3) from optical photons (ω_1, ω_2). It is important to note that these various nonlinear processes do not occur all at once, but rather each process must meet its corresponding phase-matching condition. For example, if we consider difference frequency generation, the condition $k_1 - k_2 = k_3$ must be met, where k_i is the wavenumber for photons at frequency ω_i.

3.1.3 Laser-Induced Gas Filamentation

A newly developed technique for generating ultrafast THz pulses is through laser-pulse-induced gas filamentation [36, 37, 234–239]. In this method, a high intensity ultrafast laser pulse centered at ω, and its second harmonic pulse centered at 2ω, are spatially focused inside a gas medium in order to generate

an ionized plasma and undergo four-wave rectification between photons with frequencies ω, ω and $2\omega + \omega_{\mathrm{THz}}$. It can be described as a third-order nonlinear process: $\chi^{(3)}(2\omega + \omega_{\mathrm{THz}} - \omega - \omega = \omega_{\mathrm{THz}})$ [37, 234, 236]. Second-order processes ($\chi^{(2)}$) are forbidden by the centrosymmetric nature of the gas and since the nonlinear coefficient of gases is very weak ($\chi^{(3)} = 0.17\ \mathrm{pm^2/V^2}$ for air compared to $2.8\ \mathrm{nm^2/V^2}$ for silicon [5]), the laser fields must be extremely intense. To a first approximation, the terahertz electric field amplitude is given by the relationship [37, 234, 236]

$$E_{\mathrm{THz}} \propto \chi^{(3)}\, E_{2\omega}\, E_{\omega}^{*}\, E_{\omega}^{*} \cos(\varphi)\,, \tag{3.4}$$

where φ is the relative phase difference between the fundamental E_ω and second-harmonic $E_{2\omega}$ beams (E_ω^* is the complex conjugate). However, a $\chi^{(3)}$ process acting alone cannot explain all of the experimental observations. Further studies have proposed that the two-color-excitation of the ionized plasma results in a third order conductivity, $\sigma^{(3)}$, giving rise to a third order current density, $J^{(3)}$, and a corresponding THz pulse, $E_{\mathrm{THz}} \propto \mathrm{d}J^{(3)}/\mathrm{d}t$ [36, 235]. An alternative technique for generating ultrafast THz pulses via laser-induced filamentation is to only use the fundamental frequency to generate the air-plasma, and then apply an external electric field to accelerate the free electrons [237].

3.2 Detection

All of the THz pulse generation techniques described in section 3.1 have a corresponding coherent detection scheme that utilizes very similar physical principles, but in a reversed geometry. These detection schemes directly sample the electric field amplitude and phase of a free-space-propagating THz pulse. The laser wavelength, laser pulse energy and signal-to-noise requirements are important considerations for selecting which generation and detection scheme to use.

The energy density of an electromagnetic wave that is propagating in vacuum is given by the expression $u = 1/2(\epsilon_0 E^2 + \mu_0 H^2) = \epsilon_0 E^2$, and the total energy

in the wave is given by $\varepsilon = A\,c\int_{-\infty}^{+\infty} u\,\mathrm{d}t$. Once the electric field waveform of the THz pulse has been obtained, the THz pulse energy can be estimated using

$$\varepsilon_{\mathrm{THz}} = \frac{A}{\eta_0}\int_{-\infty}^{+\infty} |E_{\mathrm{THz}}(t)|^2\,\mathrm{d}t\,, \tag{3.5}$$

where $E_{\mathrm{THz}}(t)$ is the terahertz electric field waveform, $\eta_0 = 377\ \Omega$ is the impedance of free space and A is the spot-size area. This value can be compared to direct measurements of the THz pulse energy using a bolometer or pyroelectric detector via the equation $\varepsilon_{\mathrm{THz,exp}} = P_{\mathrm{THz}}/f_{\mathrm{rep}}$, where P_{THz} is the measured average power of the THz beam and f_{rep} is the repetition rate of the laser.

3.2.1 Photoconductive Sampling

The electric field waveform of an ultrafast THz pulse is routinely acquired by focusing the THz pulse onto a photoconductive antenna, coincident with a femtosecond optical pulse, and measuring the resulting d.c. current as function of the relative time delay between the pulses [151, 152, 155, 156, 255]. Essentially, the optical pulse excites a thin layer of charge carriers near the semiconductor surface, while the local THz field provides a quasi-static bias voltage that drives a transient current across the metal electrodes of the antenna. Since the optical pulse duration ($\ll$ 1 ps) is much shorter than the THz pulse duration ($\sim$ 1 ps), the photocurrent is triggered in a narrow time-window at some phase of the THz pulse, as set by the relative time delay, τ, between the pulses. In this way, the measured current is sensitive to the phase and amplitude of the THz pulse, enabling coherent detection of the THz pulse electric field waveform, $E_{\mathrm{THz}}(t)$. However, the ultrafast transient current density that is generated across the photoconductive antenna, $J(t)$, does not get measured directly. Instead, the measured d.c. , current, $I(\tau)$, is the integrated response of $J(t,\tau)$, at a rate of f_{rep} as given by the expression [255]

$$I(\tau) = A\,f_{\mathrm{rep}}\int_{-\infty}^{+\infty} J(t,\tau)\,\mathrm{d}t\,, \tag{3.6}$$

where A is the contact area. In the limiting case where the photoexcited carriers are only present during the optical pulse, the photo-induced current, $I(\tau)$, is directly proportional to $E_{\mathrm{THz}}(t)$. This limiting case is nearly realized with semiconductors that have extremely short carrier lifetime ($t_{\mathrm{c}} < 1$ ps). Such short carrier lifetimes are due to a high concentration of trapping centers in the crystal structure, which is readily achieved using ion-implanted semiconductors [36] or low-temperature growth [258, 259]. On the other hand, if the carrier lifetime is extremely long ($t_{\mathrm{c}} \gg 1$ ps) [155], the detector acts as an integrator ($I(\tau) \propto \int_{\tau}^{\infty} E_{\mathrm{THz}}(t)\,\mathrm{d}t$). If the carrier lifetime is comparable to the THz pulse duration ($t_{\mathrm{c}} \sim 1$ ps), the photocurrent response, $I(\tau)$, is a convolution between $E_{\mathrm{THz}}(t)$ and $n(t-\tau)$, where $n(t-\tau)$ is the time-dependent carrier density after photoexcitation, decaying on a timescale of t_{c}. The expression for the current density is given by [255]

$$J(t,\tau) = \mu\, e\, n(t-\tau)\, E_{\mathrm{THz}}(t)\,, \tag{3.7}$$

where μ is the carrier mobility and e is the elementary charge.

3.2.2 Electro-Optic Sampling

A non-centrosymmetric crystal has a non-zero second-order electric susceptibility and under specific phase-matching conditions it can exhibit the linear electro-optic (EO) effect, $\chi^{(2)}(\omega + 0 = \omega)$ [5, 36, 37]. This process, which is also known as the Pockels effect, is a reciprocal process to optical rectification, and in a lossless medium, $\chi^{(2)}(\omega + 0 = \omega) = \chi^{(2)}(\omega - \omega = 0)$ [5]. Early pioneering work with electro-optic sampling of picosecond circuits [265, 266] paved the way for modern electro-optic sampling of free-space-propagating electromagnetic waves at terahertz [154, 240, 241, 243, 244, 250], multi-terahertz [246–248, 251], and near-infrared [267] frequencies. An important requirement for these measurements is that temporal duration of the sampling pulse is significantly shorter than the half-cycle duration of the electromagnetic pulse under investigation. In conventional electro-optic sampling, a femtosecond optical pulse and a far-infrared THz pulse are separated by a time-delay, τ,

and are coincident onto a nonlinear crystal such as ZnTe [243, 244, 250, 251], $LiNbO_3$ [240], $LiTaO_3$ [154], GaP [71, 241], GaSe [247, 248], BaB_2O_4 [267] or Lemke/amorphous polycarbonate [245]. The nonlinear crystal is usually orientated along a crystallographic direction that maximizes the strength of the EO effect. As the THz pulse and optical pulse co-propagate through the EO crystal, the THz pulse electric field induces a birefringence in the medium that modifies the polarization state of the optical pulse. However, all EO crystals have an intrinsic bandwidth due to the presence of phonon resonances. Accordingly, as the THz pulse propagates through the EO crystal, chromatic dispersion distorts the true THz waveform by suppressing frequencies that are close to the phonon resonances. These effects can be minimized by using a very thin EO crystal ($\ll 1$ mm). However, this comes at the cost of a smaller signal-to-noise ratio because the polarization rotation occurs across a shorter distance.

A very useful crystal for electo-optic detection at THz frequencies is ZnTe. This is because of a matching optical group velocity and THz phase velocity at 812 nm and 1.7 THz, respectively, a large EO coefficient, $\chi^{(2)}/2 = r_{41} = 4$ pm/V, and a high transmission for both frequencies [36, 268]. With ZnTe, the electro-optic effect is maximized when both of the electromagnetic waves are incident onto the crystal along the [110] direction and the polarization of both pulses is parallel to the $[1\bar{1}0]$ direction [36]. The THz pulse electric field, $E_{\mathrm{THz}}(\tau)$, is given by the expression [36]

$$E_{\mathrm{THz}}(\tau) \;=\; \frac{\lambda}{2\pi\, {n_{\mathrm{O}}}^3\, r_{41}\, L}\, \Delta\varphi(\tau)\,, \tag{3.8}$$

where $\lambda = 800$ nm is the center frequency of the sampling pulse, $n_{\mathrm{O}} = 2.853$ is the refractive index of ZnTe at 800 nm, and $\Delta\varphi(\tau)$ is the differential phase retardation that the sampling pulse experiences as it propagates a distance, L, through the EO crystal. After the sampling pulse has passed through the EO crystal, a quarter-wave-plate ($\lambda/4$) and a Wollaston prism are used to spatially separate the x and y components of its polarization into a pair of balanced photodiode detectors that are connected to a differential amplifier.

The differential phase, $\Delta\varphi$, is given by

$$\Delta\varphi = \sin^{-1}\left(\frac{I_y - I_x}{I_y + I_x}\right) \approx \frac{I_y - I_x}{I_y + I_x} \tag{3.9}$$

where I_x and I_y are the individual intensities of the two balanced photodiode detectors (if $E_{\mathrm{THz}} = 0$, $I_x = I_y$). Reflection losses at the interface of the EO crystal should also be considered when calculating the calibrated electric field value using Eq. 3.8 [241]. The refractive index for ZnTe is approximately 3.2 for frequencies near 1 THz [36]; at normal incidence, this corresponds to a amplitude transmission factor of 0.48.

3.2.3 Air-Biased Coherent Detection

Air-biased coherent detection (ABCD) of ultrafast THz transients is a newly developed technique that avoids the bandwidth limitations of EO crystals by performing four-wave mixing in gases, $\chi^{(3)}(\omega + \omega \pm \omega_{\mathrm{THz}} = 2\omega \pm \omega_{\mathrm{THz}})$ [36, 37, 252–254]. This process is the reciprocal of four-wave rectification, which was described in section 3.1.3. Since gases do not have phonon resonances or a well-defined interface, an incident ultrabroadband THz pulse will remain unperturbed as it propagates through the medium. However, while ABCD has an extremely large bandwidth, it comes at the cost of a lower signal-to-noise ratio. This is because gases have a significantly smaller nonlinear susceptibility as compared to solids, and as a result they require very intense laser fields for adequate signal-to-noise. Furthermore, since gases are isotropic (and therefore centrosymmetric), the first non-zero nonlinear susceptibility is $\chi^{(3)}$, and thus, the generated second-harmonic intensity, $I_{2\omega}$, is proportional to the square of the THz electric field and the phase information is lost.

To circumvent this problem, the initial demonstration of coherent detection in gases was performed using a homodyne technique, which resulted in a second-harmonic intensity that had one term linearly proportional to E_{THz}, and a second term that was quadratic in E_{THz} [37, 252]. In order to suppress the incoherent quadratic term, coherent detection was limited to a range of THz field strengths and sampling pulse intensities. These issues can be addressed

through a heterodyne detection technique [37, 253], where the measured second harmonic intensity is given by

$$I_{2\omega} \propto \left(\chi^{(3)} I_{\omega}\right)^2 \left[(E_{\mathrm{THz}})^2 + 2\, E_{\mathrm{THz}}\, E_{\mathrm{d.c.}} + (E_{\mathrm{d.c.}})^2\right], \tag{3.10}$$

where I_{ω} is intensity of the fundamental wave. For coherent detection, a lock-in amplifier is used to isolate the second term in Eq. 3.10 by referencing to a modulated quasi-static electric field bias, $E_{\mathrm{d.c.}}$, that is synchronized to change polarity at the repetition rate of the laser. The dynamic range and signal-to-noise ratio of heterodyne ABCD can be further enhanced by using a pair of balanced photomultiplier tubes [254].

Chapter 4

Terahertz Scanning Tunneling Microscopy

There have significant challenges to the development of a widespread ultrafast STM that is capable of retaining extremely high spatial resolution, while also simultaneously probing temporal dynamics on ultrafast timescales ($\sim$ 0.1–100 ps). All-electronic STM techniques readily maintain high spatial resolution at millisecond [118], microsecond [119, 120, 122, 124, 126, 269], nanosecond [121, 123, 125, 127] and sub-nanosecond timescales [129]. Ultrafast THz pulses have proven to be an effective way of coherently controlling electron tunneling phenomena in bulk materials [158, 160–164]. Here, we demonstrate that ultrafast THz pulses can be used to coherently modulate the bias voltage across the junction of a scanning tunneling microscope (THz-STM), and locally probe ultrafast electron dynamics with sub-picosecond time resolution. This has significant implications for future investigations because the fundamental timescale of several condensed matter phenomena covers the THz regime [34–43], including molecular vibrations [135, 270, 271], carrier thermalization [272], topological insulators [273], charge-density-waves [7, 138, 274], excitons [275, 276], polaritons [277] and magnons [278]. In order to demonstrate the viability of THz pulses to modulate the tunnel junction bias, a preliminary study was first performed with the STM scanhead located on the optics table at ambient pressure and temperature (Fig. 4.1).

4.1 Experimental Details

The laser system was a Ti:sapphire regenerative amplifier (Coherent RegA) seeded by a mode-locked oscillator (Coherent Micra). The output pulse was centered at 800 nm with a temporal duration of 100 fs, a repetition rate of $f_{\text{rep}} = 250$ kHz, and a pulse energy of approximately 4 µJ. In general, a high repetition rate laser is desirable for laser-assisted scanning probe microscopy in order to minimize lengthy acquisition times for 2D imaging and high resolution spectroscopy. Furthermore, a higher repetition rate improves the pulse-induced tunnel current sensitivity by directly increasing the number of laser pulses that reach the STM junction per second, thereby increasing the average pulse-induced current. For example, in the case of $f_{\text{rep}} = 250$ kHz, a single tunneling electron per laser pulse produces a current of $e \times f_{\text{rep}} = 40$ fA (where e is the elementary charge), and similarly, 0.16 fA (13 pA) for $f_{\text{rep}} = 1$ kHz (80 MHz). Femtoampere sensitivity can be achieved with state-of-the-art current amplifiers and low-pass filters; however, a standard STM amplifier typically operates in the nanoampere regime, which implies thousands of tunneling electrons per laser pulse. For THz-STM, there is a delicate balance between increasing the laser repetition rate for an improved tunnel

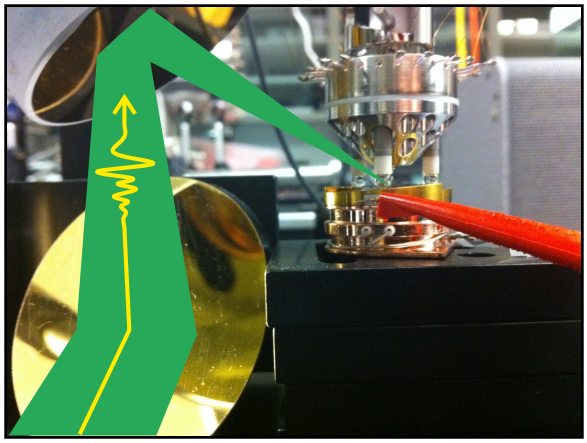

Figure 4.1: Photograph of the experimental setup for ambient THz-STM. Free-space-propagating terahertz pulses are focused onto the tip of a scanning tunneling microscope using an off-axis parabolic mirror with a focal length of 4 inches. The red banana clip on the right applies a d.c. bias voltage, $V_{\text{d.c.}}$, to the sample.

current sensitivity, and maintaining sufficient energy in the optical pulse to generate THz pulses that induce electron tunneling at the STM junction. The regenerative amplifier laser system used here provided enough optical pulse energy for THz pulse generation, while also supporting a repetition rate that enabled fast acquisition times for 2D imaging with the THz-STM.

The amplified optical pulse was split into three different beams (see Appendix B.2), which were used for THz pulse generation, photoexcitation of the sample and electro-optic sampling (EOS) of the far-field THz pulse waveform. Each of these three pulses were sent into a set of delay stages that were used to adjust the relative temporal position of the three pulses (Fig. 4.2). The THz generation pulse and the sample pump pulse were also sent through computer-controlled delay stages (Thorlabs NRT150) that were used to perform scans in 50 fs time steps (7.5 µm steps for a two-pass delay stage). The THz pulse source was a photoconductive antenna with a 1 mm gap between chrome-gold contacts deposited on a 0.5 mm thick semi-insulating GaAs wafer. A constant-voltage (0–260 V) was applied across the contacts in parallel with a 50 Ω load resistor that dissipated most of the electrical power. A 2 kΩ safety resistor was placed in series with the THz pulse source to limit the current in the case of a short-circuit. Also, the power dissipation in the antenna was reduced by pulsing the high voltage supply (Lambda Electronics Model 71), using a high-voltage-pulser (Directed Energy HV1000) that operated at positive voltages only. The HV pulser was triggered by a delay generator (Stanford Research Systems DG645) that was triggered by a silicon-based avalanche photodiode (Thorlabs APD110C). The delay generator (which set to –176 ns) was an important instrument as it synchronized the high voltage pulse at the THz source with the incident optical pulse, and also set the duty cycle by controlling the voltage pulse width. The width was set to 55 ns as this was the minimum value that the HV pulser would support, resulting in a duty cycle of 1.4% $= 55\ \text{ns} \times 250\ \text{kHz} \times 100\%$. The fast photodiode signal and the high voltage transient (with a 1/100 divider) were monitored using an oscilloscope (see also [130]).

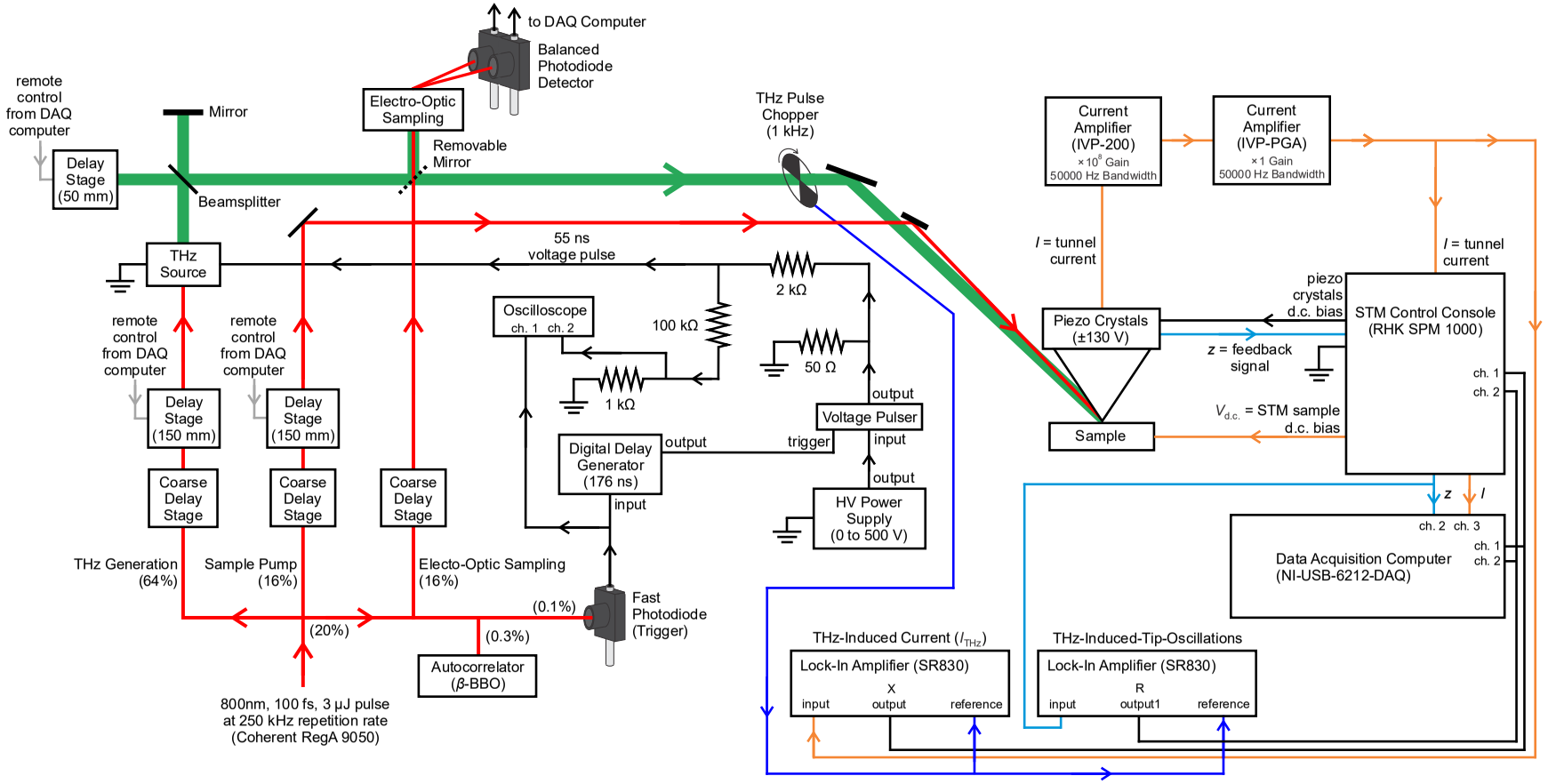

Figure 4.2: Electronics setup for data acquisition with the ambient THz-STM. The red solid line represents the optical-pulse-train, while the thick green solid line represents the THz-pulse-train. The orange and light blue lines represent electronic connections that carry the measured current, $I_{\mathrm{THz,avg}}$, and relative tip height, $z_{\mathrm{measured}} = z - z_0$, respectively. The black and dark blue solid lines represent electronic connections between instruments in the form of BNC connectors.

The optical pulse for THz pulse generation was focused onto the photoconductive antenna by a 0.5" diameter off-axis parabolic mirror with a 1" focal length, and the generated THz pulse was collimated by a 2" diameter parabolic mirror with a 4" focal length (see Fig. 4.3). A large beam size is important for long-distance THz pulse propagation because of losses due to diffraction. This is understood quantitatively by assuming Gaussian-like beam propagation, where the Rayleigh range, z_{R}, defines the distance until the beam spot area has doubled in size [36]. It is given by the formula

$$z_{\mathrm{R}} = \frac{\pi\, w^2}{\lambda} \tag{4.1}$$

where w is the beam waist (1/2 of the beam spot diameter) and λ is the wavelength. For a THz pulse with a 1" beam waist and a bandwidth centered at 0.5 THz, $z_{\mathrm{R}} = 3.4$ m. Significant losses in the field amplitude occur if the propagation distance between the THz pulse source and the STM tip is longer

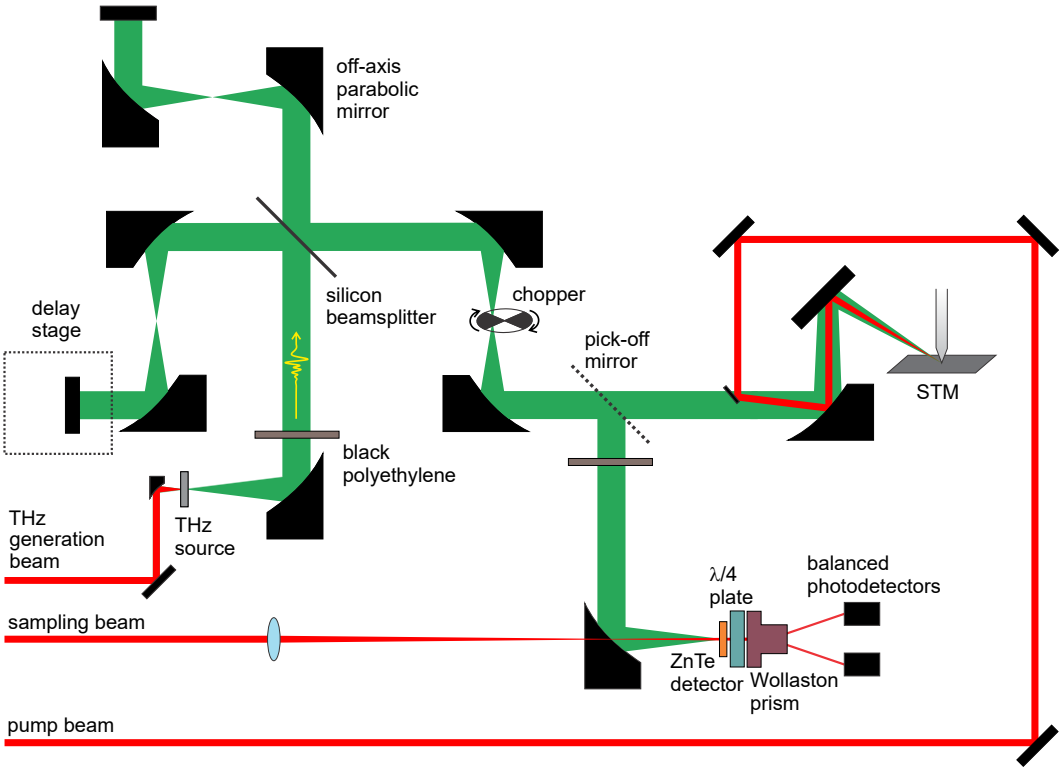

Figure 4.3: Optical setup for ambient THz-STM where the red solid line represents the optical-pulse-train and the thick green solid line represents the THz-pulse-train.

than this distance. Two layers of black polyethylene blocked any leakage of the optical pulse and transmitted the THz pulse. The THz pulse was sent through a Michelson interferometer where a 0.5 mm thick high resistivity 4" wide silicon wafer reflected and transmitted approximately 50% of the incident THz intensity. One arm of the interferometer used a linear delay stage (Thorlabs MTS50-Z8) to control the temporal delay, $\Delta\tau$, between the two the THz pulses of the interferometer. For alignment of the THz pulse, the silicon wafer was replaced with a 1 mm thick optically transparent glass slide. Alternatively, the silicon wafer was substituted with a high reflectivity gold mirror in order to increase the dynamic range of $E_{\mathrm{THz}}(t)$ by a factor of ~ 2. The THz pulse was then sent through a 1 kHz mechanical chopper for lock-in detection of the signal, before finally being routed towards the STM tip, along with the optical pump pulse. Both pulses were brought near-collinear, focused onto the tip by a 2" wide parabolic mirror with a 4" focal length (Fig. 4.1), and then reflected down towards the tip at an angle of approximately 40° above the horizontal plane (Fig. 4.4). Alternatively, the THz pulse could be rerouted using a removable pick-off mirror for electro-optic detection of the THz pulse electric field waveform. The phase and amplitude of the THz pulse were measured using electro-optic detection with a 1 mm thick ZnTe(110) crystal (see section 3.2.2 for details). The propagation path length of the THz pulse from the pick-off mirror to the ZnTe detection crystal was set to approximately match the path length from the pick-off mirror to the STM tip. A 4" focal length parabolic mirror was used to focus the THz pulses onto the ZnTe crystal. The energy of the sampling pulse was reduced until the balanced photodiode detectors (Thorlabs PDB210A) were operating in a linear regime ($\sim$ 60 mV, see figure 8.8 in [130]). The photodiodes were connected to a voltmeter for electric field calibration calibration (I_x and I_y in Eq. 3.9) and a lock-in amplifier (Stanford Research SR830) for detection with a high signal-to-noise ratio (red solid line in Fig. 4.5).

A steady-state bias voltage, $V_{\mathrm{d.c.}}$, was applied to the sample, which generated a d.c. tunnel current, $I_{\mathrm{d.c.}}$. The STM tip was electrically isolated and connected

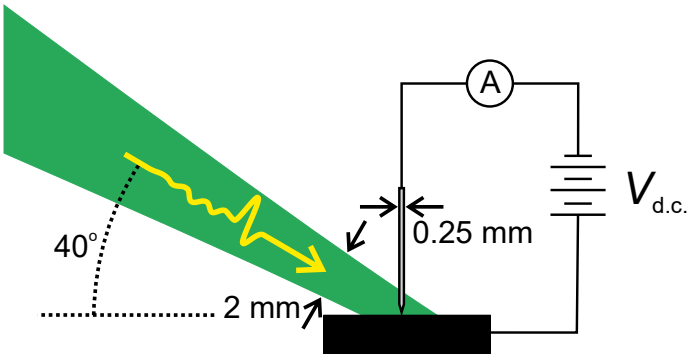

Figure 4.4: Ultrafast THz pulses were focused to 2 mm spot size at the base of a mechanically cut Pt/Ir(90:10) STM tip at an angle of 40° above the horizontal plane. This angle was chosen to match the geometry of the ultrahigh vacuum chamber that is introduced in chapter 5. A steady-state bias voltage, $V_{\mathrm{d.c.}}$, was applied to the sample, while a feedback loop controlled the tip height and maintained a constant total tunnel current, $I_{\mathrm{total}} = I_{\mathrm{d.c.}} + I_{\mathrm{THz,avg}}$.

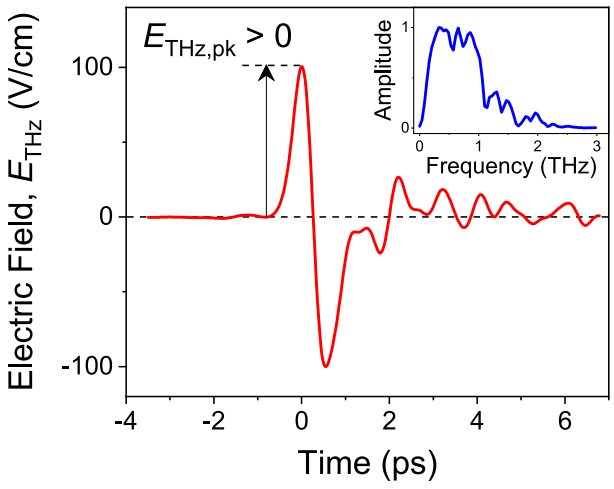

Figure 4.5: THz pulse electric field waveform generated by a photoconductive antenna with a 1 mm gap and electro-optically sampled using a 1 mm thick ZnTe crystal. The electric field calibration was performed using Eq. 3.8. Inset: corresponding amplitude spectrum. The THz pulse peak electric field is denoted by $E_{\mathrm{THz,pk}}$. For a symmetric pulse there is no dominant polarity and thus, $E_{\mathrm{THz,pk}} = E_{\mathrm{THz,max}} = |E_{\mathrm{THz,min}}|$.

to the first-stage tunnel current amplifier (RHK IVP-200) that had a gain of 10^8 and a bandwidth of 50 kHz (see Fig. 5.4 for details). The second-stage amplifier (RHK IVP-PGA) had unity gain and a bandwidth of 15 kHz (see Fig. 5.3 for details). Overall, this resulted in a minimum detectable current of approximately 8 pA, or equivalently, 200 electrons per pulse at a rate of 250 kHz. The number of electrons rectified by each THz pulse was determined from the measured average THz-pulse-induced current ($I_{\mathrm{THz,avg}}$), via $N_{\mathrm{e^-}} = (I_{\mathrm{THz,avg}})/(e \times f_{\mathrm{rep}})$. A lock-in amplifier was used to isolate $I_{\mathrm{THz,avg}}$ from the total measured current, $I_{\mathrm{measured}} = I_{\mathrm{d.c.}} + I_{\mathrm{THz,avg}}$. The lock-in amplifier output was connected to the STM control console, thereby creating a new data channel for the STM ($I_{\mathrm{THz,avg}}$) in addition to the tip height, z, tunnel current, I_{measured}, differential conductance, $\mathrm{d}I/\mathrm{d}V$, etc. A second lock-in amplifier was used to measure the THz-pulse-induced-tip-oscillations. Recording this channel ensured that the tip height was not oscillating at the THz pulse modulation frequency (chopper frequency), as that would strongly suppress $I_{\mathrm{THz,avg}}$. The THz-induced-current lock-in was set to X-mode, enabling a positive or negative $I_{\mathrm{THz,avg}}$ to be measured, while the THz-induced-tip-height lock-in was set to R-mode, since we were only interested in the magnitude of the THz-induced tip oscillations. Both of these output channels were connected to the data acquisition controller (National Instruments USB-6212-DAQ), which was connected a personal computer (Microsoft Windows) that controlled all of the THz pulse generation software (LabView) and delay stages.

4.2 Coupling THz Pulses to the STM

Coupling free-space-propagating THz pulses to the tip of a scanning tunneling microscope offers a new way of modulating the voltage across the tunnel junction on ultrafast timescales. The static STM bias, $V_{\mathrm{d.c.}}$, is added to the transient THz pulse bias, $V_{\mathrm{THz}}(t)$, as shown in Fig. 4.6 for a symmetric THz pulse where $V_{\mathrm{THz,pk}} > V_{\mathrm{d.c.}}$. This produces a static d.c. tunnel current, $I_{\mathrm{d.c.}}$, and a transient ultrafast tunnel current $I_{\mathrm{THz}}(t)$, as shown in Fig. 4.7.

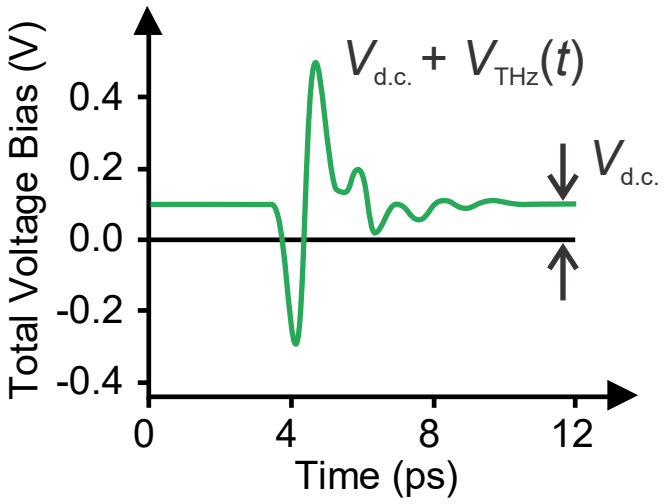

Figure 4.6: The total voltage across the tunnel junction is determined by the sum of $V_{\mathrm{d.c.}}$ and the time-dependent THz-pulse-induced voltage, $V_{\mathrm{THz}}(t)$.

Since the sub-picosecond tunnel current, $I_{\mathrm{THz}}(t)$, is much too fast for the sub-millisecond response time of the tunnel current amplifier, it cannot be measured directly. Instead, the rectified response, $I_{\mathrm{THz,avg}} = (e\, f_{\mathrm{rep}}) \times N_{\mathrm{e^-}} = (f_{\mathrm{rep}}) \times \int_{-\infty}^{+\infty} I_{\mathrm{THz}}(t)\, \mathrm{d}t$, is measured. Since any free-space-propagating electromagnetic wave with an electric field, $E(t)$, must satisfy $\int_{-\infty}^{+\infty} E(t)\, \mathrm{d}t = 0$, the nonlinear I–V characteristic of the tunnel junction is necessary to enable a non-zero THz-pulse-induced rectified current ($N_{\mathrm{e^-}} \neq 0$). Furthermore, since the nonlinearity occurs strictly at the STM junction, the THz-pulse-induced current response is spatially localized to the tunnel junction contact area. In principle, there is nothing preventing the THz-STM from ultimately combining the ultrafast time resolution (< 1 ps) of single-cycle THz pulses, with the sub-nanometer spatial resolution of the STM to enable studies of atomically resolved electron dynamics on sub-picosecond timescales.

During this initial development phase of the THz-STM, it was not known if the available experimental equipment would provide enough laser power, repetition rate and tunnel current sensitivity to produce a measurable THz-pulse-induced tunnel current. In a first experiment, the effect of THz pulses on the STM junction was investigated by measuring a standard STM I–V characteristic

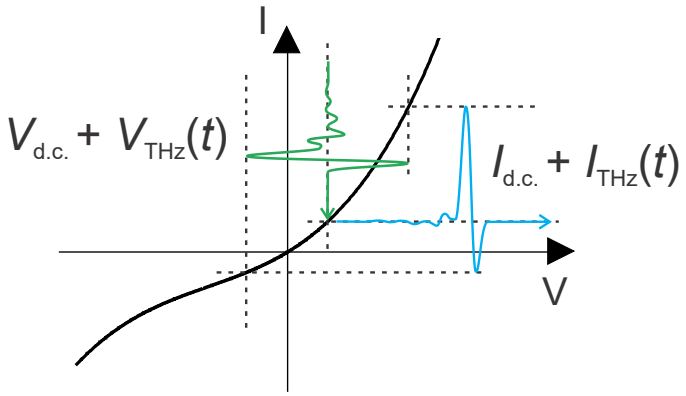

Figure 4.7: Schematic of the nonlinear tunneling I–V curve of an STM (black solid line), where the d.c. bias, $V_{\mathrm{d.c.}}$, drives a d.c. current, $I_{\mathrm{d.c.}}$. A free-space-propagating THz pulse couples to the STM tip and generates a time-dependent voltage, $V_{\mathrm{THz}}(t)$ (green solid line), that drives an ultrafast THz-pulse-induced tunnel current, $I_{\mathrm{THz}}(t)$ (blue solid line), which results in an average rectified tunnel current of $I_{\mathrm{THz,avg}} = f_{\mathrm{rep}} \times \int I_{\mathrm{THz}}(t)\ \mathrm{d}t$.

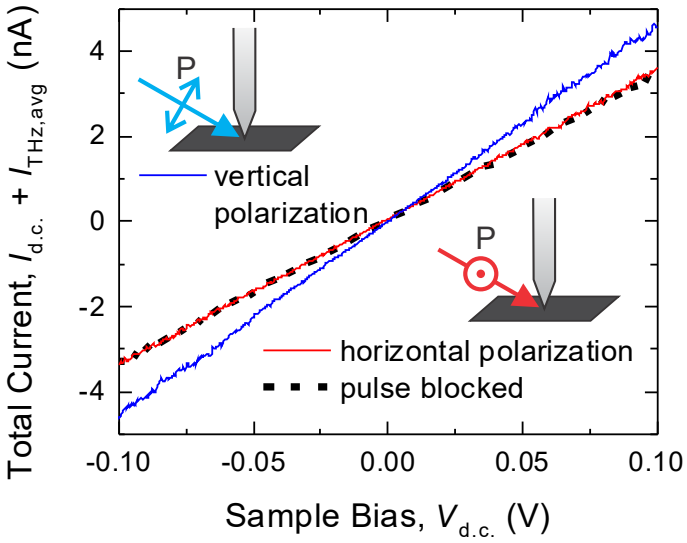

Figure 4.8: Measured I–V curves for an HOPG surface using a Pt/Ir tip with vertically polarized THz pulses incident onto the STM tip at $E_{\mathrm{THz,pk}} = 120$ V/cm (blue solid line). Horizontally polarized THz pulses at the same electric field strength do not couple to the tip and thus, the measured I–V curve (red solid line) matches the I–V curve with the pulses blocked (black dashed line). The feedback loop was disengaged at $V_{\mathrm{d.c.}} = +0.03$ V, $I_{\mathrm{d.c.}} = +1$ nA, and $E_{\mathrm{THz,pk}} = 0$ V/cm.

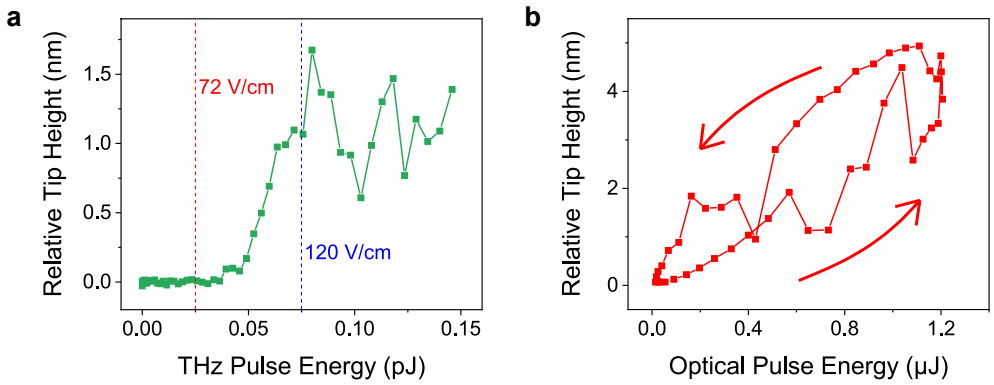

Figure 4.9: Tip height retraction as a function of the incident energy per pulse at, **a**, THz and **b**, optical frequencies. During acquisition the feedback loop is engaged and its bandwidth is much larger than the modulation frequency of 20 Hz that was used to chop the optical and THz pulses. The optical pulse had a center wavelength of 800 nm and a pulse duration of 150 fs. The scans were acquired under ambient conditions in constant-current mode at $V_{\text{d.c.}} = +30$ mV and $I_{\text{d.c.}} + I_{\text{THz,avg}} = +1$ nA for **a** and $I_{\text{d.c.}} + I_{\text{Optical,avg}} = +1$ nA for **b**. For both scans the pulse energy was gradually changed over a ~ 5 minute period and the pulses were polarized vertically along the tip-axis.

with the THz pulse polarized along the tip axis (blue solid line in Fig. 4.8), and then with the THz pulse polarized parallel to the sample surface (red solid line in Fig. 4.8). The THz pulse coupled to the tunnel junction only if it was vertically polarized, consistent with THz pulse coupling to antennas and metal wires [71, 72, 83, 165, 168–170]. As a result, the measured I–V curve with the horizontally polarized THz pulses matched the I–V curve with the THz pulses blocked (black dashed line in Fig. 4.8).

The STM tunnel junction has picometer-scale sensitivity in the z-direction, making it extremely vulnerable to laser-induced thermal expansion effects. Due to the low photon energy of THz pulses as compared to optical pulses, thermal effects play a negligible role in generating the ultrafast THz-pulse-induced current. In order to confirm that the measured THz-induced current, $I_{\text{THz,avg}}$, was not an artifact of any thermal expansion effects, we performed tip retraction scans as a function of the incident pulse energy for both THz pulses (Fig. 4.9a) and optical pulses (Fig. 4.9b). Thermal effects in the STM at optical carrier frequencies are well-understood [139–142]. If the optical pulse

energy becomes too large ($\varepsilon \gg$ 1–10 nJ), thermal effects limit the spatio-temporal resolution of the laser-assisted STM. By lowering the average optical power incident onto the tip to the milliwatt [105, 109, 111] and microwatt [110, 112–115] regimes, thermally-induced optical effects become increasingly reduced. During the tip retraction scans using optical pulses (Fig. 4.9b), the pulse energy was increased up to 1.2 µJ = (300 mW / f_{rep}), while recording a tip height retraction of, $z - z_0 = 4.5$ nm. Meanwhile, at a THz pulse field strength of $E_{\mathrm{THz,pk}} = 120$ V/cm, which was the maximum used for THz-STM measurements, a similar relative tip height retraction of 1.5 nm was achieved (Fig. 4.9a). However, the THz pulse had a pulse energy of 75 fJ, five million times less energy than the 0.4 µJ optical pulse at $z - z_0 \approx 1.5$ nm. Clearly, thermal effects are not responsible for the measured THz-pulse-induced current, $I_{\mathrm{THz,avg}}$ (see [130, 131] for additional details).

In order to demonstrate the temporal resolution of the THz-STM, THz pulse autocorrelations were performed (Fig. 4.10). The sample was a highly-oriented-pyrolytic-graphite (HOPG) substrate with gold nanoislands deposited on the surface in order to provide THz-STM signal contrast through differences in their I–V characteristics. THz-STM autocorrelations were performed with the tip positioned over a gold nanoisland (Fig. 4.11a–c), and over the HOPG

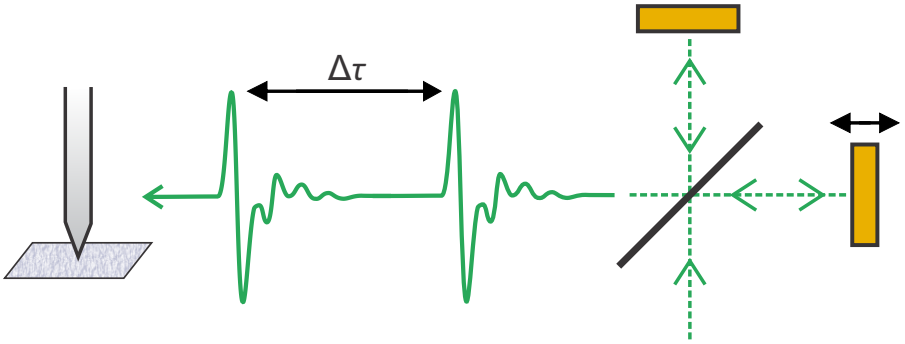

Figure 4.10: THz pulses were sent through a Michelson interferometer to enable autocorrelation measurements. A high-resistivity two-side-polished silicon wafer separated the single THz pulse into two nearly-equal-amplitude pulses with the path-length of one pulse modulated by a computer-controlled delay stage in order to adjust the relative temporal delay between the two pulses, $\Delta\tau$.

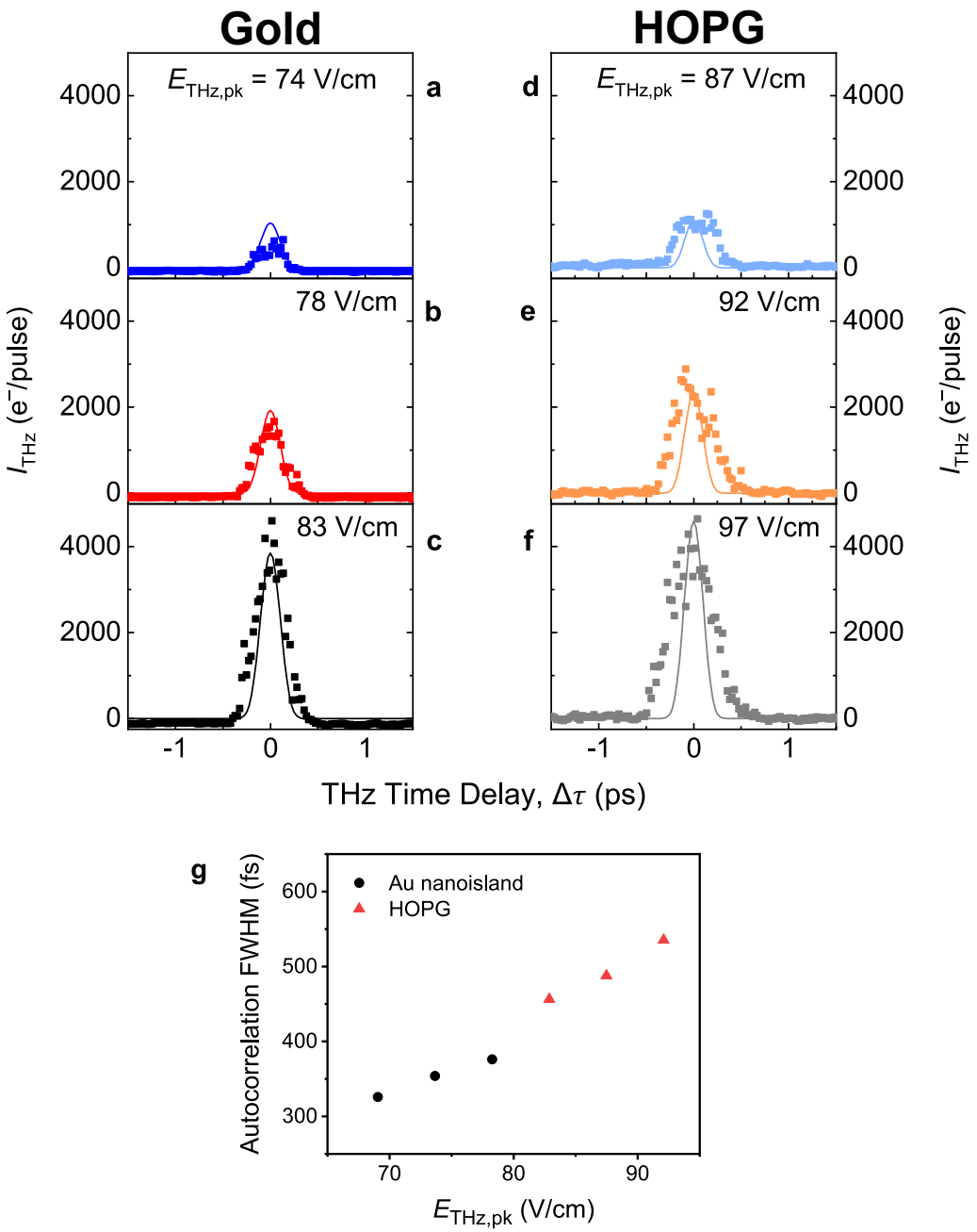

Figure 4.11: **a**–**f**, THz-pulse-induced tunnel current as a function of the arrival of two equal amplitude THz pulses (coloured squares). The THz-STM autocorrelations were performed at $E_{\mathrm{THz,pk}} = 74$ V/cm (**a**), $E_{\mathrm{THz,pk}} = 78$ V/cm (**b**), and $E_{\mathrm{THz,pk}} = 83$ V/cm (**c**) for gold, and $E_{\mathrm{THz,pk}} = 87$ V/cm (**d**), $E_{\mathrm{THz,pk}} = 92$ V/cm (**e**), and $E_{\mathrm{THz,pk}} = 97$ V/cm (**f**) for HOPG. The measurements were acquired at $V_{\mathrm{d.c.}} = +30$ mV and $I_{\mathrm{d.c.}} + I_{\mathrm{THz,avg}} = +1$ nA, while in constant-current mode ($I_{\mathrm{THz,avg}} \ll I_{\mathrm{d.c.}}$), and with the feedback loop bandwidth below the modulation frequency of the THz-pulse-train. The solid lines are fits based on the Simmons model (see section 4.3). **g**, Full-width-half-maxiumum (FWHM) of Gaussian fits to the data in **a**–**f**.

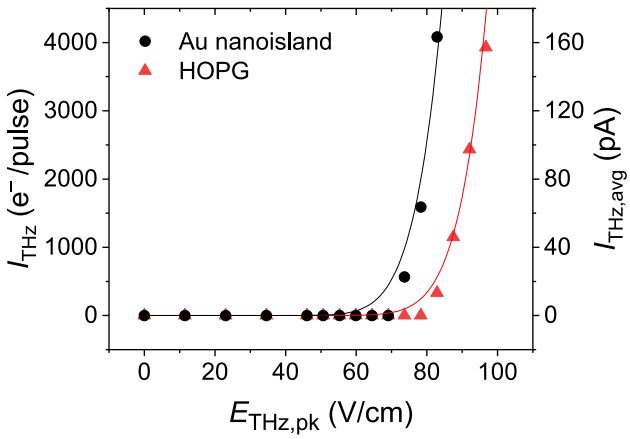

Figure 4.12: THz-pulse-induced tunnel current versus incident peak electric field (THz I–E) curves over gold nanoislands (black circles) and HOPG (red triangles). The data points are peaks of Gaussian fits to the autocorrelations in Fig. 4.11. The red and black solid lines are Simmons model fits to the data (see section 4.3).

substrate (Fig. 4.11d–f) at various $E_{\mathrm{THz,pk}}$. The full-width-half-maximum (FWHM) of Gaussian fits to the autocorrelations provide an estimate for the timescale over which the ultrafast THz current occurred. A FWHM of 350 fs was observed for autocorrelations over gold at $E_{\mathrm{THz,pk}} = 74$ V/cm. A plot of the THz pulse peak electric field versus, $E_{\mathrm{THz,pk}}$, versus the THz-pulse-induced current, I_{THz}, is shown in Fig. 4.12 (THz I–E curve). The solid lines in Fig. 4.11 and Fig. 4.12 are Simmons model fits to the data.

4.3 Modeling the THz-Pulse-Induced Current

In general, the Simmons model provides an estimate of the tunnel current that flows between two biased conductors that are separated by a thin insulating barrier (see section 2.3.1). The model ignores the energy dependence of the tip and sample local density of states, and instead, places emphasis on calculating the tunnel current from the energy-dependent transmission probability of the tunnel junction [228–230]. As a first approximation, the I–V characteristic of the STM tunnel junction can be described by the Simmons model. A pair of Simmons model I–V curves are shown in Fig. 4.13a on a linear-scale, and in

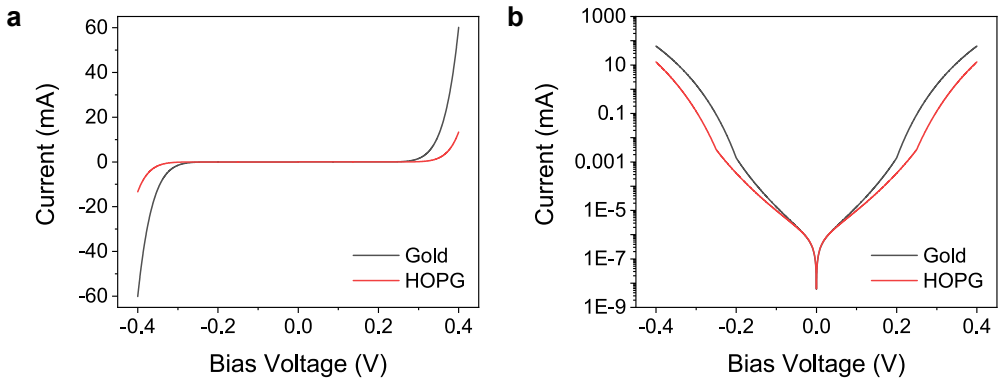

Figure 4.13: **a**, **b**, Simulated Simmons model I–V curves for STM of gold nanoislands (black solid line) and HOPG (red solid line) plotted on a linear scale (**a**) and a log scale (**b**). The model parameters are determined from a global fit to measured I–z curves and THz-STM autocorrelations on gold and HOPG. The simulation parameters that were used to generate the I–V curves shown here were, $\phi_{\mathrm{Au}} = 0.2$ eV, $\phi_{\mathrm{HOPG}} = 0.25 \pm 0.04$ eV, $z_{\mathrm{Au}} = 5.9 \pm 0.6$ nm, $z_{\mathrm{HOPG}} = 5.6 \pm 0.6$ nm, $I_0 = +1\,\mathrm{nA}$ and $V_0 = +30\,\mathrm{mV}$.

Fig. 4.13b on a log-scale. The THz-pulse-induced current was calculated using the Simmons model (Eq. 2.16) via the expression

$$
\begin{aligned}
I_{\mathrm{THz}}(t) \;= \pm \frac{1}{\zeta_0\,(\beta\,\delta)^2} \Bigg[& \overline{\phi}\, e^{-2\hbar^{-1}\beta\delta\sqrt{2m}\sqrt{\overline{\phi}}} \;\ldots \\
\ldots \;- \left(\overline{\phi} + e|V_{\mathrm{d.c.}} + V_{\mathrm{THz}}(t)|\right) & e^{-2\hbar^{-1}\beta\delta\sqrt{2m}\sqrt{\overline{\phi}+e|V_{\mathrm{d.c.}}+V_{\mathrm{THz}}(t)|}} \Bigg] \ldots \\
\ldots \mp \frac{1}{\zeta_0\,(\beta_{\mathrm{d.c.}}\,\delta_{\mathrm{d.c.}})^2} \Bigg[& \overline{\phi}_{\mathrm{d.c.}}\, e^{-2\hbar^{-1}\beta_{\mathrm{d.c.}}\delta_{\mathrm{d.c.}}\sqrt{2m}\sqrt{\overline{\phi}_{\mathrm{d.c.}}}} \;\ldots \\
\ldots \;- \left(\overline{\phi}_{\mathrm{d.c.}} + e|V_{\mathrm{d.c.}}|\right) & e^{-2\hbar^{-1}\beta_{\mathrm{d.c.}}\delta_{\mathrm{d.c.}}\sqrt{2m}\sqrt{\overline{\phi}_{\mathrm{d.c.}}+e|V_{\mathrm{d.c.}}|}} \Bigg],
\end{aligned}
\tag{4.2}
$$

where $\hbar$ is the reduced Planck constant, m is the electron mass and e is the elementary charge. The term ζ_0 is a normalization constant that is given by the expression

$$
\begin{aligned}
\zeta_0 \;= \frac{1}{|I_0|\,(\beta_0\,\delta_0)^2} \Bigg[& \overline{\phi}_0\, e^{-2\hbar^{-1}\beta_0\delta_0\sqrt{2m}\sqrt{\overline{\phi}_0}} \;\ldots \\
\ldots \;- \left(\overline{\phi}_0 + e|V_0|\right) & e^{-2\hbar^{-1}\beta_0\delta_0\sqrt{2m}\sqrt{\overline{\phi}_0+e|V_0|}} \Bigg],
\end{aligned}
\tag{4.3}
$$

where I_0 is tunnel current setpoint, and V_0 is the d.c. voltage setpoint. The variables δ (Eq. 2.12), β (Eq. 2.15), and $\overline{\phi}$ (Eq. 2.13) are evaluated at $V = V_{\text{d.c.}} + V_{\text{THz}}(t)$ and similarly, the variables $\delta_{\text{d.c.}}$, $\beta_{\text{d.c.}}$, $\overline{\phi}_{\text{d.c.}}$, δ_0, β_0, and $\overline{\phi}_0$ are evaluate at either $V_{\text{d.c.}}$ or V_0. Also, in the first term of Eq. 4.2, the $\pm$ case is positive for $V_{\text{d.c.}} + V_{\text{THz}}(t) > 0$, and negative for $V_{\text{d.c.}} + V_{\text{THz}}(t) < 0$. The $\mp$ case in the second term of Eq. 4.2 is negative for $V_{\text{d.c.}} > 0$ and positive for $V_{\text{d.c.}} < 0$. The THz pulse voltage waveform, $V_{\text{THz}}(t)$, was modeled using the expression

$$V_{\text{THz}}(t) = 1.278\, V_{\text{THz,pk}}\, e^{-\frac{t^2}{2\sigma^2}} \sin(\omega\, t)\,, \tag{4.4}$$

where $\sigma = 0.4$ ps, $\omega = 2\pi(0.8\text{ THz})$, and $V_{\text{THz,pk}}$ is the peak of the THz-pulse-induced voltage, $V_{\text{THz}}(t)$. The numerical values for Eq. 4.4 were chosen such that $V_{\text{THz}}(t)$ (Fig. 4.14a) had an amplitude spectrum (Fig. 4.14b) that was similar to the electro-optically sampled THz waveform (Fig. 4.5).

A global fit was performed to multiple measured THz-STM autocorrelations at various $E_{\text{THz,pk}}$, with the tip positioned over both gold and HOPG (Fig. 4.11 and Fig. 4.12). STM I–z curves were acquired over gold and used to determined $\phi_{\text{Au}} \approx 0.20$ eV, a value which is consistent with reports of a reduced material work function (and therefore barrier height) while operating at ambient pressure and temperature [59, 66]. The significantly reduced barrier height, ϕ_{exp}, resulted in an increased tunnel gap, where $z\sqrt{\phi_{\text{exp}}} \approx$ constant.

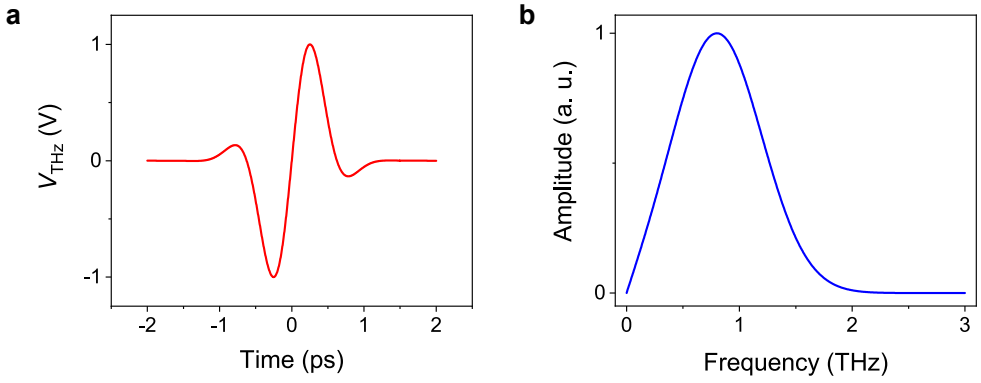

Figure 4.14: **a**, Simulated THz pulse voltage waveform, $V_{\text{THz}}(t)$, (Eq. 4.4) and **b**, its corresponding amplitude spectrum.

The global fit parameters are $\phi_{\mathrm{HOPG}} = 0.25 \pm 0.04$ eV, $z_{\mathrm{Au}} = 5.9 \pm 0.6$ nm, $z_{\mathrm{HOPG}} = 5.6 \pm 0.6$ nm and THz pulse electric field enhancement, $F = 8000 \pm 1000$. The input parameters $I_0 = +1$ nA and $V_0 = +30$ mV were used to normalize the tunnel current equations and account for the tunnel junction contact area in Eq. 2.16. The field enhancement factor, F, was quite large due to the nanoscale localization of the THz pulse electric field by the sharp metallic STM tip, and the close proximity of a conductive surface. A study of the optical-field enhancement in laser-assisted STM has reported field enhancements of 300–600 for gold and 1000–2000 for HOPG [279]. Furthermore, since the conductivity of metals is significantly larger at THz frequencies as compared to optical frequencies, a larger field enhancement factor for THz-STM is expected.

The ultrafast THz pulse induces a transient voltage across the STM tunnel junction (Fig. 4.15a) that generates an ultrafast transient current (Fig. 4.15b), which results in a measurable rectified THz-pulse-induced tunnel current (Fig. 4.15c). According to the model, in order to generate a measurable average tunnel current, $I_{\mathrm{THz,avg}}$, an extremely large instantaneous tunnel current, $I_{\mathrm{THz}}(t)$, must be driven by the THz pulse. In particular, the model finds that milliampere-scale currents occur over hundreds of femtoseconds (Fig. 4.15b, driven by

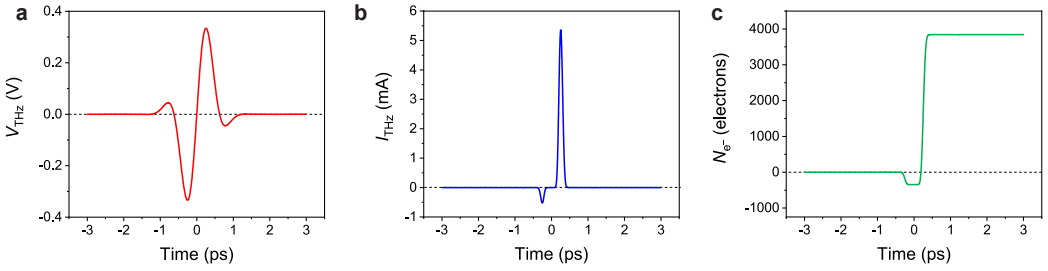

Figure 4.15: Simulation of the THz-pulse-induced tunnel current using the Simmons model (Eq. 4.2). The free parameters are defined in the text. **a**, THz-pulse-induced voltage $V_{\mathrm{THz}}(t)$, between tip and sample for an incident THz pulse with $E_{\mathrm{THz,pk}} = 83$ V/cm. **b**, The THz-pulse-induced current transient, $I_{\mathrm{THz}}(t)$. **c**, The number of electrons that tunnel across the junction (running integral of **b**). After the THz pulse has passed (beyond 2 ps), the number of electrons rectified is 3800. At 250,000 terahertz pulses per second, this is equivalent to $I_{\mathrm{THz,avg}} = +150$ pA.

volt-scale transient THz fields (Fig. 4.15a). Such an extremely fast THz-pulse-induced tunnel current is consistent with the sub-picosecond autocorrelation FWHM measurements in Fig. 4.11g. This extreme current regime can be accessed because $V_{\mathrm{THz,pk}}$ is much larger than the setpoint d.c. bias voltage. Field emission occurred at these large THz peak voltages with values significantly larger than ϕ_{exp} (Eq. 2.6).

The total energy coupled to the tunnel junction was estimated from the expression

$$\varepsilon_{\mathrm{Junction}} = \int_{-\infty}^{+\infty} I_{\mathrm{THz}}(t)\, V_{\mathrm{THz}}(t)\, \mathrm{d}t\,. \tag{4.5}$$

The simulated voltage transient, $V_{\mathrm{THz}}(t)$, and ultrafast current transient, $I_{\mathrm{THz}}(t)$, that are shown in Fig. 4.15, resulted in 0.23 fJ of energy coupled to the tunnel junction. This energy was compared to the energy of the incident free-space-propagating THz pulse (Fig. 4.5) using Eq. 3.5. For $E_{\mathrm{THz,pk}} =$ 83 V/cm and a 1.5 mm spot-size-diameter, the incident THz pulse energy is 34 fJ. This results in a 0.7% THz pulse coupling efficiency to the tunnel junction, which is comparable to previous reports of THz pulse coupling to metal wires [168].

4.4 Ultrafast THz-STM Imaging

The spatial and temporal resolution of ambient THz-STM was explored by performing THz-STM imaging of gold nanoislands on an HOPG substrate (Fig. 4.16). The sample was created by evaporating a thin layer of gold ($\sim$ 3 nm) onto the HOPG substrate. However, for thicknesses below the percolation threshold, surface wetting effects prevented the formation of a well-defined thin film, leading to the formation of large gold nanoislands with a thickness of $\sim$ 10 nm. The incident THz pulse electric field strength, $E_{\mathrm{THz,pk}}$, was set such that $I_{\mathrm{THz,avg}}$ was much larger with the STM tip position over a gold nanoisland, as compared to the HOPG substrate. This occurred at $E_{\mathrm{THz,pk}} \approx$ 80 V/cm, where the corresponding difference in signal strength between gold and HOPG can be seen in Fig. 4.12. The STM topography (Fig. 4.16a) was

acquired simultaneously with the THz-STM image (Fig. 4.16b) as a function of the relative temporal separation, $\Delta\tau$, between two (nearly) identical THz pulses. The THz-STM image at $\Delta\tau = 0$ fs demonstrates a spatial resolution on the order of 2 nm, as demonstrated by the distance required for N_{e^-} to go from 10% to 90% of its maximum value. A simultaneous temporal resolution of ~ 500 fs is demonstrated by the reduced THz-STM signal at $\Delta\tau = \pm 250$ fs, and even more significantly reduced at $\Delta\tau = \pm 500$ fs. An autocorrelation

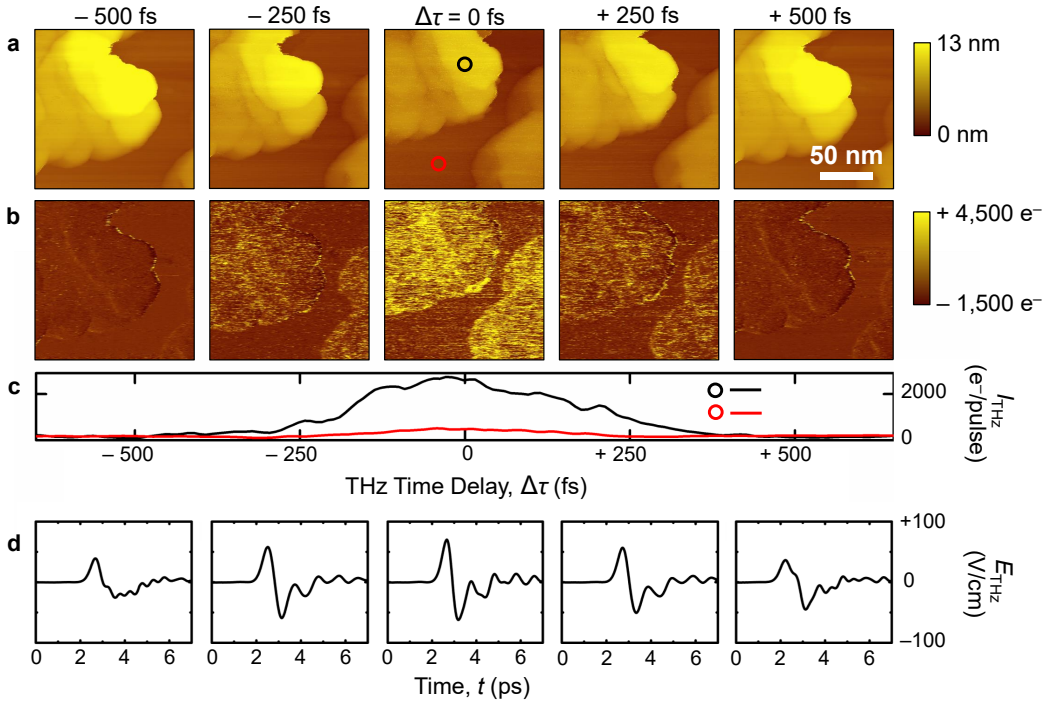

Figure 4.16: THz-STM spatio-temporal autocorrelation of gold nanoislands on HOPG. **a**, STM topography images a junction between two gold nanoisland and **b**, the simultaneously acquired THz-pulse-induced tunnel current images, $N_{e^-}(x, y)$. Each pair of images (topography and THz-STM) was acquired with a relative time delay between THz pulses equal to -500 fs, -250 fs, 0 fs, $+250$ fs and $+500$ fs from left to right, respectively. **c**, THz-STM autocorrelations acquired with the tip located over the top-left nanoisland (black circle, black solid line) and the HOPG substrate (red circle, red solid line. **d**, The THz pulse electric field waveforms for time delays of -500 fs, -250 fs, 0 fs, $+250$ fs and $+500$ fs from left to right, respectively. The THz-STM measurements were acquired in air and at room temperature while in constant-current mode at $V_{\text{d.c.}} = +30$ mV and $I_{\text{d.c.}} + I_{\text{THz,avg}} = +1$ nA. The feedback loop bandwidth was kept well below the modulation frequency of the THz-pulse-train and also, $I_{\text{THz,avg}} \ll I_{\text{d.c.}}$.

measurement was acquired (Fig. 4.16c) with the tip positioned over a gold nanoisland (black solid line) and over the HOPG substrate (red solid line). The temporal profile of the incident THz pulse, $E_{\mathrm{THz}}(t)$, is shown in Fig. 4.16d for each corresponding value of $\Delta\tau$. According to these results, the spatial resolution of the THz-STM was only limited by the spatial variation of the I–V characteristic and the tip wavefunction, as is the case with conventional STM imaging. Meanwhile, the temporal resolution was only limited by the bandwidth of the coupled THz pulse. With improved experimental conditions, there does not appear to be any physical principles that would prevent the THz-STM from achieving atomic spatial resolution with simultaneous sub-picosecond temporal resolution.

4.5 Optical Pump – THz-STM Probe Imaging

The THz-STM can probe ultrafast carrier dynamics near surfaces through its sensitivity to ultrafast changes in the local surface potential. However, these measurements can only be acquired stroboscopically, eliminating the possibility of capturing unique non-repeating events. As the STM tip is scanned across the sample surface along a digitized grid, an optical pump pulse excite carriers in the sample multiple times per pixel, while a time-delayed THz pulse probes the local dynamics. In this sense, the THz-STM images are not single-moment-in-time snapshots of electron dynamics, but rather, they are a

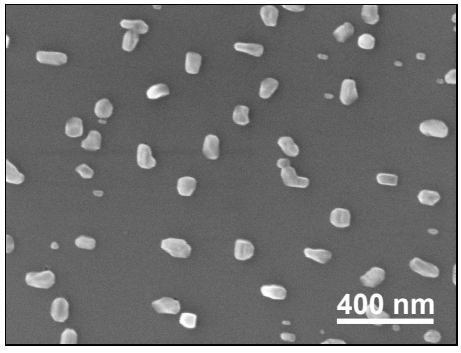

Figure 4.17: Scanning electron microscope (SEM) image of InAs nanodots on a GaAs wetting layer. This sample was used for the THz-STM measurements in Fig. 4.18, Fig. 4.19 and Fig. 4.20.

time-resolved average of multiple excitation events at some spatial location. In order to demonstrate optical pump – THz-STM probe imaging, the ideal sample should have photo-excitable carrier dynamics on the picosecond timescale, with spatial variations on the order of nanometers. Furthermore, it would be appropriate to study a system that has been previously explored using both optical techniques and scanning probe microscopes. Accordingly, we have chosen to study heteroepitaxically grown InAs nanodots on a GaAs substrate because of their picosecond-scale carrier dynamics [98, 280–282], strong absorption at near 800 nm and strongly contrasting features between the nanodots and the substrate. The InAs nanodots and GaAs substrate were moderately doped to provide sufficient conductivity for tunneling microscopy. The InAs nanodots were grown by Manisha Gupta using molecular beam epitaxy on an epi-ready n-type GaAs(100) wafer doped with silicon as the dopant at 5×10^{17} cm^{-3}. The oxide on the GaAs surface was desorbed at 615 °C for 10 min at an arsenic pressure of 5×10^{-6} torr. No buffer layer was grown, while the InAs nanodot growth was conducted at 520 °C, with an In-to-As flux ratio of ~ 30. The InAs nanodots formed due to lateral strain from a lattice mismatch between InAs and GaAs [283]. The nanodots were grown for 30 seconds and afterwards they were cooled to room temperature in an arsenic pressure. A scanning electron microscope (SEM) image is shown in Fig. 4.17, confirming the presence of the nanodots. The nanodots ranged in size from 10–100 nm, with an average separation of ~ 100 nm that varied slightly across the sample. Auger electron spectroscopy was used to confirm a near-50% composition of indium for the nanodots and trace amounts in the surrounding wetting layer. The SEM imaging and Auger spectroscopy was performed by Shihong Xu of the nanoFAB Fabrication & Characterization Facility at the University of Alberta.

The relative arrival time of the THz pulse with respect to the optical pump pulse, $\tau_{\text{Optical–THz}}$, was varied with the tip positioned above the nanodot (red solid line in Fig. 4.18a) and above the GaAs wetting layer (blue solid line in Fig. 4.18a). An asymmetric optical pump – THz-STM probe (OPP-THz-STM) scan was obtained (Fig. 4.18b), showing a rise time of ~ 500 fs, and verifying

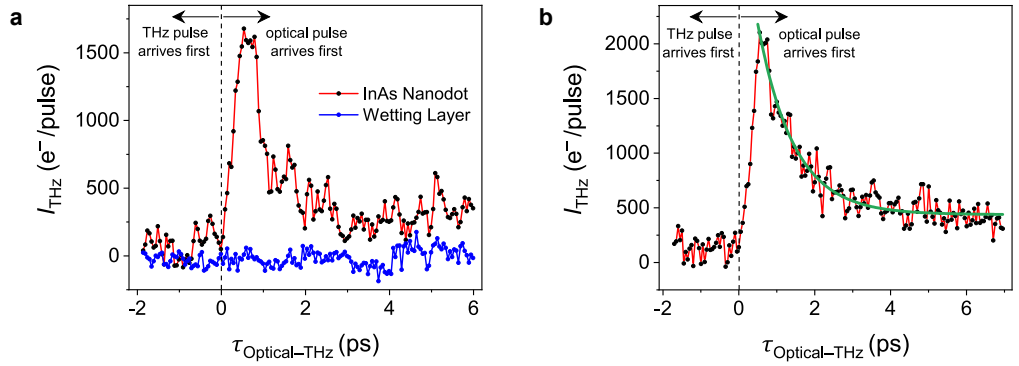

Figure 4.18: Optical pump – THz-STM probe time delay scans (OPP-THz-STM scans) acquired with the tip positioned over an InAs nanodot (black circles connected by the red solid line) and over the GaAs wetting layer (blue circles connected by the blue solid line). The measurements in **a** were acquired with the tip positioned above the InAs nanodot and wetting layer shown in Fig. 4.19. The measurement in **b** was acquired with the tip positioned above the InAs nanodot in Fig. 4.20b. The pump–probe scans were acquired with the same settings as their respective figures. Both pump–probe scans in **a** were acquired using two averages, while the scan in **b** was acquired using five averages. The solid green line in **b** is a single exponential fit with a decay time of 1 ps and an offset of 440 rectified electrons.

that THz-STM can indeed probe sub-picosecond temporal dynamics. With additional averaging, a single-exponential fit was obtain with a decay time of 1 ps and a y-offset of 440 rectified electrons. This decay time agrees with the hole trapping times that have been reported in previous work with InAs nanodots [98, 280–282]. This carrier trapping process manifests as an increase in the THz-pulse-induced current because electrons and holes exhibit different trapping times into the nanodot, with electrons captured several hundred femtoseconds faster than the holes. A slower capture time for holes is the result of a potential energy barrier that arises from strain extending laterally due to the lattice mismatch between the nanodot and the wetting layer [98, 264]. In this way, the InAs nanodot remains negatively charged until both electrons and holes are trapped in the nanodot. During this brief moment when the nanodot is negatively charged, the local I–V characteristic seen by the THz pulse is enhanced by the trap-induced transient bias voltage, resulting in an enhanced THz-pulse-induced current, $I_{\mathrm{THz}}(t)$. The y-offset in Fig. 4.18b may

be due to long-lived electron re-escape and re-capture due to a local temperature increase from the laser pulse. Another possibility is that the electrons and holes did not recombine inside the nanodot for several hundred picoseconds [98]; the unique I–V characteristic of this transient state could have enhanced the THz-pulse-induced current until carrier recombination occurred.

An STM (Fig. 4.19a) and THz-STM (Fig. 4.19b) image of a single InAs nanodot were acquired simultaneously with the the time delay, $\tau_{\text{Optical–THz}}$, set such that the THz pulse arrived 500 femtoseconds before the optical pulse (Fig. 4.19c). This resulted in a relatively small THz-pulse-induced current, $I_{\text{THz}}(t)$ (blue solid line in Fig. 4.19d). A second pair of STM (Fig. 4.19e) and THz-STM (Fig. 4.19f) images were acquired with $\tau_{\text{Optical–THz}}$ set such that the THz pulse arrived 500 fs after photoexcitation (Fig. 4.19g). A difference in the electron and hole trapping times into the InAs nanodot generated a local transient bias voltage that enhanced the THz-pulse-induced current (Fig. 4.19h). The spatial resolution of the THz-STM image was estimated to be 6 nm from Fig. 4.19. However, additional STM (Fig. 4.20a,d) and THz-STM (Fig. 4.20b,e) images of different nanodots confirm that the spatial resolution of THz-STM in ambient conditions can reach 2 nm (Fig. 4.20c). Furthermore, because the THz-STM signal strength is strongly dependent on the local I–V characteristics, the edge definition can be quite pronounced (red line in Fig. 4.20c,f), whereas conventional STM topography has a much more gradual slope (blue line in Fig. 4.20c,f). For all of the images that were acquired, the optical-pulse-train was was not modulated (as is standard for optical-pump/THz-probe spectroscopy [38, 257, 280]) in order to minimize thermally induced tip oscillations and other thermoelectric effects [141, 142]. While, there may have been a non-zero d.c. optical-pulse-induced current contributing to the total measured d.c. current, modulating the THz pulses ensured that the measured current was strictly induced by the THz pulses. Furthermore, thermal effects occur on sub-nanosecond timescales [141], which is not consistent with the measured few-picosecond dynamics (Fig. 4.18 and Fig. 4.19). Also, thermal effects cannot explain why the THz-pulse-induced

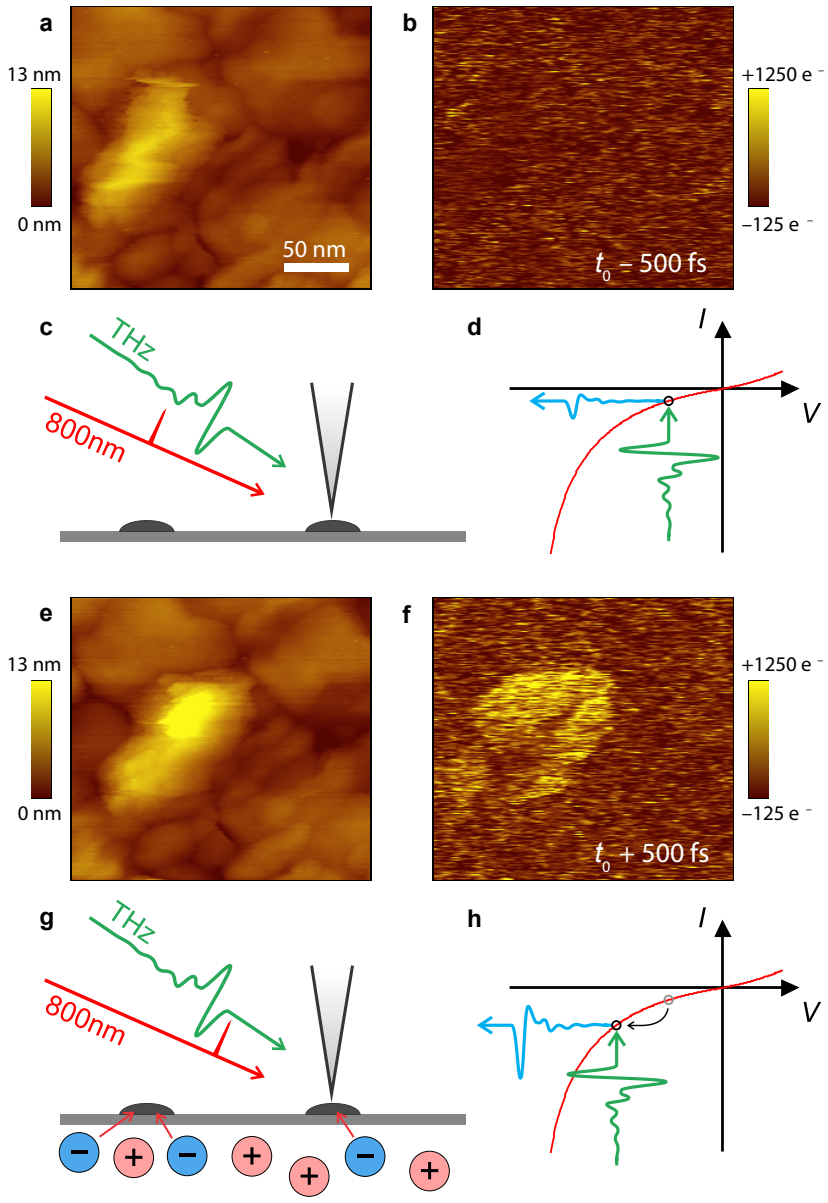

Figure 4.19: Ultrafast optical pump – THz-STM probe imaging of photoexcited InAs nanodots on GaAs. **a**–**d**, At $\tau_{\text{Optical–THz}} = -500$ fs before photoexcitation, the topography image (**a**) reveals a nanodot on the surface but the THz-STM image (**b**) does not exhibit any features. **c**, **d**, At negative time delay, the THz-pulse-induced current, $I_{\text{THz}}(t)$, was below the noise floor. **e**–**h**, At $\tau_{\text{Optical–THz}} = +500$ fs after photoexcitation, both of the topography (**e**) and THz-STM (**f**) images reveal an InAs nanodot. **g**, **h**, Electron trapping by the InAs nanodot resulted in a local enhancement of the bias voltage and led to an enhanced THz-pulse-induced current, $I_{\text{THz}}(t)$. The optical pulse has a center wavelength of 800 nm, a pulse duration of 150 fs and a fluence of $110\,\mu\text{J/cm}^2$. The images were acquired under ambient conditions in constant-current mode at $V_{\text{d.c.}} = -3.5$ V, $I_{\text{d.c.}} + I_{\text{THz,avg}} = -0.5$ nA and $E_{\text{THz,pk}} = +100$ V/cm ($E_{\text{THz,max}} \approx -E_{\text{THz,min}}$).

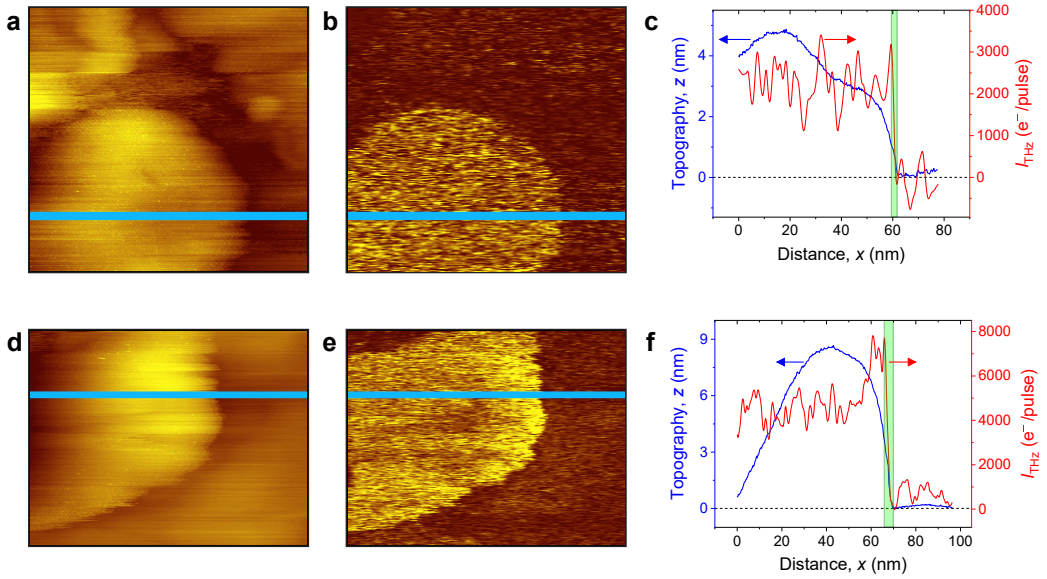

Figure 4.20: Spatial resolution of optical pump – THz-STM probe imaging of photoexcited InAs nanodots on GaAs. **a**, Topography image, **b**, THz-STM image and **c**, corresponding line scans (blue solid lines in **a** and **b**) for a photoexcited InAs nanodot at $\tau_{\text{Optical–THz}} = +1$ ps. A spatial resolution of 2 nm is estimated from the line scan. **d**, Topography image, **e**, THz-STM image and **f**, corresponding line scans (blue solid lines in **d** and **e**) for another photoexcited InAs nanodot at $\tau_{\text{Optical–THz}} = +0.5$ ps. A spatial resolution of 4 nm is estimated from the line scan. The optical pump pulse has a center wavelength of 800 nm, a pulse duration of 150 fs and a fluence of 200 μJ/cm^2. The images were acquired in air and at room temperature while in constant-current mode at $V_{\text{d.c.}} = -3$ V, $I_{\text{d.c.}} + I_{\text{THz,avg}} = -0.5$ nA and $E_{\text{THz,pk}} = +70$ V/cm.

current changes so rapidly when the tip moves laterally 2 nm from the nanodot onto the the GaAs wetting layer (Fig. 4.20c).

Chapter 5

Ultrahigh Vacuum THz-STM

The proof-of-principle demonstration of ultrafast THz-STM imaging under ambient pressure and temperature, which was described in chapter 4, provided motivation for developing a new ultrahigh-vacuum-compatible THz-STM system. Ultrahigh vacuum (UHV) conditions ($< 10^{-9}$ torr) are ideal for surface science experiments [284] because the electronic properties of the surface are extremely dependent upon the presence of any adsorbates. Accordingly, STM measurements are particularly prone to imaging and spectroscopy artifacts, especially with tips and samples that have a high chemical reactivity. These types of materials can only be used and studied under UHV conditions, where they can remain clean for several days (well beyond the duration of the experiment). Additional stability and even lower pressures in UHV can be achieved by cryogenically cooling the STM. While UHV has many benefits, designing a THz-STM in such an environment brings with it a new set of challenges and experimental procedures that were not necessary to consider under ambient pressure and temperature. The experimental details of the UHV THz-STM are summarized in this chapter, including the optical and electronic setups, along with the various tip and sample preparation techniques that were used.

5.1 Experimental Details

The UHV THz-STM experiments that are presented in chapters 6, 7 and 8 were all performed using a commercial UHV STM system (RHK-UHV-SPM 3000) with a base pressure of 5×10^{-11} torr and an open-flow-cryostat cooling the sample to a minimum temperature of about 30 K (see Fig. 5.1). A summary of the electronics setup for UHV THz-STM data acquisition is shown in Fig. 5.2. The output laser pulse is split into three different beams with slightly different split-off percentages compared to chapter 4 (see Appendix B.2 for details). The coarse delay stage positions in Fig. 5.2 were determined with sub-nanosecond accuracy using a silicon-based avalanche photodiode (Thorlabs APD120A2) that was connected to a 300 MHz oscilloscope (Tektronix DPO3032). The computer-controlled fine-delay stages (Thorlabs NRT150) were used for automated data acquisition. An optical pulse autocorrelator (Angewandte Physik & Elektronik Mini) was used to characterize the output pulses from the re-

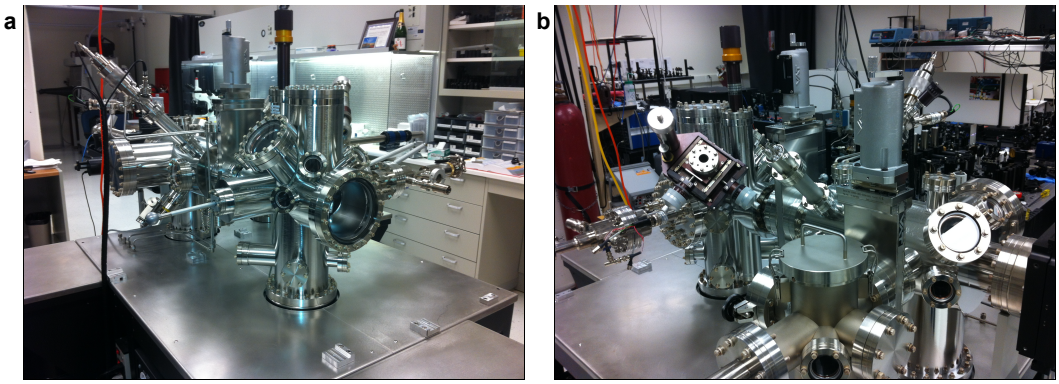

Figure 5.1: Photographs of the ultrahigh vacuum scanning tunneling microscope system. **a**, The STM chamber (without the STM scanhead in place) is in the foreground along with the large 6" and 8" windows for *in situ* manipulation with the wobble stick (which is visible in the middle left of the image). Three small 2.75" windows are used for coupling the optical pump pulse to the STM and setting up the two alignment cameras. The laser-alignment camera is angled at 35° above the horizontal plane, while the tip-exchange-alignment camera is placed horizontal to the tip–sample tunnel junction. The preparation chamber is visible in the background. **b**, The loadlock chamber is visible in the foreground, while the inverted xyz-viewport and open-flow cryostat are located in the middle left of the image.

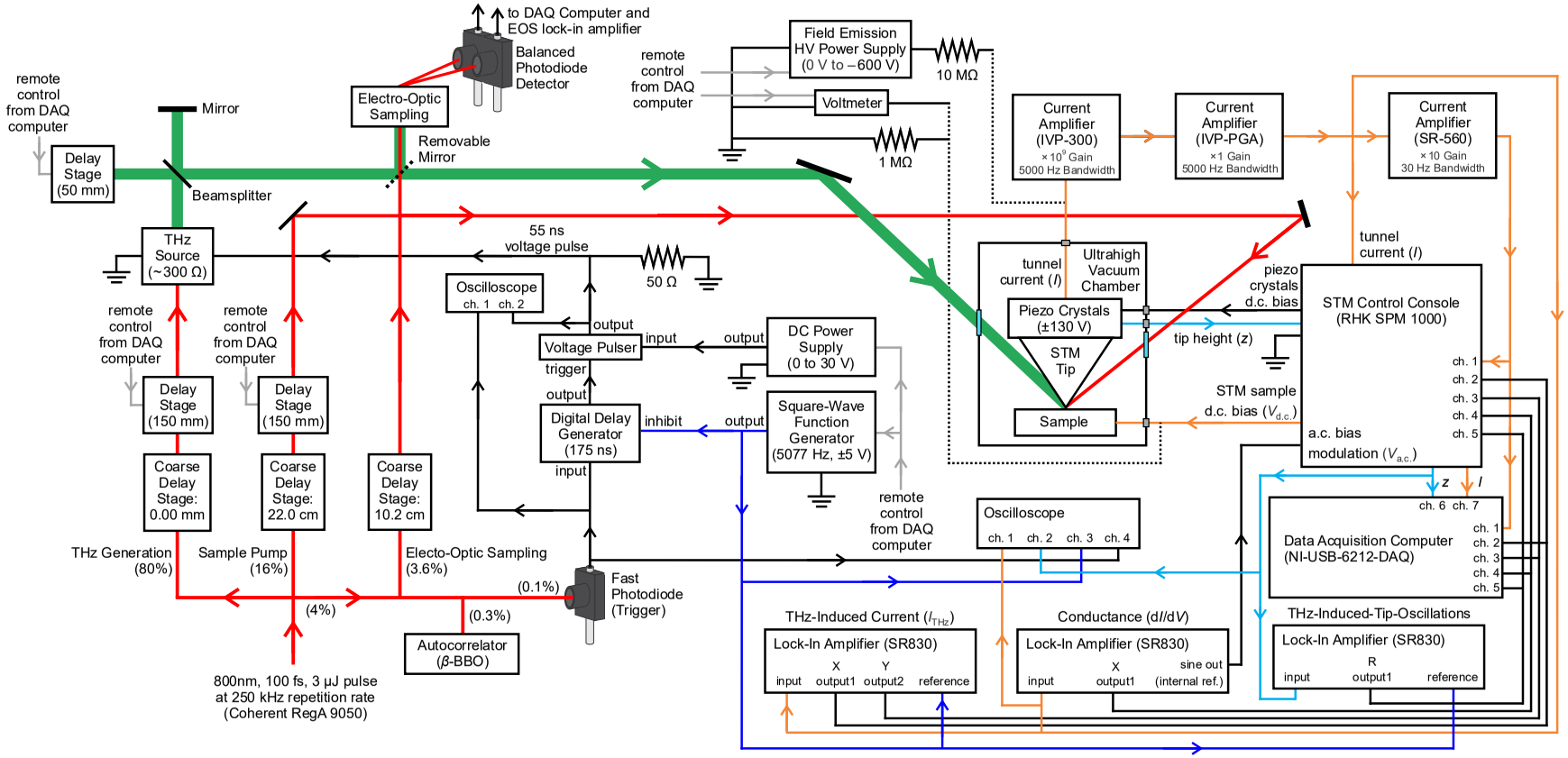

Figure 5.2: Electronics setup for data acquisition with the ultrahigh vacuum THz-STM. The red solid line represents the optical-pulse-train, while the thick green solid line represents the THz-pulse-train. The orange and light blue lines represent electronic connections that carry the measured current, $I_{\mathrm{THz,avg}}$, and relative tip height, $z_{\mathrm{measured}} = z - z_0$, respectively. The black and dark blue solid lines represent electronic connections between instruments in the form of BNC connectors.

generative amplifier, while a silicon-based avalanche photodiode triggered the electronics that were used to generate the THz pulses. The digital delay generator (Stanford Research Systems DG645) was an essential instrument that synchronized the voltage and laser pulses together at the THz source, set the corresponding duty cycle, and modulated the THz-pulse-train via an inhibit input that was driven by a square-wave function generator operating at 5077 Hz (BK Precision BK4052). This enabled lock-in detection of the THz-induced current, THz-induced-tip-oscillations and electro-optically sampled THz pulse waveform, without the use of a mechanical chopper. The fast photodiode trigger (Thorlabs PDB210A) and the pulsed bias voltage (Directed Energy HV1000 & BK Precision 9122A) were monitored using an oscilloscope (Tektronix DPO2002B). A third lock-in amplifier was used for $\mathrm{d}I/\mathrm{d}V$ spectroscopy

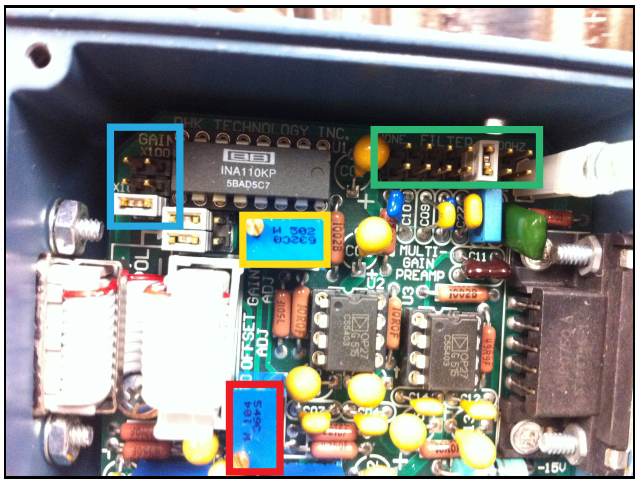

Figure 5.3: Photograph of the IVP-PGA second stage current amplifier. The red rectangle on the bottom highlights the potentiometer that was used to zero the tunnel current with the tip retracted (via a d.c. offset) to within approximately $\pm\,40$ fA. The yellow rectangle in the middle highlights the potentiometer that controls the fine-adjust-gain of the second-stage amplifier. This potentiometer has never been adjusted from its initial setting of $\times 1.04$ (this value was determined from calibration with a GΩ resistor). The blue rectangle on the left highlights the pins that control the coarse-adjust-gain of the second-stage amplifier, from top to bottom the settings are: $\times 100$, $\times 10$ and $\times 1$ (setting in the image). The green rectangle on the right highlights the pins that control the low-pass-filter setting of the second-stage amplifier, from left to right the settings are: No Filter, 150 kHz, 50 kHz, 15 kHz, 5 kHz (setting in the image), 1.5 kHz and 0.5 kHz.

as discussed in section 2.1. All of the relevant data channels were monitored simultaneously by the National Instrument DAQ, the STM control console, and a 4-channel oscilloscope (Tektronix MSO2024B). The lock-in amplifier that was used for electro-optic sampling is not depicted in Fig. 5.2.

5.1.1 Tunnel Current Detection

The tip and sample were electrically isolated and electromagnetically shielded by the stainless steel UHV chamber walls. A d.c. bias voltage, $V_{\mathrm{d.c.}}$, was applied to the sample. The tunnel current was measured by one of three possible first-stage current amplifiers (RHK IVP-100, IVP-200, or IVP-300) that had

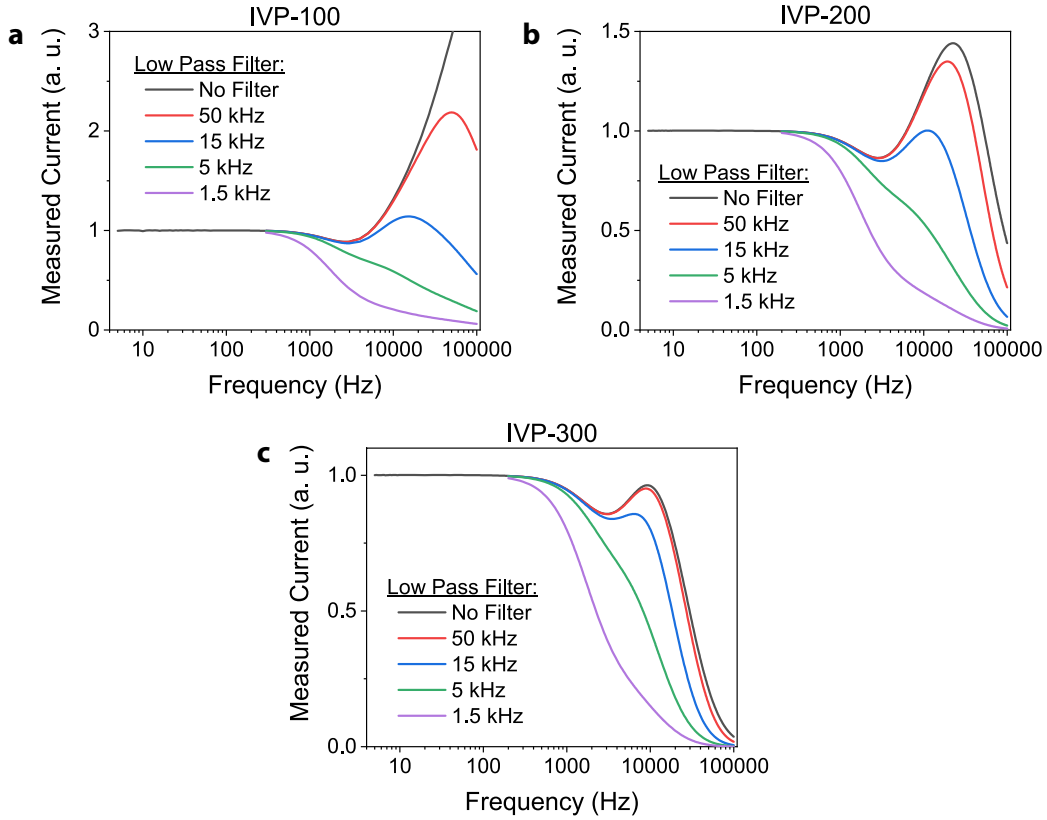

Figure 5.4: Measured frequency response of the first-stage current amplifiers for the different filter settings that are described in Fig. 5.3. **a**, IVP-100, **b**, IVP-200 and **c**, IVP-300. The amplifiers were connected to a GΩ resistor that was driven by a sine-wave modulation with a peak amplitude of ±3 V. The time constant on the lock-in amplifier was at least 5 cycles of the modulation, while the acquisition time per frequency step was set to 3 times the lock-in time constant. The lock-in amplifier output was set to R-mode.

gains of 10^7, 10^8, and 10^9 V/A, and bandwidths of 250, 50, and 5 kHz, respectively (see Fig. 5.4). For all of the experiments performed in UHV, the highest gain first-stage amplifier was used (IVP-300). The second-stage amplifier (RHK IVP-PGA) was set to unity gain and a bandwidth of 5 kHz (see Fig. 5.3). This resulted in a minimum detectable current of approximately 0.4 pA or 10 rectified electrons per pulse, for constant-current imaging (feedback loop engaged). A third amplifier (Stanford Research Systems SR560) with a gain of 10 with a bandwidth of 30 Hz was used for constant-height THz-STM at zero bias ($V_{\text{d.c.}} = 0$ V), resulting in a minimum detectable current of 40 fA or 1 rectified electron per pulse. The number of electrons rectified by each THz pulse was determined from the average THz-pulse-induced current ($I_{\text{THz,avg}}$) via $N_{\text{e}^-} = (I_{\text{THz,avg}})/(e \times f_{\text{rep}})$. For all of the measurements at $V_{\text{d.c.}} = 0$ V the THz-pulse-train modulation was turned off and the steady-state voltage was confirmed to be less than 50 µV. A square-wave bias modulation across the THz pulse source allowed the THz-pulse-train to be modulated at a frequency of 5077 Hz for lock-in detection of the THz-pulse-induced current[1]. This modulation frequency was kept well-above the bandwidth of the feedback loop and near the edge of the IVP-300 current amplifier bandwidth (Fig. 5.4). Accordingly, a multiplicative factor specific to this modulation frequency, K_{5077}, was necessary for calibrating $I_{\text{THz,avg}}$ if it was acquired using a lock-in amplifier (which was necessary only if $V_{\text{d.c.}} \neq 0$ V). The expression used for calibrating the lock-in voltage output, V_{out}, is given by

$$I_{\text{THz,avg}} = (e\, f_{\text{rep}}) \times N_{\text{e}^-} = g\, s\, K_{5077}\, \frac{V_{\text{out}}}{10\ \text{V}}\,, \tag{5.1}$$

where e is the elementary charge, $f_{\text{rep}} = 250$ kHz is the laser repetition rate, g is the gain of the first-stage amplifier in amperes per volt, s is the lock-in sensitivity setting in volts and V_{out} is the lock-in amplifier output. For the IVP-300 amplifier that was used in our system, $g = 1.04$ nA/V, resulting in a calibration factor of $N_{\text{e}^-} = K_{5077} \times s \times 2596\,[\text{e}^-/\text{V}^2] \times V_{\text{out}}$. A value of $K_{5077} \approx 1.7$ was

[1]Since 5077 Hz is not a multiple of the laser repetition rate, there is a minor reduction in the signal-to-noise that occurs because every 2 modulation cycles 25 THz pulses occur during the active half-cycle of the square-wave modulation, instead of 24.

determined from the IVP-300 frequency response function (Fig. 5.4) and corroborated during the THz-STM experiment via THz-pulse-driven ($V_{\mathrm{d.c.}} = 0$ V) I–z measurements with the THz-pulse-train modulation turned on. This measurement allowed for a direct comparison between the high sensitivity output of the SR560 amplifier ($\pm\,40$ fA), and the THz-induced-current lock-in amplifier (with $V_{\mathrm{d.c.}} = 0$ V, these two channels should be equivalent). During this unique situation where the THz-pulse-train modulation was turned on at $V_{\mathrm{d.c.}} = 0$ V, the feedback loop bandwidth had to be set very low. Otherwise, the tip would have repeatedly crash into the sample surface, as THz pulses were not present to induce a rectified tunnel current and drive the feedback loop during the inactive half-cycle of the 5077 Hz modulation. These tip crashes were not an issue with the THz-pulse-train modulation turned off because $f_{\mathrm{rep}} = 250$ kHz was several orders of magnitude larger than the feedback loop bandwidth. The sign ($\pm$) of $E_{\mathrm{THz}}(t)$ was chosen such that a negative $E_{\mathrm{THz,pk}}$ generated a negative average THz-pulse-induced tunnel current (electrons tunneling from the sample to the tip), when incident onto a tungsten tip and an n-type Si(111)-(7×7) sample at $V_{\mathrm{d.c.}} = 0$ V. The lock-in amplifier responsible for measuring the THz-induced-tip-oscillations, z_{osc}, was calibrated via

$$z_{\mathrm{osc}} \;=\; s\,K_{\mathrm{pz}}\,\frac{13\,C_{\mathrm{zp}}}{g_{\mathrm{A/D}}}\,\frac{V_{\mathrm{out}}}{10\ \mathrm{V}}\,, \tag{5.2}$$

where s is the lock-in sensitivity setting in volts, $g_{\mathrm{A/D}}$ is analog-to-digital gain setting on the STM control console, the factor 13 is a default tip-piezo-voltage gain, $C_{\mathrm{zp}} = 3.0$ nm/V is the z-piezo calibration constant and K_{pz} is a constant that depends on both the modulation frequency and the bandwidth of the piezoelectric crystal ($K_{\mathrm{pz}} = 1$ for the kHz modulation frequencies used here). Finally, the lock-in amplifier for $\mathrm{d}I/\mathrm{d}V$ spectroscopy was calibrated via

$$G \;=\; g\,s\,K_{7177}\,\frac{V_{\mathrm{out}}}{10\ \mathrm{V}}\frac{\sqrt{2}}{V_{\mathrm{a.c.,pk}}}\,, \tag{5.3}$$

where G is the differential conductance, g is the gain of the first-stage amplifier in amperes per volt, s is the lock-in sensitivity setting in volts, V_{out} is the lock-in amplifier output in volts, $V_{\mathrm{a.c.,pk}}/\sqrt{2}$ is the root-mean-square amplitude of

the a.c. voltage modulation and $K_{7177} \approx 1.9$ is the calibration factor for the frequency response of the IVP-300 at a modulation frequency of 7177 Hz.

5.1.2 Optical Setup

A schematic of the optical setup for UHV THz-STM operation and free-space electro-optic detection of THz pulses is shown in Fig. 5.5. An ultrafast Ti:sapphire regenerative amplifier laser pulse with approximately 2 µJ of energy illuminated an interdigitated photoconductive antenna, which served as the THz pulse source (Laser Quantum Tera-SED10; [244]). The antenna was mounted on a motorized rotation stage (Thorlabs PRM1Z8) for THz pulse polarity control and THz I–E measurements. A wire-grid polarizer (MicroTech G30×10-S) also rotated with the stage to ensure that the emitted THz pulse was linearly polarized. The bias voltage across the THz source was pulsed with peak values up to 30 V synchronized with the laser system repetition rate, generating free-space propagating THz pulses with peak electric fields up to ∼ 1 kV/cm at a focus. A polymethylpentene lens (Menlo Systems TPX lens) was used to collimate the THz beam. The TPX lens has a refractive index of ∼1.46 at both optical and THz frequencies, enabling straightforward alignment using a diode laser. For THz pulse autocorrelation measurements a high resistivity

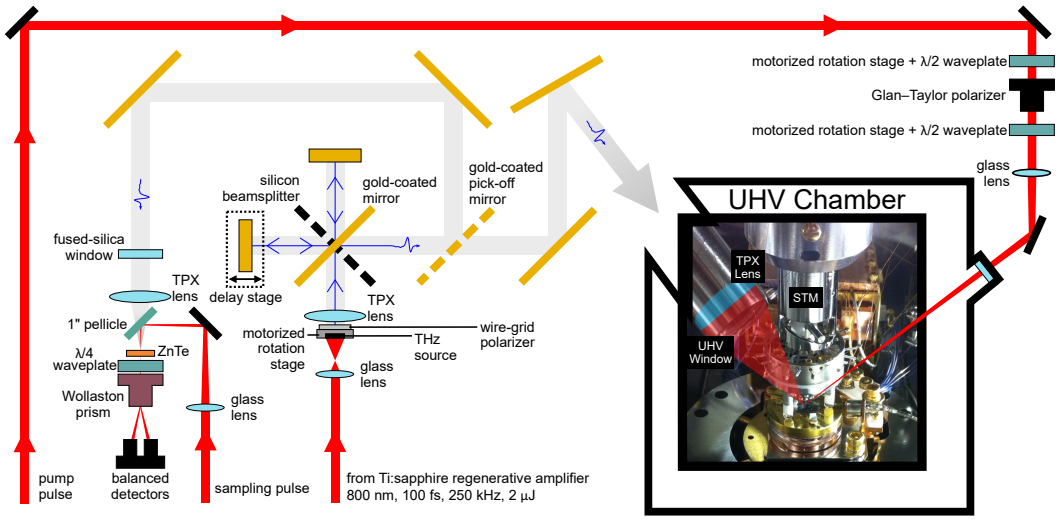

Figure 5.5: Optical setup for the UHV THz-STM system.

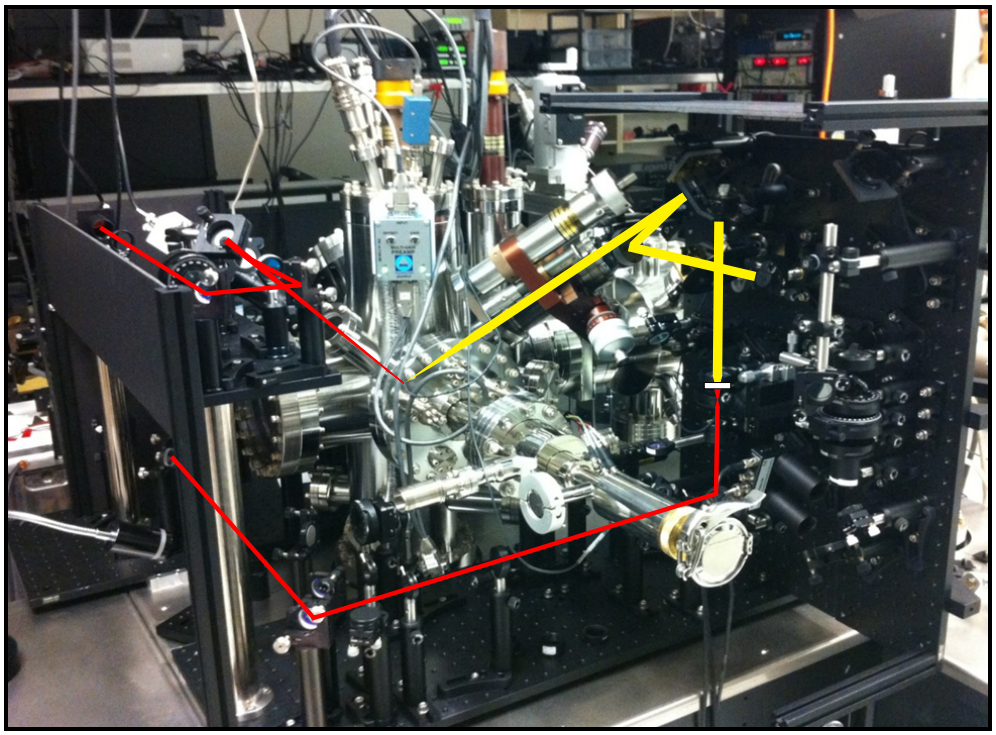

Figure 5.6: Photograph of the UHV THz-STM setup where the optical-pulse-train is represented by red lines and the THz-pulse-train is represented by thicker yellow lines. The optical-pulse-train is focused onto the tip at an angle of 120° (top-down view) with respect to the THz-pulse-train.

silicon wafer acted as the beamsplitter for a THz pulse interferometer where the optical path length of one arm was varied by a motorized linear stage (Thorlabs MTS50-Z8). Occasionally, the beamsplitter was exchanged with a gold mirror to maximize the dynamic range of the THz pulse electric field. The THz pulse was directed to the STM tip at an angle of 35° above the horizontal plane by two gold-coated mirrors. A triple-axis inverted viewport (MDC Vacuum Products PSM-1502) with an inner diameter of 22 mm held a 54 mm focal length TPX lens just before the UHV window (see photograph in Fig. 5.5). For THz-STM measurements, the incident THz pulse polarization was verified to be parallel to the tip. For electro-optic detection, the THz pulse was diverted with a gold-coated pick-off mirror and focused onto a ZnTe(110) crystal by a 54 mm focal length TPX lens. Just before the TPX lens, the THz pulse was sent through a 4 mm thick fused-silica window to emulate trans-

mission through the window of the UHV inverted viewport. Also, the optical path length from the THz source to the ZnTe detection crystal was similar to the distance from the THz source to the STM tip. A low energy optical pulse was brought coincident with the THz pulse for electro-optic sampling of the THz waveform. The pump pulse, which had a center frequency of 800 nm and a temporal duration of 100 fs, was attenuated by the combination of a half-wave-plate and a polarizer. A second half-wave-plate after the polarizer set the polarization of the pump pulse to be either horizontal or vertical with respect to the tip axis. A photograph of the UHV THz-STM optical setup is shown in Fig. 5.6.

5.2 Tip Preparation

The preparation of the tip is one of the most critical aspects of STM (see discussion in section 2.2). For THz-STM, the role of the tip becomes even more important because the tip is also an antenna that couples the free-space-propagating THz radiation. Hence, both the macroscopic and microscopic tip structure determine the overall THz-pulse coupling efficiency and spatio-temporal resolution. Furthermore, since extremely high transient currents are routinely achieved with the THz-STM, it places additional constraints on the necessary structural stability of the tip apex. Significant damage can occur to the tip apex due to the extremely high current density that is inherent to both STM and THz-STM. Accordingly, it is important to select an electrically conductive element or alloy that is resilient under extremely high current densities, electric fields, and mechanical stress. Furthermore, a relatively constant density of states near the Fermi level for the tip, aids in extracting physically meaningful information from measurements of the sample. Such a strict criteria limits the possible materials one can use for STM and THz-STM tips.

Tungsten is the most commonly used material for creating sharp metal tips because it is one of the toughest known elements. It has the lowest coefficient of thermal expansion of any elemental metal (4.5 K^{-1}), the highest melting

point and boiling point of any element (3695 K & 6203 K), one of the highest mass densities (19.3 g/cm^3) and the highest critical field for field-induced-evaporation ($\sim$ 6 V/Å) [56, 58]. While these attributes make tungsten the ideal choice in most cases, under ambient pressure and temperature, tungsten readily reacts with oxygen to form a thin non-conductive oxide along the surface of the tip. Hence, inert metals such as platinum, iridium and gold are typically used for STM measurements in ambient air. However, since these three noble metals are relatively soft, the tip apex can be easily damaged due to unintentional tip–surface contact. Accordingly, platinum and iridium are often alloyed together (in ratios of 90:10 or 80:20) in order to increase the hardness of the tip. Gold and silver tips are used for their broad plasmonic response at optical frequencies to enhance the coupling efficiency of optical photons into [285] and out-of [212, 213] the tunnel junction.

Hundreds of methods have been developed for creating sharp metal tips due to their wide-spread use among scientists throughout the 20th century. The sharpest and highest quality tips are first created by a chemical etching process, and then refined with additional treatment inside of the vacuum chamber

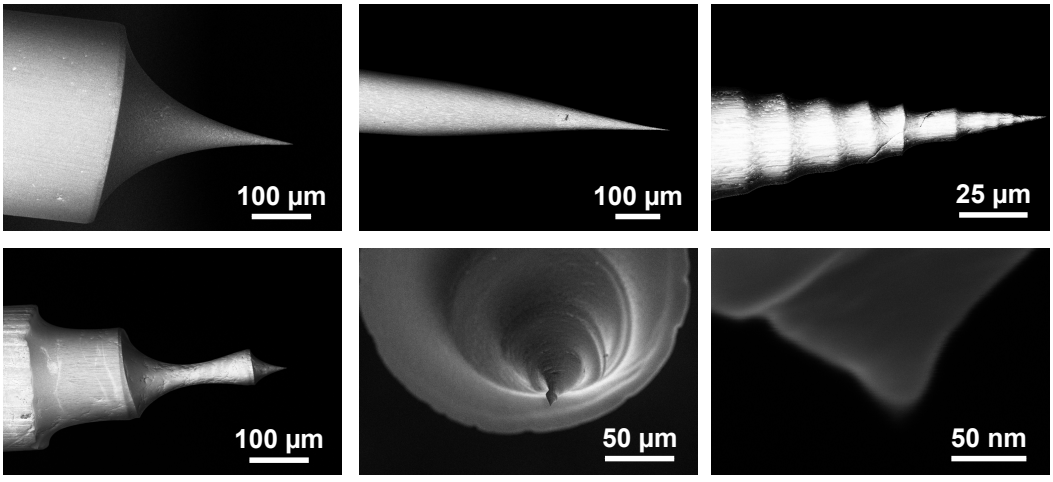

Figure 5.7: Scanning electron microscope images of tungsten tips that were used with the THz-STM. The images were all acquired using the in-lens detector with a 5 keV electron beam propagating at 90° with respect to the tip axis. The bottom-middle image was acquired at 10° with respect to the tip axis.

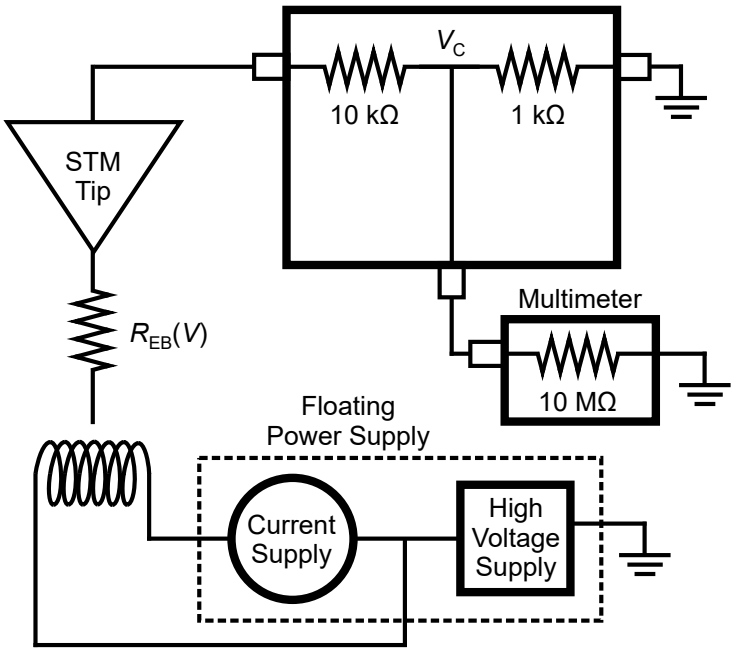

Figure 5.8: Electronics setup for electron bombardment of the STM tip. A floating power supply (Prevac Heat-2PS) sourced a constant-current output of a few amperes through a thoriated-tungsten filament, while floating several hundred volts below ground (negative voltage). The voltage V_C was measured using a multimeter and used to determine the the current travelling through the tip via $I_{EB} = (1\ \text{mA/V}) \times V_C$. The 10 kΩ resistor was a safety precaution in the case of an electrical short, $R_{EB}(V) \approx 0$. The resistor can support 11 W of power dissipation at 1080 V, and transiently 110 W for 5 seconds. Caution: do note raise the current through the thoriated-tungsten filament much more than 1.4 A as it will evaporate considerable amounts of tungsten onto the surrounding ceramic insulation, eventually creating an electrical short that requires breaking vacuum to remove. For reference, this layer was easily removed by placing the ceramic insulation into a beaker of 3 M NaOH and placing the beaker into an ultrasonic bath for several hours.

[66, 286–289]. Tips made from Pt/Ir alloy are most often created by mechanically cutting and simultaneously pulling the wire with high precision shears. Although it is a rudimentary procedure, this method routinely produces STM tips that can acquire atomic resolution images [290]. However, for tungsten tips, high precision shears cannot be used to create the tip apex as the element is quite brittle, and does not reliably form a sharp apex under the application of mechanical stress by the shears.

For all the UHV THz-STM experiments described in this thesis, the tips were

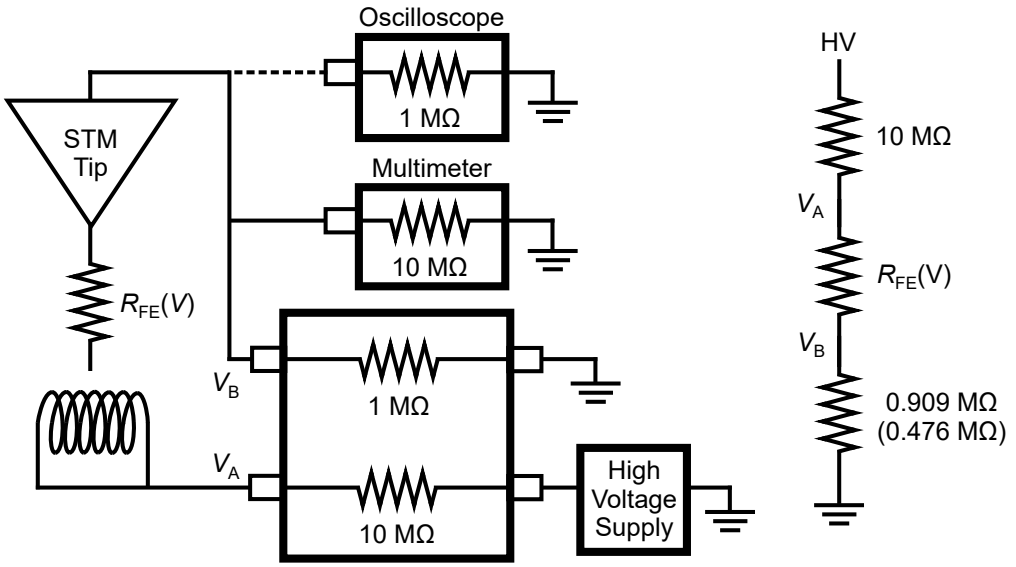

Figure 5.9: Electronics setup for field emission of the tip. A field emission bias voltage up to +5000 V was provided by the high voltage power supply (Stanford Research Systems PS350). The voltage V_B was measured using a multimeter and used to determine the the current travelling through the tip via $I_{FE} = (1.1\,\mu A/V) \times V_B$. The 10 MΩ resistor was a safety precaution in the case of an electrical short, $R_{FE}(V) \approx 0$. The resistor can support 0.75 W of power dissipation at 7500 V. An oscilloscope may be used to monitor the field emission current. If the oscilloscope was connected, the overall effective resistance was lowered from 0.909 MΩ to 0.476 MΩ, changing the calibration factor to 2.1 µA/V. A simplified equivalent circuit representation is shown on the right, it was used to find $V_{FE} = V_A - V_B$.

electrochemically etched from 0.25 mm diameter polycrystalline tungsten wire using a double-lamella drop-off technique [291, 292] with 3 M NaOH as the etchant[2]. Variability in the formation of the meniscus during the etching process provided a wide variety of tip geometries (see Fig. 5.7). Nearly all of the tip shapes were found to couple THz pulses; however, the microscopic apex of most tips was often altered by the extremely large THz electric fields and THz-pulse-induced currents that were present during THz-STM (the sample surface was often altered as well, see chapter 8 for details). In order to create a sharp tip apex that had long-term stability with the THz-STM, several days of preparation were often required. This preparation involved multiple annealing cycles that restructured the tip apex and removed adsorbates on

[2]Use the tungsten carbide shears to cut the tungsten wire.

the surface of the tip, including the thin layer of tungsten oxide that was present on all of the tungsten tips that were prepared in ambient air. The tungsten tips were annealed *in situ* using electron bombardment heating at microampere-to-milliampere currents, depending on the distance of the tip to the tungsten filament and the desired annealing temperature. Electron bombardment heating was performed with the tip loaded into the RHK-tip-exchange-holder and positioned (using the wobble stick) onto a high-voltage-safe tip-conditioning-station. A floating power supply sourced the electron bombardment current and it was measured using a computer-controlled digital multimeter (see Fig. 5.8).

After treating the STM tip with electron bombardment heating, the electronic connections were changed following Fig. 5.9 and field-induced electron emission was performed at room temperature. The strong electric field was provided by a static d.c. high-voltage, V_{FE}, that was also locally enhanced at the tip apex. The basic theory of electron field emission was developed by R. Fowler and L. Nordheim in their 1928 seminal paper [172]. More recent developments have

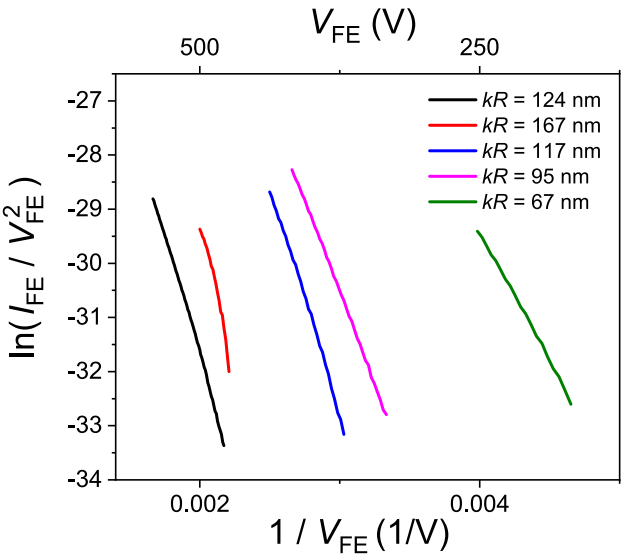

Figure 5.10: Measured Fowler-Nordheim plots for several polycrystalline tungsten tips that were prepared for use with the THz-STM. The legend shows the radius of curvature estimate for each tip apex based on the slope of its corresponding Fowler-Nordheim plot (see text for details).

improved their original equation by taking into account the contribution of the image potential when calculating the effective barrier height, ϕ_{eff}, for the field emitting electrons [293–296]. These improvements to the original equation manifest as two prefactors, $t(y)$ and $v(y)$, with the full equation given by

$$I_{\text{FE}} = \frac{e^3 A}{8\pi\hbar\phi t^2(y)}\left(\frac{V_{\text{FE}}}{kR}\right)^2 \exp\left[-\frac{4}{3}\frac{\sqrt{2m\phi^3}}{\hbar e}\left(\frac{kR}{V_{\text{FE}}}\right)v(y)\right], \qquad (5.4)$$

where $y = \sqrt{e^3 V_{\text{FE}}}/\sqrt{kR\phi^2}$, A is the emitting surface area, $\hbar$ is the reduced Planck constant, ϕ is the barrier height ($\sim$ material work function), R is the tip radius of curvature and k is a dimensionless factor that is determined by the local geometry of the tip. The prefactors $t(y)$ and $v(y)$ are typically very close to unity; a table of their values can be found in [293].

A current–voltage characteristic that follows Eq. 5.4 will produce a straight line on a plot of $\ln(I/V^2)$ versus $1/V$ (Fig. 5.10). This particular type of linearization is called a Fowler-Nordheim plot, and it can be used to provide an estimate of the tip radius of curvature, R, provided that ϕ and k are known. However, since k is very difficult to determine, it is usually ignored and just written alongside R as a reminder that the calculation is only accurate to within an order of magnitude. Furthermore, if the tips are extremely sharp,

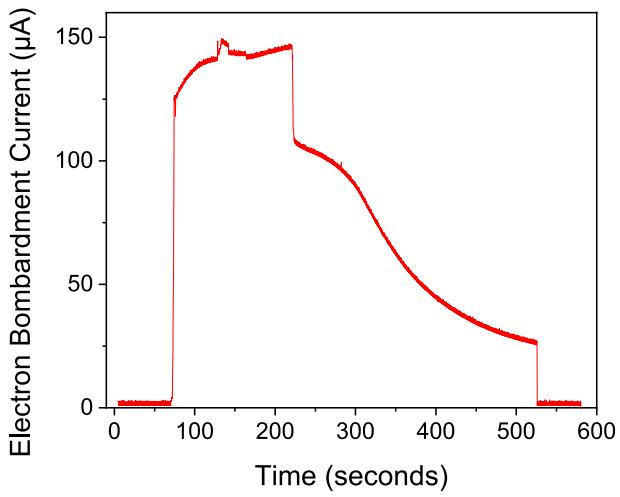

Figure 5.11: Measured electron bombardment current versus time with 1.3 A travelling through the tungsten filament (see Fig. 5.8). The floating voltage supply was turned to –900 V after 75 seconds, changed to –800 V after 225 seconds and then turned off after 525 seconds.

their I–V characteristics will deviate from Fowler-Nordheim behaviour [294–296]. The Fowler-Nordheim equation (Eq. 5.4) agrees with the Simmons model (Eq. 2.16) at very large voltages relative to the barrier height.

Field emission and electron bombardment were routinely cycled back-and-forth, in order to sharpen the tip apex (see also [297]). The slopes of the Fowler-Nordheim plots were a good indicator if the tip was getting sharper or blunter during the *in situ* treatment cycles. However, rather than performing a Fowler-Nordheim plot after every treatment cycle, we typically only recorded the onset voltage, V_{FE}, that was required to achieve a field emission current of 1 nA. The tips underwent repeated cycles of electron bombardment and field emission until the onset voltage was significantly lower compared to its starting value. In a few extreme cases, a tip that would not field emit up to 5000 V, was reconfigured into a sharp nano-tip requiring only several hundred volts for field emission. An electron bombardment current versus time plot for such a case is shown in Fig. 5.11. From trial-and-error it was determined that a decreasing electron bombardment current with time would produce a considerably lower field emission onset voltage. As a result, during the bombardment treatment in Fig. 5.11, when the electron bombardment current

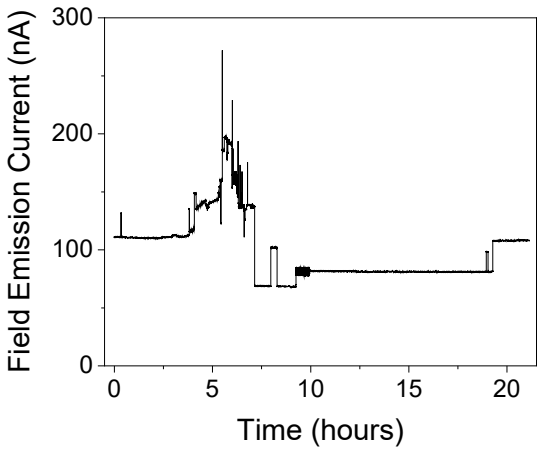

Figure 5.12: Measured field emission current versus time at $V_{\mathrm{FE}} = 700$ V. The current was sampled every 200 ms for more than 20 hours. The high field emission current induced numerous structural changes to the tip apex (between 5 and 10 hours), until eventually a stable configuration was reached.

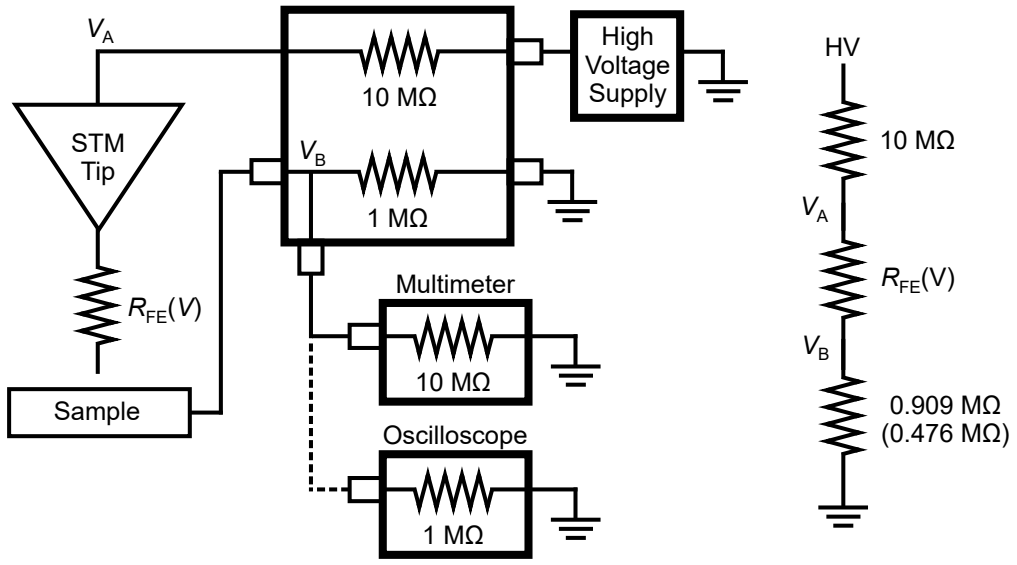

Figure 5.13: Electronics setup for field emission of the tip while mounted in the STM scanhead and located several hundred nanometers above the sample surface. A field emission bias voltage up to −600 V was provided by the high voltage power supply (Stanford Research Systems PS350). The voltage V_B was measured using a multimeter and used to determine the the current travelling through the tip via $I_{FE} = (1.1\,\mu A/V) \times V_B$. The 10 MΩ resistor was a safety precaution in the case of an electrical short, $R_{FE}(V) \approx 0$. The resistor can support 0.75 W of power dissipation at 7500 V. An oscilloscope may be used to monitor the field emission current. If the oscilloscope was connected, the overall effective resistance was lowered from 0.909 MΩ to 0.476 MΩ, changing the calibration factor to 2.1 µA/V. A simplified equivalent circuit representation is shown on the right, it was used to find $V_{FE} = V_A - V_B$.

was found to be increasing with time, the applied voltage was lowered until a stable downward trend began (occasionally the voltage was raised when looking for a downward trend). Long-term field emission was also used to reconfigure the shape of the tip apex and improve the overall tip stability at very high currents (Fig. 5.12). However, unlike electron bombardment, the structural reshaping that occurred during the field emission process was completely unpredictable and would sometimes result in a lower onset voltage afterwards. Nonetheless, long-term field emission proved to be an effective way of obtaining and maintaining high quality THz-STM tips that were capable of acquiring high resolution images, while operating at extremely large transient tunnel currents. Occasionally, field emission was also performed with the tip

positioned several hundred nanometers above the sample surface[3]. In this case, the tunnel current amplifier was disconnected from the STM scanhead and the electronics were connected as shown in Fig. 5.13.

Very recent THz-STM experiments have confirmed that the macroscopic tip shape determines the precise temporal structure of the transient THz voltage pulse, $V_{\mathrm{THz}}(t)$, at the tip apex [137]. In particular, certain macroscopic tip shapes were found to significantly alter the carrier-envelope-phase of the incident THz pulse from the expected value that was determined from electro-optic sampling the free-space-propagating THz waveform. In chapter 7 we further elucidate this phenomenon by directly sampling of the THz pulse near-field in the THz-STM and exploring its spatial dependence on the GaAs(110) surface.

5.3 Sample Preparation

Proper sample preparation is essential for obtaining high quality surfaces that are atomically flat, free of adsorbates, and ready for high resolution imaging [298]. All of the samples that were investigated here are frequently studied by researchers that use the STM and other surface science instruments. This section summarizes the standard experimental procedure for preparation of these surfaces within the context of our experimental setup. The height of the sample is an important consideration for THz-STM due to the beetle-style design of our STM scanhead. In the beetle-style design, three piezo legs are used to coarsely position the STM tip just before approach. These three piezo legs simultaneously obstruct direct line-of-sight to the tip–sample junction for all four window viewports that are used to couple light into the UHV chamber. Hence, before mounting any tips and samples into the UHV system, the user must ensure that the tip–sample separation is approximately 0.25–0.5

[3]Note that in this particular field emission configuration, a negative bias voltage is applied to the tip, instead of a positive bias voltage on the filament. Therefore, the applied voltage in this configuration should not exceed more than −600 V because the insulation of the tunnel current wire does not support high voltages. Significant damage may occur to the STM scanhead if this warning is not followed! Also, the high voltage supply must be completely turned off when switching its polarity.

mm upon landing with the piezo legs onto the RHK sample holder. At this tip–sample separation, the coarse positioning piezo legs will all simultaneously rotate by about 30° during the approach, enabling electromagnetic radiation from all four viewports to see the tunnel junction.

5.3.1 Si(111)-(7×7)

The primary sample was an n-type Si(111) wafer that was 0.25 mm thick with an arsenic concentration of 4×10^{19} cm^{-3} (p-type samples with a similar concentration of boron were seldom prepared following the same recipe). The sample was cleaved into a rectangular shape (8 mm × 5 mm) and placed into the sample holder where it was electrically isolated from its surroundings. Sapphire washers pressed the sample down onto two tantalum sheets that were placed on opposite sides of the sample, providing an ohmic contact to the sample. For this highly doped sample, a low-voltage (< 20 V) constant-current power supply (Agilent 6542A) was directly connected to the electrically isolated sample. The silicon sample was first degassed for 12 hours at 900 K, while maintaining a pressure below 5×10^{-10} torr. The temperature was recorded using an infrared thermometer (Land Instruments Cyclops160L) and the pressure was recorded using a nude Bayard-Alpert ionization gauge (Granville Phillips 274) with a thoria-coated iridium filament[4]. After cooling the sample to room temperature, it was flashed with multiple heating cycles up to 1500 K, while maintaining a chamber pressure less than 5×10^{-10} torr. Just after the final flash, the sample was brought to 1200 K and subsequently cooled through the Si(111)-(7×7) phase transition temperature near 1100 K. Finally, the sample was brought to room temperature and transferred to the STM chamber. By varying the annealing time of the sample, the large-scale structure of the surface was altered as shown in Fig. 2.4 and Fig. 2.5.

An n-type Si(111) sample with a phosphorus concentration of 10^{15} cm^{-3} was

[4]Use a thoria-coated iridium filament instead of a tungsten filament for the ionization gauge in the UHV system. This is because tungsten filaments can coat the inner chamber with a tungsten oxide powder if the filament is still hot when the vacuum chamber is vented to atmosphere.

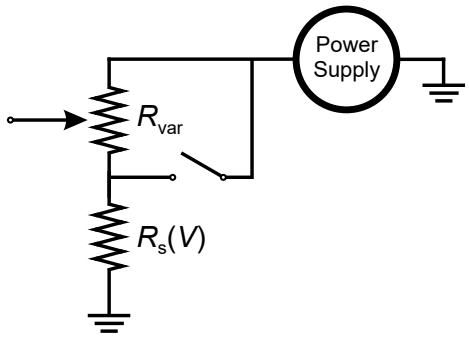

Figure 5.14: Electronics setup for direct current resistive heating of the sample, $R_s(V)$. The in-series variable resistor, R_{var} = 0.1–500 Ω, can only support a power dissipation of 0.5 W and should be circumvented by using the switch when necessary. Both constant-current and constant-voltage power supplies were used, depending on the value of $R_s(V)$ (see text for details).

also prepared following a similar recipe. However, due to its low doping concentration, the bulk resistance of the sample at room temperature was very high ($\sim$ MΩ). As a result, a higher voltage power supply (BK Precision 9206) was used to generate the milliampere currents that were necessary to begin resistively heating the sample. As the d.c. current flowing through the sample was increased, resistive heating raised the temperature of the sample, until suddenly the resistance of the sample changed dramatically from MΩ to Ω in the span of a few milliseconds. Since a constant-current power supply cannot regulate the voltage that quickly, a variable resistor was placed in-series with the sample, such that the variable resistor limited the current draw from the power supply (Fig. 5.14). Once the current draw from the power supply had stabilized and the voltage was being safely regulated, the variable resistor was slowly turned down to 0.1 Ω and then shorted out of the circuit[5]. The current and voltage values that were necessary for flashing and annealing the silicon surface are quite different compared to the higher doped sample. However, both samples should have a similar resistive power dissipation for each corresponding temperature setting: approximately 25 W for 1500 K, and 4 W for 900 K. For samples with a particularly low dopant concentration, the 150 V

[5]After shorting out the variable resistor, make sure to set the resistance back to 500 Ω before increasing the current. The variable resistor used here can only dissipate 0.5 W of power.

output of the BK9206 power supply was not strong enough to generate the milliampere currents that were necessary to begin resistively heating the sample. In this case, a 500 V power supply was used (Lambda Electronics Model 71), but due to its current limit of 200 mA, it had to be switched out for the BK9206 power supply once the average temperature of the sample had been sufficiently increased.

5.3.2 H-Si(100)-(2×1)

The electronic properties of a clean silicon surface can be completely altered by passivating the highly reactive adatoms with a hydrogen capping layer [124–127, 188, 269, 287, 299–307]. The Si(100)-(2×1) surface is typically chosen as the starting sample as it readily passivates into H-Si(100)-(2×1)[6] [302]. This surface is of great technological importance as individual hydrogen adatoms can be selectively removed by the STM tip, forming a conducting channel of silicon dangling bonds laterally along the surface that can be used to fabricate atomic-scale circuitry [269, 304, 306, 307] and memory [188].

[6]Passivation of Si(111) into H-Si(111)-(1×1) is complicated by the formation of silicon hydrides along the surface [301, 302].

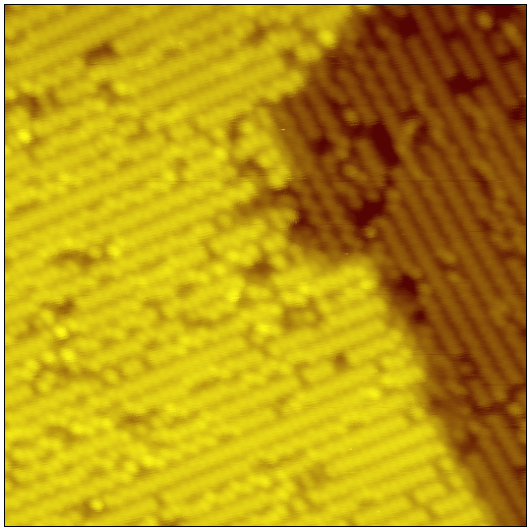

Figure 5.15: STM image of the Si(100)-(2×1) surface acquired in constant-current mode at $V_{\text{d.c.}} = -1.4$ V and $I_{\text{d.c.}} = -50$ pA. Image size 20 nm × 20 nm.

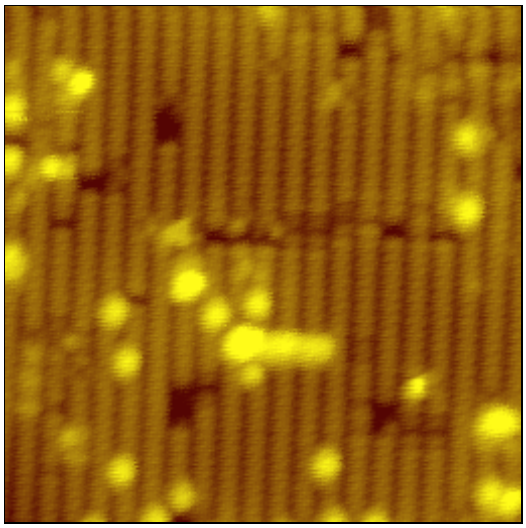

Figure 5.16: STM image of the H-Si(100)-(2×1) surface acquired in constant-current mode at $V_{\text{d.c.}} = -1.5$ V and $I_{\text{d.c.}} = -100$ pA. Image size 15 nm × 15 nm.

We performed hydrogen termination of dangling bonds on an atomically flat Si(100)-(2×1) surface that was prepared as follows. First, the sample was degassed for 12 hours at 900 K, while maintaining a pressure below 5×10^{-10} torr. Next, the sample was flashed several times up to 1500 K, while maintaining a chamber pressure less than 5×10^{-10} torr. After the surface was free of adsorbates (Fig. 5.15), the sample temperature was brought to 600 K and an atomic hydrogen source (RIBER) was used to dose the Si(100)-(2×1) surface with approximately 10 langmuir[7] (Fig. 5.16). Hydrogen gas was introduced into the chamber by a high-purity gas cylinder and regulated by a mass-flow-controller (Bronkhorst) that was set to a flow-rate of 0.1 standard-cubic-centimeter-per-minute (3.3% of maximum flow-rate). The atomic hydrogen was generated by a tungsten filament operating at 40 V and 16 A (85% of maximum power), corresponding to a filament temperature reading of 1130 °C[8].

[7] One langmuir (L) is defined as 1 second of exposure at 10^{-6} torr, or equivalently 100 seconds of exposure at 10^{-8} torr. Our samples were dosed at 10^{-7} torr for 100 seconds, or equivalently, 10 L.

[8] The actual temperature of the tungsten filament is ∼2600 K. This temperature is hot enough to radiatively melt the insulation on the wires of the Preparation Chamber manipulator arm. Accordingly, the exposure time was kept brief, the UHV chamber walls were water-cooled, and the sample was not held directly underneath the filament.

5.3.3 Ag-Si(111)-($\sqrt{3}\times\sqrt{3}$)

Ag-Si(111)-($\sqrt{3}\times\sqrt{3}$) is a well-known surface superstructure that is formed upon adsorption of silver atoms onto a clean Si(111) surface. The silver atoms form a crystalline monolayer on top of the silicon that supports a two-dimensional metallic-like surface-state with a relatively low conductivity (it is about an order of magnitude more conductive than the Si(111)-(7×7) surface [308, 309]). Its unique electronic properties arise from the formation of two inequivalent triangles within the unit cell of the surface superstructure [308, 309].

First, a Si(111)-(7×7) surface was prepared following the recipe in section 5.3.1. Next, the sample was transferred to the deposition chamber, which was connected to the preparation chamber of the UHV system. A current of approximately 40 A (RD Mathis LV400) was used to resistively heat a standard tungsten boat containing high-purity silver pellets. The deposition rate was stabilized to 0.1 Å/s before exposing the silicon surface for 1–2 seconds, providing a sub-monolayer coverage of silver. The deposition rate was monitored

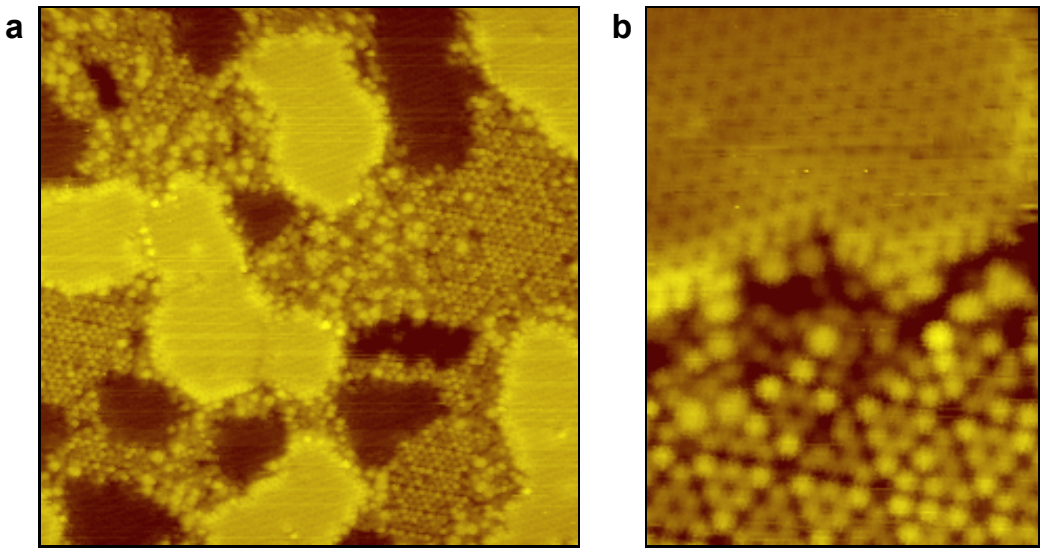

Figure 5.17: STM images of the Ag-Si(111)-($\sqrt{3}\times\sqrt{3}$) surface with only partial coverage of the underlying Si(111)-(7×7) layer. The images were acquired in constant-current mode at $V_{\text{d.c.}} = -1$ V and $I_{\text{d.c.}} = -100$ pA. **a**, image size 50 nm × 50 nm. **b**, image size 10.5 nm × 14.4 nm.

using a gold-coated quartz crystal monitor (Inficon). A closed-flow water cooling system was used to prevent the electrodes and the quartz crystal monitors from overheating. The silicon sample was kept at ambient temperature during the deposition. Immediately after the deposition, the sample was resistively heated to 790 K for 2 minutes. After the sample had cooled down to room temperature, it was transferred to the STM chamber for analysis (Fig. 5.17).

5.3.4 GaAs(110)

Atomically flat surfaces of GaAs(110) were prepared by cleaving a vertically oriented n-type GaAs(100) wafer with a silicon concentration of 3×10^{18} cm^{-3}, and a thickness of 0.35 mm. The STM tip landed on the freshly exposed (110) facet of the GaAs crystal (Fig. 5.18). The sample was mounted vertically into the RHK sample holder and held in place by tightening a set-screw that sandwiched the GaAs wafer between two molybdenum blocks. In order to provide an ohmic contact between the molybdenum and the GaAs, a 10 nm chromium film, and a 50 nm gold film were evaporated onto the unpolished surface of the GaAs wafer. A small notch of about 1 mm in length was inscribed near the middle of the sample in order to set the location of the cleave.



Figure 5.18: Photograph of the tip during THz-STM of a freshly cleaved GaAs(110) surface in ultrahigh vacuum.

Chapter 6

THz-STM of Si(111)-(7×7)

Ultrafast control of current on the atomic scale is essential for future innovations in nanoelectronics. Extremely localized transient electric fields on the nanoscale can be achieved by coupling picosecond duration THz pulses to metallic nanostructures. Here, we demonstrate terahertz scanning tunnelling microscopy (THz-STM) in ultrahigh vacuum as a new platform for exploring ultrafast non-equilibrium tunnelling dynamics with atomic precision. Extreme THz-pulse-driven tunnel currents up to 10^7 times larger than steady-state currents in conventional STM are used to image individual atoms on a silicon surface with 0.3 nm spatial resolution. At THz frequencies, the metallic-like Si(111)-(7×7) surface is unable to screen the electric field from the bulk, resulting in a terahertz tunnel conductance that is fundamentally different than that of the steady-state. Ultrafast THz-pulse-induced band bending and non-equilibrium charging of surface states opens new conduction pathways to the bulk, enabling extreme transient tunnel currents to flow between the tip and sample.

The Si(111)-(7×7) surface has been studied extensively with conventional STM [51, 66, 67, 87, 218, 225, 226, 310–327] and other techniques [52–55, 220–224, 328–335], and the nature of its metallic-like state is a topic of intense interest [312, 314, 318, 319, 323, 328–334]. Here, we perform for the first time atomic-resolution THz-STM in ultrahigh vacuum on a Si(111)-(7×7) surface

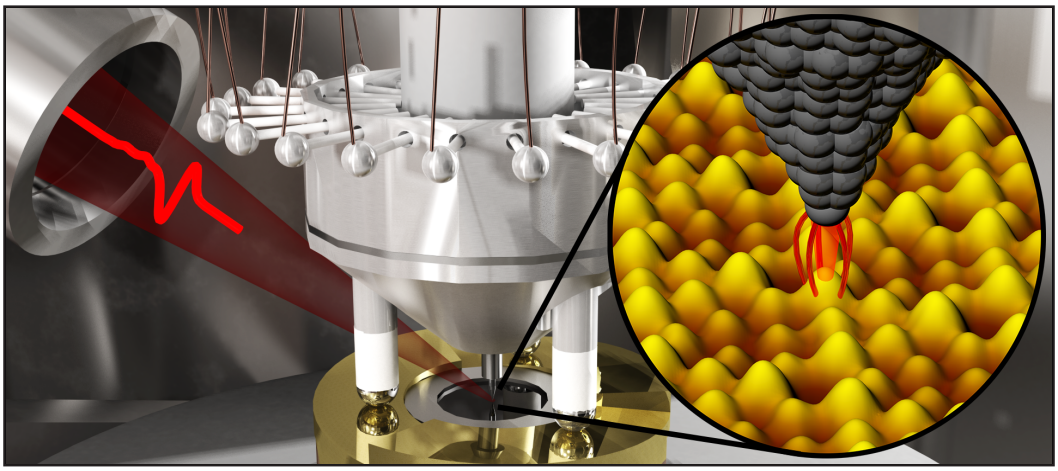

Figure 6.1: Ultrafast THz pulses are focused by a lens in an inverted viewport (left) onto an STM tip in ultrahigh vacuum (center), inducing a tunnel current at the junction (inset).

and establish that ultrafast THz-pulse-driven tunneling at high current levels can indeed be localized to single atoms. Further, we show that interpreting the atomic corrugations of a terahertz-driven STM (TD-STM) image on Si(111)-(7×7), where hundreds of electrons tunnel within subpicosecond timescales, requires an understanding of the non-equilibrium charging dynamics induced by THz pulse at the silicon surface. Atomic resolution is preserved during TD-STM imaging while achieving a transient tunnel current density greater than[1] 10^{11} A/cm^2, tens-to-hundreds of times greater than some of the highest current densities reported by conventional STM while imaging a metallic surface [205, 336]. It is remarkable that such an extreme transient current density does not adversely affect the single-atom tip or the surface atom under investigation, as would happen with conventional STM of Si(111)-(7×7) at d.c. currents of such magnitude [311] (see chapter 8 for details on THz-pulse-induced surface modifications). Furthermore, the direction of the THz-driven tunnel current through a single atom can be controlled by the polarity of the THz pulse electric field, and at high terahertz electric fields an additional contribution to the tunnel current from hot electrons is observed.

[1] In Fig. 6.28 the spatial resolution is approximately 3 Å at $N_{e^-} = 1000$ rectified electrons per THz pulse. According to our model this corresponds to a peak transient current of approximately 2 mA (Fig. 6.24c): 7.1×10^{11} A/cm^2 = (2 mA)/(π [3×10^{-8} cm]^2).

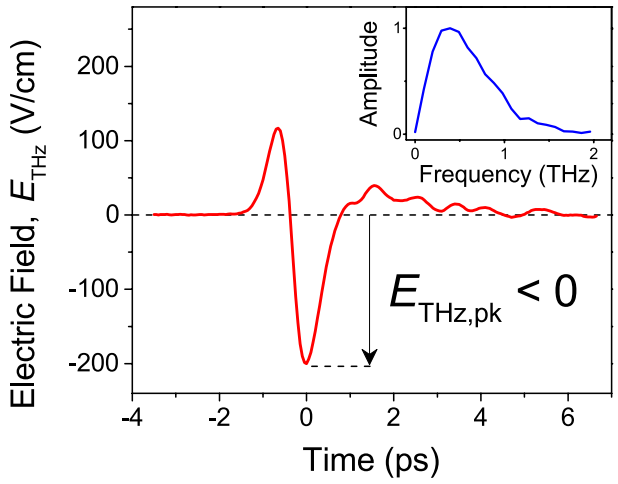

Figure 6.2: THz pulse electric field waveform and its corresponding frequency spectrum peaked at 0.4 THz (inset).

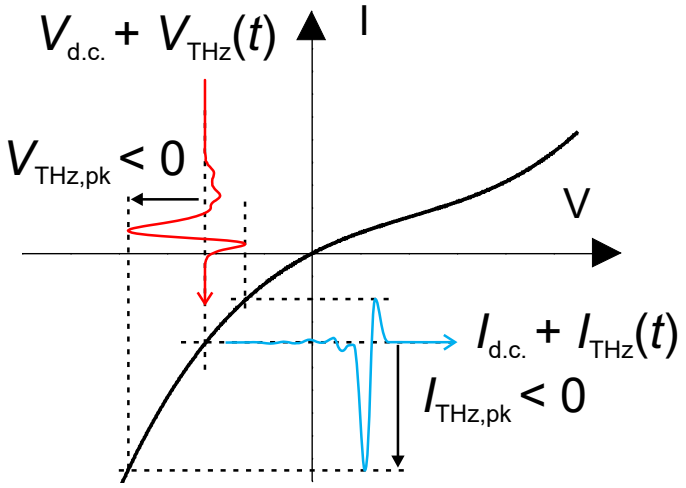

Figure 6.3: Schematic of the nonlinear tunneling I–V curve of an STM (black solid line), where the d.c. bias, $V_{\mathrm{d.c.}}$, drives a d.c. current, $I_{\mathrm{d.c.}}$ and an ultrafast THz pulse with asymmetric half-cycle amplitudes generates a time-dependent voltage, $V_{\mathrm{THz}}(t)$ (red solid line), that drives an ultrafast terahertz-induced current, $I_{\mathrm{THz}}(t)$ (blue solid line), resulting in a rectified average tunnel current, $I_{\mathrm{THz,avg}}$.

6.1 Atomic Resolution THz-Driven STM

A single-cycle THz pulse is guided into an ultrahigh vacuum chamber and focused onto the tip of an STM (Fig. 6.1). The THz pulse (Fig. 6.2) induces a transient voltage $V_{\mathrm{THz}}(\mathrm{t})$ across the STM tunnel junction that drives an extremely localized ($\lambda/10^6$) ultrafast tunnel current. The total current is the sum of the d.c. component, $I_{\mathrm{d.c.}}$, and the time-dependent response, $I_{\mathrm{THz}}(t)$, induced by the THz pulse, as illustrated in Fig. 6.3. However, the electronics of an STM operate well below THz frequencies, so only the rectified response, I_{THz} (e^-/pulse) $= e^{-1} \int I_{\mathrm{THz}}(t)\ \mathrm{d}t$, is measured. To demonstrate the presence of THz-pulse-induced tunneling, point spectroscopy was performed with and without THz pulses incident on the tip. Typically in STM, the current–voltage characteristic (I–V curve) crosses through the origin (Fig. 6.4a); however, with THz pulses incident on the tip, the I–V curve is modified, including a -12 pA shift at $V_{\mathrm{d.c.}} = 0$ V, where $I_{\mathrm{THz,avg}} = -12$ pA corresponds to I_{THz} (e^- /pulse) $= N_{\mathrm{e}^-} = 300$ rectified electrons per pulse at 250 kHz tunneling from the sample to the tip. The exponential decay of the current–distance characteristic (I–z curve) does not change significantly when THz pulses are incident (Fig. 6.4b), evidence that both the d.c. bias and the terahertz voltage are inducing a tunneling process. Linearly polarized THz pulses that have asymmet-

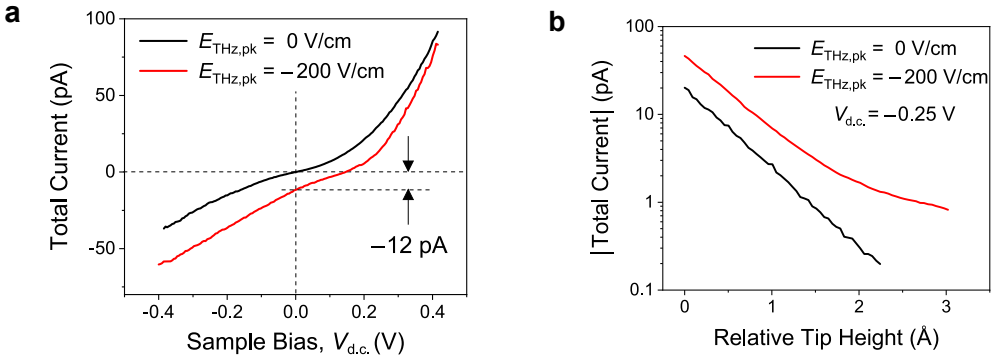

Figure 6.4: **a**, Measured I–V curves and **b**, I–z curves acquired without THz pulses incident (black solid line) and with THz pulses incident (red solid line). The measurements were acquired with the tip positioned over an unfaulted centre adatom and the tip–sample separation set by $V_{\mathrm{d.c.}} = -0.25$ V, $I_{\mathrm{d.c.}} = -20$ pA, and $E_{\mathrm{THz,pk}} = 0$ V/cm.

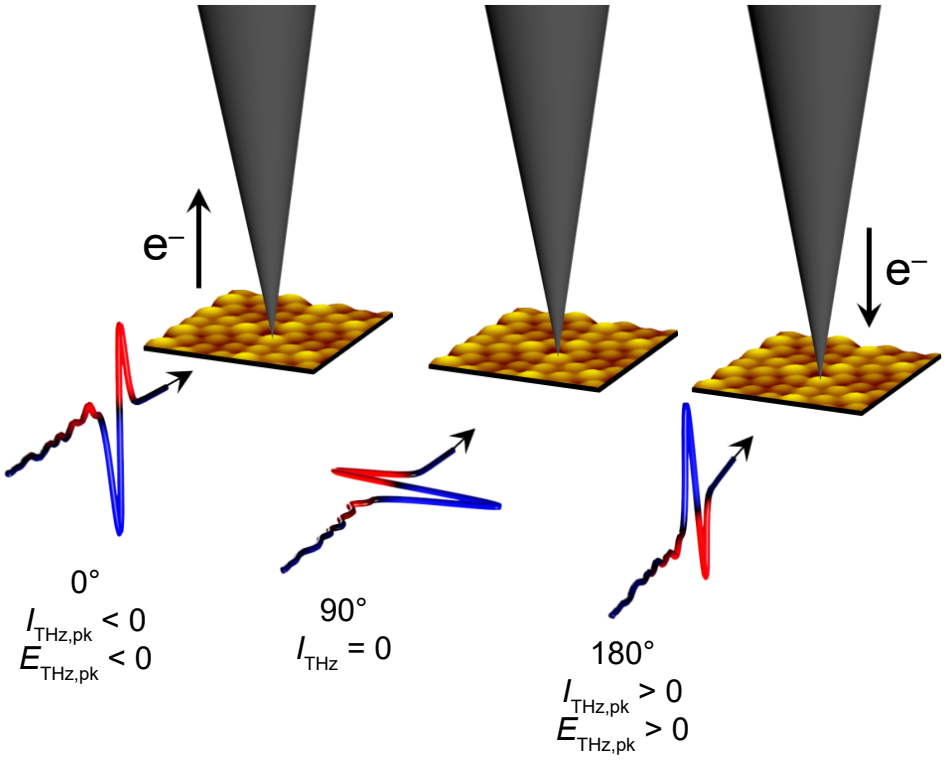

Figure 6.5: The THz pulse polarity (0°, 90°, 180°) is used to control the THz-pulse-induced rectified tunnel current. Electrons flow from the sample to the tip for a negative THz polarity and from the tip to the sample for a positive THz polarity.

ric half-cycle amplitudes (Fig. 6.2) are used to control the direction of current flow at the tip–sample junction (Fig. 6.5). When rotating the THz pulse polarization (Fig. 6.6), I_{THz} approaches zero as the THz pulse becomes polarized perpendicular to the tip, consistent with antenna-like coupling. Upon rotation of 180°, a reversal of the terahertz current is demonstrated, indicating that the larger THz half-cycle drives more current than the smaller half-cycle. Measurements of the THz-pulse-induced current versus incident peak electric field (THz I–E), demonstrate that a negative $V_{\mathrm{d.c.}}$ enhances I_{THz} at negative $E_{\mathrm{THz,pk}}$ and suppresses I_{THz} at positive $E_{\mathrm{THz,pk}}$, while a positive $V_{\mathrm{d.c.}}$ acts oppositely (Fig. 6.7).

Atomically-resolved images of a Si(111)-(7×7) surface were acquired with standard STM (Fig. 6.8a) and with TD-STM (Fig. 6.8b) over the same region. The

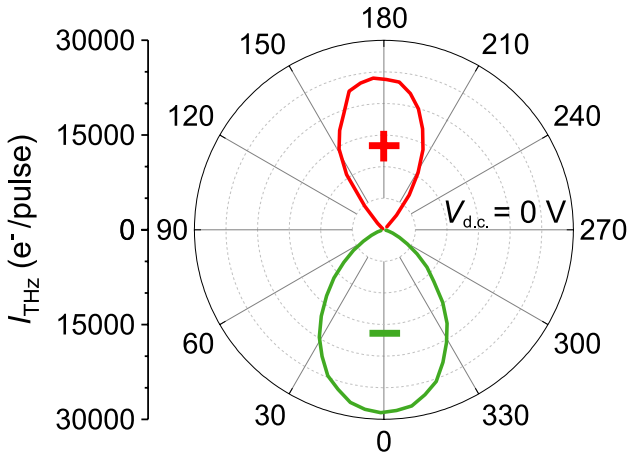

Figure 6.6: Terahertz pulse polarization dependence at $|E_{\mathrm{THz,pk}}| = 500$ V/cm and $V_{\mathrm{d.c.}} = 0$ V, demonstrating terahertz control of positive (red solid line) and negative (green solid line) extreme transient currents. For $I_{\mathrm{THz,avg}} = 0.1$ nA, 2500 electrons are rectified by each THz pulse at a rate of 250 kHz. The measurements were acquired with the feedback loop disengaged at $V_{\mathrm{d.c.}} = 0$ V, $I_{\mathrm{THz,avg}} = -20$ pA, and $E_{\mathrm{THz,pk}} = -150$ V/cm

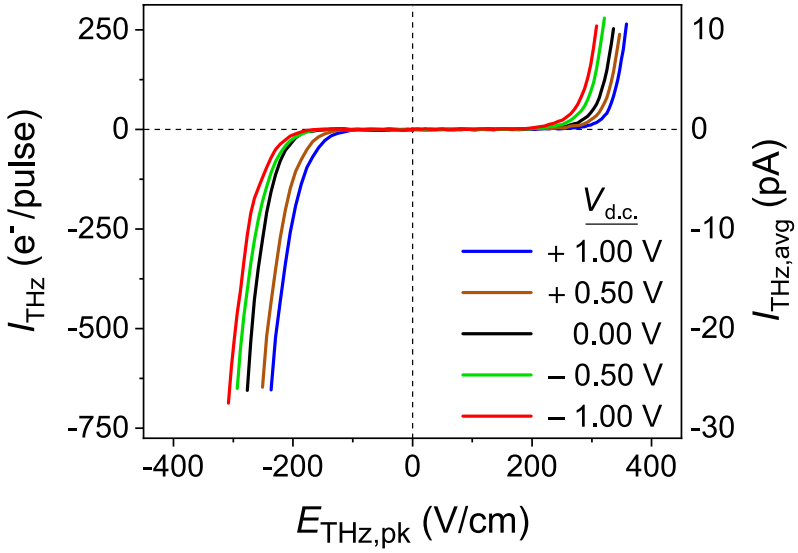

Figure 6.7: Measured THz I–E curves (THz-pulse-induced current versus peak THz pulse electric field) as a function of $V_{\mathrm{d.c.}}$. The measurements were acquired with the feedback loop disengaged at $V_{\mathrm{d.c.}} = -1.3$ V, $I_{\mathrm{d.c.}} = -20$ pA, and $E_{\mathrm{THz,pk}} = 0$ V/cm, maintaining $|I_{\mathrm{d.c.}}| < 10$ pA at $V_{\mathrm{d.c.}} = \pm 1$ V.

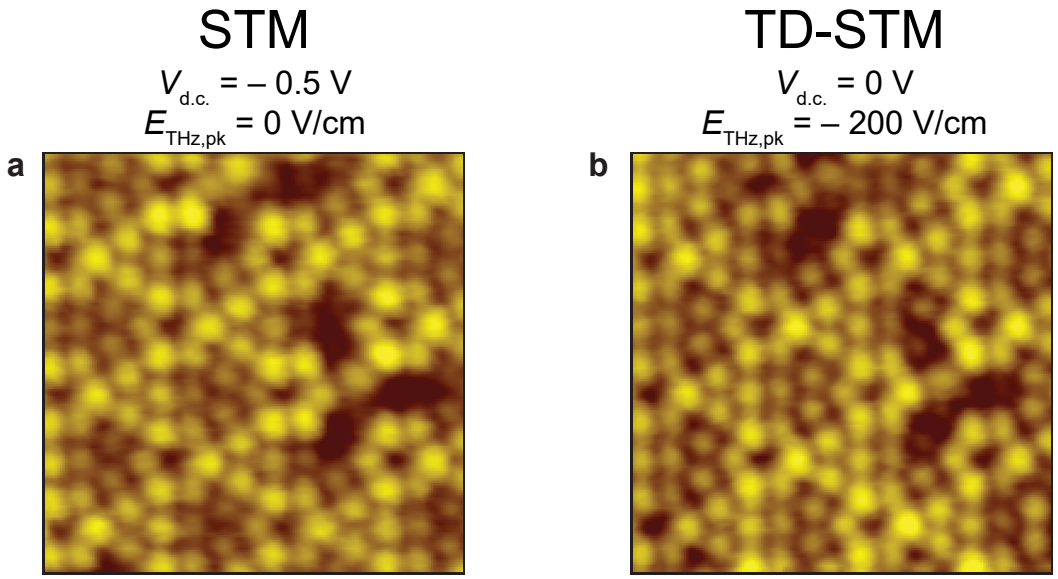

Figure 6.8: Topographic images of the Si(111)-(7×7) surface measured in constant-current mode with **a**, standard STM at $V_{\mathrm{d.c.}} = -0.5$ V, $E_{\mathrm{THz,pk}} = 0$ V/cm, $I_{\mathrm{d.c.}} = -20$ pA and **b**, TD-STM of the same region with $V_{\mathrm{d.c.}} = 0$ V, $E_{\mathrm{THz,pk}} = -200$ V/cm and $I_{\mathrm{THz,avg}} = -20$ pA. Image size 8.5 nm × 8.5 nm; scan speed 13 nm/s; low-pass-filtered with a 3×3 smoothing matrix.

TD-STM image demonstrates well-defined atomic resolution, clearly showing adatoms and defects on the 7×7 surface. Strikingly, the TD-STM image looks nearly identical to the STM image, suggesting that THz-driven electrons are tunneling through the same spatially localized surface states as standard STM. Furthermore, both images were acquired using a feedback loop current of −20 pA. For the STM image with $V_{\mathrm{d.c.}} = -0.5$ V and no THz pulses present, this current corresponds to a steady-state flow of 1.2 electrons every 10 ns. However, since $V_{\mathrm{d.c.}} = 0$ V in TD-STM, any current flow in the feedback loop circuit must arise exclusively from THz-pulse-induced tunnel currents over ∼ 0.5 ps time scales at the repetition rate of the THz pulse source. Therefore, the average THz-driven current of −20 pA used to acquire the atomically-resolved TD-STM image in Fig. 6.8b corresponds to 500 rectified electrons per THz pulse, or a peak THz-pulse-induced current of $I_{\mathrm{THz,pk}} = \Delta Q/\Delta t \approx (500\ \mathrm{e}^-)/(0.5\ \mathrm{ps}) = 160\,\mu\mathrm{A}$, which is 8 million times higher than the steady-state current used to acquire the STM image in Fig. 6.8a. The larger area

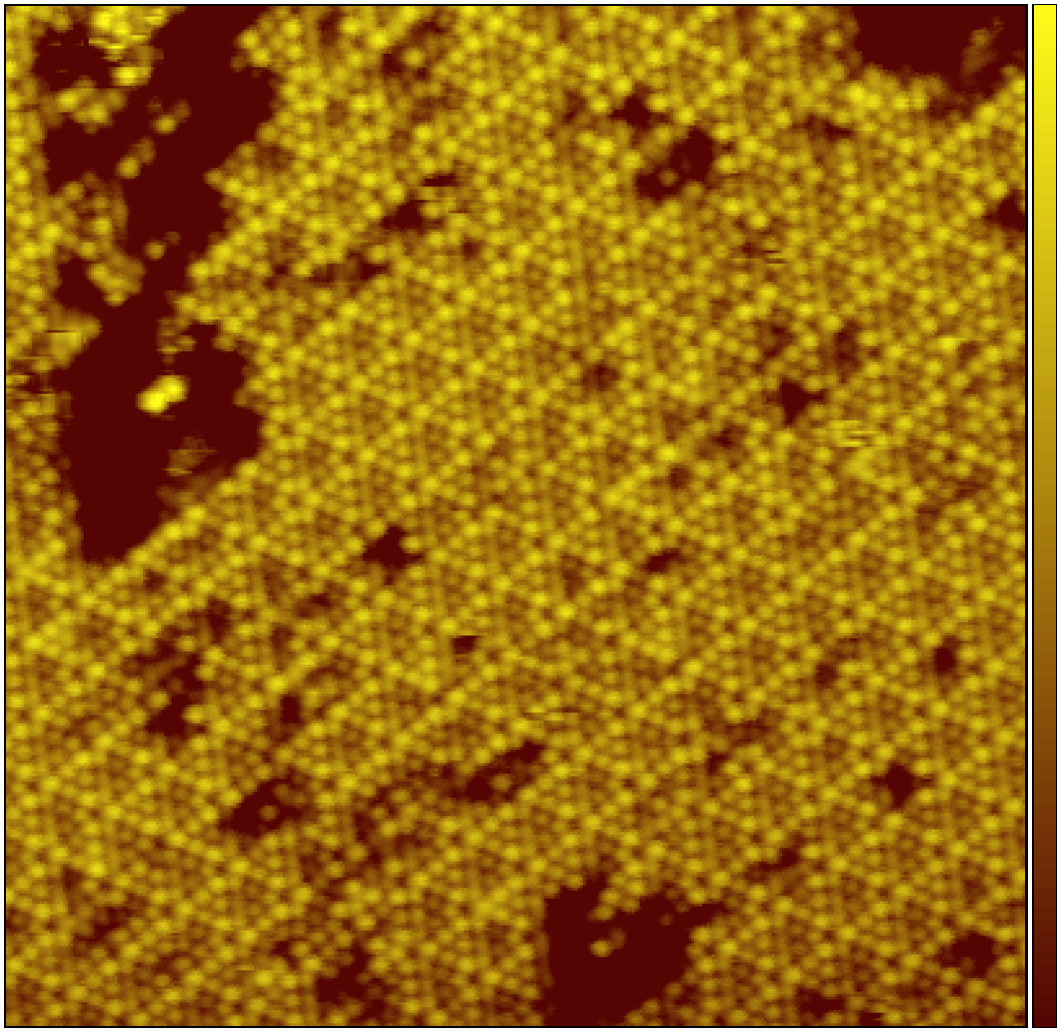

Figure 6.9: Large area TD-STM image acquired at $V_{\text{d.c.}} = 0$ V, $E_{\text{THz,pk}} = -200$ V/cm and $I_{\text{THz,avg}} = -20$ pA. Image size 40 nm × 40 nm; scan speed 25 nm/s; colourmap range 0.2 nm.

TD-STM image shown in Fig. 6.9 demonstrates that tunneling at these extreme transient current levels through single atoms can be maintained over long periods without damaging the surface or the tip (see chapter 8 for more details on THz-pulse-induced surface modifications). As shown in Fig. 6.10a, the 7×7 unit cell of the Si(111) surface is divided into two halves, faulted and unfaulted, each with 6 adatoms. Line scans performed through the unit cell (Fig. 6.10b) establish a spatial resolution of 0.3 nm for TD-STM, equivalent to what is observed with STM [218]. Thus, the transient current density achieved by TD-STM in Fig. 6.8b and Fig. 6.9 is greater than 10^{11} A/cm^2. THz pulse

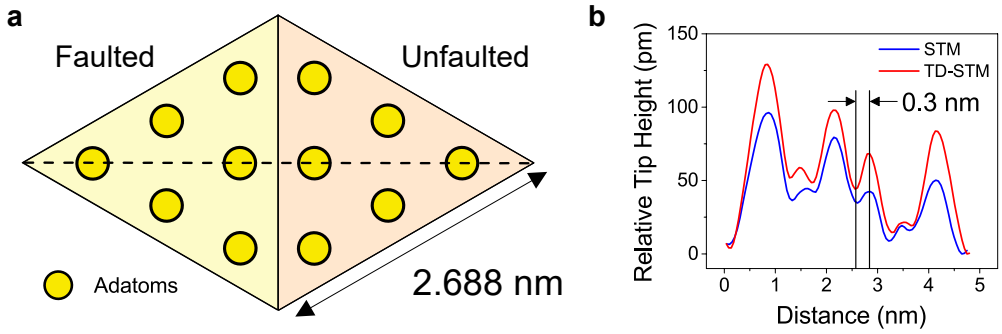

Figure 6.10: **a**, Unit cell for the Si(111)-(7×7) surface reconstruction with adatoms as yellow circles. The orientation of faulted and unfaulted unit cell halves matches the orientation in the images. **b**, Cross-sectional linescans through the 7×7 unit cell (dashed line in **a**) for STM (blue solid line) and TD-STM (red solid line), showing a spatial resolution of 0.3 nm.

autocorrelations (Fig. 4.10) are used to determine the temporal localization of the ultrafast current, $I_{\mathrm{THz}}(t)$. Constant-height TD-STM autocorrelation images (Fig. 6.11) verify that THz-pulse-induced tunnel currents are indeed spatio-temporally localized to the subnanometer and subpicosecond regimes.

Cross-sectional inescans through the 7×7 unit cell (Fig. 6.10a) reveal larger corrugations for TD-STM compared to standard STM. This is attributed to the absolute tip height being about 0.1 nm closer to the sample during TD-STM operation as compared to standard STM at $V_{\mathrm{d.c.}} = -0.5$ V. The smaller tip–sample distance may result in more localized wavefunctions contributing to the tunnel current [65, 66, 215] effectively sharpening the tip. Also, tip–sample interactions [337] and tunneling of states with large $k_{\parallel}$ [194, 338] cause

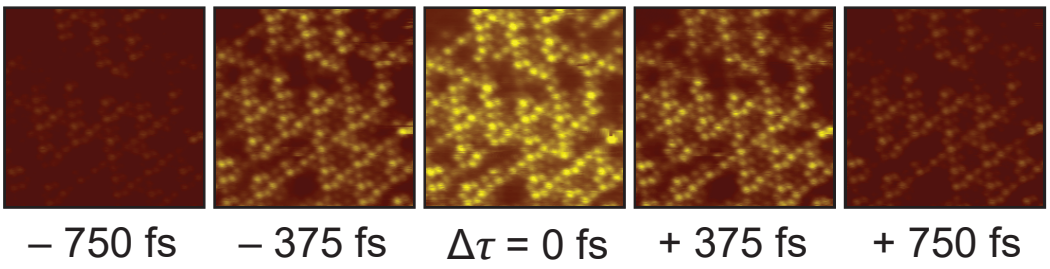

Figure 6.11: Constant-height spatio-temporal autocorrelation at $E_{\mathrm{THz,pk}} = -100$ V/cm for each pulse. The time delay between THz pulses is given by $\Delta\tau$ for each image. Image size 13 nm × 13 nm; scan speed 12 nm/s; colourmap -25 e$^-$/pulse (brown) to -450 e$^-$/pulse (gold).

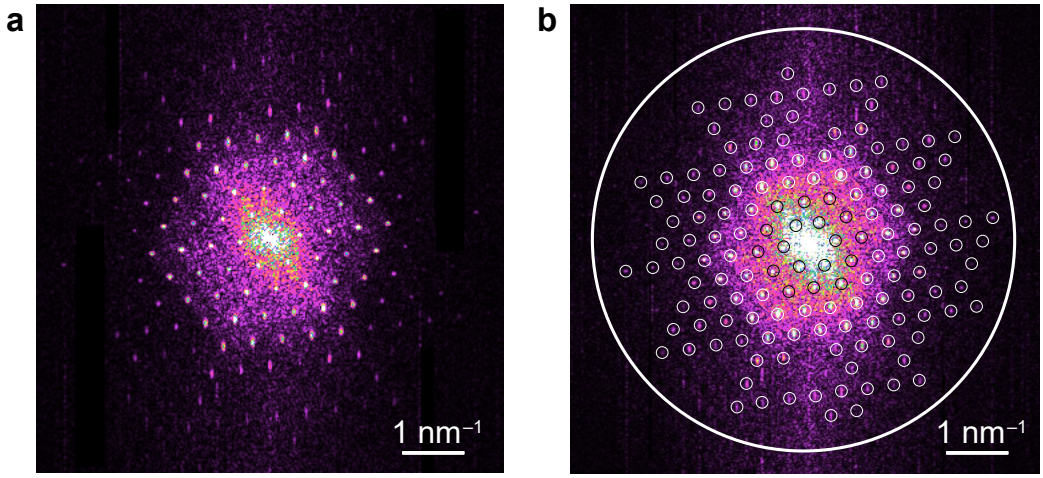

Figure 6.12: **a**, 2D-FFT of the TD-STM image in Fig. 6.9. **b**, The same 2D-FFT with small white and black circles as guides to the eye for locating peaks in k-space. The large white circle has a radius of 3.33 nm^{-1}.

an increase in the apparent barrier-height, which results in a smaller tunnel current area (Eq. 2.5) and larger corrugations [65, 66, 215]. In STM, surface corrugation is primarily determined by the tip/surface geometry, tip–sample separation and local density of states [64–67, 215]. Relative heights between inequivalent adatoms of the Si(111)-(7×7) unit cell serve as a quantitative comparison of STM junctions across literature. Our TD-STM adatom heights match well with previous STM studies (Table 6.1). Atomic force microscopy (AFM) and low energy electron diffraction (LEED) measure smaller adatom heights when compared to STM because they are not as sensitive to the lo-

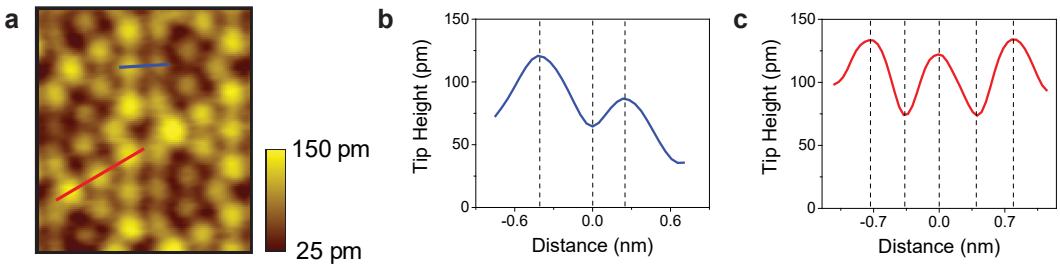

Figure 6.13: **a**, High resolution TD-STM image acquired at $V_{\mathrm{d.c.}} = 0$ V, $I_{\mathrm{THz,avg}} = -20$ pA and $E_{\mathrm{THz,pk}} = -200$ V/cm. Image size 4.8 nm × 5.5 nm; scan speed 13 nm/s; low-pass-filtered with a 3×3 smoothing matrix. **b**, **c**, Constant-current TD-STM linescans for nearest-neighbour adatoms (**b**) and next-nearest-neighbour adatoms (**c**).

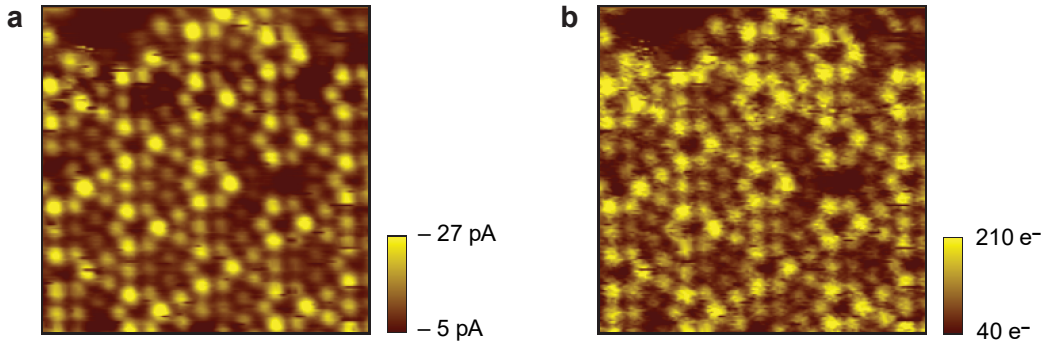

Figure 6.14: **a**, Constant-height total current image, low-pass-filtered during acquisition and **b**, the simultaneously acquired THz-STM image, $N_{e^-}(x, y)$. The average total current is −12 pA, while the average terahertz current is −4 pA (or equivalently 100 rectified electrons per pulse tunneling from the sample to the tip). $V_{\mathrm{d.c.}} = -0.30$ V; $E_{\mathrm{THz,pk}} = -200$ V/cm; image size 10 nm × 10 nm; scan speed 11 nm/s.

cal density of states. The simulated adatom heights [220–224] are geometric coordinates of atomic nuclei obtained using density functional theory.

The spatial and temporal resolution of THz-STM on the Si(111)-(7×7) surface is further demonstrated in Fig. 6.12, Fig. 6.13, Fig. 6.14 and Fig. 6.15. The two-dimensional Fourier transform of Fig. 6.9 is shown in Fig. 6.12 and reveals spatial frequencies up to 3 nm^{-1}. A high resolution TD-STM image (Fig. 6.12a) and its corresponding linescans (Fig. 6.12b,c) demonstrate that

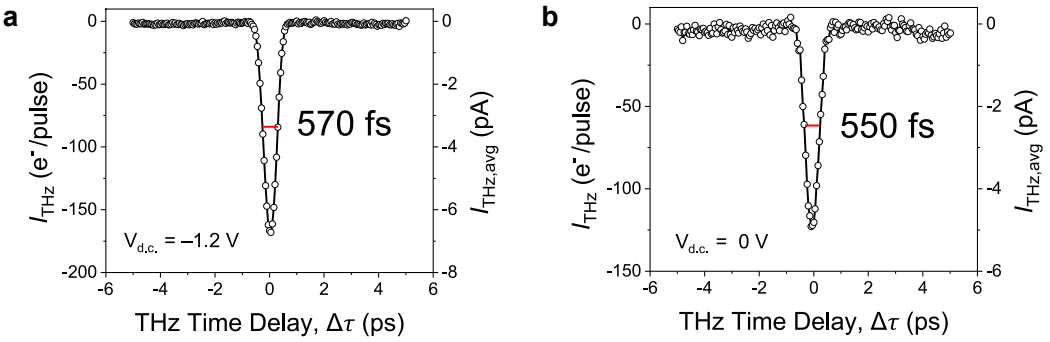

Figure 6.15: Constant-height THz pulse autocorrelations on Si(111)-(7×7). **a**, The feedback loop was disengaged at $V_{\mathrm{d.c.}} = -1.20$ V, $I_{\mathrm{d.c.}} = -30$ pA, $E_{\mathrm{THz,pk}} = 0$ V/cm and the parameters during acquisition were $V_{\mathrm{d.c.}} = -1.20$ V, $E_{\mathrm{THz,pk}} = -115$ V/cm (each pulse). **b**, The feedback loop was disengaged at $V_{\mathrm{d.c.}} = +1.00$ V, $I_{\mathrm{d.c.}} = +200$ pA, $E_{\mathrm{THz,pk}} = 0$ V/cm and the parameters during acquisition were $V_{\mathrm{d.c.}} = 0$ V, $E_{\mathrm{THz,pk}} = -90$ V/cm (each pulse).

		Tip Height (pm)			Experimental Conditions				
		F-Co	F-Ce	UF-Co	Sample Bias (V)	Current (pA)	Tip	Sample Doping	Notes
STM	TD-STM (Fig. 6.8b)	61	30	16	0	−20	W	As: 4e19	$E_{\mathrm{THz,pk}} = -200$ V/cm
	STM (Fig. 6.8a)	54	37	8	−0.50	−20	W	As: 4e19	$E_{\mathrm{THz,pk}} = 0$ V/cm
	[324] Donati 2013	61	40	20	−1.50	−2200	Cr	-	graphical interpolation
	[51] Erlandsson 1996	53	25	15	−2.20	−100	W	high n-type	
	[218] Hamers 1986	53	25	15	-	-	W	Sb: 1e19	values found only in [223]
	[325] Sutter 2003	46	22	16	−1.00	−300	InAs(001)	-	graphical interpolation
	[225] Wang 2004	43	24	12	−1.50	−300	W	Sb: 5e17	graphical interpolation
	[326] Nishikawa 1991	42	22	15	−2.00	−200	W(111)	n-type	graphical interpolation
	[327] Chaika 2008	26	12	9	−1.40	−80	W	B: 1e17	graphical interpolation
	[226] Paz 2005	35	54	−15	1.5	200	W	-	graphical interpolation
AFM	[53] Giessibl 2000	34	19	15	−1.60		W	p-type	
	[52] Uchihashi 1997	25	15	5			Si	-	
	[55] Eguchi 2002	14	10	6			Si	As: 4e19	graphical interpolation
	[54] Lantz 2000	−7	10	0			Si	B: 2e19	
	[51] Erlandsson 1996	−13	0	−13			W	high n-type	
LEED	[335] Tong 1988	12	8	4				-	
Simulation	[223] Ke 2000	13	7	2					values for $n = 8$ layers
	[224] Smeu 2012	10	5	3					
	[222] Brommer 1992	8	3	4					
	[220] Qian 1987	8	1	3					
	[221] Stich 1992	4	0.2	0.3					values found only in [223]

Table 6.1: Experimental and theoretical relative heights between inequivalent adatoms on the Si(111)-(7×7) surface. This table is a partial summary of the Si(111)-(7×7) inequivalent adatom heights reported in literature. Several results were graphically interpolated and should be considered estimates to within a few picometers. If an experimental condition was not specified, a dash is displayed. The faulted corner (F-Co), faulted-centre (F-Ce) and unfaulted-corner (UF-Co) adatom heights are relative to the unfaulted-centre-adatom.

interatomic distances are clearly resolved. A constant-height image at $V_{\mathrm{d.c.}} = -0.30$ V confirms the same spatial resolution for total current (Fig. 6.14a) and the simultaneously acquired THz-pulse-induced current (Fig. 6.14b). Ultrafast scanning probe microscopes often use autocorrelations to assess their temporal resolution [92, 102, 104, 129, 135]. Autocorrelations with full-width half-maxima (FWHM) below 600 fs have been measured with the THz-STM (Fig. 6.15).

6.2 Modeling THz-STM on Si(111)-(7×7)

The THz-pulse-induced tunnel current, $I_{\mathrm{THz}}(t)$, generated by $V_{\mathrm{THz}}(t)$ at each time step was calculated using the Bardeen tunneling model (Eq. 2.23), including the image potential contribution (Eq. 2.19) via

$$\begin{aligned} I_{\mathrm{THz}}(t) = & \frac{\pm 1}{\zeta_0} \int_0^{e|V_{\mathrm{d.c.}}+V_{\mathrm{THz}}(t)|} \rho_{\mathrm{s}}(\varepsilon)\, T(\phi_{\mathrm{t}}, \phi_{\mathrm{s}}, \varepsilon, V_{\mathrm{d.c.}} + V_{\mathrm{THz}}(t), z)\, \mathrm{d}\varepsilon \ldots \\ & \ldots \mp \frac{1}{\zeta_0} \int_0^{e|V_{\mathrm{d.c.}}|} \rho_{\mathrm{s}}(\varepsilon)\, T(\phi_{\mathrm{t}}, \phi_{\mathrm{s}}, \varepsilon, V_{\mathrm{d.c.}}, z)\, \mathrm{d}\varepsilon\,, \end{aligned} \tag{6.1}$$

where e is the elementary charge, ϕ_{t} is the tip barrier-height, ϕ_{s} is the sample barrier-height, $V_{\mathrm{d.c.}}$ is the quiescent STM bias voltage, $V_{\mathrm{THz}}(t)$ is the instantaneous THz-pulse-induced bias voltage (Fig. 6.16a), z is the tip–sample separation, $\rho_{\mathrm{s}}(\varepsilon)$ is the sample density of states, and we have assumed a constant value for the tip density of states, $\rho_{\mathrm{t}}(\varepsilon)$. The constant ζ_0 is a scaling factor that is set by the operating current setpoint (I_0) and voltage setpoint (V_0), as the feedback loop is disengaged, just before the THz-STM measurement is acquired; it is given by

$$\zeta_0 = \frac{1}{|I_0|} \int_0^{e|V_0|} \rho_{\mathrm{s}}(\varepsilon)\, T(\phi_{\mathrm{t}}, \phi_{\mathrm{s}}, \varepsilon, V_0, z)\mathrm{d}\varepsilon\,. \tag{6.2}$$

In the first term of Eq. 6.1, the $\pm$ symbol is positive for $V_{\mathrm{d.c.}} + V_{\mathrm{THz}}(t) > 0$ and negative for $V_{\mathrm{d.c.}} + V_{\mathrm{THz}}(t) < 0$. The $\mp$ symbol in the second term is negative for $V_{\mathrm{d.c.}} > 0$ and positive for $V_{\mathrm{d.c.}} < 0$. Also, at negative bias ($V_{\mathrm{d.c.}} + V_{\mathrm{THz}}(t) < 0$; $V_{\mathrm{d.c.}} < 0$; $V_0 < 0$), the substitution $\varepsilon \to \varepsilon - eV$ is made in $\rho_{\mathrm{s}}(\varepsilon)$ and $T(\varepsilon)$. The scaling factor, ζ_0, allows the density of states to be defined

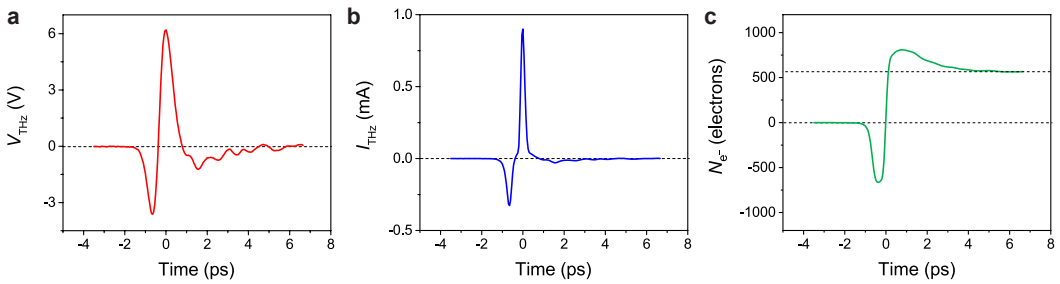

Figure 6.16: Simulated temporal profile of the THz-pulse-induced tunnel current using the Bardeen model. **a**, Total applied voltage $V_{\mathrm{THz}}(t)$ between tip and sample ($V_{\mathrm{d.c.}} = 0$ V). **b**, The THz-induced current transient, $I_{\mathrm{THz}}(t)$, calculated using Eq. 6.1. **c**, The number of electrons that tunnel across the junction (running integral of **b**). After the THz pulse has passed (beyond 6 ps), the number of electrons rectified is 570. At 250,000 terahertz pulses per second, this is equivalent to $I_{\mathrm{THz,avg}} = +23$ pA.

in arbitrary units within the tunneling model and also takes into account the multiplicative prefactor ξ in Eq. 2.24 that contains unknown parameters such as the tunneling area. The THz-pulse-induced tunnel current, $I_{\mathrm{THz}}(t)$ (Fig. 6.16b), is then integrated over the duration of the THz pulse (Fig. 6.16c) to obtain the number of rectified electrons per pulse ($N_{\mathrm{e^-}}$) via

$$I_{\mathrm{THz}}\ (\mathrm{e^-/pulse}) = N_{\mathrm{e^-}} = \frac{1}{e}\int_{-\infty}^{+\infty} I_{\mathrm{THz}}(t)\,\mathrm{d}t\,. \tag{6.3}$$

For the Bardeen tunneling model which includes image potential effects, the transmission factor is given by

$$T(\phi_{\mathrm{t}}, \phi_{\mathrm{s}}, \varepsilon, V, z) \;=\; \xi \cdot \overline{\phi}_{\mathrm{eff}}(\phi_{\mathrm{t}}, \phi_{\mathrm{s}}, \varepsilon, V, z) \cdot e^{-2\delta\sqrt{\frac{2m}{\hbar^2}\overline{\phi}_{\mathrm{eff}}(\phi_{\mathrm{t}},\phi_{\mathrm{s}},\varepsilon,V,z)}}\,, \tag{6.4}$$

where $\xi = 2[\hbar\, A\, \psi_i(0)\, \psi_f(z)]^2/m$ is a constant, ε is the electron energy between 0 eV and $eV_{\mathrm{d.c.}}$, δ is the effective barrier-width and $\overline{\phi}_{\mathrm{eff}}$ is the average effective barrier-height that is calculated from $\phi_{\mathrm{eff}}(x)$ via (Eq. 2.10)

$$\overline{\phi}_{\mathrm{eff}}(\phi_{\mathrm{t}}, \phi_{\mathrm{s}}, \varepsilon, V, z) = \frac{1}{\delta}\int_{s_1}^{s_2} \phi_{\mathrm{eff}}(x, \phi_{\mathrm{t}}, \phi_{\mathrm{s}}, \varepsilon, V, z)\,\mathrm{d}x\,, \tag{6.5}$$

where $s_2 - s_1 = \delta$ is the effective barrier-width due to image potential narrowing and the effective barrier-height, $\phi_{\mathrm{eff}}(x)$, is given by

$$\begin{aligned}\phi_{\mathrm{eff}}(x, \phi_{\mathrm{t}}, \phi_{\mathrm{s}}, \varepsilon, V, z) = \phi_{\mathrm{t}} \pm e|V| \mp |\varepsilon| + \frac{x}{z}(\phi_{\mathrm{s}} - \phi_{\mathrm{t}} \mp e|V|)\,... \\ ... - \frac{1.15e^2\ln 2}{16\pi\epsilon_0}\frac{z}{x(z-x)}\,,\end{aligned} \tag{6.6}$$

where ϵ_0 is the permittivity of free space. The average effective barrier-height, $\overline{\phi}_{\text{eff}}$, is obtained by placing Eq. 6.6 into Eq. 6.5, yielding

$$\begin{aligned}\overline{\phi}_{\text{eff}}(\phi_{\text{t}}, \phi_{\text{s}}, \varepsilon, V, z) = \phi_{\text{t}} \pm e|V| \mp |\varepsilon| + \frac{s_1 + s_2}{2z}(\phi_{\text{s}} - \phi_{\text{t}} \mp e|V|) \ldots \\ \ldots - \frac{1.15}{s_2 - s_1}\frac{e^2 \ln 2}{16\pi\epsilon_0}\ln\left(\frac{s_2(z - s_1)}{s_1(z - s_2)}\right).\end{aligned} \tag{6.7}$$

The values s_1 and s_2 are determined by the two positive real roots of the equation $\phi_{\text{eff}}(x, \phi_{\text{t}}, \phi_{\text{s}}, \varepsilon, V, z) = 0$. This cubic expression can be rearranged to obtain

$$\begin{aligned}x^3\left(\frac{\phi_{\text{t}} - \phi_{\text{s}} \pm e|V|}{z}\right) + x^2\big(\phi_{\text{s}} - 2\phi_{\text{t}} \mp 2e|V| \pm |\varepsilon|\big) \ldots \\ \ldots + xz\big(\phi_{\text{t}} \pm e|V| \mp |\varepsilon|\big) - z\frac{1.15e^2 \ln 2}{16\pi\epsilon_0} = 0\,.\end{aligned} \tag{6.8}$$

In Eq. 6.6, Eq. 6.7 and Eq. 6.8 the top case ($\pm$, $\mp$) is used for positive bias (V > 0), and the bottom case is used for negative bias (V < 0). Also at negative bias, the substitution $|\varepsilon| \rightarrow e|V| - |\varepsilon|$ is made in Eq. 6.6, Eq. 6.7 and Eq. 6.8.

The following is a list of assumptions that were made when calculating $I_{\text{THz}}(t)$ from $V_{\text{THz}}(t)$ with the Bardeen tunneling model:

1. Sum of states in Eq. 2.21 is represented as an integral over a density of states (DOS).
2. One dimensional approximation.
3. Zero temperature (T = 0 K).
4. Tip and sample barrier-heights are equal ($\phi_{\text{t}} = \phi_{\text{s}}$).
5. Tip DOS, $\rho_{\text{t}}(\varepsilon)$, is constant.
6. No phase delay between $I_{\text{THz}}(t)$ and $V_{\text{THz}}(t)$.
7. Electrons in the silicon bulk respond to the THz field and form an image potential. Electron screening occurs on a timescale comparable to the inverse plasma frequency [339], approximately several tens to hundreds of femtoseconds in heavily doped silicon.

8. $V_{\mathrm{THz}}(t)$ has the same temporal profile as the electro-optically measured $E_{\mathrm{THz}}(t)$. This assumption is supported by the 3D electromagnetic simulations in section 6.4.

9. A scaling factor is defined in Eq. 6.2 and its value is determined by the current and voltage setpoints, I_0 and V_0, before the feedback loop is disengaged. This permits the density of states to be defined in arbitrary units within the tunneling model and accounts for the prefactor ξ in Eq. 2.24 and Eq. 6.4 (see equation 20.53 in [67] for details).

10. A modified I–V curve is used for THz-STM measurements to account for ultrafast non-equilibrium tunneling dynamics.

11. A quasi-static model is sufficient for describing subpicosecond dynamics. Band bending at THz frequencies has been demonstrated by Schottky barrier mixer diodes operating at 2.5 THz [340]. Also, tunnel current rectification at 30 THz has been shown with laser-driven STM [341]. The Keldysh parameter [342] of our system is much smaller than one ($\gamma \sim 0.01$), and thus we are in the tunneling regime ($\gamma \ll 1$). The Keldysh parameter is defined as

$$\gamma = \omega \frac{\sqrt{2mV_{\mathrm{IP}}}}{eE}, \tag{6.9}$$

where ω is the frequency ($2\pi \times 0.5$ THz), V_{IP} is the ionization potential (on the order of eV), E is the electric field (200 V/cm $\times$ 220,000), m is the electron mass and e is the elementary charge. Quasi-static models successfully describe phenomena even down to the attosecond regime [19, 30].

STM and THz-STM tunneling was simulated using Eq. 6.1 via a global fit across multiple STM and THz-STM measurements at identical tip–sample separation over the same atom. The temporal profile of the electro-optically measured THz pulse electric field waveform (Fig. 6.2) defines the shape of $V_{\mathrm{THz}}(t)$ in the tunneling model (this is supported by COMSOL simulations of THz pulse coupling to an STM, see Fig. 6.31). The global fit parameters are

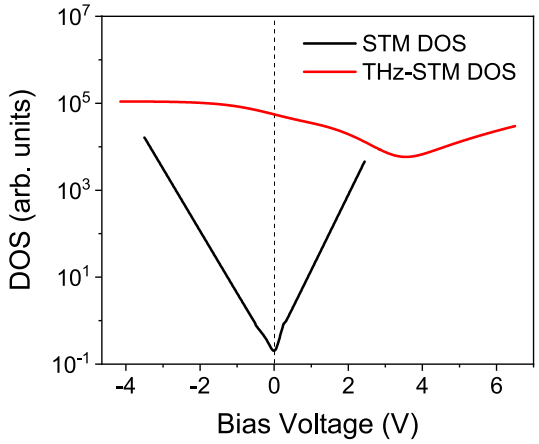

Figure 6.17: Density of states (DOS) used in the tunneling model for STM (black solid line) and THz-STM (red solid line).

barrier-height ($\phi_t = \phi_s = \phi_{Simulation} = 4.9 \pm 0.1$ eV), tip–sample separation ($z = 0.7 \pm 0.2$ nm), THz pulse field enhancement ($F = 220{,}000 \pm 50{,}000$) and density of states (Fig. 6.17). As shown in Fig. 6.18, the model produces an I–V curve for steady-state STM that matches measurements of $I_{d.c.}$ as a function of $V_{d.c.}$ taken at multiple tip heights. I–V curves were acquired at multiple tip–sample separations in order to map out the tunneling characteristics out to several volts while maintaining current levels within the dynamic range of the STM current amplifier [343]. The I–V curves are renormalized by the multiplicative factor, $\exp(2\kappa\Delta z)$, where κ is the inverse decay length ($\kappa[\text{Å}^{-1}] = 0.51\sqrt{\phi_{exp}[\text{eV}]}$) and Δz is the relative height difference between the I–V curves. The global fit predicts $V_{THz,pk} = -3.1$ V for an incident field of $E_{THz,pk} = -200$ V/cm. The THz pulse peak voltage ($V_{THz,pk}$) is larger than the work under ambient conditions (see chapter 4) because operation in ultrahigh vacuum results in a significantly larger barrier height for the tunnel junction and thus a larger $V_{THz,pk}$ is required to generate a measurable THz-pulse-induced current. Fits for I–V (Fig. 6.19), I–z (Fig. 6.20), THz I–E (Fig. 6.21 and Fig. 6.22) and autocorrelations (Fig. 6.23) show good agreement with the data.

The total energy coupled to the tunnel junction was estimated using Eq. 4.5.

For the simulated voltage transient, $V_{\mathrm{THz}}(t)$, and ultrafast current transient, $I_{\mathrm{THz}}(t)$, that are shown in Fig. 6.16, the energy coupled to the junction was 0.25 fJ. We can compared this to the energy of the incident free-space-propagating THz pulse (Fig. 6.2), using Eq. 3.5. For $E_{\mathrm{THz,pk}} = -200$ V/cm and a 2.4 mm spot-size-diameter at a frequency of 0.4 THz (position of peak in Fig. 6.2 inset), the incident THz pulse energy was 3.4 pJ. This result is comparable to the to the pyroelectric detector measurement of 7.4 pJ. The THz pulse coupling efficiency to the tunnel junction was found to be 0.007%. This value is slightly lower than, but still comparable to, the Simmons model prediction in ambient conditions (section 4.3) and previous reports of THz pulse coupling to metal wires [168].

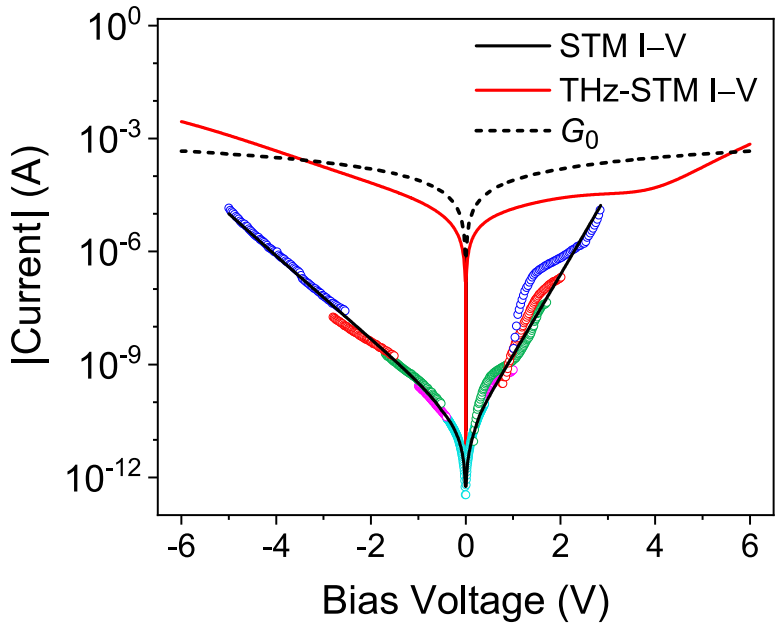

Figure 6.18: I–V curves obtained from a global fit of multiple data sets to the Bardeen tunneling model for STM (black solid line) and THz-STM (red solid line). Experimental STM I–V curves (circles) were acquired at five different tip–sample separations ($\Delta z = z - z_0 = 500$ pm, 375 pm, 250 pm, 125 pm and 0 pm for blue, red, green, magenta and cyan circles, respectively) and then normalized to the initial tip height. The dashed line represents the quantum of conductance, $G_0 \approx 77.5\,\mu$A. The initial tip–sample separation, z_0, was set by $V_{\mathrm{d.c.}} = -0.25$ V, $I_{\mathrm{d.c.}} = -20$ pA, $E_{\mathrm{THz,pk}} = 0$ V/cm over an unfaulted-centre-adatom and measurements were performed over the same atom.

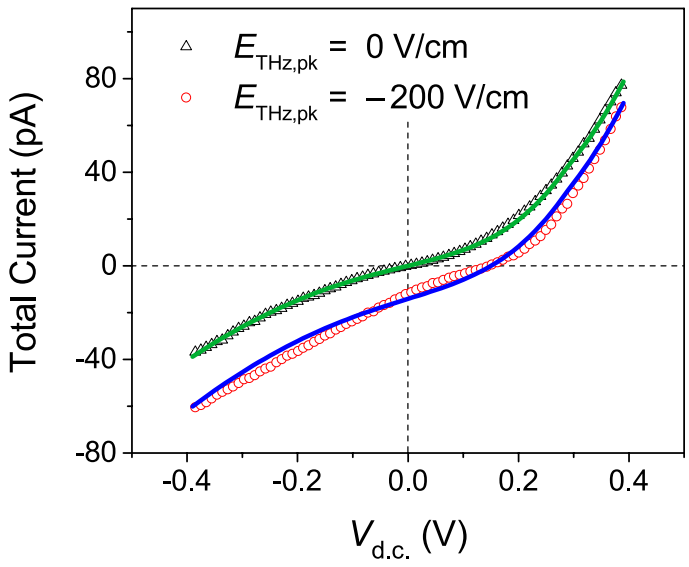

Figure 6.19: Simulated and experimental I–V curves taken without (black triangles, green solid line) and with (red circles, blue solid line) THz pulses incident on the tip. The initial tip–sample separation was set by $V_{\mathrm{d.c.}} = -0.25$ V, $I_{\mathrm{d.c.}} = -20$ pA, $E_{\mathrm{THz,pk}} = 0$ V/cm over an unfaulted-centre-adatom and measurements were performed over the same atom.

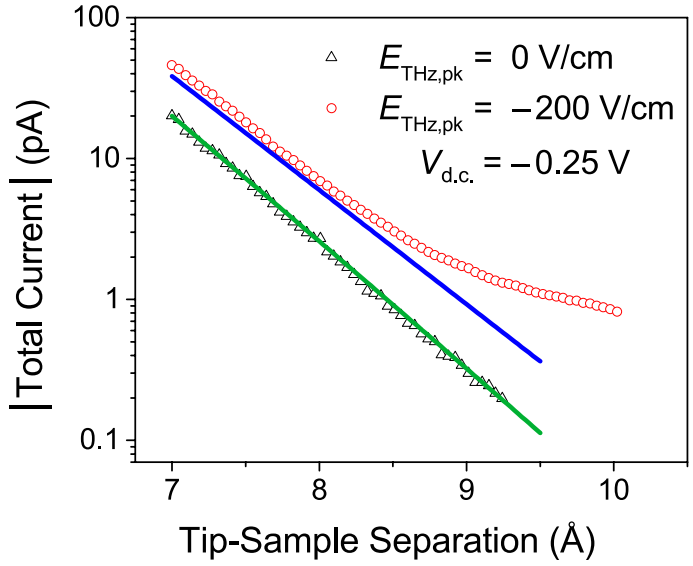

Figure 6.20: Simulated and experimental I–z curves taken without (black triangles, green solid line) and with (red circles, blue solid line) THz pulses incident on the tip. The initial tip–sample separation was set by $V_{\mathrm{d.c.}} = -0.25$ V, $I_{\mathrm{d.c.}} = -20$ pA, $E_{\mathrm{THz,pk}} = 0$ V/cm over an unfaulted-centre-adatom and measurements were performed over the same atom.

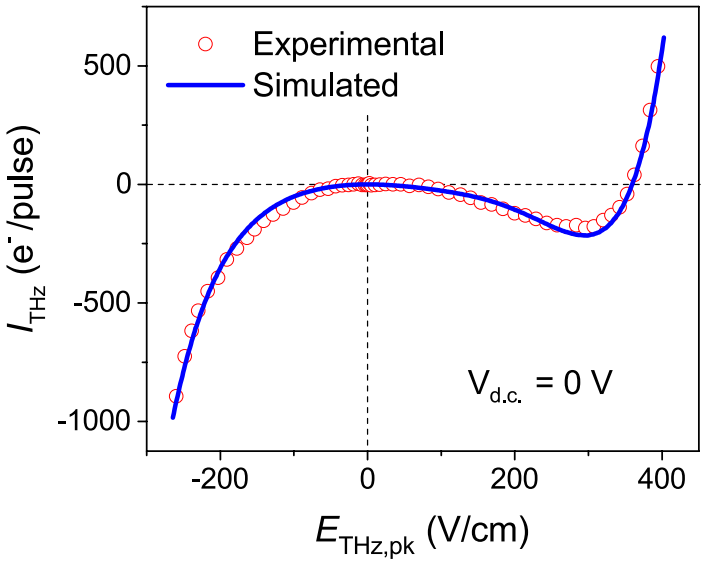

Figure 6.21: Simulated (blue solid line) and experimental (red circles) THz I–E curves. The initial tip–sample separation was set by $V_{\mathrm{d.c.}} = -0.25$ V, $I_{\mathrm{d.c.}} = -20$ pA, $E_{\mathrm{THz,pk}} = 0$ V/cm over an unfaulted-centre-adatom and measurements were performed over the same atom.

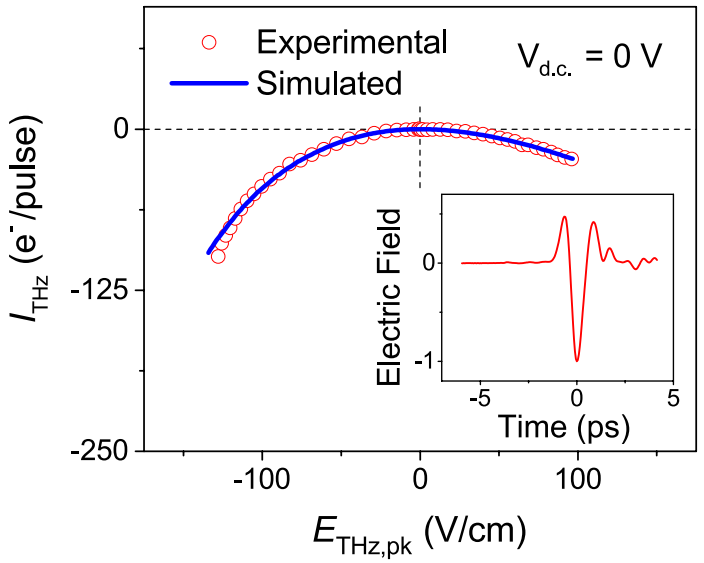

Figure 6.22: Simulated (blue solid line) and experimental (red circles) THz I–E curves measured with the THz pulse silicon beamsplitter in place (see Fig. 5.2). The initial tip–sample separation was set by $V_{\mathrm{d.c.}} = -0.25$ V, $I_{\mathrm{d.c.}} = -20$ pA, $E_{\mathrm{THz,pk}} = 0$ V/cm over an unfaulted-centre-adatom and measurements were performed over the same atom. Inset: Electro-optically measured THz pulse waveform with the silicon beamsplitter in place.

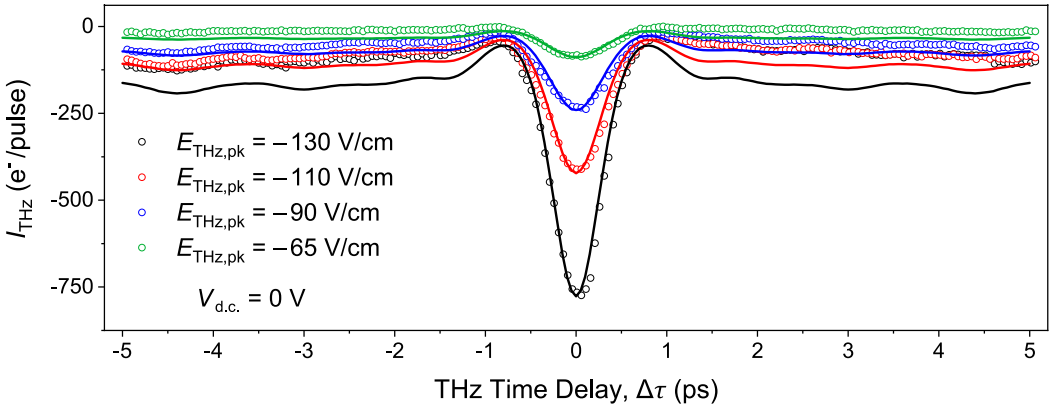

Figure 6.23: Simulated (solid lines) and experimental (circles) THz pulse autocorrelations with the THz pulse peak electric field in each arm of the autocorrelator denoted by $E_{\mathrm{THz,pk}}$. The THz pulse waveform in Fig. 6.22 was used to model $V_{\mathrm{THz}}(t)$ for the autocorrelation fits in this figure. The initial tip–sample separation was set by $V_{\mathrm{d.c.}} = -0.25$ V, $I_{\mathrm{d.c.}} = -20$ pA, $E_{\mathrm{THz,pk}} = 0$ V/cm over an unfaulted-centre-adatom and measurements were performed over the same atom.

The THz-pulse-induced tunnel current, $I_{\mathrm{THz}}(t)$, was simulated for $E_{\mathrm{THz,pk}} = -200$ V/cm (Fig. 6.24a), $E_{\mathrm{THz,pk}} = +300$ V/cm (Fig. 6.24b) and $E_{\mathrm{THz,pk}} = +400$ V/cm (Fig. 6.24c), where the electro-optically measured THz pulse waveform provided a reasonable approximation to the temporal profile of $V_{\mathrm{THz}}(t)$ at the tunnel junction, as verified by electromagnetic simulations (see Fig. 6.31). The tunneling simulation finds that extreme transient tunnel currents with peak magnitudes up to 200 µA over 400 fs and 1 mA over 240 fs occur at peak terahertz fields of −200 V/cm and +400 V/cm, respectively, corresponding to peak current densities in excess of 10^{11} A/cm^2. The integrated response of $I_{\mathrm{THz}}(t)$ as a function of $E_{\mathrm{THz,pk}}$ (THz I–E curve) exhibits three distinct regions (Fig. 6.25a). In region I, $V_{\mathrm{THz}}(t)$ drives a large negative current with a much smaller positive current (Fig. 6.25b). In region II the peaks for $I_{\mathrm{THz}}(t)$ are similar in magnitude, but $I_{\mathrm{THz,avg}} < 0$ even though $E_{\mathrm{THz,pk}} > 0$ (Fig. 6.25c). Region III has large transient currents in both directions, with an overall net positive current (Fig. 6.25d). This THz I–E behavior is a direct consequence of the drastically different tunnel conductance seen by the THz pulse compared to the steady-state I–V characteristic.

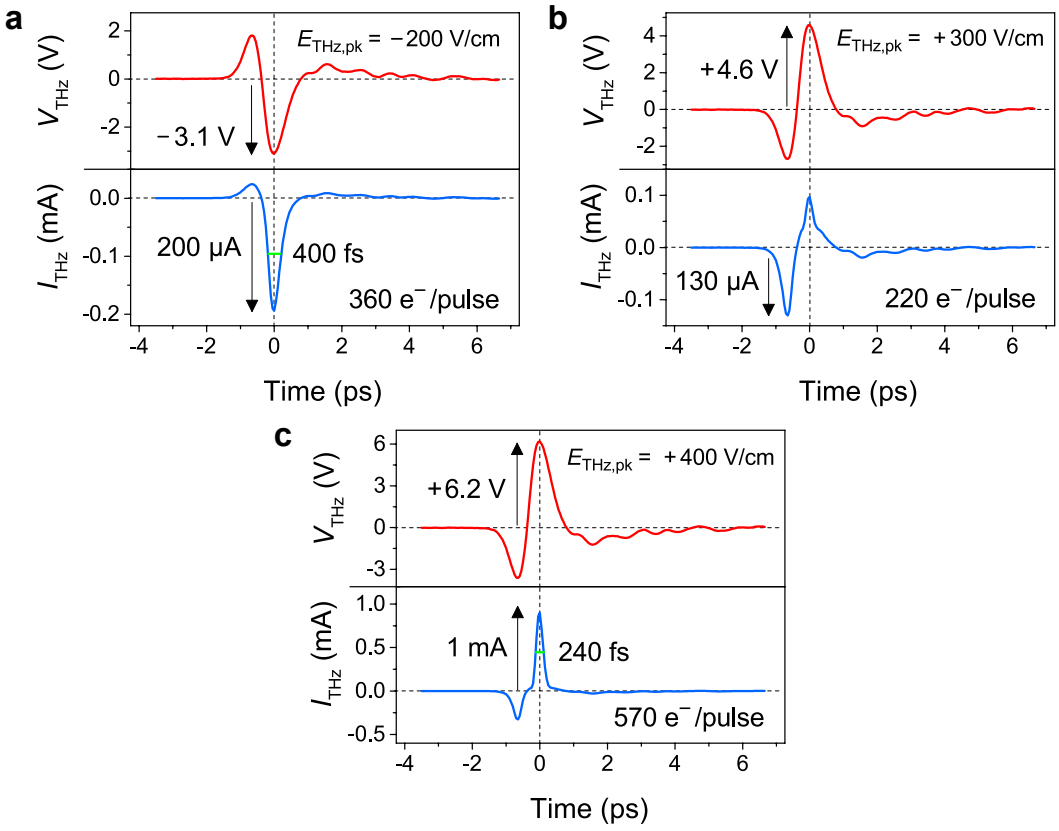

Figure 6.24: THz pulse voltage transient (red solid line) and simulated ultrafast THz-pulse-induced current transient (blue solid line) based on the THz-STM I–V curve in a for $E_{\mathrm{THz,pk}} = -200$ V/cm (**a**), $E_{\mathrm{THz,pk}} = +300$ V/cm (**b**) and $E_{\mathrm{THz,pk}} = +400$ V/cm (**c**), reaching peak THz-pulse-induced tunnel currents of 1 mA over 240 fs (full-width half-maximum). The rectified terahertz current ($I_{\mathrm{THz,avg}}$) is negative for **a**, **b** and positive for **c**.

For THz-STM, an I–V curve that represents the instantaneous value of I_{THz} at a given V_{THz} is produced by the model and found to be several orders of magnitude larger than the STM I–V curve, accounting for extreme tunnel currents observed at THz frequencies. Such a large difference between STM and THz-STM I–V curves is consistent with four-point-probe measurements on Si(111)-(7×7) that have shown an increase in the conductance by several orders of magnitude when transitioning from surface-dominated transport to bulk-dominated transport [333]. Furthermore, a large asymmetry in the THz-STM I–V curve is consistent with heavy n-type bulk doping and limited transport at positive voltages and high currents [313–315]. The quan-

tum of conductance, G_0 (dashed line in Fig. 6.18), shows that THz-STM at high currents on Si(111)-(7×7) operates in a regime very close to 1D ballistic transport [66]. This could arise from an adatom dangling bond forming a 1D conducting channel between the bulk and the tip [344–346]. The crossover of the THz-STM I–V above G_0 is attributed to hot electrons at high terahertz fields (see section 6.7).

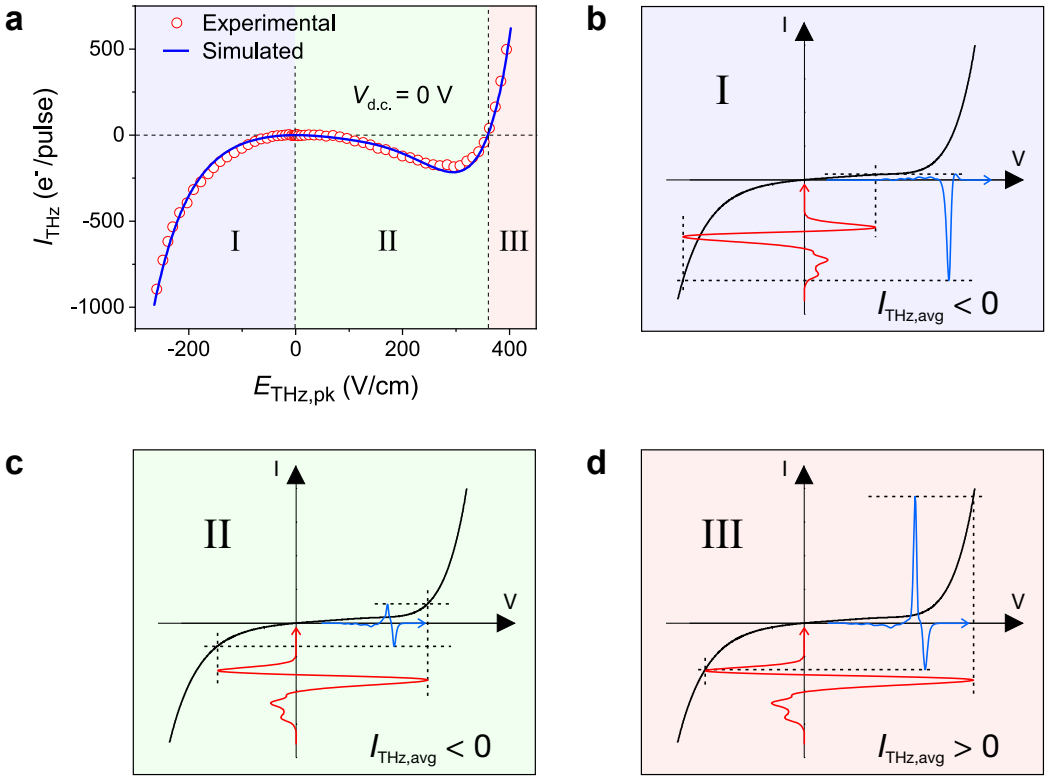

Figure 6.25: Modeling TD-STM on Si(111)-(7×7) in the extreme tunnel current regime. **a**, Experimental and simulated THz I–E curve exhibiting three distinct regimes designated by I (blue), II (green) and III (red) (see also Fig. 6.21). **b**–**d**, Schematic of $V_{\mathrm{THz}}(t)$ (red solid line) superimposed on the THz-STM I–V (black solid line), generating an ultrafast tunnel current, $I_{\mathrm{THz}}(t)$ (blue solid line) for $E_{\mathrm{THz,pk}} < 0$ V/cm (**b**), 0 V/cm $< E_{\mathrm{THz,pk}} < +360$ V/cm (**c**) and $E_{\mathrm{THz,pk}} > +360$ V/cm (**d**). The rectified terahertz current ($I_{\mathrm{THz,avg}}$) is negative for **b**, **c** and positive for **d**.

6.3 Ultrafast Band Bending

STM measurements on Si(111)-(7×7) have demonstrated non-equilibrium charging of the surface in the steady-state at nanoamp-level d.c. tunnel currents, attributed to limited transport between surface states and bulk states at high currents [313–315]. A d.c. current of 1 nA corresponds to 1 tunnel electron every 160 ps, suggesting that the timescale for non-equilibrium charging of the 7×7 surface is on the order of 100 ps. The THz-STM investigates ultrafast non-equilibrium tunneling using extremely large transient tunnel currents over subpicosecond timescales to charge and discharge the 7×7 surface faster than the rate of electron transport between surface states and bulk states. In STM of Si(111)-(7×7), bulk states are typically forbidden from directly contributing to the tunnel current due to the subsurface depletion region and the metallic-like 7×7 surface that screens the electric field of the tip from the bulk [142, 313–315, 333]. However, the 7×7 surface has a low conductivity [318, 319, 330, 333, 334] that is believed to be dominated by hopping transport between adatom dangling bonds [323, 334]. Owing to its poor conductivity, the

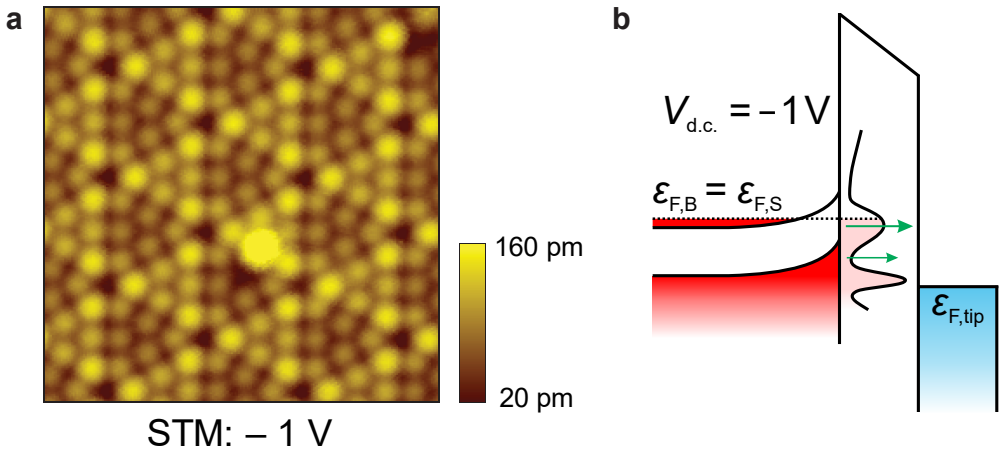

Figure 6.26: **a**, Constant-current STM image at $V_{\mathrm{d.c.}} = -1$ V, $I_{\mathrm{d.c.}} = -100$ pA and $E_{\mathrm{THz,pk}} = 0$ V/cm. Image size 9 nm × 9 nm; scan speed 9 nm/s. **b**, Band diagram for steady-state equilibrium tunneling from occupied surface states (occupied states are shaded). Green arrows indicate the direction and magnitude of electron tunneling. Fermi levels for bulk, tip and surface are given by $\varepsilon_{\mathrm{F,B}}$, $\varepsilon_{\mathrm{F,tip}}$ and $\varepsilon_{\mathrm{F,S}}$, respectively, where $eV_{\mathrm{d.c.}} = \varepsilon_{\mathrm{F,tip}} - \varepsilon_{\mathrm{F,B}}$.

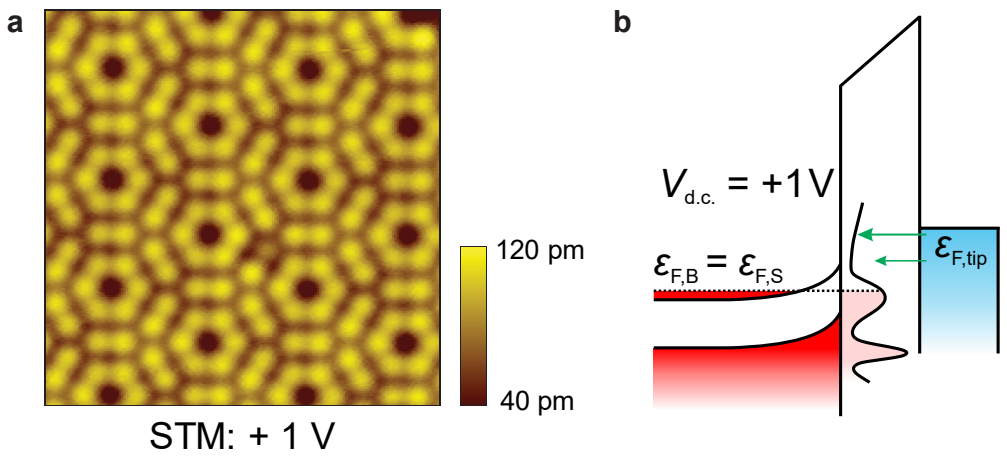

Figure 6.27: **a**, Constant-current STM image at $V_{\mathrm{d.c.}} = +1$ V, $I_{\mathrm{d.c.}} = +100$ pA and $E_{\mathrm{THz,pk}} = 0$ V/cm. Image size 9 nm × 9 nm; scan speed 9 nm/s. **b**, Band diagram for equilibrium tunneling into unoccupied surface states. Green arrows indicate the direction and magnitude of electron tunneling. Fermi levels for bulk, tip and surface are given by $\varepsilon_{\mathrm{F,B}}$, $\varepsilon_{\mathrm{F,tip}}$ and $\varepsilon_{\mathrm{F,S}}$, respectively, where $eV_{\mathrm{d.c.}} = \varepsilon_{\mathrm{F,tip}} - \varepsilon_{\mathrm{F,B}}$.

metallic-like Si(111)-(7×7) surface cannot effectively screen terahertz electric fields from the bulk, leading to THz-pulse-induced band bending in the subsurface depletion layer and enabling transport between the surface and the bulk. This sensitivity to bulk states enables THz-STM imaging of subsurface features (see section 6.8). Furthermore, poor carrier mobility on the 7×7 surface limits electron transport and leads to a non-equilibrium carrier occupation of the 7×7 surface.

In equilibrium, the surface Fermi level ($\varepsilon_{\mathrm{F,S}}$) remains pinned to the bulk Fermi level ($\varepsilon_{\mathrm{F,B}}$) and band bending through the depletion region does not change because the 7×7 surface can effectively screen the external field [142, 313–315, 333]. The d.c. tunnel current probes occupied (Fig. 6.26) and unoccupied (Fig. 6.27) surface states in an energy window between $eV_{\mathrm{d.c.}}$ and $\varepsilon_{\mathrm{F,S}}$. However, for THz-STM, the THz electric field is not screened effectively by the weakly-conducting Si(111)-(7×7) surface [318, 319, 330, 333, 334] leading to THz-pulse-induced band banding across the subsurface depletion region and new conduction pathways between surface states and bulk states. Ultrafast THz-pulse-induced band bending results in a non-equilibrium carrier occupa-

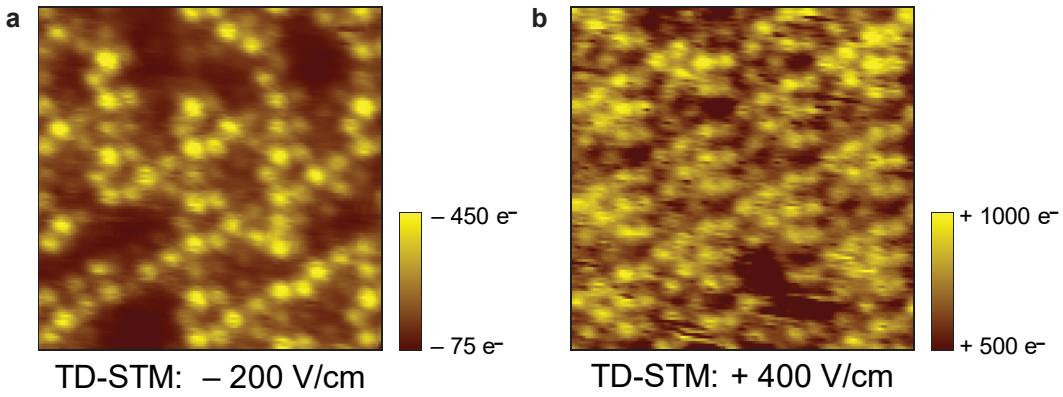

Figure 6.28: **a**, Constant-height image of the THz-pulse-driven tunnel current at $V_{\mathrm{d.c.}} = 0$ V and $E_{\mathrm{THz,pk}} = -200$ V/cm. **b**, Constant-height TD-STM image at $V_{\mathrm{d.c.}} = 0$ V and $E_{\mathrm{THz,pk}} = +400$ V/cm. Image size 9 nm × 9 nm; scan speed 12 nm/s.

tion of the 7×7 surface ($\varepsilon_{\mathrm{F,S}} \neq \varepsilon_{\mathrm{F,B}}$), which strongly enhances the tunneling probability of surface states at $\varepsilon_{\mathrm{F,S}}$. This enhancement is caused by electrons tunneling onto the 7×7 surface and rapidly thermalizing to a Fermi-Dirac distribution over tens of femtoseconds [320, 322, 332], resulting in surface states near $\varepsilon_{\mathrm{F,S}}$ that are constantly being replenished with new electrons. In this way, an extremely large THz-pulse-induced tunnel current flows via surface states near $\varepsilon_{\mathrm{F,S}}$ into the bulk, as shown in Fig. 6.29 and Fig. 6.30. Constant-

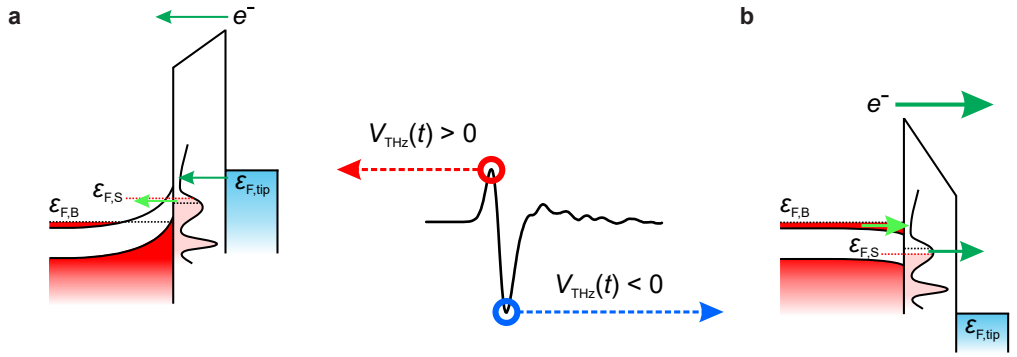

Figure 6.29: Band diagrams for THz-pulse-induced non-equilibrium tunneling at $E_{\mathrm{THz,pk}} = -200$ V/cm during the initial positive THz pulse half-cycle (**a**) and final negative THz pulse half-cycle (**b**). Green arrows indicate the direction and magnitude of electron tunneling. Fermi levels for bulk, tip and surface are given by $\varepsilon_{\mathrm{F,B}}$, $\varepsilon_{\mathrm{F,tip}}$ and $\varepsilon_{\mathrm{F,S}}$, respectively, where $eV_{\mathrm{d.c.}} = \varepsilon_{\mathrm{F,tip}} - \varepsilon_{\mathrm{F,B}}$. $\varepsilon_{\mathrm{F,S}}$ is shifted from $\varepsilon_{\mathrm{F,B}}$ due to a transient surface charge, where $eV_{\mathrm{THz}}(t) = \varepsilon_{\mathrm{F,tip}} - \varepsilon_{\mathrm{F,B}}$.

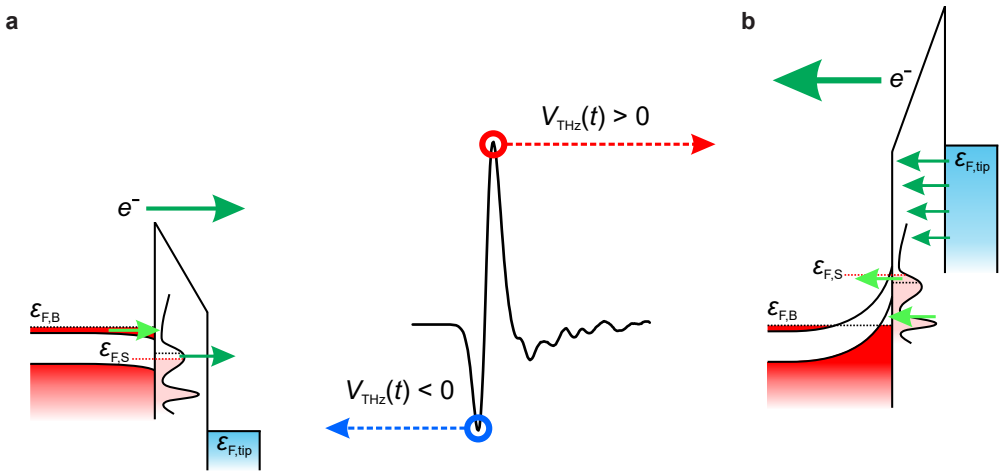

Figure 6.30: Band diagrams for ultrafast non-equilibrium tunneling at $E_{\mathrm{THz,pk}} = +400$ V/cm during the initial negative THz pulse half-cycle (**a**) and final positive THz pulse half-cycle (**b**). Green arrows indicate the direction and magnitude of electron tunneling. Fermi levels for bulk, tip and surface are given by $\varepsilon_{\mathrm{F,B}}$, $\varepsilon_{\mathrm{F,tip}}$ and $\varepsilon_{\mathrm{F,S}}$, respectively, where $eV_{\mathrm{d.c.}} = \varepsilon_{\mathrm{F,tip}} - \varepsilon_{\mathrm{F,B}}$. $\varepsilon_{\mathrm{F,S}}$ is shifted from $\varepsilon_{\mathrm{F,B}}$ due to a transient surface charge, where $eV_{\mathrm{THz}}(t) = \varepsilon_{\mathrm{F,tip}} - \varepsilon_{\mathrm{F,B}}$.

height TD-STM images at $E_{\mathrm{THz,pk}} = -200$ V/cm (Fig. 6.28a) and $E_{\mathrm{THz,pk}} = +400$ V/cm (Fig. 6.28b) reveal the same faulted–unfaulted asymmetry evident in d.c. STM occupied state imaging (Fig. 6.26a). This occurs because the surface state responsible for the asymmetry [218] is positioned near $\varepsilon_{\mathrm{F,S}}$ (see section 6.6 for details), resulting in a high tunneling probability for that surface state with STM imaging at $V_{\mathrm{d.c.}} < 0$. However, unoccupied-state STM imaging (Fig. 6.27a) is not sensitive to states near $\varepsilon_{\mathrm{F,S}}$ since the highest tunneling probability occurs for surface states with energy $\varepsilon_{\mathrm{F,S}} + eV_{\mathrm{d.c.}}$. For TD-STM, the surface state responsible for the faulted–unfaulted asymmetry always contributes to the THz-pulse-induced tunnel current since it lies near $\varepsilon_{\mathrm{F,S}}$. Band diagrams are shown for each half-cycle of the THz pulse for $E_{\mathrm{THz,pk}} = -200$ V/cm (Fig. 6.29) and $E_{\mathrm{THz,pk}} = +400$ V/cm (Fig. 6.30). The negative half-cycle causes ultrafast electron depletion of surface states, positively charging the surface ($\varepsilon_{\mathrm{F,S}} < \varepsilon_{\mathrm{F,B}}$) and reducing the amount of band bending until transport of electrons from the bulk through the depletion layer becomes effective (Fig. 6.29b and Fig. 6.30a). At positive $V_{\mathrm{THz}}(t)$, ultrafast charging

of surface states by electrons tunneling from the tip ($\varepsilon_{F,S} > \varepsilon_{F,B}$) causes upward band bending until tunneling into empty bulk states becomes effective (Fig. 6.29a and Fig. 6.30b).

A very small THz-pulse-induced tunnel current was observed on Si(111)-(7×7) with a bulk carrier concentration of 10^{15} cm^{-3}, indicating that bulk states are necessary for resupplying the surface with charge. Furthermore, a longer depletion layer limits how many electrons can reach the junction for the duration of a THz pulse half-cycle. If all the rectified electrons were supplied by states on the 7×7 surface, the THz-pulse-induced current would not depend on the bulk carrier concentration because the 7×7 surface conductivity is independent of bulk doping [333].

6.4 THz Pulse Electric Field Penetration

Terahertz pulse coupling to the STM tip and the subsequent field penetration into the silicon bulk was explored using 3D electromagnetic simulations solved with the finite element method. Free-space propagation of THz radiation requires millimeter length scales; however, computation limits prevented the

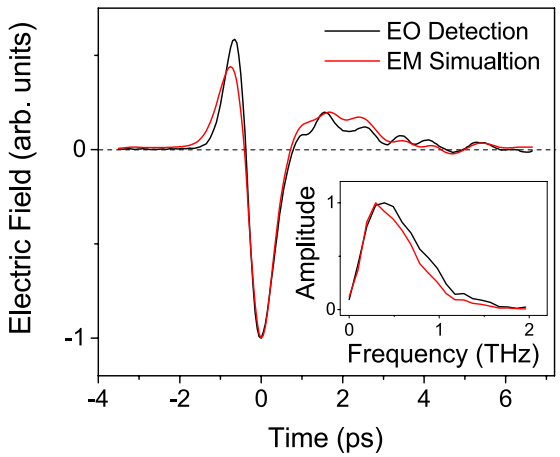

Figure 6.31: Simulated THz pulse at STM tip apex. The temporal profile of an electro-optically (EO) measured THz pulse waveform (black solid line) is used as an input for the electromagnetic (EM) simulation of THz pulse coupling to an STM tip. The electric field transient at the tip apex is extracted from the simulation (red solid line). Inset: corresponding amplitude spectra.

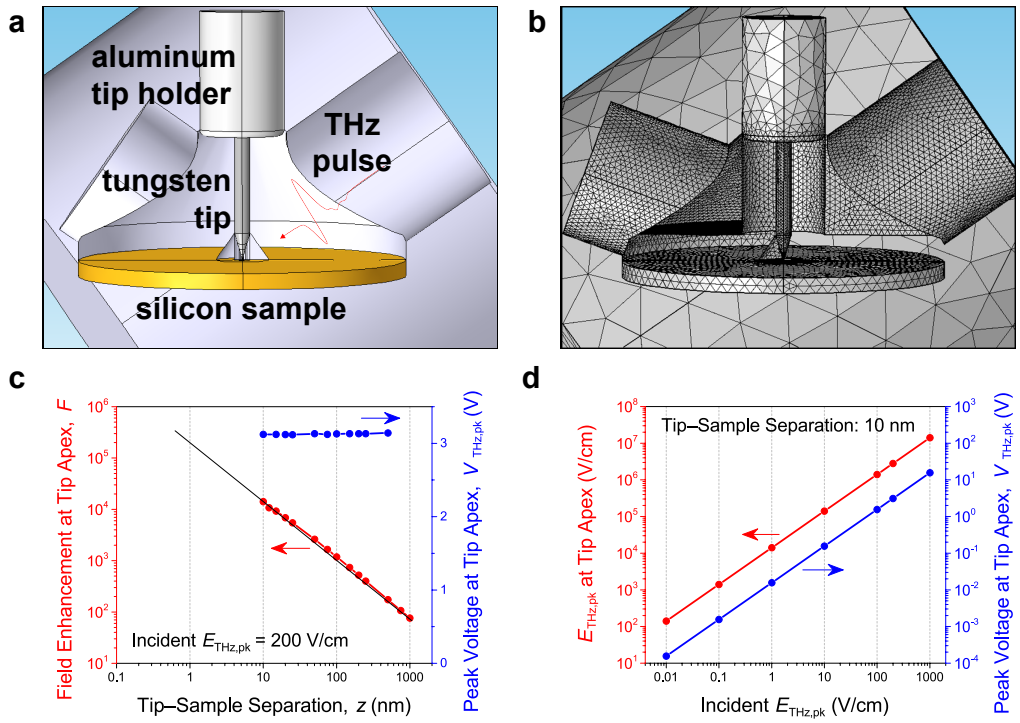

Figure 6.32: Electromagnetic simulation of THz pulse coupling to an STM tip. **a**, Simulation geometry and **b**, finite element mesh. **c**, THz pulse electric field enhancement (red circles) and THz pulse peak voltage (blue circles) at the STM junction for several tip–sample separations. **d**, THz pulse peak electric field at the tip apex (red circles) and THz pulse peak voltage at the tip apex (blue circles) for several incident fields.

simulation mesh from reaching subnanometer tip–sample separations ($z = 10$ nm was used with 2 nm meshing). The simulated electric field transient at the tip apex had a temporal profile that was very similar to the electro-optically measured free-space THz pulse waveform (Fig. 6.31). The simulation geometry is shown in Fig. 6.32a,b. Simulations were performed for gap widths ranging from 10 nm to 1000 nm (Fig. 6.32c). The simulation found that $V_{\mathrm{THz,pk}}$ did not change with the gap width for distances less than 1 µm and that the THz pulse electric field enhancement at the junction was greater than 10^5 at typical tunneling distances (Fig. 6.32c). In our experiment, we have an extremely large field enhancement, F, because an atomically sharp tip is in subnanometer proximity of a conductive sample, allowing free-space THz pulses with peak fields below 1 kV/cm to reach several V/nm at the tip apex. This is consistent

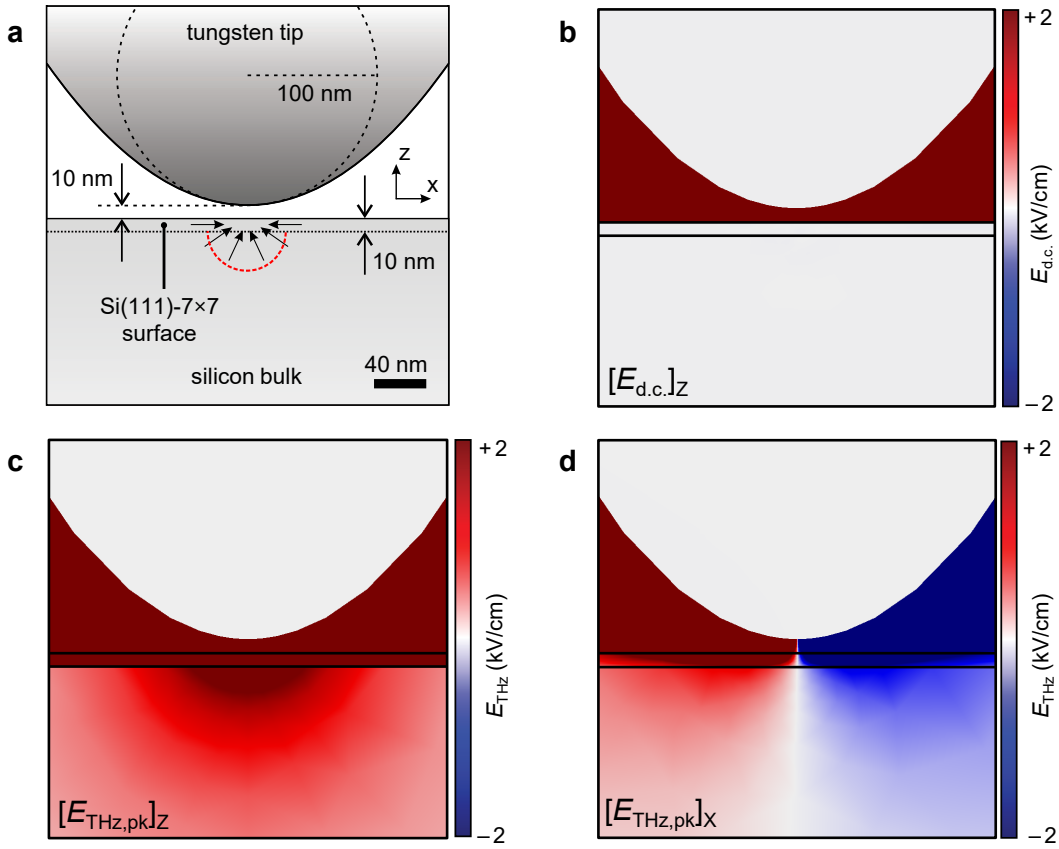

Figure 6.33: Electric field spatial profiles obtained from 3D electromagnetic simulations. **a**, Simulation geometry with a tip–sample separation of 10 nm and tip radius of curvature of 100 nm. The bulk was modeled using a conductivity of 20,000 S/m, while the 7×7 surface was approximated as a 10 nm slab with a conductivity of 500 S/m (10 nm × 500 S/m = 5 µS/□) [316]. The red dashed line outlines a 30 nm radius half-sphere in the silicon bulk that contains 500 electrons and the arrows illustrate carriers within tens of nanometers of the tunnel junction being accelerated by the THz pulse electric field. The free-space THz pulse has a field strength of $E_{\mathrm{THz,pk}} = 100$ V/cm and is incident onto the tungsten tip at 35° above the x-axis (see Fig. 6.32 for details). **b**, Simulated spatial profile of the vertical component of the steady-state electric field, $[E_{\mathrm{d.c.}}]_Z$, with $V_{\mathrm{d.c.}} = 1$ V applied to the sample. The d.c. electric field does not penetrate significantly into the bulk under steady-state. **c**, **d**, Simulated spatial profile of the THz pulse electric field for the vertical component, $[E_{\mathrm{THz,pk}}]_Z$ (**c**), and horizontal component, $[E_{\mathrm{THz,pk}}]_X$ (**d**), when the larger THz pulse half-cycle undergoes maximum enhancement at the junction. The colourmap range was chosen to emphasize the terahertz electric field penetration into the bulk (the electric field in the gap is saturated dark red/blue). For a 0.7 nm tunnel gap and an incident field free-space THz pulse electric field of $E_{\mathrm{THz,pk}} = 200$ V/cm, the electric field obtained from the simulation is enhanced by a factor of 28.

with recent reports of terahertz field enhancement up to 10^5 in antennas with subnanometer gap widths [347]. Also, the relationship between the incident and enhanced fields was verified to be linear (Fig. 6.32d).

A schematic of the simulation geometry in the tunnel junction region is shown in Fig. 6.33a. The spatial profile of the vertical component of the steady-state electric field, $[E_{\text{d.c.}}]_{\text{Z}}$, is shown in Fig. 6.33b, while the spatial profile of the peak THz electric field within the silicon sample is shown in Fig. 6.33c for the vertical field component, $[E_{\text{THz,pk}}]_{\text{Z}}$, and in Fig. 6.33d for the horizontal field component, $[E_{\text{THz,pk}}]_{\text{X}}$. In the steady-state, the metallic-like surface screens the d.c. field from the silicon bulk. However, due to the relatively low conductivity [318, 319, 330, 333, 334] and low carrier density [328, 330–332] of the metallic-like Si(111)-(7×7) surface, the THz electric field is not effectively screened by the surface and is able to penetrate several tens of nanometers into the bulk. The penetration of the THz electric field, therefore, is able to induce band bending in the subsurface depletion layer, opening new conduction pathways to the bulk that resupply the 7×7 surface with charge.

6.5 Charge Transport Dynamics

The Si(111)-(7×7) surface has two conduction electrons per unit cell [328, 330, 331], which results in a carrier density of $n_{7\times7} = 0.32$ nm^{-2}. These electrons are responsible for the metallic-like nature of the 7×7 surface [328, 330]. If we assume the 7×7 surface supplies all the electrons for the THz-pulse-induced tunnel current, then there would have to be N_{e^-} electrons within a circle of radius $R = \sqrt{N_{\text{e}^-}/(\pi n_{7\times7})}$. For $N_{\text{e}^-} = 500$ rectified electrons per THz pulse, $R = 22$ nm. A surface mobility of 1–7 cm^2/(V·s) can be estimated from a scattering time [334] of 0.6-4 fs and an effective mass of unity [329] for the Si(111)-(7×7) surface. With a maximum in-plane electric field at the surface of 170 kV/cm, as estimated from the simulation results of the horizontal terahertz field component (Fig. 6.33d) and accounting for the 0.7 nm gap and 200 V/cm incident terahertz field, it would take an electron 13–1.8 ps (depending on the

scattering time) to travel 22 nm on the 7×7 surface. Therefore, the electrons on the Si(111)-(7×7) surface are not mobile enough to arrive at the tunnel junction within the subpicosecond timescale of the THz pulse half-cycle to account for the total number of measured rectified tunnel electrons. Similarly, if we assume that the bulk supplies all the electrons for the THz-pulse-induced current, then the radius for a half-sphere containing $N_{e^-} = 500$ electrons at a carrier concentration of 10^{19} cm^{-3} is 30 nm (red dashed line in Fig. 6.33a). The peak THz pulse electric field is estimated from Fig. 6.33c,d to be at least 50 kV/cm (after scaling) within 30 nm of the tunnel junction. At this electric field and for a bulk electron mobility of 120 cm^2/(V·s) [348], an electron takes 0.5 ps to travel 30 nm, indicating that a significant component of the rectified tunnel current must originate from the bulk. However, electrons from the 7×7 surface may still contribute to the overall tunnel current.

We estimate the far-field terahertz electric field penetration using the Drude model. A $1/e$ skin depth of 3.6 µm is obtained for a frequency of 1 THz using the permittivity of bulk silicon, 11.7 [264], electron effective mass, 0.26 m [349], and electron mobility, 120 cm^2/(V·s) [348] at a carrier concentration of 10^{19} cm^{-3}. The terahertz field penetration that is simulated in Fig. 6.33c,d is significantly smaller than 3.6 µm because the tip-enhanced near-field decays much faster.

The mean-free path of electrons in the metallic-like Si(111)-(7×7) surface can be estimated from $l = v_F\tau$, where v_F is the surface Fermi velocity and τ is scattering time (0.6–4 fs). Estimates of the surface Fermi velocity for the 7×7 surface range from 5×10^4 m/s [328, 334] to 3×10^5 m/s [331, 334], producing mean-free paths between 0.03–0.2 nm and 0.2–1.2 nm, respectively. These distances are close to the nearest-neighbour adatom distance of 0.7 nm, which indicates a collapse of the Drude and Boltzmann models for the Si(111)-(7×7) surface [334]. However, it is interesting to note that for the lower surface Fermi velocity value of 5×10^4 m/s and 2D density of states, $D_{2D} = 7.7 \times 10^{14}$ cm^{-2}eV^{-1} [313], the Boltzmann equation [308, 309, 334] predicts

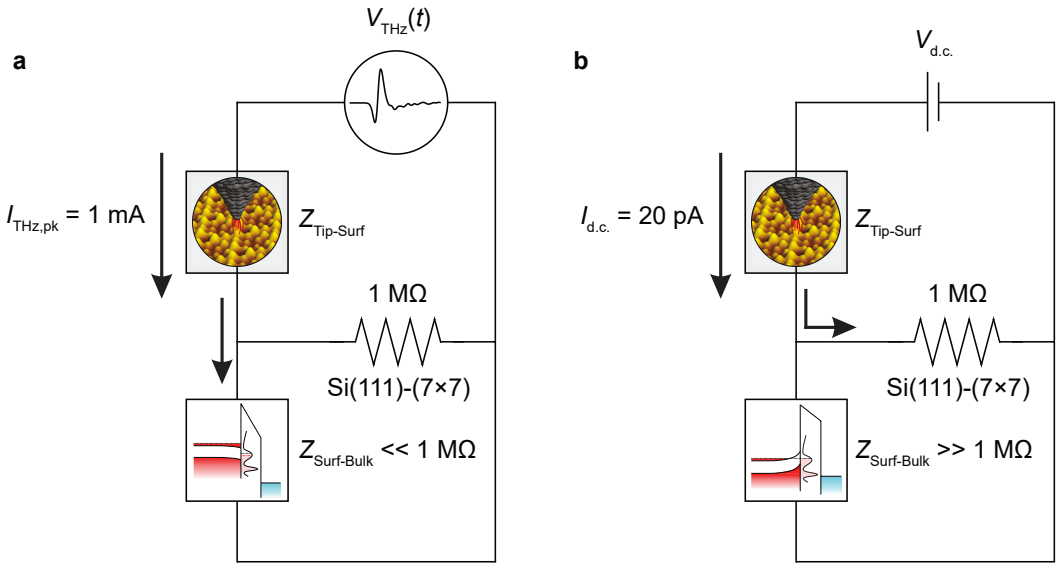

Figure 6.34: Simplified equivalent circuit representation of the tunnel current pathways at THz frequencies and in steady-state. The impedance of the tunnel junction is given by $Z_{\text{Tip-Surf}}$, while the impedance between the surface and the bulk is given by $Z_{\text{Surf-Bulk}}$. Charge carriers on the Si(111)-(7×7) surface can either propagate along the surface, or travel directly from surface states into bulk states. The conductivity of the Si(111)-(7×7) surface is approximately 1 µS/□ [318, 319, 330, 334], corresponding to a resistance of ∼ 1 MΩ. **a**, A free-space THz pulse induces a transient voltage at the tunnel junction, $V_{\text{THz}}(t)$, that drives an ultrafast transient current, $I_{\text{THz}}(t)$, with peak currents up to 1 mA. The impedance for electrons tunneling from surface states to bulk states is small at high frequencies due to THz-pulse-induced band bending ($Z_{\text{Surf-Bulk}} \ll$ 1 MΩ). **b**, Under steady-state operation the depletion layer prevents charge carriers from accessing the bulk directly ($Z_{\text{Surf-Bulk}} \gg 1$ MΩ). The charge carriers propagate on the Si(111)-(7×7) surface before eventually scattering into the bulk.

the 7×7 surface conductivity, $\sigma_{7\times7} = lv_{\text{F}}D_{\text{2D}}/2$, to be between 0.9 µS/□ and 6 µS/□, which is within an order of magnitude of recently measured values [318, 319, 330, 334] (using the larger Fermi velocity [331, 334] overestimates $\sigma_{7\times7}$). Similar values for the scattering time, 2D electron density, surface conductivity, surface Fermi velocity and mean-free path have been reported for the Ag-Si(111)-($\sqrt{3}\times\sqrt{3}$) surface [308, 309].

A simplified equivalent circuit representation of the STM tunnel current pathways is shown in Fig. 6.34. As demonstrated in Fig. 6.24c, the THz pulse drives transient tunnel currents up to 1 mA. If this current was to flow en-

tirely through the Si(111)-(7×7) surface, $V_{\mathrm{THz,pk}}$ would need to be greater than 1000 V (1 MΩ × 1 mA). Since this cannot be the case, there must be conduction pathways to the bulk. In the steady-state, the depletion layer prevents conduction between the surface and the bulk. However, subsurface terahertz field penetration leads to ultrafast band bending and the subsequent formation of an accumulation layer ($V_{\mathrm{THz}}(t) < 0$) or extreme narrowing of the depletion layer in the reverse bias condition ($V_{\mathrm{THz}}(t) > 0$). The depletion layer width [264] is ∼ 10 nm at a carrier concentration of 10^{19} cm^{-3}.

6.6 Steady-State Bias Voltage Dependence

For d.c. STM images, the faulted half of the unit cell often appears taller than the unfaulted half. This occurs at all negative bias and at positive bias only if $V_{\mathrm{d.c.}} < 0.15$ V [218, 219]. The asymmetry is due to a stacking fault in the first two layers of the 7×7 reconstruction, resulting in a higher density of states near the Fermi level for the faulted half compared to the unfaulted half. When probing occupied states, electrons just below the Fermi level always contribute to the tunnel current with a large transmission probability. Therefore, the stacking fault asymmetry is evident in all negative bias images. However, at positive bias the same asymmetry is evident only if $V_{\mathrm{d.c.}} < 0.15$ V. A reversed asymmetry appears near $V_{\mathrm{d.c.}} = 1.4$ V. For details on STM imaging of Si(111)-(7×7), see [64–67, 218, 219].

A TD-STM image (Fig. 6.35a) and STM images of the same region for $V_{\mathrm{d.c.}} = -0.5$ V (Fig. 6.35b), $V_{\mathrm{d.c.}} = -0.7$ V (Fig. 6.35c) and $V_{\mathrm{d.c.}} = -1$ V (Fig. 6.35d) demonstrate that THz-pulse-induced tunneling is not occurring from occupied surface states greater than 0.5 eV below the surface Fermi level ($\varepsilon_{\mathrm{F,S}}$). This is evident from the TD-STM image not showing protrusions at either of the two defect sites, as seen in STM images with $V_{\mathrm{d.c.}} < -0.5$ V. Furthermore, a d.c. bias dependence of the region in Fig. 6.9 was performed in constant-current mode from −1.500 V to 0 V in 125 mV steps at constant $E_{\mathrm{THz,pk}}$ with topography (Fig. 6.36) and THz-STM (Fig. 6.37) images measured simulta-

neously. The TD-STM image ($V_{\mathrm{d.c.}} = 0$ V) does not exhibit any protrusions for defects and non-crystalline regions on the 7×7 surface, indicating that TD-STM is strictly occurring through states near $\varepsilon_{\mathrm{F,S}}$.

Non-equilibrium tunneling must be considered when studying transport on semiconductor surfaces [113, 115, 303, 305, 312–315, 317, 350–359]. For $V_{\mathrm{THz}}(t) < 0$, THz-pulse-induced charging of the Si(111)-(7×7) surface creates a localized subsurface accumulation layer underneath the tip that couples bulk state electrons to the 7×7 surface. These bulk electrons scatter onto the surface and rapidly thermalize to a Fermi-Dirac distribution within tens of femtoseconds [320, 322, 332] before tunneling to the tip via surface states near $\varepsilon_{\mathrm{F,S}}$. In the reverse direction, $V_{\mathrm{THz}}(t) > 0$, the subsurface layer is in depletion, allowing charge to build up on the surface until the formation of an inversion layer and until the electric field becomes strong enough to tunnel electrons directly into conduction band states. The THz-STM current–voltage characteristic is fundamentally different from d.c. STM due to THz-pulse-induced band bending and ultrafast charging of the surface. THz-STM in the extreme current regime is not a measure of the ultrafast differential conductance ($\mathrm{d}I/\mathrm{d}V$).

During TD-STM (Fig. 6.35a; Fig. 6.36) the tip approaches the surface while scanning defects and non-crystalline regions because they do not have surface states near $\varepsilon_{\mathrm{F,S}}$. However, for STM with $V_{\mathrm{d.c.}} < -0.5$ V (Fig. 6.35c,d), a large density of defect states moves into the bias window, causing the tip to retract (or current to increase in constant-height mode). The strong signal at low bias for THz-STM images (Fig. 6.37) is due to the THz-pulse-induced current being heavily modulated by tip height changes while scanning the surface with a d.c. bias present in constant-current mode. When scanning with THz-STM in constant-current mode and $V_{\mathrm{d.c.}} \neq 0$ V, the feedback response is a convolution of both $I_{\mathrm{THz,avg}}$ and $I_{\mathrm{d.c.}}$ (similar discussion in [290]). A scenario is possible where the tip height is changing primarily in response to $I_{\mathrm{d.c.}}$ and the much smaller THz-induced contribution, $I_{\mathrm{THz,avg}}$, is also changing, but only

because of its strong exponential dependence with distance. Even if THz-induced tunneling was completely delocalized, the STM tip would trace out atomic features in response to $I_{\mathrm{d.c.}}$ and spatially modulate $I_{\mathrm{THz,avg}}$ due to its exponential dependence. By setting $V_{\mathrm{d.c.}} = 0$ V, the true resolution of THz-STM on silicon is established, which was one of the motivations for TD-STM.

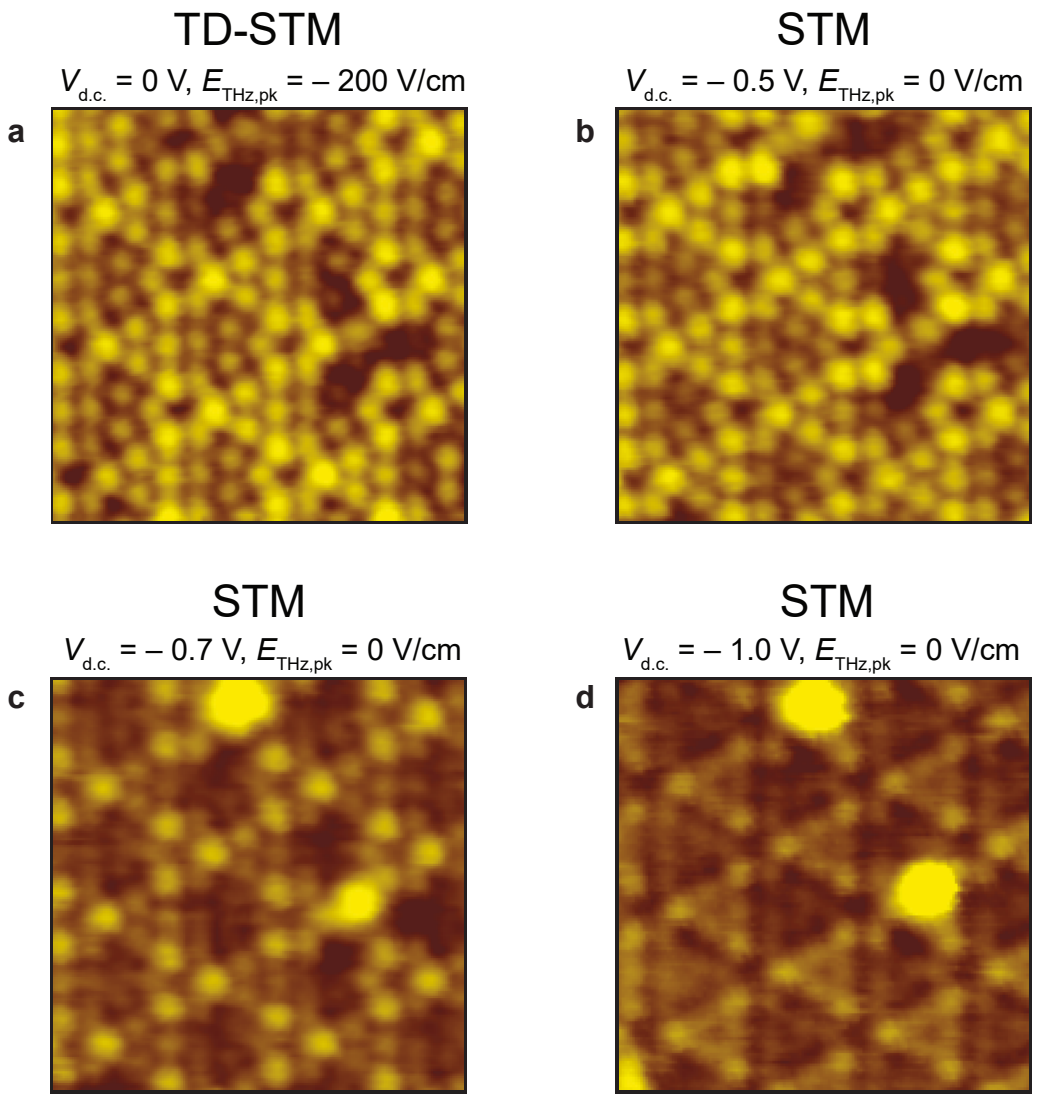

Figure 6.35: STM and TD-STM constant-current topographs. **a**, TD-STM image from Fig. 6.8b acquired at $V_{\mathrm{d.c.}} = 0$ V and $E_{\mathrm{THz,pk}} = -200$ V/cm. **b**, STM image from Fig. 6.8a acquired at $V_{\mathrm{d.c.}} = -0.5$ V. **c**, **d**, STM images of the same region at $V_{\mathrm{d.c.}} = -0.7$ V (**c**) and $V_{\mathrm{d.c.}} = -1$ V (**d**). Image size 8.5 nm × 8.5 nm; scan speed 13 nm/s; low-pass filtered with a 3×3 smoothing matrix; feedback loop setpoint −20 pA.

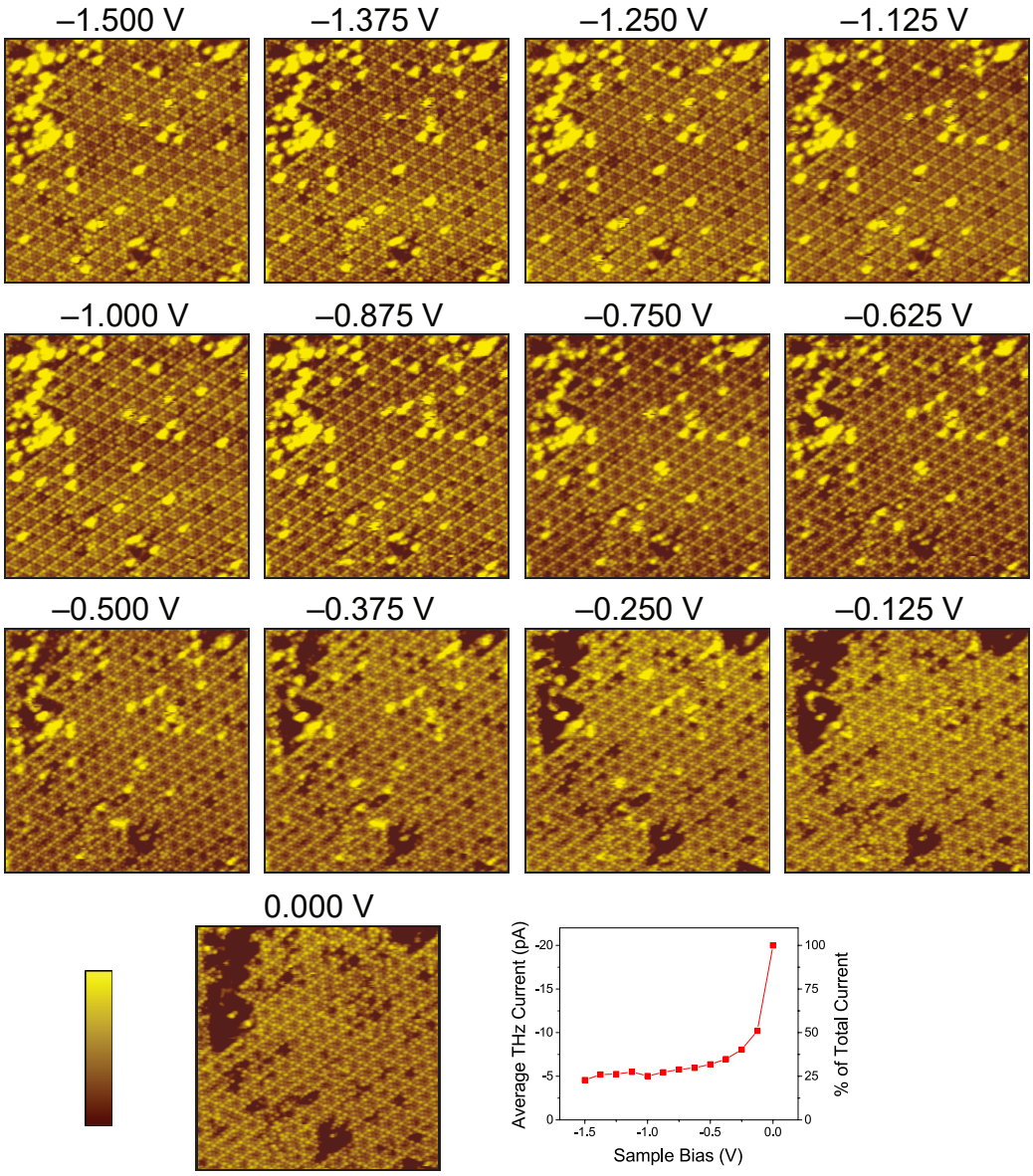

Figure 6.36: Constant-current topography of Si(111)-(7×7) at several $V_{\mathrm{d.c.}}$ and $E_{\mathrm{THz,pk}} = -200$ V/cm. The images are acquired at a feedback loop setpoint of -20 pA ($I_{\mathrm{d.c.}} + I_{\mathrm{THz,avg}} = -20$ pA). At $V_{\mathrm{d.c.}} = 0$ V, the 50% duty cycle THz pulse modulation is switched off, doubling $I_{\mathrm{THz,avg}}$ at constant tip height. Image size 40 nm × 40 nm; scan speed 40 nm/s.

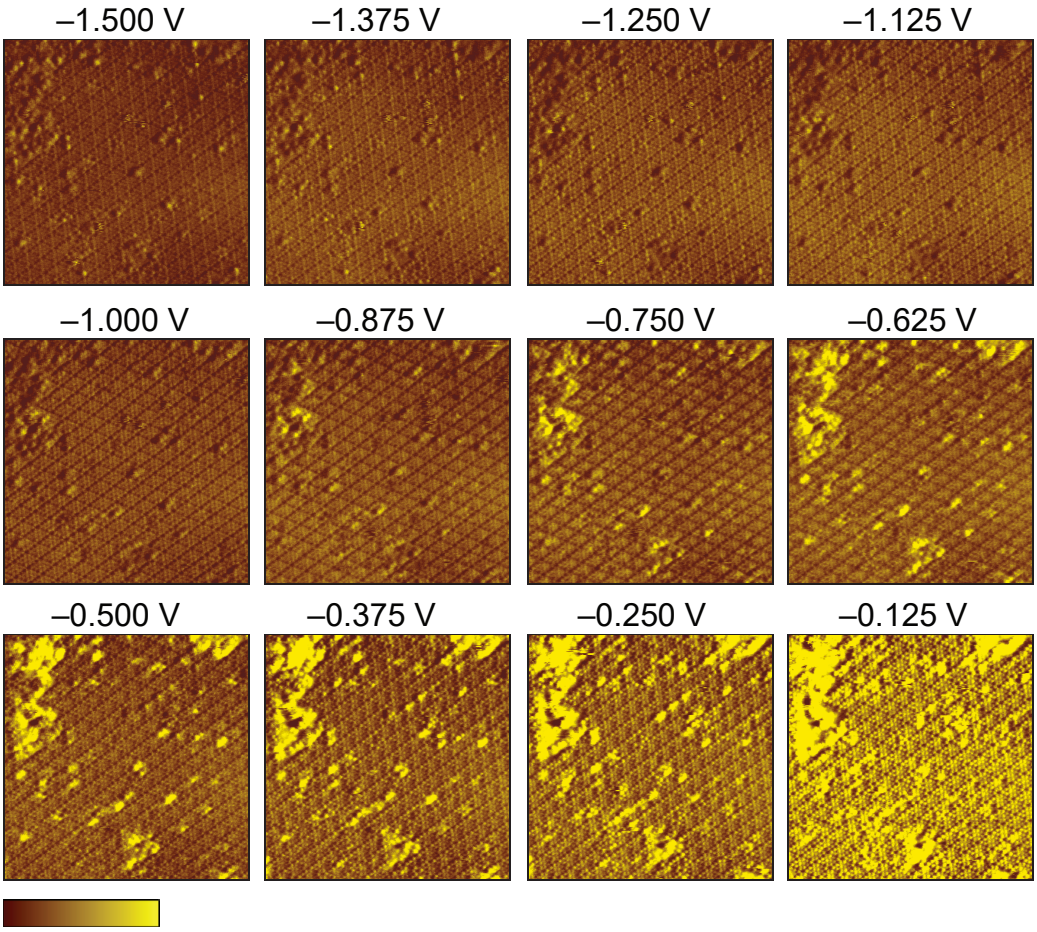

Figure 6.37: THz-STM of Si(111)-(7×7) at several $V_{\text{d.c.}}$ and $E_{\text{THz,pk}} = -200$ V/cm. The THz-STM images, $N_{\text{e}^-}(x, y)$, are acquired simultaneously with the constant-current topography images in Fig. 6.36. The lock-in time constant was set to 1 ms with an average pixel-time during scanning at 2.4 ms. The colourmap ranges from 80 to 350 rectified electrons per pulse for brown to gold, respectively.

6.7 Hot Electron Effects

TD-STM I–z curves (Fig. 6.38a,b,c) reveal two distinct exponential decay, fast and slow. At low THz fields, tunneling of electrons via surface states near $\varepsilon_{\mathrm{F,S}}$ is the primary contribution to I_{THz}, resulting in a strong dependence on the tip–sample separation (fast decay). However, for larger negative peak terahertz fields, band bending beyond the flatband condition accelerates conduction band electrons towards the tunnel junction (inset Fig. 6.38b). These hot electrons have an enhanced tunneling probability and less dependence on the tip–sample separation (slow decay). Similar I–z behavior [104, 140] and hot electron effects [101] have been reported in laser-assisted STM at optical frequencies. Interestingly, the study in [140], which was performed at optical frequencies, finds that the photoelectron component (slow decay) has a $\sim 45°$ difference in the lock-in phase as compared to the tunneling component (fast decay). This may prove useful in future studies that attempt to separate the contributions of the fast decay and slow decay components in the measured current.

In THz-STM, hot electrons can be accelerated to electronvolt energies by the THz electric field, resulting in a reduced apparent barrier-height (Fig. 6.38d). High energy electrons have been reported by studies of intense THz pulses in silicon [360, 361] and ultrafast THz field emission from nanostructures [160–164]. Furthermore, Monte Carlo simulations of electron velocity overshoot in silicon [362, 363] find that an electric field of 50 kV/cm can generate 0.3 eV electrons within subpicosecond timescales. Terahertz electric fields can penetrate several nanometers into the bulk since the Si(111)-(7×7) surface cannot screen the field effectively at THz frequencies due to its low conductivity (see section 6.4 and Fig. 6.33 for details). The Bardeen tunneling model predicts 44 MV/cm at the tip apex (3.1 V/ 7 Å) (see section 6.2).

In tunneling spectroscopy, the exponential decay of an I–z curve defines the apparent barrier-height (Eq. 2.6), ϕ_{exp} [66, 67]. The apparent barrier-heights of TD-STM I–z curves as a function of $E_{\mathrm{THz,pk}}$ (Fig. 6.38d) yield $\phi_{\mathrm{exp}} \approx 5$ eV

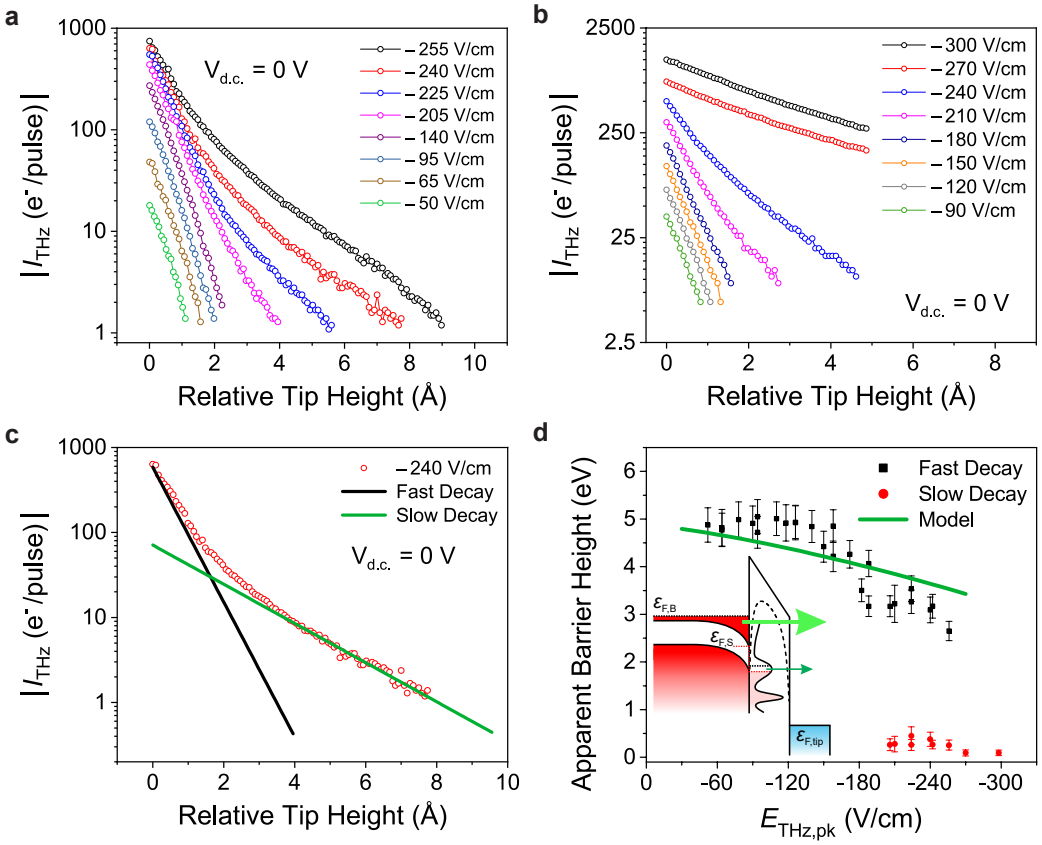

Figure 6.38: Hot electrons in the THz-pulse-induced current. **a**, I–z curves measured at $V_{\mathrm{d.c.}} = 0$ V for several $E_{\mathrm{THz,pk}}$. The initial tip–sample separation was set by $V_{\mathrm{d.c.}} = 0$ V, $I_{\mathrm{THz,avg}} = -20$ pA, $E_{\mathrm{THz,pk}} = -225$ V/cm. **b**, I–z curves measured at $V_{\mathrm{d.c.}} = 0$ V for several $E_{\mathrm{THz,pk}}$ with the initial tip–sample separation set by $V_{\mathrm{d.c.}} = 0$ V, $I_{\mathrm{THz,avg}} = -20$ pA, $E_{\mathrm{THz,pk}} = -240$ V/cm. **c**, A bi-exponential fit was used if the I–z curve exhibited fast and slow decay components. **d**, A plot of the apparent barrier-height obtained from the exponential decay of experimental (symbols) and simulated (green solid line) I–z curves in **a** and **b**. The error bars are determined from an uncertainty in the z-piezo calibration and exponential fits to the I–z curves. Inset: non-equilibrium band diagram for large negative terahertz fields. Incorporating an image potential into the modeling (dashed line) lowers the effective barrier height and width (see section 6.2 for details).

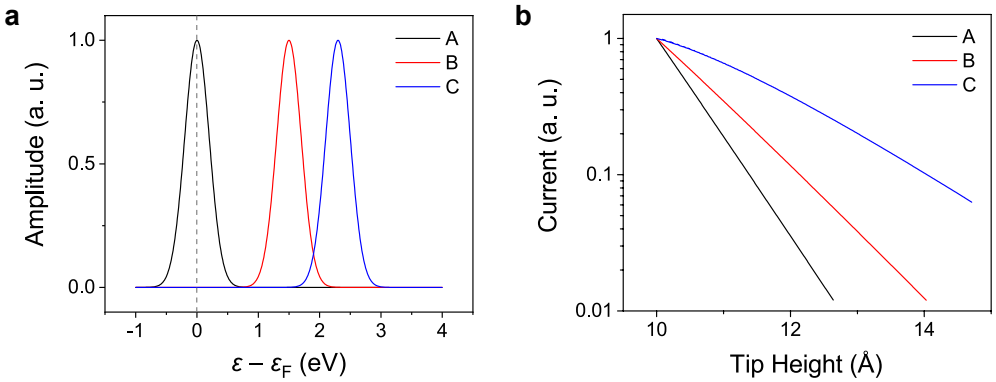

Figure 6.39: Simulated I–z curves for a hot electron energy distribution. **a**, Hot electrons are modeled as a density of states above the Fermi level using Gaussians centered at 0 eV (A), 1.5 eV (B) and 2.3 eV (C). **a**, Simulated I–z curves and their corresponding apparent barrier-heights. The apparent barrier-heights are 2.7 eV, 1.1 eV and 0.3 eV for electron energies centered at 0 eV (A), 1.5 eV (B) and 2.3 eV (C), respectively. The Bardeen tunneling model parameters are: $V_{\mathrm{THz,pk}} = -3$ V, z = 1 nm and $\phi_{\mathrm{sim}} = 5$ eV.

for low fields, decreasing to $\phi_{\mathrm{exp}} \approx 3$ eV with increasing $|E_{\mathrm{THz,pk}}|$ for the fast decay component, as described by our model, while the slow decay component yields $\phi_{\mathrm{exp}} < 0.5$ eV. This dramatic decrease in ϕ_{exp} can be accounted for by a reduced tunnel barrier height and width seen by the hot electron distribution tunneling from the conduction band to the tip (Fig. 6.39). The tunnel current due to hot electrons was calculated using Eq. 6.1 with hot electrons modeled as a large density of states above the sample Fermi level (Fig. 6.39a). A Gaussian distribution was used to select a relatively narrow range of electron energies and investigate their effect on the apparent barrier-height. Simulated I–z retraction scans show a decreasing apparent barrier-height for increasing electron energies (Fig. 6.39b), similar to what is observed experimentally (Fig. 6.38d). Apparent barrier-heights of 0.3 eV are obtained for energies 2–3 eV above the Fermi level, indicating that hot electron tunneling is consistent with the observations.

The current flowing through a high quality STM tunnel junction has an extremely strong dependence on the tip–sample separation (about a decade of current per 1 Å) and will measure ϕ_{exp} to be 4–5 eV [64–67]. A large ϕ_{exp}

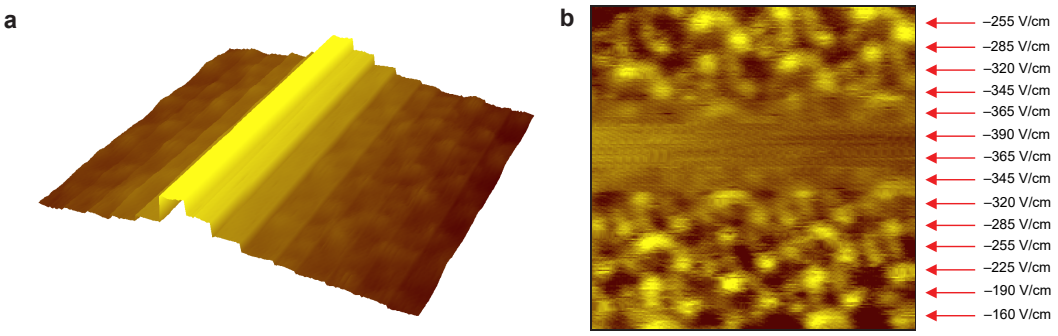

Figure 6.40: Constant-current TD-STM image with increasing and decreasing $E_{\mathrm{THz,pk}}$. **a**, 3D perspective view of TD-STM topography acquired at $V_{\mathrm{d.c.}} = 0$ V, $I_{\mathrm{THz,avg}} = -20$ pA and various $E_{\mathrm{THz,pk}}$. The topography appears stepped because the tip jumps when $E_{\mathrm{THz,pk}}$ is changed (constant-current mode). Topography z-range, 0.4 nm. **b**, Processed image where the average of every line is set to zero. $E_{\mathrm{THz,pk}}$ is changed fourteen times throughout the scan. Image size 9 nm × 9 nm; scan speed 14 nm/s.

is essential for localizing the tunnel current to the atom under investigation and the apex atom of the tip. This can be understood from an estimate of the spatial extent of the tunnel current as a function of lateral position Δx and tip radius of curvature (Eq. 2.5). For $\phi = 5$ eV, the tunnel area is narrower by a factor of 5, as compared to $\phi = 0.2$ eV. Furthermore, multiple protrusions on the tip can delocalize the tunnel current if ϕ is small. A loss of spatial resolution was observed for TD-STM imaging at large negative $E_{\mathrm{THz,pk}}$ (Fig. 6.40). While imaging in constant-current TD-STM mode, an increasing $|E_{\mathrm{THz,pk}}|$ caused the tip to retract (Fig. 6.40a), but only the slow decay component contributed significantly to the THz-pulse-induced current at large tip–sample separations (Fig. 6.38a,b), resulting in a loss of spatial resolution at large negative $E_{\mathrm{THz,pk}}$ (Fig. 6.40b). At large tip–sample separations the tip height is no longer determined by atomically localized tunneling of bulk electrons via adatom surface states, but rather hot electron tunneling over a broad area. Furthermore, the tunnel junction is no longer confined to single atoms at the tip apex and sample surface, and the terahertz tunnel conductance may exceed that of 1D ballistic transport [66]. THz-pulse-induced hot electron effects may find application with ballistic electron emission microscopy [364].

6.8 Subsurface Features

Terahertz pulses coupled to sharp metal tips have demonstrated subsurface imaging at the nanoscale [77]. The THz-STM images in Fig. 6.41–6.43 reveal a large-scale variation in the background signal level. Topography images (Fig. 6.41a; Fig. 6.42a; Fig. 6.43a,d) show a typical Si(111)-(7×7) surface with crystalline and non-crystalline regions. However, the simultaneously acquired THz-STM images (Fig. 6.41b; Fig. 6.42b; Fig. 6.43b,e) show localized enhancements of the THz-pulse-induced current. Differential conductance maps, $\mathrm{d}I/\mathrm{d}V$ (Fig. 6.42c; Fig. 6.43c,f), confirm that these features are not detected with conventional STM. Cross-sectional linescans performed on topography (Fig. 6.41c; Fig. 6.42d; Fig. 6.43g), THz-STM (Fig. 6.41d; Fig. 6.42e; Fig. 6.43h) and $\mathrm{d}I/\mathrm{d}V$ (Fig. 6.42f; Fig. 6.43i) emphasize that there is very little correlation between the localized THz-STM enhancements and the simultaneously measured STM topography and $\mathrm{d}I/\mathrm{d}V$. These local enhancements of THz-pulse-induced current are attributed to subsurface dopant concentrations. The silicon sample is heated several times to clean the surface and form the 7×7 reconstruction. This procedure migrates dopants and forms areas with varying dopant concentration. Recent studies found that a dopant depletion layer is formed below the silicon surface, resulting in a reduced dopant concentration near the surface compared to the bulk [351, 365–367]. They determined a correlation between the subsurface dopant concentration and the maximum temperature reached during sample preparation. A reduction of the dopant concentration near the surface compared to that of the bulk was qualitatively verified in our sample by secondary ion mass spectrometry at the University of nanoFAB facility.

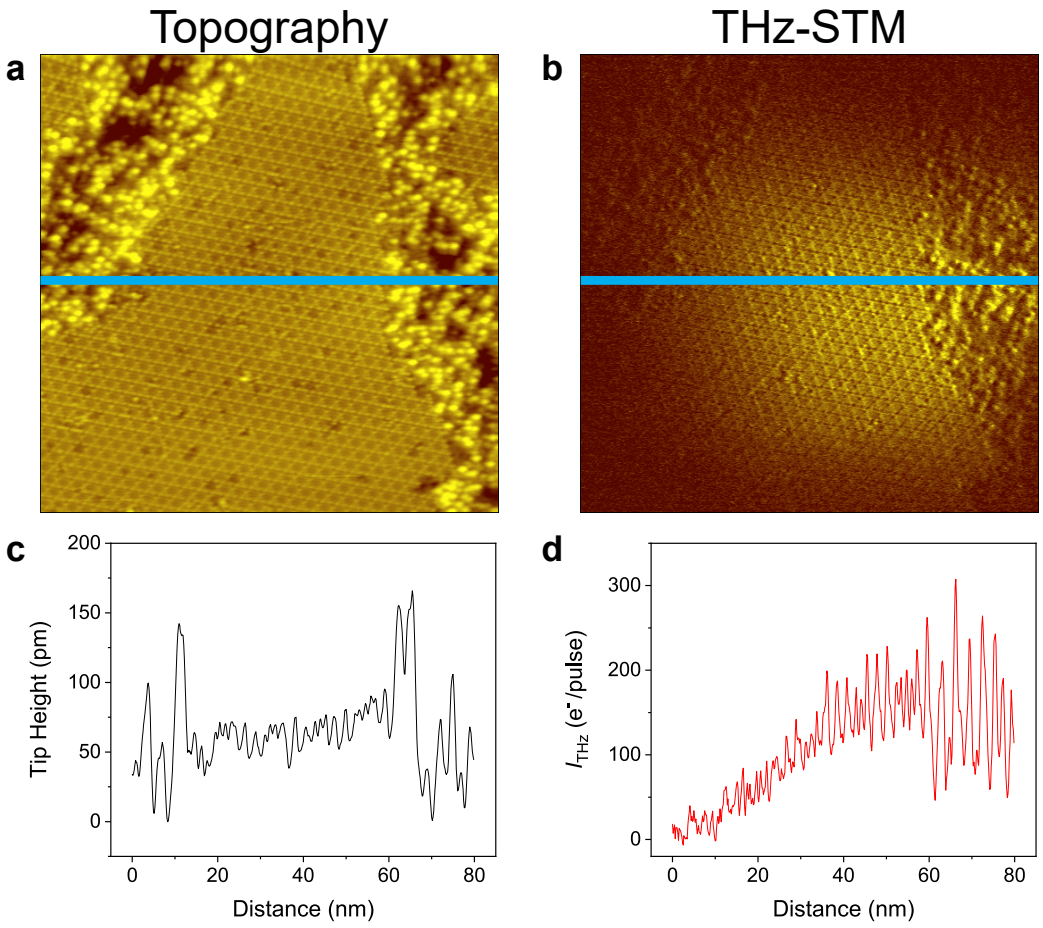

Figure 6.41: THz-STM revealing subsurface features on Si(111)-(7×7). **a**, Constant-current topography image at $V_{\mathrm{d.c.}} = -1.2$ V and **b**, simultaneously acquired THz-STM at $E_{\mathrm{THz,pk}} = -60$ V/cm and $I_{\mathrm{d.c.}} + I_{\mathrm{THz,avg}} = -200$ pA. Image size 80 nm × 80 nm; scan speed 72 nm/s; $I_{\mathrm{THz,avg}}$ is less than 10% of the total current ($I_{\mathrm{d.c.}} \gg I_{\mathrm{THz,avg}}$). **c**, **d**, Cross-sectional linescans for the topography image in **a** and THz-STM image in **b**, as indicated the by the blue lines in the insets.

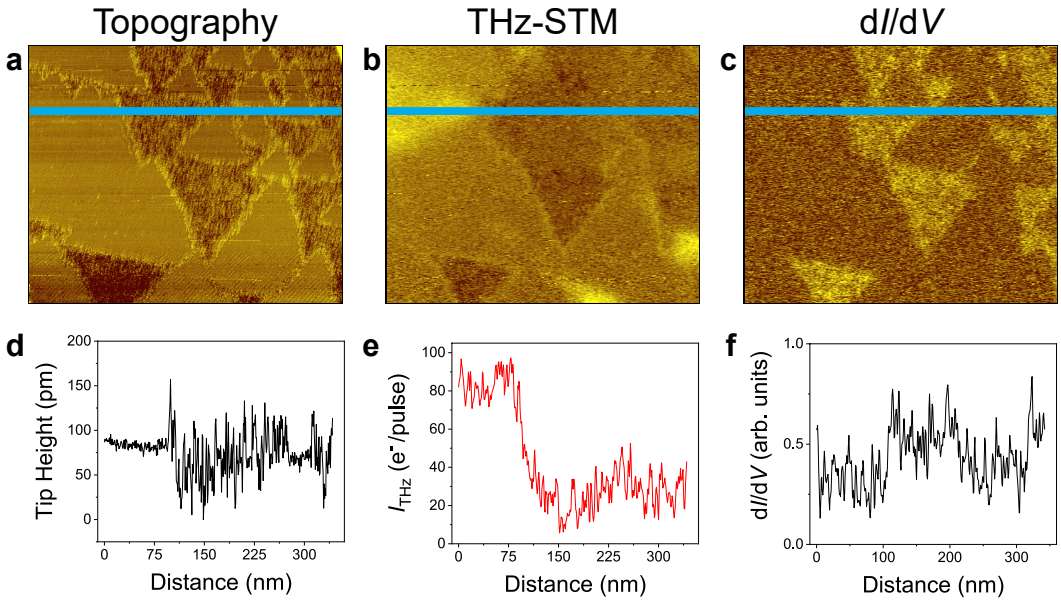

Figure 6.42: Comparison between topography, THz-STM and differential conductance images on Si(111)-(7×7). **a**, Constant-current topography image at $V_{\mathrm{d.c.}} = -1.2$ V. **b**, The simultaneously acquired THz-STM image at $E_{\mathrm{THz,pk}} = -110$ V/cm. **c**, The simultaneously acquired differential conductance ($\mathrm{d}I/\mathrm{d}V$) image at 25 mV $\mathrm{d}I/\mathrm{d}V$ modulation amplitude. Image size 340 nm × 280 nm; scan speed 160 nm/s; $I_{\mathrm{d.c.}} + I_{\mathrm{THz,avg}} = -200$ pA with $I_{\mathrm{d.c.}} \gg I_{\mathrm{THz,avg}}$. **d**, **e**, **f**, Cross-sectional linescans as indicated by the blue lines in **a**–**c** for topography (**d**), THz-STM (**e**) and $\mathrm{d}I/\mathrm{d}V$ (**f**).

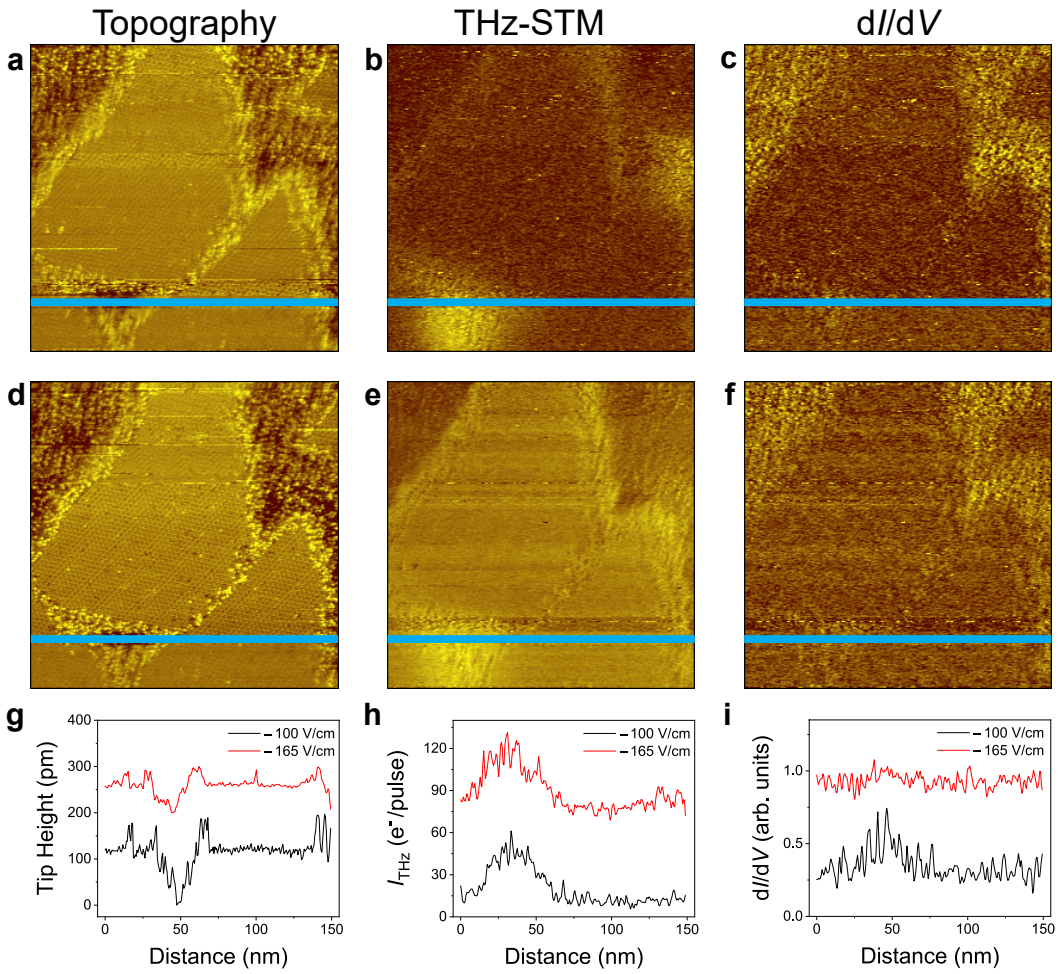

Figure 6.43: Subsurface features on Si(111)-(7×7) at two different $E_{\mathrm{THz,pk}}$. **a**, Constant-current topography image at $V_{\mathrm{d.c.}} = -1.2$ V. **b**, The simultaneously acquired THz-STM image at $E_{\mathrm{THz,pk}} = -100$ V/cm. **c**, The simultaneously acquired differential conductance image. **d**, Constant-current topography image at $V_{\mathrm{d.c.}} = -1.2$ V. **e**, The simultaneously acquired THz-STM image at $E_{\mathrm{THz,pk}} = -165$ V/cm. **f**, The simultaneously acquired differential conductance image. The average of every line was set to zero for the topography images because of minor tip changes (instead of plane-fit-subtraction). For both sets of scans: image size 150 nm × 150 nm; scan speed 120 nm/s; $I_{\mathrm{d.c.}} + I_{\mathrm{THz,avg}} = -200$ pA with $I_{\mathrm{d.c.}} \gg I_{\mathrm{THz,avg}}$; 25 mV $\mathrm{d}I/\mathrm{d}V$ modulation amplitude. **g**, **h**, **i**, Cross-sectional linescans as indicated by the blue lines in **a**–**f** for topography (**g**), THz-STM (**h**) and $\mathrm{d}I/\mathrm{d}V$ (**i**). The linescans for topography and $\mathrm{d}I/\mathrm{d}V$ were shifted along the y-axis for clarity.

Chapter 7

Optical Pump – THz-STM Probe of GaAs(110)

Our ability to control, characterize and image ultrafast non-equilibrium carrier transport on the atomic scale is essential for guiding future applications that aim to couple our macroscopic world to individual atoms. The THz-STM is a newly developed platform for exploring the evolution of electrons and other charged quasi-particles at sub-nanometer lengthscales and sub-picosecond timescales. Here, we demonstrate time-resolved THz-STM imaging and spectroscopy of an optically excited silicon-doped GaAs(110) surface. The THz-pulse-induced tunnel current was locally enhanced by the optical-pulse-induced transient surface photovoltage (SPV) that surrounded charged surface defects. However, when the tip was positioned within a screening-length distance of the defect, the transient SPV was completely suppressed. At perturbative THz field strengths, the single-cycle pulses coherently controlled the tunneling of optically-excited carriers in a nearly-linear regime, such that the THz pulse near-field at the apex of individual tips was photoconductively sampled. Meanwhile, for strong THz pulses, the field penetrated deep into the sample and the resulting transient tunnel current response developed a complex temporal structure that was described by a convolution of the incident THz pulse with the subsurface carrier dynamics of the sample, within the framework of a nonlinear tunnel junction.

Gallium arsenide (GaAs) is a III–V semiconductor with a cubic zincblende crystal structure, where every Ga atom is tetrahedrally bonded with an As atom and similarly, every As atom is tetrahedrally bonded to a Ga atom[1]. This configuration leads to bonding that is partially covalent and partially ionic, with the former due to four singly occupied s^1p^3 orbitals, and the latter due to the charged Ga^{3+} and As^{3-} ions [368]. There are some key differences between the GaAs(110) surface studied here, and the Si(111)-(7×7) surface that was studied in chapters 6 and 8. At a temperature of 100 K, GaAs has a direct band gap of $\sim$ 1.45 eV, compared to an indirect band gap of $\sim$ 1.17 eV for silicon [369]. This leads to efficient generation of electron–hole pairs in the GaAs sample upon photoexcitation with 1.55 eV photons (λ = 800 nm). Another unique feature of GaAs is that its principle cleavage plane[2] is the (110) face, and not the (111) face, as expected for a tetrahedrally bonded crystal structure. This is because the (111) face must terminate with either Ga atoms or As atoms[3], and as a result, the surface is electrically polarized. Meanwhile, the (110) face contains an equal number of Ga atoms and As atoms, generating a nonpolar surface with less surface energy per unit area compared to the (111) face. Upon cleaving, the GaAs(110) surface undergoes a 1×1 surface relaxation (buckling) that slightly repositions the adatoms in order to minimize their energy [343, 368]. This relaxation shifts the energy of the Ga–As hybridized dangling-bond-states beyond the edges of the valence and conduction bands, and as a result, intrinsic surface states are not present on GaAs(110) within the fundamental band gap[4]. This is similar to the Si(100)-(2×1) and H-Si(100)-(2×1) surfaces, and in strong contrast to the metallic-like Si(111)-(7×7) surface, which had a surface state density of $\sim 10^{15}$ cm^{-2}eV^{-1}

[1] The zincblende crystal structure is identical to the diamond crystal structure except with alternating atoms in the lattice sites (eg. ZnTe, GaAs, InAs). Accordingly, the zincblende structure is inherently non-centrosymmetric, resulting in a non-zero second-order susceptibility, $\chi^{(2)}$ (Eq. 3.2).

[2] The principle cleavage plane minimizes the energy of broken bonds per unit area.

[3] These two polar surfaces are labeled as either GaAs(111)A or GaAs(111)B.

[4] There are intrinsic surface states at approximately 1.75 eV above the valence band edge with a 0.25 eV FWHM and a 2D DOS of $\sim 10^{15}$ cm^{-2}eV^{-1} [370, 371]. Extrinsic in-gap surface states may still be present due to defects, adsorbates and dopants.

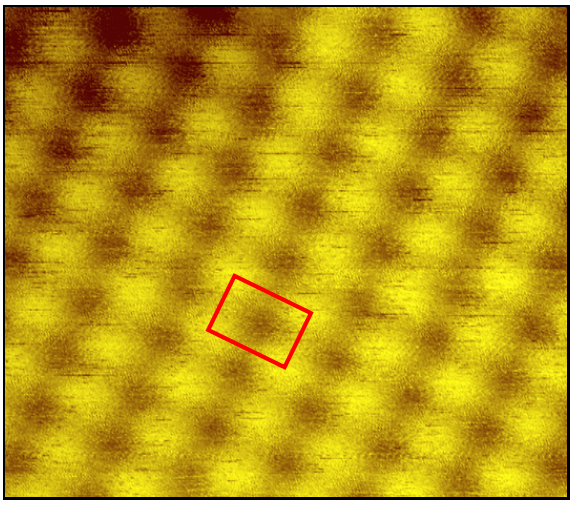

Figure 7.1: STM image of the GaAs(110) surface acquired in constant-current mode at $V_{\text{d.c.}} = +1.5$ V, $I_{\text{d.c.}} = +150$ pA and $T = 295$ K. A red rectangle with dimensions 5.6 Å × 4.0 Å shows the unit cell of the surface. Image size 3.9 nm × 3.4 nm; scan speed 15 nm/s; colourmap range 100 pm.

at the Fermi level [313, 314]. Due to the absence of intrinsic surface states on GaAs(110), an externally applied electric field readily penetrates into the semiconductor bulk and produces significant tip-induced-band-bending (TIBB) of the subsurface potential [352, 353, 370–373].

The electron tunneling dynamics of the GaAs(110) surface have been carefully studied using conventional STM imaging and spectroscopy [189, 227, 343, 352, 353, 368, 370, 374–383], optically-excited STM [113, 371, 373, 384–388], and time-resolved optical pump-probe STM [100, 105, 109–112, 114, 115]. An atomically resolved STM image of a silicon-doped GaAs(110) surface is shown in Fig. 7.1. At positive bias, the peaks in the STM image represent the location of gallium atoms on the surface because the unoccupied states are localized on gallium atoms, while the occupied states are localized on arsenic atoms. This property enables atom-selective imaging of the GaAs(110) surface by switching the polarity of the bias voltage [374]. Further studies have shown that surface resonances through the back-bonded atoms can significantly alter the atomically resolved electronic properties of (110)-oriented III–V semiconductor surfaces, whereby a sudden 90° rotation of the measured atomic rows occurs

at particular bias voltages [353, 378]. Also, TIBB in the semiconductor bulk can lead to the formation of an accumulation layer of majority carriers ($V_{\mathrm{d.c.}} \lesssim -0.2$ V), an inversion layer of minority carriers ($V_{\mathrm{d.c.}} \gtrsim +2.2$ V), or a carrier depletion layer (-0.2 V $\lesssim V_{\mathrm{d.c.}} \lesssim +2.2$ V)[5] [382]. Comprehensive studies of the silicon-doped GaAs(110) surface have successfully characterized many of the various defects, adsorbates and dopant configurations that can occur [368, 370, 375, 379, 380, 382, 383]. For Si-doped GaAs, silicon acceptors start to limit the bulk conductivity at doping concentrations in excess of 2×10^{18} cm^{-3} [379, 380, 383]. This occurs because a silicon impurity in GaAs is an amphoteric dopant, acting primarily as a donor at low doping concentrations, while both a donor and an acceptor at high doping concentrations (at a dopant concentration of 5×10^{18} cm^{-3}, about 20% of the silicon atoms are acceptors [383]).

Optically excited GaAs(110) surfaces have been studied with the STM using continuous-wave illumination [113, 371, 373, 384–388], electrostatic simulations [371, 373], and ultrafast pump-probe measurements [100, 105, 109–112, 114, 115]. The optical excitation generates electron–hole pairs that get spatially separated by the potential drop across the tunnel junction[6]. The photoexcited electrons accumulate in a small volume underneath the tip at negative bias voltages, and similarly holes accumulate underneath the tip at at positive bias voltages. For n-type samples, a majority carrier accumulation layer naturally forms underneath the tip at negative bias voltages due to TIBB. Under these conditions (forward bias), TIBB eliminates the carrier depletion layer and enables direct coupling between the surface states and the bulk band structure. While this increases the steady-state conductivity, it negates the impact of the optically-induced transient photoconductivity. This is because the majority carriers that are already present under forward bias,

[5]The precise values depend on the dopant concentration, tip–sample separation and tip work function.

[6]Photoexcited electron–hole pairs separate naturally (without a tip present) only if there is a space-charge-layer underneath the surface [389]. However, since the GaAs(110) surface does not have any intrinsic in-gap surface states, only extrinsic surface states can separate the photoexcited electron–hole pairs (in addition to the tip-induced field).

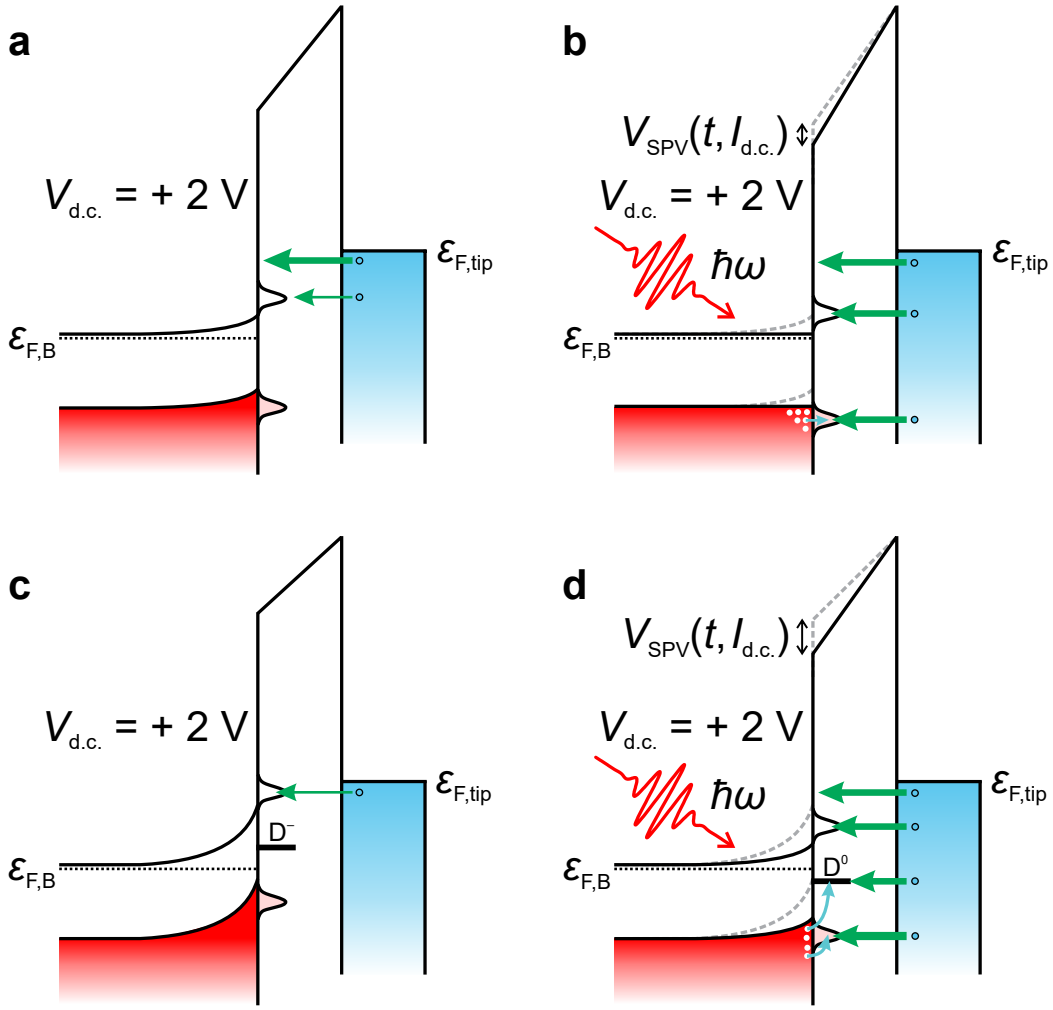

Figure 7.2: Band diagrams for STM of n-type GaAs(110) under reverse bias at $V_{\mathrm{d.c.}} = +2$ V. **a**, **b**, A pair of band diagrams for an atomically clean GaAs(110) surface before (**a**) and after (**b**) photoexcitation by an optical pulse that creates electron–hole pairs in the sample. **c**, **d**, A pair of band diagrams for a negatively charged surface defect on GaAs(110) before (**c**) and after (**d**) photoexcitation. The two small Gaussians represent the intrinsic surface states of GaAs(110), while a solid black bar represents a negatively charged (D^-) or neutral (D^0) extrinsic in-gap surface state. Green arrows indicate the direction of electron tunneling, with thicker arrows indicating a higher tunneling probability. Small blue and white circles are used to represent electrons and holes, respectively. The Fermi levels of the tip and sample bulk are given by $\varepsilon_{\mathrm{F,tip}}$ and $\varepsilon_{\mathrm{F,B}}$, respectively, where $eV_{\mathrm{d.c.}} = \varepsilon_{\mathrm{F,tip}} - \varepsilon_{\mathrm{F,B}}$. The dashed grey lines in **b** and **d** show the change in band bending due to the surface photovoltage (SPV). The occupied states for the sample, surface and tip are colored red, pink and blue, respectively.

efficiently screen any electric fields that are present at the surface [114, 373]. However, under reverse bias conditions (Fig. 7.2a), the photoexcited minority carriers are localized underneath the tip apex, generating a surface potential that screens the tip-induced field from the semiconductor bulk (Fig. 7.2b). This change in the surface potential compared to a dark sample is known the surface photovoltage (SPV). The SPV is strongest at positive bias voltages for n-type samples and negative voltages for p-type samples [388]. Also, the SPV is strongly enhanced by defect-induced gap states (Fig. 7.2c), such as a single-gallium-atom vacancy on the surface [387]. This is because negatively charged defects, D^-, readily attract nearby photoexcited holes, which places them into a neutral state, D^0, that reduces the local potential barrier and increases the electron tunneling probability (Fig. 7.2d). The transient SPV, $V_{\mathrm{SPV}}(t-\tau, I_{\mathrm{d.c.}})$, is strongly dependent on the steady-state tunnel current, $I_{\mathrm{d.c.}}$, if the tunneling rate is comparable to the hole trapping time [113] (160 pA corresponds to 1 tunneling electron per nanosecond). For a pulsed photoexcitation, the SPV fades away once the electrons and holes have been annihilated by the STM tunnel current, or once the carriers have decayed via natural processes[7]. An additional modification to the surface potential can occur due to the photo-Dember effect (see section 3.1.1); however, this effects turns out to be fairly negligible for GaAs surfaces [262]. Time-resolved optical pump-probe STM measurements of an atomically clean silicon-doped GaAs(110) surface at room temperature have revealed two decay mechanisms for the photoexcited electron–hole pairs [109, 111]. The first decay mechanism is a bulk-side recombination due to carrier diffusion and drift, $\tau_{\mathrm{b}} \approx 5$ ns, while the second is a surface-side decay of trapped minority carriers after photoexcitation, $\tau_{\mathrm{s}} > 100$ ns. In the presence of an extrinsic in-gap state (such as an adsorbate), the decay times were found to be 1–2 orders of magnitude faster [109–111].

[7]Bulk carrier decay times in GaAs vary from several nanoseconds to hundreds of femtoseconds, depending on the concentration of trapping sites in the sample [109, 257–259].

7.1 Sampling the THz-STM Near-Field

An n-type silicon-doped GaAs(110) surface was investigated by the THz-STM just before and after photoexcitation by an optical pulse that had a center wavelength of 800 nm and a temporal duration of 70 fs. The relative time delay of the optical pulse with respect to the THz pulse was scanned as the THz-pulse-induced tunnel current was measured, $I_{\mathrm{THz,avg}}(\tau_{\mathrm{THz–Optical}})$[8]; this measurement was referred to as an 'optical pump – THz-STM probe waveform' (OPP-THz-STM waveform). Unless otherwise specified, all of the THz-STM measurements in this chapter were performed in constant-current mode in order to maintain a safe tip–sample separation during the long acquisition times. Constant-current mode was a valid alternative to constant-height mode because the tip height did not change considerably throughout the acquisition in response to the modulation of $I_{\mathrm{THz,avg}}$. This was ensured by setting the feedback loop current such that $I_{\mathrm{THz,avg}}$ was less than 5% of the total measured current, $I_{\mathrm{d.c.}} + I_{\mathrm{THz,avg}}$. In other words, the tip–sample separation throughout the acquisition, was primarily determined by $I_{\mathrm{d.c.}}$ and not $I_{\mathrm{THz,avg}}$.

Etched polycrystalline tungsten tips were treated *in situ* as described in section 5.2. The THz-pulse-induced structural modifications on the GaAs(110) surface were found to be minimized at low sample temperatures, similar to the results of chapter 8 for the Si(111)-(7×7) and H-Si(100)-(2×1) surfaces. Accordingly, all of the measurements were acquired at $T = 100$ K, using low-amplitude THz pulses ($|E_{\mathrm{THz,pk}}| \lesssim 100$ V/cm; Fig. 7.3a). The polarization of the optical pulse was set perpendicular to the tip axis (horizontal), while the THz pulse was polarized parallel to the tip axis (vertical). The maximum average optical power incident onto the STM tip was 750 µW (3 nJ per pulse), or ~ 400 µW when accounting for reflections from the polished GaAs surface[9]

[8] All pump-probe measurements in this chapter have positive time representing the arrival of the optical pulse after the THz pulse ($\tau_{\mathrm{THz–Optical}}$). This is opposite to chapter 4, where positive time represented the THz pulse arriving after the optical pulse ($\tau_{\mathrm{Optical–THz}}$).

[9] For a polished GaAs surface with 800 nm light incident at 35° above the surface, the reflectance is 0.525 and 0.136 for s-polarized and p-polarized light, respectively [390]. A reflectance and transmission calculator is available at: *http://refractiveindex.info/*

(the former value is quoted). This was just below the few-milliwatt threshold where thermal effects start to occur [139–142]. In fact, during our experiments on the Si(111)-(7×7) surface, well-defined atomic resolution was maintained with up to 5 mW of incident average optical power (20 nJ per pulse). Notably, OPP-THz-STM waveforms that were acquired on the Si(111)-(7×7) surface did not exhibit any temporal structure until more than 50 mW of average optical power was applied. This is consistent with reports of SPV effects on the Si(111)-(7×7) surface requiring intense optical excitation [310].

An OPP-THz-STM waveform was acquired using an atomically sharp tungsten tip on a GaAs(110) surface (Fig. 7.3b). Its temporal profile was found to be remarkably similar in appearance to the electro-optically sampled (EOS) waveform, except for a minor shift in the carrier-envelope-phase[10] (CEP) and amplitude spectrum. These spectral and phase shifts were caused by dispersion of the THz pulse upon coupling to the metal-wire-antenna and then propagating to the tip apex. In fact, early studies found that the temporal profile of the THz pulse near-field closely resembled the time-integrated far-field THz waveform [71]. However, recent 3D electromagnetic simulations have shown that the THz pulse electric near-field at the tip apex has a significantly altered temporal profile within the vacuum gap, as compared to inside the sample[11]. Specifically, the time-derivative of the THz pulse waveform within the vacuum gap region was found to be present inside the sample bulk. Furthermore, a very recent study with the THz-STM has demonstrated that the macroscopic tip shape modifies the CEP of the THz pulse near-field, with respect to the far-field pulse [137]. This CEP shift was found to range from 0 to $\pi/2$, using standard STM tip shapes. In the experiments presented here, a wide variety of tip shapes were used (Fig. 5.7), ensuring a range of CEP shifts between the near-field and far-field waveforms throughout day-to-day experiments.

The remarkable similarity between the EOS waveform (Fig. 7.3a) and the THz-

[10]The amplitude of each THz pulse half-cycle varies cyclically with the CEP from 0 to 2π. A CEP shift of π is equivalent to inverting the temporal profile ($\pm E_{\mathrm{THz,pk}}$).

[11]Private communication with Peter H. Nguyen. To be published.

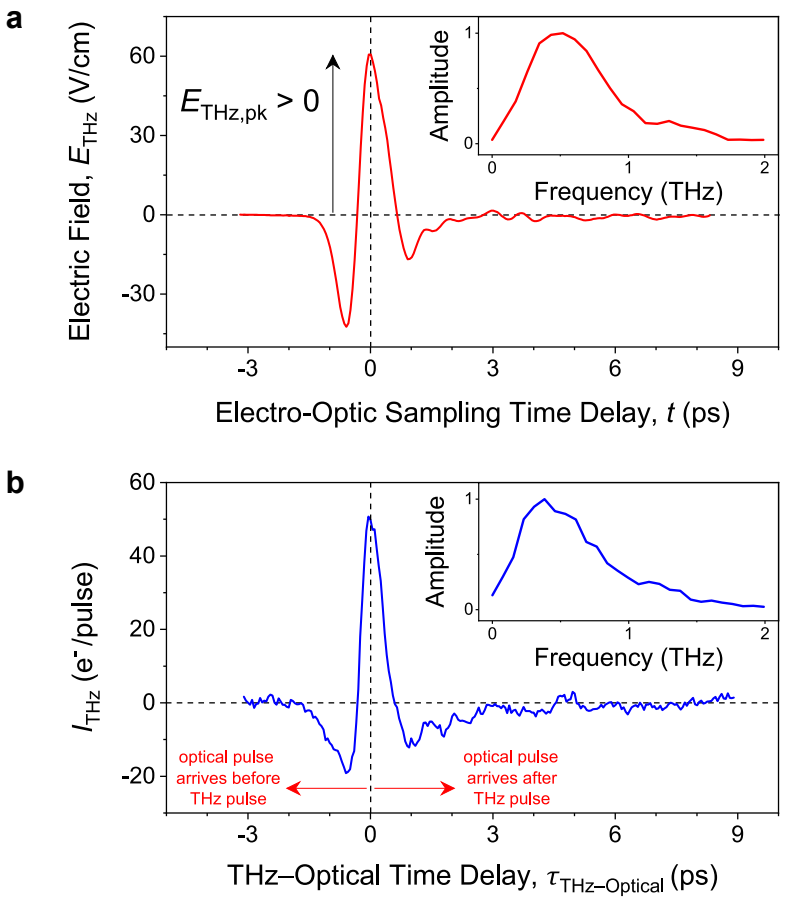

Figure 7.3: Photoconductive sampling of the THz pulse in the far-field and the STM near-field. **a**, Electro-optically sampled THz pulse electric field waveform and its corresponding frequency spectrum (inset). The magnitude of the smaller THz pulse half-cycle is approximately ~ 75 % of the larger half-cycle. **b**, Measured THz-pulse-induced rectified tunnel current, I_{THz} (e^-/pulse) = $N_{\mathrm{e}^-} = I_{\mathrm{THz,avg}}/(e\, f_{\mathrm{rep}})$, as a function of arrival time between the optical pulse and THz pulse onto the STM junction (OPP-THz-STM waveform). The measurements were acquired on a GaAs(110) surface at $V_{\mathrm{d.c.}} = +2$ V, $I_{\mathrm{d.c.}} + I_{\mathrm{THz,avg}} = +50$ pA, $E_{\mathrm{THz,pk}} = +40$ V/cm and $\varepsilon_{\mathrm{Optical}} = 1$ nJ.

STM near-field waveform (Fig. 7.3b) indicates that the local carrier lifetime underneath the tip must be extremely short, less than one picosecond. This is well understood for photoconductive sampling of free-space-propagating THz pulses, as discussed in section 3.2.1. Essentially, the negative THz pulse half-cycle at -0.6 ps (and positive $E_{\mathrm{THz,pk}}$) can only be accurately represented through photoconductive sampling if the local carrier lifetime, θ, is less than the temporal duration of a THz pulse half-cycle. Otherwise if $\theta \gtrsim 1$ ps, pho-

toexcited carriers will be present during both of the THz pulse half-cycles at negative time delay ($\tau < 0$ ps). In this case, the larger THz pulse half-cycle will dominate the overall response and the rectified THz-pulse-induced tunnel current will be non-zero at large negative time delay, τ. Clearly, this was not the case in Fig. 7.3b, as the THz-pulse-induced tunnel current was below the noise floor if the optical pulse arrived just two picoseconds before the THz pulse. If $\theta \rightarrow \infty$, and the junction is ohmic, the THz-pulse-induced tunnel current waveform is related to the time-integrated waveform of the incident THz pulse via $I_{\mathrm{THz,avg}}(\tau) \propto \int_{\tau}^{\infty} E_{\mathrm{THz}}(t)\,\mathrm{d}t$. However, in general, the measured THz-pulse-induced tunnel current, $I_{\mathrm{THz,avg}}(\tau)$, is the result of a nonlinear convolution between the locally enhanced instantaneous THz electric field $E_{\mathrm{THz}}(t)$, and the transient carrier density, $n(\theta, \varepsilon, t-\tau)$, together with the transient SPV of the local sample surface, $V_{\mathrm{SPV}}(t-\tau)$. In other words, the general expression for the THz-pulse-induced instantaneous tunnel current, $I_{\mathrm{THz}}(t,\tau)$, depended nonlinearly on the local carrier density, local transient SPV, and THz pulse voltage transient: $V_{\mathrm{THz}}(t) = F \times z \times E_{\mathrm{THz}}(t)$, where F is the field enhancement and z is the tip–sample separation. Accordingly, the measured THz-pulse-induced tunnel current waveform is easily distorted with respect to the incident far-field THz pulse. These nonlinear distortions often emerged in the OPP-THz-STM waveforms at moderate THz pulse electric fields (Fig. 7.4a), while at strong THz fields, a time-independent background signal completely dominated the response (Fig. 7.4b). By using perturbative low-field THz pulses, the nonlinearity of the tunnel junction was largely avoided[12], and the measured THz-pulse-induced tunnel current waveform, $I_{\mathrm{THz,avg}}(\tau)$, was an accurate representation of the THz pulse electric near-field at the tunnel junction. This THz-STM near-field sampling technique is analogous to far-field photoconductive sampling of ultrafast THz pulses (see section 3.2.1).

The physical significance of the parameter, θ, is that it represents the local

[12]In an optical pump – THz-STM probe geometry, a linear I–V curve can generate a non-zero rectified THz-pulse-induced tunnel current because the optical pulse can selectively enhance the tunneling probability for a brief temporal window during either half-cycle of the incident THz pulse.

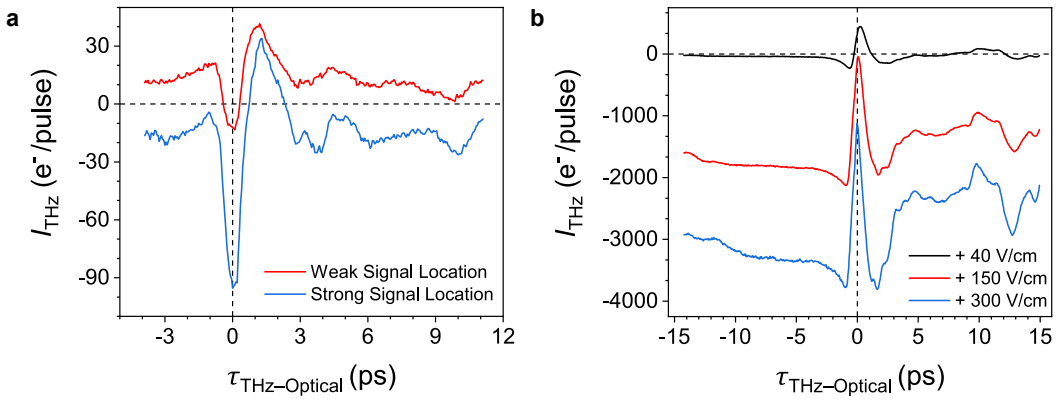

Figure 7.4: Nonlinear behaviour in optical pump – THz-STM probe waveforms on GaAs. **a**, Measured OPP-THz-STM waveforms that were acquired at two different locations on the sample surface with $V_{\mathrm{d.c.}} = +2$ V, $I_{\mathrm{d.c.}} + I_{\mathrm{THz,avg}} = +50$ pA, $\varepsilon_{\mathrm{Optical}} = 2.6$ nJ and $E_{\mathrm{THz,pk}} = -120$ V/cm. **b**, Measured THz-pulse-driven OPP-THz-STM waveforms that were acquired with the tip gently contacted to the sample surface at $V_{\mathrm{d.c.}} = 0$ V and $\varepsilon_{\mathrm{Optical}} = 100$ nJ. The feedback loop was disengaged after the tip–sample separation had established equilibrium due to the optical-pulse-induced thermal expansion.

decay of photoexcited carriers near the tunnel junction (it is also referred to as the local carrier lifetime). The THz-STM measures a much smaller value for θ than expected, due to reports of nanosecond carrier lifetimes by time-resolved THz spectroscopy of bulk GaAs [257] and ultrafast optical-pump – optical-probe STM of the GaAs(110) surface [109, 111]. These techniques reported carrier lifetimes of a few nanoseconds for the bulk [109, 111, 257], and tens to hundreds of nanoseconds for the surface [109, 111]. However, sub-picosecond carrier lifetimes have been reported by time-resolved THz spectroscopy measurements of low-temperature-grown GaAs (LT-GaAs) [258, 259]. The first of these studies determined a bulk carrier lifetime of 1 ps [258], while the second study identified three relaxation processes with time constants of 0.26 ps, 0.85 ps and 1.25 ps [259]. The LT-GaAs sample is created under a flux of excess arsenic and at a relatively low substrate temperature of 450–570 K. This creates a very high concentration of point defects throughout the bulk via As atom antisites, As atom interstitials and Ga atom vacancies. These defects are efficient trapping sites for photoexcited carriers, resulting in an extremely short carrier lifetime for bulk LT-GaAs. While LT-GaAs was not specifically

studied here, the THz-STM is sensitive to the local carrier dynamics of the sample surface, especially near charged surface defects (see section 7.3). Accordingly, the sub-picosecond timescale required for θ was most likely due to the THz-STM locally probing the carrier lifetime near these surface defects.

However, another consideration for why the carrier lifetime measured by the THz-STM does not match the nanosecond lifetime measured by SPPX-STM [109, 111], is that the two ultrafast microscopy techniques operate under fundamentally different physical principles. With the SPPX-STM technique, the ultrafast current is generated by photoexcitation using two nearly-identical time-delayed optical pulses, and the carrier dynamics of the sample are subsequently extracted from the temporal decay of pump–pump autocorrelations. In this case, the photoexcited carriers naturally decay following their locally available mechanisms, which take anywhere from a few nanoseconds to hundreds of nanoseconds [109, 111]. However, in an optical pump – THz-STM probe experiment, the ultrafast THz voltage drives non-equilibrium transport of the photoexcited carriers, which can modify the physical significance of the parameter, θ. A situation can arise where the photoexcited carriers are generated deep within the bulk, beyond the extent of the steady-state tip-induced field, and the carriers simply continue to diffuse into the bulk. However, if the optical pulse arrives at the same time as the THz pulse, the photoexcited carriers that would have otherwise diffused away, are accelerated towards the tunnel junction by the deeply penetrating THz pulse electric field. In this case, the physical significance of θ would not only be the local carrier trapping time, but it would also include effects from the spatio-temporal distribution of the photoexcited carriers, and their subsequent THz-pulse-induced transport through the semiconductor bulk.

Three different tips were used to acquire a set of OPP-THz-STM waveforms on the GaAs(110) surface as a function of the THz pulse peak electric field (Fig. 7.5). The waveforms show a notable variability in their temporal profiles. Most of the tips that were tested did not generate a THz-STM near-field

waveform that was so clearly matched to the incident THz waveform. The OPP-THz-STM waveforms shown in Fig. 7.5 were all capable of sub-nanometer spatial resolution. The tip that had the finest spatial resolution[13] (tip #1), also produced the most-accurate THz pulse near-field with respect to the incident THz pulse (Fig. 7.5a). At large negative $E_{\mathrm{THz,pk}}$ (Fig. 7.5b), the temporal structure of the OPP-THz-STM waveform began to change in a way that indicated the onset of longer carrier lifetimes contributing to the THz-pulse-induced tunnel current. This was confirmed by simulating these temporal distortions with a variable local carrier-decay time-constant, θ, within the framework of a time-dependent Bardeen tunneling model (see section 7.2).

The OPP-THz-STM waveforms that were acquired by tip #2 and tip #3 in Fig. 7.5c–f share many of the same general features as the waveforms acquired by tip #1 in Fig. 7.5a,b; however, their precise temporal structure and spectral bandwidth varied greatly with different tip geometries. This was due to the combination of both spectral modifications to the THz waveform during THz-STM coupling, and the convolution of two electromagnetic pulses in a nonlinear tunnel junction. The OPP-THz-STM waveforms in Fig. 7.5d show a reduction of the smaller half-cycle ($\tau_{\mathrm{THz–Optical}} = -0.9$ ps) at large $E_{\mathrm{THz,pk}}$, similar to Fig. 7.5b. Also, the number of rectified electron per pulse in Fig. 7.5c,d was much larger than the other scans because the tip was about 1 Å closer to the surface due to the higher tunnel current setpoint (300 pA compared to 50 pA). The OPP-THz-STM waveforms in Fig. 7.5e,f are unique because they have a notable difference between the temporal durations of the positive and negative half-cycles. Understanding how these various phenomena shape the OPP-THz-STM waveforms is important for obtaining valuable quantitative information about the local carrier dynamics of the sample, and establishing an efficient coupling geometry between the free-space-propagating THz pulse and the atomically sharp tunnel junction.

[13] Atomic-row resolution on the GaAs(110) surface requires a spatial resolution of $\lesssim 3$ Å, while true atomic resolution (Fig. 7.1) requires a spatial resolution of $\lesssim 1$ Å. This tip achieved the former spatial resolution. See section 7.3 for details.

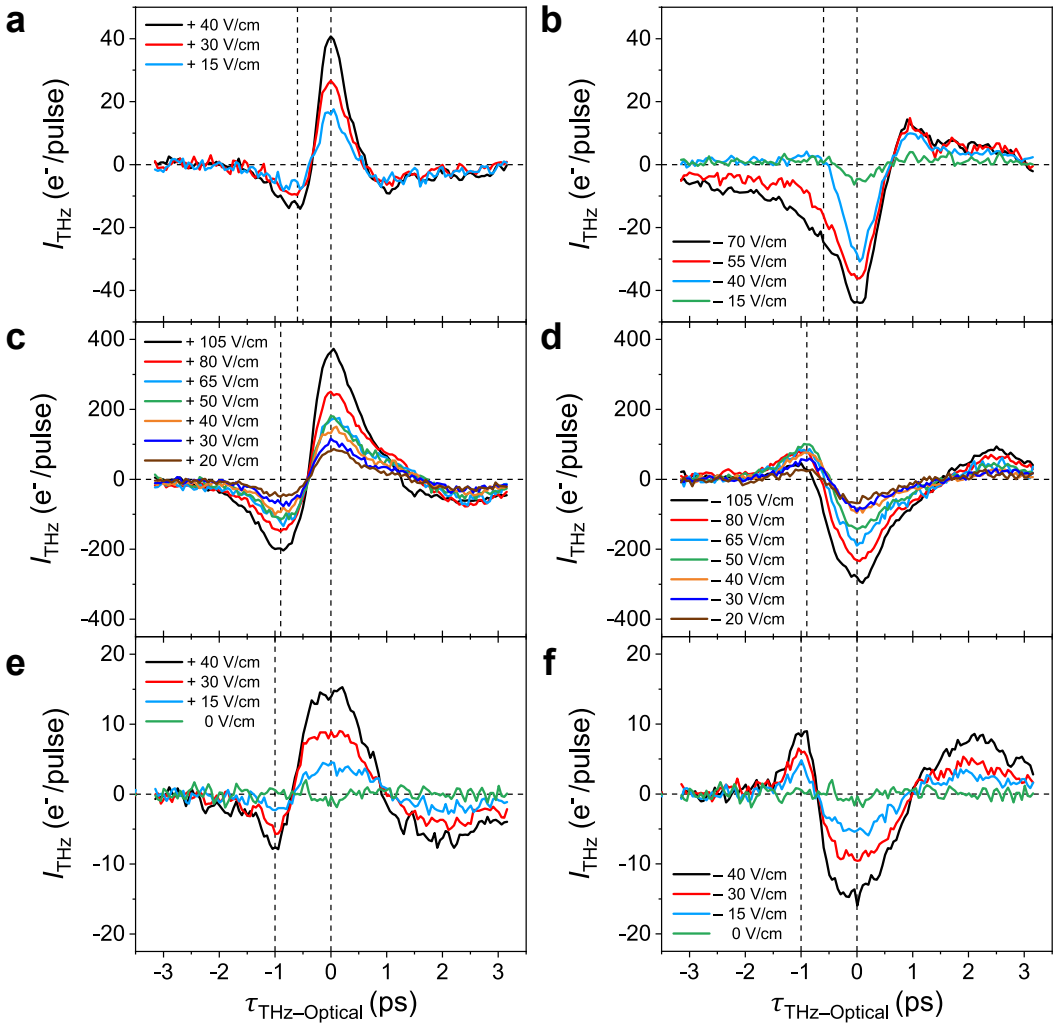

Figure 7.5: Coherent control of photoexcited carriers on the GaAs(110) surface with the THz-STM. All of the waveforms were acquired in constant-current mode at $V_{\text{d.c.}} = +2$ V, and $E_{\text{THz,pk}}$ as shown in the legend. **a**, **b**, OPP-THz-STM waveforms acquired with tip #1 at $I_{\text{d.c.}} + I_{\text{THz,avg}} = +50$ pA and $\varepsilon_{\text{Optical}} = 1$ nJ. **c**, **d**, OPP-THz-STM waveforms acquired with tip #2 at $I_{\text{d.c.}} + I_{\text{THz,avg}} = +300$ pA and $\varepsilon_{\text{Optical}} = 2.6$ nJ. **e**, **f**, OPP-THz-STM waveforms acquired with tip #3 at $I_{\text{d.c.}} + I_{\text{THz,avg}} = +50$ pA and $\varepsilon_{\text{Optical}} = 2.4$ nJ. The vertical dashed lines represent the temporal location of each half-cycle of the THz-pulse-induced tunnel current waveform. The relative position of the larger half-cycle was set to 0 ps for each data set, while the smaller-half cycle occurred at –0.6 ps for **a** and **b**, –0.9 ps for **c** and **d**, and –1 ps for **e** and **f**.

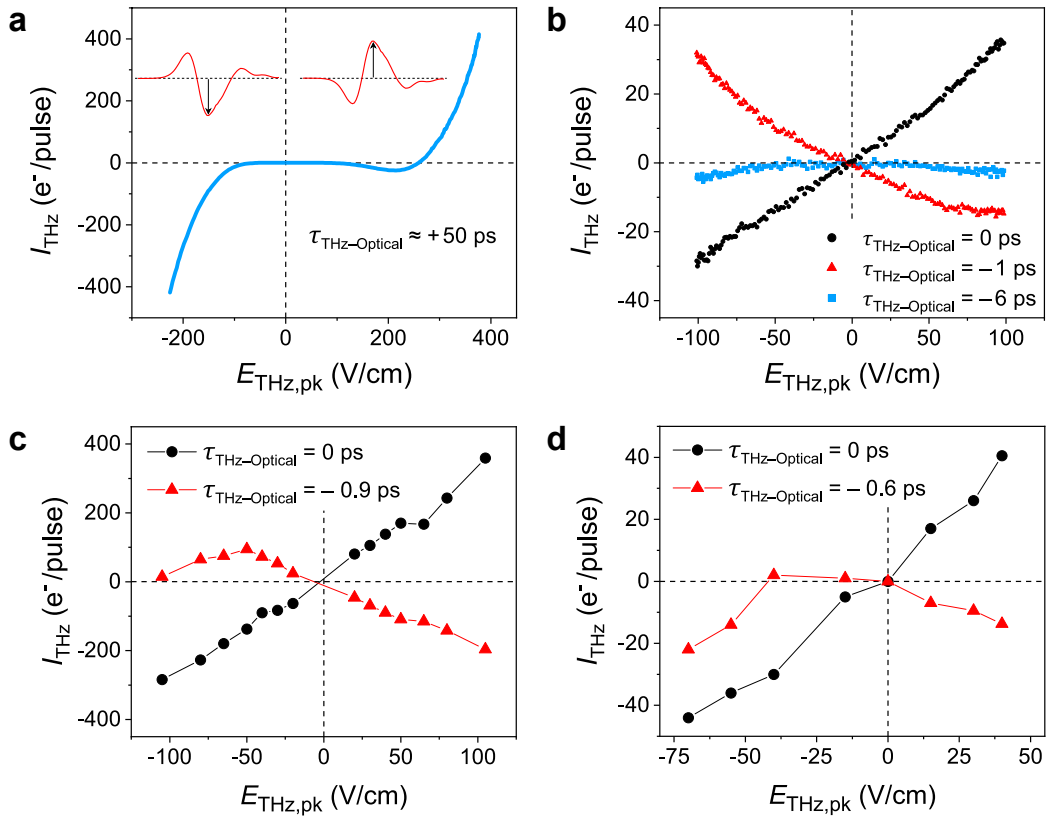

Figure 7.6: Time-resolved THz I–E curves acquired on the GaAs(110) surface. **a**, The measurements were acquired at $V_{\text{d.c.}} = +2$ V, $I_{\text{d.c.}} + I_{\text{THz,avg}} = +200$ pA, $\tau_{\text{THz–Optical}} \approx +50$ ps and $\varepsilon_{\text{Optical}} = 3.6$ nJ. **b**, THz I–E curves acquired using tip #3 with the same settings as Fig. 7.5e,f. **c**, **d**, The data points for **c** and **d** were extrapolated from the OPP-THz-STM waveforms in Fig. 7.5c,d and Fig. 7.5a,b, respectively.

The THz pulse electric field dependence of the rectified tunnel current was explored at various time delays between the optical pulse and the THz pulse ($\tau_{\text{THz–Optical}}$). Four data sets of time-resolved THz I–E curves were acquired using four different THz-STM tips (Fig. 7.6). When the optical pulse and the THz pulse were temporally decoupled (Fig. 7.6a), the THz I–E curve exhibited a similar shape to what was observed for the Si(111)-(7×7) surface (Fig. 6.25). In particular, at positive $E_{\text{THz,pk}}$, the THz-pulse-induced tunnel current, $I_{\text{THz,avg}}$, initially turned negative, before turning positive above $E_{\text{THz,pk}} = +260$ V/cm. Such behavior was routinely observed on n-type semiconductor samples, while a reversed situation was observed on p-type samples, where $I_{\text{THz,avg}}$ would initially become positive at negative $E_{\text{THz,pk}}$, before

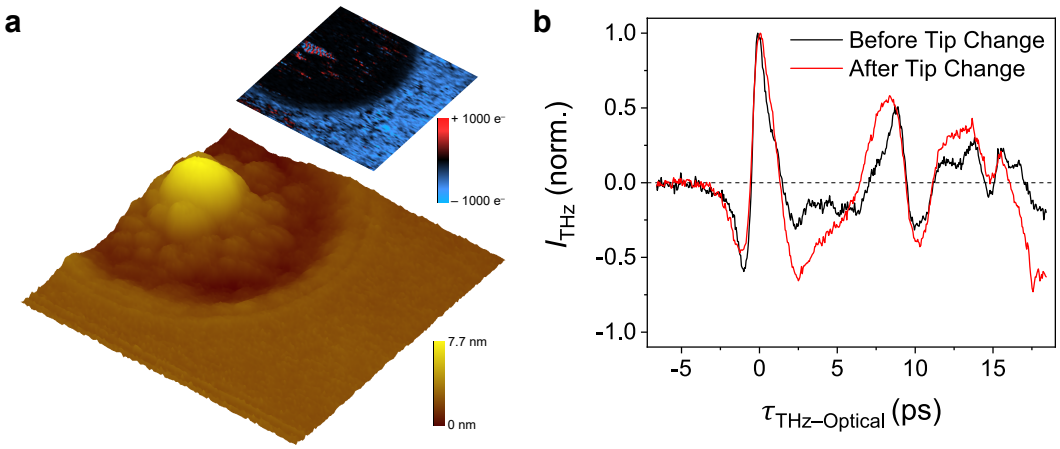

Figure 7.7: The effect of a microscopic tip restructuring on the measured THz-STM near-field waveform. **a**, STM and THz-STM images of the GaAs(110) surface after the tip restructuring event. The images were acquired at $V_{\text{d.c.}} = +2$ V, $I_{\text{d.c.}} + I_{\text{THz,avg}} = +50$ pA, $E_{\text{THz,pk}} = -500$ V/cm, $\varepsilon_{\text{Optical}} = 2.6$ nJ and $\tau_{\text{THz–Optical}} = 0$ ps. Image size 300 nm × 300 nm. **b**, Measured OPP-THz-STM waveforms before and after the tip restructuring event, acquired at $V_{\text{d.c.}} = +2$ V, $I_{\text{d.c.}} + I_{\text{THz,avg}} = +50$ pA, $E_{\text{THz,pk}} = +60$ V/cm and $\varepsilon_{\text{Optical}} = 2.6$ nJ.

turning negative at larger negative $E_{\text{THz,pk}}$. This dependence of the THz I–E curve shape for n-type versus p-type samples was attributed to the significant availability of majority carriers in the sample upon achieving the flat-band condition under forward bias (which occurs at opposite polarities for n-type versus p-type samples). The time-resolved THz I–E curves that were acquired with the optical pulse and THz pulse arriving together (Fig. 7.6b–d), reveal a linear relationship for the larger half-cycle at $\tau_{\text{THz–Optical}} = 0$ ps, and a non-linear relationship for the smaller half-cycle at $\tau_{\text{THz–Optical}} = -1$ ps, -0.9 ps, and -0.6 ps. In order to accurately sample the THz pulse near-field at the tip, both of the THz pulse half-cycles need to be in a linear regime. Clearly, this only occurred at relatively low THz fields, if at all. With $|E_{\text{THz,pk}}| < 50$ V/cm, the system was usually in a nearly-linear regime throughout most of the near-field waveform acquisition. The nonlinearity of the THz I–E curves during the smaller half-cycle (red triangles) was caused by the variability of the local carrier-decay time-constant, θ, as discussed earlier.

The measured THz pulse near-field waveform showed notable temporal distortions after a spontaneous restructuring of the tip apex (Fig. 7.7a). This catastrophic event was caused by the extremely large THz-pulse-induced transient tunnel currents that were being generated just before the event occurred (about 500 electrons per pulse). The STM image in Fig. 7.7a shows a massive crater that is several hundred nanometers across, while the simultaneously acquired THz-STM image shows that the crater does not produce any rectified electrons up to $E_{\mathrm{THz,pk}} = -500$ V/cm. A pair of OPP-THz-STM waveforms were acquired before and after the tip restructuring event (Fig. 7.7b). These

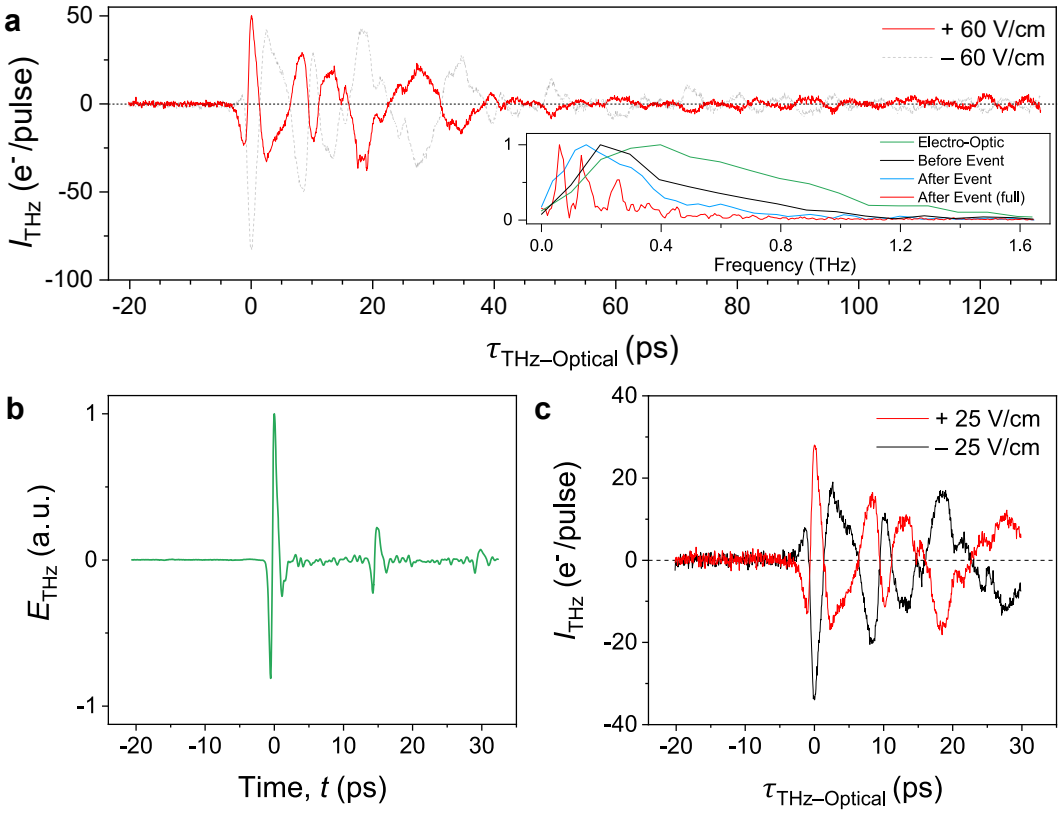

Figure 7.8: Near-field photoconductive sampling of a complex temporal structure. **a**, Measured OPP-THz-STM waveforms acquired at $V_{\mathrm{d.c.}} = +2$ V, $I_{\mathrm{d.c.}} + I_{\mathrm{THz,avg}} = +50$ pA, $E_{\mathrm{THz,pk}} = \pm 60$ V/cm and $\varepsilon_{\mathrm{Optical}} = 2.6$ nJ. Normalized amplitude spectra are shown for the incident THz pulse (green line), before the restructuring event (black line), after the restructuring event (blue line), and the full waveform in **a** (red line). The amplitude spectrum for the full waveform had notable peaks at 60 GHz, 125 GHz and 260 GHz. **b**, Electro-optically sampled THz pulse electric field waveform. **c**, Measured OPP-THz-STM waveforms with the same settings as **a** except with $E_{\mathrm{THz,pk}} = \pm 25$ V/cm.

measurements were acquired with the same tip that acquired the OPP-THz-STM waveforms in Fig. 7.5c,d (tip #2). After the tip change, two extremely long waveforms were acquired in order to assess the new temporal structure of the near-field (Fig. 7.8a). Several amplitude spectra are shown in the inset of Fig. 7.8a for the following waveforms: the incident THz pulse (Fig. 7.8b), the OPP-THz-STM waveform before the tip change, and the OPP-THz-STM waveform after the tip change, with and without the post-pulse reflections included. These temporal and spectral distortions were attributed to the significant nano-scale structural modification that occurred to the tip apex in-between the measurements. The incident THz pulse (Fig. 7.8b) did not show any significant oscillations after the main pulse until $t = +15$ ps[14].

The distortions of the THz-pulse-induced tunnel current waveform were attributed to reflections of THz-SPPs travelling along the surface of the metal. These reflections have been routinely observed near sharp edges and corners in 3D electromagnetic simulations of THz pulse coupling to the STM tip. Several of our THz-STM tips had sharp concentric edges (Fig. 5.7) that could have easily produced several THz pulse echoes in the THz-STM near-field waveform. For the average tip shape that was used, the THz-SPPs travelled along the surface of the tip for 100–1000 µm before reflecting off of a naturally occurring sharp edge that was formed by the etching process. For THz-SPPs travelling at $0.99\,c$[15] [165, 167], a single reflection from the apex and back can take anywhere between 0.7–7 ps, consistent with the observations. To verify that the observed THz pulse reflections were indeed real, the THz pulse electric field magnitude was reduced until the OPP-THz-STM waveforms at both polarities were nearly identical inverted copies of each other (Fig. 7.8c). This ensured that the measured near-field waveform was not distorted by the nonlinearity of the tunnel junction.

[14]The THz pulse echoes in Fig. 7.8b at $t \approx +15$ ps and $t \approx +30$ ps occurred inside the GaAs crystal of the THz pulse source. This was confirmed by EOS sampling with a 2 mm thick ZnTe crystal, where the THz pulse reflection occurred at $t \approx +44$ ps.

[15]This value is a rough estimate because the phase and group velocities of THz-SPPs depend on the diameter of the metallic wire [167], which changes continuously for an atomically sharp metal tip.

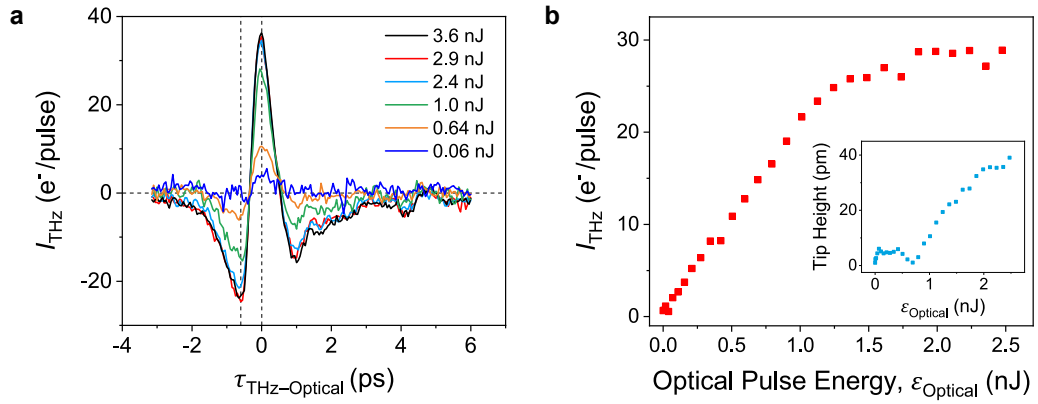

Figure 7.9: **a**, Incident optical pulse energy, $\varepsilon_{\text{Optical}}$, dependence of OPP-THz-STM waveforms on GaAs(110) using tip #1 at $V_{\text{d.c.}} = +2$ V, $I_{\text{d.c.}} + I_{\text{THz,avg}} = +50$ pA and $E_{\text{THz,pk}} = +105$ V/cm. A vertical dashed line is shown at $\tau_{\text{THz–Optical}} = -0.6$ ps and $\tau_{\text{THz–Optical}} = 0$ ps. **b**, A single scan was acquired at $\tau_{\text{THz–Optical}} = 0$ ps with the same settings as **a**. The inset shows the relative tip height throughout the acquisition; a steady 0.5 pm/s background drift towards the sample was subtracted from the measurement.

The effect of the optical pulse energy on the THz-pulse-induced tunnel current was evaluated using OPP-THz-STM waveforms (Fig. 7.9a), and a single high-resolution scan acquired at $\tau_{\text{THz–Optical}} = 0$ ps (Fig. 7.9b). The linear behaviour that was observed for optical pulse energies below 1.2 nJ was a result of the photoexcited carrier density increasing linearly with the number of photons in the pulse. This occurred because only one photon was required to produce a single electron–hole pair, and the number of photons in the pulse scaled linearly with the pulse energy, $\varepsilon_{\text{Optical}}$. For energies above 1.2 nJ, the THz-pulse-induced tunnel current began to saturate for all values of $\tau_{\text{THz–Optical}}$ (Fig. 7.9a). This saturation effect was most likely caused by the steadily increasing tip–sample distance throughout the acquisition due to optical-pulse-induced thermal expansion. An average optical power of 1 mW (4 nJ per pulse at 250 kHz) is right at the threshold for the onset of picometer-scale thermal effects in the STM (approximately 20 pm/mW) [140, 142]. Accordingly, a steadily increasing average optical power eventually caused the tip–sample distance to start expanding (inset of Fig. 7.9b), which reduced the magnitude of the THz-pulse-induced tunnel current. Another possibility to consider is

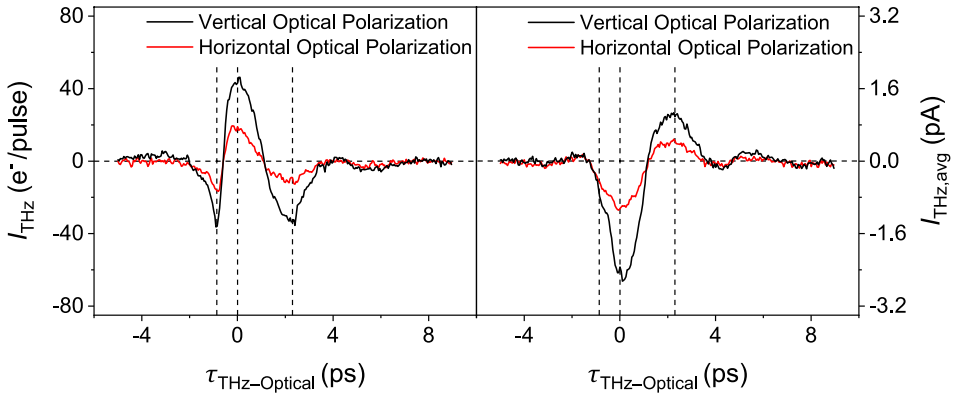

Figure 7.10: Optical pulse polarization dependence of OPP-THz-STM waveforms on GaAs(110). The measurements were acquired with tip #3 at $V_{\text{d.c.}} = +2$ V, $I_{\text{d.c.}} + I_{\text{THz,avg}} = +50$ pA, $E_{\text{THz,pk}} = \pm 105$ V/cm and $\varepsilon_{\text{Optical}} = 0.64$ nJ. The vertical dashed lines are centered at $\tau_{\text{THz–Optical}} = -0.85$ ps, $\tau_{\text{THz–Optical}} = 0$ ps, and $\tau_{\text{THz–Optical}} = +2.3$ ps.

that the observed saturation above 1.2 nJ may be due to the saturation of the SPV (Fig. 7.2), which occurs at relatively low optical intensities [111, 115, 387, 388]. The SPV determines the number of minor carriers localized underneath the tip, awaiting annihilation by the tunnel current. Under saturation, adding more electron–hole pairs with higher optical pulse intensities does not create a larger population of minority carriers underneath the tip apex because the tip-induced field is effectively screened by the SPV.

The optical pulse polarization was set perpendicular to the tip axis for all of the measurements in order minimize any coupling of the optical pulse to the tunnel junction. The purpose of the optical pulse was to simply generate a transient population of free carriers in the GaAs sample. Nevertheless, the effect of the optical pulse polarization on the THz-pulse-induced rectified tunnel current was investigated by a set of OPP-THz-STM waveforms that were acquired at both THz polarities (Fig. 7.10). The number of rectified electrons per pulse increased significantly upon a 90° rotation of the optical pulse polarization. This was primarily attributed to an increased electric field enhancement for optical pulses polarized along the tip axis [44, 279], which directly increased the number of photons near the tunnel junction. However, the increased amplitude of the THz-pulse-induced tunnel current waveform

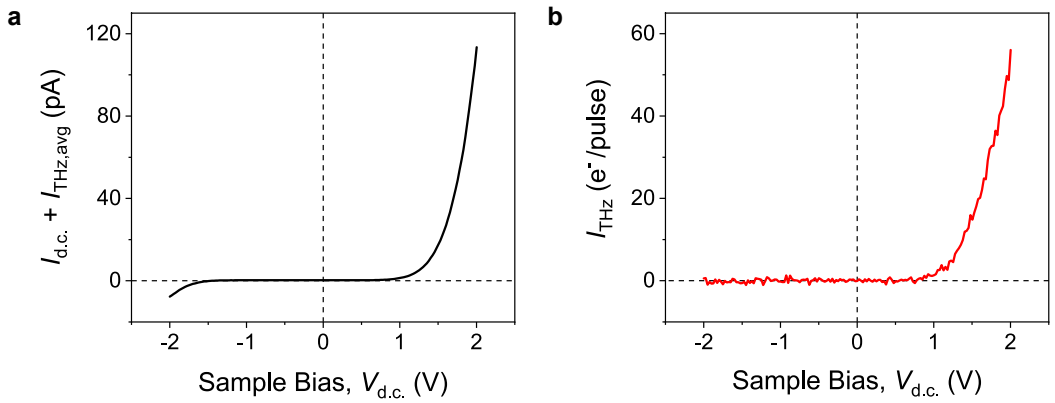

Figure 7.11: Constant-tip-height d.c. bias voltage dependence of THz-STM on GaAs(110). **a**, Current–voltage characteristic (I–V) acquired with the feedback loop disengaged at $V_{\text{d.c.}} = +2$ V, $I_{\text{d.c.}} + I_{\text{THz,avg}} = +110$ pA, $E_{\text{THz,pk}} = +50$ V/cm, $\varepsilon_{\text{Optical}} = 2.6$ nJ and $\tau_{\text{THz–Optical}} = 0$ ps. **b**, The simultaneously acquired rectified electrons per THz pulse. $I_{\text{THz,avg}}$ only contributes about 2% of the total measured current at $V_{\text{d.c.}} = +2$ V.

was also influenced by a difference in the absorption for vertically and horizontally polarized optical pulses. Specifically, 800 nm wavelength horizontally polarized light incident on the sample at an angle of 35° with respect to the surface has a 52.5% reflectance; however, the same vertically polarized light has a 13.6% reflectance [390]. Accordingly, the THz-pulse-induced tunnel current was amplified for vertically polarized optical pulses due to both the increased optical field enhancement, and increased transmission into the sample. Future experiments may take advantage of the increased field enhancement for vertically polarized optical pulses by reducing the incident energy $\varepsilon_{\text{Optical}}$, and still observing a time-dependent THz-pulse-induced tunnel current.

The d.c. bias dependence of the optically-enhanced THz-pulse-induced tunnel current was investigated using an I–V curve with THz pulse and optical pulse incident onto the tip at $\tau_{\text{THz–Optical}} = 0$ ps (Fig. 7.11). The steady-state current–voltage characteristic (Fig. 7.11a) and the THz-pulse-induced tunnel current (Fig. 7.11b) both followed a similar curvature. A positive d.c. bias voltage enhanced the THz-pulse-induced tunnel current because the steady-state bias helped accumulate holes underneath the tip apex, which then the THz pulse could coherently control. As the d.c. bias voltage was reduced to

zero, the THz pulse penetration depth around the tip also decreased due to the reduced steady-state band bending and increased majority carrier concentration near the surface. As a result, this reduced the amount of photoexcited holes that could be accelerated towards the tunnel junction[16]. The absence of a THz-pulse-induced tunnel current at negative bias voltages was attributed to electric field screening of the photoexcited carriers by the large availability of majority carriers upon achieving the flat-band-condition ($V_{\mathrm{d.c.}} \approx -0.2$ V). In other words, without the presence of a subsurface depletion layer at negative d.c. bias, conduction band electrons accumulated near the surface and screened photoexcited electron–hole pairs in the bulk. This reduced the transient SPV underneath the tip and maintained a small THz-pulse-induced tunnel current.

7.2 Modeling Pump-Probe THz-STM

The Bardeen tunneling model including image potential effects that was developed in chapter 6 was further expanded upon to account for the transient photoconductivity due to the optical pulse. The transient carrier density was a free parameter within the model that was approximated as a Gaussian centered at the sample Fermi level ($\varepsilon_{\mathrm{c}} = 0$ eV). In reality, several dynamic processes determined the temporal evolution of the free carrier energy distribution after photoexciation [391, 392]. The time-resolved tunneling simulations performed here were not intended to accurately model the evolution of the free carrier energy distribution, but rather show that the observed temporal distortions in Fig. 7.5a,b were caused by a variability in the decay constant, θ. The time and energy dependence of the photoexcited free carriers was incorporated into the tunneling model as a transient carrier density, $n(\varepsilon, t)$, which was composed of the steady-state LDOS of the sample, $\rho_{\mathrm{s}}(\varepsilon)$ and the transient optical-pulse-induced term, $n(\varepsilon, t) - \rho_{\mathrm{s}}(\varepsilon)$. The energy dependence of this latter term was modeled to a first approximation as a Gaussian with a

[16]Nevertheless, with the tip and sample in gentle contact, and at very high optical pulse energies, a THz-pulse-driven tunnel current was still observed (Fig. 7.4b).

full-width-half-maximum of $2.35\,\sigma$ and an amplitude of A_0, centered at ε_c with respect to the Fermi level of the sample. The full expression for the transient carrier density is given by

$$n(\varepsilon,t) \;=\; \rho_\mathrm{s}(\varepsilon) + A_0\,\exp\!\left(-\frac{t}{\theta}\right)\cdot\exp\!\left(-\frac{(\varepsilon-\varepsilon_\mathrm{c})^2}{2\,\sigma^2}\right)\cdot\;\frac{1}{2}\left[\mathrm{erf}\!\left(\frac{t}{\gamma_\mathrm{rt}}\right)+1\right], \quad (7.1)$$

where θ is the temporal decay constant, σ is the standard deviation of the energy distribution and γ_rt a parameter that sets the risetime of the transient carrier density. This equation was evaluated at $t-\tau$, where t represents the time axis of the THz pulse, and $\tau = \tau_\mathrm{THz–Optical}$, represents the time delay of the THz pulse with respect to the optical pulse. The energy dependence was integrated to give the instantaneous THz-pulse-induced tunnel current

$$\begin{aligned} I_\mathrm{THz}(t,\tau) = \frac{\pm 1}{\Sigma_0}\int_0^{e|V_\mathrm{d.c.}+V_\mathrm{THz}(t)|} & n(\varepsilon,t-\tau)\,T(\phi_\mathrm{t},\phi_\mathrm{s},\varepsilon,V_\mathrm{d.c.}+V_\mathrm{THz}(t),z)\,\mathrm{d}\varepsilon ... \\ ... \mp \frac{1}{\Sigma_0}\int_0^{e|V_\mathrm{d.c.}|} & n(\varepsilon,t-\tau)\,T(\phi_\mathrm{t},\phi_\mathrm{s},\varepsilon,V_\mathrm{d.c.},z)\,\mathrm{d}\varepsilon\,, \end{aligned} \quad (7.2)$$

where the tip density of states, $\rho_\mathrm{t}(\varepsilon)$, has been set to unity, $T(\phi_\mathrm{t},\phi_\mathrm{s},\varepsilon,V,z)$ is given by Eq. 6.4 and Σ_0 is a scaling factor that was set by the operating current setpoint (I_0) and voltage setpoint (V_0) during the THz-STM measurement, as given by

$$\Sigma_0 = \frac{1}{|I_0|}\int_0^{e|V_0|}\rho_\mathrm{s}(\varepsilon)\,T(\phi_\mathrm{t},\phi_\mathrm{s},\varepsilon,V_0,z)\,\mathrm{d}\varepsilon\,. \quad (7.3)$$

Finally, the instantaneous THz-pulse-induced current was integrated with respect to t, and multiplied by the repetition rate, f_rep, to get the simulated THz-pulse-induced tunnel current waveform,

$$I_\mathrm{THz}(\tau) = f_\mathrm{rep}\int_{-\infty}^{+\infty} I_\mathrm{THz}(t,\tau)\,\mathrm{d}t\,. \quad (7.4)$$

The following list summarizes the assumptions that were made when calculating $I_\mathrm{THz}(\tau)$ from $E_\mathrm{THz}(t)$ and $n(\varepsilon,t-\tau)$ with the time-resolved Bardeen tunneling model. From the previous list of assumptions in section 6.2, items 1–6, 8, 9 and 11 all apply, including the following:

1. Electrons in the GaAs bulk respond to the THz field and form an image potential. Screening occurs on a timescale comparable to the inverse plasma frequency, approximately 60 fs in heavily doped GaAs [339, 393].

2. The local density of states of the tip, $\rho_t(\varepsilon)$, and sample, $\rho_s(\varepsilon)$, were both set to unity.

3. θ decays much faster than the time between successive laser pulses ($\theta \lll 1/f_{rep}$). This implies that the transient carrier density had a negligible effect on the average d.c. current.

4. The transient carrier density, $n(\varepsilon, t)$, was dimensionless due to the renormalization factor, Σ_0 (Eq. 7.3).

5. The transient SPV, $V_{SPV}(t-\tau)$, was not considered within the time-resolved tunneling simulation. This is because the transient SPV is a non-equilibrium effect at the semiconductor surface that cannot be modeled by simply inserting $V_{SPV}(t-\tau)$ into Eq. 7.2, along with $V_{d.c.}$ and $V_{THz}(t)$. The transient SPV is taken into account by the parameters θ and A_0 of the transient carrier density in Eq. 7.1. For a complete analysis, a new model is required that takes into account the non-equilibrium and non-Markovian nature of this problem [359].

6. The value of A_0 in Eq. 7.1 had two roles. First, it accounted for the increased local density of free carriers after photoexcitation (10^{18}–10^{19} cm^{-3} for semi-insulating GaAs [339, 391, 392], and 6×10^{20} cm^{-3} for heavily doped GaAs [373]). Second, the amplitude coefficient, A_0, accounted for an increased tunnel current due to the ultrafast non-equilibrium charging dynamics of photoexcited carriers in the GaAs subsurface (Fig. 7.15). This THz-pulse-induced charging also strongly modulated the transient SPV, $V_{SPV}(t-\tau, I_{THz})$. The THz pulse electric field penetrated deeper into the bulk than the steady-state field (Fig. 6.33), inducing ultrafast band bending of the subsurface potential, and enabling a large instantaneous THz-pulse-induced tunnel current to flow.

The time-dependent Bardeen tunneling model was used to simulate a set of measured OPP-THz-STM waveforms (Fig. 7.12a–c). Within the model, the only parameters that were capable of radically broadening the temporal profile

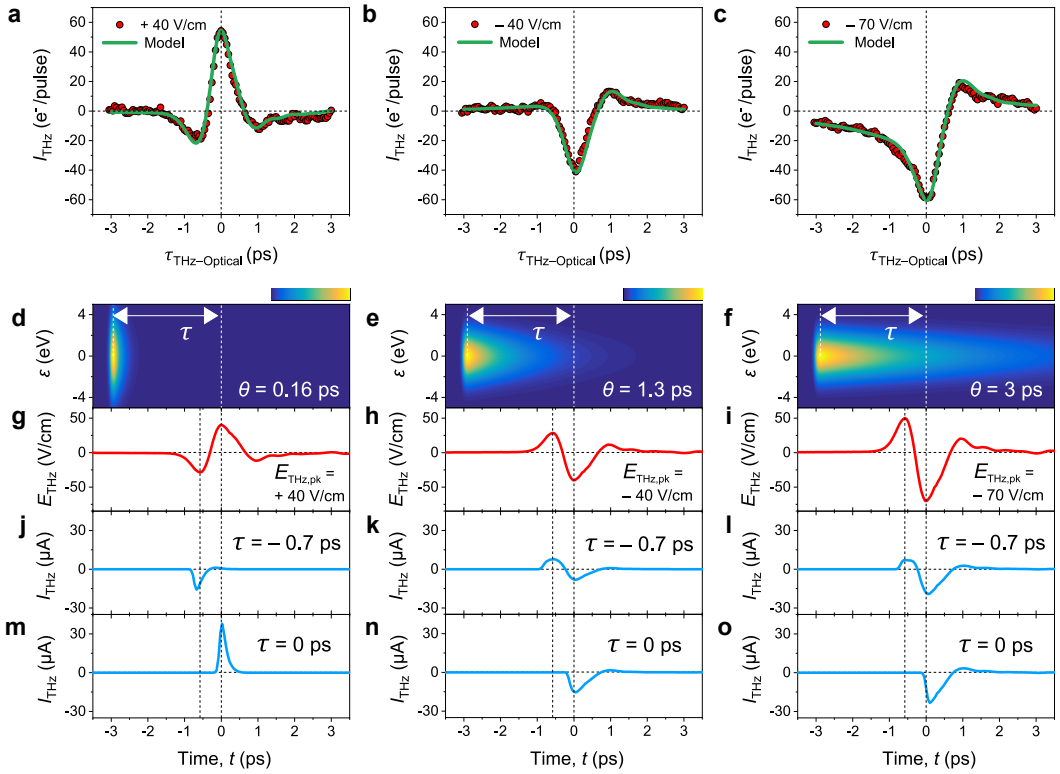

Figure 7.12: Modeling time-resolved THz-STM on GaAs(110) in the extreme tunnel current regime. **a**–**c**, Experimental (red circles) and simulated (green solid lines) OPP-THz-STM waveforms at three different $E_{\mathrm{THz,pk}}$. The experimental waveforms are from the data set in Fig. 7.5a,b, where they were acquired at $V_{\mathrm{d.c.}} = +2$ V, $I_{\mathrm{d.c.}} + I_{\mathrm{THz,avg}} = +50$ pA and $\varepsilon_{\mathrm{Optical}} = 1$ nJ. **d**–**f**, The optically-induced transient carrier density, $n(\varepsilon, t)$, of the local GaAs(110) surface for carrier-decay time-constants of 0.16 ps (**d**), 1.3 ps (**e**) and 3 ps (**f**), where τ is the relative time delay of the optically-induced transient carrier density with respect to the THz pulse. **g**–**i**, The THz pulse waveform incident onto the tip as measured by free-space electro-optic sampling. **j**–**o**, The simulated instantaneous THz-pulse-induced tunnel current, $I_{\mathrm{THz}}(t, \tau)$, generated by the THz voltage transient, $V_{\mathrm{THz}}(t)$, at time delays of $\tau = -0.7$ ps for **j**–**l** and $\tau = 0$ ps for **m**–**o**. The simulated OPP-THz-STM waveforms, $N_{\mathrm{e^-}}(\tau) = e^{-1} \times \int_{-\infty}^{+\infty} I_{\mathrm{THz}}(t, \tau)\, \mathrm{d}t$, were acquired with similar parameters as in section 6.2: barrier-height $\phi_{\mathrm{t}} = \phi_{\mathrm{s}} = 4.9 \pm 0.5$ eV, tip–sample separation $z = 0.8 \pm 0.2$ nm, THz pulse field enhancement $F = 275{,}000 \pm 25{,}000$, and the time-dependent carrier densities in **d**–**f**, which were calculated using Eq. 7.1, with $\rho_{\mathrm{s}}(\varepsilon) = 1$, $\varepsilon_{\mathrm{c}} = 0$ eV, $\gamma_{\mathrm{rt}} = 70$ fs, $\sigma = 1.8 \pm 0.3$ eV, and $A_0 = 10^6 \pm 10^5$.

of the simulated OPP-THz-STM waveforms were the carrier lifetime, θ, and the rise-time parameter, γ_{rt}. This last parameter was set to 70 fs, corresponding to the minimum temporal width of our ultrafast optical pulses. A global fit was not performed to several measurements simultaneously, as was done in section 6.2; instead, the results of the global fit in section 6.2 were used as a guide for determining the free parameters in the simulation (Fig. 7.12). The four unrestricted parameters within the tunneling model were barrier-height $\phi_{\mathrm{t}} = \phi_{\mathrm{s}} = 4.9 \pm 0.5$ eV, tip–sample separation $z = 0.8 \pm 0.2$ nm, THz pulse field enhancement $F = 275{,}000 \pm 25{,}000$ and the transient carrier density $n(\varepsilon, t)$. The transient carrier density (Fig. 7.12d–f) was modeled using the parameters: $\rho_{\mathrm{s}}(\varepsilon) = 1$, $\varepsilon_{\mathrm{c}} = 0$ eV, $\gamma_{\mathrm{rt}} = 70$ fs, $\sigma = 1.8 \pm 0.3$ eV, $A_0 = 10^6 \pm 10^5$ and $\theta = 0.16$ ps, 1.3 ps, 3.0 ps for $E_{\mathrm{THz,pk}} = +40$ V/cm, -40 V/cm, -70 V/cm, respectively. The incident THz pulse waveform (Fig. 7.12g–i) was measured using electro-optic sampling and multiplied by the THz pulse field enhancement factor, F, and tip–sample separation, z, in order to obtain the simulated THz-pulse-induced voltage transient at the tunnel junction, $V_{\mathrm{THz}}(t)$. A value of $V_{\mathrm{THz,pk}} = 0.9$–$1.5$ V was simulated for an incident field of $E_{\mathrm{THz,pk}} =$ 40–70 V/cm. The simulated instantaneous THz-pulse-induced tunnel current, $I_{\mathrm{THz}}(t, \tau)$, is shown for $\tau = -0.7$ ps in Fig. 7.12j–l, and $\tau = 0$ ps in Fig. 7.12m–o. The subsurface GaAs decay constant, θ, was found to increase from 0.16 ps at $E_{\mathrm{THz,pk}} = +40$ V/cm, to 1.3 ps at $E_{\mathrm{THz,pk}} = -40$ V/cm, and finally to 3.0 ps at $E_{\mathrm{THz,pk}} = -70$ V/cm. The increase in θ that occurred for increasingly negative $E_{\mathrm{THz,pk}}$ may have been caused by different trapping times for carriers coming from deep within the bulk, or alternatively, non-equilibrium effects that modified the physical significance of θ, as described earlier. It is not clear why a larger θ was only required for increasingly more negative $E_{\mathrm{THz,pk}}$, and not positive $E_{\mathrm{THz,pk}}$ as well. One possible explanation for this asymmetry may have to do with the large difference in the carrier mobility between electrons and holes in doped GaAs[17]. The positive THz pulse half-cycle depended on the field-assisted diffusion of low-mobility holes towards the tunnel junction,

[17] $\mu_{\mathrm{e}} \sim 2500$ cm^2/(V·s) and $\mu_{\mathrm{h}} \sim 150$ cm^2/(V·s) [264]

while the negative THz pulse half-cycle accelerated high-mobility electrons from deep within the bulk. These electrons could have reached the tunnel junction from a position within the bulk where holes would not have been able to make it from (assuming equal and opposite driving fields). This may also explain why the THz-pulse-induced tunnel current is strictly negative at very high THz electric fields (Fig. 7.4b and Fig. 7.7a).

7.3 Imaging Ultrafast Carrier Dynamics

Time-resolved THz-STM imaging the GaAs(110) surface revealed a unique spatio-temporal dependence for the THz-pulse-induced tunnel current near charged surface defects. Two independent OPP-THz-STM waveforms were acquired at nearby locations to reveal a time-dependent THz-pulse-induced tunnel current that very accurately reassembled the temporal profile of the incident THz pulse (Fig. 7.13a). The dark brown surface defects in the STM topography images (Fig. 7.13b) were identified as single gallium atom vacancies (V^{-}_{Ga}) on the surface of the sample. Single gallium vacancies are extremely common negatively charged surface defects on heavily doped n-type GaAs(110)[18]. They lie within the fundamental band gap of GaAs and create an upward band bending near the defect. This band bending locally reduced the tunnel current at positive bias voltages, which caused the single-atom-defect to be imaged as a relatively large topographic depression [227, 377, 379, 382, 386, 387]. The size of this depression was comparable to the screening length of a single gallium vacancy, approximately 15 Å [377]. One of the four surface defects in Fig. 7.13 was unique because it had a small protrusion located right beside it. This particular defect is located in the middle-top-right portion of the image, and it is another very common defect on the GaAs(110) surface known as silicon–vacancy complex, Si^{+}_{Ga}–V^{-}_{Ga} [227, 379]. A silicon–vacancy complex is the combination of a silicon atom that has replaced a gallium

[18]Spatially-resolved surface photovoltage images of V^{-}_{Ga} defects on GaAs(110) have suggested the presence of a charge state as high as $-3e$ [387]. Note: arsenic surface vacancies (V^{+}_{As}) are not energetically favorable on heavily-doped n-type GaAs(110). Instead, they occur readily on heavily-doped p-type samples [376, 377].

atom, coupled to a next-nearest-neighbour gallium vacancy. Either of these two individual defects can be right at surface or one layer below the surface, giving rise to four unique arrangements [227]. The silicon–vacancy complex often produces an asymmetric structure in the STM image due to its weak dipole [379]. The third type of surface feature that was readily observed in the STM topography images was a small bright yellow protrusion. This fea-

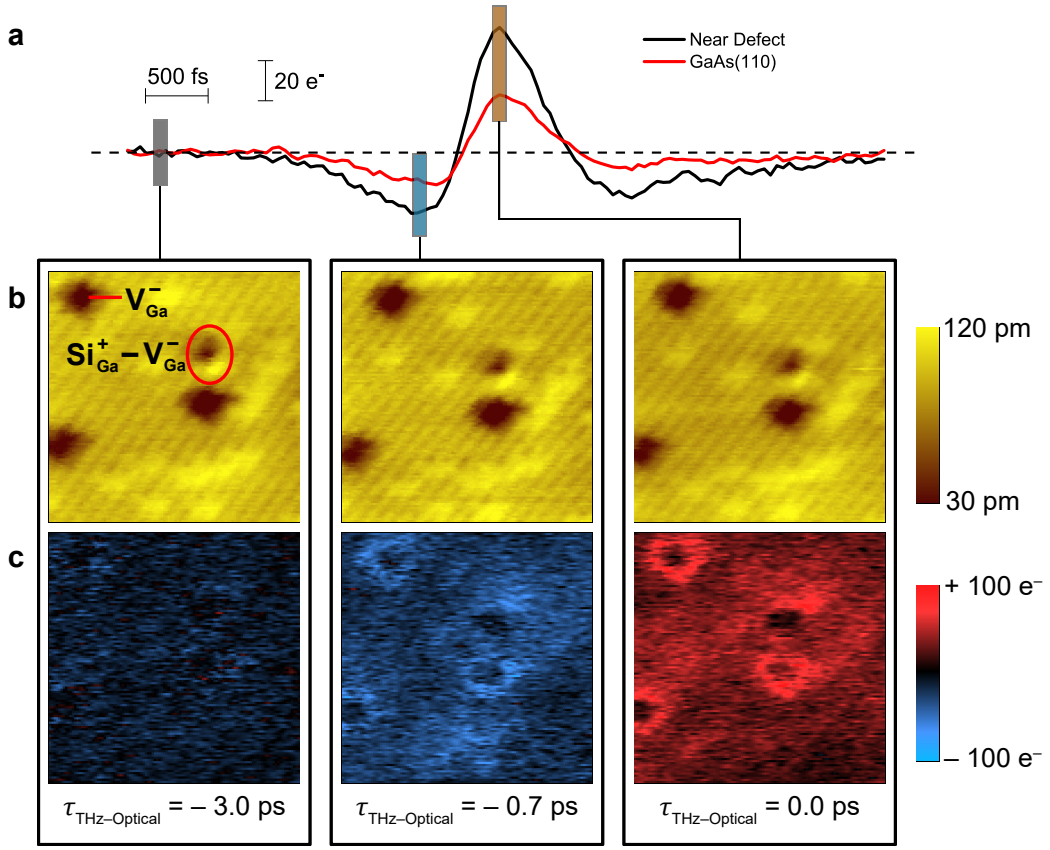

Figure 7.13: Ultrafast THz-STM imaging of gallium vacancies on the silicon-doped GaAs(110) surface. **a**, Measured optical pump – THz-STM probe time delay scan acquired at $V_{\mathrm{d.c.}} = +2$ V, $I_{\mathrm{d.c.}} + I_{\mathrm{THz,avg}} = +50$ pA, $E_{\mathrm{THz,pk}} = +40$ V/cm and $\varepsilon_{\mathrm{Optical}} = 1$ nJ at two different locations on the surface. **b**, Atomic-row-resolved STM constant-current topographic images of the GaAs(110) surface acquired at $V_{\mathrm{d.c.}} = +1.5$ V, $I_{\mathrm{d.c.}} + I_{\mathrm{THz,avg}} = +75$ pA, $E_{\mathrm{THz,pk}} = +70$ V/cm and $\varepsilon_{\mathrm{Optical}} = 1$ nJ, at three different time delays, $\tau_{\mathrm{THz–Optical}}$. **c**, Rectified THz-pulse-induced tunnel current images, $N_{\mathrm{e^-}}(x, y)$, acquired simultaneously with the corresponding topography images in **b**. All topographic data has been plane-fit-subtracted to account for the piezo thermal drift throughout the scan. Image size 10 nm × 10 nm; scan speed 21 nm/s.

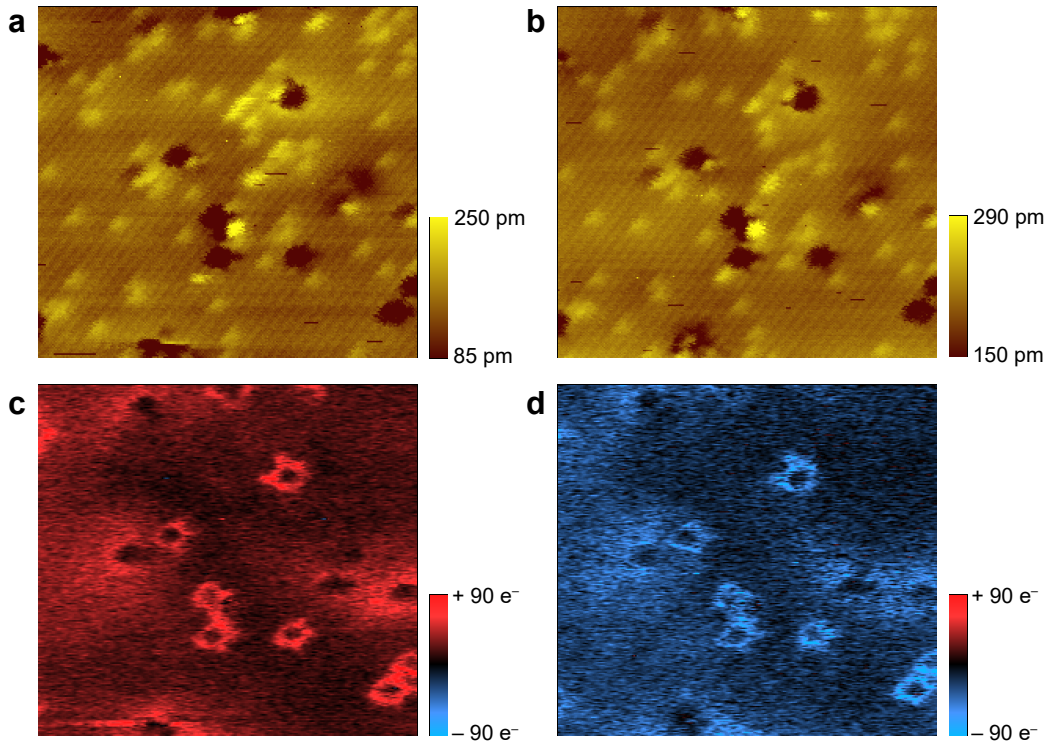

Figure 7.14: Ultrafast defect-enhanced carrier trapping for two types of surface defects. **a**, **b**, STM images and **c**, **d**, ultrafast THz-STM images of the photoexcited GaAs(110) surface at time delays of $\tau_{\text{THz–Optical}} = 0$ ps (**a**, **c**) and $\tau_{\text{THz–Optical}} = -0.7$ ps (**b**, **d**). The images were acquired at $V_{\text{d.c.}} = +1.5$ V, $I_{\text{d.c.}} + I_{\text{THz,avg}} = +75$ pA, $\varepsilon_{\text{Optical}} = 1$ nJ and $E_{\text{THz,pk}} = +60$ V/cm. Image size 19 nm × 19 nm; scan speed 20 nm/s.

ture represented the location of a subsurface silicon donor ($\text{Si}^{+}_{\text{Ga}}$), with shallow donors exhibiting a larger protrusion [383].

The ultrafast THz-STM images were acquired simultaneously with each corresponding STM topography image at three different time delays, $\tau_{\text{THz–Optical}}$ (Fig. 7.13c). If the optical pulse arrived 3 ps before the THz pulse, the THz-STM image showed indiscernible features. At time delays where the optical pulse arrived during either half-cycle of the THz pulse, the THz-STM images showed well-defined rings of an enhanced THz-pulse-induced tunnel current around the edges of gallium vacancies, and an asymmetric feature for the silicon–vacancy complex. Meanwhile, the accumulation of several subsurface silicon donors at the bottom of the image set provided a small localized enhancement of $N_{\text{e}^-}(x, y)$ at $\tau_{\text{THz–Optical}} = -0.7$ ps, which did not occur at

$\tau_{\text{THz–Optical}} = 0$ ps (Fig. 7.13c). Another set of STM (Fig. 7.14a,b) and THz-STM (Fig. 7.14c,d) images reveal that the isolated silicon–donor complexes produce a spatially broader crater-like enhancement compared to the gallium vacancies. In addition to this, they have a pronounced asymmetry due to their local dipole [379]. The observation of this asymmetry in the THz-STM images confirmed that THz-pulse-induced tunnel current was strongly modulated by the local charge state of the sample surface. For nearly all of the defects that were imaged, the THz-pulse-induced tunnel current was strongly suppressed in a 5–15 Å diameter circle that was positioned at the topographic center of any individual defect. In fact, the center of the defects typically had a smaller THz-pulse-induced tunnel current than the surrounding GaAs(110) surface.

A very similar crater-like spatial modulation of the SPV has been reported by an STM study of negatively charged oxygen atoms adsorbed on a GaAs(110) surface [386]. The spatial width of the area and the amount of SPV suppression within the central region of the oxygen adsorbate was found to be strongly dependent on the sample doping, and weakly dependent on the applied bias voltage. Also, for the heavily-doped sample (2×10^{18} cm^{-3}), the SPV inside the central region of the oxygen adsorbate was lower than the surrounding clean GaAs(110) surface. In the experiments described by [386], if the tip was positioned near a charged defect, but not close enough to alter its physical properties, the SPV was enhanced by the local upward band bending of the negatively charged surface defect. Similarly, a positively charged surface defect enhanced the SPV for the opposite polarity.

The observed reduction in the THz-pulse-induced tunnel current directly above charged surface defects was attributed to three possible effects. First, a local suppression of the SPV may have occurred when the tip was positioned within a Debye-screening-length distance of the charged defect, due to a Coulombic modification of its local density of states [386]. This gave rise to an effective increase in the local band-gap, which then suppressed the SPV. Second, the strong Coulombic potential may have also modified the ability of the defect

to accommodate electrons with particular momenta [353], decreasing the local SPV [386]. Third, the ultrafast THz-pulse-induced tunnel current maybe have locally charged the defect, which is known to cause spatial variations in the SPV, and in some cases completely invert it [385]. Previous reports have demonstrated that the reduced SPV directly above the defect was unlikely to have been caused by a lateral variation of the recombination rate, or local Fermi level pinning by the defect [384, 386].

The THz-pulse-induced tunnel current was locally enhanced near negatively charged surface defects because they were able to support a large population of photoexcited holes (SPV) that could be efficiently resupplied from the bulk due the local band bending induced by the defect. A single gallium defect supported a maximum local SPV that was significantly higher than the maximum SPV of the clean GaAs(110) surface (approximately 1.5 V, compared to 0.65 V at $V_{\text{d.c.}} = +2$ V [387]; see also Fig. 7.2). At low THz fields where $V_{\text{THz,pk}} \sim V_{\text{SPV,pk}}$, the THz-pulse-induced tunnel current was enhanced by the increased local carrier density and resulting transient SPV, $V_{\text{SPV}}(t-\tau)$ (Fig. 7.15a,b). If the optical pulse arrived during the positive THz pulse half-cycle (Fig. 7.15a), there was a sufficient population of photoexcited holes at the surface to supply all of the necessary carriers for THz-pulse-driven electrons tunneling from the tip. However, if the optical pulse arrived during the negative THz pulse half-cycle (Fig. 7.15b), the tunnel current that would normally flow due to the steady-state voltage (Fig. 7.2d), was suppressed by $V_{\text{THz}}(t)$. At strong THz fields where $V_{\text{THz,pk}} \gg V_{\text{SPV,pk}}$, the THz-pulse-induced tunnel current, $I_{\text{THz}}(t, \tau)$, locally modified the transient SPV by rapidly annihilating any photoexcited holes near the surface. The THz-pulse-induced voltage transient, $V_{\text{THz}}(t)$, induced ultrafast band bending of the subsurface potential, which drove non-equilibrium charging of the GaAs subsurface and high-field transport of free carriers (Fig. 7.15c,d). This resulted in a transient SPV, $V_{\text{SPV}}(t-\tau, I_{\text{THz}})$, that was now also strongly dependent on the THz-pulse-induced tunnel current, $I_{\text{THz}}(t)$, in addition to the local decay constant (θ), energy of the incident optical pulse ($\varepsilon_{\text{Optical}}$), and the relative arrival time

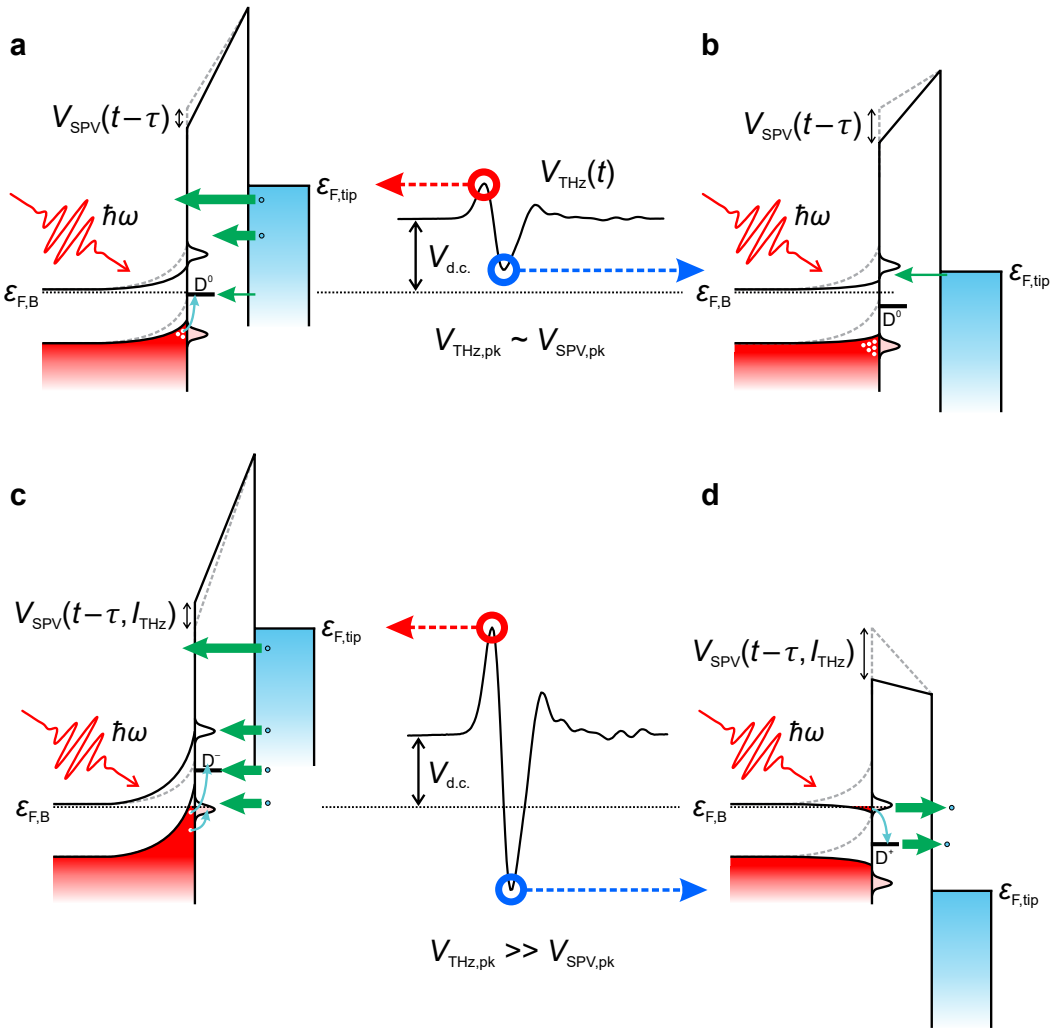

Figure 7.15: Band diagrams for THz-STM of a photoexcited n-type GaAs(110) sample under a steady-state reverse bias, $V_{\mathrm{d.c.}}$, with the THz pulse electric field strength in the **a**, **b**, weak-field regime and **c**, **d**, strong-field regime. Electrons and holes are represented as small blue and white circles, respectively. The two small Gaussians represents the intrinsic surface states of GaAs(110), while a solid black bar represents the extrinsic in-gap surface state (D^-, D^0, D^+). The dashed grey lines show the change in band bending due to the transient THz-current-modified surface photovoltage. Green arrows indicate the direction of electron tunneling, while blue arrows indicate the non-equilibrium transport of electrons and holes through the surface states. The Fermi levels of the tip, surface and sample bulk are given by $\varepsilon_{\mathrm{F,tip}}$, $\varepsilon_{\mathrm{F,S}}$ and $\varepsilon_{\mathrm{F,B}}$, respectively, where $eV_{\mathrm{d.c.}} + eV_{\mathrm{THz}}(t) = \varepsilon_{\mathrm{F,tip}} - \varepsilon_{\mathrm{F,B}}$ and $\varepsilon_{\mathrm{F,S}} = \varepsilon_{\mathrm{F,B}} - eV_{\mathrm{SVP}}(t-\tau, I_{\mathrm{THz}})$. The occupied states for the sample, surface and tip are colored red, pink and blue, respectively.

between the optical and THz pulses ($\tau_{\text{THz–Optical}}$).

Non-equilibrium tunneling with the STM has been explored on the photoexcited GaAs(110) surface [113, 115, 371, 373] and the photoexcited Si(111)-(2×1) surface [394]. For the case of GaAs(110), a diffusive hole capture rate of 25 fA/μW was reported along with a dopant-field-driven capture rate of 200 fA/μW at $V_{\text{d.c.}} = +2$ V. These capture rates determine the onset current for non-equilibrium effects at a particular incident optical power. Evidently, even with a moderate incident optical power, these capture rates are insignificant compared to the timescale and current density of the THz-pulse-induced tunnel current. For the clean Si(111)-(2×1) surface, the magnitude of the tunnel current under reverse bias was found to increase the local SPV by 6.5 mV/nA, and even more for surface defects [394]. The d.c. tunnel current induced excess charging of surface defects, over-saturating them with more charge than they could normally hold. In this way, a large positive THz pulse half-cycle overloaded the sample with negative charge and annihilated the photo-generated holes at the surface that were providing the local SPV (Fig. 7.15c). Ultrafast THz-pulse-induced band bending created a huge potential well for photoexcited holes in the bulk, accelerating them towards the tunnel junction and increasing the THz-pulse-induced current. Similarly, during the negative half-cycle of a large THz pulse, electrons were accelerated from the bulk towards the tunnel junction, where they were rapidly depleted by tunneling into the unoccupied tip states (Fig. 7.15b).

A rich environment of ultrafast dynamics was observed in a THz-STM image containing a gallium vacancy and a few other unidentified defects (Fig. 7.16). These unidentified defects exhibited very small topographic features (Fig. 7.16a), and were found to completely invert the polarity of the rectified THz-pulse-induced tunnel current (Fig. 7.16b). One defect in particular at the bottom left of the image was particularly unique, as it produced both polarities of the tunnel current within its vicinity. Such extreme spatial variability in the polarity of the THz-pulse-induced rectified tunnel current around particular

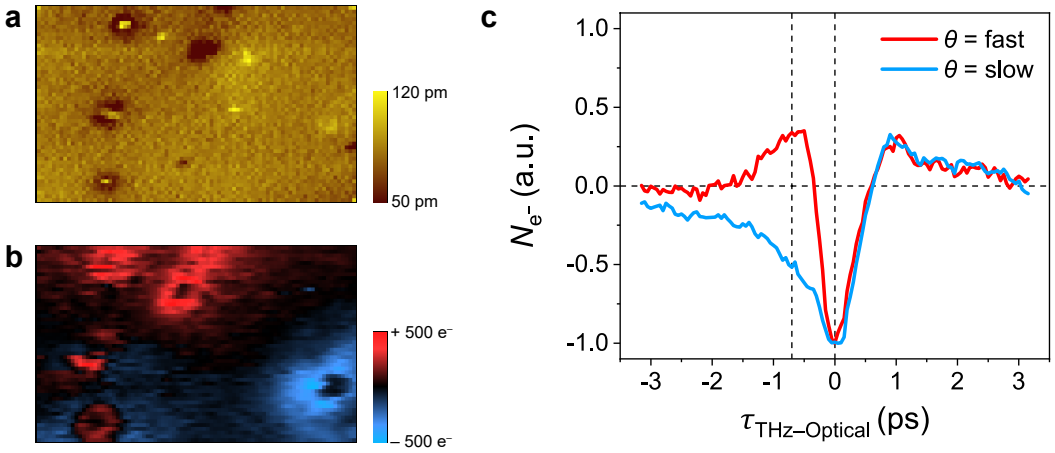

Figure 7.16: Time-resolved THz-STM imaging of ultrafast carrier dynamics near surface defects on GaAs(110). **a**, STM topography and **b**, the ultrafast THz-STM image acquired at $V_{\text{d.c.}} = +2.5$ V, $I_{\text{d.c.}} + I_{\text{THz,avg}} = +200$ pA, $\varepsilon_{\text{Optical}} = 2.6$ nJ, $\tau_{\text{THz–Optical}} = -0.7$ ps and $E_{\text{THz,pk}} = -105$ V/cm. Image size 40 nm × 20 nm; scan speed 70 nm/s. **c**, OPP-THz-STM waveforms that demonstrate how a bipolar THz-pulse-induced rectified tunnel current can occur at particular time delays for different values of the carrier-decay time-constant, θ. The vertical dashed lines are centered at $\tau_{\text{THz–Optical}} = -0.7$ ps and $\tau_{\text{THz–Optical}} = 0$ ps.

surface defects was primarily attributed to a spatially modulated carrier-decay time-constant, $\theta(x, y)$. At certain values of $\tau_{\text{THz–Optical}}$ (Fig. 7.16c), the same incident THz pulse generated a rectified THz-pulse-induced tunnel current, $I_{\text{THz,avg}}(x, y)$, with a modulated polarity across the image. Another possibility is that the polarity of the local SPV was strongly modulated by the Coulombic potential of the tip, such that the spatial proximity of the tip determined the charge state of the defect. In this case, the polarity of $I_{\text{THz,avg}}(x, y)$ would be strongly modulated due to an inversion of the local transient SPV as the tip was scanned across the defect. There are several possible effects one may hope to explore in future studies of optical-pump – THz-STM probe on the GaAs(110) surface, including: the local carrier trapping time, carrier screening effects, local charging by the tunnel current [384–386, 394], high-field transport effects such as velocity overshoot [264, 359, 362, 363], intervalley scattering [359, 392], and additional free carrier generation through impact ionization [264, 359] and Zener tunneling [158]. The time-resolved THz-STM is an excit-

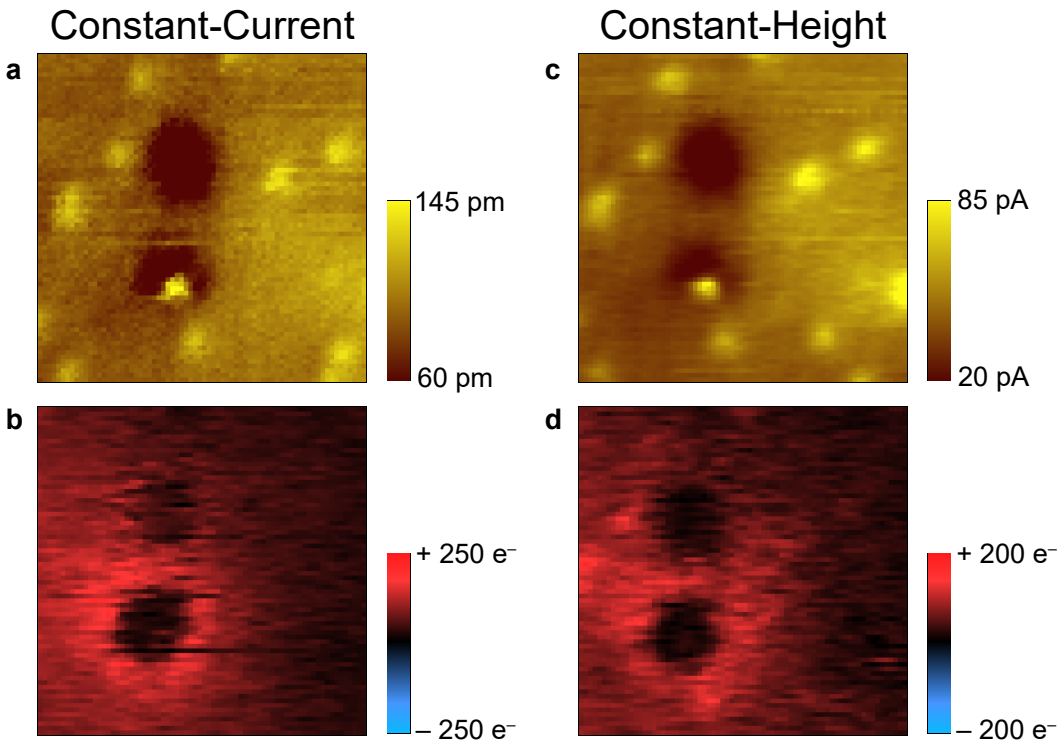

Figure 7.17: Comparison between constant-current and constant-height ultrafast THz-STM images of atomic-scale defects on the GaAs(110) surface. **a**, Constant-current STM topography $z(x, y)$, and **b**, the simultaneously acquired THz-STM image $I_{\mathrm{THz,avg}}(x, y)$. **c**, Constant-height total current image $I_{\mathrm{d.c.}}(x, y) + I_{\mathrm{THz,avg}}(x, y)$, and **d**, simultaneously acquired THz-STM image $I_{\mathrm{THz,avg}}(x, y)$. The images were acquired at acquired at $V_{\mathrm{d.c.}} = +2.5$ V, $\varepsilon_{\mathrm{Optical}} = 2.6$ nJ, $E_{\mathrm{THz,pk}} = +90$ V/cm and $\tau_{\mathrm{THz–Optical}} = 0$ ps. For **a** and **b**, the tunnel current was regulated at $+50$ pA, while for **c** and **d**, the feedback loop was disengaged at $+50$ pA and $V_{\mathrm{d.c.}} = +2.5$ V on the defect-free GaAs(110) surface. Image size 11 nm $\times$ 11 nm; scan speed 130 nm/s.

ing new platform for exploring these various ultrafast processes on the atomic scale.

The crater-like structures that were observed in the THz-STM images were not due to a modulation of the tip height while scanning across the surface with the feedback loop active. This was confirmed by a pair of constant-current (Fig. 7.17a,b) and constant-height (Fig. 7.17c,d) STM and THz-STM images. The notable similarity between the OPP-THz-STM images confirmed that the images were not affected by the modulation of the tip height during constant-current mode as long as the steady-state current, $I_{\mathrm{d.c.}}$, was significantly larger

than the average THz-pulse-induced tunnel current, $I_{\mathrm{THz,avg}}$.

High-resolution STM (Fig. 7.18a) and THz-STM (Fig. 7.18b) images reveal that the crater-like structures occur right at the edges of the topographic depressions, following their non-circular contours fairly accurately. A pair of cross-sectional linescans for STM and THz-STM were acquired across a gallium vacancy that was located beside a prominent topographic protrusion (Fig. 7.18c), and across an isolated gallium vacancy (Fig. 7.18d). The linescans emphasize that the THz-pulse-induced tunnel current was most strongly enhanced along the inner topographic edge of the surface defects. Also, the THz-STM linescan in region II largely ignored the pronounced topographic protrusion (likely an adsorbate). A spatial resolution of approximately 0.3 nm was deduced from the images.

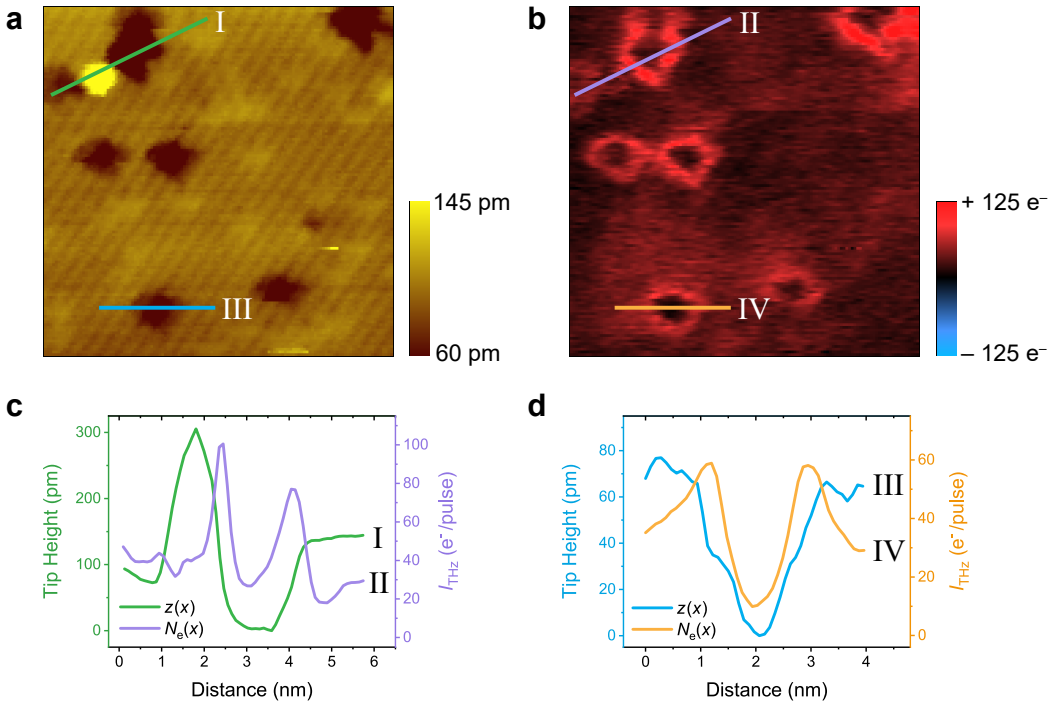

Figure 7.18: High spatial resolution THz-STM imaging of atomic-scale defects on the GaAs(110) surface. **a**, STM topography and **b**, the ultrafast THz-STM image acquired at $V_{\mathrm{d.c.}} = +1.5$ V, $I_{\mathrm{d.c.}} + I_{\mathrm{THz,avg}} = +75$ pA, $\varepsilon_{\mathrm{Optical}} = 1$ nJ, $\tau_{\mathrm{THz–Optical}} = 0$ ps and $E_{\mathrm{THz,pk}} = +70$ V/cm. Image size 12 nm × 12 nm; scan speed 8.5 nm/s. **c**, **d**, Cross-sectional linescans for two different regions of the STM image (solid blue lines) and THz-STM image (solid gold lines).

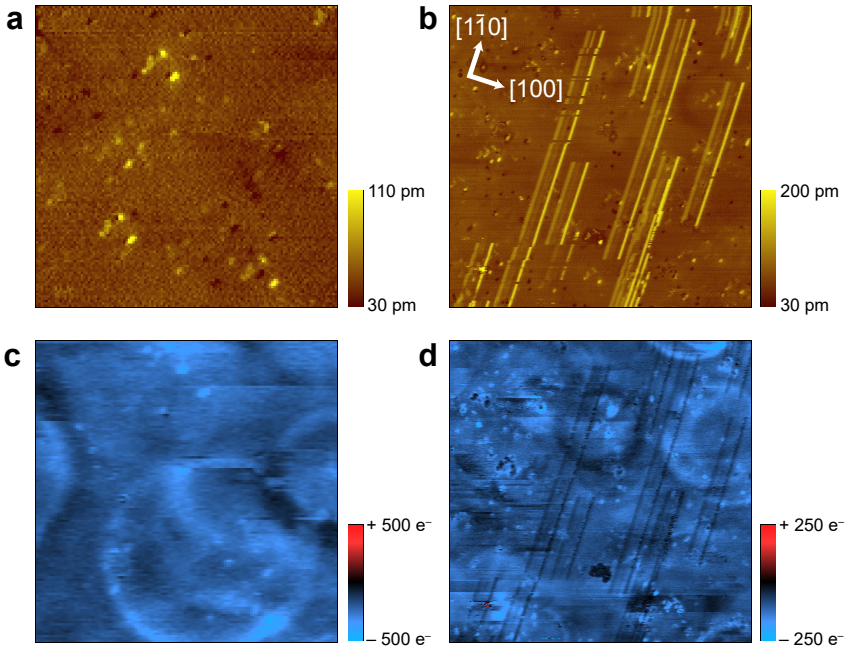

Figure 7.19: **a**, **b**, STM images and **c**, **d**, ultrafast THz-STM images of the photoexcited GaAs(110) surface acquired at $V_{\text{d.c.}} = +2.5$ V, $I_{\text{d.c.}} + I_{\text{THz,avg}} = +200$ pA, $\varepsilon_{\text{Optical}} = 2.6$ nJ, $\tau_{\text{THz–Optical}} = 0$ ps and $E_{\text{THz,pk}} = -105$ V/cm. **a**, **c**, Image size 50 nm × 50 nm; scan speed 75 nm/s. **b**, **d**, Image size 100 nm × 100 nm; scan speed 45 nm/s.

Large-scale subsurface features have also been observed during THz-STM of the GaAs(110) surface, similar to what was reported for the Si(111)-(7×7) surface in section 6.8. The STM topography appeared relatively featureless[19] (Fig. 7.19a,b), while the THz-STM image showed distinct circles about 35 nm in diameter and other large-scale structure (Fig. 7.19c,d). A possible source for these large-scale subsurface features in the THz-STM image may be the deeply penetrating charge densities of defect-induced-gap-states, which can stretch for several nanometers into the bulk under forward bias [356]. Such features may be too deep to be imaged with conventional STM, as a steady-state potential bias of $V_{\text{d.c.}} = +3$ V only penetrates 10–15 nm into the heavily-doped GaAs bulk [371–373]. Although, the penetration depth of the tip-induced field strongly depends on the tip radius of curvature [372]. These subsurface effects may be interesting to fully explore in future experiments.

[19] The long protrusions in Fig. 7.19b,d are [1$\bar{1}$0]-oriented atomic-chains that were created by the THz pulse (see section 8.4 for more details).

A complementary data set to the one shown in Fig. 7.13 was acquired with tip #2 (Fig. 7.20). This tip exhibited notable temporal distortions in its near-field waveform (Fig. 7.8). Two consecutive OPP-THz-STM waveforms were acquired on different areas of the sample surface, where only the positive values were found to increased in amplitude (Fig. 7.20a). The STM topography images show numerous gallium vacancies, subsurface dopants, adsorbates and several unidentified surface defect complexes (Fig. 7.20b). The THz-STM images share many of the same features described earlier.

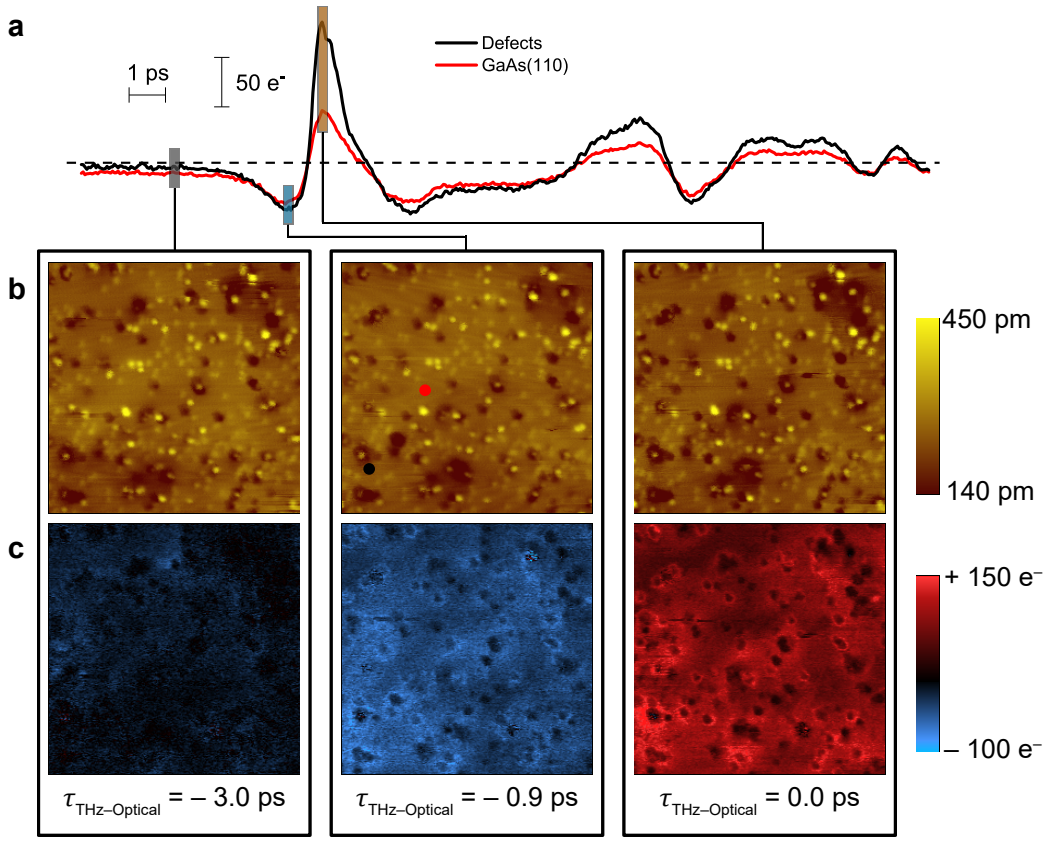

Figure 7.20: Ultrafast THz-STM imaging of surface defects on silicon-doped GaAs(110) using tip #2. All of the measurements were acquired at $V_{\mathrm{d.c.}} = +2$ V, $I_{\mathrm{d.c.}} + I_{\mathrm{THz,avg}} = +50$ pA, $\varepsilon_{\mathrm{Optical}} = 2.6$ nJ and $E_{\mathrm{THz,pk}} = +105$ V/cm. **a**, Measured OPP-THz-STM waveforms at the two different locations on the sample surface shown by the red and black circles in the topography image of the middle frame. **b**, STM images and **c**, ultrafast THz-STM images of the photoexcited GaAs(110) surface at time delays of $\tau_{\mathrm{THz–Optical}} = -3$ ps (left), $\tau_{\mathrm{THz–Optical}} = -0.9$ ps (middle) and $\tau_{\mathrm{THz–Optical}} = 0$ ps (right). Image size 45 nm × 45 nm; scan speed 23 nm/s.

Chapter 8

THz-Pulse-Induced Structural Modifications

During STM and THz-STM, the bias voltage and tunnel current can cause irreversible structural damage to both the tip apex and sample surface. These modifications are due to a variety of physical mechanisms that can arise from the large electric fields and current densities near the tunnel junction. We explored THz-pulse-induced structural modifications using a standard tungsten tip on the Si(111)-(7×7), H-Si(100)-(2×1) and GaAs(110) surfaces. Numerous studies have reported STM-induced modifications with these surfaces, making them well-suited for investigating the physical mechanisms behind the THz-pulse-induced effects.

8.1 Structural Modifications with the STM

Shortly after the STM was developed, it was realized that the atomically sharp metal tip could be used to manipulate the position of individual atoms on surfaces [204, 395–401], along with their charge states [125, 126, 305, 307, 402, 403] and spin states [118–123, 404, 405]. The idea that Richard Feynman had considered back in 1959 during his famous lecture [406] had finally been realized. Feynman proposed that the manipulation of individual atoms would open the door to miniaturized computers, atomic scale circuitry and ultimately molecular synthesis. While there have been major advancements in atomic-

scale memory [120, 186, 188, 404] and atomic-scale circuitry [269, 304, 306, 307], there remains plenty of room for new developments.

The STM tip is routinely used to push and pull adsorbed atoms [67, 206, 395, 396, 407–411] and molecules [206–209, 211, 412, 413] on surfaces. In order to minimize thermally-activated surface diffusion, the measurements are typically performed at low temperature, locking the position of any adsorbates. However, adsorbates can be easily moved around using the strong electric fields and current densities that are present during tunneling microscopy. Considering the typical values during STM: 1 V bias, 1 nm tip height and 1 nA tunnel current, this corresponds to an electric field of 10 MV/cm and a current density of $\sim 10^5$ A/cm^2 through a single silicon atom[1] (metals begin to break down around 10^6 A/cm^2 [414, 415]). At these field strengths and current densities, weak bonds are easily broken, enabling straight-forward maneuvering of physisorbed (van der Waals bonded) atoms and molecules. These techniques have been used to create atomic-scale structures that scatter the 2D electron gas of a metal surface (also called a Shockley state [416]), and exhibit unique standing wave patterns at certain bias voltages (tunneling electron energies) [206, 407–410]. While the tip can be used to directly push and pull adsorbed atoms, there are other surface modification effects that can occur including electric-field-gradient-induced diffusion, electric-field-induced evaporation, and current-induced effects such as Joule heating and electromigration.

Electric-field-gradient-induced surface diffusion readily occurs at V/nm field strengths on both the tip [417, 418] and the sample [397]. This phenomenon is understood by considering the response of the electric dipole moment, $\boldsymbol{p}$, under an applied electric field, $\boldsymbol{E}(\boldsymbol{r})$, and assuming a uniform field across the adsorbate. The total dipole moment (static + induced), $\boldsymbol{p}$=(p_x, p_y, p_z), of the adsorbate can be expanded using perturbation theory to give [419, 420]

$$p_i = \sum_{j,k,l...}^{3} \left[\mu_i + \alpha_{ij} E_j + \frac{1}{2}\beta_{ijk} E_j E_k + \frac{1}{6}\gamma_{ijkl} E_j E_k E_l + ... \right], \tag{8.1}$$

[1] Assuming a spatial resolution of 3 Å for STM and TD-STM of Si(111)-(7×7) as shown in [218] and Fig. 6.13, respectively: 3.5×10^5 A/cm^2 $= (1 \times 10^{-9}$ A$)/(\pi\,[3 \times 10^{-8}$ cm$]^2$)

where $j, k, l, ...$ are summed over the three Cartesian components, E_j is the component of the field in the j direction, $\boldsymbol{\mu}$=(μ_x, μ_y, μ_z) is the static dipole moment, α_{ij} is the electric polarizability tensor (rank 2), β_{ijk} is the first order hyperpolarizability tensor (rank 3) and γ_{ijkl} is the second order hyperpolarizability tensor (rank 4). These polarizability terms are microscopic analogues of the dielectric susceptibility, $\chi^{(1)}_{ij}$, and the nonlinear susceptibilities, $\chi^{(2)}_{ijk}$ and $\chi^{(3)}_{ijkl}$ (see Eq. 3.2). There are additional higher order terms that can arise in Eq. 8.1 due to a non-uniform field across the adsorbate (for a complete theoretical analysis see [419]). For atomic adsorbates the first order hyperpolarizability (β_{ijk}) is neglected due to the inherent radial symmetry of the atom, but this term can play an important role for asymmetric molecular adsorbates [420]. This symmetry is analogous to the inability of a centrosymmetric medium to exhibit second order ($\chi^{(2)}$) nonlinear optical effects [5]. Under an applied electric field, the potential energy, $U(r)$, of an adsorbate will be modified by (ignoring quadrupolar effects, see [419] for details)

$$U = \sum_{i,j,k,l...}^{3} \Big[-\mu_i E_i - \frac{1}{2}\alpha_{ij} E_i E_j - \frac{1}{6}\beta_{ijk} E_i E_j E_k - \frac{1}{24}\gamma_{ijkl} E_i E_j E_k E_l - ... \Big]. \quad (8.2)$$

Due to the physical asymmetry of the tip–sample junction, there is a radial electric field gradient that arises naturally during STM. This induces a spatially dependent force that acts on any adsorbate, leading to field-gradient-induced surface diffusion. By assuming an isotropic polarizability in the radial direction the summation indices can be ignored to obtain the radial force on the adsorbate

$$F_r = -\frac{dU}{dr} = \left(\mu + \alpha\, E + \frac{1}{2}\,\beta\, E^2 + \frac{1}{6}\,\gamma\, E^3 + ... \right) \frac{dE}{dr}, \quad (8.3)$$

where dU/dr is the field-induced potential energy gradient and dE/dr is the electric field gradient. Note the asymmetry in the equation for different signs of the electric field, which can lead to a preferred polarity for field-gradient-induced surface diffusion [397, 418]. For more reactive surfaces such as silicon dangling bonds, the adsorbate may become chemisorbed, increasing the activation energy for diffusion. However, if the force acting on the adsorbate is

strong enough ($E \sim 0.1$ V/Å), it can result in field-induced-desorption [417, 421–424].

Electric-field-induced evaporation is the dissociation of bulk atoms into an ionized plasma gas due to an extremely skewed local potential energy. An electric field of several V/Å can locally reduce the evaporation temperature from several thousand Kelvin to cryogenic temperatures. Field evaporation was first observed prior to the invention of the STM using kilovolt potentials applied to free-standing tips in another type of high resolution microscopy called field ion microscopy [56, 58, 286, 288]. The term *field evaporation* implies that the atoms were part of the bulk crystal lattice, while *field desorption* implies that the atoms or molecules were adsorbed to the surface. Atoms that are near the surface and located in sharp protruding volumes will experience a very high local electric field that drastically alters their potential energy landscape, and enables spontaneous atomic evaporation in the form of ions [57, 58, 425]. Specifically, an evaporating ion with a positive charge state[2] overcomes its nearest-neighbour chemical bonds that hold it in place by tunneling through the field-dependent activation energy, $Q(E)$. Several models have been developed to describe this phenomenon such as the image-charge-hump model [58, 428], the charge-exchange model [57, 421, 426–428] and first-principles kinetic theory [425, 429]. The image-charge-hump model (also called the Schottkey-hump model) approximates the evaporation rate, r, as [58, 401, 429]

$$r \;=\; A(E)\,\nu(E)\,\exp\!\left(\frac{-Q(E)}{k_{\mathrm{B}}\,T}\right) \tag{8.4}$$

where E is the electric field, T is temperature, $A(E)$ is the ionization probability, $\nu(E)$ is the characteristic vibrational frequency, $Q(E)$ is the field dependent activation energy and k_{B} is the Boltzmann constant. For a free-standing tungsten tip, typical values of the activation energy range from 0.90 eV to 0.12 eV for 4.7 V/Å and 5.9 V/Å, respectively [57]. Experimental studies have

[2]Field evaporation of ions with a negative charge state has only been observed with the STM [418, 426, 427]. This is because at negative potentials the onset of electron field emission occurs several thousand voltages before the onset of field evaporation. If the negative bias voltage is further increased, field emission currents melt the tip apex before the onset of negative ion evaporation.

confirmed that the temperature dependence of the evaporation rate in Eq. 8.4 becomes negligible at low temperature (< 600 K) and very high field strengths (~ 6 V/Å) [56, 57, 428, 430]. In fact, by operating below a critical temperature (depending on the tip material), the evaporation becomes dominated by a field-driven tunneling process with a very weak dependence on temperature [428, 430]. These general principles have been applied to the development of techniques such as field ion microscopy [56, 58, 286, 288], atom probe tomography [58, 431], focused ion beam lithography [432], helium ion microscopy [433] and single-atom-tip formation [286, 288, 433].

Electric-field-induced evaporation in the STM has been routinely observed on metallic surfaces [427, 434, 435], semiconductor surfaces [204, 311, 398–401, 423, 426, 427, 436–442] and metallic tips [418, 443]. Accordingly, STM tips are often made from tungsten because it has an extremely high resistance to field evaporation, with critical fields between 5.7 V/Å and 6.3 V/Å, depending on the crystallographic orientation and temperature [56, 58], (for comparison, silicon is ~ 3.8 V/Å [58]). In the STM tunnel junction, the electric field strength required for evaporation is significantly lower than in FIM measurements using a free-standing tip. This has to do with the tip–sample interactions that occur when the absolute distance of the STM tunnel junction falls below 4 Å (sometimes called chemically-assisted field evaporation [65, 398, 423, 434, 436]). Theoretical modeling has demonstrated that the onset for field-induced evaporation in the STM geometry becomes 1/2 of the FIM value at a tip–sample distance of ~ 4 Å [417]. A 1 V/Å electric field is more than enough to cause significant surface modifications with the STM tip [422, 426, 427, 438]. However, at these very small tip–sample distances, determining the dominant mechanism becomes quite challenging as chemical and physical adhesion between the tip and sample cannot be ignored [202, 399]. In fact, Pascual et al. [344] argue that field evaporation is not the dominant physical mechanism in the formation of large mounds with the STM [418, 443, 444]. Furthermore, theoretical studies of field-induced single atom transfer in the STM have demonstrated activation energy lowering from 1.6 eV at 5 Å to 0.5

eV at 4 Å, which was attributed to both chemical bonding between atoms and field-induced effects [445].

Performing field-effect manipulations on the atomic-scale is a delicate procedure that requires an extremely sharp tip without any small protruding mini-tips [400]. This can be quite a difficult task, and even if one follows the standard tip preparation procedure (section 5.2), success is not guaranteed. However, higher reproducibility has been reported using tips etched from single crystal W(111) wire [439, 440]. Field-induced evaporation may also result in unexpected nonlocal surface modifications due to adatom diffusion and surface restructuring [434]. Also, additional details arise when considering different tip materials. In the case of a platinum tip compared to a tungsten tip, it was reported that the tungsten tip would redeposit some evaporated silicon atoms back onto the surface, while the platinum tip did not show the same effect [441, 442]. Furthermore, due to the higher work function of platinum as compared to tungsten, its tip–sample distance is smaller and hence a platinum tip requires less voltage to extract a single silicon adatom as compared to a tungsten tip [441, 442].

In conventional STM, the current density of a metal-to-metal tunnel junction can approach values up to[3] 10^{10} A/cm^2 [205, 346], while a semiconductor-to-metal tunnel junction typically has a current density near[4] 10^6 A/cm^2. Even STM imaging of individual molecular orbitals [135, 183–185, 195, 210–213], which typically occurs at a tunnel current of few picoamperes, results in a current density of approximately[5] 10^4 A/cm^2. These current densities are comparable to the breakdown values for bulk metals (10^6 A/cm^2 [414, 415]), modern copper interconnects (10^8 A/cm^2 [447, 448]), carbon nanotubes (10^9 A/cm^2 [449]), and metal nanobridges (10^{10} A/cm^2 [346, 446]). At these ex-

[3] In figure 3 of Barth et al. [205], the spatial resolution is approximately 0.5 Å at a tunnel current of 631 nA: 0.8×10^{10} A/cm^2 = (631 nA)/($\pi\,[0.5 \times 10^{-8}$ cm$]^2$). A similar current density was achieved by Yanson et al. [346] for a one-dimensional metal-to-metal break-junction in an STM configuration, and by Ralls et al. [446] for an atomically thin metal nanobridge.

[4] 1.3×10^6 A/cm^2 = (100 pA)/($\pi\,[0.5 \times 10^{-8}$ cm$]^2$).

[5] 1.3×10^4 A/cm^2 = (1 pA)/($\pi\,[0.5 \times 10^{-8}$ cm$]^2$).

tremely high current densities, the crystal structure of the conducting metal begins to break down due to mass transfer from the cathode to the anode, which arises from the momentum transfer of electron-ion scattering events. This effect is known as electromigration [396, 399, 414, 415, 446–448, 450], and it is extremely important to consider when the current density is greater than 10^5 A/cm^2. Electromigration typically refers to a variety of current-induced effects; however, all of these effects contribute to the eventual failure of the circuit or connection. The failure of a metallic interconnect due to electromigration can be described phenomenologically by Black's equation [450]

$$\mathrm{MTTF} \;=\; \frac{A}{J^2}\,\exp\!\left(\frac{Q}{k_{\mathrm{B}}\,T}\right), \tag{8.5}$$

where MTTF is the mean-time-to-failure (typically maximized), J is the current density, A is a constant and Q is the activation energy. Electromigration effects have been observed for single defects in metal nanobridges [446] and even single-atom-transfer in the STM [396, 451]. On clean metallic surfaces in UHV, electromigration occurs primarily along the surface [414, 415].

Several current-induced effects have been explored with the STM across a wide range of samples including metals [186, 187, 336, 344], semiconductors [299, 300, 311, 377], single molecules [184, 320–322, 452–456] and glassy metal alloys [457, 458]. Surprisingly, the large current densities that occur during STM typically result in a negligible temperature increase near the tunnel junction. The local temperature increase of the STM junction can be approximated by [65, 459]

$$\Delta T \;\approx\; \frac{I\,V}{4\,\pi\,\kappa\,\lambda}\,, \tag{8.6}$$

where I is the current, V is the voltage, κ is the thermal conductivity and λ is the electron mean-free-path. For typical values of the STM: $I = 1$ nA, $V = 1$ V, and a relatively low conductivity sample[6] with $\lambda = 1$ nm and $\kappa = 1$ W/(K·m), the local temperature increase is only 0.08 K. Therefore, in order to observe significant current-induced heating with the STM, microampere-scale tunnel currents must be used on low resistivity materials that have a poor thermal

[6]For a high conductivity metal with $\lambda = 30$ nm and $\kappa = 300$ W/(K·m), $\Delta T = 10^{-5}$ K.

conductivity such as glassy metal alloys [457, 458]. However, according to a quantum mechanical description of energy dissipation in the STM [460], whose results agree with Eq. 8.6, the local temperature of the surface can be increased by several thousand degrees if the tunnel junction resistance is very low $\sim 10^5$ Ω and a moderate bias voltage is applied. In this case, the large increase in the local temperature near the tunnel junction is due to the excitation of plasmons and electron–hole pairs, followed by a corresponding reduction in the local surface thermal conductivity [460]. Furthermore, thermal runaway of metal nano-tips has been demonstrated during intense electron field emission under high electron fields [461].

Single molecules and atoms that are adsorbed on the surface are much more sensitive to current-induced effects. Hence, there are a variety of processes that can occur such as molecular disassociation [452, 453, 455], molecular switching [184], lateral hopping [454], hydrogen tautomerization [184], hydrogen desorption [299, 300] and inelastic tunneling spectroscopy [456]. Recent work has also demonstrated localized molecular desorption of toluene and chlorobenzene on Si(111)-(7×7) using hot electron charge injection with the STM tip [320–322].

8.2 Si(111)-(7×7)

There have been numerous studies that have investigated STM-induced modifications of the Si(111)-(7×7) surface [398, 400, 401, 436, 438–442]. The observations, which range from single-adatom-removal [398, 400, 401, 439, 440, 442] to large-scale nanometer-sized trenches [436, 438, 441], have been mainly attributed to chemically-assisted field evaporation [398, 423, 436]. Although, further studies have demonstrated an 'unassisted' field evaporation process at a larger tip–sample separation ($\sim$ 1 nm), where chemical interactions are weak [400, 401, 439, 440, 442]. Current-induced effects may be present in some cases [311, 320–322, 460, 461], but they are typically negligible in comparison to the field-induced effects [401].

Terahertz-pulse-induced surface modifications were performed on the Si(111)-

(7×7) surface with the UHV THz-STM system described in chapter 5. The etched polycrystalline tungsten tips were treated *in situ* as described in section 5.2, and the incident single-cycle THz pulses had the same temporal profile as Fig. 6.2. The experiments were performed at room temperature (T = 295 K) and low temperature (T = 100 K) with a low-doped silicon sample (P: 10^{15} cm^{-3}) and a high-doped silicon sample (As: 10^{19} cm^{-3}). The THz-pulse-induced surface modification effects were found to be strongly dependent on both the sample temperature and the doping concentration. In particular, the high-doped sample at high temperature (T = 295 K) required the lowest $E_{\mathrm{THz,pk}}$ to induce tip or surface modifications. The reduced probability for damage at lower doping concentration was expected because of the decreased availability of free-carriers. This led to a smaller THz-pulse-induced current and less field enhancement at the tip apex due to a weaker image charge (see also the discussion in section 6.3). However, the strong temperature dependence that was observed for both doping concentrations was indeed quite surprising.

At low temperature, THz pulses with $E_{\mathrm{THz,pk}} = -200$ V/cm (Fig. 6.9) and even $E_{\mathrm{THz,pk}} = +400$ V/cm (Fig. 6.28) can drive the tunnel current without

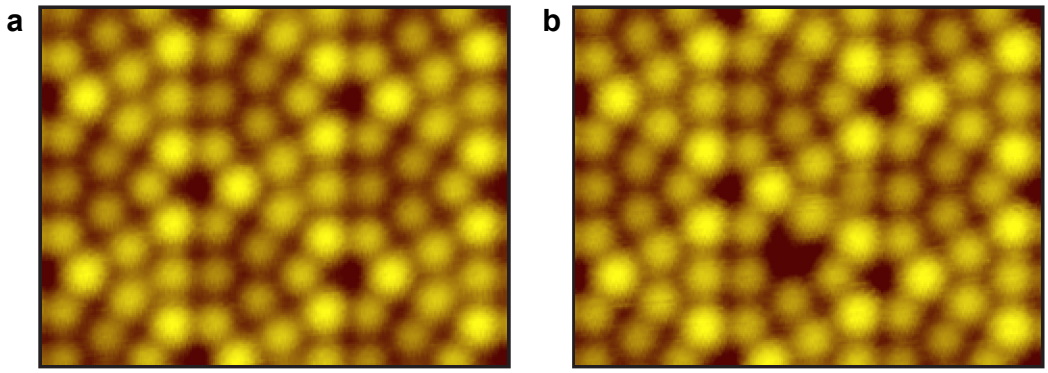

Figure 8.1: THz-pulse-induced single-adatom removal from the Si(111)-(7×7) surface. STM images of the same surface were acquired at $V_{\mathrm{d.c.}} = -0.9$ V and $I_{\mathrm{d.c.}} = -100$ pA, before (**a**) and after (**b**) exposing the STM tip to THz pulses for $t_{\mathrm{dmg}} \approx 5$ s at $E_{\mathrm{THz,pk}} = -150$ V/cm, $V_0 = V_{\mathrm{d.c.}}$ and $I_0 = I_{\mathrm{d.c.}}$. Image size 7.0 nm × 5.4 nm. Note: the adatom that was actually removed in **b** was positioned directly northeast of the brown topographic depression. This was revealed by STM images of the defect at other bias voltages.

significant modifications to either the tip or sample. However, at room temperature, the same THz electric fields instantly cause irreversible damage to both the tip apex and local sample surface. The onset $E_{\mathrm{THz,pk}}$ for THz-pulse-induced surface modifications was found to vary greatly with temperature, but also with the tip geometry and the initial tip–sample separation prior to THz pulse exposure. Also, some tips did not exhibit any THz-pulse-induced effects at room temperature, nor low temperature, while some other tips would continue to exhibit surface modification effects even down to $T = 50$ K. On average, tungsten tips that exhibited a stable long-term field emission profile (Fig. 5.12), with consistent day-to-day atomic resolution STM imaging (Fig. 2.6), would have THz-pulse-induced surface modifications start to occur at $E_{\mathrm{THz,pk}} \approx -150$ V/cm, while at room temperature and standard tunneling conditions (Fig. 8.1).

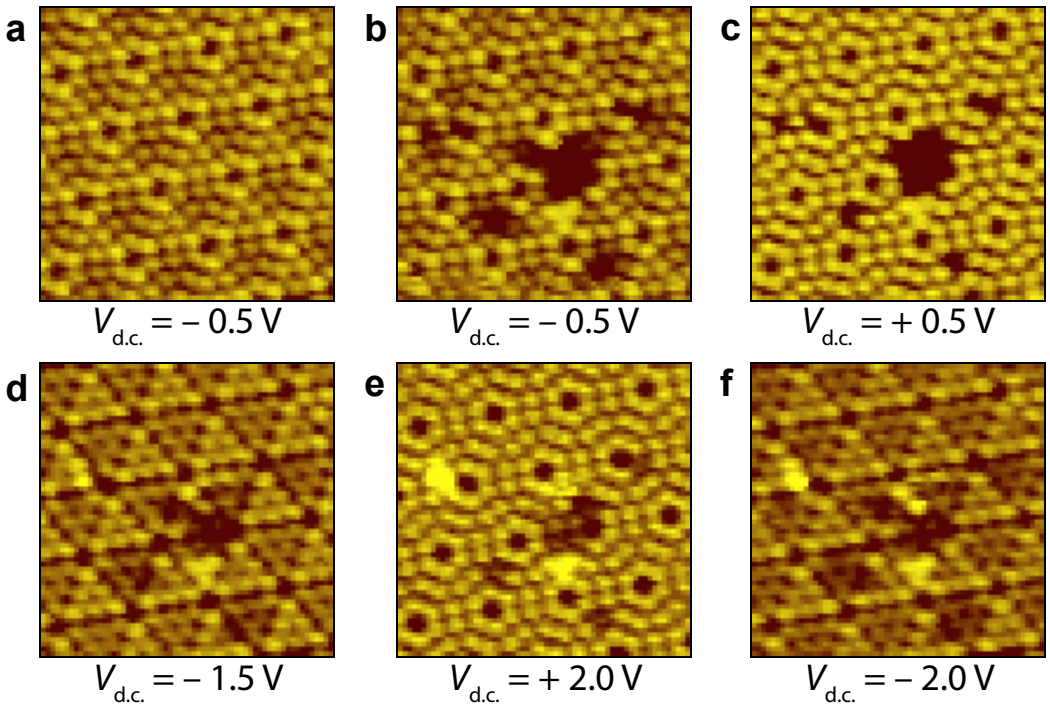

Figure 8.2: Imaging voltage dependence of an atomic-scale THz-pulse-induced surface modification. STM images of the same Si(111)-(7×7) surface were acquired at $|I_{\mathrm{d.c.}}| = 150$ pA, and a range of bias voltages before (**a**) and after (**b**–**f**) exposing the STM tip to THz pulses for $t_{\mathrm{dmg}} \approx 3$ s at $E_{\mathrm{THz,pk}} = -200$ V/cm, $V_0 = -0.5$ V and $I_0 = I_{\mathrm{d.c.}}$. Image size 10 nm × 10 nm.

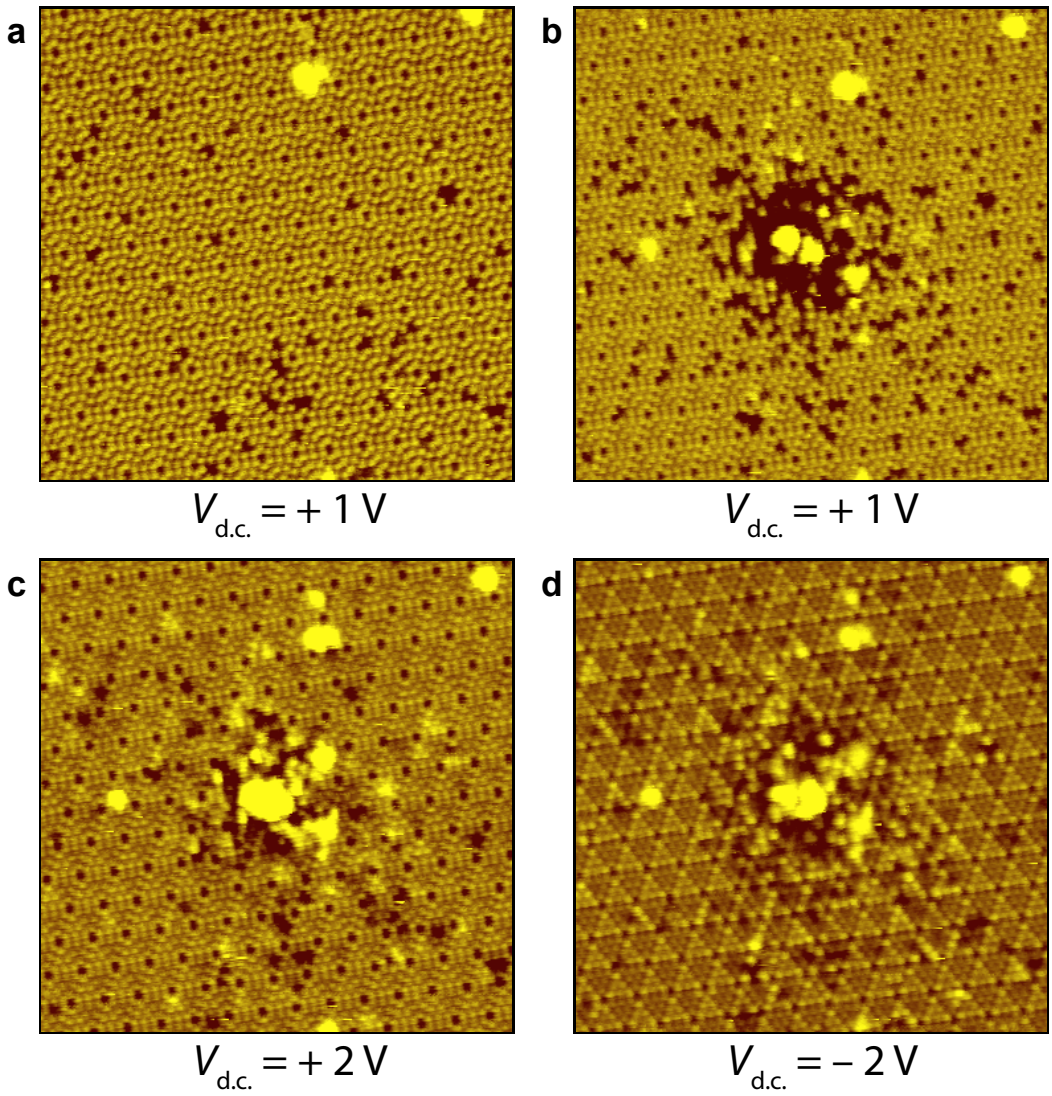

Figure 8.3: Imaging voltage dependence of a nanometer-scale THz-pulse-induced surface modification. STM images of the same Si(111)-(7×7) surface were acquired at $|I_{\mathrm{d.c.}}| = 35$ pA, and a range of bias voltages before (**a**) and after (**b**–**d**) exposing the STM tip to THz pulses for $t_{\mathrm{dmg}} \approx 3$ s at $E_{\mathrm{THz,pk}} = -400$ V/cm, $V_0 = +1$ V and $I_0 = I_{\mathrm{d.c.}}$. Image size 35 nm × 35 nm.

If the THz pulse electric field is increased to about $E_{\mathrm{THz,pk}} \approx -200$ V/cm, more atoms are removed (Fig. 8.2a,b). However, due to drastic changes to the local density of states near the defect, the same surface defect can appear quite different at different bias voltages (Fig. 8.2b–f). In particular, the defect has a lack of electron states near the Fermi level, so when the STM tip is positioned near the defect, while at a low bias voltage, the tip will get closer to the surface

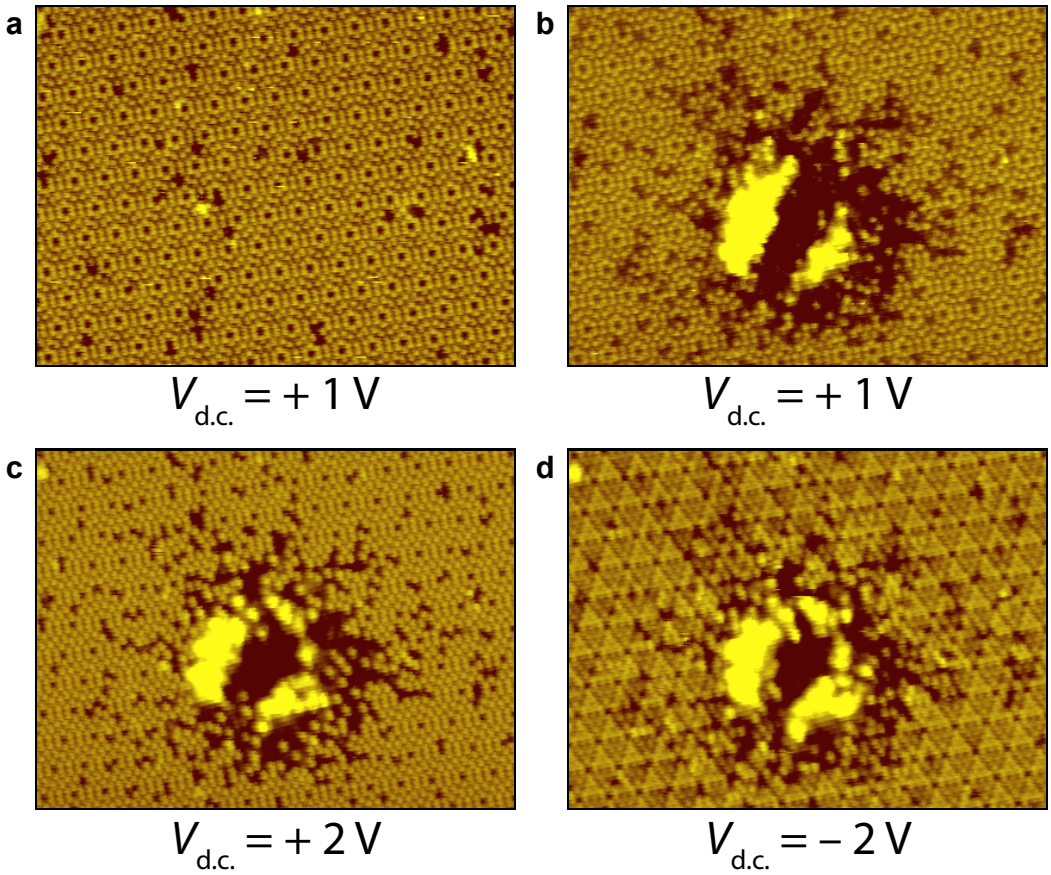

Figure 8.4: Imaging voltage dependence of a nanometer-scale THz-pulse-induced surface modification. STM images of the same Si(111)-(7×7) surface were acquired at $|I_{\mathrm{d.c.}}| = 35$ pA, and a range of bias voltages before (**a**) and after (**b**–**d**) exposing the STM tip to THz pulses for $t_{\mathrm{dmg}} \approx 3$ s at $E_{\mathrm{THz,pk}} = -450$ V/cm, $V_0 = +1$ V and $I_0 = I_{\mathrm{d.c.}}$. Image size 40 nm × 30 nm.

in order to maintain a constant tunnel current. Accordingly, the surface may appear to be missing more atoms than have actually been displaced. This is evident when comparing the images in Fig. 8.2b,c and Fig. 8.3b at low-bias, to the images in Fig. 8.2d–f and Fig. 8.3c at high-bias, respectively. These artifacts can be largely avoided by imaging the surface at a bias voltage where the tip follows a path that closely resembles the geometric contour of the surface; for Si(111)-(7×7), this occurs at approximately $V_{\mathrm{d.c.}} = +2.0$ V [218]. For even larger THz pulse electric fields of $E_{\mathrm{THz,pk}} = -400$ V/cm (Fig. 8.3) and $E_{\mathrm{THz,pk}} = -450$ V/cm (Fig. 8.4), the damage becomes increasingly significant, such that the modification effects can be accurately resolved at several bias

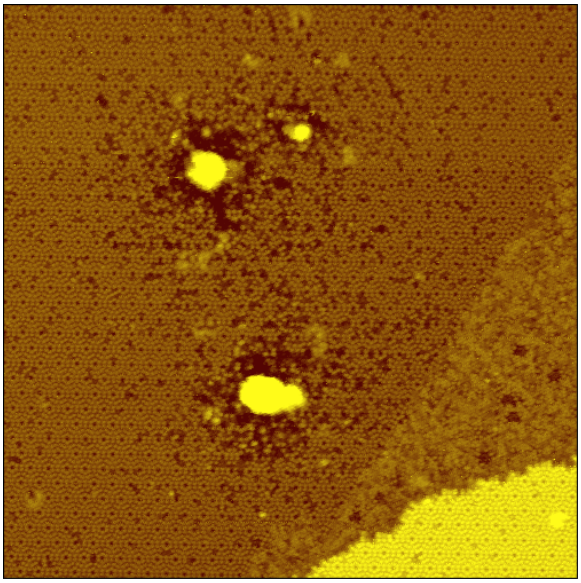

Figure 8.5: THz-pulse-induced surface modification and tip material deposition. An STM image of the Si(111)-(7×7) surface was acquired at $I_{\text{d.c.}} = 150$ pA and $V_{\text{d.c.}} = +1.5$ V, after the STM tip was exposed to THz pulses for $t_{\text{dmg}} \approx 5$ s at $E_{\text{THz,pk}} = -400$ V/cm for the top middle event and $E_{\text{THz,pk}} = -500$ V/cm for the other two events. Image size 100 nm × 100 nm.

voltages.

At high THz electric fields (> 300 V/cm), the tip eventually starts to deposit mass onto the surface, in addition to causing local surface modifications (Fig. 8.3, Fig. 8.4 and Fig. 8.5). The mass deposits are a few nanometers tall, while the depressions surrounding them are only 1–2 atomic layers deep, no more than a few ångströms. Thus, the mass lost by the surrounding 7×7 surface cannot account for the size of the deposits and as a result, the deposits are largely attributed to THz-pulse-induced mass transfer from the tungsten tip. Significant mass transfer is also possible at lower THz fields by decreasing the tip–sample separation. This is shown in Fig. 8.6, which was exposed to THz pulses at $E_{\text{THz,pk}} = -350$ V/cm, where the tip–sample separation was set by 0.5 V and 50 pA. However, the same THz pulse electric field at a tip–sample separation set by 2 V and 50 pA (the tip retracts by approximately 2 Å), produced significantly less damage (Fig. 8.7). Although the d.c. bias does change considerably between these two measurements, it does not have a sig-

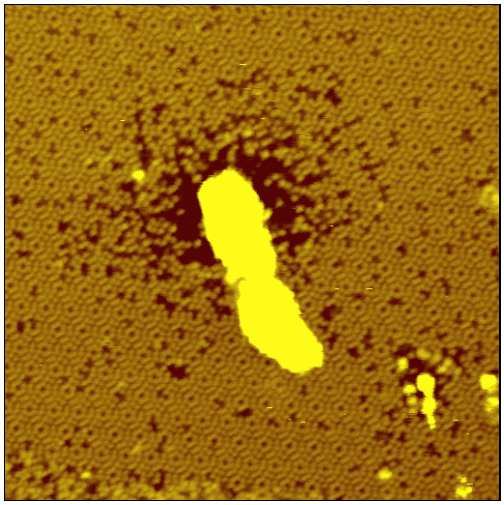

Figure 8.6: THz-pulse-induced surface modifications and tip material depositions. An STM image of the Si(111)-(7×7) surface was acquired at $I_{\text{d.c.}} = 50$ pA and $V_{\text{d.c.}} = +1$ V, after the STM tip was exposed to THz pulses at $E_{\text{THz,pk}} = -350$ V/cm, $V_0 = +0.5$ V and $I_0 = I_{\text{d.c.}}$ for $t_{\text{dmg}} \approx 5$ s. Image size 50 nm × 50 nm.

nificant role in determining the size of the surface modification[7]. Instead, with a smaller tip–sample separation, the local THz pulse field enhancement increases (Fig. 6.32c), which causes more significant damage to occur due to the larger THz pulse electric field that drives extreme transient currents.

There are a variety of physical mechanisms that may be responsible for the observed THz-pulse-induced modifications. These effects include field-assisted evaporation, field-assisted diffusion, current-induced electromigration and current-induced heating. For weak-field effects such as single-adatom-removal (Fig. 8.1), field evaporation is the most likely mechanism, as was the case with conventional STM [398, 400, 401, 423, 436, 439, 440]. Although, single atom transfer due to vibration excitation via inelastic electron tunneling has also been observed in cases where the atoms are weakly bonding [396, 451]. For high-field effects that involve THz-pulse-induced mass transfer, the dominant mechanism is even less clear. This is because in THz-STM, an extremely large transient current density can occur that is several orders of magnitude greater than

[7]If the d.c. bias had any notable effect on the magnitude of the THz-pulse-induced surface modification, the higher voltage event should have caused more damage, not less.

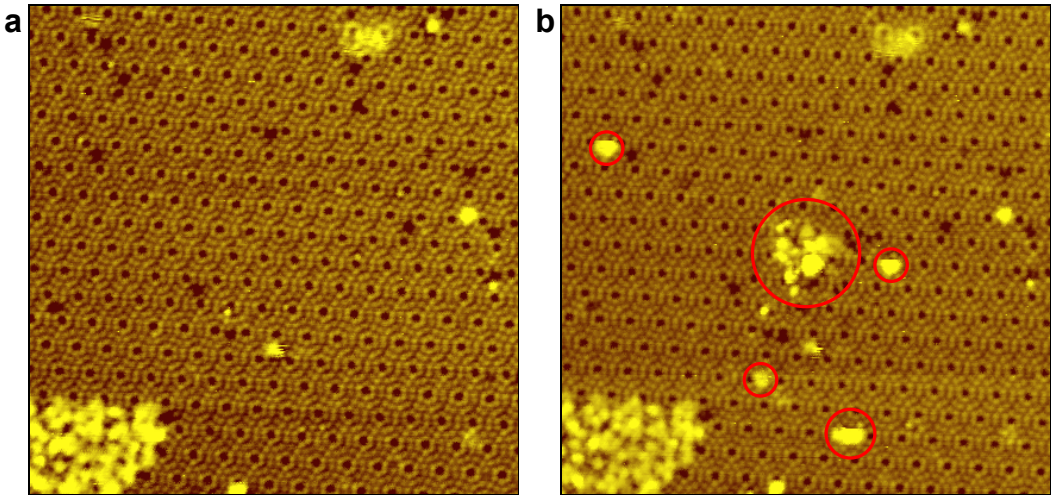

Figure 8.7: **a**, **b**, Local and nonlocal THz-pulse-induced surface modifications on the nanometer-scale. STM images of the same Si(111)-(7×7) surface were acquired at $V_{\text{d.c.}} = +2$ V and $I_{\text{d.c.}} = 50$ pA, before (**a**) and after (**b**) exposing the STM tip to THz pulses for $t_{\text{dmg}} \approx 3$ s at $E_{\text{THz,pk}} = -350$ V/cm, $V_0 = V_{\text{d.c.}}$ and $I_0 = I_{\text{d.c.}}$. Image size 40 nm × 40 nm. The red circles are guides to the eye for locating the THz-pulse-induced modifications.

the upper limit for electromigration-induced breakdown at steady-state currents[8]. As a result, electromigration effects likely play a role in creating the THz-pulse-induced tip and surface modifications. Furthermore, field-assisted diffusion readily occurs on clean surfaces in ultrahigh vacuum [414, 415], such as the tip shank [417, 418] and sample surface [397], and it may be contributing to the observed modifications by migrating adsorbates near the tip apex (Fig. 8.7).

The physical processes of field evaporation (Eq. 8.4), surface diffusion [415, 421] and electromigration (Eq. 8.5) all exhibit an exponential temperature dependence, whereby a lower temperature reduces the probability of the effect occurring. Although, field evaporation has a relatively weak dependence on

[8]In Fig. 6.28 the spatial resolution is approximately 0.3 nm for $N_{e^-} \approx 1000$ rectified electrons per pulse. According to our model (Fig. 6.24), this corresponds to a 2 mA peak current occurring over several hundred femtoseconds, resulting in a transient tunnel current density of 7×10^{11} A/cm^2 $= (2 \times 10^{-3}\text{ A})/(\pi\,[3 \times 10^{-8}\text{ cm}]^2)$. This current density is orders of magnitude greater than the maximum steady-state current density that has been sustained in bulk metals (10^6 A/cm^2 [414, 415]), modern copper interconnects (10^8 A/cm^2 [447, 448]), carbon nanotubes (10^9 A/cm^2 [449]) and metal nanobridges (10^{10} A/cm^2 [346, 446]).

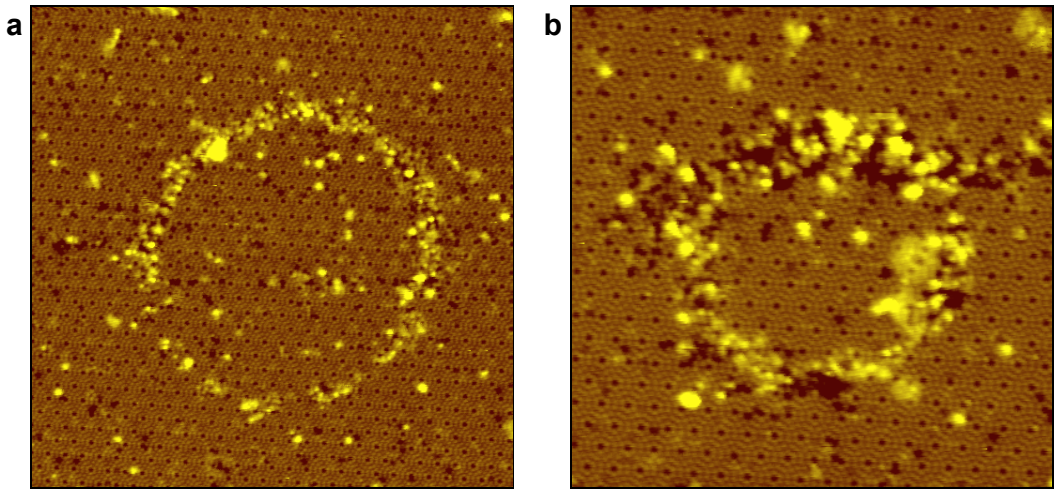

Figure 8.8: **a**, **b**, STM images of THz-pulse-induced nano-patterned circles on the Si(111)-(7×7) surface acquired at $I_{\text{d.c.}} = +30$ pA and $V_{\text{d.c.}} = +2$ V. Prior to the image acquisition, the STM tip was exposed to THz pulses at $V_0 = V_{\text{d.c.}}$, $I_0 = I_{\text{d.c.}}$ and $E_{\text{THz,pk}} = -400$ V/cm for $t_{\text{dmg}} \sim 60$ s as the tip was translated along a 40 nm diameter circle (**a**) and a 25 nm diameter circle (**b**). Image size 70 nm × 70 nm for **a** and 45 nm × 45 nm for **b**.

temperature below ∼ 600 K [56, 57, 428, 430], and as a result, it may not be the primary physical mechanism responsible for the observed surface modifications during THz-STM of Si(111)-(7×7). This is in contrast to conventional STM, where the surface modifications have been largely attributed to field evaporation [400, 401, 439, 440] or chemically-assisted field evaporation [398, 423, 436]. For THz-STM at extremely high transient current densities, the effects of electromigration [396, 399, 415, 446, 451] and local heating of the tunnel junction [460, 461] need to be taken into consideration when attempting to establish the physical mechanism that is responsible for the observed large-scale THz-pulse-induced modifications. The surface temperature of the tunnel junction can reach several thousand degrees if the resistivity of the tunnel junction is very low (∼ 10 kΩ) and a few volts bias are applied [460, 461]. Such extreme tunnel junction conditions are readily achieved during THz-STM of Si(111)-(7×7) at high THz pulse electric fields, as discussed in chapter 6. Also, heating effects are naturally suppressed by a reduction of the sample temperature, consistent with the observations. Accordingly, the

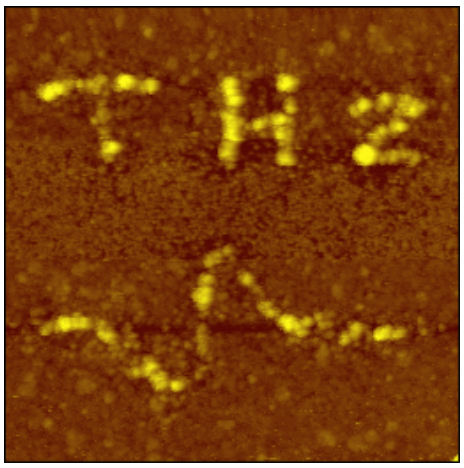

Figure 8.9: STM image of THz-pulse-induced nano-patterning on the Si(111)-(7×7) surface acquired at $V_{\text{d.c.}} = +1.7$ V and $I_{\text{d.c.}} = +200$ pA. Prior to the image acquisition, the STM tip was exposed to THz pulses at $V_0 = V_{\text{d.c.}}$, $I_0 = I_{\text{d.c.}}$ and $E_{\text{THz,pk}} = -300$ V/cm for $t_{\text{dmg}} \sim 30$ s. Image size 100 nm × 100 nm.

effects of local heating may play a significant role during THz-STM of the Si(111)-(7×7) surface at these high transient tunnel currents.

There are several possible applications to consider for THz-pulse-induced modifications. One straightforward example is to locally induce surface damage with the STM tip, in order to pattern out a structure across the surface. THz-pulse-induced nano-patterning was used to create unique structures on the Si(111)-(7×7) surface via the formation of either nanometer-sized mounds underneath the tip (Fig. 8.8 and Fig. 8.9), or removing adatoms within a couple nanometers of the tip apex (Fig. 8.10). However, nano-patterning techniques on the Si(111)-(7×7) surface have already been explored using steady-state bias voltages. In fact, atomic-scale-patterning has been demonstrated via the extraction and re-deposition of individual silicon adatoms in a completely reversible process [439, 440]. Accordingly, the ideal application for THz-pulse-induced surface modifications should utilize the ultrafast nature of the THz pulse in a manner that conventional STM cannot replicate. There are several molecular-scale effects that become available upon adjusting the THz pulse amplitude to a more perturbative regime (such as in Fig. 8.1), with examples including isomerization [462], tautomerization [184], molecular dissocia-

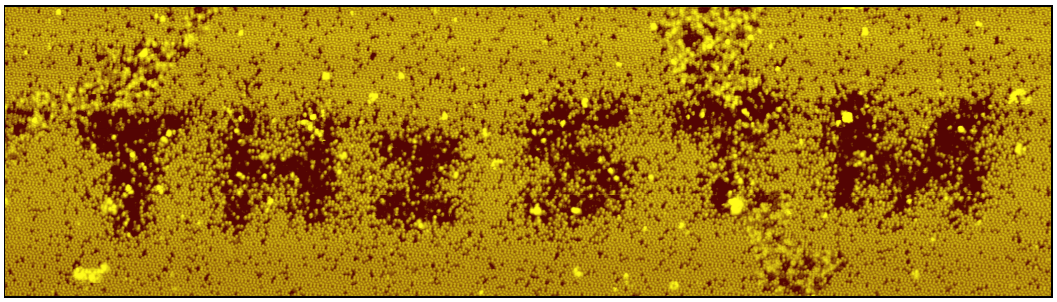

Figure 8.10: Large-scale atomically-resolved STM image of THz-pulse-induced nano-patterning on the Si(111)-(7×7) surface acquired at $V_{\text{d.c.}} = +1$ V and $I_{\text{d.c.}} = +50$ pA. Prior to the image acquisition, the STM tip was exposed to THz pulses at $V_0 = V_{\text{d.c.}}$, $I_0 = I_{\text{d.c.}}$ and $E_{\text{THz,pk}} = -300$ V/cm for $t_{\text{dmg}} \sim 60$ s. Image size 210 nm × 60 nm.

tion [452, 453, 455], molecular hopping [454], conductance switching [184], inelastic tunneling spectroscopy [456] and hydrogen desorption [299, 300]. Future experiments may trigger these effects with sub-picosecond accuracy using an ultrafast THz pulse, and then probe the subsequent dynamics with a time-delayed THz-STM-coupled pulse.

8.3 H-Si(100)-(2×1)

In conventional STM, hydrogen desorption from the H-Si(100)-(2×1) surface can occur via either non-resonant vibronic excitations, or resonant electronic excitations [300]. The low voltage (2–3 V) vibronic excitations are the result of inelastic electron tunneling in the STM, while resonant excitations (6–8 V) break the silicon–hydrogen bonds directly [300]. Here, we performed a preliminary study of ultrafast THz-pulse-induced hydrogen desorption on the H-Si(100)-(2×1) surface. The etched polycrystalline tungsten tips were treated *in situ* following section 5.2, and the sample surface was prepared following section 5.3.2. The incident THz pulses had the same temporal profile as Fig. 6.2. The experiments were performed at low temperature ($T = 160$ K), with a high-doped silicon sample (As: 10^{19} cm^{-3}).

At first, the THz pulse electric field, $E_{\text{THz,pk}}$, was increased throughout the scan until the onset for hydrogen desorption was observed (Fig. 8.11). Hy-

drogen desorption began to occur at $E_{\mathrm{THz,pk}} \approx -200$ V/cm, consistent with vibronic excitations as the THz peak voltage was approximately, $V_{\mathrm{THz,pk}} \approx -3$ V, as determine in section 6.2, for the same THz field strength on the Si(111)-(7x7) surface (with a similar bulk doping). Following the same assumptions, at $E_{\mathrm{THz,pk}} \approx -400$ V/cm, the peak THz voltage was $V_{\mathrm{THz,pk}} \approx -6$ V, which agrees with the reported voltage onset for direct resonant excitation of the silicon–hydrogen bond [300]. Next, the STM tip was scanned in a 7 nm × 7 nm square for 30 seconds at $E_{\mathrm{THz,pk}} = -300$ V/cm (Fig. 8.12) and $E_{\mathrm{THz,pk}} = -450$ V/cm (Fig. 8.13). The hydrogen was effectively desorbed by the THz pulse at both field strengths, with the larger field strength having a greater

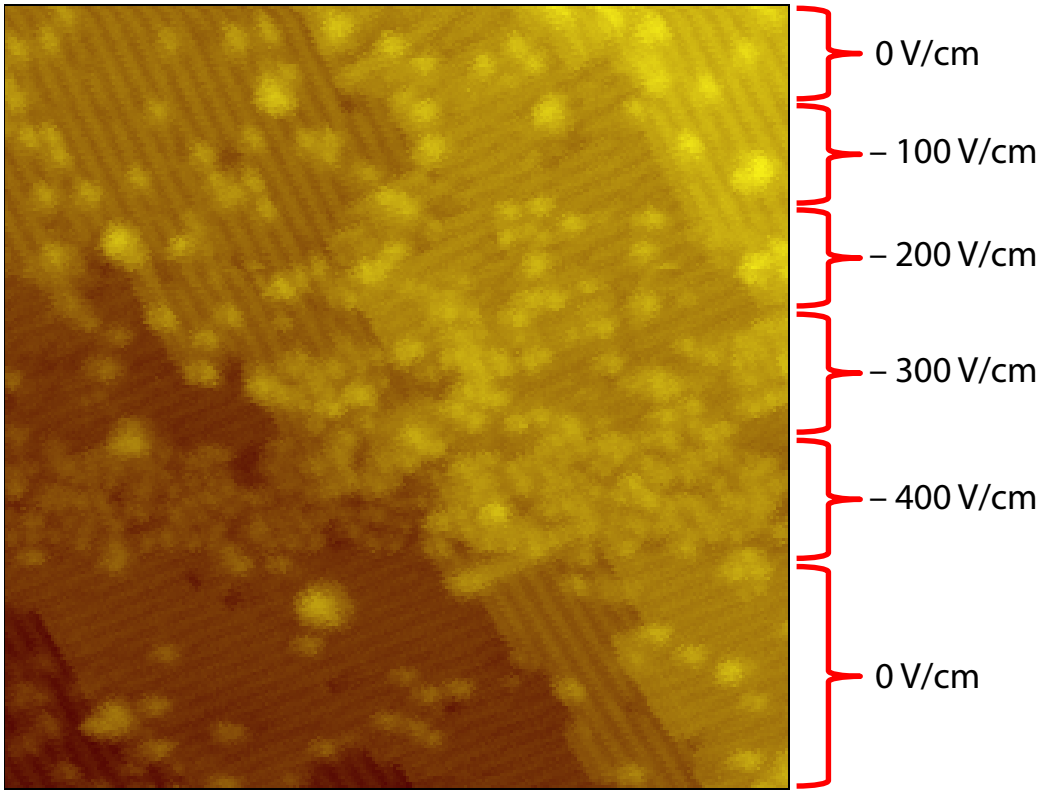

Figure 8.11: An STM image of the H-Si(100)-(2×1) surface that was acquired after THz-pulse-induced hydrogen desorption was performed during the previous scan, where the THz pulse electric field, $E_{\mathrm{THz,pk}}$, was increased progressively throughout the scan. The fast scan direction is leftward-travelling and the slow scan direction is downward-travelling. The image was acquired at $V_{\mathrm{d.c.}} = -1.5$ V and $I_{\mathrm{d.c.}} = -100$ pA, and the same settings were used during the THz-pulse-induced hydrogen desorption. Image size 30 nm × 30 nm.

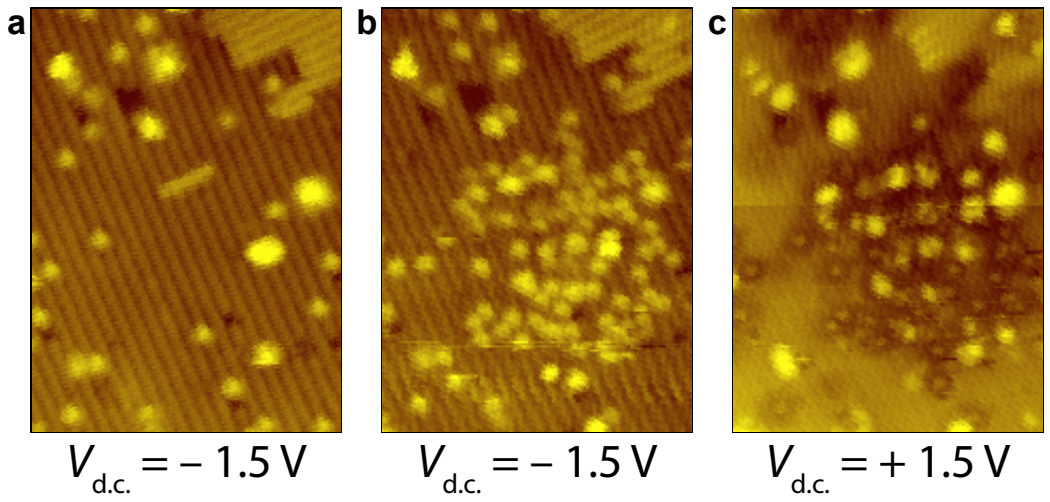

Figure 8.12: STM images of the H-Si(100)-(2×1) surface that were acquired **a**, before, and **b**, **c**, after THz-pulse-induced hydrogen desorption was performed at $E_{\mathrm{THz,pk}} = -300$ V/cm, $V_0 = -1.5$ V and $I_0 = -100$ pA. The images were acquired in constant current mode at $|I_{\mathrm{d.c.}}| = 100$ pA. Image size 17 nm × 23 nm.

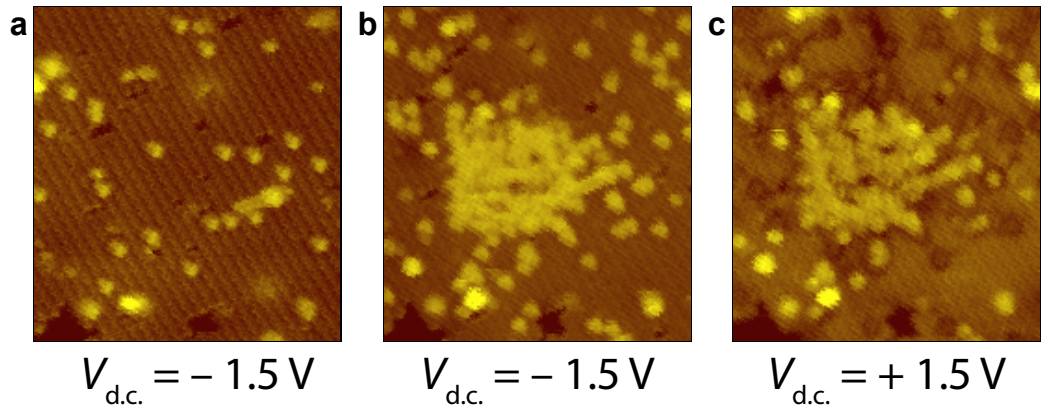

Figure 8.13: STM images of the H-Si(100)-(2×1) surface that were acquired **a**, before, and **b**, **c**, after THz-pulse-induced hydrogen desorption was performed at $E_{\mathrm{THz,pk}} = -450$ V/cm, $V_0 = -1.5$ V and $I_0 = -100$ pA. The images were acquired in constant-current mode at $|I_{\mathrm{d.c.}}| = 100$ pA. Image size 19 nm × 21 nm.

desorption yield. The THz-pulse-induced defects were confirmed to be individual dangling bonds by the presence of a dark halo surrounding an isolated dangling bond [304, 305, 365], while STM imaging at a positive bias, as shown in Fig. 8.12c and Fig. 8.13c.

8.4 GaAs(110)

Conventional STM studies of field-induced and current-induced changes on the GaAs(110) surface have reported the formation of extremely straight atomic chains along the $[1\bar{1}0]$ direction of the sample surface. This was attributed to field-induced surface diffusion of adsorbates on the sample surface. A very similar behavior has been observed in a set of STM (Fig. 8.14a,b and Fig. 7.19b) and THz-STM (Fig. 8.14c,d and Fig. 7.19d) images that were acquired on the GaAs(110) surface. The THz-STM images share many of the same features described in section 7.3, but the STM topography images reveal several extremely straight 150 pm protrusions along the $[1\bar{1}0]$ direction of the sample.

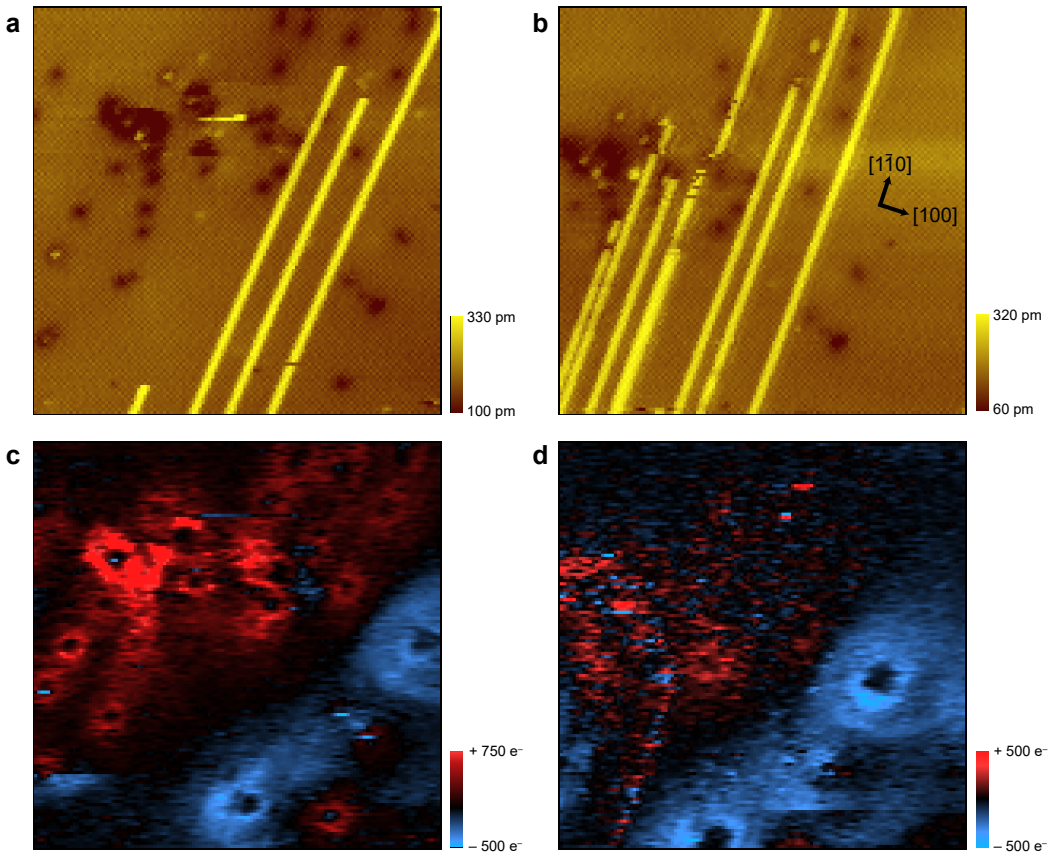

Figure 8.14: Spontaneous creation of atomic chains during time-resolved THz-STM imaging of GaAs(110). **a**, **b**, STM topography and **c**, **d**, the ultrafast THz-STM images of the same surface acquired at $V_{\text{d.c.}} = +2.5$ V, $I_{\text{d.c.}} + I_{\text{THz,avg}} = +200$ pA, $\varepsilon_{\text{Optical}} = 2.6$ nJ, $\tau_{\text{THz–Optical}} = -0.7$ ps and $E_{\text{THz,pk}} = -105$ V/cm. Image size 40 nm × 40 nm; scan speed 70 nm/s.

These topographic features were attributed to the spontaneous creation of atomic-chains on the GaAs(110) surface during THz-STM imaging. However, unlike the intentionally deposited cesium atoms in Whitman et al. [397], in our experiments it was not so obvious what atoms were forming the long and uniform chains. Most likely, due to their relatively high rate of spontaneous formation during THz-STM of GaAs(110), they were composed of Ga or As atoms that had locally melted or field evaporated, and then diffused towards the tip apex. This spontaneous creation of vacancies and other complexes on the GaAs(110) surface was also frequently observed during THz-STM imaging (Fig. 8.15) due to the large THz-pulse-induced tunnel currents and electric fields. These results are consistent with a study that has reported STM-induced vacancy migration on GaAs(110) at a relatively moderate steady-state tunnel current of 100 pA [376]. The STM-induced defect migration was attributed to minority carrier trapping by adatom vacancies on the GaAs(110) surface. As a result, it is not too surprising that the THz-pulse-induced tunnel current and electric field often created adatom vacancies during scanning. Surprisingly, the atomic-chains were almost completely invisible in the THz-STM images (Fig. 8.14c,d), indicating that the THz-pulse-induced tunnel current on GaAs(110) is sensitive to the subsurface carrier dynamics of the sample. However, this was not always the case, as shown in Fig. 7.19d. Unfortunately,

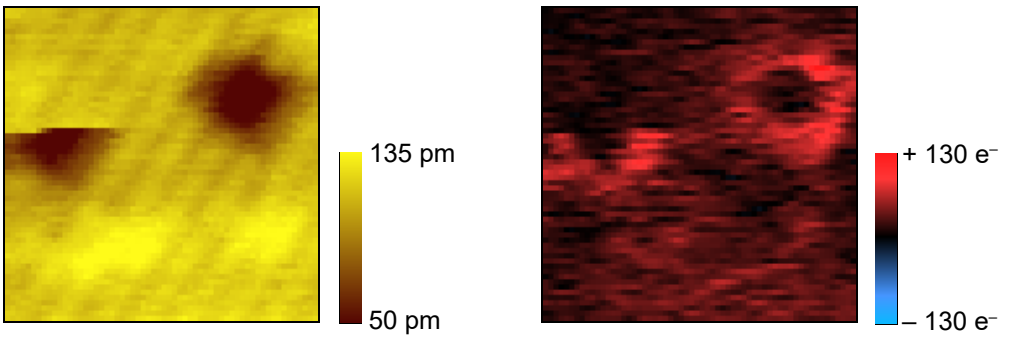

Figure 8.15: Spontaneous removal of a single gallium atom from the GaAs(110) surface during THz-STM imaging at $V_{\text{d.c.}} = +1.5$ V, $I_{\text{d.c.}} + I_{\text{THz,avg}} = +75$ pA, $\varepsilon_{\text{Optical}} = 1$ nJ, $\tau_{\text{THz–Optical}} = 0$ ps and $E_{\text{THz,pk}} = +70$ V/cm. Image size 4.7 nm × 4.7 nm; scan speed 21 nm/s.

the continued appearance of these atomic chains around this unique region of the surface (and others like it) prevented any long-term measurement of the area.

The large THz-pulse-induced topographic depression in Fig. 8.14 is a negatively charged gallium vacancy complex as evident from the strong locally enhanced THz-pulse-induced tunnel current (Fig. 8.14c). In a subsequent scan, the atomic chains had accumulated near the large topographic depression and sharply reduced the local enhancement of $I_{\mathrm{THz,avg}}$. This may be due to gallium atoms in atomic chains re-filling the surface vacancies and reducing the net negative charge locally. Additional large-scale defect creation can also be seen in Fig. 7.20 as new features that appear inbetween successive scans (the images were acquired in order from right to left).

Chapter 9

Summary and Outlook

A new time-resolved imaging and spectroscopy technique has been developed for resolving the sub-picosecond dynamics of electrons with sub-nanometer precision. The THz-pulse-coupled scanning tunneling microscope (THz-STM) can characterize and manipulate the properties of single atoms on a timescale that is intrinsic to their local interactions. This thesis has shown that ultrafast single-cycle THz pulses can be used to coherently drive an extremely large transient tunnel current through an atomically sharp metal tip and a relatively conductive sample surface. The THz-pulse-induced tunnel currents were characterized across a wide range of sample surfaces. The THz-STM was shown to: induce ultrafast non-equilibrium charging of surface states, probe the photoexcited local carrier dynamics of surfaces, and photo-conductively sample the THz pulse near-field waveform at the end of the tip apex.

The initial THz-STM experiments that were performed under ambient conditions are described in chapter 4. Single-cycle THz pulses that were polarized along the central axis of the metal tip were able to modulate the measured d.c. tunnel current with relatively modest peak electric fields. A spatio-temporal imaging resolution of 2 nm and 500 fs was demonstrated for gold nanoislands that were deposited onto a highly-oriented-pyrolytic-graphite substrate. The THz-STM was then used to spatially and temporally resolve the ultrafast dynamics of photoexcited free carriers near a single InAs nanodot.

Specifically, the photoexcitation induced ultrafast charging of the nanodot, which was attributed to a local variability in the electron and hole trapping times.

The THz-STM system was then redesigned for an ultrahigh vacuum environment, as described in chapter 5. Various techniques were used to characterize the tip apex and modify its structure until the tip could support a large transient THz-pulse-induced tunnel current. In chapter 6, the ultrahigh vacuum THz-STM system was used to demonstrate a 0.3 nm and 500 fs spatio-temporal resolution on the Si(111)-(7×7) surface. The THz pulse electric field was used to coherently tunnel several hundred electrons through single atoms on a silicon surface, which produced transient tunnel current densities in excess of 10^{11} A/cm^2. These extreme transient tunnel currents were enabled by the subsurface penetration of the THz pulse electric field into the silicon bulk. This induced ultrafast band bending throughout the naturally occurring depletion region below the surface, which opened up a new conduction channel to the bulk that resulted in a fundamentally different terahertz tunneling conductance, and led to non-equilibrium charging of the Si(111)-(7×7) surface.

In chapter 7, an optically-excited GaAs(110) surface was spatio-temporally resolved with the THz-STM. A large steady-state reverse bias created a deep potential well within the sample that attracted minority carriers towards the tunnel junction. This resulted in a transient surface photovoltage that was coherently enhanced or suppressed by the THz pulse, depending on which half-cycle of the THz pulse the surface photovoltage was generated on. In this way, the transient surface photovoltage was used to sample the temporal profile of the THz-pulse-induced voltage at the tunnel junction. However, at high THz pulse electric fields, non-equilibrium charging and high-field transport dominated the overall response.

Chapter 8 explored how the large THz-pulse-induced electric fields and current densities were able to cause structural modifications to the tip apex and sample surface. A significant temperature dependence was observed whereby

the THz-pulse-induced surface modifications were sharply suppressed at low temperatures ($T < 200$ K). The physical mechanisms behind these structural modifications include both field-induced effects and current-induced effects.

The burgeoning field of THz-STM has seen incredible growth since its initial demonstration in 2013 [130–138]. Several new THz-STM systems are emerging all around the world, suggesting that the field will see rapid growth in the near-future. There are several possible avenues to explore with this powerful technique. For example, several new exotic nano-materials have recently emerged with potentially groundbreaking implications for future real-world applications [7, 138, 187, 273–277, 463]. By fully characterizing the ultrafast dynamics of these nano-materials down to the atomic scale, new applications will inevitably emerge that harness the unique properties of these nano-materials. Another possible direction is pushing the temporal resolution of the technique down to tens of femtoseconds using ultrabroadband single-cycle pulses with center frequencies in the mid-infrared [248, 341]. In fact, field-driven electron tunneling with few-cycle optical pulses has already been demonstrated [143], suggesting that the ultimate temporal resolution of ultrafast STM may one day approach the attosecond regime [29–33]. Yet another possible avenue to explore is using the THz-pulse-induced voltage and current transients to actively control the internal and external degrees of freedom of particles on surfaces, such as charge state [125, 126, 305, 307, 402, 403], spin state [118–123, 404, 405], vibrational state [135], molecular orientation [184], many-body transitions [185], lateral position [209, 211] and local field emission [233]. In this way, the THz pulse acts as an ultrafast gate for time-dependent interactions between atoms, molecules and other charged quasi-particles. Another possibility is that modern STM/AFM systems [188, 306, 307] may open the door to THz-STM of insulating samples. Some additional avenues to explore are: time-resolved THz-pulse-induced-electroluminescence [212], THz-tunnel-current-induced single photon emission [213], ultrafast atomic force microscopy [85] and multi-probe THz-STM [318, 319].

References

1. Rohrer, H. STM: 10 years after. *Ultramicroscopy* **42–44,** 1–6 (1992) (cit. on pp. vi, 2, 7, 9).
2. Fattahi, H., Barros, H. G., Gorjan, M., Nubbemeyer, T., Alsaif, B., Teisset, C. Y., Schultze, M., Prinz, S., Haefner, M., Ueffing, M., Alismail, A., Vámos, L., Schwarz, A., Pronin, O., Brons, J., Geng, X. T., Arisholm, G., Ciappina, M., Yakovlev, V. S., Kim, D.-E., Azzeer, A. M., Karpowicz, N., Sutter, D., Major, Z., Metzger, T. & Krausz, F. Third-generation femtosecond technology. *Optica* **1,** 45–63 (2014) (cit. on pp. 1, 27).
3. Bloembergen, N. Nobel Lecture: Nonlinear optics and spectroscopy. *Reviews of Modern Physics* **54,** 685–695 (1982) (cit. on p. 1).
4. Schawlow, A. L. Nobel Lecture: Spectroscopy in a new light. *Reviews of Modern Physics* **54,** 697–707 (1982) (cit. on p. 1).
5. Boyd, R. W. *Nonlinear Optics* 3rd Edition (Academic Press, 2008) (cit. on pp. 1, 30–32, 34, 173).
6. Zewail, A. H. Nobel Lecture: Femtochemistry: Atomic-scale dynamics of the chemical bond using ultrafast lasers. *Angewandte Chemie International Edition* **39,** 2586–2631 (2000) (cit. on pp. 1, 2).
7. Eichberger, M., Schäfer, H., Krumova, M., Beyer, M., Demsar, J., Berger, H., Moriena, G., Sciaini, G. & Miller, R. J. D. Snapshots of cooperative atomic motions in the optical suppression of charge density waves. *Nature* **468,** 799–802 (2010) (cit. on pp. 1, 2, 38, 196).
8. Sciaini, G. & Miller, R. J. D. Femtosecond electron diffraction: heralding the era of atomically resolved dynamics. *Reports on Progress in Physics* **74,** 096101 (2011) (cit. on pp. 1, 2).
9. Kealhofer, C., Schneider, W., Ehberger, D., Ryabov, A., Krausz, F. & Baum, P. All-optical control and metrology of electron pulses. *Science* **352,** 429–433 (2016) (cit. on pp. 1, 2).
10. Hall, J. L. Nobel Lecture: Defining and measuring optical frequencies. *Reviews of Modern Physics* **78,** 1279–1295 (2006) (cit. on p. 1).
11. Hänsch, T. W. Nobel Lecture: Passion for precision. *Reviews of Modern Physics* **78,** 1297–1309 (2006) (cit. on p. 1).
12. Glauber, R. J. Nobel Lecture: One hundred years of light quanta. *Reviews of Modern Physics* **78,** 1267–1278 (2006) (cit. on p. 1).
13. Kao, C. K. Nobel Lecture: Sand from centuries past: Send future voices fast. *Reviews of Modern Physics* **82,** 2299–2303 (2010) (cit. on p. 1).

14. Betzig, E. Nobel Lecture: Single molecules, cells, and super-resolution optics. *Reviews of Modern Physics* **87,** 1153–1168 (2015) (cit. on p. 1).
15. Hell, S. W. Nobel Lecture: Nanoscopy with freely propagating light. *Reviews of Modern Physics* **87,** 1169–1181 (2015) (cit. on p. 1).
16. Moerner, W. E. Nobel Lecture: Single-molecule spectroscopy, imaging, and photocontrol: Foundations for super-resolution microscopy. *Reviews of Modern Physics* **87,** 1183–1212 (2015) (cit. on p. 1).
17. Strickland, D. & Mourou, G. Compression of amplified chirped optical pulses. *Optics Communications* **55,** 447–449 (1985) (cit. on p. 1).
18. Ashkin, A., Dziedzic, J. M., Bjorkholm, J. E. & Chu, S. Observation of a single-beam gradient force optical trap for dielectric particles. *Optics Letters* **11,** 288–290 (1986) (cit. on p. 1).
19. Corkum, P. B. Plasma perspective on strong field multiphoton ionization. *Physical Review Letters* **71,** 1994–1997 (1993) (cit. on pp. 1, 102).
20. Paul, P. M., Toma, E. S., Breger, P., Mullot, G., Augé, F., Balcou, P., Muller, H. G. & Agostini, P. Observation of a train of attosecond pulses from high harmonic generation. *Science* **292,** 1689–1692 (2001) (cit. on p. 1).
21. Itatani, J., Levesque, J., Zeidler, D., Niikura, H., Pépin, H., Kieffer, J. C., Corkum, P. B. & Villeneuve, D. M. Tomographic imaging of molecular orbitals. *Nature* **432,** 867–871 (2004) (cit. on p. 1).
22. Ndabashimiye, G., Ghimire, S., Wu, M., Browne, D. A., Schafer, K. J., Gaarde, M. B. & Reis, D. A. Solid-state harmonics beyond the atomic limit. *Nature* **534,** 520–523 (2016) (cit. on p. 1).
23. Ghimire, S., DiChiara, A. D., Sistrunk, E., Agostini, P., DiMauro, L. F. & Reis, D. A. Observation of high-order harmonic generation in a bulk crystal. *Nature Physics* **7,** 138–141 (2011) (cit. on p. 1).
24. Schubert, O., Hohenleutner, M., Langer, F., Urbanek, B., Lange, C., Huttner, U., Golde, D., Meier, T., Kira, M., Koch, S. W. & Huber, R. Sub-cycle control of terahertz high-harmonic generation by dynamical Bloch oscillations. *Nature Photonics* **8,** 119–123 (2014) (cit. on pp. 1, 5, 27).
25. Vampa, G., Hammond, T. J., Thiré, N., Schmidt, B. E., Légaré, F., McDonald, C. R., Brabec, T. & Corkum, P. B. Linking high harmonics from gases and solids. *Nature* **522,** 462–464 (2015) (cit. on p. 1).
26. Langer, F., Hohenleutner, M., Schmid, C. P., Poellmann, C., Nagler, P., Korn, T., Schüller, C., Sherwin, M. S., Huttner, U., Steiner, J. T., Koch, S. W., Kira, M. & Huber, R. Lightwave-driven quasiparticle collisions on a subcycle timescale. *Nature* **533,** 225–229 (2016) (cit. on pp. 1, 5, 27).
27. Yoshikawa, N., Tamaya, T. & Tanaka, K. High-harmonic generation in graphene enhanced by elliptically polarized light excitation. *Science* **356,** 736–738 (2017) (cit. on p. 1).
28. Hafez, H. A., Kovalev, S., Deinert, J.-C., Mics, Z., Green, B., Awari, N., Chen, M., Germanskiy, S., Lehnert, U., Teichert, J., Wang, Z., Tielrooij,

K.-J., Liu, Z., Chen, Z., Narita, A., Müllen, K., Bonn, M., Gensch, M. & Turchinovich, D. Extremely efficient terahertz high-harmonic generation in graphene by hot Dirac fermions. **561,** 507–511 (2018) (cit. on p. 1).
29. Goulielmakis, E., Yakovlev, V. S., Cavalieri, A. L., Uiberacker, M., Pervak, V., Apolonski, A., Kienberger, R., Kleineberg, U. & Krausz, F. Attosecond control and measurement: lightwave electronics. *Science* **317,** 769–775 (2007) (cit. on pp. 1, 4, 196).
30. Krausz, F. & Ivanov, M. Attosecond physics. *Reviews of Modern Physics* **81,** 163–234 (2009) (cit. on pp. 1, 4, 102, 196).
31. Hassan, M. T., Luu, T. T., Moulet, A., Raskazovskaya, O., Zhokhov, P., Garg, M., Karpowicz, N., Zheltikov, A. M., Pervak, V., Krausz, F. & Goulielmakis, E. Optical attosecond pulses and tracking the nonlinear response of bound electrons. *Nature* **530,** 66–70 (2016) (cit. on pp. 1, 4, 196).
32. Ciappina, M. F., Pérez-Hernández, J. A., Landsman, A. S., Okell, W. A., Zherebtsov, S., Förg, B., Schötz, J., Seiffert, L., Fennel, T., Shaaran, T., Zimmermann, T., Chacón, A., Guichard, R., Zaïr, A., Tisch, J. W. G., Marangos, J. P., Witting, T., Braun, A., Maier, S. A., Roso, L., Krüger, M., Hommelhoff, P., Kling, M. F., Krausz, F. & Lewenstein, M. Attosecond physics at the nanoscale. *Reports on Progress in Physics* **80,** 054401 (2017) (cit. on pp. 1, 4, 196).
33. Vampa, G., Fattahi, H., Vuckovic, J. & Krausz, F. Attosecond nanophotonics. *Nature Photonics* **11,** 210–212 (2017) (cit. on pp. 1, 196).
34. Mittleman, D. *Sensing with Terahertz Radiation* (Springer, Berlin, Heidelberg, 2003) (cit. on pp. 1, 27, 31, 38).
35. Ganichev, S. & Prettl, W. *Intense Terahertz Excitation of Semiconductors* (Oxford University Press, 2005) (cit. on pp. 1, 27, 38).
36. Lee, Y.-S. *Principles of Terahertz Science and Technology* (Springer, Boston, MA, 2008) (cit. on pp. 1, 27, 29, 31, 32, 34–36, 38, 42, 260).
37. Zhang, X.-C. & Xu, J. *Introduction to THz Wave Photonics* (Springer, Boston, MA, 2010) (cit. on pp. 1, 27, 31, 32, 34, 36–38).
38. Schmuttenmaer, C. A. Exploring dynamics in the far-infrared with terahertz spectroscopy. *Chemical Reviews* **104,** 1759–1780 (2004) (cit. on pp. 1, 27, 38, 60).
39. Tonouchi, M. Cutting-edge terahertz technology. *Nature Photonics* **1,** 97–105 (2007) (cit. on pp. 1, 27, 38).
40. Baxter, J. B. & Guglietta, G. W. Terahertz Spectroscopy. *Analytical Chemistry* **83,** 4342–4368 (2011) (cit. on pp. 1, 27, 38).
41. Jepsen, P., Cooke, D. & Koch, M. Terahertz spectroscopy and imaging – Modern techniques and applications. *Laser & Photonics Reviews* **5,** 124–166 (2011) (cit. on pp. 1, 27, 38).
42. Ulbricht, R., Hendry, E., Shan, J., Heinz, T. F. & Bonn, M. Carrier dynamics in semiconductors studied with time-resolved terahertz spectroscopy. *Reviews of Modern Physics* **83,** 543–586 (2011) (cit. on pp. 1, 27, 38).

43. Kampfrath, T., Tanaka, K. & Nelson, K. A. Resonant and nonresonant control over matter and light by intense terahertz transients. *Nature Photonics* **7,** 680–690 (2013) (cit. on pp. 1, 5, 27, 38).
44. Novotny, L. & Hecht, B. *Principles of Nano-Optics* (Cambridge University Press, 2012) (cit. on pp. 2, 152).
45. McGurn, A. *Nanophotonics* (Springer, Cham, 2018) (cit. on p. 2).
46. Haider, M., Uhlemann, S., Schwan, E., Rose, H., Kabius, B. & Urban, K. Electron microscopy image enhanced. *Nature* **392,** 768–769 (1998) (cit. on p. 2).
47. Nellist, P. D., Chisholm, M. F., Dellby, N., Krivanek, O. L., Murfitt, M. F., Szilagyi, Z. S., Lupini, A. R., Borisevich, A., Sides, W. H. & Pennycook, S. J. Direct sub-angstrom imaging of a crystal lattice. *Science* **305,** 1741–1741 (2004) (cit. on p. 2).
48. Zuo, J. M., Vartanyants, I., Gao, M., Zhang, R. & Nagahara, L. A. Atomic resolution imaging of a carbon nanotube from diffraction intensities. *Science* **300,** 1419–1421 (2003) (cit. on p. 2).
49. Kohl, H. & Reimer, L. *Transmission Electron Microscopy* 5th Edition (Springer, New York, NY, 2008) (cit. on p. 2).
50. Giessibl, F. J. Atomic resolution of the silicon (111)-(7×7) surface by atomic force microscopy. *Science* **267,** 68–71 (1995) (cit. on p. 2).
51. Erlandsson, R., Olsson, L. & Mårtensson, P. Inequivalent atoms and imaging mechanisms in ac-mode atomic-force microscopy of Si(111)7×7. *Physical Review B* **54,** R8309–R8312 (1996) (cit. on pp. 2, 87, 98).
52. Uchihashi, T., Sugawara, Y., Tsukamoto, T., Ohta, M., Morita, S. & Suzuki, M. Role of a covalent bonding interaction in noncontact-mode atomic-force microscopy on Si(111)7×7. *Physical Review B* **56,** 9834–9840 (1997) (cit. on pp. 2, 87, 98).
53. Giessibl, F. J., Hembacher, S., Bielefeldt, H. & Mannhart, J. Subatomic features on the silicon (111)-(7×7) surface observed by atomic force microscopy. *Science* **289,** 422–425 (2000) (cit. on pp. 2, 87, 98).
54. Lantz, M. A., Hug, H. J., van Schendel, P. J. A., Hoffmann, R., Martin, S., Baratoff, A., Abdurixit, A., Güntherodt, H.-J. & Gerber, C. Low temperature scanning force microscopy of the Si(111)-(7×7) surface. *Physical Review Letters* **84,** 2642–2645 (2000) (cit. on pp. 2, 87, 98).
55. Eguchi, T. & Hasegawa, Y. High resolution atomic force microscopic imaging of the Si(111)-(7×7) surface: Contribution of short-range force to the images. *Physical Review Letters* **89,** 266105 (2002) (cit. on pp. 2, 87, 98).
56. Tsong, T. T. Field ion image formation. *Surface Science* **70,** 211–233 (1978) (cit. on pp. 2, 73, 174, 175, 186).
57. Kellogg, G. L. Measurement of activation energies for field evaporation of tungsten ions as a function of electric field. *Physical Review B* **29,** 4304–4312 (1984) (cit. on pp. 2, 174, 175, 186).

58. Tsong, T. T. *Atom-Probe Field Ion Microscopy: Field Ion Emission, and Surfaces and Interfaces at Atomic Resolution* (Cambridge University Press, 1990) (cit. on pp. 2, 7, 73, 174, 175).
59. Binnig, G., Rohrer, H., Gerber, C. & Weibel, E. Tunneling through a controllable vacuum gap. *Applied Physics Letters* **40,** 178–180 (1982) (cit. on pp. 2, 7, 15, 53).
60. Binnig, G., Rohrer, H., Gerber, C. & Weibel, E. Surface studies by scanning tunneling microscopy. *Physical Review Letters* **49,** 57–61 (1982) (cit. on pp. 2, 7, 15).
61. Binnig, G., Rohrer, H., Gerber, C. & Weibel, E. 7×7 Reconstruction on Si(111) resolved in real space. *Physical Review Letters* **50,** 120–123 (1983) (cit. on pp. 2, 7, 15, 16).
62. Binnig, G. & Rohrer, H. Nobel Lecture: Scanning tunneling microscopy – from birth to adolescence. *Reviews of Modern Physics* **59,** 615–625 (1987) (cit. on pp. 2, 7).
63. Hallmark, V. M., Chiang, S., Rabolt, J. F., Swalen, J. D. & Wilson, R. J. Observation of atomic corrugation on Au(111) by scanning tunneling microscopy. *Physical Review Letters* **59,** 2879–2882 (1987) (cit. on pp. 2, 16).
64. Güntherodt, H.-J. & Wiesendanger, R. *Scanning Tunneling Microscopy I* (Springer, Berlin, Heidelberg, 1992) (cit. on pp. 2, 20, 22, 96, 120, 127).
65. Wiesendanger, R. *Scanning Probe Microscopy and Spectroscopy: Methods and Applications* (Cambridge University Press, 1994) (cit. on pp. 2, 15, 16, 20, 22, 95, 96, 120, 127, 175, 177).
66. Chen, C. J. *Introduction to Scanning Tunneling Microscopy* 2nd Edition (Oxford University Press, 2008) (cit. on pp. 2, 11, 16, 17, 20, 22, 25, 53, 74, 87, 95, 96, 109, 120, 125, 127, 128).
67. Voigtländer, B. *Scanning Probe Microscopy: Atomic Force Microscopy and Scanning Tunneling Microscopy* (Springer, Berlin, Heidelberg, 2015) (cit. on pp. 2, 9–12, 14, 17, 20, 22, 25, 26, 87, 96, 102, 120, 125, 127, 172, 261).
68. Van der Valk, N. C. J. & Planken, P. C. M. Electro-optic detection of subwavelength terahertz spot sizes in the near field of a metal tip. *Applied Physics Letters* **81,** 1558–1560 (2002) (cit. on pp. 2–4).
69. Chen, H.-T., Kersting, R. & Cho, G. C. Terahertz imaging with nanometer resolution. *Applied Physics Letters* **83,** 3009–3011 (2003) (cit. on pp. 2–4).
70. Chen, H.-T., Kraatz, S., Cho, G. C. & Kersting, R. Identification of a resonant imaging process in apertureless near-field microscopy. *Physical Review Letters* **93,** 267401 (2004) (cit. on pp. 2–4).
71. Wang, K., Mittleman, D. M., van der Valk, N. C. J. & Planken, P. C. M. Antenna effects in terahertz apertureless near-field optical microscopy. *Applied Physics Letters* **85,** 2715–2717 (2004) (cit. on pp. 2–5, 35, 48, 140).

72. Planken, P. C. M. & van der Valk, N. C. J. Spot-size reduction in terahertz apertureless near-field imaging. *Optics Letters* **29,** 2306–2308 (2004) (cit. on pp. 2–5, 48).
73. Buersgens, F., Kersting, R. & Chen, H.-T. Terahertz microscopy of charge carriers in semiconductors. *Applied Physics Letters* **88,** 112115 (2006) (cit. on pp. 2–4).
74. Buersgens, F., Acuna, G., Lang, C. H., Potrebic, S. I., Manus, S. & Kersting, R. Shear force control for a terahertz near field microscope. *Review of Scientific Instruments* **78,** 113701 (2007) (cit. on pp. 2–4).
75. Zhan, H., Astley, V., Hvasta, M., Deibel, J. A., Mittleman, D. M. & Lim, Y.-S. The metal-insulator transition in VO_2 studied using terahertz apertureless near-field microscopy. *Applied Physics Letters* **91,** 162110 (2007) (cit. on pp. 2–4).
76. Von Ribbeck, H.-G., Brehm, M., van der Weide, D., Winnerl, S., Drachenko, O., Helm, M. & Keilmann, F. Spectroscopic THz near-field microscope. *Optics Express* **16,** 3430–3438 (2008) (cit. on pp. 2–4).
77. Moon, K., Park, H., Kim, J., Do, Y., Lee, S., Lee, G., Kang, H. & Han, H. Subsurface nanoimaging by broadband terahertz pulse near-field microscopy. *Nano Letters* **15,** 549–552 (2015) (cit. on pp. 2–4, 129).
78. Eisele, M., Cocker, T. L., Huber, M. A., Plankl, M., Viti, L., Ercolani, D., Sorba, L., Vitiello, M. S. & Huber, R. Ultrafast multi-terahertz nano-spectroscopy with sub-cycle temporal resolution. *Nature Photonics* **8,** 841–845 (2014) (cit. on pp. 2–4).
79. Huber, M. A., Mooshammer, F., Plankl, M., Viti, L., Sandner, F., Kastner, L. Z., Frank, T., Fabian, J., Vitiello, M. S., Cocker, T. L. & Huber, R. Femtosecond photo-switching of interface polaritons in black phosphorus heterostructures. *Nature Nanotechnology* **12,** 207–211 (2016) (cit. on pp. 2–4).
80. Wagner, M., Fei, Z., McLeod, A. S., Rodin, A. S., Bao, W., Iwinski, E. G., Zhao, Z., Goldflam, M., Liu, M., Dominguez, G., Thiemens, M., Fogler, M. M., Castro Neto, A. H., Lau, C. N., Amarie, S., Keilmann, F. & Basov, D. N. Ultrafast and nanoscale plasmonic phenomena in exfoliated graphene revealed by infrared pump–probe nanoscopy. *Nano Letters* **14,** 894–900 (2014) (cit. on pp. 2–4).
81. Wagner, M., McLeod, A. S., Maddox, S. J., Fei, Z., Liu, M., Averitt, R. D., Fogler, M. M., Bank, S. R., Keilmann, F. & Basov, D. N. Ultrafast dynamics of surface plasmons in InAs by time-resolved infrared nanospectroscopy. *Nano Letters* **14,** 4529–4534 (2014) (cit. on pp. 2–4).
82. Ni, G. X., Wang, L., Goldflam, M. D., Wagner, M., Fei, Z., McLeod, A. S., Liu, M. K., Keilmann, F., Özyilmaz, B., Castro Neto, A. H., Hone, J., Fogler, M. M. & Basov, D. N. Ultrafast optical switching of infrared plasmon polaritons in high-mobility graphene. *Nature Photonics* **10,** 244–247 (2016) (cit. on pp. 2–4).

83. Klarskov, P., Kim, H., Colvin, V. L. & Mittleman, D. M. Nanoscale laser terahertz emission microscopy. *ACS Photonics* **4,** 2676–2680 (2017) (cit. on pp. 2, 3, 5, 29, 48).
84. Kravtsov, V., Ulbricht, R., Atkin, J. M. & Raschke, M. B. Plasmonic nanofocused four-wave mixing for femtosecond near-field imaging. *Nature Nanotechnology* **11,** 459–464 (2016) (cit. on pp. 2, 3).
85. Schumacher, Z., Spielhofer, A., Miyahara, Y. & Grutter, P. The limit of time resolution in frequency modulation atomic force microscopy by a pump-probe approach. *Applied Physics Letters* **110,** 053111 (2017) (cit. on pp. 2, 3, 196).
86. Sadewasser, S. & Nicoara, N. Time-Resolved Electrostatic and Kelvin Probe Force Microscopy. *Kelvin Probe Force Microscopy: From Single Charge Detection to Device Characterization,* (eds Sadewasser, S. & Glatzel, T.) pgs 119–143 (Springer, Cham, 2018) (cit. on pp. 2, 3).
87. Hamers, R. J. & Cahill, D. G. Ultrafast time resolution in scanned probe microscopies. *Applied Physics Letters* **57,** 2031–2033 (1990) (cit. on pp. 2, 3, 87).
88. Nunes, G. & Freeman, M. R. Picosecond resolution in scanning tunneling microscopy. *Science* **262,** 1029–1032 (1993) (cit. on pp. 2, 3, 21).
89. Steeves, G. M., Elezzabi, A. Y. & Freeman, M. R. Advances in picosecond scanning tunneling microscopy via junction mixing. *Applied Physics Letters* **70,** 1909–1911 (1997) (cit. on pp. 2, 3).
90. Steeves, G. M., Elezzabi, A. Y., Teshima, R., Said, R. A. & Freeman, M. R. Circuit analysis of an ultrafast junction mixing scanning tunneling microscope. *IEEE Journal of Quantum Electronics* **34,** 1415–1418 (1998) (cit. on pp. 2, 3).
91. Steeves, G. M., Elezzabi, A. Y. & Freeman, M. R. Nanometer-scale imaging with an ultrafast scanning tunneling microscope. *Applied Physics Letters* **72,** 504–506 (1998) (cit. on pp. 2, 3, 21).
92. Khusnatdinov, N. N., Nagle, T. J. & Nunes, G. Ultrafast scanning tunneling microscopy with 1 nm resolution. *Applied Physics Letters* **77,** 4434–4436 (2000) (cit. on pp. 2, 3, 21, 99).
93. Weiss, S., Ogletree, D. F., Botkin, D., Salmeron, M. & Chemla, D. S. Ultrafast scanning probe microscopy. *Applied Physics Letters* **63,** 2567–2569 (1993) (cit. on pp. 2, 3).
94. Weiss, S., Botkin, D., Ogletree, D. F., Salmeron, M. & Chemla, D. S. The ultrafast response of a scanning tunneling microscope. *Physica Status Solidi B* **188,** 343–359 (1993) (cit. on pp. 2, 3).
95. Botkin, D., Glass, J., Chemla, D. S., Ogletree, D. F., Salmeron, M. & Weiss, S. Advances in ultrafast scanning tunneling microscopy. *Applied Physics Letters* **69,** 1321–1323 (1996) (cit. on pp. 2, 3).
96. Groeneveld, R. H. M. & van Kempen, H. The capacitive origin of the picosecond electrical transients detected by a photoconductively gated

scanning tunneling microscope. *Applied Physics Letters* **69,** 2294–2296 (1996) (cit. on pp. 2, 3).
97. Donati, G. P., Rodriguez, G. & Taylor, A. J. Ultrafast, dynamical imaging of surfaces by use of a scanning tunneling microscope with a photoexcited, low-temperature-grown GaAs tip. *Journal of the Optical Society of America B* **17,** 1077–1083 (2000) (cit. on pp. 2, 3).
98. Yarotski, D. A., Averitt, R. D., Negre, N., Crooker, S. A., Taylor, A. J., Donati, G. P., Stintz, A., Lester, L. F. & Malloy, K. J. Ultrafast carrier-relaxation dynamics in self-assembled InAs/GaAs quantum dots. *Journal of the Optical Society of America B* **19,** 1480–1484 (2002) (cit. on pp. 2, 3, 58–60).
99. Feldstein, M. J., Vöhringer, P., Wang, W. & Scherer, N. F. Femtosecond optical spectroscopy and scanning probe microscopy. *The Journal of Physical Chemistry* **100,** 4739–4748 (1996) (cit. on pp. 2–4).
100. Pfeiffer, W., Sattler, F., Vogler, S., Gerber, G., Grand, J.-Y. & Möller, R. Photoelectron emission in femtosecond laser assisted scanning tunneling microscopy. *Applied Physics B* **64,** 265–268 (1997) (cit. on pp. 2–4, 135, 136).
101. Merschdorf, M., Pfeiffer, W., Thon, A. & Gerber, G. Hot electron tunneling in femtosecond laser-assisted scanning tunneling microscopy. *Applied Physics Letters* **81,** 286–288 (2002) (cit. on pp. 2–4, 125).
102. Wu, S. W. & Ho, W. Two-photon-induced hot-electron transfer to a single molecule in a scanning tunneling microscope. *Physical Review B* **82,** 085444 (2010) (cit. on pp. 2–4, 99).
103. Dolocan, A., Acharya, D. P., Zahl, P., Sutter, P. & Camillone, N. Two-color ultrafast photoexcited scanning tunneling microscopy. *The Journal of Physical Chemistry C* **115,** 10033–10043 (2011) (cit. on pp. 2–4).
104. Dey, S., Mirell, D., Perez, A. R., Lee, J. & Apkarian, V. A. Nonlinear femtosecond laser induced scanning tunneling microscopy. *Journal of Chemical Physics* **138,** 154202 (2013) (cit. on pp. 2–4, 99, 125).
105. Yoshida, S., Aizawa, Y., Wang, Z.-h., Oshima, R., Mera, Y., Matsuyama, E., Oigawa, H., Takeuchi, O. & Shigekawa, H. Probing ultrafast spin dynamics with optical pump-probe scanning tunnelling microscopy. *Nature Nanotechnology* **9,** 588–593 (2014) (cit. on pp. 2, 3, 49, 135, 136).
106. Takeuchi, O., Morita, R., Yamashita, M. & Shigekawa, H. Development of time-resolved scanning tunneling microscopy in femtosecond range. *Japanese Journal of Applied Physics* **41,** 4994–4997 (2002) (cit. on pp. 2, 3).
107. Takeuchi, O., Aoyama, M., Oshima, R., Okada, Y., Oigawa, H., Sano, N., Shigekawa, H., Morita, R. & Yamashita, M. Probing subpicosecond dynamics using pulsed laser combined scanning tunneling microscopy. *Applied Physics Letters* **85,** 3268–3270 (2004) (cit. on pp. 2, 3).
108. Terada, Y., Aoyama, M., Kondo, H., Taninaka, A., Takeuchi, O. & Shigekawa, H. Ultrafast photoinduced carrier dynamics in GaNAs probed

using femtosecond time-resolved scanning tunnelling microscopy. *Nanotechnology* **18,** 044028 (2007) (cit. on pp. 2, 3).
109. Terada, Y., Yoshida, S., Takeuchi, O. & Shigekawa, H. Real-space imaging of transient carrier dynamics by nanoscale pump-probe microscopy. *Nature Photonics* **4,** 869–874 (2010) (cit. on pp. 2, 3, 49, 135, 136, 138, 143, 144).
110. Yoshida, S., Yokota, M., Takeuchi, O., Oigawa, H., Mera, Y. & Shigekawa, H. Single-atomic level probe of transient carrier dynamics by laser-combined scanning tunneling microscopy. *Applied Physics Express* **6,** 032401 (2013) (cit. on pp. 2, 3, 49, 135, 136, 138).
111. Yokota, M., Yoshida, S., Mera, Y., Takeuchi, O., Oigawa, H. & Shigekawa, H. Bases for time-resolved probing of transient carrier dynamics by optical pump-probe scanning tunneling microscopy. *Nanoscale* **5,** 9170–9175 (2013) (cit. on pp. 2, 3, 49, 135, 136, 138, 143, 144, 152).
112. Yoshida, S., Terada, Y., Yokota, M., Takeuchi, O., Oigawa, H. & Shigekawa, H. Optical pump-probe scanning tunneling microscopy for probing ultrafast dynamics on the nanoscale. *European Physical Journal Special Topics* **222,** 1161–1175 (2013) (cit. on pp. 2, 3, 49, 135, 136).
113. Kloth, P., Kaiser, K. & Wenderoth, M. Controlling the screening process of a nanoscaled space charge region by minority carriers. *Nature Communications* **7,** 10108 (2016) (cit. on pp. 2, 3, 49, 121, 135, 136, 138, 165).
114. Kloth, P., Thias, T., Bunjes, O., von der Haar, J. & Wenderoth, M. A versatile implementation of pulsed optical excitation in scanning tunneling microscopy. *Review of Scientific Instruments* **87,** 123702 (2016) (cit. on pp. 2, 3, 49, 135, 136, 138).
115. Kloth, P. & Wenderoth, M. From time-resolved atomic-scale imaging of individual donors to their cooperative dynamics. *Science Advances* **3,** e1601552 (2017) (cit. on pp. 2, 3, 49, 121, 135, 136, 152, 165).
116. Swartzentruber, B. S., Smith, A. P. & Jónsson, H. Experimental and theoretical study of the rotation of Si ad-dimers on the Si(100) surface. *Physical Review Letters* **77,** 2518–2521 (1996) (cit. on pp. 2, 3).
117. Van Houselt, A. & Zandvliet, H. J. W. *Colloquium*: Time-resolved scanning tunneling microscopy. *Reviews of Modern Physics* **82,** 1593–1605 (2010) (cit. on pp. 2, 3).
118. Paul, W., Yang, K., Baumann, S., Romming, N., Choi, T., Lutz, C. P. & Heinrich, A. J. Control of the millisecond spin lifetime of an electrically probed atom. *Nature Physics* **13,** 403–407 (2016) (cit. on pp. 2, 3, 38, 171, 196).
119. Baumann, S., Paul, W., Choi, T., Lutz, C. P., Ardavan, A. & Heinrich, A. J. Electron paramagnetic resonance of individual atoms on a surface. *Science* **350,** 417–420 (2015) (cit. on pp. 2–4, 38, 171, 196).
120. Natterer, F. D., Donati, F., Patthey, F. & Brune, H. Thermal and magnetic-field stability of holmium single-atom magnets. *Physical Review Letters* **121,** 027201 (2018) (cit. on pp. 2–4, 38, 171, 172, 196).

121. Loth, S., Etzkorn, M., Lutz, C. P., Eigler, D. M. & Heinrich, A. J. Measurement of fast electron spin relaxation times with atomic resolution. *Science* **329,** 1628–1630 (2010) (cit. on pp. 2–4, 38, 171, 196).
122. Yan, S., Choi, D.-J., Burgess, J. A. J., Rolf-Pissarczyk, S. & Loth, S. Control of quantum magnets by atomic exchange bias. *Nature Nanotechnology* **10,** 40–45 (2015) (cit. on pp. 2–4, 38, 171, 196).
123. Yan, S., Malavolti, L., Burgess, J. A. J., Droghetti, A., Rubio, A. & Loth, S. Nonlocally sensing the magnetic states of nanoscale antiferromagnets with an atomic spin sensor. *Science Advances* **3,** e1603137 (2017) (cit. on pp. 2–4, 38, 171, 196).
124. Rashidi, M., Burgess, J. A. J., Taucer, M., Achal, R., Pitters, J. L., Loth, S. & Wolkow, R. A. Time-resolved single dopant charge dynamics in silicon. *Nature Communications* **7,** 13258 (2016) (cit. on pp. 2–4, 38, 83).
125. Rashidi, M., Taucer, M., Ozfidan, I., Lloyd, E., Koleini, M., Labidi, H., Pitters, J. L., Maciejko, J. & Wolkow, R. A. Time-resolved imaging of negative differential resistance on the atomic scale. *Physical Review Letters* **117,** 276805 (2016) (cit. on pp. 2–4, 38, 83, 171, 196).
126. Rashidi, M., Lloyd, E., Huff, T. R., Achal, R., Taucer, M., Croshaw, J. J. & Wolkow, R. A. Resolving and tuning carrier capture rates at a single silicon atom gap state. *ACS Nano* **11,** 11732–11738 (2017) (cit. on pp. 2–4, 38, 83, 171, 196).
127. Rashidi, M., Vine, W., Burgess, J. A. J., Taucer, M., Achal, R., Pitters, J. L., Loth, S. & Wolkow, R. A. All-electronic nanosecond-resolved scanning tunneling microscopy: Facilitating the investigation of single dopant charge dynamics. *Journal of Visualized Experiments* **131,** e56861 (2018) (cit. on pp. 2–4, 38, 83).
128. Moult, I., Herve, M. & Pennec, Y. Ultrafast spectroscopy with a scanning tunneling microscope. *Applied Physics Letters* **98,** 233103 (2011) (cit. on pp. 2–4).
129. Saunus, C., Raphael Bindel, J., Pratzer, M. & Morgenstern, M. Versatile scanning tunneling microscopy with 120 ps time resolution. *Applied Physics Letters* **102,** 051601 (2013) (cit. on pp. 2–4, 38, 99).
130. Cocker, T. L. *Exploring conductivity in nanomaterials with terahertz pulses* (University of Alberta Dissertation, 2012) (cit. on pp. 2, 3, 5, 6, 40, 43, 49, 196).
131. Cocker, T. L., Jelic, V., Gupta, M., Molesky, S. J., Burgess, J. A. J., Reyes, G. D. L., Titova, L. V., Tsui, Y. Y., Freeman, M. R. & Hegmann, F. A. An ultrafast terahertz scanning tunnelling microscope. *Nature Photonics* **7,** 620–625 (2013) (cit. on pp. 2, 3, 5, 6, 49, 196).
132. Cocker, T. L., Jelic, V., Hoffman, J. R., Gupta, M., Miller, R., Molesky, S. J., Burgess, J. A. J., Reyes, G. D. L., Titova, L. V., Tsui, Y. Y., Freeman, M. R. & Hegmann, F. A. Imaging ultrafast dynamics on the nanoscale with a THz-STM. *Proceedings of SPIE* **8984,** 898411 (2014) (cit. on pp. 2, 3, 196).

133. Jelic, V., Cocker, T. L., Hoffman, J. R., Gupta, M., Miller, R., Molesky, S. J., Burgess, J. A. J., Reyes, G. B. D. L., Titova, L. V., Tsui, Y. Y., Freeman, M. R. & Hegmann, F. A. Ultrafast THz-pulse-induced tunneling dynamics in an STM. *Proceedings of SPIE* **8984,** 898412 (2014) (cit. on pp. 2, 3, 196).
134. Jelic, V., Iwaszczuk, K., Nguyen, P. H., Rathje, C., Hornig, G. J., Sharum, H. M., Hoffman, J. R., Freeman, M. R. & Hegmann, F. A. Ultrafast terahertz control of extreme tunnel currents through single atoms on a silicon surface. *Nature Physics* **13,** 591–598 (2017) (cit. on pp. 2, 3, 6, 196).
135. Cocker, T. L., Peller, D., Yu, P., Repp, J. & Huber, R. Tracking the ultrafast motion of a single molecule by femtosecond orbital imaging. *Nature* **539,** 263–267 (2016) (cit. on pp. 2, 3, 5, 12, 16, 38, 99, 176, 196).
136. Yoshioka, K., Katayama, I., Minami, Y., Kitajima, M., Yoshida, S., Shigekawa, H. & Takeda, J. Real-space coherent manipulation of electrons in a single tunnel junction by single-cycle terahertz electric fields. *Nature Photonics* **10,** 762–765 (2016) (cit. on pp. 2, 3, 5, 21, 26, 196).
137. Yoshioka, K., Katayama, I., Arashida, Y., Ban, A., Kawada, Y., Konishi, K., Takahashi, H. & Takeda, J. Tailoring single-cycle near field in a tunnel junction with carrier-envelope phase-controlled terahertz electric fields. *Nano Letters* **18,** 5198–5204 (2018) (cit. on pp. 2, 3, 5, 21, 80, 140, 196).
138. Rolf-Pissarczyk, S. *Atomically resolved dynamics of correlated quantum systems* (Universität Hamburg Dissertation, 2018) (cit. on pp. 2, 3, 5, 12, 38, 196).
139. Huber, R., Koch, M. & Feldmann, J. Laser-induced thermal expansion of a scanning tunneling microscope tip measured with an atomic force microscope cantilever. *Applied Physics Letters* **73,** 2521–2523 (1998) (cit. on pp. 2, 48, 140).
140. Gerstner, V., Knoll, A., Pfeiffer, W., Thon, A. & Gerber, G. Femtosecond laser assisted scanning tunneling microscopy. *Journal of Applied Physics* **88,** 4851–4859 (2000) (cit. on pp. 2, 48, 125, 140, 151).
141. Gerstner, V., Thon, A. & Pfeiffer, W. Thermal effects in pulsed laser assisted scanning tunneling microscopy. *Journal of Applied Physics* **87,** 2574–2580 (2000) (cit. on pp. 2, 48, 60, 140).
142. Grafström, S. Photoassisted scanning tunneling microscopy. *Journal of Applied Physics* **91,** 1717–1753 (2002) (cit. on pp. 2, 48, 60, 110, 111, 140, 151).
143. Rybka, T., Ludwig, M., Schmalz, M. F., Knittel, V., Brida, D. & Leitenstorfer, A. Sub-cycle optical phase control of nanotunnelling in the single-electron regime. *Nature Photonics* **10,** 667–670 (2016) (cit. on pp. 4, 196).

144. Cerullo, G., Baltuška, A., Mücke, O. D. & Vozzi, C. Few-optical-cycle light pulses with passive carrier-envelope phase stabilization. *Laser & Photonics Reviews* **5,** 323–351 (2011) (cit. on p. 4).
145. Brida, D., Krauss, G., Sell, A. & Leitenstorfer, A. Ultrabroadband Er:fiber lasers. *Laser & Photonics Reviews* **8,** 409–428 (2014) (cit. on p. 4).
146. Büttiker, M. & Landauer, R. Traversal time for tunneling. *Physical Review Letters* **49,** 1739–1742 (1982) (cit. on pp. 4, 7).
147. Nguyen, H. Q., Cutler, P. H., Feuchtwang, T. E., Huang, Z.-H., Kuk, Y., Silverman, P. J., Lucas, A. A. & Sullivan, T. E. Mechanisms of current rectification in an STM tunnel junction and the measurement of an operational tunneling time. *IEEE Transactions on Electron Devices* **36,** 2671–2678 (1989) (cit. on pp. 4, 7).
148. Landauer, R. & Martin, T. Barrier interaction time in tunneling. *Reviews of Modern Physics* **66,** 217–228 (1994) (cit. on pp. 4, 7).
149. Shafir, D., Soifer, H., Bruner, B. D., Dagan, M., Mairesse, Y., Patchkovskii, S., Ivanov, M. Y., Smirnova, O. & Dudovich, N. Resolving the time when an electron exits a tunnelling barrier. *Nature* **485,** 343–346 (2012) (cit. on pp. 4, 7).
150. Février, P. & Gabelli, J. Tunneling time probed by quantum shot noise. *Nature Communications* **9,** 4940 (2018) (cit. on p. 4).
151. Auston, D. H., Cheung, K. P. & Smith, P. R. Picosecond photoconducting Hertzian dipoles. *Applied Physics Letters* **45,** 284–286 (1984) (cit. on pp. 4, 27, 28, 33).
152. Smith, P. R., Auston, D. H. & Nuss, M. C. Subpicosecond photoconducting dipole antennas. *IEEE Journal of Quantum Electronics* **24,** 255–260 (1988) (cit. on pp. 4, 27, 28, 33).
153. Xu, L., Zhang, X. & Auston, D. H. Terahertz beam generation by femtosecond optical pulses in electro-optic materials. *Applied Physics Letters* **61,** 1784–1786 (1992) (cit. on pp. 4, 27, 30).
154. Wu, Q. & Zhang, X. Free-space electro-optic sampling of terahertz beams. *Applied Physics Letters* **67,** 3523–3525 (1995) (cit. on pp. 4, 27, 34, 35).
155. Sun, F. G., Wagoner, G. A. & Zhang, X. Measurement of free-space terahertz pulses via long-lifetime photoconductors. *Applied Physics Letters* **67,** 1656–1658 (1995) (cit. on pp. 4, 27, 28, 33, 34).
156. Jepsen, P. U., Jacobsen, R. H. & Keiding, S. R. Generation and detection of terahertz pulses from biased semiconductor antennas. *Journal of the Optical Society of America B* **13,** 2424–2436 (1996) (cit. on pp. 4, 27, 28, 33).
157. Wimmer, L., Herink, G., Solli, D. R., Yalunin, S. V., Echternkamp, K. E. & Ropers, C. Terahertz control of nanotip photoemission. *Nature Physics* **10,** 432–436 (2014) (cit. on pp. 5, 27).
158. Lange, C., Maag, T., Hohenleutner, M., Baierl, S., Schubert, O., Edwards, E. R. J., Bougeard, D., Woltersdorf, G. & Huber, R. Extremely nonperturbative nonlinearities in GaAs driven by atomically strong ter-

ahertz fields in gold metamaterials. *Physical Review Letters* **113,** 227401 (2014) (cit. on pp. 5, 27, 38, 166).
159. Kang, T., Kim, R. H. J.-Y., Choi, G., Lee, J., Park, H., Jeon, H., Park, C.-H. & Kim, D.-S. Terahertz rectification in ring-shaped quantum barriers. *Nature Communications* **9,** 4914 (2018) (cit. on pp. 5, 27).
160. Herink, G., Wimmer, L. & Ropers, C. Field emission at terahertz frequencies: AC-tunneling and ultrafast carrier dynamics. *New Journal of Physics* **16,** 123005 (2014) (cit. on pp. 5, 27, 38, 125).
161. Iwaszczuk, K., Zalkovskij, M., Strikwerda, A. C. & Jepsen, P. U. Nitrogen plasma formation through terahertz-induced ultrafast electron field emission. *Optica* **2,** 116–123 (2015) (cit. on pp. 5, 27, 38, 125).
162. Yoshioka, K., Minami, Y., Shudo, K., Dao, T. D., Nagao, T., Kitajima, M., Takeda, J. & Katayama, I. Terahertz-field-induced nonlinear electron delocalization in Au nanostructures. *Nano Letters* **15,** 1036–1040 (2015) (cit. on pp. 5, 27, 38, 125).
163. Li, S. & Jones, R. R. High-energy electron emission from metallic nanotips driven by intense single-cycle terahertz pulses. *Nature Communications* **7,** 13405 (2016) (cit. on pp. 5, 27, 38, 125).
164. Mittleman, D. M. Perspective: Terahertz science and technology. *Journal of Applied Physics* **122,** 230901 (2017) (cit. on pp. 5, 27, 38, 125).
165. Wang, K. & Mittleman, D. M. Metal wires for terahertz wave guiding. *Nature* **432,** 376–379 (2004) (cit. on pp. 5, 48, 150).
166. Maier, S. A., Andrews, S. R., Martín-Moreno, L. & García-Vidal, F. J. Terahertz surface plasmon-polariton propagation and focusing on periodically corrugated metal wires. *Physical Review Letters* **97,** 176805 (2006) (cit. on p. 5).
167. Wang, K. & Mittleman, D. M. Dispersion of surface plasmon polaritons on metal wires in the terahertz frequency range. *Physical Review Letters* **96,** 157401 (2006) (cit. on pp. 5, 150).
168. Deibel, J. A., Wang, K., Escarra, M., Berndsen, N. & Mittleman, D. M. The excitation and emission of terahertz surface plasmon polaritons on metal wire waveguides. *Comptes Rendus Physique* **9,** 215–231 (2008) (cit. on pp. 5, 48, 55, 104).
169. Walther, M., Chambers, G. S., Liu, Z., Freeman, M. R. & Hegmann, F. A. Emission and detection of terahertz pulses from a metal-tip antenna. *Journal of the Optical Society of America B* **22,** 2357–2365 (2005) (cit. on pp. 5, 48).
170. Adam, A. J., van der Valk, N. C. & Planken, P. C. Measurement and calculation of the near field of a terahertz apertureless scanning optical microscope. *Journal of the Optical Society of America B* **24,** 1080–1090 (2007) (cit. on pp. 5, 48).
171. Astley, V., Mendis, R. & Mittleman, D. M. Characterization of terahertz field confinement at the end of a tapered metal wire waveguide. *Applied Physics Letters* **95,** 031104 (2009) (cit. on p. 5).

172. Fowler, R. H. & Nordheim, L. Electron emission in intense electric fields. *Proceedings of the Royal Society of London A* **119,** 173–181 (1928) (cit. on pp. 7, 76).
173. Zener, C. A theory of the electrical breakdown of solid dielectrics. *Proceedings of the Royal Society of London A* **145,** 523–529 (1934) (cit. on p. 7).
174. Müller, E. W. Elektronenmikroskopische beobachtungen von feldkathoden. *Zeitschrift für Physik* **106,** 541–550 (1937) (cit. on p. 7).
175. Bardeen, J. Tunnelling from a many-particle point of view. *Physical Review Letters* **6,** 57–59 (1961) (cit. on pp. 7, 25).
176. Young, R., Ward, J. & Scire, F. Observation of metal-vacuum-metal tunneling, field emission, and the transition region. *Physical Review Letters* **27,** 922–924 (1971) (cit. on p. 7).
177. Gamow, G. Zur auantentheorie des qtomkernes. *Zeitschrift für Physik* **51,** 204–212 (1928) (cit. on p. 7).
178. Hawking, S. W. Black hole explosions? *Nature* **248,** 30–31 (1974) (cit. on p. 7).
179. Vault, D. D. & Chance, B. Studies of photosynthesis using a pulsed laser: Temperature dependence of cytochrome oxidation rate in *Chromatium*, evidence for tunneling. *Biophysical Journal* **6,** 825–847 (1966) (cit. on p. 7).
180. Young, R., Ward, J. & Scire, F. The topografiner: An instrument for measuring surface microtopography. *Review of Scientific Instruments* **43,** 999–1011 (1972) (cit. on p. 7).
181. Jelic, V. & Marsiglio, F. The double-well potential in quantum mechanics: a simple, numerically exact formulation. *European Journal of Physics* **33,** 1651–1666 (2012) (cit. on p. 10).
182. Haynes, W. M. *CRC Handbook of Chemistry and Physics* 99th Edition (Taylor & Francis, 2018) (cit. on pp. 11, 22).
183. Repp, J., Meyer, G., Stojković, S. M., Gourdon, A. & Joachim, C. Molecules on insulating films: scanning-tunneling microscopy imaging of individual molecular orbitals. *Physical Review Letters* **94,** 026803 (2005) (cit. on pp. 12, 16, 176).
184. Liljeroth, P., Repp, J. & Meyer, G. Current-induced hydrogen tautomerization and conductance switching of naphthalocyanine molecules. *Science* **317,** 1203–1206 (2007) (cit. on pp. 12, 16, 176–178, 187, 188, 196).
185. Schulz, F., Ijäs, M., Drost, R., Hämäläinen, S. K., Harju, A., Seitsonen, A. P. & Liljeroth, P. Many-body transitions in a single molecule visualized by scanning tunnelling microscopy. *Nature Physics* **11,** 229–234 (2015) (cit. on pp. 12, 16, 176, 196).
186. Kalff, F. E., Rebergen, M. P., Fahrenfort, E., Girovsky, J., Toskovic, R., Lado, J. L., Fernández-Rossier, J. & Otte, A. F. A kilobyte rewritable atomic memory. *Nature Nanotechnology* **11,** 926–929 (2016) (cit. on pp. 12, 172, 177).

187. Drost, R., Ojanen, T., Harju, A. & Liljeroth, P. Topological states in engineered atomic lattices. *Nature Physics* **13,** 668–671 (2017) (cit. on pp. 12, 177, 196).
188. Achal, R., Rashidi, M., Croshaw, J., Churchill, D., Taucer, M., Huff, T., Cloutier, M., Pitters, J. & Wolkow, R. A. Lithography for robust and editable atomic-scale silicon devices and memories. *Nature Communications* **9,** 2778 (2018) (cit. on pp. 12, 83, 172, 196).
189. Feenstra, R. M. Tunneling spectroscopy of the (110) surface of direct-gap III-V semiconductors. *Physical Review B* **50,** 4561–4570 (1994) (cit. on pp. 13, 135).
190. Koslowski, B., Dietrich, C., Tschetschetkin, A. & Ziemann, P. Evaluation of scanning tunneling spectroscopy data: Approaching a quantitative determination of the electronic density of states. *Physical Review B* **75,** 035421 (2007) (cit. on p. 14).
191. Koslowski, B., Pfeifer, H. & Ziemann, P. Deconvolution of the electronic density of states of tip and sample from scanning tunneling spectroscopy data: Proof of principle. *Physical Review B* **80,** 165419 (2009) (cit. on p. 14).
192. Passoni, M., Donati, F., Li Bassi, A., Casari, C. S. & Bottani, C. E. Recovery of local density of states using scanning tunneling spectroscopy. *Physical Review B* **79,** 045404 (2009) (cit. on p. 14).
193. Naydenov, B. & Boland, J. J. Variable-height scanning tunneling spectroscopy for local density of states recovery based on the one-dimensional WKB approximation. *Physical Review B* **82,** 245411 (2010) (cit. on p. 14).
194. De Vries, R. J., Saedi, A., Kockmann, D., van Houselt, A., Poelsema, B. & Zandvliet, H. J. W. Spatial mapping of the inverse decay length using scanning tunneling microscopy. *Applied Physics Letters* **92,** 174101 (2008) (cit. on pp. 14, 95).
195. Albrecht, F., Fleischmann, M., Scheer, M., Gross, L. & Repp, J. Local tunneling decay length and Kelvin probe force spectroscopy. *Physical Review B* **92,** 235443 (2015) (cit. on pp. 15, 16, 176).
196. Ziegler, M., Néel, N., Sperl, A., Kröger, J. & Berndt, R. Local density of states from constant-current tunneling spectra. *Physical Review B* **80,** 125402 (2009) (cit. on p. 15).
197. Pronschinske, A., Mardit, D. J. & Dougherty, D. B. Modeling the constant-current distance-voltage mode of scanning tunneling spectroscopy. *Physical Review B* **84,** 205427 (2011) (cit. on p. 15).
198. Hellenthal, C., Heimbuch, R., Sotthewes, K., Kooij, E. S. & Zandvliet, H. J. W. Determining the local density of states in the constant current STM mode. *Physical Review B* **88,** 035425 (2013) (cit. on p. 15).
199. Becker, R. S., Golovchenko, J. A. & Swartzentruber, B. S. Electron interferometry at crystal surfaces. *Physical Review Letters* **55,** 987–990 (1985) (cit. on p. 15).

200. Binnig, G., Rohrer, H., Gerber, C. & Weibel, E. (111) facets as the origin of reconstructed Au(110) surfaces. *Surface Science Letters* **131,** L379–L384 (1983) (cit. on p. 15).
201. Chen, C. J. Origin of atomic resolution on metal surfaces in scanning tunneling microscopy. *Physical Review Letters* **65,** 448–451 (1990) (cit. on p. 16).
202. Wintterlin, J., Wiechers, J., Brune, H., Gritsch, T., Höfer, H. & Behm, R. J. Atomic-resolution imaging of close-packed metal surfaces by scanning tunneling microscopy. *Physical Review Letters* **62,** 59–62 (1989) (cit. on pp. 16, 175).
203. Binnig, G. & Rohrer, H. Scanning tunneling microscopy. *Helvetica Physica Acta* **55,** 726–735 (1982) (cit. on p. 16).
204. Becker, R. S., Golovchenko, J. A. & Swartzentruber, B. S. Atomic-scale surface modifications using a tunnelling microscope. *Nature* **325,** 419–421 (1987) (cit. on pp. 16, 171, 175).
205. Barth, J. V., Brune, H., Ertl, G. & Behm, R. J. Scanning tunneling microscopy observations on the reconstructed Au(111) surface: Atomic structure, long-range superstructure, rotational domains, and surface defects. *Physical Review B* **42,** 9307–9318 (1990) (cit. on pp. 16, 88, 176).
206. Meyer, G., Moresco, F., Hla, S. W., Repp, J., Braun, K.-F., Fölsch, S. & Rieder, K. H. Manipulation of atoms and molecules with the low-temperature scanning tunneling microscope. *Japanese Journal of Applied Physics* **40,** 4409–4413 (2001) (cit. on pp. 16, 172).
207. Bartels, L., Meyer, G. & Rieder, K.-H. Basic steps of lateral manipulation of single atoms and diatomic clusters with a scanning tunneling microscope tip. *Physical Review Letters* **79,** 697–700 (1997) (cit. on pp. 16, 172).
208. Bartels, L., Meyer, G., Rieder, K.-H., Velic, D., Knoesel, E., Hotzel, A., Wolf, M. & Ertl, G. Dynamics of electron-induced manipulation of individual CO molecules on Cu(111). *Physical Review Letters* **80,** 2004–2007 (1998) (cit. on pp. 16, 172).
209. Heinrich, A. J., Lutz, C. P., Gupta, J. A. & Eigler, D. M. Molecule cascades. *Science* **298,** 1381–1387 (2002) (cit. on pp. 16, 172, 196).
210. Feng, M., Zhao, J. & Petek, H. Atomlike, hollow-core–bound molecular orbitals of C_{60}. *Science* **320,** 359–362 (2008) (cit. on pp. 16, 176).
211. Swart, I., Sonnleitner, T., Niedenführ, J. & Repp, J. Controlled lateral manipulation of molecules on insulating films by STM. *Nano Letters* **12,** 1070–1074 (2012) (cit. on pp. 16, 172, 176, 196).
212. Kuhnke, K., Große, C., Merino, P. & Kern, K. Atomic-scale imaging and spectroscopy of electroluminescence at molecular interfaces. *Chemical Reviews* **117,** 5174–5222 (2017) (cit. on pp. 16, 73, 176, 196).
213. Zhang, L., Yu, Y.-J., Chen, L.-G., Luo, Y., Yang, B., Kong, F.-F., Chen, G., Zhang, Y., Zhang, Q., Luo, Y., Yang, J.-L., Dong, Z.-C. & Hou, J. G. Electrically driven single-photon emission from an isolated single

molecule. *Nature Communications* **8,** 580 (2017) (cit. on pp. 16, 73, 176, 196).
214. Chen, C. J. Tunneling matrix elements in three-dimensional space: The derivative rule and the sum rule. *Physical Review B* **42,** 8841–8857 (1990) (cit. on p. 16).
215. Chen, C. J. Microscopic view of scanning tunneling microscopy. *Journal of Vacuum Science & Technology A* **9,** 44–50 (1991) (cit. on pp. 16, 95, 96).
216. Pelz, J. P. Tip-related electronic artifacts in scanning tunneling spectroscopy. *Physical Review B* **43,** 6746–6749 (1991) (cit. on p. 17).
217. Chen, C. J. Effects of $m \neq 0$ tip states in scanning tunneling microscopy: The explanations of corrugation reversal. *Physical Review Letters* **69,** 1656–1659 (1992) (cit. on p. 17).
218. Hamers, R. J., Tromp, R. M. & Demuth, J. E. Surface electronic structure of Si(111)-(7×7) resolved in real space. *Physical Review Letters* **56,** 1972–1975 (1986) (cit. on pp. 20, 87, 94, 98, 113, 120, 172, 182).
219. Hamers, R., Tromp, R. & Demuth, J. Electronic and geometric structure of Si(111)-(7×7) and Si(001) surfaces. *Surface Science* **181,** 346–355 (1987) (cit. on pp. 20, 120).
220. Qian, G.-X. & Chadi, D. J. Si(111)-7×7 surface: Energy-minimization calculation for the dimer–adatom–stacking-fault model. *Physical Review B* **35,** 1288–1293 (1987) (cit. on pp. 21, 87, 97, 98).
221. Štich, I., Payne, M. C., King-Smith, R. D., Lin, J.-S. & Clarke, L. J. *Ab initio* total-energy calculations for extremely large systems: Application to the Takayanagi reconstruction of Si(111). *Physical Review Letters* **68,** 1351–1354 (1992) (cit. on pp. 21, 87, 97, 98).
222. Brommer, K. D., Needels, M., Larson, B. & Joannopoulos, J. D. *Ab initio* theory of the Si(111)-(7×7) surface reconstruction: A challenge for massively parallel computation. *Physical Review Letters* **68,** 1355–1358 (1992) (cit. on pp. 21, 87, 97, 98).
223. Ke, S. H., Uda, T. & Terakura, K. Surface topography of the Si(111)-7×7 reconstruction. *Physical Review B* **62,** 15319–15322 (2000) (cit. on pp. 21, 87, 97, 98).
224. Smeu, M., Guo, H., Ji, W. & Wolkow, R. A. Electronic properties of Si(111)-7×7 and related reconstructions: Density functional theory calculations. *Physical Review B* **85,** 195315 (2012) (cit. on pp. 21, 87, 97, 98).
225. Wang, Y. L., Gao, H.-J., Guo, H. M., Liu, H. W., Batyrev, I. G., McMahon, W. E. & Zhang, S. B. Tip size effect on the appearance of a STM image for complex surfaces: Theory versus experiment for Si(111)-(7×7). *Physical Review B* **70,** 073312 (2004) (cit. on pp. 21, 87, 98).
226. Paz, Ó., Brihuega, I., Gómez-Rodríguez, J. M. & Soler, J. M. Tip and surface determination from experiments and simulations of scanning tunneling microscopy and spectroscopy. *Physical Review Letters* **94,** 056103 (2005) (cit. on pp. 21, 87, 98).

227. Duan, X., Peressi, M. & Baroni, S. Characterization of Si-doped GaAs cross-sectional surfaces via *ab initio* simulations. *Physical Review B* **72,** 085341 (2005) (cit. on pp. 21, 135, 159, 160).
228. Simmons, J. G. Generalized formula for the electric tunnel effect between similar electrodes separated by a thin insulating film. *Journal of Applied Physics* **34,** 1793–1803 (1963) (cit. on pp. 21–24, 51).
229. Simmons, J. G. Electric tunnel effect between dissimilar electrodes separated by a thin insulating film. *Journal of Applied Physics* **34,** 2581–2590 (1963) (cit. on pp. 21–24, 51).
230. Bâldea, I. & Köppel, H. Transition voltage spectroscopy in vacuum break junction: The standard tunneling barrier model and beyond. *Physica Status Solidi B* **249,** 1791–1804 (2012) (cit. on pp. 21–24, 51).
231. Gottlieb, A. D. & Wesoloski, L. Bardeen's tunnelling theory as applied to scanning tunnelling microscopy: a technical guide to the traditional interpretation. *Nanotechnology* **17,** R57–R65 (2006) (cit. on p. 25).
232. Zhang, P. Scaling for quantum tunneling current in nano- and subnanoscale plasmonic junctions. *Scientific Reports* **5,** 9826 (2015) (cit. on p. 26).
233. Esat, T., Friedrich, N., Tautz, F. S. & Temirov, R. A standing molecule as a single-electron field emitter. *Nature* **558,** 573–576 (2018) (cit. on pp. 26, 196).
234. Cook, D. J. & Hochstrasser, R. M. Intense terahertz pulses by four-wave rectification in air. *Optics Letters* **25,** 1210–1212 (2000) (cit. on pp. 27, 31, 32).
235. Kress, M., Löffler, T., Eden, S., Thomson, M. & Roskos, H. G. Terahertz-pulse generation by photoionization of air with laser pulses composed of both fundamental and second-harmonic waves. *Optics Letters* **29,** 1120–1122 (2004) (cit. on pp. 27, 31, 32).
236. Xie, X., Dai, J. & Zhang, X.-C. Coherent control of THz wave generation in ambient air. *Physical Review Letters* **96,** 075005 (2006) (cit. on pp. 27, 31, 32).
237. Lu, X. & Zhang, X.-C. Generation of elliptically polarized terahertz waves from laser-induced plasma with double helix electrodes. *Physical Review Letters* **108,** 123903 (2012) (cit. on pp. 27, 31, 32).
238. Klarskov, P., Strikwerda, A. C., Iwaszczuk, K. & Jepsen, P. U. Experimental three-dimensional beam profiling and modeling of a terahertz beam generated from a two-color air plasma. *New Journal of Physics* **15,** 075012 (2013) (cit. on pp. 27, 31).
239. Zhang, Z., Chen, Y., Cui, S., He, F., Chen, M., Zhang, Z., Yu, J., Chen, L., Sheng, Z. & Zhang, J. Manipulation of polarizations for broadband terahertz waves emitted from laser plasma filaments. *Nature Photonics* **12,** 554–559 (2018) (cit. on pp. 27, 31).
240. Yeh, K.-L., Hoffmann, M. C., Hebling, J. & Nelson, K. A. Generation of 10 µJ ultrashort terahertz pulses by optical rectification. *Applied Physics Letters* **90,** 171121 (2007) (cit. on pp. 27, 30, 34, 35).

241. Hirori, H., Doi, A., Blanchard, F. & Tanaka, K. Single-cycle terahertz pulses with amplitudes exceeding 1 MV/cm generated by optical rectification in $LiNbO_3$. *Applied Physics Letters* **98,** 091106 (2011) (cit. on pp. 27, 30, 34–36).
242. Hoffmann, M. C., Yeh, K.-L., Hebling, J. & Nelson, K. A. Efficient terahertz generation by optical rectification at 1035 nm. *Optics Express* **15,** 11706–11713 (2007) (cit. on pp. 27, 30).
243. Blanchard, F., Razzari, L., Bandulet, H.-C., Sharma, G., Morandotti, R., Kieffer, J.-C., Ozaki, T., Reid, M., Tiedje, H. F., Haugen, H. K. & Hegmann, F. A. Generation of 1.5 µJ single-cycle terahertz pulses by optical rectification from a large aperture ZnTe crystal. *Optics Express* **15,** 13212–13220 (2007) (cit. on pp. 27, 30, 34, 35).
244. Beck, M., Schäfer, H., Klatt, G., Demsar, J., Winnerl, S., Helm, M. & Dekorsy, T. Impulsive terahertz radiation with high electric fields from an amplifier-driven large-area photoconductive antenna. *Optics Express* **18,** 9251–9257 (2010) (cit. on pp. 27, 28, 34, 35, 70).
245. Seifert, T., Jaiswal, S., Martens, U., Hannegan, J., Braun, L., Maldonado, P., Freimuth, F., Kronenberg, A., Henrizi, J., Radu, I., Beaurepaire, E., Mokrousov, Y., Oppeneer, P. M., Jourdan, M., Jakob, G., Turchinovich, D., Hayden, L. M., Wolf, M., Münzenberg, M., Kläui, M. & Kampfrath, T. Efficient metallic spintronic emitters of ultrabroadband terahertz radiation. *Nature Photonics* **10,** 483–488 (2016) (cit. on pp. 27, 35).
246. Kübler, C., Huber, R., Tübel, S. & Leitenstorfer, A. Ultrabroadband detection of multi-terahertz field transients with GaSe electro-optic sensors: Approaching the near infrared. *Applied Physics Letters* **85,** 3360–3362 (2004) (cit. on pp. 27, 30, 34).
247. Sell, A., Leitenstorfer, A. & Huber, R. Phase-locked generation and field-resolved detection of widely tunable terahertz pulses with amplitudes exceeding 100 MV/cm. *Optics Letters* **33,** 2767–2769 (2008) (cit. on pp. 27, 30, 34, 35).
248. Junginger, F., Sell, A., Schubert, O., Mayer, B., Brida, D., Marangoni, M., Cerullo, G., Leitenstorfer, A. & Huber, R. Single-cycle multiterahertz transients with peak fields above 10 MV/cm. *Optics Letters* **35,** 2645–2647 (2010) (cit. on pp. 27, 30, 34, 35, 196).
249. Yardimci, N. T. & Jarrahi, M. Nanostructure-enhanced photoconductive terahertz emission and detection. *Small* **14,** 1802437 (2018) (cit. on pp. 27, 28).
250. Lu, Z. G., Campbell, P. & Zhang, X.-C. Free-space electro-optic sampling with a high-repetition-rate regenerative amplified laser. *Applied Physics Letters* **71,** 593–595 (1997) (cit. on pp. 27, 28, 34, 35).
251. Wu, Q. & Zhang, X.-C. Free-space electro-optics sampling of mid-infrared pulses. *Applied Physics Letters* **71,** 1285–1286 (1997) (cit. on pp. 27, 30, 34, 35).

252. Dai, J., Xie, X. & Zhang, X.-C. Detection of broadband terahertz waves with a laser-induced plasma in gases. *Physical Review Letters* **97,** 103903 (2006) (cit. on pp. 27, 36).
253. Karpowicz, N., Dai, J., Lu, X., Chen, Y., Yamaguchi, M., Zhao, H., Zhang, X.-C., Zhang, L., Zhang, C., Price-Gallagher, M., Fletcher, C., Mamer, O., Lesimple, A. & Johnson, K. Coherent heterodyne time-domain spectrometry covering the entire "terahertz gap". *Applied Physics Letters* **92,** 011131 (2008) (cit. on pp. 27, 36, 37).
254. Lu, X. & Zhang, X.-C. Balanced terahertz wave air-biased-coherent-detection. *Applied Physics Letters* **98,** 151111 (2011) (cit. on pp. 27, 36, 37).
255. Castro-Camus, E., Fu, L., Lloyd-Hughes, J., Tan, H. H., Jagadish, C. & Johnston, M. B. Photoconductive response correction for detectors of terahertz radiation. *Journal of Applied Physics* **104,** 053113 (2008) (cit. on pp. 27, 28, 33, 34).
256. Van Exter, M., Fattinger, C. & Grischkowsky, D. Terahertz time-domain spectroscopy of water vapor. *Optics Letters* **14,** 1128–1130 (1989) (cit. on pp. 27, 28).
257. Beard, M. C., Turner, G. M. & Schmuttenmaer, C. A. Transient photoconductivity in GaAs as measured by time-resolved terahertz spectroscopy. *Physical Review B* **62,** 15764–15777 (2000) (cit. on pp. 27, 60, 138, 143).
258. Beard, M. C., Turner, G. M. & Schmuttenmaer, C. A. Subpicosecond carrier dynamics in low-temperature grown GaAs as measured by time-resolved terahertz spectroscopy. *Journal of Applied Physics* **90,** 5915–5923 (2001) (cit. on pp. 27, 34, 138, 143).
259. Tonouchi, M., Kawasaki, N., Yoshimura, T., Wald, H. & Seidel, P. Pump and probe terahertz generation study of ultrafast carrier dynamics in low-temperature grown-GaAs. *Japanese Journal of Applied Physics* **41,** L706–L709 (2002) (cit. on pp. 27, 34, 138, 143).
260. Greene, B. I., Saeta, P. N., Dykaar, D. R., Schmitt-Rink, S. & Chuang, S. L. Far-infrared light generation at semiconductor surfaces and its spectroscopic applications. *IEEE Journal of Quantum Electronics* **28,** 2302–2312 (1992) (cit. on p. 29).
261. Dekorsy, T., Auer, H., Waschke, C., Bakker, H. J., Roskos, H. G., Kurz, H., Wagner, V. & Grosse, P. Emission of submillimeter electromagnetic waves by coherent phonons. *Physical Review Letters* **74,** 738–741 (1995) (cit. on p. 29).
262. Gu, P., Tani, M., Kono, S., Sakai, K. & Zhang, X.-C. Study of terahertz radiation from InAs and InSb. *Journal of Applied Physics* **91,** 5533–5537 (2002) (cit. on pp. 29, 138).
263. Apostolopoulos, V. & Barnes, M. E. THz emitters based on the photo-Dember effect. *Journal of Physics D: Applied Physics* **47,** 374002 (2014) (cit. on p. 29).

264. Grundmann, M. *The Physics of Semiconductors* 3rd Edition (Springer, Cham, 2016) (cit. on pp. 29, 59, 118, 120, 158, 166).
265. Kolner, B. & Bloom, D. Electrooptic sampling in GaAs integrated circuits. *IEEE Journal of Quantum Electronics* **22,** 79–93 (1986) (cit. on p. 34).
266. Valdmanis, J. & Mourou, G. Subpicosecond electrooptic sampling: Principles and applications. *IEEE Journal of Quantum Electronics* **22,** 69–78 (1986) (cit. on p. 34).
267. Keiber, S., Sederberg, S., Schwarz, A., Trubetskov, M., Pervak, V., Krausz, F. & Karpowicz, N. Electro-optic sampling of near-infrared waveforms. *Nature Photonics* **10,** 159–162 (2016) (cit. on pp. 34, 35).
268. Blanchard, F., Doi, A., Tanaka, T. & Tanaka, K. Real-time, subwavelength terahertz imaging. *Annual Review of Materials Research* **43,** 237–259 (2013) (cit. on pp. 35, 260).
269. Rashidi, M. & Wolkow, R. A. Autonomous scanning probe microscopy *in situ* tip conditioning through machine learning. *ACS Nano* **12,** 5185–5189 (2018) (cit. on pp. 38, 83, 172).
270. Dantus, M., Bowman, R. M. & Zewail, A. H. Femtosecond laser observations of molecular vibration and rotation. *Nature* **343,** 737–739 (1990) (cit. on p. 38).
271. Scholes, G. D., Fleming, G. R., Chen, L. X., Aspuru-Guzik, A., Buchleitner, A., Coker, D. F., Engel, G. S., van Grondelle, R., Ishizaki, A., Jonas, D. M., Lundeen, J. S., McCusker, J. K., Mukamel, S., Ogilvie, J. P., Olaya-Castro, A., Ratner, M. A., Spano, F. C., Whaley, K. B. & Zhu, X. Using coherence to enhance function in chemical and biophysical systems. *Nature* **543,** 647–656 (2017) (cit. on p. 38).
272. Bernardi, M., Vigil-Fowler, D., Lischner, J., Neaton, J. B. & Louie, S. G. *Ab initio* study of hot carriers in the first picosecond after sunlight absorption in silicon. *Physical Review Letters* **112,** 257402 (2014) (cit. on p. 38).
273. Reimann, J., Schlauderer, S., Schmid, C. P., Langer, F., Baierl, S., Kokh, K. A., Tereshchenko, O. E., Kimura, A., Lange, C., Güdde, J., Höfer, U. & Huber, R. Subcycle observation of lightwave-driven Dirac currents in a topological surface band. *Nature* **562,** 396–400 (2018) (cit. on pp. 38, 196).
274. Porer, M., Leierseder, U., Ménard, J.-M., Dachraoui, H., Mouchliadis, L., Perakis, I. E., Heinzmann, U., Demsar, J., Rossnagel, K. & Huber, R. Non-thermal separation of electronic and structural orders in a persisting charge density wave. *Nature Materials* **13,** 857–861 (2014) (cit. on pp. 38, 196).
275. Jailaubekov, A. E., Willard, A. P., Tritsch, J. R., Chan, W.-L., Sai, N., Gearba, R., Kaake, L. G., Williams, K. J., Leung, K., Rossky, P. J. & Zhu, X.-Y. Hot charge-transfer excitons set the time limit for charge separation at donor/acceptor interfaces in organic photovoltaics. *Nature Materials* **12,** 66–73 (2012) (cit. on pp. 38, 196).

276. Hong, X., Kim, J., Shi, S.-F., Zhang, Y., Jin, C., Sun, Y., Tongay, S., Wu, J., Zhang, Y. & Wang, F. Ultrafast charge transfer in atomically thin MoS_2/WS_2 heterostructures. *Nature Nanotechnology* **9,** 682–686 (2014) (cit. on pp. 38, 196).
277. Basov, D. N., Fogler, M. M. & García de Abajo, F. J. Polaritons in van der Waals materials. *Science* **354,** aag1992 (2016) (cit. on pp. 38, 196).
278. Baierl, S., Hohenleutner, M., Kampfrath, T., Zvezdin, A. K., Kimel, A. V., Huber, R. & Mikhaylovskiy, R. V. Nonlinear spin control by terahertz-driven anisotropy fields. *Nature Photonics* **10,** 715–718 (2016) (cit. on p. 38).
279. Bragas, A. V., Landi, S. M. & Martíne, O. Laser field enhancement at the scanning tunneling microscope junction measured by optical rectification. *Applied Physics Letters* **72,** 2075–2077 (1998) (cit. on pp. 54, 152).
280. Cooke, D. G., Hegmann, F. A., Mazur, Y. I., Ma, W. Q., Wang, X., Wang, Z. M., Salamo, G. J., Xiao, M., Mishima, T. D. & Johnson, M. B. Anisotropic photoconductivity of InGaAs quantum dot chains measured by terahertz pulse spectroscopy. *Applied Physics Letters* **85,** 3839–3841 (2004) (cit. on pp. 58–60).
281. Liu, H.-Y., Meng, Z.-M., Dai, Q.-F., Wu, L.-J., Guo, Q., Hu, W., Liu, S.-H., Lan, S. & Yang, T. Ultrafast carrier dynamics in undoped and p-doped InAs/GaAs quantum dots characterized by pump-probe reflection measurements. *Journal of Applied Physics* **103,** 083121 (2008) (cit. on pp. 58, 59).
282. Porte, H. P., Uhd Jepsen, P., Daghestani, N., Rafailov, E. U. & Turchinovich, D. Ultrafast release and capture of carriers in InGaAs/GaAs quantum dots observed by time-resolved terahertz spectroscopy. *Applied Physics Letters* **94,** 262104 (2009) (cit. on pp. 58, 59).
283. Grundmann, M., Stier, O. & Bimberg, D. InAs/GaAs pyramidal quantum dots: Strain distribution, optical phonons, and electronic structure. *Physical Review B* **52,** 11969–11981 (1995) (cit. on p. 58).
284. Oura, K., Katayama, M., Zotov, A. V., Lifshits, V. G. & Saranin, A. A. *Surface Science* (Springer, Berlin, Heidelberg, 2003) (cit. on p. 63).
285. Zhang, R., Zhang, Y., Dong, Z. C., Jiang, S., Zhang, C., Chen, L. G., Zhang, L., Liao, Y., Aizpurua, J., Luo, Y., Yang, J. L. & Hou, J. G. Chemical mapping of a single molecule by plasmon-enhanced Raman scattering. *Nature* **498,** 82–86 (2013) (cit. on p. 73).
286. Rezeq, M., Pitters, J. & Wolkow, R. Tungsten nanotip fabrication by spatially controlled field-assisted reaction with nitrogen. *Journal of Chemical Physics* **124,** 204716 (2006) (cit. on pp. 74, 174, 175).
287. Schmucker, S. W., Kumar, N., Abelson, J. R., Daly, S. R., Girolami, G. S., Bischof, M. R., Jaeger, D. L., Reidy, R. F., Gorman, B. P., Alexander, J., Ballard, J. B., Randall, J. N. & Lyding, J. W. Field-directed sputter sharpening for tailored probe materials and atomic-scale lithography. *Nature Communications* **3,** 935 (2012) (cit. on pp. 74, 83).

288. Kim, K.-I., Kim, Y. H., Ogawa, T., Choi, S., Cho, B., Ahn, S. J. & Park, I.-Y. Fabrication of a trimer/single atom tip for gas field ion sources by means of field evaporation without tip heating. *Ultramicroscopy* **192,** 50–56 (2018) (cit. on pp. 74, 174, 175).
289. Suzuki, Y. & Kizuka, T. Single-atom-sharpened tungsten tips: The ultimate finest structures. *Applied Physics Express* **11,** 045201 (2018) (cit. on p. 74).
290. Lee, J., Long, C. J., Yang, H., Xiang, X.-D. & Takeuchi, I. Atomic resolution imaging at 2.5 GHz using near-field microwave microscopy. *Applied Physics Letters* **97,** 183111 (2010) (cit. on pp. 74, 121).
291. Kulawik, M., Nowicki, M., Thielsch, G., Cramer, L., Rust, H.-P., Freund, H.-J., Pearl, T. P. & Weiss, P. S. A double lamellae dropoff etching procedure for tungsten tips attached to tuning fork atomic force microscopy/scanning tunneling microscopy sensors. *Review of Scientific Instruments* **74,** 1027–1030 (2003) (cit. on p. 75).
292. Schoelz, J. K., Xu, P., Barber, S. D., Qi, D., Ackerman, M. L., Basnet, G., Cook, C. T. & Thibado, P. M. High-percentage success method for preparing and pre-evaluating tungsten tips for atomic-resolution scanning tunneling microscopy. *Journal of Vacuum Science & Technology B* **30,** 033201 (2012) (cit. on p. 75).
293. Miller, H. C. Values of Fowler-Nordheim field emission functions: $v(y)$, $t(y)$, and $s(y)$. *Journal of the Franklin Institute* **282,** 382–388 (1966) (cit. on p. 77).
294. Binh, V. T., Garcia, N. & Purcell, S. T. Electron field emission from atom-sources: Fabrication, properties, and applications of nanotips. *Advances in Imaging and Electron Physics* **95,** 63–153 (1996) (cit. on pp. 77, 78).
295. Fursey, G. N. & Glazanov, D. V. Deviations from the Fowler–Nordheim theory and peculiarities of field electron emission from small-scale objects. *Journal of Vacuum Science & Technology B* **16,** 910–915 (1998) (cit. on pp. 77, 78).
296. Yeong, K. S. & Thong, J. T. L. Field-emission properties of ultrathin 5 nm tungsten nanowire. *Journal of Applied Physics* **100,** 114325 (2006) (cit. on pp. 77, 78).
297. Yamada, T. K., Abe, T., Nazriq, N. M. K. & Irisawa, T. Electron-bombarded <110>-oriented tungsten tips for stable tunneling electron emission. *Review of Scientific Instruments* **87,** 033703 (2016) (cit. on p. 78).
298. Musket, R. G., McLean, W., Colemenares, C. A. & Siekhaus, W. J. Atomically Clean Surfaces of Elemental Solids. *Specimen Handling, Preparation, and Treatments in Surface Characterization,* (eds Czanderna, A. W., Powell, C. J., Madey, T. E., Hercules, D. M. & Yates, J. T.) pgs 63–143 (Springer, Boston, MA, 1998) (cit. on pp. 80, 246).
299. Becker, R. S., Higashi, G. S., Chabal, Y. J. & Becker, A. J. Atomic-scale conversion of clean Si(111):H-1×1 to Si(111)-2×1 by electron-

stimulated desorption. *Physical Review Letters* **65,** 1917–1920 (1990) (cit. on pp. 83, 177, 178, 188).
300. Shen, T.-C., Wang, C., Abeln, G. C., Tucker, J. R., Lyding, J. W., Avouris, P. & Walkup, R. E. Atomic-scale desorption through electronic and vibrational excitation mechanisms. *Science* **268,** 1590–1592 (1995) (cit. on pp. 83, 177, 178, 188, 189).
301. Owman, F. & Mårtensson, P. STM study of structural defects on in situ prepared Si(111)1×1-H surfaces. *Surface Science* **324,** 211–225 (1995) (cit. on p. 83).
302. Oura, K., Lifshits, V. G., Saranin, A. A., Zotov, A. V. & Katayama, M. Hydrogen interaction with clean and modified silicon surfaces. *Surface Science Reports* **35,** 1–69 (1999) (cit. on p. 83).
303. Schofield, S. R., Studer, P., Hirjibehedin, C. F., Curson, N. J., Aeppli, G. & Bowler, D. R. Quantum engineering at the silicon surface using dangling bonds. *Nature Communications* **4,** 1649 (2013) (cit. on pp. 83, 121).
304. Wolkow, R. A., Livadaru, L., Pitters, J., Taucer, M., Piva, P., Salomons, M., Cloutier, M. & Martins, B. V. C. Silicon Atomic Quantum Dots Enable Beyond-CMOS Electronics. *Field-Coupled Nanocomputing: Paradigms, Progress, and Perspectives,* (eds Anderson, N. G. & Bhanja, S.) pgs 33–58 (Springer, Berlin, Heidelberg, 2014) (cit. on pp. 83, 172, 190).
305. Taucer, M., Livadaru, L., Piva, P. G., Achal, R., Labidi, H., Pitters, J. L. & Wolkow, R. A. Single-electron dynamics of an atomic silicon quantum dot on the H-Si(100)-(2×1) surface. *Physical Review Letters* **112,** 256801 (2014) (cit. on pp. 83, 121, 171, 190, 196).
306. Huff, T., Labidi, H., Rashidi, M., Achal, R., Livadaru, L., Dienel, T., Pitters, J. & Wolkow, R. A. Binary atomic silicon logic, arXiv:1706.07427v4 (2017) (cit. on pp. 83, 172, 196).
307. Rashidi, M., Vine, W., Dienel, T., Livadaru, L., Retallick, J., Huff, T., Walus, K. & Wolkow, R. A. Initiating and monitoring the evolution of single electrons within atom-defined structures. *Physical Review Letters* **121,** 166801 (2018) (cit. on pp. 83, 171, 172, 196).
308. Matsuda, I., Hirahara, T., Konishi, M., Liu, C., Morikawa, H., D'angelo, M., Hasegawa, S., Okuda, T. & Kinoshita, T. Evolution of Fermi surface by electron filling into a free-electronlike surface state. *Physical Review B* **71,** 235315 (2005) (cit. on pp. 85, 118, 119).
309. Matsuda, I. & Hasegawa, S. Fermiology and transport in metallic monatomic layers on semiconductor surfaces. *Journal of Physics: Condensed Matter* **19,** 355007 (2007) (cit. on pp. 85, 118, 119).
310. Hamers, R. J. & Markert, K. Surface photovoltage on Si(111)-(7×7) probed by optically pumped scanning tunneling microscopy. *Journal of Vacuum Science & Technology A* **8,** 3524–3530 (1990) (cit. on pp. 87, 140).

311. Hasunuma, R., Komeda, T., Mukaida, H. & Tokumoto, H. Atom manipulation on Si(111)-7×7 surface by contact formation of biased scanning tunneling microscope tip: Surface structures and tip current variation with atom removal. *Journal of Vacuum Science & Technology A* **15,** 1482–1487 (1997) (cit. on pp. 87, 88, 175, 177, 178).
312. Heike, S., Watanabe, S., Wada, Y. & Hashizume, T. Electron conduction through surface states of the Si(111)-(7×7) surface. *Physical Review Letters* **81,** 890–893 (1998) (cit. on pp. 87, 121).
313. Mysliveček, J., Stróżecka, A., Steffl, J., Sobotík, P., Ošt'ádal, I. & Voigtländer, B. Structure of the adatom electron band of the Si(111)-7×7 surface. *Physical Review B* **73,** 161302 (2006) (cit. on pp. 87, 108, 110, 111, 118, 121, 135).
314. Modesti, S., Gutzmann, H., Wiebe, J. & Wiesendanger, R. Correction of systematic errors in scanning tunneling spectra on semiconductor surfaces: The energy gap of Si(111)-7×7 at 0.3 K. *Physical Review B* **80,** 125326 (2009) (cit. on pp. 87, 108, 110, 111, 121, 135).
315. Liao, Y. C., Yang, C. K., Wu, T. L., Hwang, I. S., Wu, M. K. & Chi, C. C. Evolution of surface to bulk tunneling spectrum by scanning tunneling microscopy. *Physical Review B* **81,** 195435 (2010) (cit. on pp. 87, 108, 110, 111, 121).
316. Wutscher, T., Weymouth, A. J. & Giessibl, F. J. Localization of the phantom force induced by the tunneling current. *Physical Review B* **85,** 195426 (2012) (cit. on pp. 87, 116).
317. Odobescu, A. B. & Zaitsev-Zotov, S. V. Energy gap revealed by low-temperature scanning–tunnelling spectroscopy of the Si(111)-7×7 surface in illuminated slightly doped crystals. *Journal of Physics: Condensed Matter* **24,** 395003 (2012) (cit. on pp. 87, 121).
318. Martins, B. V. C., Smeu, M., Livadaru, L., Guo, H. & Wolkow, R. A. Conductivity of Si(111)-(7×7): The role of a single atomic step. *Physical Review Letters* **112,** 246802 (2014) (cit. on pp. 87, 110, 111, 117, 119, 196).
319. Just, S., Blab, M., Korte, S., Cherepanov, V., Soltner, H. & Voigtländer, B. Surface and step conductivities on Si(111) surfaces. *Physical Review Letters* **115,** 066801 (2015) (cit. on pp. 87, 110, 111, 117, 119, 196).
320. Lock, D., Rusimova, K. R., Pan, T. L., Palmer, R. E. & Sloan, P. A. Atomically resolved real-space imaging of hot electron dynamics. *Nature Communications* **6,** 8365 (2015) (cit. on pp. 87, 112, 121, 177, 178).
321. Rusimova, K. R., Bannister, N., Harrison, P., Lock, D., Crampin, S., Palmer, R. E. & Sloan, P. A. Initiating and imaging the coherent surface dynamics of charge carriers in real space. *Nature Communications* **7,** 12839 (2016) (cit. on pp. 87, 177, 178).
322. Rusimova, K. R., Purkiss, R. M., Howes, R., Lee, F., Crampin, S. & Sloan, P. A. Regulating the femtosecond excited-state lifetime of a single molecule. *Science* **361,** 1012–1016 (2018) (cit. on pp. 87, 112, 121, 177, 178).

323. Odobescu, A. B., Maizlakh, A. A. & Zaitsev-Zotov, S. V. Electron correlation effects in transport and tunneling spectroscopy of the Si(111)-7×7 surface. *Physical Review B* **92,** 165313 (2015) (cit. on pp. 87, 110).
324. Donati, F., Fratesi, G., Ning, L., Brambilla, A., Trioni, M. I., Li Bassi, A., Casari, C. S. & Passoni, M. Electronic and magnetic properties of bulk Cr tips for scanning tunneling spectroscopy. *Physical Review B* **87,** 235431 (2013) (cit. on pp. 87, 98).
325. Sutter, P., Zahl, P., Sutter, E. & Bernard, J. E. Energy-filtered scanning tunneling microscopy using a semiconductor tip. *Physical Review Letters* **90,** 166101 (2003) (cit. on pp. 87, 98).
326. Nishikawa, O., Tomitori, M. & Iwawaki, F. Atomic configurations of tip apexes and scanning tunnelling microscopy-spectroscopy. *Materials Science and Engineering: B* **8,** 81–97 (1991) (cit. on pp. 87, 98).
327. Chaika, A. N. & Myagkov, A. N. Imaging atomic orbitals in STM experiments on a Si(111)-(7×7) surface. *Chemical Physics Letters* **453,** 217–221 (2008) (cit. on pp. 87, 98).
328. Ortega, J., Flores, F. & Yeyati, A. L. Electron correlation effects in the Si(111)-7×7 surface. *Physical Review B* **58,** 4584–4588 (1998) (cit. on pp. 87, 117, 118).
329. Losio, R., Altmann, K. N. & Himpsel, F. J. Fermi surface of Si(111)7×7. *Physical Review B* **61,** 10845–10853 (2000) (cit. on pp. 87, 117).
330. Tanikawa, T., Yoo, K., Matsuda, I., Hasegawa, S. & Hasegawa, Y. Nonmetallic transport property of the Si(111)7×7 surface. *Physical Review B* **68,** 113303 (2003) (cit. on pp. 87, 110, 111, 117, 119).
331. Barke, I., Zheng, F., Konicek, A. R., Hatch, R. C. & Himpsel, F. J. Electron-phonon interaction at the Si(111)-7×7 surface. *Physical Review Letters* **96,** 216801 (2006) (cit. on pp. 87, 117–119).
332. Mauerer, M., Shumay, I. L., Berthold, W. & Höfer, U. Ultrafast carrier dynamics in Si(111)7×7 dangling bonds probed by time-resolved second-harmonic generation and two-photon photoemission. *Physical Review B* **73,** 245305 (2006) (cit. on pp. 87, 112, 117, 121).
333. Wells, J. W., Kallehauge, J. F., Hansen, T. M. & Hofmann, P. Disentangling surface, bulk, and space-charge-layer conductivity in Si(111)-(7×7). *Physical Review Letters* **97,** 206803 (2006) (cit. on pp. 87, 108, 110, 111, 114, 117).
334. D'angelo, M., Takase, K., Miyata, N., Hirahara, T., Hasegawa, S., Nishide, A., Ogawa, M. & Matsuda, I. Conductivity of the Si(111)7×7 dangling-bond state. *Physical Review B* **79,** 035318 (2009) (cit. on pp. 87, 110, 111, 117–119).
335. Tong, S. Y., Huang, H., Wei, C. M., Packard, W. E., Men, F. K., Glander, G. & Webb, M. B. Low-energy electron diffraction analysis of the Si(111)7×7 structure. *Journal of Vacuum Science & Technology A* **6,** 615–624 (1988) (cit. on pp. 87, 98).
336. Krause, S., Berbil-Bautista, L., Herzog, G., Bode, M. & Wiesendanger, R. Current-induced magnetization switching with a spin-polarized

scanning tunneling microscope. *Science* **317,** 1537–1540 (2007) (cit. on pp. 88, 177).
337. Chen, C. J. & Hamers, R. J. Role of atomic force in tunneling-barrier measurements. *Journal of Vacuum Science & Technology B* **9,** 503–505 (1991) (cit. on p. 95).
338. Feenstra, R., Stroscio, J. A. & Fein, A. Tunneling spectroscopy of the Si(111)2×1 surface. *Surface Science* **181,** 295–306 (1987) (cit. on p. 95).
339. Huber, R., Tauser, F., Brodschelm, A., Bichler, M., Abstreiter, G. & Leitenstorfer, A. How many-particle interactions develop after ultrafast excitation of an electron-hole plasma. *Nature* **414,** 286–289 (2001) (cit. on pp. 101, 155, 156).
340. Peatman, W. C. B., Wood, P. A. D., Porterfield, D., Crowe, T. W. & Rooks, M. J. Quarter-micrometer GaAs Schottky barrier diode with high video responsivity at 118 µm. *Applied Physics Letters* **61,** 294–296 (1992) (cit. on p. 102).
341. Völcker, M., Krieger, W. & Walther, H. Laser-driven scanning tunneling microscope. *Physical Review Letters* **66,** 1717–1720 (1991) (cit. on pp. 102, 196).
342. Keldysh, L. V. Ionization in the field of a strong electromagnetic wave. *Soviet Physics – Journal of Experimental and Theoretical Physics* **20,** 1307–1314 (1965) (cit. on p. 102).
343. Feenstra, R. M. & Stroscio, J. A. Tunneling spectroscopy of the GaAs-(110) surface. *Journal of Vacuum Science & Technology B* **5,** 923–929 (1987) (cit. on pp. 103, 134, 135).
344. Pascual, J. I., Méndez, J., Gómez-Herrero, J., Baró, A. M., García, N. & Binh, V. T. Quantum contact in gold nanostructures by scanning tunneling microscopy. *Physical Review Letters* **71,** 1852–1855 (1993) (cit. on pp. 109, 175, 177).
345. Ohnishi, H., Kondo, Y. & Takayanagi, K. Quantized conductance through individual rows of suspended gold atoms. *Nature* **395,** 780–783 (1998) (cit. on p. 109).
346. Yanson, A. I., Bollinger, G. R., van den Brom, H. E., Agraït, N. & van Ruitenbeek, J. M. Formation and manipulation of a metallic wire of single gold atoms. *Nature* **395,** 783–785 (1998) (cit. on pp. 109, 176, 185).
347. Yoshida, K., Shibata, K. & Hirakawa, K. Terahertz field enhancement and photon-assisted tunneling in single-molecule transistors. *Physical Review Letters* **115,** 138302 (2015) (cit. on p. 117).
348. Baccarani, G. & Ostoja, P. Electron mobility empirically related to the phosphorus concentration in silicon. *Solid-State Electronics* **18,** 579–580 (1975) (cit. on p. 118).
349. Riffe, D. M. Temperature dependence of silicon carrier effective masses with application to femtosecond reflectivity measurements. *Journal of the Optical Society of America B* **19,** 1092–1100 (2002) (cit. on p. 118).

350. Feenstra, R. M., Gaan, S., Meyer, G. & Rieder, K. H. Low-temperature tunneling spectroscopy of Ge(111)c(2×8) surfaces. *Physical Review B* **71,** 125316 (2005) (cit. on p. 121).
351. Piva, P. G., DiLabio, G. A., Livadaru, L. & Wolkow, R. A. Atom-scale surface reactivity mediated by long-ranged equilibrium charge transfer. *Physical Review B* **90,** 155422 (2014) (cit. on pp. 121, 129).
352. Jäger, N. D., Ebert, P., Urban, K., Krause-Rehberg, R. & Weber, E. R. Scanning tunneling microscopy and spectroscopy of semi-insulating GaAs. *Physical Review B* **65,** 195318 (2002) (cit. on pp. 121, 135).
353. Jäger, N. D., Weber, E. R., Urban, K. & Ebert, P. Importance of carrier dynamics and conservation of momentum in atom-selective STM imaging and band gap determination of GaAs(110). *Physical Review B* **67,** 165327 (2003) (cit. on pp. 121, 135, 136, 163).
354. Feenstra, R. M., Meyer, G. & Rieder, K. H. Transport limitations in tunneling spectroscopy of Ge(111)c(2×8) surfaces. *Physical Review B* **69,** 081309 (2004) (cit. on p. 121).
355. Nie, S., Feenstra, R. M., Ke, Y., Devaty, R. P. & Choyke, W. J. Electronic states of chemically treated SiC surfaces. *Journal of Applied Physics* **103,** 013709 (2008) (cit. on p. 121).
356. Feenstra, R. A prospective: Quantitative scanning tunneling spectroscopy of semiconductor surfaces. *Surface Science* **603,** 2841–2844 (2009) (cit. on pp. 121, 169).
357. Mysliveček, J., Dvořák, F., Stróżecka, A. & Voigtländer, B. Scanning tunneling microscopy contrast in lateral Ge-Si nanostructures on Si(111)-$\sqrt{3}\times\sqrt{3}$-Bi. *Physical Review B* **81,** 245427 (2010) (cit. on p. 121).
358. Livadaru, L., Pitters, J., Taucer, M. & Wolkow, R. A. Theory of nonequilibrium single-electron dynamics in STM imaging of dangling bonds on a hydrogenated silicon surface. *Physical Review B* **84,** 205416 (2011) (cit. on p. 121).
359. Jacoboni, C. *Theory of Electron Transport in Semiconductors* (Springer, Berlin, Heidelberg, 2010) (cit. on pp. 121, 156, 166).
360. Al-Naib, I., Sharma, G., Dignam, M. M., Hafez, H., Ibrahim, A., Cooke, D. G., Ozaki, T. & Morandotti, R. Effect of local field enhancement on the nonlinear terahertz response of a silicon-based metamaterial. *Physical Review B* **88,** 195203 (2013) (cit. on p. 125).
361. Tarekegne, A. T., Iwaszczuk, K., Zalkovskij, M., Strikwerda, A. C. & Jepsen, P. U. Impact ionization in high resistivity silicon induced by an intense terahertz field enhanced by an antenna array. *New Journal of Physics* **17,** 043002 (2015) (cit. on p. 125).
362. Teitel, S. L. & Wilkins, J. W. Ballistic transport and velocity overshoot in semiconductors: Part I – uniform field effects. *IEEE Transactions on Electron Devices* **30,** 150–153 (1983) (cit. on pp. 125, 166).
363. Chen, R. Y. & Pan, D. A Monte Carlo study of many-valley effects on the temporal electron transient transport in silicon. *Journal of Applied Physics* **70,** 4938–4945 (1991) (cit. on pp. 125, 166).

364. Yi, W., Stollenwerk, A. & Narayanamurti, V. Ballistic electron microscopy and spectroscopy of metal and semiconductor nanostructures. *Surface Science Reports* **64,** 169–190 (2009) (cit. on p. 128).
365. Pitters, J. L., Piva, P. G. & Wolkow, R. A. Dopant depletion in the near surface region of thermally prepared silicon (100) in UHV. *Journal of Vacuum Science & Technology B* **30,** 021806 (2012) (cit. on pp. 129, 190).
366. Sinthiptharakoon, K., Schofield, S. R., Studer, P., Brázdová, V., Hirjibehedin, C. F., Bowler, D. R. & Curson, N. J. Investigating individual arsenic dopant atoms in silicon using low-temperature scanning tunnelling microscopy. *Journal of Physics: Condensed Matter* **26,** 012001 (2014) (cit. on p. 129).
367. Sakata, T., Takeda, S. N., Ayob, N. I. & Daimon, H. Effect of the flash annealing on the impurity distribution and the electronic structure in the inversion layer. *e-Journal of Surface Science and Nanotechnology* **13,** 75–78 (2015) (cit. on p. 129).
368. Münnich, G. *Cross-sectional scanning probe microscopy on GaAs: Tip-induced band bending, buried acceptors and adsorbed molecules* (Universität Regensburg Dissertation, 2014) (cit. on pp. 134–136).
369. O'Donnell, K. P. & Chen, X. Temperature dependence of semiconductor band gaps. *Applied Physics Letters* **58,** 2924–2926 (1991) (cit. on p. 134).
370. Ishida, N., Sueoka, K. & Feenstra, R. M. Influence of surface states on tunneling spectra of *n*-type GaAs(110) surfaces. *Physical Review B* **80,** 075320 (2009) (cit. on pp. 134–136).
371. Schnedler, M., Dunin-Borkowski, R. E. & Ebert, P. Importance of quantum correction for the quantitative simulation of photoexcited scanning tunneling spectra of semiconductor surfaces. *Physical Review B* **93,** 195444 (2016) (cit. on pp. 134–136, 165, 169).
372. Feenstra, R. M. Electrostatic potential for a hyperbolic probe tip near a semiconductor. *Journal of Vacuum Science & Technology B* **21,** 2080–2088 (2003) (cit. on pp. 135, 169).
373. Schnedler, M., Portz, V., Weidlich, P. H., Dunin-Borkowski, R. E. & Ebert, P. Quantitative description of photoexcited scanning tunneling spectroscopy and its application to the GaAs(110) surface. *Physical Review B* **91,** 235305 (2015) (cit. on pp. 135, 136, 138, 156, 165, 169).
374. Feenstra, R. M., Stroscio, J. A., Tersoff, J. & Fein, A. P. Atom-selective imaging of the GaAs(110) surface. *Physical Review Letters* **58,** 1192–1195 (1987) (cit. on p. 135).
375. Stroscio, J. A., Feenstra, R. M. & Fein, A. P. Local state density and long-range screening of adsorbed oxygen atoms on the GaAs(110) surface. *Physical Review Letters* **58,** 1668–1671 (1987) (cit. on pp. 135, 136).
376. Lengel, G., Weimer, M., Gryko, J. & Allen, R. E. Carrier capture as a mechanism for defect migration at semiconductor surfaces. *Journal of*

Vacuum Science & Technology B **13,** 1144–1149 (1995) (cit. on pp. 135, 159, 192).

377. Lengel, G., Harper, J. & Weimer, M. Charge injection and STM-induced vacancy migration on GaAs(110). *Physical Review Letters* **76,** 4725–4728 (1996) (cit. on pp. 135, 159, 177).
378. Ebert, P., Engels, B., Richard, P., Schroeder, K., Blügel, S., Domke, C., Heinrich, M. & Urban, K. Contribution of surface resonances to scanning tunneling microscopy images: (110) surfaces of III-V semiconductors. *Physical Review Letters* **77,** 2997–3000 (1996) (cit. on pp. 135, 136).
379. Domke, C., Ebert, P., Heinrich, M. & Urban, K. Microscopic identification of the compensation mechanisms in Si-doped GaAs. *Physical Review B* **54,** 10288–10291 (1996) (cit. on pp. 135, 136, 159, 160, 162).
380. Domke, C., Ebert, P. & Urban, K. Atomic-scale properties of the amphoteric dopant Si in GaAs(110) surfaces. *Surface Science* **415,** 285–298 (1998) (cit. on pp. 135, 136).
381. De la Broïse, X., Delerue, C., Lannoo, M., Grandidier, B. & Stiévenard, D. Theory of scanning tunneling microscopy of defects on semiconductor surfaces. *Physical Review B* **61,** 2138–2145 (2000) (cit. on p. 135).
382. Feenstra, R. M., Meyer, G., Moresco, F. & Rieder, K. H. Low-temperature scanning tunneling spectroscopy of *n*-type GaAs(110) surfaces. *Physical Review B* **66,** 165204 (2002) (cit. on pp. 135, 136, 159).
383. Loth, S. *Atomic scale images of acceptors in III–V semiconductors: Band bending, tunneling paths and wave functions* (Universität Göttingen Dissertation, 2008) (cit. on pp. 135, 136, 161).
384. Aloni, S., Nevo, I. & Haase, G. Local Fermi-level pinning at a single adatom (Cs) or vacancy (As) on a GaAs(110) surface. *Physical Review B* **60,** R2165–R2168 (1999) (cit. on pp. 135, 136, 163, 166).
385. Aloni, S., Nevo, I. & Haase, G. Photovoltage imaging of a single As-vacancy at a GaAs(110) surface: Evidence for electron trapping by a charged defect? *The Journal of Chemical Physics* **115,** 1875–1881 (2001) (cit. on pp. 135, 136, 163, 166).
386. Nevo, I., Aloni, S., Cohen, S. R. & Haase, G. The effect of adsorbed oxygen on the surface potential of *n*-GaAs(110). *The Journal of Chemical Physics* **123,** 064705 (2005) (cit. on pp. 135, 136, 159, 162, 163, 166).
387. Yoshida, S., Kanitani, Y., Takeuchi, O. & Shigekawa, H. Probing nanoscale potential modulation by defect-induced gap states on GaAs(110) with light-modulated scanning tunneling spectroscopy. *Applied Physics Letters* **92,** 102105 (2008) (cit. on pp. 135, 136, 138, 152, 159, 163).
388. Yoshida, S., Kanitani, Y., Oshima, R., Okada, Y., Takeuchi, O. & Shigekawa, H. Nanoscale mapping of built-in potential in GaAs p–n junction using light-modulated scanning tunneling microscopy. *Japanese Journal of Applied Physics* **47,** 6117–6120 (2008) (cit. on pp. 135, 136, 138, 152).

389. Dekorsy, T., Pfeifer, T., Kütt, W. & Kurz, H. Subpicosecond carrier transport in GaAs surface-space-charge fields. *Physical Review B* **47,** 3842–3849 (1993) (cit. on p. 136).
390. Aspnes, D. E., Kelso, S. M., Logan, R. A. & Bhat, R. Optical properties of $Al_xGa_{1-x}As$. *Journal of Applied Physics* **60,** 754–767 (1986) (cit. on pp. 139, 153).
391. Clady, R., Tayebjee, M. J. Y., Aliberti, P., König, D., Ekins-Daukes, N. J., Conibeer, G. J., Schmidt, T. W. & Green, M. A. Interplay between the hot phonon effect and intervalley scattering on the cooling rate of hot carriers in GaAs and InP. *Progress in Photovoltaics: Research and Applications* **20,** 82–92 (2012) (cit. on pp. 154, 156).
392. Purschke, D. N., Na, M., Longman, A., Titova, L. V. & Hegmann, F. A. Enhancement of hot-carrier photoluminescence with intense terahertz pulses. *Applied Physics Letters* **112,** 072105 (2018) (cit. on pp. 154, 156, 166).
393. Cada, M., Blazek, D., Pistora, J., Postava, K. & Siroky, P. Theoretical and experimental study of plasmonic effects in heavily doped gallium arsenide and indium phosphide. *Optical Materials Express* **5,** 340–352 (2015) (cit. on p. 155).
394. Cahill, D. G. & Feenstra, R. M. Carrier injection and scanning tunneling microscopy at the Si(111)-2×1 surface. *Journal of Vacuum Science & Technology A* **11,** 792–796 (1993) (cit. on pp. 165, 166).
395. Eigler, D. M. & Schweizer, E. K. Positioning single atoms with a scanning tunnelling microscope. *Nature* **344,** 524–526 (1990) (cit. on pp. 171, 172).
396. Eigler, D. M., Lutz, C. P. & Rudge, W. E. An atomic switch realized with the scanning tunnelling microscope. *Nature* **352,** 600–603 (1991) (cit. on pp. 171, 172, 177, 184, 186).
397. Whitman, L. J., Stroscio, J. A., Dragoset, R. A. & Celotta, R. J. Manipulation of adsorbed atoms and creation of new structures on room-temperature surfaces with a scanning tunneling microscope. *Science* **251,** 1206–1210 (1991) (cit. on pp. 171–173, 185, 192).
398. Lyo, I.-W. & Avouris, P. Field-induced nanometer- to atomic-scale manipulation of silicon surfaces with the STM. *Science* **253,** 173–176 (1991) (cit. on pp. 171, 175, 178, 184, 186).
399. Stroscio, J. A. & Eigler, D. M. Atomic and molecular manipulation with the scanning tunneling microscope. *Science* **254,** 1319–1326 (1991) (cit. on pp. 171, 175, 177, 186).
400. Huang, D., Uchida, H. & Aono, M. Fabrication of atomic-scale structures on Si(111)-7×7 using a scanning tunneling microscope (STM). *Japanese Journal of Applied Physics* **31,** 4501–4503 (1992) (cit. on pp. 171, 175, 176, 178, 184, 186).
401. Aono, M., Kobayashi, A., Grey, F., Uchida, H. & Huang, D.-H. Tip-sample interactions in the scanning tunneling microscope for atomic-

scale structure fabrication. *Japanese Journal of Applied Physics* **32,** 1470–1477 (1993) (cit. on pp. 171, 174, 175, 178, 184, 186).
402. Repp, J., Meyer, G., Olsson, F. E. & Persson, M. Controlling the charge state of individual gold adatoms. *Science* **305,** 493–495 (2004) (cit. on pp. 171, 196).
403. Olsson, F. E., Paavilainen, S., Persson, M., Repp, J. & Meyer, G. Multiple charge states of Ag atoms on ultrathin NaCl films. *Physical Review Letters* **98,** 176803 (2007) (cit. on pp. 171, 196).
404. Natterer, F. D., Yang, K., Paul, W., Willke, P., Choi, T., Greber, T., Heinrich, A. J. & Lutz, C. P. Reading and writing single-atom magnets. *Nature* **543,** 226–228 (2017) (cit. on pp. 171, 172, 196).
405. Hsu, P.-J., Kubetzka, A., Finco, A., Romming, N., von Bergmann, K. & Wiesendanger, R. Electric-field-driven switching of individual magnetic skyrmions. *Nature Nanotechnology* **12,** 123–126 (2016) (cit. on pp. 171, 196).
406. Feynman, R. P. There's plenty of room at the bottom: After-dinner speech on December 29, 1959 at the annual meeting of the American Physical Society at the California Institute of Technology. *Journal of Microelectromechanical Systems* **1,** 60–66 (1992) (cit. on p. 171).
407. Crommie, M. F., Lutz, C. P. & Eigler, D. M. Confinement of electrons to quantum corrals on a metal surface. *Science* **262,** 218–220 (1993) (cit. on p. 172).
408. Heller, E. J., Crommie, M. F., Lutz, C. P. & Eigler, D. M. Scattering and absorption of surface electron waves in quantum corrals. *Nature* **369,** 464–466 (1994) (cit. on p. 172).
409. Crommie, M., Lutz, C., Eigler, D. & Heller, E. Waves on a metal surface and quantum corrals. *Surface Review and Letters* **02,** 127–137 (1995) (cit. on p. 172).
410. Manoharan, H. C., Lutz, C. P. & Eigler, D. M. Quantum mirages formed by coherent projection of electronic structure. *Nature* **403,** 512–515 (2000) (cit. on p. 172).
411. Stroscio, J. A. & Celotta, R. J. Controlling the dynamics of a single atom in lateral atom manipulation. *Science* **306,** 242–247 (2004) (cit. on p. 172).
412. Stróżecka, A., Mysliveček, J. & Voigtländer, B. Scanning tunneling spectroscopy and manipulation of C_{60} on Cu(111). *Applied Physics A* **87,** 475–478 (2007) (cit. on p. 172).
413. Jiang, N., Zhang, Y. Y., Liu, Q., Cheng, Z. H., Deng, Z. T., Du, S. X., Gao, H.-J., Beck, M. J. & Pantelides, S. T. Diffusivity control in molecule-on-metal systems using electric fields. *Nano Letters* **10,** 1184–1188 (2010) (cit. on p. 172).
414. Jo, B. H. & Vook, R. W. In-situ ultra-high vacuum studies of electromigration in copper films. *Thin Solid Films* **262,** 129–134 (1995) (cit. on pp. 172, 176, 177, 185).

415. Choi, Z.-S., Mönig, R. & Thompson, C. V. Activation energy and prefactor for surface electromigration and void drift in Cu interconnects. *Journal of Applied Physics* **102,** 083509 (2007) (cit. on pp. 172, 176, 177, 185, 186).
416. Shockley, W. On the surface states associated with a periodic potential. *Physical Review* **56,** 317–323 (1939) (cit. on p. 172).
417. Tsong, T. T. Effects of an electric field in atomic manipulations. *Physical Review B* **44,** 13703–13710 (1991) (cit. on pp. 172, 174, 175, 185).
418. Chang, C. S., Su, W. B. & Tsong, T. T. Field evaporation between a gold tip and a gold surface in the scanning tunneling microscope configuration. *Physical Review Letters* **72,** 574–577 (1994) (cit. on pp. 172–175, 185).
419. Buckingham, A. D. Permanent and induced molecular moments and long-range intermolecular forces. *Advances in Chemical Physics* **12,** 107–142 (1967) (cit. on pp. 172, 173).
420. Hurst, G. J. B., Dupuis, M. & Clementi, E. *Ab initio* analytic polarizability, first and second hyperpolarizabilities of large conjugated organic molecules: Applications to polyenes C_4H_6 to $C_{22}H_{24}$. *Journal of Chemical Physics* **89,** 385–395 (1988) (cit. on pp. 172, 173).
421. Gomer, R. Theory of field desorption. *Journal of Chemical Physics* **38,** 1613–1629 (1963) (cit. on pp. 174, 185).
422. Gomer, R. Possible mechanisms of atom transfer in scanning tunneling microscopy. *IBM Journal of Research and Development* **30,** 428–430 (1986) (cit. on pp. 174, 175).
423. Avouris, P. & Lyo, I.-W. Probing and inducing surface chemistry with the STM: the reactions of Si(111)-7×7 with H_2O and O_2. *Surface Science* **242,** 1–11 (1991) (cit. on pp. 174, 175, 178, 184, 186).
424. Boland, J. J. Manipulating chlorine atom bonding on the Si(100)-(2×1) surface with the STM. *Science* **262,** 1703–1706 (1993) (cit. on p. 174).
425. Wang, L. & Kreuzer, H. Kinetic theory of field evaporation of metals. *Surface Science* **237,** 337–346 (1990) (cit. on p. 174).
426. Miskovsky, N. M., Wei, C. M. & Tsong, T. T. Field evaporation of silicon in the field ion microscope and scanning tunneling microscope configurations. *Physical Review Letters* **69,** 2427–2430 (1992) (cit. on pp. 174, 175).
427. Miskovsky, N. M. & Tsong, T. T. Field evaporation of gold in single- and double-electrode systems. *Physical Review B* **46,** 2640–2643 (1992) (cit. on pp. 174, 175).
428. Ernst, N. Experimental investigation on field evaporation of singly and doubly charged rhodium. *Surface Science* **87,** 469–482 (1979) (cit. on pp. 174, 175, 186).
429. Karahka, M. & Kreuzer, H. Kinetics of silicon field evaporation. *Materials Characterization* **146,** 319–323 (2018) (cit. on p. 174).
430. Brandon, D. G. On field evaporation. *The Philosophical Magazine* **14,** 803–820 (1966) (cit. on pp. 175, 186).

431. Blavette, D., Bostel, A., Sarrau, J. M., Deconihout, B. & Menand, A. An atom probe for three-dimensional tomography. *Nature* **363,** 432–435 (1993) (cit. on p. 175).
432. Utke, I., Hoffmann, P. & Melngailis, J. Gas-assisted focused electron beam and ion beam processing and fabrication. *Journal of Vacuum Science & Technology B* **26,** 1197–1276 (2008) (cit. on p. 175).
433. Gregor Hlawacek, A. G. *Helium Ion Microscopy* (Springer, Cham, 2016) (cit. on p. 175).
434. Hasegawa, Y. & Avouris, P. Manipulation of the reconstruction of the Au(111) surface with the STM. *Science* **258,** 1763–1765 (1992) (cit. on pp. 175, 176).
435. Nakayama, T., Huang, D.-H. & Aono, M. Extraction, deposition, and displacement of atoms by STM. *Microelectronic Engineering* **32,** 191–201 (1996) (cit. on p. 175).
436. Avouris, P., Lyo, I. & Hasegawa, Y. Scanning tunneling microscope tip–sample interactions: Atomic modification of Si and nanometer Si Schottky diodes. *Journal of Vacuum Science & Technology A* **11,** 1725–1732 (1993) (cit. on pp. 175, 178, 184, 186).
437. Hosoki, S., Hosaka, S. & Hasegawa, T. Surface modification of MoS_2 using an STM. *Applied Surface Science* **60–61,** 643–647 (1992) (cit. on p. 175).
438. Kobayashi, A., Grey, F., Williams, R. S. & Aono, M. Formation of nanometer-scale grooves in silicon with a scanning tunneling microscope. *Science* **259,** 1724–1726 (1993) (cit. on pp. 175, 178).
439. Huang, D. H., Uchida, H. & Aono, M. Deposition and subsequent removal of single Si atoms on the Si(111)-7×7 surface by a scanning tunneling microscope. *Journal of Vacuum Science & Technology B* **12,** 2429–2433 (1994) (cit. on pp. 175, 176, 178, 184, 186, 187).
440. Huang, D. H. & Yamamoto, Y. Manipulating atoms one by one with a scanning tunneling microscope. *Surface Review and Letters* **3,** 1463–1472 (1996) (cit. on pp. 175, 176, 178, 184, 186, 187).
441. Huang, D. H. & Aono, M. Scanning tunneling microscopy fabrication of an Si atom chain. *Surface Science* **386,** 166–168 (1997) (cit. on pp. 175, 176, 178).
442. Huang, D. H. & Aono, M. STM atom manipulation with different material tips. *Journal of Surface Analysis* **4,** 264–267 (1998) (cit. on pp. 175, 176, 178).
443. Mamin, H. J., Guethner, P. H. & Rugar, D. Atomic emission from a gold scanning-tunneling-microscope tip. *Physical Review Letters* **65,** 2418–2421 (1990) (cit. on p. 175).
444. Huang, D. H., Nakayama, T. & Aono, M. Platinum nanodot formation by atomic point contact with a scanning tunneling microscope platinum tip. *Applied Physics Letters* **73,** 3360–3362 (1998) (cit. on p. 175).

445. Lang, N. D. Field-induced transfer of an atom between two closely spaced electrodes. *Physical Review B* **45,** 13599–13606 (1992) (cit. on p. 176).
446. Ralls, K. S., Ralph, D. C. & Buhrman, R. A. Individual-defect electromigration in metal nanobridges. *Physical Review B* **40,** 11561–11570 (1989) (cit. on pp. 176, 177, 185, 186).
447. Lloyd, J. R. & Clement, J. J. Electromigration in copper conductors. *Thin Solid Films* **262,** 135–141 (1995) (cit. on pp. 176, 177, 185).
448. Schindler, G., Steinlesberger, G., Engelhardt, M. & Steinhögl, W. Electrical characterization of copper interconnects with end-of-roadmap feature sizes. *Solid-State Electronics* **47,** 1233–1236 (2003) (cit. on pp. 176, 177, 185).
449. Wong, H.-S. P. & Akinwande, D. *Carbon Nanotube and Graphene Device Physics* (Cambridge University Press, 2010) (cit. on pp. 176, 185).
450. Black, J. R. Electromigration–A brief survey and some recent results. *IEEE Transactions on Electron Devices* **16,** 338–347 (1969) (cit. on p. 177).
451. Walkup, R. E., Newns, D. M. & Avouris, P. Role of multiple inelastic transitions in atom transfer with the scanning tunneling microscope. *Physical Review B* **48,** 1858–1861 (1993) (cit. on pp. 177, 184, 186).
452. Dujardin, G., Walkup, R. E. & Avouris, P. Dissociation of individual molecules with electrons from the tip of a scanning tunneling microscope. *Science* **255,** 1232–1235 (1992) (cit. on pp. 177, 178, 188).
453. Stipe, B. C., Rezaei, M. A., Ho, W., Gao, S., Persson, M. & Lundqvist, B. I. Single-molecule dissociation by tunneling electrons. *Physical Review Letters* **78,** 4410–4413 (1997) (cit. on pp. 177, 178, 188).
454. Komeda, T., Kim, Y., Kawai, M., Persson, B. N. J. & Ueba, H. Lateral hopping of molecules induced by excitation of internal vibration mode. *Science* **295,** 2055–2058 (2002) (cit. on pp. 177, 178, 188).
455. Schulze, G., Franke, K. J., Gagliardi, A., Romano, G., Lin, C. S., Rosa, A. L., Niehaus, T. A., Frauenheim, T., Di Carlo, A., Pecchia, A. & Pascual, J. I. Resonant electron heating and molecular phonon cooling in single C_{60} junctions. *Physical Review Letters* **100,** 136801 (2008) (cit. on pp. 177, 178, 188).
456. Okabayashi, N., Konda, Y. & Komeda, T. Inelastic electron tunneling spectroscopy of an alkanethiol self-assembled monolayer using scanning tunneling microscopy. *Physical Review Letters* **100,** 217801 (2008) (cit. on pp. 177, 178, 188).
457. Staufer, U., Scandella, L. & Wiesendanger, R. Direct writing of nanometer scale structures on glassy metals by the scanning tunneling microscope. *Zeitschrift für Physik B Condensed Matter* **77,** 281–286 (1989) (cit. on pp. 177, 178).
458. Staufer, U., Scandella, L., Rudin, H., Güntherodt, H. & Garçia, N. Tailoring nanostructures with a scanning tunneling microscope. *Journal of*

Vacuum Science & Technology B **9,** 1389–1393 (1991) (cit. on pp. 177, 178).

459. Persson, B. & Demuth, J. Inelastic electron tunnelling from a metal tip. *Solid State Communications* **57,** 769–772 (1986) (cit. on p. 177).
460. Flores, F., Echenique, P. M. & Ritchie, R. H. Energy dissipation processes in scanning tunneling microscopy. *Physical Review B* **34,** 2899–2902 (1986) (cit. on pp. 178, 186).
461. Kyritsakis, A., Veske, M., Eimre, K., Zadin, V. & Djurabekova, F. Thermal runaway of metal nano-tips during intense electron emission. *Journal of Physics D: Applied Physics* **51,** 225203 (2018) (cit. on pp. 178, 186).
462. Alemani, M., Peters, M. V., Hecht, S., Rieder, K.-H., Moresco, F. & Grill, L. Electric field-induced isomerization of azobenzene by STM. *Journal of the American Chemical Society* **128,** 14446–14447 (2006) (cit. on p. 187).
463. Beidenkopf, H., Roushan, P., Seo, J., Gorman, L., Drozdov, I., Hor, Y. S., Cava, R. J. & Yazdani, A. Spatial fluctuations of helical Dirac fermions on the surface of topological insulators. *Nature Physics* **7,** 939–943 (2011) (cit. on p. 196).

Appendix A

Ultrafast Movie of an InAs Nano-Island

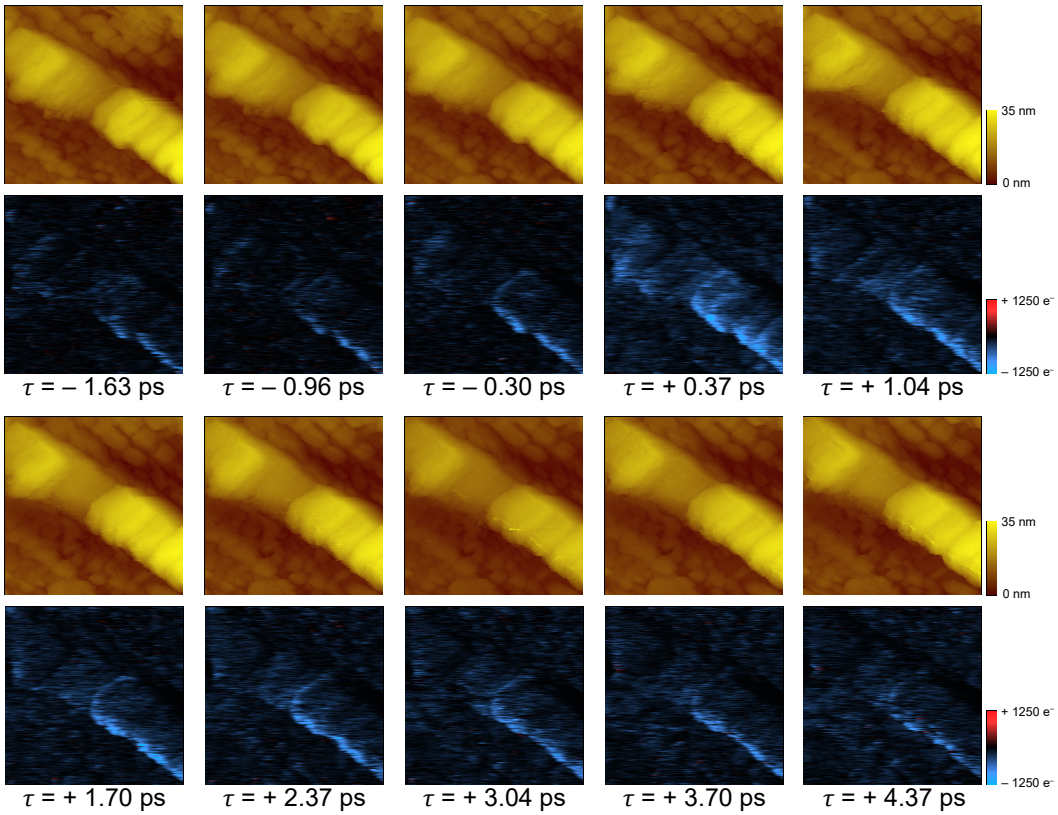

Figure A.1: Ultrafast movie of an InAs nano-island. The STM images (first and third rows) and THz-STM images (second and fourth rows) were acquired with the tip travelling in the right scan direction at $V_{\text{d.c.}} = -2.1$ V, $I_{\text{d.c.}} = -500$ pA, $E_{\text{THz,pk}} = 100$ V/cm and the time delay, $\tau_{\text{Optical–THz}}$, as given below the pairs of images. Image size 400 nm × 400 nm; scan speed 1300 nm/s.

A set of STM images and ultrafast THz-STM images were acquired of a photoexcited InAs nano-island on a GaAs surface (Fig. A.1 and Fig. A.2). The STM and THz-STM images were acquired simultaneously at different time delays between the incident optical and THz pulses, $\tau_{\text{Optical–THz}}$. The data in Fig. A.1 was acquired with the fast scan direction going from left to right, while the data in Fig. A.2 was acquired with the fast scan direction going from right to left. The enhanced THz-pulse-induced current near the edge of the nano-island is an imaging artifact, along with the suppression of the THz-pulse-induced current on the opposite edge of the nano-island for the same scan direction. These effects are due to the fast scan speed of 1300 nm/s, together with the slow feedback loop response time, causing the tip to travel too close to the sample surface while scanning protruding features like the 35 nm tall nano-island. This imaging artifact is clearly evident when comparing between the the two image sets in Fig. A.1 and Fig. A.2, which only differ in their respective scan directions. Nevertheless for both scan directions, there is a strong enhancement of the THz-pulse-induced current that occurs when the THz pulse arrives at the same time as the optical pulse ($\tau = +0.37$ ps).

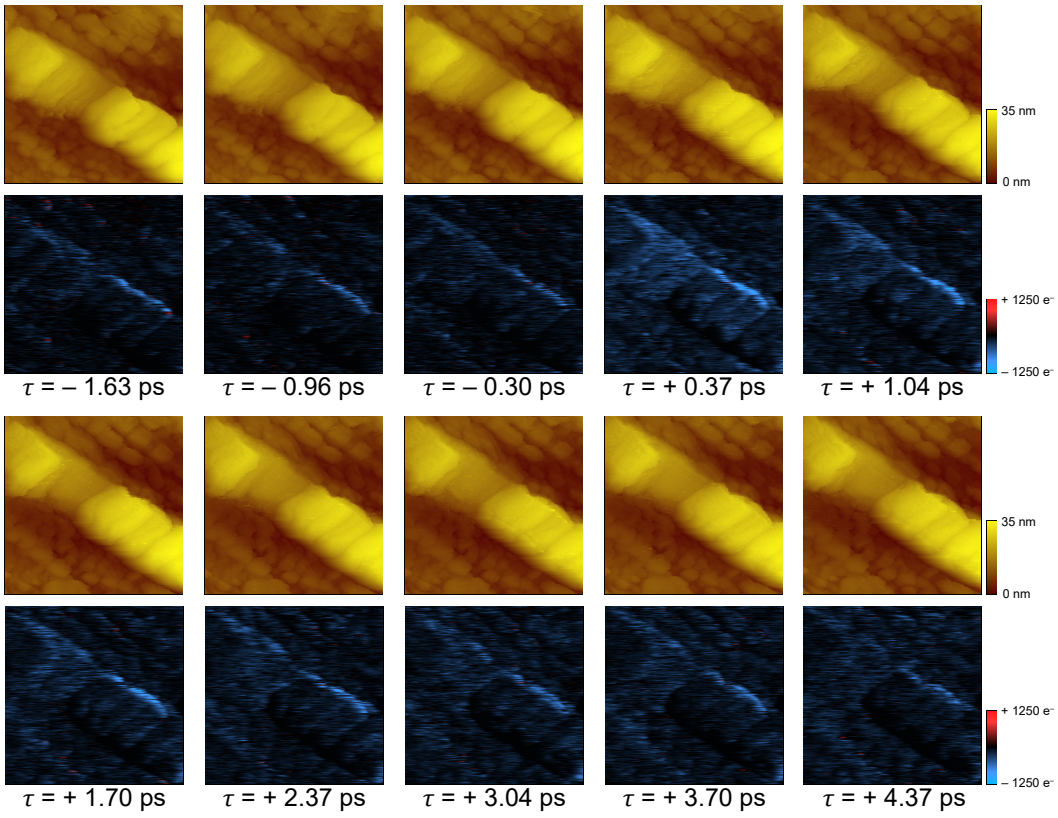

Figure A.2: Ultrafast movie of an InAs nano-island. The STM images (first and third rows) and THz-STM images (second and fourth rows) were acquired with the tip travelling in the left scan direction at $V_{\text{d.c.}} = -2.1$ V, $I_{\text{d.c.}} = -500$ pA, $E_{\text{THz,pk}} = 100$ V/cm and the time delay, $\tau_{\text{Optical–THz}}$, as given below the pairs of images. Image size 400 nm × 400 nm; scan speed 1300 nm/s.

Appendix B

Ultrafast Laser System Details

B.1 RegA Laser

Ultrafast femtosecond laser pulses with a spectral bandwidth of more than 30 nm FWHM are temporally stretched to 10–100 ps by a four-pass grating system (Coherent EC9150) before being injected into the regenerative amplifier cavity (Fig. B.1). The seed pulse is passed through a Faraday Isolator and diffracted into the laser cavity by the SiO_2 'Cavity Dumper' (acousto-optic crystal). The seed pulse, which has a repetition rate of 80 MHz, is amplified inside the cavity for approximately 22 round trips, and then ejected as a few-microjoule pulse at a repetition rate of 250 kHz. The average power of the output beam prior to compression should be more than 2 W. The output pulse is compressed using a four-pass holographic grating that has an efficiency of 60%, generating $\sim$ 6 µJ pulses at 75 fs FWHM. To turn on the laser system, first turn on the chillers, wait 5–10 minutes, and then turn on the Micra and RegA laser systems on their respective controllers.

The RegA cavity occasionally requires re-alignment. The cavity alignment procedure is briefly summarized here (see also the notes by Lyuba Titova and the RegA manual).

1. **Align the RegA cavity**
   Goal: Optimize the cavity alignment by maximizing the power of the 800 nm beam that is generated by the 15 W c.w. pump laser. A value of 3.2 W was achieved during installation.

   - Block the seed (Micra needs to be on for Alignment of the RegA).
   - Replace M1 (high reflector) with M0 (output coupler), M0 is kept inside a capsule at the bottom left area of the RegA, make sure that the arrow on M0 points towards the cavity.
   - Place a power meter after the output coupler (M0) that works up to 3.5 W.

- Use RegA Alignment Menu #1 (Cavity Dumper and Q-Switch off).
- Overlap the Ti:Sapphire fluorescence spots onto the center of the mirrors M2 and then M0 (use an IR viewer). Use M3 to center the fluorescence on M2, and M2 to center it onto M0. M0 should center the fluorescence spot back onto M2.
- Repeat the same procedure for M5 $\rightarrow$ M6 $\rightarrow$ M7 $\rightarrow$ M8.
- There should be lasing at this point. Center the laser onto the mirrors as accurately as possible. This step should be repeated if any large adjustments are made to the position of the Q-Switch or Cavity Dumper.
- Use the fine adjust for the pump steering mirrors to optimize the cavity.
- Clean the mirrors and crystals with HPLC methanol. Also, try translating the Q-Switch crystal vertically to increase the power.

2. **Align the Q-Switch**
   Goal: Optimize the position of the Q-Switch in order to obtain the highest possible power inside the cavity, while also using the lowest possible Q-Switch amplitude setting (QS AMPLITUDE) to spoil lasing.

   - Use RegA Alignment Menu #2 (Cavity Dumper off, Q-Switch c.w.).
   - Set the QS AMPLITUDE to anywhere less than 150 (not enough to destroy lasing). Rotate the QS to the nearest Bragg peak (there are multiple orders) where the lasing output power is minimized. Try translating the stage horizontally and vertically as well.
   - Changing the position of the Q-Switch can misalign the cavity. Return to alignment step #1 and re-optimize the cavity.
   - Increase the QS AMPLITUDE until lasing is extinguished. This should occur at 160–190. If it is occurring at higher values, the Q-Switch is not aligned properly (ensure that you are at the global minimum for the Bragg angle setting, not just a local minimum.
   - Set the QS AMPLITUDE to 150% of the hold-off value (~ 220).

3. **Q-Switch Timing**
   Goal: Optimize the timing of the Q-Switch.

   - Use RegA Alignment Menu #3 (Cavity Dumper off, Q-Switch pulsed).
   - Check the oscilloscope, there should be a clean Q-Switched pulse of several hundred nanoseconds. Use the QS WIDTH setting to clip the fall time to about twice the rise time.
   - Set the QS DELAY setting to ~ 11, this can be adjusted later.

4. **Align the Cavity Dumper**
   Goal: Optimize the position of the Cavity Dumper crystal in order to maximize the diffracted c.w. power.

   - Use RegA Alignment Menu #4 (Cavity Dumper off, Q-Switch pulsed).
   - Set the radio frequency amplitude (RF AMPLITUDE) to 100+.

- Place a power meter after the Faraday Isolator to measure the dumped c.w. power.
- Maximize this power by adjusting the 5-axis translation stage for the Cavity Dumper. The z-axis is an extremely important setting that should be adjusted such that the beam passes quite close to the base of the crystal. The x and y controls should center the beam near the middle of the crystal. The Bragg angle (left knob) is critical to the alignment of the cavity dumper.

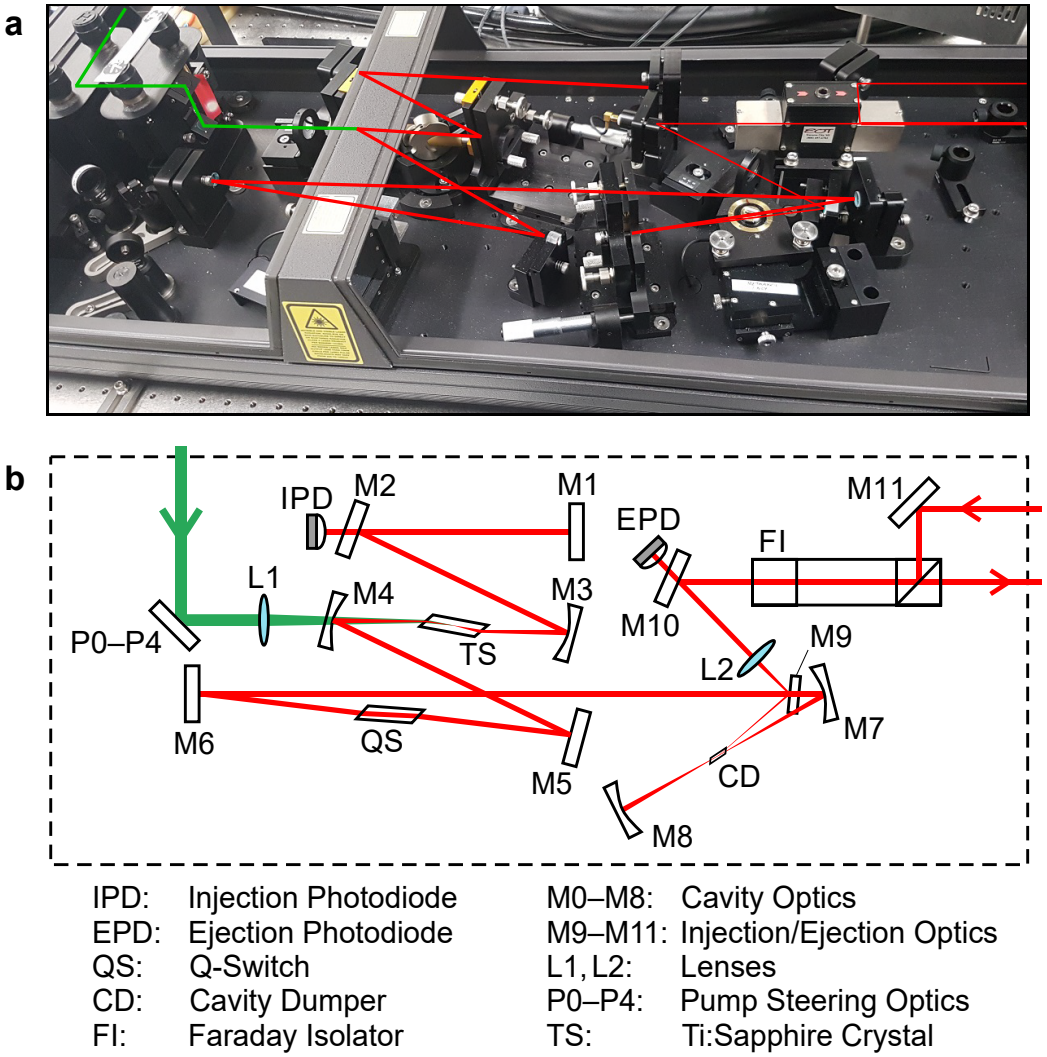

Figure B.1: **a**, Photograph and **b**, schematic of the Ti:sapphire regenerative amplifier laser (Coherent RegA 9050). The green beam is a 532 nm c.w. 15 W pump laser (Coherent Verdi-V18), while the thin red beam is a seed pulse from the oscillator (Coherent Micra) that gets coupled into the cavity and then amplified for approximately 22 round trips (thick red beam). The input seed pulse and output amplified pulse are routed into and out-of the cavity by an acousto-optic modulator. A Faraday Isolator separates the two beam paths.

- Changing the cavity dumper position can misalign the cavity. Return to Alignment #1 and re-optimize the cavity.
- The Cavity Dumper crystal is aligned if the diffracted optical power (c.w.) measured after the Faraday Isolator is more than 500 mW.

5. **Seed the Amplifier**
   Goal: Align the seed pulse from the Micra into the RegA such that it is collinear with the Cavity Dumped beam.

   - Do not use RegA Alignment Menu #5 (glitch), instead use standard RegA operation.
   - Use the LMR1-mounted white-card irises to align the two beams collinearly.
   - Once the beams are nearly collinear, the amplified seed pulse within the cavity can be monitored using the injection photodiode (IPD).
   - Optimize the injection of the seed pulse into the cavity using M11 and the mirror that routes the seed pulse towards M11 (not shown). Monitor the injection photodiode (IPD) on an oscilloscope and maximize the amplification of the seed pulse inside the cavity.
   - Adjust the Cavity Dumper (x, y, z, Bragg angle and tilt angle) to optimize the ejection.
   - Use Alignment Menu #6 to check that the cavity dumper is positioned correctly for double-pass operation. If it is, when the ejection phase is swept, the efficiency of the Cavity Dumper is modulated. This can also be confirmed by placing a white card after the Faraday Isolator while sweeping the ejection phase; the intensity of the laser on the card should be spatially modulated such that horizontal lines appears to be travelling across the beam spot.
   - If the alignment is good, the fine adjust knob of the vertical pump steering mirror should cause the injection and ejection peaks on the cavity photodiode (IPD) to move in opposite vertical directions.
   - Set the ejection delay to produce 20–28 round trips in the cavity.
   - Replace the output coupler, M0, with the end-mirror, M1. Upon replacing this mirror, the cavity will have to be re-aligned one last time using only the x and y controls for this one mirror that was just replaced.
   - Optimize the output power using the injection/ejection delay and phase settings.
   - Ensure that the beam is not being clipped by the Faraday Isolator. An uncompressed average output power of 2.1 W was obtained during installation.
   - After the number of round trips within the cavity is set, adjust the compressor in order to minimize the FWHM of the output pulse as measured by the autocorrelator ($\sim$75 fs). After the compressor, the average output power should be about 1.5 W, or equivalently 6 µJ per pulse.

B.2 Optical Setup for the Delay Stages

The peak amplitude of the ultrafast THz pulse electric field, $E_{\mathrm{THz,pk}}$, was maximized by modifying the optical setup of the delay stages. The optics was re-aligned to have 80% of the total laser beam going towards generation of THz pulses (Fig. B.2), compared to the 64% of the previous setup (Fig. B.3). The optical alignment into the delay stages was adjusted on a daily basis with the assistance of two silicon photodiode quadrant detectors.

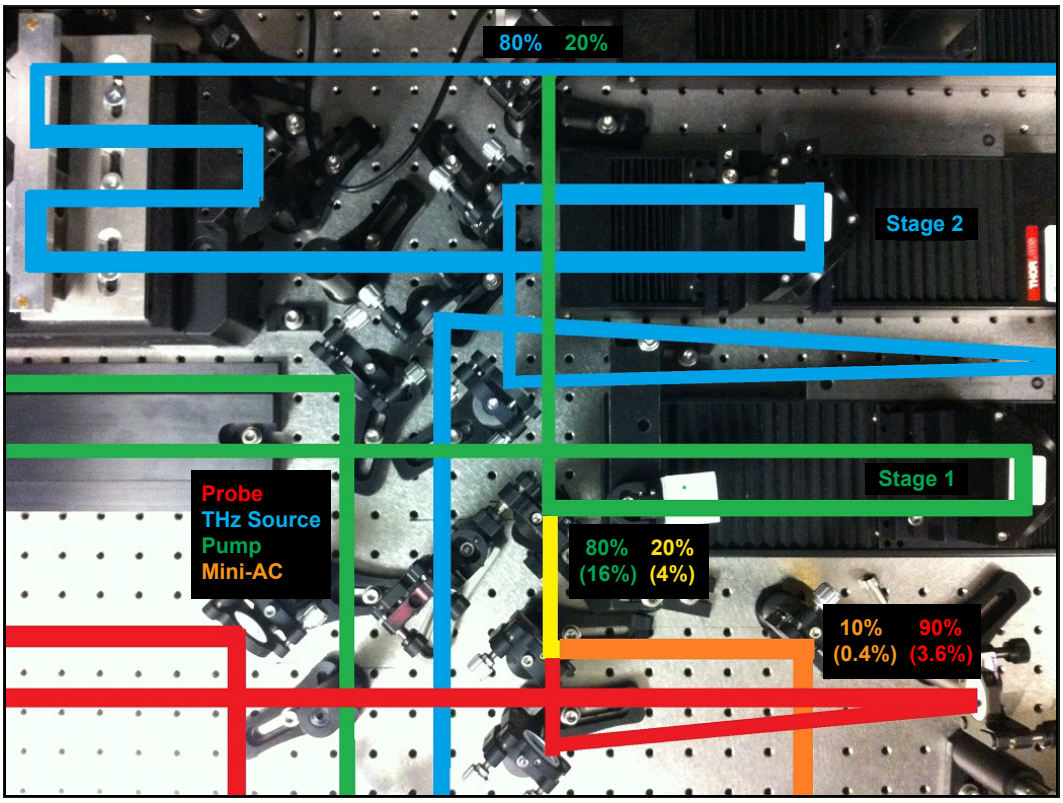

Figure B.2: Photograph of the optical beam path through the delay stages for the new setup that has 80% of the full laser power going towards THz pulse generation. The red beam is the electro-optic sampling pulse, the green beam is the pump pulse, and the orange beam goes to the autocorrelator and photodiode trigger (see also Fig. 5.2).

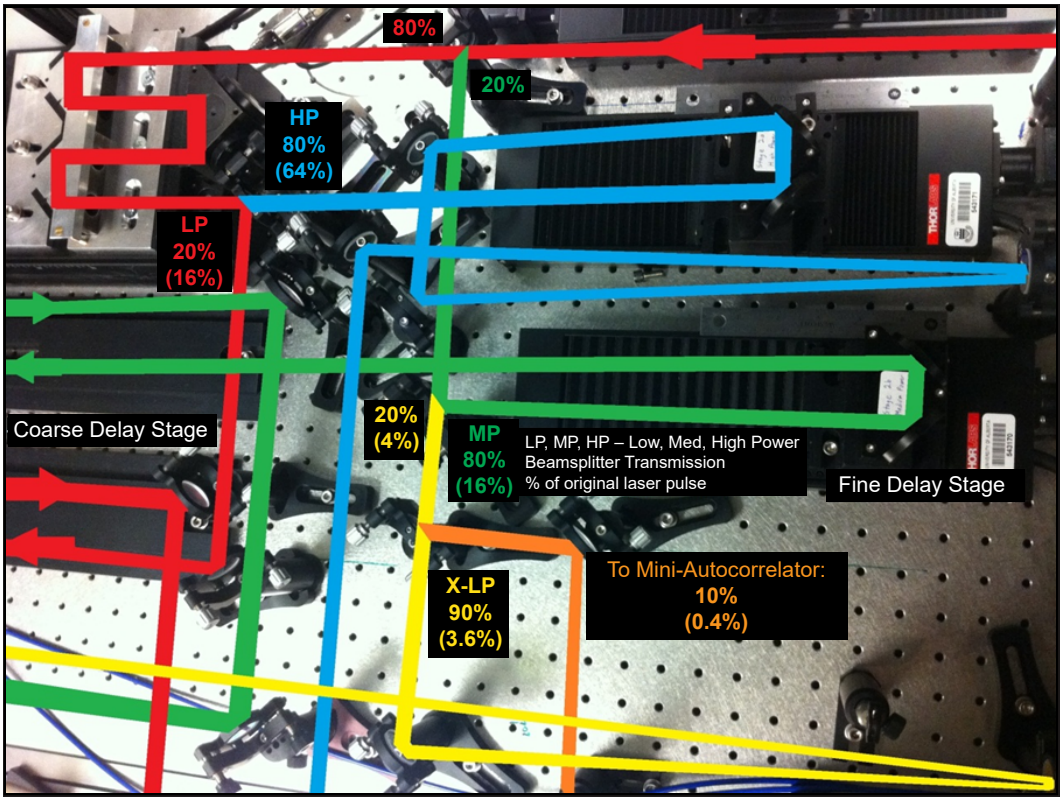

Figure B.3: Photograph of the optical beam path through the delay stages for the old setup that had only 64% of the full laser power going towards THz pulse generation. The red beam is the electro-optic sampling pulse, the green beam is the pump pulse, the yellow beam is used by another experiment, and the orange beam goes to the autocorrelator and photodiode trigger (see also Fig. 4.2).

Appendix C

UHV THz-STM System Details

This appendix provides a complete walkthrough of the ultrahigh vacuum (UHV) terahertz scanning tunneling microscope (THz-STM) system that is located in the Ultrafast Nanotools Laboratory at the University of Alberta. A summary of the equipment that was used with the UHV THz-STM system is presented in section C.1, followed by a step-by-step guide for preparing high quality tips in section C.2. Section C.3 highlights the necessary steps for acquiring high quality data, while a brief summary of the analysis methods is provided in section C.4.

C.1 Equipment

The UHV THz-STM system has several auxiliary electronics that control various aspects of the STM, THz generation and data acquisition (Fig. C.1). This section outlines the purpose of these various instruments within the THz-STM experiment. Most of the instruments in Fig. C.1 have already been introduced in Fig. 5.2. This appendix provides additional details regarding the daily operation of these instruments.

C.1.1 Ultrahigh Vacuum System

The schematic in Fig. C.3 outlines all of the equipment that was connected to the UHV system. A full chamber bake should be performed if the system has been exposed to atmospheric pressure, or if the base pressure of either the STM chamber or Preparation chamber is greater than 2×10^{-10} torr.

Full Chamber Bake

1. First, begin pumping down the system using the roughing pump (Agilent IDP-7, 2.5 L/s) with the inlet valve open (energized), the purge valve closed (energized), the manual purge valve closed and both of the

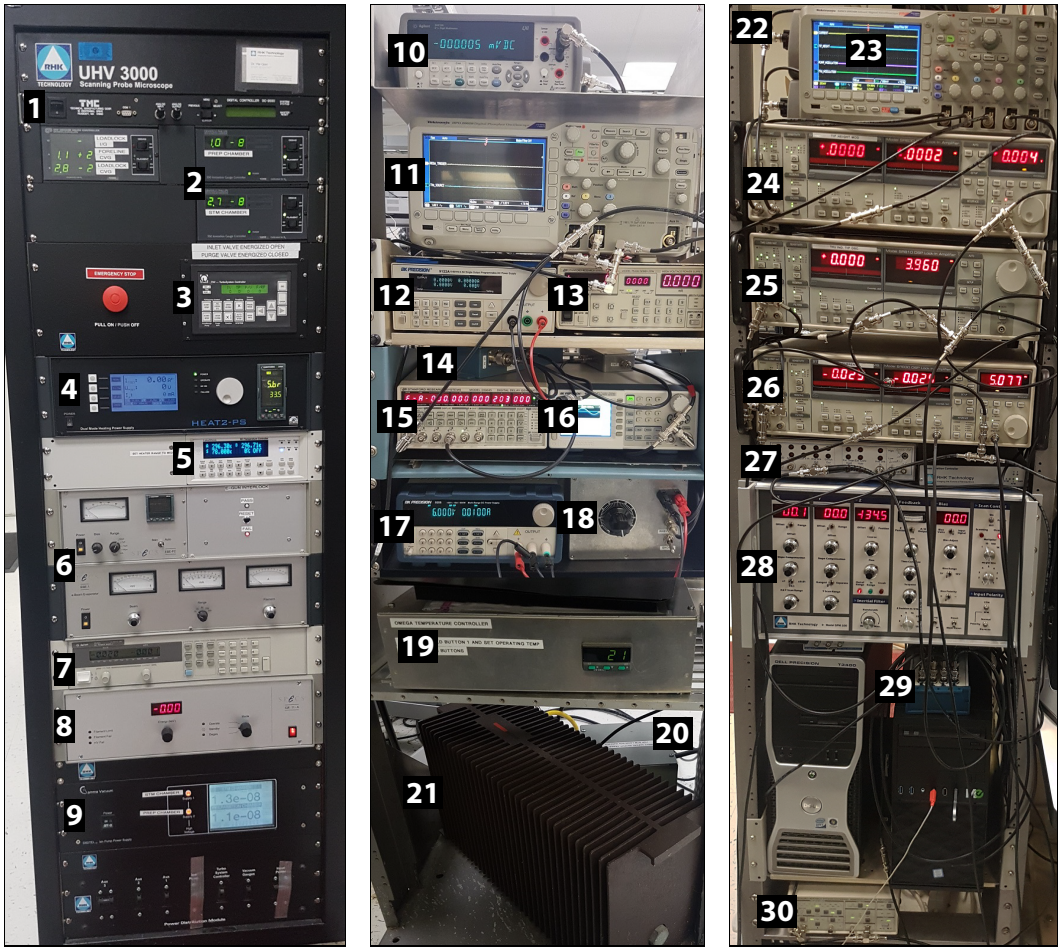

Figure C.1: Photographs of the three THz-STM electronics racks. 1 – controller for the vibration isolation system (TMC Stacis 2100), 2 – ionization gauge controllers (Granville-Phillips 350), 3 – turbomolecular pump controller (Leybold), 4 – electron bombardment heater (Prevac Heat-2PS), 5 – temperature controller (Lakeshore 331), 6 – electron evaporator controllers (SPECS), 7 – low voltage power supply (Agilent 6542A), 8 – argon gun controller (SPECS), 9 – ion pump controller (Gamma Vacuum). 10 – digital multimeter (Agilent 34401A), 11 – oscilloscope (Tektronix DPO2002B), 12 – THz source power supply (BK Precision 9122A), 13 – high voltage power supply (Stanford Research PS350), 14 – voltage pulser (Directed Energy HV1000), 15 – delay generator (Stanford Research Systems DG645), 16 – function generator (BK Precision BK4052), 17 – multi-range power supply (BK Precision 9206), 18 – variable resistor, 19 – temperature controller, 20 – external loadlock heater, 21 – 50 Ω load resistor, 22 – digital multimeters (Agilent 34401A), 23 – oscilloscope (Tektronix MSO2024B), 24, 25, 26 – lock-in amplifier (Stanford Research Systems SR830), 27 – single-shot THz pulse controller, 28 – STM control console (RHK SPM1000), 29 – data acquisition analog-to-digital converter (National Instruments USB6212DAQ), 30 – low-noise voltage amplifier (Stanford Research Systems SR560).

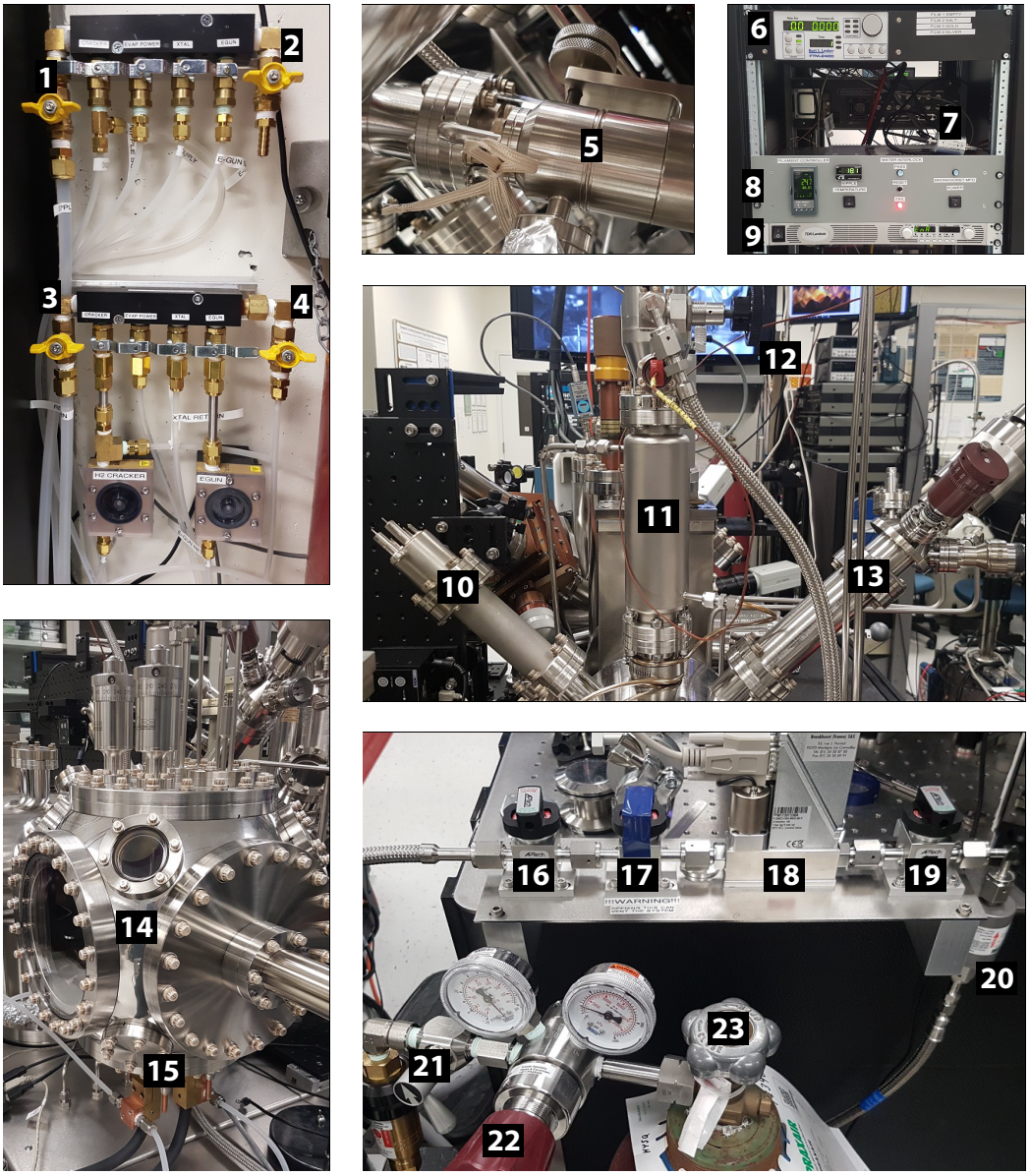

Figure C.2: Photographs of the various equipment used to operate instruments inside the Preparation Chamber of the UHV system. 1 – main water valve, 2 – nitrogen purge inlet, 3 – main return valve, 4 – water purge valve, 5 – argon gun (SPECS IQE-11/35), 6 – controller for the quartz crystal thickness monitor inside the deposition chamber (Inficon FTM-2400), 7 – quartz crystal oscillator (Inficon OSC-100A), 8, 9 – controllers and power supplies for the atomic hydrogen source (TDK-Lambda GEN 40-38), 10 – residual gas analyzer (Extorr XT100M), 11 – atomic hydrogen source (RIBER), 12 – hydrogen gas inlet valve, 13 – electron evaporator (SPECS EBE-1), 14 – deposition chamber, 15 – water-cooled leads from the high ampere power supply (RD Mathis LV400), 16, 17, 18, 19 – manual and electronic valves of the mass-flow-controller (Bronkhorst), 20 – hydrogen gas purifier, 21, 22, 23 – manual valves and regulator for the hydrogen gas cylinder.

UHV gate valves open (Fig. C.3). Once the base pressure of the vacuum chamber has reached 2 torr or less, turn on the turbomolecular pump (Leybold TURBOVAC-TW70H, 70 L/s), and keep both of the ion pumps off (Gamma Vacuum 300T-DI, 240 L/s). After the pressure reading on the convection gauge bottoms out, wait a few minutes before turning on the ionization gauges. The pressure reading on the ionization gauges can be monitored in Labview (National Instruments) using 'PressureMonitor.vi'.

2. Next, remove all of the optics and cables connected to the UHV system in the following order:
   - SHV tip conditioning cables and residual gas analyzer controller
   - cables, hoses, and O-rings connected to the STM cryostat
   - the cameras, their cables, and all of the USB cables
   - the heavy (>50 lbs) vertical breadboard[1]
   - the TPX lens at the bottom of the inverted viewport
   - the pump optics breadboard and the horizontal breadboards
   - the cables and preamplifiers connected to the STM scanhead
   - the magnetic handles of the two magnetic transfer arms[2]
   - the motor that controls the manipulator arm and any cables attached to the electron beam evaporator, atomic hydrogen source, and deposition chamber (the argon gun cable can stay plugged in)
   - empty the water inside the stainless steel water lines of the atomic hydrogen source and electron beam evaporator (attach a dry nitrogen cylinder to #2 in Fig. C.2, the water will flow out of #4)
3. After the stainless steel vacuum chamber has been cleared of any auxiliary equipment (Fig. 5.1), secure the tent poles into their respective slots, bolt in the main external heater, and then cover the vacuum system and transfer arms with the insulating tent. The magnetic transfer arm for the deposition chamber should be wrapped up with heat tape and then with tin foil. Before closing the tent, re-attach any K-type thermocouples that may have been removed during the initial step. The thermocouple that is connected to the Lakeshore temperature controller (#5 in Fig. C.1) can be used to monitor the STM sample stage temperature throughout the bake using the Labview VI 'TemperatureMonitor.vi'.
4. Plug in and lock all of the cables for the: bakeout power rack, main external heater, magnetic transfer arm heater, manipulator arm heater and external loadlock heater (#20 in Fig. C.1).
5. Start the bake by turning on the safety switches for every row of the power rack that is in use and then flipping on the 'Mains' switch. Next, set the timer to 60 hours, and finally press the 'Start Bake' button (the

[1] Make sure to disconnect all of the electronics on the vertical breadboard before attempting to move it. The bottom of the breadboard can be rested on the upper thigh as it is gently lifted off the STM table. Take note of the 2" circular mirror closest to the inverted viewport and the two routing mirrors at the bottom, making sure they do not get misoriented or damaged in any way during the breadboard removal. Ask for help if necessary.

[2] Make sure to lock the arms in place before removing the magnetic handles.

button should light up). The temperature controller for the external loadlock heater should be set to 130 °C, the main external heater knob should be set to about 70%, and the voltage output for the heat tape should be set to around 40–50 V. Throughout the bake, record the pressure and temperature of the vacuum chambers in the bakeout logbook. The temperature of the bake should not exceed 135 °C.

6. After approximately 24 hours, turn on the two ion pumps. The pressure will rise from the mid 10^{-7} torr to 10^{-5} torr or higher, due an initial degas from the ion pumps. After a couple of hours, turn on all of the titanium sublimation pumps (TSPs) in reverse order: #6, #3, #5, #2, #4, #1.For each TSP, keep the on button pressed down until the screen flashes. Set a timer for 60–90 seconds, and then turn off the TSP by again holding down the button until the screen flashes. After this step, continue using TSP #1 and TSP #4 for the STM Chamber and Preparation Chamber, respectively. Degas all of the ionization gauges several times throughout the bake.
7. Turn off the bake after about 60–120 hours. Close both UHV gate valves (use heat-resistant gloves).
8. After the STM sample stage has cooled down to room temperature (∼ 24 h), remove the bakeout tent and re-attach the equipment that was

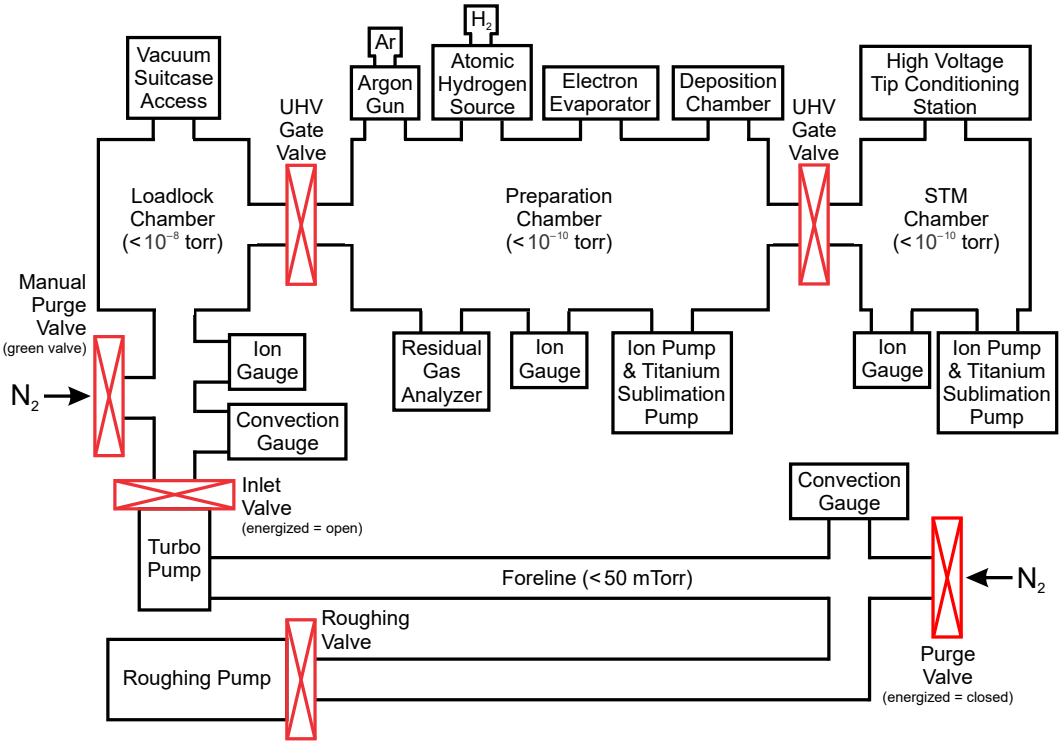

Figure C.3: Schematic of the vacuum system for the THz-STM. The inlet valve, purge valve, turbomoleular pump and roughing pump+valve are operated electronically using the turbo pump controller (#3 in Fig. C.1), while the green purge valve and the UHV gate valves are operated manually.

removed in step #2. The pressure in the UHV chambers should be 10^{-11}–10^{-10} torr. Run the TSPs as necessary to maintain this pressure.

9. Add tips and samples into the UHV chamber via the Loadlock Chamber. Vent the Loadlock Chamber by first turning off the turbo pump and the roughing pump, and then quickly toggling the purge vent to slow down the turbo pump with tiny bursts of nitrogen gas. Once the turbo has slowed down, open the purge vent, and adjust the flow-rate of the nitrogen gas cylinder as necessary.

Argon Gun

The argon ion sputter gun is the primary tool for cleaning the surfaces of metals in UHV [298]. Use the following procedure to operate the argon gun (#1 in Fig. C.2 and #8 in Fig. C.1).

1. Before starting, ensure that the turbomolecular pump is pumping down the Loadlock Chamber. The turbomolecular pump will be used later to pump out the argon gas that gets introduced into the Preparation Chamber.
2. Monitor the pressure of the Preparation Chamber using the Labview VI 'PressureMonitor.vi'.
3. If the argon gun filament has not been degassed recently, isolate the sample from the Preparation Chamber until the filament has been degassed.
4. Place the sample onto the manipulator arm and then close the UHV gate valve that separates the STM Chamber and the Preparation Chamber.
5. Turn off the ion pump in the Preparation Chamber.
6. With the sample on the manipulator arm, place the x-position of the arm to 132 mm, the y-position to 14 mm (red numbers), the z-position to 12 mm (red numbers), and the angle to $\sim 110°$.
7. Open the leak valve by rotating the knurled stainless steel knob that is attached to the argon gun by 3.5 full turns (#5 in Fig. C.2).
8. Close the leak valve once the pressure reaches $\sim 10^{-5}$ torr. If the pressure does not increase, leak more argon into the line by opening the valves on the regulator and the argon cylinder.
9. To start the operation of the argon gun, turn the switch on the argon gun controller to 'OPERATE' and then set the acceleration voltage to the desired valve (#8 in Fig. C.1). An acceleration voltage of 0.5–1 kV is typically enough. The magnitude of the ion current can be estimated by consulting the calibration curve inside the manual.
10. After the sputter and annealing cycles are done [298], turn off the acceleration voltage, and then turn off the argon gun controller.
11. Pump out the argon gas using the turbomolecular pump by briefly opening the UHV gate valve that separates the Preparation Chamber and the Loadlock Chamber. Close the UHV gate valve after 5–10 seconds, and then turn on the ion pump in the Preparation Chamber. The pressure should recover to the high 10^{-10} torr in a few minutes and the low 10^{-10} torr in a few hours.

Atomic Hydrogen Source

The atomic hydrogen source (#8, #9, #11 and #12 in Fig. C.2) was briefly introduced in section 5.3.2. The step-by-step procedure for operating this instrument is presented here.

1. Before starting, ensure that the turbomolecular pump is pumping down the Loadlock Chamber. The turbomolecular pump will be used later to pump out the hydrogen gas that gets introduced into the Preparation Chamber.
2. Monitor the pressure of the Preparation Chamber using the Labview VI 'PressureMonitor.vi'.
3. If the hydrogen cracker filament has not been degassed recently, isolate the sample from the Preparation Chamber until the filament has been degassed.
4. Obtain an atomically clean Si(100)-(2×1) surface following the procedure outlined in section 5.3.2.
5. Place the sample onto the manipulator arm, and move the arm such that the sample is **not** positioned directly underneath the atomic hydrogen source. Make sure to close the UHV gate valve that separates the STM Chamber and the Preparation Chamber.
6. Open the valves that control the flow of water for the stainless steel encasing of the hydrogen cracker. Specifically, open the main in-flow valve (#1 in Fig. C.2), the main out-flow valve (#3 in Fig. C.2), the hydrogen cracker in-flow valve (CRACKER), and the hydrogen cracker out-flow valve (CRACKER).
7. Turn off the ion pump in the Preparation Chamber.
8. To leak in hydrogen gas, slowly turn the valve located on top of the stainless steel vacuum encasing (#12 in Fig. C.2). Close the valve once the pressure reaches $\sim 10^{-7}$ torr.
9. If there is not enough hydrogen within the gas line, open the first valve of the mass-flow-controller (#16 in Fig. C.2). If there is still not enough hydrogen, then the mass-flow-controller (#18) should be operated at a flow-rate of approximately 0.1 standard-cubic-centimeter-per-minute, or equivalently, 3.3% of maximum flow-rate. The mass-flow-controller is operated remotely by a computer, while the power switch for the mass-flow-controller is located on right side of the controller in #8 of Fig. C.2. Open valves #19, #21, #22 and #23 in Fig. C.2 as necessary. Warning: opening valve #17 exposes the high-purity hydrogen gas line to atmospheric pressure. It should only be opened in the case of a contamination so that the line can be pumped out. In this case, make sure that valve #19 stays closed until the contamination has been eliminated.
10. Reset the water interlock on controller #8 in Fig. C.2. The water interlock should light-up green if the water cooling system was turned on correctly in step #6.
11. Turn on the 'FILAMENT CONTROLLER' and 'NIPPLE TEMPERATURE' monitor on the controller in #8 of Fig. C.2. Turn on the power

supply for the the filament (#9 in Fig. C.2).

12. Set the filament power to 80% using the 'FILAMENT CONTROLLER'. Once the filament temperature reaches 1130 °C, as read by the 'FILAMENT CONTROLLER', the cracker is operating near maximum efficiency. Set the sample temperature to 600 K and dose the sample for 100 seconds (10 langmuir).
13. Power down the filament. Turn off the sample heating.
14. Wait a few minutes for everything to cool down. Keep monitoring the nipple temperature and wait to turn off the water cooling system until the nipple temperature is below 300 K. Turn off all of the equipment that was used.
15. If there is a high load of hydrogen gas ($> 10^{-7}$ torr), it should be pumped out using the turbomolecular pump by briefly opening the UHV gate valve that separates the Preparation Chamber and the Loadlock Chamber. Close the UHV gate valve after 5–10 seconds, and then turn on the ion pump in the Preparation Chamber. The pressure should recover to the high 10^{-10} torr in a few minutes and to the low 10^{-10} torr in a few hours. If there a relatively low amount of hydrogen gas ($< 10^{-7}$ torr), the ion pumps can be turned on and the turbomolecular pump does not need to be used (to avoid any potential sample contamination from the Loadlock Chamber).

Deposition Chamber

The Deposition Chamber (#6, #7, #14 and #15 in Fig. C.2) was briefly introduced in section 5.3.3. The pumps and ionization gauges for this chamber are shared with the Preparation Chamber. The step-by-step procedure for the deposition of a single monolayer film is presented here.

1. Monitor the pressure of the Preparation Chamber using the Labview VI 'PressureMonitor.vi'.
2. If the deposition sources have not been degassed since the previous exposure to atmospheric pressure, isolate the sample from the Preparation Chamber until the sources have been degassed.
3. Place the sample onto the manipulator arm, transfer the sample onto the magnetic transfer arm of the Deposition Chamber, and then close the UHV gate valve that separates the STM Chamber and the Preparation Chamber.
4. Rotate the magnetic transfer arm such that the sample surface is facing the deposition source. Make sure that the manual shutter blocks the line-of-sight between the sample surface and the deposition source. Be careful to not hit the quartz detection crystal with the transfer arm.
5. Attach the water-cooled leads of the RD Mathis LV400 power supply to the desired source (#15 in Fig. C.2). Connect the water lines of the leads.
6. Open the valves that control the flow of water for the quartz crystal monitor and the water-cooled leads. Specifically, open the main in-flow

valve (#1 in Fig. C.2), the main out-flow valve (#3 in Fig. C.2), the in-flow valve for the quartz crystal monitor (XTAL), the in-flow valve for the water-cooled leads (EVAP POWER), the out-flow valve for the quartz crystal monitor (XTAL), and the out-flow valve for the water-cooled leads (EVAP POWER).

7. Keep the ion pump on during the deposition. The pressure in the preparation chamber should not exceed 10^{-5} torr.
8. Connect the quartz crystal oscillator (#7 in Fig. C.2) to the quartz crystal monitor on top of the Deposition Chamber (#14 in Fig. C.2). Turn on the quartz crystal controller (#6 in Fig. C.2). Make sure the quartz crystal controller is correctly calibrated for the sample being deposited. Also, make sure to change the preset values for the controller if the sources inside the Deposition Chamber are modified.
9. Start the deposition by slowly ramping up the current through the tungsten boat (make sure the knob on the power supply is set to zero before turning the power supply on). Start with a few amperes and over the course of a minute increase the current to the desired value. The following values were used: Au – 60 A; Ag – 38 A; NaCl – 30 A. Watch the deposition rate on the crystal monitor as current is increased. In order to apply a monolayer, a very slow deposition rate is required. Steady the deposition rate to 0.1 Å/s or less. If the crystal monitor reads 0.0 Å/s, you can manually time how long it takes the thickness to increase by 1 Å to determine the deposition rate.
10. Once a steady deposition rate has been established, briefly expose the surface by rotating the shutters (2–3 s). Make sure to block the line-of-sight between the source and sample after the deposition is complete.
11. Slowly turn down the current that is being used to heat the source.
12. Wait a couple of minutes for everything to cool down. Turn off the water cooling system and then turn off all of the equipment that was used.
13. Transfer the sample onto the manipulator arm and anneal the sample as necessary.

Electron Beam Evaporator

The electron beam evaporator (#13 in Fig. C.2) and its controllers (#6 in Fig. C.1) were seldom operated. The step-by-step procedure presented here should only be used as an outline. Before operating the electron evaporator, contact the local technician and consult the instrument manual. The source that is currently mounted is a titanium rod.

1. Monitor the pressure of the Preparation Chamber using the Labview VI 'PressureMonitor.vi'.
2. Plug in the three cables required for the electron evaporator.
3. If the source has not been degassed since the previous exposure to atmospheric pressure, isolate the sample from the Preparation Chamber until the source has been degassed.
4. Position the sample surface towards the electron evaporator nozzle. Close

the UHV gate valve that separates the STM Chamber and the Preparation Chamber.

5. Open the valves that control the flow of water for the electron evaporator. Specifically, open the main in-flow valve (#1 in Fig. C.2), the main out-flow valve (#3 in Fig. C.2), the electron evaporator in-flow valve (EGUN), and the electron evaporator out-flow valve (EGUN).
6. Turn on the electron evaporator power supply, turn on the flux monitor and reset the water interlock (#6 in Fig. C.1). The water interlock should light up 'PASS' if the water cooling system was turned on correctly in step #5.
7. Run the evaporation. Use the manual shutter on the electron evaporator to expose the sample surface.
8. After the evaporation, turn off all of the equipment that was used.

Residual Gas Analyzer

The partial pressure of gases inside the Preparation Chamber can be measured using the residual gas analyzer (RGA). Our particular RGA (Extorr XT100M) measures the partial pressure of atoms and molecules that have an atomic mass of less than 100 amu, with a sensitive down to 10^{-14} torr. To run the RGA, connect the RGA controller to the ultrahigh vacuum chamber (#10 in Fig. C.2), and then connect the power cable and the RS232-to-USB cable to the RGA controller. Next, run the Extorr 'Vacuum Plus' software on the computer (make sure the correct COMM port is selected), set the desired sweep parameters, and then turn on the filament. Degas the filament if the RGA has not been operated recently. If an extremely high sensitivity is required, consult

amu	Residual Gas	amu	Residual Gas	amu	Residual Gas
1	H^+	19	F^+	41	$C_3H_5{}^+$
2	$H_2{}^+$	20	HF^+, Ne^+, Ar^{2+}	43	$C_3H_7{}^+$
4	He^+	22	Ne^+	44	$CO_2{}^+, C_3H_8{}^+$
6	C^{2+}	26	$C_2H_2{}^+$	55	$C_4H_7{}^+$
8	O^{2+}	28	$N_2{}^+, CO^+, C_2H_4{}^+$	57	$C_4H_9{}^+$
12	C^+	29	$C_2H_5{}^+$	58	$C_3H_6O^+, C_4H_{10}{}^+$
14	$CH_2{}^+, N^+$	30	$C_2H_6{}^+$	60	$C_3H_8O^+$
15	$CH_3{}^+$	32	$O_2{}^+, CH_3OH^+$	69	$C_5H_9{}^+$
16	$NH_2{}^+, CH_4{}^+, O^+$	34	$H_2S_2{}^+$	71	$C_5H_{11}{}^+$
17	$NH_3{}^+, OH^+$	36	Ar^+	78	$C_6H_6{}^+$
18	H_2O^+	40	Ar^+	84	Kr^+

Table C.1: A list of common residual gases in ultrahigh vacuum chambers and their corresponding atomic mass units (amu). CH_2 – methylene; CH_4 – methane; NH_3 – ammonia; C_2H_2 – acetylene; C_2H_4 – ethylene; C_2H_2 – methylene; C_2H_6 – ethane; C_3H_3OH – methanol; C_3H_8 – propane; C_4H_{10} – butane; C_3H_6O – acetone; C_3H_8O – isopropanol; C_6H_6 – benzene.

the Extorr manual for operating with the electron multiplier. Use Table C.1 to help identify the contaminant gases inside the vacuum chamber.

Cooling with Cryogens

Cryogenic liquids were often used to cool the sample stage using the open-flow cryostat (CryoIndustries RC-110) and corresponding transfer line. For a relatively gentle flow-rate that minimizes local vibrations, a sample temperature of 30 K (100 K) can be achieved using liquid helium (liquid nitrogen). The temperature of the sample stage and cryostat was regulated by the Lakeshore temperature controller, which was operated remotely using the Labview VI 'TemperatureMonitor.vi'.

Ionization Gauges

All three ionization gauges (#2 in Fig. C.1) must be turned off during experiments. They generate excessive noise, limiting the resolution of the microscope. Also, they should be kept off inbetween experiments if the same surface is going to be studied again. Degas the ionization gauges regularly and corroborate their measured pressure with the ion pump pressure reading (#9 in Fig. C.1). The ion pump pressure should be in the low 10^{-11} torr if the ionization gauges are off, and in the mid 10^{-8} torr if the ionization gauges are on.

Vacuum Suitcase

A portable vacuum suitcase with a 3 L/s ion pump (Gamma Vacuum 3S-CV) can be attached onto the Loadlock Chamber for transferring delicate samples between different vacuum systems. However, in order for the vacuum suitcase to properly function, one of the two forks on the magnetic arm inside the Loadlock Chamber must be removed. The vacuum suitcase was not used for any of the samples that were studied in this thesis.

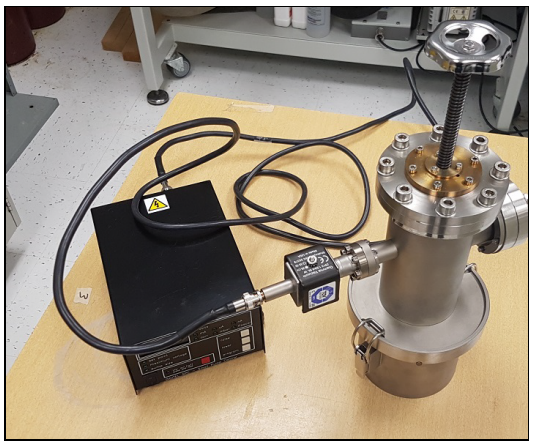

Figure C.4: Photograph of the vacuum suitcase and the ion pump controller.

C.1.2 STM Control Console

A brief overview of the BNC connections to the STM control console is presented in this section (Fig. C.5 and #28 in Fig. C.1). Every connection that falls under the 'OUTPUTS TO SPM' heading, except the connection labeled 'BIAS', applies a steady-state voltage to the piezoelectric crystals that control the tip motion. Their connections are outlined in the SPM100 manual and are not discussed here. The 'PREAMP MONITOR' connection under the 'MONITOR OUTPUTS' heading provides the input for the THz-pulse-induced current lock-in amplifier (#26 in Fig. C.1), $\mathrm{d}I/\mathrm{d}V$ lock-in amplifier (Fig. 5.2), NI-DAQ (#29 in Fig. C.1), low-noise voltage amplifier (#30 in Fig. C.1), and oscilloscope (#23 in Fig. C.1). Similarly, the 'Z SCAN' connection also provides the input for the THz-pulse-induced tip-oscillations lock-in amplfier (#25 in Fig. C.1), NI-DAQ (#29 in Fig. C.1), and oscilloscope (#23 in Fig. C.1). The 'INERTIAL INPUT' label under the 'EXTERNAL CONTROLS' heading should always be connected to the top-most connection, 'A D/A 1', under the 'OUTPUT' heading. Two of the remaining three outputs should be connected to the 'Z SCAN #2' and 'BIAS #1' connections under the 'MODULATION INPUTS' heading. Ensure that the correct output channel is being swept when performing I–z and I–V spectroscopy with the STM. The second bias modulation, 'BIAS #2', is connected to the sine-wave output of the $\mathrm{d}I/\mathrm{d}V$ lock-in amplifier (Fig. 5.2). The outputs of the lock-in amplifiers are connected to four of the six auxiliary inputs under the 'AUX INPUTS' label, while the output of the low-noise voltage amplifier (#30 in Fig. C.1) is connected to the fifth auxiliary input.

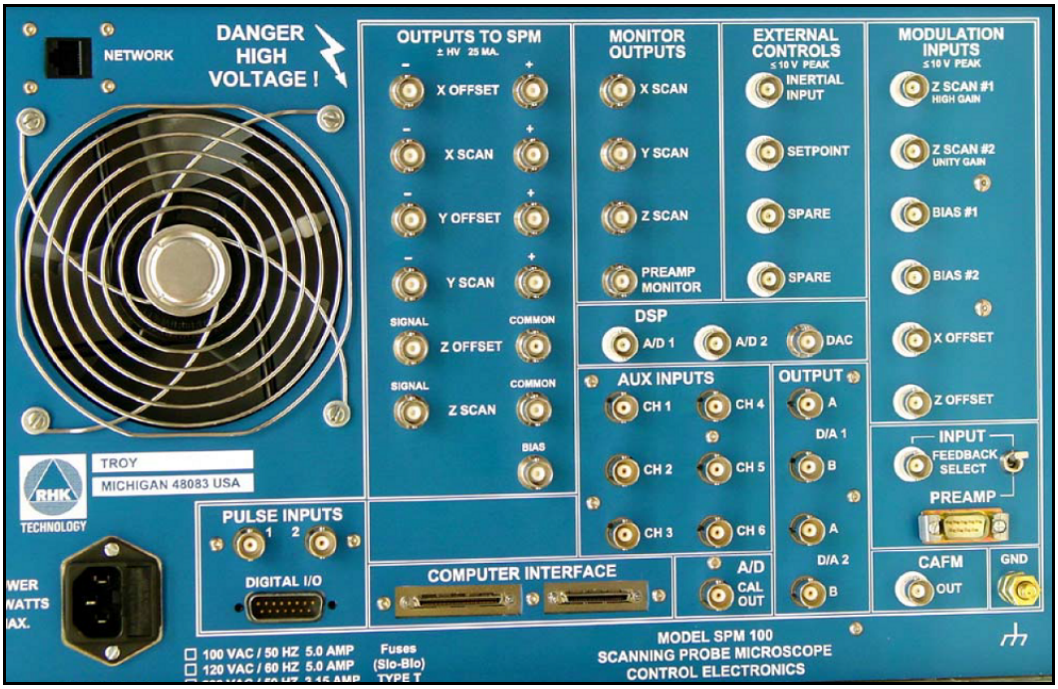

Figure C.5: Back panel of the RHK SPM100 control console.

C.2 Preparing Tips

Tip preparation was discussed in section 5.2. This section provides a step-by-step guide for etching tips, mounting tips, and performing *in situ* tip conditioning.

C.2.1 Etching Tips

The step-by-step guide for the double-lamella etching technique that was briefly mentioned in section 5.2 is presented in this section, along with another more standard etching technique that has been recently adopted (Fig. C.6a).

Double Lamella Etching Technique

1. Cut a 2–4 cm long tungsten wire using the tungsten carbide high precision cutters.
2. Use the set screw to attach the tungsten wire and then move the micrometer to move the wire down so that it travels through the center of the gold rings of the double-lamella apparatus.
3. Attach the positive voltage (red wire) to the bottom gold ring, and the ground (black wire) to the top gold ring.
4. Using a small beaker of 3 M NaOH, submerge the two gold rings in order to create a double-lamella with the tungsten wire located along the center. Move the tip catcher underneath the rings.
5. Using the 'Schrödinger Sharpener' etching controller, set the brake mode to 'arm', set the etch mode to 'DC' and adjust the output voltage to 4–6 V.
6. Press 'etch' on the controller. Monitor the current. The etching process takes about 10 minutes. An alarm will sound when the etch is finished. Stop the alarm by pressing 'rst'.
7. Carefully rinse the tips with distilled water.
8. Using the tungsten carbide high precision cutters shorten the tips so that they can fit into the STM tip holder, approximately 8–15 mm.

Standard Etching Technique

1. Cut a 2 cm long tungsten wire using the tungsten carbide high precision cutters.
2. Attach the tungsten wire to the apparatus by tightening the set screw (Fig. C.6b).
3. Submerge the platinum ring and tungsten wire into the etchant using a 20 mL beaker of 2 M NaOH. Rotate the micrometer to move the wire vertically. About 0.5–1 mm of the tungsten wire should be submerged (Fig. C.6c).
4. Attach the positive voltage (red wire) to the tungsten wire, and the ground (black wire) to the platinum ring (Fig. C.6b).

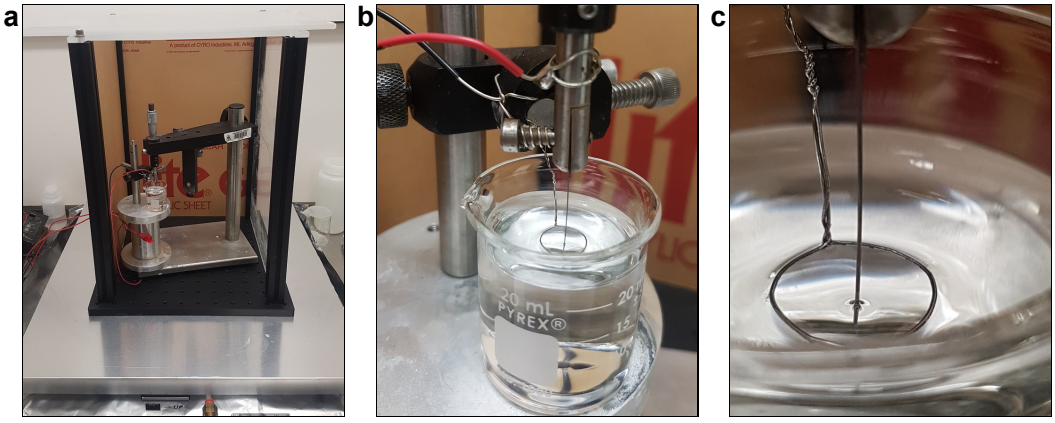

Figure C.6: Photographs of the new tip etching station. **a**, The entire assembly rests on a vibration isolation table (TMC 66-501). **b**, A small beaker is used to hold solution of 2 M NaOH, while electrical connections are made to the etching wire and the platinum wire. **c**, The platinum wire is bent into the shape of a ring, orientated parallel to the surface of the etchant, and gently submersed into the solution.

5. Turn on the etching power supply (BK Precision 9120A). Using the Labview VI 'Control BK9120A.vi', set the output voltage to 4–6 V.
6. Enable the voltage output. The etching process takes about 10 minutes. The Labview program automatically turns off the voltage when the current falls below 0.5 mA.
7. Carefully rinse the tips with hot distilled water.
8. Use the tungsten carbide cutters to shorten the tips so that they can fit into the STM tip holder, approximately 8–15 mm.

C.2.2 Mounting Tips

1. Ensure that the length of the tip is between 8–15 mm.
2. Carefully mount the tip into the stainless steel tip holder (Fig. C.7a). The tip is held in place inside the tip holder by slightly bending the wire about 20° before sliding it into the tip holder.
3. The exposed tip length that is necessary will vary with the thickness of the sample and the thickness of anything that is placed underneath the sample. For the relatively thin semiconductor wafers that were investigated here, the STM tip length that was exposed beyond the edge of the stainless steel tip holder was about 1.5 mm. This ensured that the tip–sample separation upon landing with the piezo legs onto the RHK sample holder was approximately 0.25–0.5 mm, as described in section 5.3. This distance can be finely tuned *in situ* by varying the insertion depth of the tip holder into the piezoelectric crystal of the STM (a few hundred micrometers).
4. Mount the tip holder into the empty tip-exchange-holder (Fig. C.7b)

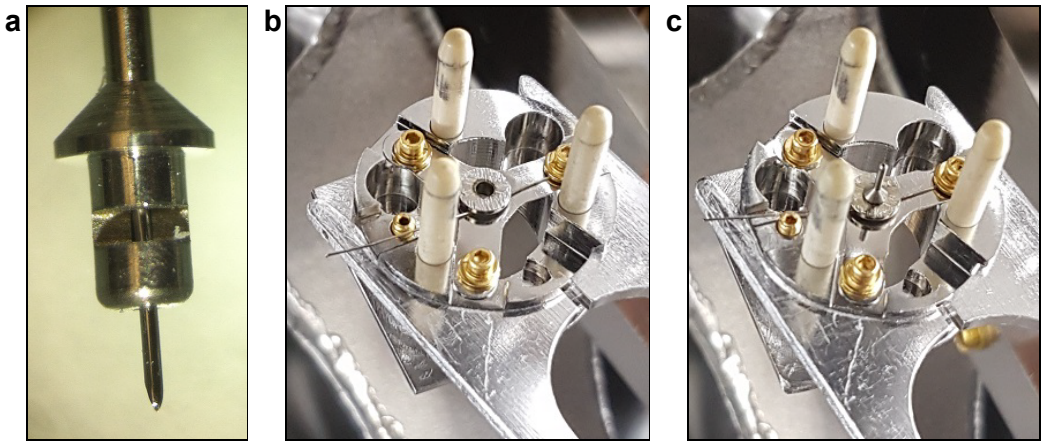

Figure C.7: Photographs of the **a**, tip holder **b**, unlocked and empty tip-exchange-holder, and **c**, locked and loaded tip-exchange-holder.

with the notched side of the tip holder pointed towards the long stainless steel holding wire of the tip-exchange-holder.

5. Lock the tip holder into the tip-exchange-holder by moving the stainless steel holding wire across the gold-coated set screw (Fig. C.7c).
6. Use the old (broken) piezoelectric crystal to confirm that the tip holder is being securely held by the tip-exchange-holder.
7. Mount the tip-exchange-holder onto the transfer fork and then carefully mount the tip-exchange-holder onto the magnetic transfer arm inside the Loadlock Chamber. Be very careful to not displace the stainless steel holding wire that is securing the tip holder in the tip-exchange-holder. The tip-exchange-holder has to be mounted upside-down inside the Loadlock Chamber[3].

C.2.3 *In situ* Tip Conditioning

Electron Bombardment

1. Mount the tip-exchange-holder onto the tip conditioning station inside the STM Chamber using the wobble stick.
2. Plug in the three safe high-voltage (SHV-5) connectors as shown in Fig. C.8a. The thick RG214 coax cables are for the high voltage connection to the filament, they plug into the top two SHV connectors. The thinner RG58 coax cable is for the connection to the floating ground of the tip conditioning station; this cable plugs into the bottom SHV connector.
3. For electron bombardment, the other ends of the cables in step #2 are

[3]If the tip falls down into the pump well (it will hit the safety-mesh just before the turbo pump), use the dedicated vacuum cleaner to recover the tip holder from the pump well. Before inserting the vacuum cleaner into the Loadlock Chamber, wash the end of the vacuum cleaner with acetone and methanol.

attached to the left-hand side of the electron bombardment breakout box (Fig. C.8b). The electron bombardment power supply (#4 in Fig. C.1) is plugged into the right-hand side of the breakout box. Match the colors of the power supply cables to the colors on the breakout box (green, black, and red from top to bottom).

4. Turn on the power supply. Set the output to electron bombardment mode, and turn the bombardment voltage to 0 V. Turn on the digital multimeter (#10 in Fig. C.1) and monitor the electron bombardment current using the Labview VI 'Field Emission and Electron Bombardment.vi'.
5. Enable the constant-current output for the filament. Set the current to approximately 1.2–1.4 A. The power supply will slowly ramp the current. The filament should glow orange/white.
6. Slowly increase the electron bombardment voltage until the onset of an electron bombardment current. See section 5.2 and Fig. 5.8 for more details.
7. Slowly decrease the electron bombardment voltage. Turn off the power supply and the multimeter.

Field Emission

1. Mount the tip-exchange-holder onto the tip conditioning station inside the STM Chamber using the wobble stick.
2. Plug in the three safe high-voltage (SHV-5) connectors as shown in Fig. C.8a. The thick RG214 coax cables are for the high voltage connection to the filament, they plug into the top two SHV connectors. The

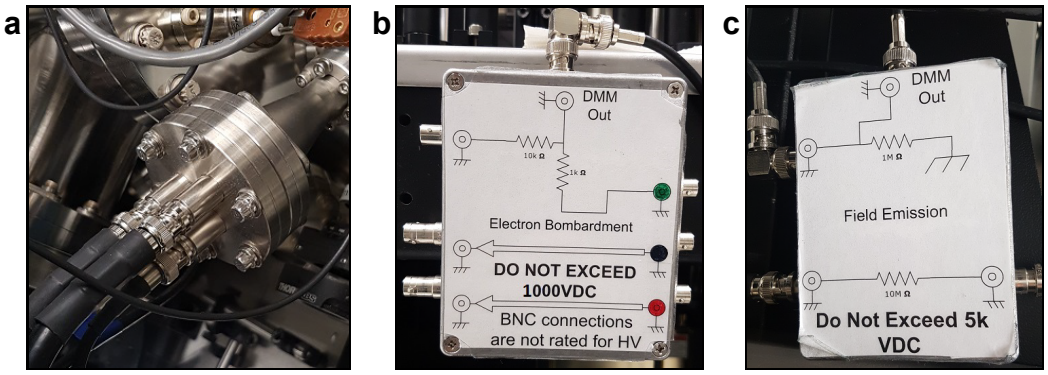

Figure C.8: Photographs of the electrical connections for *in situ* tip conditioning. **a**, The three safe high-voltage (SHV-5) connections into the UHV chamber. The top two connections are for the high voltage, while the bottom connection is for floating ground. **b**, The electrical breakout box for electron bombardment. The color-coded connections from the power supply are attached to the red, black and green connections on the box. **c**, The electrical breakout box for electron field emission. The high voltage is connected at the bottom right, just before the 10 MΩ safety-resistor.

thinner RG58 coax cable is for the connection to the floating ground of the tip conditioning station; this cable plugs into the bottom SHV connector.

3. For field emission, the other ends of the high voltage cables in step #2 are attached to a tee-adapter that is connected to the bottom left-hand side of the field emission breakout box (Fig. C.8c). The field emission power supply (#13 in Fig. C.1) is plugged into the right-hand side of the breakout box.
4. Turn on the power supply and the digital multimeter (#10 in Fig. C.1). Monitor the field emission current using the Labview VI 'Field Emission and Electron Bombardment.vi'. Alternatively, use the Labview VI 'FowlerNordheim.vi' to control the field emission power supply and perform Fowler-Nordheim curves.
5. Increase the field emission voltage in steps of 100 V until the onset of a field emission current. If the oxide layer on the tip apex has not been removed, once the field emission current starts, it may suddenly increase to dangerous levels where spontaneous melting and massive restructuring of the apex can occur. Make sure to decrease the applied voltage before this occurs, or simply perform electron bombardment first. See section 5.2 and Fig. 5.9 for more details.
6. Stop the field emission voltage. Turn off the power supply and the digital multimeter.

C.3 THz-STM Data Acquisition

This section summarizes the basic measurements that can be performed with the THz-STM system (consult the microscope manual for more details). The THz-STM measurements were acquired using two computers, where one computer controlled the STM, while the other computer controlled the motorized delay stages, motorized rotation stages, and other electrical equipment. The THz-STM data was acquiring using the Labview VI 'Stages, DMMs, Voltage Supply, Function Generator, Rotation Stage.vi'.

C.3.1 Point Spectroscopy

Point spectroscopy measurements with the THz-STM system can be divided into two categories. The first category involves measurements that are operated using the STM control console such as I–V, I–z and z–V curves (see section 2.1), while the second category involves measurements that vary the properties of the incident light pulses, such as THz I–E curves, OPP-THz-STM waveforms, THz pulse autocorrelations, and polarity/fluence dependencies. Constant-height point spectroscopy measurements can be very difficult to perform because of the inevitable vertical and horizontal drift that occurs (as discussed in section 2.1). Accordingly, it is extremely important to maintain a stable tip–sample separation throughout the acquisition.

For STM and THz-STM measurements in the first category, the scan settings can be changed clicking on the 'Spectroscopy' label, under the 'Settings' heading. Here, various settings can be adjusted such as the sweep range, sweep velocity, sampling time, pre-sampling time, sample count, output channels[4] and other details. The total time per spectrum is shown in the 'Control' label (consult the microscope manual for default values if necessary). If multiple spectra are acquired, it may be worthwhile to consider using the feedback stability feature (under the 'Adv. Modes' label.). In this case, the feedback loop is briefly engaged in-between successive spectra in order to account for any vertical drift that may have occurred throughout the constant-height measurement. It is important to note that this feature should not be used if the scan settings are modified just before the acquisition. For example, this feature was not used to acquire the data in Fig. 6.38 or Fig. 6.18–6.23 because the settings throughout the acquisition were different from the settings that determined the initial tip–sample separation. Another useful advanced mode was the 'Variable Gap Mode', where the tip height was automatically adjusted by a predetermined amount just before the acquisition (see microscope manual for details). This feature was used to acquire the data set in Fig. 6.18. If the point spectroscopy measurement requires the output channel of a lock-in amplifier, it is important to set the time-per-pixel for the 1D scan to be at least two times greater than the time constant on the lock-in amplifier. Most often for 1D measurements, the lock-in time constant ranged from 10 ms to 300 ms, depending on the signal-to-noise ratio.

For THz-STM measurements that vary the properties of the incident light pulses, such as THz I–E curves, OPP-THz-STM waveforms, THz pulse autocorrelations, and polarity/fluence dependencies, the scan settings can be adjusted in the Labview program. These settings include the sweep range, sampling time, pre-sampling time and sampling count. The instruments that are controlled by the Labview program include: the function generator for the THz pulse modulation (#16 in Fig. C.1), the power supply for the THz pulse source (#12 in Fig. C.1), the motorized rotation stages for the THz pulse polarity, pump pulse polarity and pump fluence (Fig. 5.5), and also the motorized linear delay stages for the THz pulse, pump pulse, and THz pulse autocorrelator (Fig. 5.2). For THz I–E curves, the THz pulse electric field waveform can be scaled by either rotating the THz source or sweeping the applied voltage on the THz source. However, due to a minor shift in the THz pulse carrier-envelope-phase between high and low voltages on the THz source, rotating the THz source is more reliable than sweeping the bias voltage. In this case, a wire-grid polarizer that is orientated along the axis of the tip should be set up after the THz pulse source (remove this polarier for THz polarity measurements such as in Fig. 6.6).

[4]For point spectroscopy measurements with the STM control console, the acquisition time per spectrum scales up with the number of channels that are being recorded. For most constant-height measurements, the only necessary output channels are the low-noise amplifier (#30 in Fig. C.1) and the THz-pulse-induced current lock-in amplifier (#26 in Fig. C.1).

A general procedure for constant height point spectroscopy measurements:

1. Ensure that the software calibrations are correct for the current preamplifier and piezoelectric crystals under the 'Configure Hardware' label under the 'Settings' heading, and for the auxiliary channels under the 'Operating Modes' label in 'Settings' heading.
2. Select the measurement to be performed and then set the appropriate sweep parameters. Note: when using the STM control console, check if the feedback stability feature is enabled under 'Adv. Modes' in the 'Spectroscopy' settings window.
3. Disengage the feedback loop. Note: when using the STM control console to acquire the data, the feedback loop will disengage automatically just before the measurement starts.
4. Change any settings if necessary.
5. Initiate the point spectroscopy acquisition.
6. After the acquisition is finished, return any settings that were changed to their setpoint values. If the same raw current is observed before and after the measurement, it is a good indicator that there were no structural modifications to the tip apex throughout the acquisition.
7. Re-engage the feedback loop.

C.3.2 Imaging

Imaging with the THz-STM requires patience. Sometimes after continuously scanning the surface for several hours, the tip apex naturally changes into a stable configuration. This process can be assisted in various ways such as intentional tip–surface contact, and tunneling spectroscopy at moderate–high tunnel currents (I–V or I–z), or simply scanning at a moderate–high bias voltage or tunnel current. Intentional tip–surface contact can be performed by first disengaging the feedback loop and then using the fine adjust knob of the z-piezo to move the tip into the surface. In cases where the linescan is composed of large triangles, the tip apex is coated with an insulating oxide and needs to be cleaned. A quick trick is to increase the bias voltage to ± 10 V for a few seconds.

Atomically resolved constant-current imaging requires a very low bandwidth on the feedback loop. This is achieved by rotating the time constant knob to ~ 10.0, and the gain knob to > 0.3. Also, the analog-to-digital gain (A/D gain) should be set to at least 32. A scan speed of 10–50 nm/s is standard, but higher scan speeds can also achieve atomic resolution if the gain and time constant settings are appropriately adjusted (for example see Fig. 2.4 and Fig. 2.5). For constant-height imaging, the signal-to-noise ratio of the image can be improved by reducing the bandwidth of the low-noise amplifier (#30 in Fig. C.1) to 30–300 Hz. For THz-STM imaging (and all other lock-in amplifier techniques), ensure that the average-time-per-pixel is at least 1–2 multiples of the lock-in amplifier time constant. This corresponds to a line-time of 1.5 seconds at 256×256 pixels for a lock-in amplifier time constant of 3 ms.

If the feedback loop is engaged during THz-STM imaging, the bandwidth of the the feedback loop should be set such that it does not respond to the kHz modulation of the THz-pulse-train. The amplitude of this modulation can be monitored through the output of the THz-pulse-induced tip oscillations lock-in amplifier (#25 in Fig. C.1).

C.3.3 Electro-Optic Detection

The amplitude and phase of the THz pulse can be measured as described in section 3.2.2. The THz-pulse-induced birefringence of the 800 nm sampling pulse was measured in a pair of balanced photodiode detectors. The output voltage from these photodiode detectors was sent to a pair of digital multimeters (#22 in Fig. C.1) and a lock-in amplifier (#24 in Fig. C.1). The THz pulse electric field waveform that was measured by the lock-in amplifier, **C**, was calibrated using the signal from the balanced photodiodes, **K** & **J**, using

$$E_{\mathrm{THz}}[\mathrm{V/cm}] \;=\; 28556 \times \frac{\mathbf{C}}{\max(\mathbf{C})} \times \left[\max\left(\frac{\mathbf{K}-\mathbf{J}}{\mathbf{K}+\mathbf{J}}\right) - \mathrm{mean}\left(\frac{\mathbf{K}-\mathbf{J}}{\mathbf{K}+\mathbf{J}}\right)\right], \quad \text{(C.1)}$$

where differential phase retardation $\Delta\varphi$ is given by $(\mathbf{K}-\mathbf{J})/(\mathbf{K}+\mathbf{J})$ (see Eq. 3.9). The factor 28556 is determined by evaluating the constants λ = 800 nm, n_{O} = 2.853 [36, 268], r_{41} = 4 pm/V [36, 268], and L = 1 mm in Eq. 3.8, and then dividing the result by the amplitude transmission factor for THz pulses incident onto ZnTe, 0.48 (ZnTe has a refractive index of 3.2 at 1 THz [36]). For an accurate calibration, the THz pulse waveform detected by the balanced photodiodes, as given by

$$E_{\mathrm{THz}}[\mathrm{V/cm}] \;=\; \max(\text{Eq. C.1}) \times \frac{\frac{\mathbf{K}-\mathbf{J}}{\mathbf{K}+\mathbf{J}} - \mathrm{mean}\left(\frac{\mathbf{K}-\mathbf{J}}{\mathbf{K}+\mathbf{J}}\right)}{\max\left(\frac{\mathbf{K}-\mathbf{J}}{\mathbf{K}+\mathbf{J}} - \mathrm{mean}\left(\frac{\mathbf{K}-\mathbf{J}}{\mathbf{K}+\mathbf{J}}\right)\right)}, \quad \text{(C.2)}$$

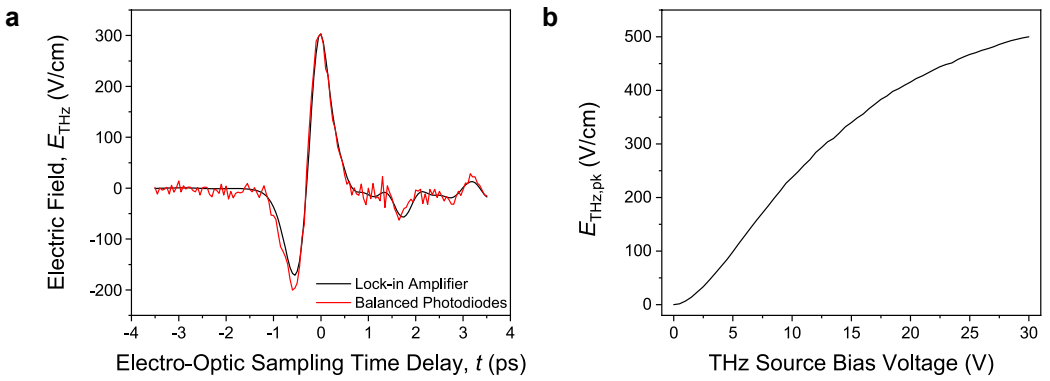

Figure C.9: Calibrating the THz Waveform. **a**, Electro-optically sampled THz waveform as measured using a lock-in amplifier (black solid line) and the raw signal from the balanced photodiode detectors (red solid line). **b**, Relationship between the applied voltage to the THz pulse source and the peak THz electric field $E_{\mathrm{THz,pk}}$. The measurement was acquired at t = 0 ps.

should be similar in shape to the waveform detected by the lock-in amplifier (Fig. C.9a). A voltage sweep of the THz pulse source at $t = 0$ ps provides a relationship between the applied bias voltage across the THz pulse source and the peak THz pulse electric field (Fig. C.9b). However, a small temporal shift of $\sim$150 fs occurs at low THz source bias voltages compared to high THz source bias voltages, resulting in an exaggerated nonlinearity near 0 V.

C.4 THz-STM Data Analysis

A script was developed in MATLAB to readily display the massive amount of data and metadata that was produced by the XPMPro acquisition software on a daily basis[5]. The code has been recently updated by Jesus Alejandro Marin Calzada to include a graphical user interface. For detailed analysis of images, the open-source software 'Gwyddion' was used, while the software 'Origin' was used to generate the 1D plots.

The STM is extremely vulnerable to electrical noise and mechanical vibrations. Various STM designs have addressed these problems in different ways, each with their own merits (see [67] for details); however, occasionally there may still be some background noise in the STM image (Fig. C.10a). Instead of searching for the source of the noise (which may be very difficult to find), it may be possible to filter-out the noise in post-processing if the noise produces a repeating pattern in the image. In this case, as long as the features of interest (atoms for example) are occurring at a different spatial periodicity than the noise, a 2D fast-Fourier-transform (2D-FFT) can be used to filter-out the noise (Fig. C.10b). After applying the filter and taking an inverse 2D-FFT, the new image does not exhibit the noise pattern (Fig. C.10c).

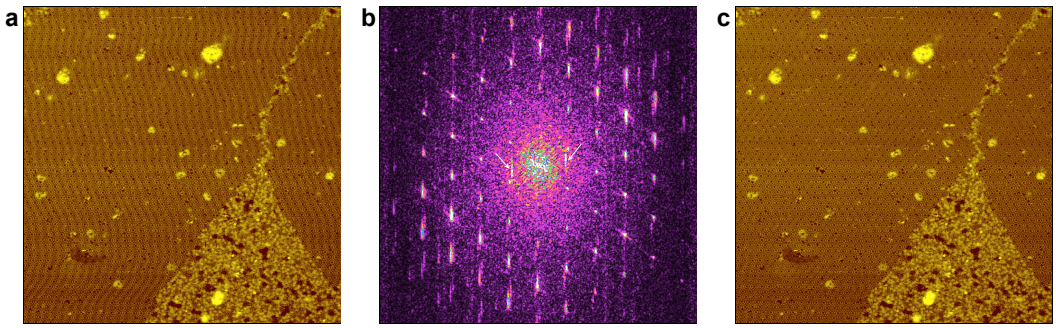

Figure C.10: Filtering noise in the STM image. **a**, STM image acquired at $V_{\text{d.c.}} = +1.5$ V and $I_{\text{d.c.}} = +150$ pA. Image size 130 nm $\times$ 130 nm. **b**, 2D-FFT of the image in **a** with white arrows in the center highlighting the frequency peaks of the noise. Image size 3.5 nm^{-1} $\times$ 3.5 nm^{-1}. **c**, Inverse FFT of **b** after filtering out the frequency peaks due to the noise.

[5]The original MATLAB code for extracting the data and metadata from the .sm4 files, 'read_sm4.m', was written by Martín Caldarola.